# BULGARIAN CHEMICAL COMMUNICATIONS

# PREFACE

The XV International Scientific Conference "Renewable Energy & Innovative Technologies" was held between 10th and 11th June 2016 at the Technical College of Smolyan, Bulgaria. Representatives of 21 countries (Bulgaria, Turkey, Russia, Cyprus, Spain, Lithuania, Kazakhstan, India, United Kingdom, Italy, Serbia, Austria, Romania, France, China, Latvia, Greece, Brazil, India, Iran and Ukraine) sent their works to the conference. Some of the reports (69 works) have been selected and are published after international peer-review in the present Special Issue of the journal "Bulgarian Chemical Communications".

It is our pleasure to be guest editors of the presented articles, which focus on new international scientific results in the field of Renewable Energy and Innovative Technologies (Solar and Hybrid Thermal Systems, Solar Photovoltaic Systems, Storages with Phase Change Materials, Energy Efficiency, Materials Science, Food Engineering and Technologies, and Biotechnologies).

Prof. Aleksandar Georgiev, PhD  (European Polytechnic University, Pernik, Bulgaria)

Assoc. Prof. Daniela Dzhonova-Atanasova (Bulgarian Academy of Sciences, Sofia, Bulgaria)

**Guest editors** of the present Special Issue

# ENERGY EFFICIENCY

# 3D modelling of heat and mass transfer processes during the combustion of liquid fuel

A. Askarova[1], S. Bolegenova[2*], N. Mazhrenova[2], R. Manatbayev[2], Sh. Ospanova[1], Symbat Bolegenova[2], I. Berezovskaya[1], V. Maximov[1], A. Nugymanova[2], Zh. Shortanbayeva[2]

[1] *SRI of Experimental and theoretical physic, Al-Farabi Kazakh National University, Almaty, Kazakhstan*
[2] *Faculty of Physics and Technology, Al-Farabi Kazakh National University, Almaty, Kazakhstan*

In this article numerical study of the processes of atomization and combustion of two kinds of liquid fuel by using the statistical model of breakup and dispersion of the drops was conducted. The octane and dodecane were used as liquid fuels in the researches. There was also constructed the model of the combustion chamber in a cylinder form. During the numerical simulation has been determined optimum combustion mode for two types of liquid fuel. The initial temperature in the combustion chamber was varied from 700 to 1500 K. It was shown that for the two types of liquid fuel the oxidant's optimal initial temperature in the combustion chamber is 900 K. It was determined the optimum value of the initial temperature in the combustion chamber. Computational experiments on research of the distribution of the maximum temperature, the concentration of the combustion products and the dispersion of liquid particles were performed.

**Keywords:** liquid fuel, numerical modeling, octane, dodecane, combustion, statistical model, initial temperature

## INTRODUCTION

At the present time, despite the ongoing efforts in the development and use of renewable energy, 85% of all energy consumed in the world are received from the combustion of fossil fuels. Statistics show that 39% of the total energy consumption are accounted for the liquid types of fuels' combustion and 97% of this total energy is used in the transport sector [1]. While still in the world widely liquid fuels are used as a primary energy source, it is paramount the increasing the efficiency of their combustion and thereby minimizing the impact on the environment.

The development of energy conversion systems with high efficiency and low emissions plays a major role in reducing of greenhouse gas emissions to the atmosphere. Necessity of a detailed study of physical and chemical processes occurring during combustion of liquid types of fuels is determined by increasing requirements for effectiveness of the various technical devices, necessity of accurately determine the moment of ignition and due to modern environmental requirements. On the other hand the results of basic research of physical and chemical processes of combustion allow to find effective modes of various technical devices, including internal combustion engines [2].

In this regard computer simulation of the physical and chemical processes of breakup, dispersion, vaporization and combustion of liquid

fuel droplets at different initial conditions in internal combustion engines is relevant. The combustion of liquid fuels has a number of specific features, due to chemical reactions in a dynamic and thermal interaction between of the reagents and the intensive mass transfer during phase transitions, as well as the dependence of the process parameters as the thermodynamic state of the system and of its structural characteristics. As the investigation of combustion is impossible without a detailed study, that comes to the fore the problem of the fundamental laws of processes of heat and mass transfer research during the combustion of various types of fuels. This article is devoted to the numerical simulation of the processes of atomization and combustion of two kinds of liquid fuel.

Atomization of the fuel jet has wide application in many fuel supply systems, as well as in combustion chambers of the modern aircraft engines. This type of flow in a radial cross-flow enhances fuel atomization characteristics which generated injection and vaporization and is used in premix and evaporative fuel-air mixture chambers. When liquid fuel is sprayed from the gas turbine engine nozzle droplets sizes may reach several microns, while the sizes of the fuel channels exceeds by several orders.

With the development of modern science of jet technology, many researchers have begun to focus on thermal and chemical processes occurring inside the engines of missile and aviation technology. So M. Gorokhovski in his work [3] has developed a

---

* To whom all correspondence should be sent:
saltanat.bolegenova@kaznu.kz

new subgrid stochastic model for liquid particles breakup at high turbulence. The developed model describes the decay of elementary particles in a space where the liquid spreads through the relaxation time in the distribution of the droplet radii. This model was implemented in the KIVA-II software package together with the Lagrangian particle trajectory tracking model.

In [4] M. Gorokhovski and V. Savel'ev in the framework of Kolmogorov decay theory for large numbers of Weber studied the decay of liquid droplets. In this paper it was given balance equation for the droplet population distribution radially in the form of the invariant under the group of large-scale transformation. In this work the authors have shown that due to the law of symmetry ultimate solution of this equation is a function of power.

Also in the [4] work the authors used subgrid stochastic model for the study of atomized liquid droplets. Following Kolmogorov concept, considering the collapse of solid particles in the form of a discrete random process, the authors studied the work of spray liquid clumps at a high relative velocity of the moving gas during the uncorrelated breakup events that turn to howl do not depend on the initial droplet size. Also the discrete model of the Kolmogorov's breakup has been modified in the form of the Fokker-Planck differential equation for the probability density function of droplet radii.

In this paper KIVA-II was used as a starting package of computer programs, which was developed by scientists from the Los Alamos National Laboratory (LANL). All the computational experiments were done by using this computer program which are used for the numerical calculation of two- and three-dimensional chemical reactive fluid flows with sprays. The KIVA-II equations and numerical solution procedure are very general and can be applied to laminar or turbulent flows, subsonic or supersonic flows and single phase or dispersed two-phase flows. With this software package is possible to explore the complex processes of ignition, combustion of the fuel and air mixtures, as well as the processes of formation of pollutants released into the atmosphere as a result of the internal combustion engine's work [3-5].

In this paper a computer package KIVA-II software has been optimized to simulate the chemical kinetics of combustion processes in diesel and aircraft engines. This software package has been adapted to the task of the incineration of the liquid fuel in the combustion chamber at high turbulence. With KIVA-II it was possible to calculate the aerodynamic of the flow, injection mass, oxidant's temperature, pressure, turbulent characteristics, the concentration of combustion products, fuel vapor and other characteristics of the process of liquid fuel combustion across the combustion chamber space.

A statistic particle method is used to calculate evaporating liquid sprays, including the effects of droplet collisions and aerodynamic breakups. The initial and boundary conditions and mesh generation have been written for internal engine calculations.

## MATHEMATICAL MODEL

In this article the Kolmogorov's discrete model has been reproduced in the form of evolution equation for distribution function of the drops' radius. The asymptotic solution of this equation has been applied to simulate the drop breakup alongside with statistical model of spray dynamics [3].

The breakup of parent drops into secondary droplets is viewed as the temporal and spatial evolution of this distribution function around the parent-droplet size according to the Fokker-Planck differential equation [4-5]:

$$\frac{\partial f(x,t)}{\partial t} + v(\xi)\frac{\partial f(x,t)}{\partial x} = \frac{1}{2}v(\xi^2)\frac{\partial^2 f(x,t)}{\partial x^2}, \quad (1)$$

where $v$ is the breakup frequency (Hz) and t is the breakup time (ms). Here, $f(x,t)$ is the distribution function for $x = \ln(r)$, and $r$ is the droplet radius (μm).

The value of the breakup frequency and the critical radius of breakup are obtained by the balance between the aerodynamic and surface tension forces. The critical radius of breakup becomes [6]:

$$r_{cr} = \left(\frac{9}{2}\frac{We_{cr}\sigma v_{lam}}{\varepsilon\rho_l}\right)^{1/3}, \quad (2)$$

where $v_{lam}$ is the kinematic viscosity (St), $\rho_l$ is the liquid density (kg/m$^3$), $\varepsilon$ is the viscous dissipation rate, $We_{cr}$ is the critical Weber number, which is assumed to be on the order of six over a wide range of Ohnesorge numbers:

$$We = \frac{\rho_g\left(u_g - u_l\right)^2 D_l}{2\sigma}, \quad (3)$$

where $u_g$ (m/s) and $u_l$ (m/s) are the velocities of liquid and gas, respectively, $D_l$ (cm) is the inlet diameter for the liquid jet.

In the statistical model the discrete particle distribution function is approximated by a discrete particle dispersion [7]:

$$f' = \sum_{p=1}^{NP} N_p \delta\left(\vec{x} - \vec{x}_p\right) \delta\left(\vec{v} - \vec{v}_p\right) \delta\left(r - r_p\right) \delta\left(T - T_{d_p}\right), \quad (4)$$
$$\delta\left(y - y_p\right) \delta\left(\dot{y} - \dot{y}_p\right)$$

where $p$ is the particle, $N_p$ - the total number of the particle, $\vec{x}_p$ - the location of the particle in space, $\vec{v}_p$ - velocity of the particle (m/s), $r_p$ - radius of the particle (μm), $\dot{y}_p$ - deviation from a spherical particle shape.

During the dispersion of the particles in a turbulent gas flow fluctuation of the velocity component is a function of the time which changes intermittently after the passage of turbulent correlation time, which in turn is determined by the following relationship [8]:

$$t_{turb} = \min\left(\frac{k}{\varepsilon}, c_{ps} \frac{k^{3/2}}{\varepsilon} \frac{1}{\left|\vec{u} + \vec{u}' - \vec{v}\right|}\right), \quad (5)$$

here $c_{ps}$ is an empirical constant with a value of 0,16432, k – turbulent kinetic energy, $\varepsilon$ - its dissipation rate. Therefore $t_{turb}$ (ms) represents the minimum of an eddy breakup time and a time required by a droplet to traverse or pass through an eddy. The sum of the mean and fluctuating velocity component is the gas velocity which a particle sees during the computation of drag, mass transfer, momentum transfer, oscillations and breakup.

When a particle moves in a turbulent gas stream with a large-scale structures whose dimensions are much greater than the particle diameter, the relative velocity between the particle and the gas flow is determined as follows:

$$\frac{d\vec{v}_p}{dt} = \frac{\left(\vec{v}_g - \vec{v}_p\right)\left|\vec{v}_g - \vec{v}_p\right|}{\tau_{St}}, \quad (6)$$

where $\tau_{St} = \dfrac{\rho_p d_p^2}{18\rho_g v_g}$ is the droplet relaxation time scale (s), where $d_p$ (μm) is the diameter of the droplet.

The majority of currents by the nature have turbulent character, a condition of turbulence strongly influences on such parameters of a current as transfer of an impulse, temperatures and concentration of substances in the mixture during the flow motion. In this chapter, the thesis shows the mathematical model describing the burning of liquid fuels on the basis of the equations of conservation of mass ($\rho$, kg/m$^3$), momentum ($\rho\vec{u}$, kg·m/s) energy ($E$, J) and concentration ($c$, kg/kg).

$$\frac{\partial \rho}{\partial t} + div(\rho\vec{u}) = S_{mass}, \quad (7)$$

where $u$ - the velocity of the fluid (m/s). The source term $S_{mass}$ is a local change of gas density due to evaporation or condensation.

The conservation equation of an impulse of gas has the following appearance:

$$\rho\frac{\partial \vec{u}}{\partial t} + \rho\left(\vec{u}\cdot grad\right)\vec{u} = div\vec{\vec{\xi}} + \rho\vec{g} + S_{mom}. \quad (8)$$

$S_{mom} = 0$ for a single-phase flow of gas; $S_{mom}$ is the local rate of change in momentum in the gas phase due to the movement of droplets for two-phase.

Conservation equation of an internal energy:

$$\rho\frac{\partial E}{\partial t} = \vec{\vec{\tau}} : \vec{\vec{D}} - \rho div\vec{u} - div\vec{q} + S_{energy}, \quad (9)$$

where $q$ – the specific heat flux (W/m$^2$), it is the Fourier law of heat transfer, $\vec{\vec{\tau}} : \vec{\vec{D}}$ is the rate of increase of the internal energy due to viscous dissipation. Source term $S_{energy}$ denotes the contribution to the change of an internal energy due to the presence of atomized liquid or solid phase.

The conservation equation of concentration of a component:

$$\frac{\partial(\rho c_m)}{\partial t} = -\frac{\partial(\rho c_m u_i)}{\partial x_i} + \frac{\partial}{\partial x_i}\left(\rho \cdot D_{c_m} \cdot \frac{\partial c_m}{\partial x_i}\right) + S_{mass}, \quad (10)$$

where $\rho_m$ - a mass density of a component $m$ (kg/m$^3$), $\rho$ - full mass density (kg/m$^3$).

More universal models in engineering calculations of turbulent flows are models with two differential equations. Using in technical flows model with two differential equations is the most

common. $k - \varepsilon$ is model when two equations for a kinetic energy of turbulence and dissipation rate are solved:

$$\rho \frac{\partial k}{\partial t} + \rho \frac{\partial \overline{u}_j k}{\partial x_j} = \frac{\partial}{\partial x_j} \left[ \left( \mu + \frac{\mu_t}{\sigma_k} \right) \frac{\partial k}{\partial x_j} \right] \frac{\partial \overline{u}_i}{\partial x_j} + \quad (11)$$

$$+ G - \frac{2}{3} \rho k \delta_{ij} \frac{\partial \overline{u}_i}{\partial x_j} - \rho \varepsilon$$

$$\rho \frac{\partial \varepsilon}{\partial t} + \rho \frac{\partial \overline{u}_j \varepsilon}{\partial x_j} - \frac{\partial}{\partial x_j} \left[ \left( \mu + \frac{\mu_t}{\sigma_\varepsilon} \right) \frac{\partial \varepsilon}{\partial x_j} \right] = c_{\varepsilon_1} \frac{\varepsilon}{k} G - \quad (12)$$

$$- \left[ \left( \frac{2}{3} c_{\varepsilon_1} - c_{\varepsilon_3} \right) \rho \varepsilon \delta_{ij} \frac{\partial \overline{u}_i}{\partial x_j} \right] - c_{\varepsilon_2} \rho \frac{\varepsilon^2}{k}$$

This is the standard $k - \varepsilon$ equations. Values $c_{\varepsilon_1}$, $c_{\varepsilon_2}$, $c_{\varepsilon_3}$, $\sigma_k$, $\sigma_\varepsilon$ are modal constants which are determined from the experiment. Typical values of these constants are commonly used in engineering calculations and are taken from the literature [4-5].

Chemical kinetics of combustion is represented as generalized chemical reactions for the two kinds of fuel - octane and dodecane:

$$2C_8H_{18} + 25O_2 \rightarrow 16CO_2 + 18H_2O, \quad (13)$$

$$2C_{12}H_{26} + 37O_2 \rightarrow 24CO_2 + 26H_2O, \quad (14)$$

as a result $CO_2$ and $H_2O$ combustion products are formed.

Octane is a hydrocarbon and an alkane. Octane has many structural isomers that differ by the amount and location of branching in the carbon chain. One of its isomers isooctane is used as a standard value in fuel octane rating scale. Octane is a part of the gasoline. Kazakhstan oil is characterized by the predominance of normal paraffins, so straight run gasoline of them have low octane numbers. As octane is used as an index of the fuel in the engine to resist the high compression ratio, which is a characteristic of the octane branched chain isomers, especially of them can be identified isooctane. Octane is contained in large amounts in the composition of oil, straight run gasoline (10%) and in a large amount in the synthetic gasoline produced from CO and H₂. In industry octane was isolated by distillation, and then purified by urea using molecular sieves.

Dodecane is a liquid hydrocarbon from class of alkane, oily liquid from the paraffin series. Dodecane is used in industrial and laboratory practice as a solvent. It is used for analytical purposes in the study of the composition of oil fractions. Also it is used for the manufacture of olefins and biodegradable detergent component as vaseline oil. In recent years it has begun n-dodecane used as a possible substitute for kerosene fuels, such as Jet-A, S-8, and other conventional aviation fuels. The fuel of the second generation, which is dodecane, ousted n-decane because of its higher molecular mass, it is best to interact with the n-alkanes in the composition of jet fuel.

In this work a model of the combustion chamber in the cylinder form the height of which is 15 cm, 4 cm in diameter has been used. General view of the combustion chamber is shown in Fig.1. Liquid fuel is injected by a nozzle which is located in the lower part of the combustion chamber. The initial temperature of the gas in the combustion chamber is 900 K, the fuel is injected at 300 K. The initial radius of the injected droplets is 25 microns.

Air was used as oxidant, stoichiometric composition of which was calculated by using the mass of used fuel. This air composition provides a complete combustion without of excessive oxidant residue. In internal combustion engines the oxidizing agent is atmospheric oxygen. An ordinary air is composed of 78% nitrogen and 21% oxygen, which are the predominant elements.

## NUMERICAL RESULTS

This work presents the results of numerical simulation of the octane and dodecane combustion depending on the oxidant's initial temperature in the combustion chamber. The initial optimal values of the pressure and mass were 6 bar and 100 mg for the octane and 80 bar and 7 mg for the dodecane, which have been identified in previous works [5, 9-13]. The initial temperature in the combustion chamber was varied from 700 to 1500 K. The results of numerical experiments of two kinds of liquid fuel combustion by using the statistical model of atomization are presented in this work.

In this work we measured the area of injection of liquid fuel spray in the combustion chamber. The investigation results are shown in Fig.2. This figure shows a comparison between the results of the numerical data and the experiment, which was staged by the authors of work [12]. The authors of work [12] used a diesel, the main component of which is tetradecane $C_{14}H_{30}$. As shown in Fig.2, the experimental points for diesel fuel (green line) and numerical calculations for dodecane (blue line) are consistent with each other better than the numerical calculations for octane (red line).
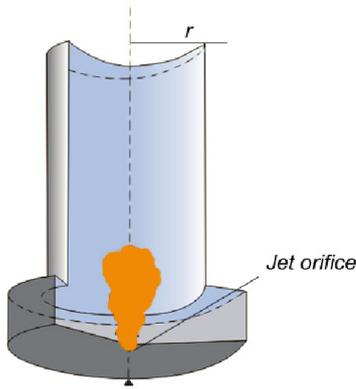
**Fig.1.** General view of the combustion chamber

Fig.3 shows the distribution of the maximum combustion temperature depending on the oxidant's initial temperature. Analysis of Fig.2 shows that if the oxidant's temperature in the combustion chamber takes values higher than 800 K, in this case the fuel burns intensively and the large amount of heat is generated and the combustion chamber is warmed up to 3000 K. The oxidant's initial temperature influences on the dodecane's combustion, since the increasing of the initial temperature from 900 to 1500 K leads to increasing of the maximum temperature from 2080.09 to 2684.69 K.
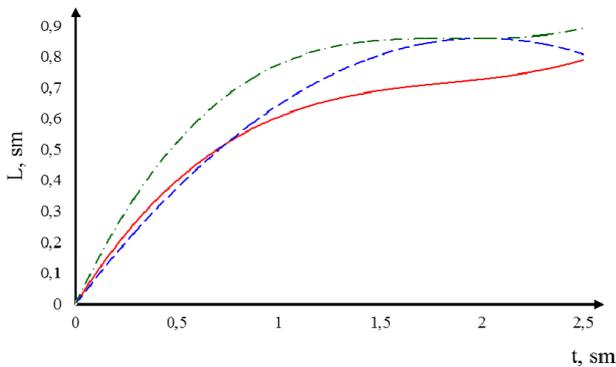


**Fig.2.** The injection area of liquid fuel spray in the combustion chamber (green line - diesel, blue line - dodecane, red line – octane)

Fig.4 shows the distribution of the maximum concentration of carbon dioxide for the two types of fuel (octane and dodecane) depending on the oxidant's initial temperature in the combustion chamber. During the dodecane's combustion the concentration of carbon dioxide takes higher values than the octane's combustion. As can be seen from the Fig.3, when the temperature increases from 900 K to 1500 K the concentration of carbon dioxide emitted by combustion of the octane reaches values from 0.08459 g/g to 0.08561 g/g and the combustion of dodecane from 0.11986 g/g to 0.14142 g/g.
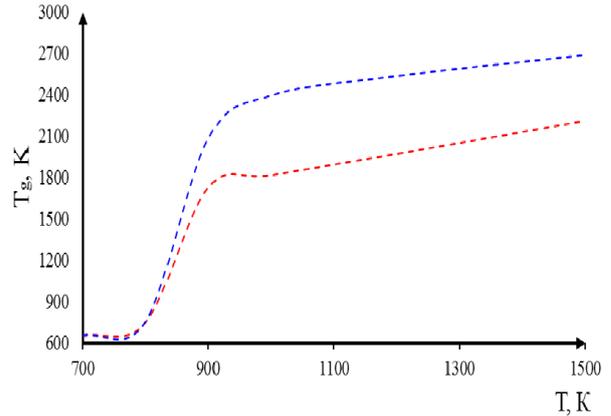


**Fig.3.** The dependence of the maximum combustion temperature on the oxidant's initial temperature in the combustion chamber during the combustion of octane and dodecane (red line is octane and blue line is dodecane)

From the analysis of the Fig.3 and Fig.4 it can be concluded that for the octane and dodecane the oxidant's optimal initial temperature in the combustion chamber begins with 900 K. Beginning from this value of the temperature the fuel reacts rapidly with the oxidant, the combustion chamber is warmed up to high values of temperature, and the concentration of generated carbon dioxide didn't exceed permissible limits.
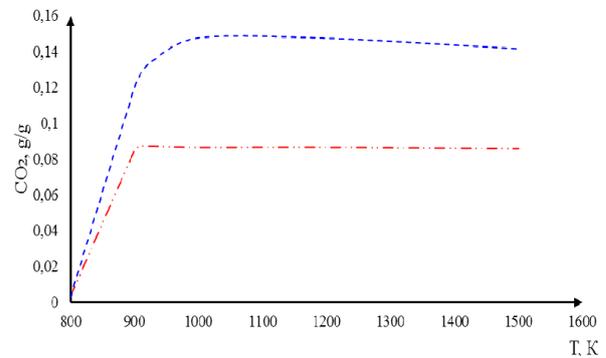


**Fig.4.** The dependence of the carbon dioxide's concentration on the oxidant's initial temperature in the combustion chamber during the combustion of octane and dodecane (red line is octane and blue line is dodecane)

This conclusion is supported by the two-dimensional distribution graphs of the basic parameters describing atomization, dispersion and combustion processes of two types of liquid fuel (octane and dodecane), which are listed below.

Fig.5 shows the temperature distribution in the combustion chamber for octane and dodecane at time t=2.5 ms for oxidant's initial temperature of 900 K. From these figure it can be seen how the temperature changes in the combustion chamber at a given time. The maximum temperature in the

combustion chamber during octane's combustion is 1726 K, and for the dodecane its value is 2080 K.

Fig.6 shows the octane and dodecane droplets distribution by temperature at time t=2.5 ms. At time t=2.5 ms octane and dodecane droplets is concentrated in a small region of the width of the combustion chamber. Droplets rise up by the height of the combustion chamber to 0.45 cm during octane's combustion. During the combustion of the dodecane at time t = 2.5 ms droplets of liquid fuel reaches the height of the chamber 0.4 cm.
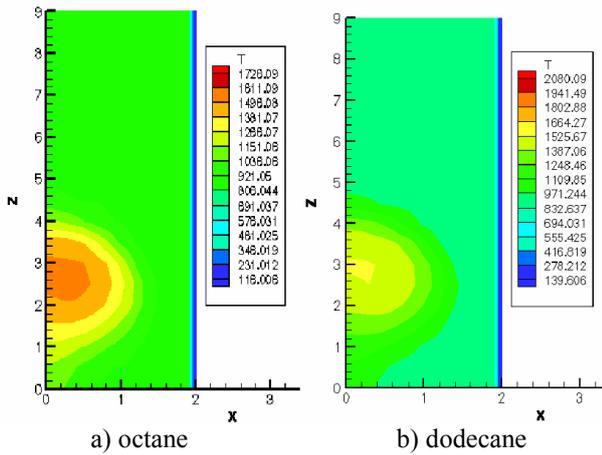


a) octane        b) dodecane

**Fig.5.** The distribution of the temperature in the combustion chamber for octane and dodecane at time t=2.5 ms
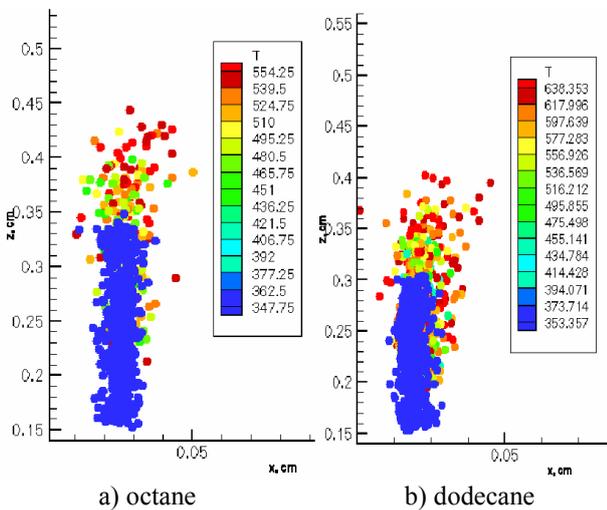


a) octane        b) dodecane

**Fig.6.** The distribution of the octane and dodecane droplets by the temperature at time t=2.5 ms

In Fig.7 it is shown the results of numerical simulation of the carbon dioxide formation during the octane and dodecane combustion at the optimal temperature. The analysis of the figure shows that the maximum amount of the carbon dioxide for octane is formed on the axis of the combustion chamber and is equal to 0.08455878 g/g. During the

dodecane combustion on the axis of the combustion chamber concentration of carbon dioxide reaches a value equal to 0.103878 g/g. At the outlet of combustion chamber the concentration of carbon dioxide is reduced and takes minimum values for both fuels.
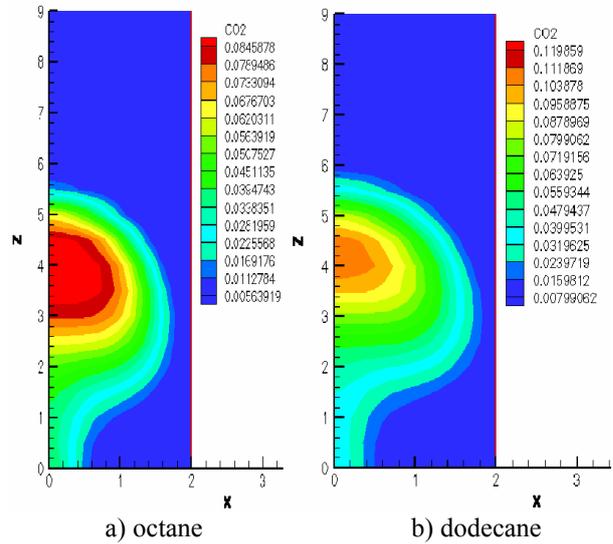


a) octane        b) dodecane

**Fig.7.** The distribution of the $CO_2$ concentrations in combustion chamber for octane and dodecane at time t=3 ms

## CONCLUSION

In this work numerical study of the influence of the oxidant's initial temperature on the combustion process of octane and dodecane was conducted. The optimal parameters for the fuel mass and pressure in the combustion chamber had been previously identified in the works of scientists, specializing in the modeling of two-phase flows [5, 9-13]. Also, similar studies have been conducted by various scientists who specialize in the field of modeling of two-phase reacting flows in real geometry areas. Various types of solid fuels are used by these authors, especially coals of Kazakhstan of various grades and ash content, which are burnt in thermal power stations and the various thermal centers of the country [14-20].

In this work it was shown that for the two types of liquid fuel the oxidant's optimal initial temperature in the combustion chamber is 900 K. Beginning from this temperature the fuel burns completely, the chamber is heated to the

sufficiently high temperature, and the produced concentration of carbon dioxide takes smallest value.

## REFERENCES

1 Mayer D.O., Business and Society Review, 105, 347 (2000).

2 Askarova, S. Bolegenova, Bolegenova Symbat, I. Berezovskaya, Zh., Ospanova Sh., Shortanbayeva, A. Maksutkhanova, G. Mukasheva and A. Ergalieva, J. of Engineering and Applied Sciences, 10, 90 (2015).

3 Gorokhovski M., Atomization and Sprays, 1, 169 (2001).

4 Gorokhovski M.A., Saveliev V.L., Physics of Fluids, 5, 184 (2003).

5 Gorokhovski, M., Chtab-Desportes, A., Voloshina, I., Askarova (AIP Conf. Proc., Xian, 2010, p. 66-73.

6 Askarova, A. S., Karpenko, E. I., Karpenko, Yu. E., Messerle, V. E., Ustimenko, A. B. (7th International Fall Seminar on Propellants, Explosives and Pyrotechnics, Xian, 2007), Xian, 2007, p. 672-683.

7 Askarova A., Bolegenova S., Bekmukhamet A., Ospanova Sh., Gabitova Z., Journal of Engineering and Applied Sciences, 9, 24 (2014).

8 Ustimenko A.B., Askarova A.S., Messerle V.E., Nagibin, Journal of Thermophysics and Aeromechanics, 7, 435 (2010).

9 Askarova, A.S., Messerle, V. E., Ustimenko, A. B., Bolegenova, S. A., Maksimov, V. Yu., Thermophysics and aeromechanics, 21, 747 (2014).

10 Bolegenova, S.A., Maximov, V.Y., Bekmukhamet, A, Beketayeva, M.T. Gabitova, ZK., High temperature, 5, 751 (2015).

11 Askarova A.S., Bolegenova S.A., Berezovskaya I.E., Ospanova Sh. (Proceedings of the 2013 Int. conf. on Applied Mathematics and Computational Methods in engineering, Rhodes Islands, Greece, 2013), Rhodes Islands, Greece, 2013, p. 155-158.

12 Arcoumanis C., Cutter P., Whitelaw D. S., Institution of Chemical Engineer Trans IChemE, 76, 124 (1998).

13 Askarova, A.S., Voloshina, I.E., Ryspayeva, M.Zh. (Abstracts of V-th International conference "Problems of industrial heat engineering", Kiev, Ukraine, 2007), Kiev, Ukraine, 2007, p. 27-28.

14 Askarova, A. S., Messerle, V. E., Ustimenko, A.B., Bolegenova, S. A., Maximov, V. Yu. Gabitova, Z. Kh., High temperature, 53, 445 (2015).

15 Askarova, A., Maximov, V., Bolegenova, S., Beketayeva, M., Safarik, P., Journal of thermal science, 24, 275 (2015).

16 A. Askarova, A. Bekmukhamet, S. Bolegenova, S.Ospanova, B. Symbat, V. Maximov, M. Beketayeva, A. Ergalieva. 3-D Modeling of Heat and MassTransfer during Combustion of Solid Fuel in Bkz-420-140-7C Combustion Chamber of Kazakhstan. J. Applied Fluid Mechanics, 9, 699 (2016).

17 Karpenko E.I., Messerle V.E., Askarova A.S., Journal of High Energy Chemistry, 40, 111 (2006).

18 Messerle V.E., Lavrishcheva Ye.I., Karpenko E.I., Askarova A.S., Ustimenko A.B., IEEE Transactions on Plasma Science, 35, 1607 (2007).

19 Askarowa A., Buchmann M.A. (Gesell Energietech, Combustion and incineration - Eighteenth Dutch-German Conference on Flames), VDI Berichte, 1997, vol.313, p. 241-244.

20 Vockrodt S., Leithner. R, Schiller A., Askarowa A.S. (VDI, 19th German Conference on Flames, Germany, VDI Gesell Energietechn; Verein Deutsch Ingn., Combustion And Incineration), VDI Berichte, 1999, vol. 1492, p. 93.

# Application of 3D modelling for solving the problem of combustion coal-dust flame

A. Askarova[1], S. Bolegenova[2]*, S. Bolegenova[2], V. Maximov[1], R. Manatbayev[2],A. Yergaliyeva[2], Z. Gabitova[2], A. Maxutkhanova[2], Zh. Shortanbayeva[2], A. Boranbayeva[2], K. Berdikhan[2]

[1] *SRI of Experimental and theoretical physic, Al-Farabi Kazakh National University, 71, al-Farabi ave., 050040, Almaty, KAZAKHSTAN*

[2] *Faculty of Physics and Technology, Al-Farabi Kazakh National University, 71, al-Farabi ave., 050040, Almaty, KAZAKHSTAN*

This article presents the results of numerical simulations on research of influence of moisture of the burned Ekibastuz coal in the combustion chamber of Kazakhstan Aksu power plant on processes of heat and mass transfer. Graphs of distribution of such characteristics as temperature, concentration of carbon oxides and nitrogen oxide are attached. It is shown that the increase in moisture of fuel leads to the reduction of average values of temperature and concentration of carbon dioxide in the combustion chamber, and to the reduction of concentration of carbon monoxide CO and nitrogen oxides NO in the field of active combustion.

**Keywords:** moisture of coal, coal-dust torch, combustion, heat power plant, heat and mass transfer

## INTRODUCTION

It is known, fuel moisture is the ballast that substantially reduces the effectiveness of its combustion. However, the studies on burning of coals of various moisture carried out by groups of scientists [1-3] showed the need for a more complete investigation.

Today, numerical modelling is rather effective method for predicting the behavior of systems difficult for analytical research, among them is the burning of low-grade coal in the combustion chambers of boilers on power plants. Computer simulation allows obtaining of qualitative and quantitative characteristics of the process and also the response of the system to the change of its parameters and initial conditions [4-7]. The main stages of process of modelling are: 1) the stage of subject modelling consisting of the formulation of basic laws, rules and approximations; 2) stage of mathematical modelling – the description of the main equations; 3) the stage of computer modelling including mathematical calculations and graphic interpretation of the obtained data.

Numerical modelling was carried out with FLOREAN [8, 9] software on the basis of the three-dimensional equations convective warm and a mass transfer for a prediction of influence of moisture of coal for the general operation of the fire chamber and formation of products of combustion [1,7]. This software package was used for a basis of numerical researches and added by us the new GEOM software, which is always written in the selection of a new object of study (the combustion chamber), taking into account the geometry, sizes of burners, their shape and location in the space of the combustion chamber [10-15]. In this model all the characteristics of complex real physical and chemical processes in the object of research chosen by us also the boundary conditions for the solution of the chosen research problem which are adequately reflecting this process are set [16, 17].

## EXPERIMENTAL

### Mathematical and physical formulation of the problem

A mathematical model describing the processes of turbulent heat and mass transfer in this case is as follows [8- 11]:

a) Continuity equation:

$$\frac{\partial \rho}{\partial t} = -\frac{\partial \left( \rho u_j \right)}{\partial x_j},\qquad(1)$$

b) Equation of motion:

$$\frac{\partial \left( \rho u_j \right)}{\partial t} = -\frac{\partial \left( \rho u_i u_j \right)}{\partial x_j} + \frac{\partial \tau_{i,j}}{\partial x_j} - \frac{\partial p}{\partial x_j} + \rho f_i,\qquad(2)$$

$f_i$ – volume forces; $\tau_{i,j}$ – tensor of viscous tension.

c) Energy equation:

$$\frac{\partial}{\partial t}(\rho h) = -\frac{\partial}{\partial x_i}(\rho u_i h) - \frac{\partial q_i^{res}}{\partial x_j} +$$
$$+\frac{\partial p}{\partial t} + u_i \frac{\partial p}{\partial x_i} + \tau_{i,j} \frac{\partial u_j}{\partial x_i} + S_h,\qquad(3)$$

* To whom all correspondence should be sent:
  saltanat.bolegenova@kaznu.kz

$h$ – enthalpy; $q_i^{res}$ – energy flux density due to molecular heat transfer, $S_h$ – a source of energy.

d) Conservation law for substance components:

$$\frac{\partial}{\partial t}(\rho c_n) + \frac{\partial}{\partial x_i}(\rho u_i c_n) = \frac{\partial}{\partial x_i}\left[\rho D_{c_n} \frac{\partial c_n}{\partial x_i}\right] + S_{c_n}, \quad (4)$$

$S_{Cn}$ – the source term taking into account the contribution of the chemical reactions in the change in the concentration of components.

e) Standard k-ε turbulence model:

$$\frac{\partial(\overline{\rho}k)}{\partial t} = -\frac{\partial(\overline{\rho}\,\overline{u}_j k)}{\partial x_j} + \frac{\partial}{\partial x_j}\left[\frac{\mu_{eff}}{\sigma_k}\frac{\partial k}{\partial x_j}\right] + P - \overline{\rho}\varepsilon, \quad (5)$$

$P$ – the production of turbulent kinetic energy, which is determined by the following equation:

$$P = \left[\mu_{turb}\left(\frac{\partial \overline{u}_i}{\partial x_j} + \frac{\partial \overline{u}_j}{\partial x_i}\right)\right]\frac{\partial \overline{u}_i}{\partial x_j} - \left[\frac{2}{3}\rho k \delta_{ij}\right]\frac{\partial \overline{u}_i}{\partial x_j} \quad (6)$$

and the equation for the turbulent kinetic energy dissipation ε:

$$\frac{\partial(\overline{\rho}\varepsilon)}{\partial t} = -\frac{\partial(\overline{\rho}\,\overline{u}_j \varepsilon)}{\partial x_j} + \frac{\partial}{\partial x_j}\left[\frac{\mu_{eff}}{\sigma_\varepsilon}\frac{\partial \varepsilon}{\partial x_j}\right] +$$
$$+ C_{\varepsilon,1}\frac{\varepsilon}{k}P - C_{\varepsilon,2}\frac{\varepsilon^2}{k}\overline{\rho}, \quad (7)$$

$\overline{\rho}\varepsilon$ – the conversion of kinetic energy pulsating movement in the internal energy (dissipation).

Empirical constants are defined and equal to the following values:

$c_\mu$=0,09; $\sigma_k$=1,00; $\sigma_\varepsilon$=1,30; $C_{\varepsilon1}$=1,44; $C_{\varepsilon2}$=1,92.

By consideration of the heat transfer processes in technical reacting flows in combustion chambers heat transfer by radiation makes the largest contribution to the total heat transfer. In a zone of a flame, the contribution of radiant heat exchange makes up to 90 % and even more.

Physical quantity, which describes heat transfer by radiation, is the spectral intensity $I_v$. In general terms, the radiation energy balance equation has the form:

$$\frac{1}{c}\frac{\partial I_v}{\partial t} + \frac{\partial I_v}{\partial s} = -\left(K_{abs,v} + K_{sca,v}\right)I_v + K_{abs,v}I_v +$$
$$+ \frac{K_{sca,v}}{4\pi}\int_{4\pi}\left(P(\Omega_i \to \Omega)\cdot I_v(\Omega_i)\right)d\Omega_i. \quad (8)$$

To describe the radiant heat exchange the six-line model in Cartesian coordinates, proposed by de

Marco and Lockwood. In this model, the distribution of radiation energy flux at appropriate sites is approximated using power series and spherical functions.

The intensity distribution in various directions is approximated using a Taylor power series over the solid angle:

$$I = A_i\left(\vec{n}_i \cdot \Omega\right) + B_i\left(\vec{n}_i \cdot \Omega\right)^2, \quad (9)$$

where $A_i$, $B_i$ – the coefficients in the Taylor series expansion – functions of intensity of radiation.

Integrating all six directions with a constant angle of integration $\Omega i = 2\pi$ and infinitely small angles in the positive and negative directions of coordinates we obtain a system of differential equations of six-line model:

$$\frac{\partial}{\partial x_j}\left[\frac{1}{K_{abs}}\frac{\partial\left(B_i b_{ij}\right)}{\partial x_j}\right] = K_{abs}B_j - K_{abs}\frac{\sigma}{\pi}T^4, \quad (10)$$

where $\sigma$=5,67*$10^{-8}$ W/$m^2$·$K^4$ – Stefan-Boltzmann constant; $b_{ij}$ is the matrix coefficient and is defined as

$$b_{ij} = \frac{1}{2}\cdot\begin{pmatrix} 1+x_i^{//2} & \dfrac{1-x_i^{//2}}{2} & \dfrac{1-x_i^{//2}}{2} \\ \dfrac{1-x_i^{//2}}{2} & 1+x_i^{//2} & \dfrac{1-x_i^{//2}}{2} \\ \dfrac{1-x_i^{//2}}{2} & \dfrac{1-x_i^{//2}}{2} & 1+x_i^{//2} \end{pmatrix} \quad (11)$$

Parameters $x_i^{//}$ depend on intensity of directing radiation and are defined by

$$x_i^{//} = \gamma_{Sca}\cdot\frac{B_i}{\sqrt{B_1^2 + B_2^2 + B_3^2}}. \quad (12)$$

The value of the constant $\gamma_{Sca}$ is defined in [18] and equals 0.1. Source term associated with radiant heat transfer in the energy equation is obtained by integrating the total intensity over the solid angle $\Omega$=4π. Thus, we have

$$S_{h,Sca} = \frac{4\pi}{3}K_{abs}(B_1 + B_2 + B_3) - 4K_{abs}\sigma T^4. \quad (13)$$

As the object of study was chosen real industrial steam boiler PK-39, mounted on the Aksu power plant (Kazakhstan) with dimensions 7,762 x 10,76 x 29,985 m. The combustion chamber of the boiler is equipped with 12 vortex coal-dust torches located

on two tiers. The scheme of the combustion chamber of the boiler and its breakdown on control volumes is submitted in Fig.1.
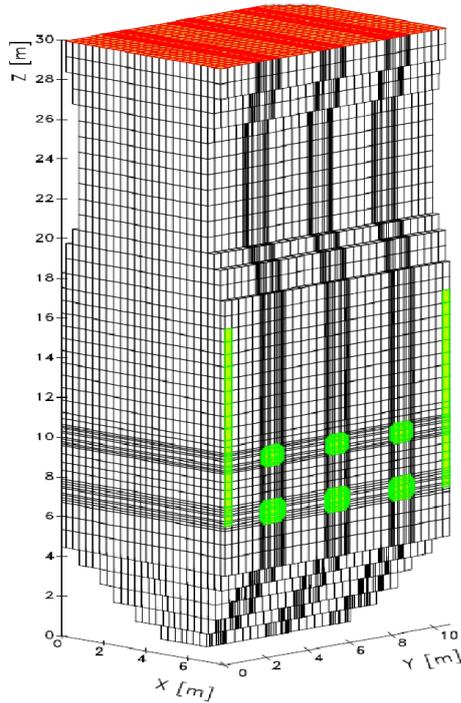


**Fig**.**1.** PK-39 boiler combustion chamber

RESULTS

Fig.2 to Fig.5 show the results of modelling experiments of the study of heat and mass transfer taking into account various value of moisture content in fuel in weight percent (wt%). As it is possible to notice, qualitatively provided characteristics don't change depending on moisture, however, it is possible to notice that curves in these drawings differ in a quantitative sense.

Along with the results of modelling experiments, Fig.2 shows the results of a natural experiment on the power plant [19] for coal with a moisture content equal to 7%. We see that the behavior of the experimental and calculated (numerical simulation) curves coincide. It is possible to see the existence of a minimum curves in areas of an arrangement of a line of torches that is connected with the low temperature of the aero mix (150 °C) given through these torches. Temperature reaches the maximum values in the central part of the combustion chamber where there is a torch core. In process of advance to an exit from the combustion chamber, the field of temperature is leveled, and the values are reduced.

The greatest differences between the calculated and experimental data (Fig.2) are observed when ignited coal torch. This can be explained by the

instability of the combustion process in this area and, accordingly, the difference between the actual physical conditions of the dust mixture and ignition of a mathematical model that describes the process of combustion of solid fuels in this area.
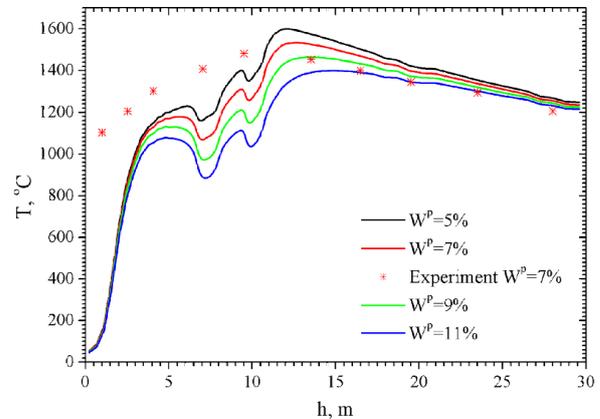


**Fig**.**2**. The temperature distribution along the height of the furnace chamber during combustion of varying moisture coal

By analyzing the curves of Fig.2, it should be noted that an increase in fuel moisture results in a decrease in average temperature in the combustion chamber (Table 1). This can be explained by the fact that moisture of fuel reduces its thermal value, as transformation of 1 kg of water into steam takes 2,5 MJ of heat.

The greatest distinctions between temperature curves for coal of different moisture can be noticed in the combustion chamber in the field of a line of torches. At the exit from the combustion chamber differences in values of temperature for coals which moisture changes from 5% to 11%, decrease and makes no more than 35 °C (Table 2).

As a result of modelling experiments on burning Ekibastuz coal concentration fields of harmful dust and gas products of combustion were calculated. In figures 3-5 schedules of distribution of concentration of CO and $CO_2$ carbon oxides and NO nitrogen oxide are submitted.

The analysis of Fig.3 shows that formation of carbon monoxide occurs mainly in the main body of the torch, where its average temperature reaches its maximum value. Moreover, with decreasing of moisture content in coal, maximum of CO concentration increases and moves to the region of the burners. In process of advance to an exit from a fire chamber, concentration of carbon monoxide decreases.

Thus, increasing the fuel moisture reduces the concentration of carbon monoxide CO in the active combustion, which coincides with the experimental data given in works [1, 19]. It can be explained to

that at low temperatures fuel carbon reaction with air oxygen with formation of carbon dioxide prevails, however at temperature increase reaction between coal and the formed carbon dioxide starts proceeding.
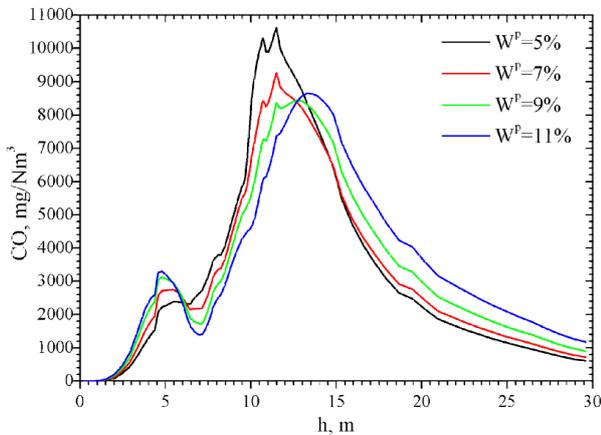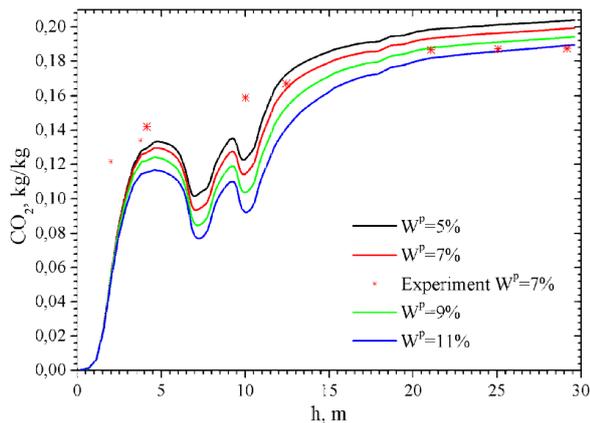


**Fig.3.** The distribution of the CO concentration along the height of the furnace chamber during combustion of varying moisture coal

Fig.4 shows the distribution of average values of the $CO_2$ concentration in each section of the height of the combustion chamber. It can be seen that increasing moisture leads to reduction of concentration of carbon dioxide that is connected with temperature conditions of process. This in turn creates worse conditions for the reaction connected with afterburning of CO to $CO_2$. Consequently, the concentration of carbon dioxide $CO_2$ at the outlet of the fire chamber with increasing fuel moisture is reduced.



**Fig.4.** The distribution of the $CO_2$ concentration along the height of the furnace chamber during combustion of varying moisture coal

Fig.4 shows the results of an experiment conducted directly at the power plant [19]. We see that the greatest distinctions in results of modelling and natural experiments are observed in the field of

ignition of gas mixture that is connected with instability of burning and distinction between the modeled and experimental conditions for aero mix ignition.

Currently distinguish 3 mechanism of formation of nitrogen oxides: thermal NOx and fast NOx formed from nitrogen of atmospheric air and fuel NOx formed from the fuel nitrogen. The greatest contribution to formation nitrogen oxides bring fuel and thermal NOx.

Thermal oxides – are formed by the oxidation of atmospheric nitrogen at high temperatures. Zel'dovich proposed the mechanism of their formation and proved that the formation of nitrogen oxides is not directly connected with the combustion reaction, and goes through the dissociation of molecular oxygen at high temperatures.

Fuel nitrogen oxides are formed as a result of transformation fuel the nitrogen which is contained in fuel oil and all types of solid fuel. Therefore, at combustion of coal dust the share of fuel NOx is very high. Considerable part (up to 80%) of NOx are formed on an initial site of a torch, in a zone of an exit and ignition of volatiles.

Fig.5 shows a field of concentration of NO nitrogen oxide on height of the combustion chamber of the boiler PK-39 Aksu power plant for different values of the moisture content of the fuel. From the figure, we can see that the greatest distinctions in average concentration fall on the central part of the furnace where burners are located.
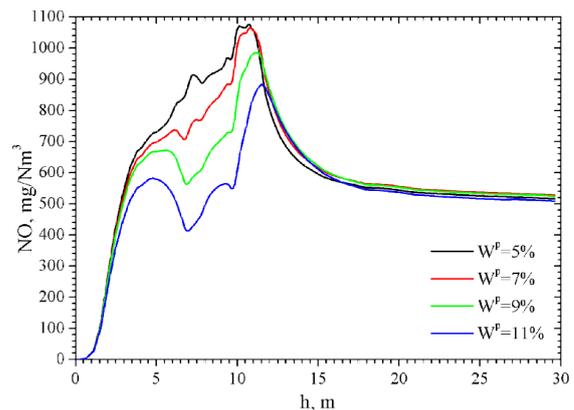


**Fig.5.** The distribution of the NO concentration along the height of the furnace chamber during combustion of varying moisture coal

Increasing the moisture of coal reduces the temperature (see. Fig.2) in a zone of active burning that conducts to reduction of concentration NO in this area. These results are confirmed by the researches described in works [1, 3, 19]. However,

it is possible to notice that to an exit from the furnace chamber a field of concentration of nitric oxide NO are aligned and differences in the concentrations according to Table 1 in the order of 3-18 mg/Nm$^3$.

**Table 1.** The distribution of average values of the temperature, concentrations of CO, $CO_2$ and NO in section of the lower tier of burners for various values of fuel moisture

| Character istics | Moisture, $W_p$ | | | |
|---|---|---|---|---|
| | 5% | 7% | 9% | 11% |
| T, °C | 1178,86 | 1079,82 | 976,46 | 885,72 |
| CO, mg/Nm$^3$ | 2938,94 | 2391,9 | 1912,79 | 1550,57 |
| $CO_2$, kg/kg | 0,104 | 0,094 | 0,085 | 0,077 |
| NO, mg/Nm$^3$ | 914,58 | 766,67 | 589,49 | 431,33 |

**Table 2.** The distribution of average values of the temperature, concentrations of CO, $CO_2$, and NO at the outlet of the combustion chamber for different fuel moisture

| Character istics | Moisture, $W_p$ | | | |
|---|---|---|---|---|
| | 5% | 7% | 9% | 11% |
| T, °C | 1247,9 | 1236,1 | 1225,0 | 1214,6 |
| CO, mg/Nm$^3$ | 614,4 | 724,5 | 907,4 | 1183,1 |
| $CO_2$, kg/kg | 0,204 | 0,199 | 0,194 | 0,189 |
| NO, mg/Nm$^3$ | 516,97 | 527,79 | 524,78 | 509,25 |

## ACKNOWLEDGMENT

## CONCLUSION

The study has shown that an increase in moisture leads to a decrease in fuel temperature and the average concentration of carbon dioxide $CO_2$ in the combustion chamber, and also to reduce the carbon monoxide concentration CO in the active burning zone (Table 1). With reduction of moisture content in coal the maximum of concentration of CO increases and is displaced to area of an arrangement of torches. Out of the combustion chamber reduces the concentration of carbon monoxide (Table 2). It is also shown that the increase in moisture of coal leads to reduction of concentration of NO in the central part (Table 1) of the combustion chamber. The greatest differences in the results of modelling and physical experiments are observed in the ignition of the combustible mixture. Concentrations of CO, $CO_2$, NO, which are the main substances polluting the atmosphere, at the outlet of the flue space does not exceed maximum permissible concentration norms adopted in the Republic of Kazakhstan.

## NOMENCLATURE LIST

$u_i$ – components of the velocity, m/s;

$t$ – time, s;

$\rho$ – density, kg/m$^3$;

$\tau_{i,j}$ – tensor of viscous tension, N/m$^2$;

$p$ – pressure, Pa;

$f_i$ – volume forces, N;

$h$ – enthalpy, kJ/kg;

$q^{res}$ – energy flux density due to molecular heat transfer, kg/s$^3$;

$S_h$ – a source of energy, kJ/m$^3$·s;

$c_n$ – mass concentration of the components of the substance, kg/kg;

$D_{c_n}$ – the diffusion coefficient of a component, m$^2$/s;

$S_{c_n}$ – the source term taking into account the contribution of the chemical reactions in the change in the concentration of components, kg/ m$^3$·s;

$k$ – turbulent kinetic energy per unit mass, m$^2$/s$^2$;

$\mu_{eff}$ – effective viscosity, kg/m·s;

$\sigma_k$, $\sigma_\varepsilon$ – turbulent Prandtl numbers – empirical constants in turbulence model;

$P$ – the production of turbulent kinetic energy, which is determined by the following equation, kg/m·s$^3$;

$\varepsilon$ – dissipation rate of turbulent kinetic energy per unit mass, m$^2$/s$^3$;

$\delta_{ij}$ – Kronecker delta;

$\mu_{turb}$ – turbulent viscosity, kg/m·s;

$c_{\varepsilon1}$, $c_{\varepsilon2}$, $c_\mu$ – empirical constants;

$I_v$ – spectral intensity, kW/m$^2$·rad;

$v$ – frequency of radiant energy emitted from the element area, s$^{-1}$;

$ds$ – length of the infinitesimal element allocated in space, m;

$K_{abs}$, $K_{sca}$ – optical absorption and scattering coefficients, m$^{-1}$;

$\Omega$ – the solid angle, rad;

$A_i$, $B_i$ – the coefficients in the Taylor series expansion – functions of intensity of radiation, kW/m$^2$·rad;

$\sigma$ – Stefan-Boltzmann constant, W/m$^2$·K$^4$;

$b_{ij}$ – the matrix coefficient.

## REFERENCES

1  Iskakov R.T., Engelsht V.S. Termodinamicheskiy analiz vliyaniya vlazhnosti na gorenie ugleroda, *Vestnik IGU*, 8, 75 (2002).

2  Kurose R., Watanabe H., Makino H. Numerical Simulations of Pulverized Coal Combustion, *KONA Powder Part. J.,* 27, 144 (2009).

3  Pinchuk V.A., Potapov B.B., Sharabura T.A. Ispolzovanie termodinamicheskih pokazateley dlya otsenki energeticheskoy i tehnologicheskoy tsennosti razlichnyih marok ugley, *Metallurgicheskaya teplotehnika. Sbornik nauchnyih trudov Natsionalnoy metallurgicheskoy akademii Ukrainyi,* Dnepropetrovsk: PP Grek OS, S. 228 (2008).

4  Askarova A.S., Messerle V.E., Ustimenko A.B., Bolegenova S.A., Maximov V.Yu. Numerical simulation of the coal combustion process initiated by a plasma source, *Thermophysics and Aeromechanics,* 21, Issue 6, 747 (2014).

5  Messerle V.E., Ustimenko A.B., Askarova A.S., Nagibin A.O. Pulverized coal torch combustion in a furnace with plasma-coal system, *Thermophysics and Aeromechanics,* 17, Issue 3, 435 (2010).

6  Askarova A.S., Karpenko EI; Lavrishcheva Y.I., Messerle V.E., Ustimenko A.B. Plasma-supported coal combustion in boiler furnace, *IEEE Trans. Plasma Sci.*, 35, Issue 6, 1607 (2007).

7  Askarova A.S., Karpenko E.I, Messerle V.E., Ustimenko A.B. Plasma enhancement of combustion of solid fuels, *High Energy Chem.,* 40, Issue 2, 111 (2006).

8  Müller, H. Numerische simulation von Feuerungen. CFD–Vorlesung, TU, Braunschweig: IWBT, 8 (1997).

9  Leithner, R. Numerical Simulation. Computational Fluid Dynamics CFD: Course of Lecture. – Braunschweig, 2006. 52 s.

10  Askarova A.S., Bolegenova S.A., Maximov V.Yu., Bekmukhamet A., Beketayeva M.T., Gabitova Z.Kh. Computational method for investigation of solid fuel combustion in combustion chambers of a heat power plant, *High Temp.*, 53, Issue 5, 751 (2015).

11  Askarova A., Bolegenova S., Maximov V., Beketayeva M., Safarik P. Numerical Modelling of Pulverized Coal Combustion at Thermal Power Plant Boilers, *J. Therm. Sci.,* 24, Issue 3, 275 (2015).

12  Askarova A.S., Messerle V.E., Ustimenko A.B., Bolegenova S.A., Maximov V.Yu., Gabitova Z.Kh. Numerical simulation of pulverized coal combustion in a power boiler furnace, *High Temp.,* 53, Issue 3, 445 (2015).

13  Askarova A.S., Karpenko E.I., Karpenko Yu.E., Messerle V.E., Ustimenko A.B. Mathematical modelling of the processes of solid fuel ignition and combustion at combustors of the power boilers, *Theory Pract. Energ. Mater., Proc. Int. Autumn Semin. Propellants, Explos. Pyrotech., 7th,* VII, 672 (2007).

14  Askarova A.S., Bolegenova S.A., Maksimov V.Yu., Bekmuhamet A., Ospanova Sh.S. Numerical research of aerodynamic characteristics of combustion chamber BKZ-75 mining thermal power station, *Procedia Eng.,* 42, 1250 (2012).

15  Askarova A., Bekmukhamet A., Bolegenova S., Beketayeva M., Maximov V., Ospanova S., Gabitova Z. Investigation of turbulence characteristics of burning process of the solid fuel in BKZ 420 combustion chamber, *WSEAS Trans. Heat Mass Transfer,* 9, 39, (2014).

16  Askarova A., Bolegenova S., Bekmukhamet A., Ospanova S., Gabitova Z. Using 3D modelling technology for investigation of conventional combustion mode of BKZ-420-140-7c combustion chamber, *J. Eng. Appl. Sci. (Faisalabad, Pak.)*, 9, Issue 1, 24 (2014).

17  Askarova A.S., Bekmukhamet A. Bolegenova S.A., Maximov Yu.V., Ospanova Sh.S., Gabitova Z.K. Numerical modelling of turbulence characteristics of burning process of the solid fuel in BKZ-420-140-7c combustion chamber, *International Journal of Mechanics,* 8, 112 (2014).

18  Lockwood F., Shah N. An improved flux model for calculation of radiation heat transfer in combustion chambers, *ASME–AIChE Heat transfer Conf.: ASME–Paper,* (*Salt Lake City*), 1, 2 (1976).

19  Aliyarov B.K., Aliyarova M.B. Szhiganie kazahstanskih ugley na TES i na krupnyih kotelnyih: opyit i problemyi, Almatyi, (2012), 306 s.

# Comparative analysis of individual house heating system based on electricity and combustion of alternative and fossil fuels

A. Majchrzycka

*West Pomeranian University of Technology, Szczecin Faculty of Mechanical Engineering and Mechatronics
Department of Thermal Engineering 70-310 Szczecin, Piastów Av.19, Poland*

The paper reports cost analysis of house heating and preparation of hot water by means of the different heating systems. The following heating systems were analyzed: electrical heating, boilers fired with the different types of biomass (firewood, wood pellets, wood briquettes, wheat straw, sunflowers husks pellets and conventional fuels (hard coal, fine coal, natural gas, light oil fuel). Based on heat demand for house heating and preparation of hot water, properties of the fuels, current prices of the biomass, fossil fuels, electricity and boilers unit costs of heat production, operational costs and economic effect covering 15 years of exploitation were determined.

**Keywords:** alternative fuels, heating systems, biomass

## INTRODUCTION

Climate and energy package for 2020 includes four targets: to reduce emissions of greenhouse gases by 20% by 2020 taking 1990 emissions as the reference, to increase energy efficiency to save 20% of EU energy consumption by 2020, to reach 20% of renewable energy in the total energy consumption in the EU by 2020, to reach 10% of biofuels in the total consumption of vehicles by 2020, [1]. EU countries have 3 times more renewable power per capita than the rest of the world put together [2]. In EU countries share of renewables for heating and cooling - 17%, transport -6%, electricity – 26 %, [2].

In 2013 share of renewable energy in gross final energy consumption in Poland was 11,3% [3]. Table 1 presents the share of renewable commodities in the total obtaining primary energy form renewable energy sources in 2013, **[3].**

The estimated technical potential of biomass in Poland amounts to 755 PJ/year, Janowicz [4]. Availability and competitive prices cause that biomass and biomass originated fuels are considered for energy production in individual houses, dwellings [5, 6], Zawistowski [7, 8] and for combined heat and power generation [9].

Presented paper is aimed at comparative analysis of the use of electricity, alternative and fossil fuels for heating and preparation of warm water in an individual house. Comparative analysis will be based on the previously determined energy demand for the house. The real object consists of the one floor individual house with attic and garage annex. The ground floor (without cellar) consists of: vestibule, wc, kitchen, dining room, saloon, hall, 2 bathrooms, 3 bedrooms, store room and garage. Attic is excluded from a living space. The house is covered with the gable roof of the slope 15°. The total house area of 225,5 m$^2$; the usable area of 146,0 m$^2$, the cubature of 496,1 m$^3$. Energy demand for heating and preparation of warm water was estimated at the following assumptions: number of the household members $n = 5$, minimal 24-hour consumption of warm water of $t = 60\ ^oC$, $V=60\ l$ /capita, comfort temperature $t_i = 20\ ^oC$, location of the house in the region of the mean ambient temperature in winter $t_e = -16^oC$ [10, 11]. Estimated thermal power demand for the house heating and preparation of the warm water $\dot{Q} = 11,4\ kW$. House heating load $Q_{co} = 68\ 149\ MJ$ was estimated taking into account the different heating periods during a year [10, 11]. The total annual energy demand for heating and preparation of the warm water for the house in question $Q_a = 88\ 795\ MJ$.

**Table 1.** Share of renewable commodities in the total obtaining primary energy form renewable energy sources in 2013, [3]

| RES | EU , [%] | Poland , [%] |
|---|---|---|
| Solid biofuels | 45,83 | 80,30 |
| Hydropower | 16,10 | 2,46 |
| Wind energy | 10,53 | 6,07 |
| Biogas | 7,05 | 2,13 |
| Liquid biofuels | 6,71 | 8,23 |
| Solar energy | 5,54 | 0,18 |
| Municipal waste | 4,64 | 0,42 |
| Geothermal energy | 3,08 | 0,22 |

* To whom all correspondence should be sent:
anna.majchrzycka@zut.edu.pl

## HEATING SYSTEMS

Selection of the heating system should be preceded with an economic analysis of the use of different fuels and heating systems. It was assumed that energy demand for the house in question will be the same for each of analysed heating systems**.** The cost effectiveness analysis will be carried out for electric heating and heating systems based on combustion of the different fuels presented in Table 2.

Table 2 presents net calorific values of biomass and fossil fuels, current prices of the fuels, electricity and purchase prices of the different types of boilers [12, 13, 14, 15, 16, 17, 18, 19, 20, 21, 22, 23].

**Table 2.** Net calorific value of the fuels and current purchase prices of the fuels and boilers

| Heating system | $Q_i$ [MJ/kg] | $k_f$ [€/t] | I [€] |
|---|---|---|---|
| Firewood (15 % of moisture) | 14,7 | 57,9 | 1134,3 |
| Willow chips | 12,0 | 46,3 | 1134,3 |
| Wheat straw | 14,3 | 50,9 | 1134,3 |
| Wood briquettes | 17,8 | 138,9 | 1134,3 |
| Pellets-wood | 18,5 | 185,2 | 2083,3 |
| Sunflowers husks pellets | 20,0 | 92,6 | 2083,3 |
| Pea-ecocoal | 26,0 | 185,2 | 2083,3 |
| Hard coal | 23,0 | 162,0 | 1134,3 |
| Fine coal | 19,0 | 138,9 | 1134,3 |
| Natural gas E | 49,5 | 578,7 | 1064,8 |
| Light fuel oil | 42,6 | 601,9 | 5248,6 |
| Electric heating G11* -24-h tariff | 0,0719 [€/kWh] | | 1851,8 |
| Electric heating G12* - the night tariff | 0,0438 [€/kWh] | | 1851,8 |

*G11     - 24-h tariff for electricity ,*
*G12     - the night tariff for electricity,*
*I         - capital cost of heat source ,[€],*
*$k_f$       - purchase price of the fuel, [€/t]*
*kf      - purchase price of electricity, [€/kWh]*
*Qi      - net calorific value of the fuel, [MJ/kg]*

Purchase prices of electricity were taken from [24] for two tariffs: G11 – 24 hour tariff and G12 - the night tariff (transmission fee is not included).

For combustion of biomass and coal (hard and fine coal) the following types of the boilers were applied: Warmet 200 Ceramic [19] - boiler designed as fit for combustion of firewood (15 % of moisture), willow chips, wood briquettes, straw, hard coal, and fine coal (it is also possible combustion of coke,), then Farmer Bio [19] designed as fit for combustion of wood pellets, sunflowers husk pellets, eco-pea coal boiler.

For combustion of natural gas and light oil fuel gas boiler Junkers Ceropur Midi ZWB 24-1 AR, [18] and light fuel oil boiler Vitoladens 300-C/300-T, produdced by Viessmann [26] were applied.

For electrical heating the programmable accumulative heaters ZP DGN 30 RTS 007, [20] were applied. Purchase prices of the fuels and the boilers were taken from actual price lists presented in bids [12, 13, 14, 15, 16, 17, 18, 19, 20, 21, 22, 24, 25, 26]. For combustion of hard coal, pea - ecocoal, fine coal and biomass efficiency of the boilers was assumed to be η= 0,80 and η = 0,90 for combustion of natural gas and light fuel oil.

## HEATING COSTS

To analyse profitability of the different heating systems, the unit cost of heat production, annual investment outlays and the running costs are determined. There are two components of heat production cost: cost of energy supplied in the fuel (electricity) and cost resulting form the investment outlays. Cost resulting from the investment outlays depends upon purchase and installation costs, annual heating consumption and the investment outlay service rate.

The unit cost of heating produced by the different heat sources can be determined from the equation presented by Rubik [27]:

$$k_c = \frac{k_z}{\eta} + \frac{p \cdot I}{Q_a} \qquad (1)$$

$k_z$ - unit cost of energy delivered in the fuel [€/GJ],
$\eta$ - heat source efficiency,
$p$ - annual investment outlays service rate,
$I$ - capital cost of heat source ,[€],
$Q_a$ - annual heat demand [GJ/a].

Heat production unit cost is determined from the following equation:

$$k_e = \frac{k_z}{\eta} \qquad (2)$$

Annual house heating load is calculated as follows:

$$Q_a = \frac{24 \, \dot{Q} \cdot S_d}{t_i - t_e} \qquad (3)$$

where:

$\dot{Q}$ - heating power demand for the house, [kW],
$S_d$ - degree-day number, $S_d$ = 3781,[10,11]
$t_i$ – comfort temperature, $t_i$ = 20°C
$t_e$ - computational temperature in space adjacent to the wall ( ambient temperature) $t_e$ = - 16 ° C, [10, 11].

Annual operating costs of the fuel is detetermined from equation;

$$k_o = \dot{B} \cdot k_f \qquad (4)$$

Rate of the fuel is determined as follows :

$$\dot{B} = \frac{\dot{Q}}{\eta \cdot Q_i} \qquad (5)$$

Annual service rate of the investment expenditures includes the rates of discount and depreciation. At calculation of profitability at the constant prices, usually the rate of discount is assumed to be 6 - 8 %, taken from Górzyński [28]. The real rate of discount was assumed 8 %, depreciation rate was assumed to be constant 5,6 %.

Capital costs given in equation (1) refer only to heat source, costs of the pipelines, fittings and heaters are not included. Estimated annual operating costs determined from annual heating demand and unit heat production costs are presented in Table 3.

**Table 3.** Production unit costs and annual operating costs for different heating systems

| Heating system | $k_z$ [€/GJ] | $k_e$ [€/GJ] | $k_c$ [€/GJ] | $k_o$ [€/year] |
|---|---|---|---|---|
| Firewood (15% of moisture) | 3,9 | 4,9 | 6,7 | 437,0 |
| Willow chips | 3,9 | 4,8 | 6,6 | 428,2 |
| Wheat straw | 3,6 | 4,5 | 6,2 | 395,3 |
| Wood briquettes | 7,8 | 9,8 | 11,5 | 866,1 |
| Wood pellets | 10,0 | 12,5 | 15,7 | 1111,0 |
| Sunflower husks pellets | 4,6 | 5,8 | 9,0 | 513,9 |
| Pea-ecocoal | 7,1 | 8,9 | 12,1 | 790,6 |
| Hard coal | 7,0 | 8,8 | 10,5 | 782,0 |
| Fine coal | 7,3 | 9,1 | 10,9 | 811,4 |
| Natural gas E | 11,7 | 13,0 | 14,6 | 1153,4 |
| Light fuel oil | 14,1 | 15,7 | 23,7 | 1393,9 |
| Electric heating G11 | | 20,0 | 22,8 | 1774,4 |
| Electric heating G12 | | 12,2 | 15,0 | 1081,4 |

$k_z$ – unit cost of energy delivered in fuel, [€/GJ]
$k_e$ – heat production unit cost , [ €/GJ]
$k_c$ -the unit cost of heat produced in the heating system,[€/GJ]
$k_o$ -operating (fuel) costs, [€/year]

Estimated annual operating costs determined from annual heating demand and heat production costs are presented in Table 3. Estimates from Table 3 enable to compare the heating unit costs, taking into consideration the fuel cost, fuel net calorific value and efficiency of the heat source and the heating costs including capital costs of the heat source and annual operating costs for the different heating systems.As it follows from Table 3 the highest unit cost of heating was obtained for heating system equipped with the boiler fired with light oil fuel, then for case of electrical heating, boiler fired with wood pellets, natural gas E, eco-peacoal, wood

briquett, hard coal and biomass (sunflowers husks pellets, fireewood, willow chips and wheat straw).

High unit cost of heat produced in boiler fired with wood pellets results from the high cost of the fuel and capital cost of the modern boiler designed as fit for combustion of the different types of biofuels, pea ecocoal and fine coal [19].

DISCOUNTED HEATING COSTS

Economic effect covering the whole exploitation period of the heating system is described as Net Predicted Value, NPV. In fact, it is total predicted profit discounted to year zero, expressed in currency of this year.

It is the objective function of the analysis in question Górzyński [28], Skorek and Kruppa [29]:

$$NPV = \sum_{t=0}^{t=n} \frac{(CI_t - CO_t)}{(1+r)^t} \qquad (6)$$

where:
$CI_t$ - cash inflow, €,
$CO_t$ - cash outflow, €,
$r$ - discount rate,
$t$ - successive year of exploitation,
$n$ - number of time periods

Fig. 1 shows discounted expenditure for house heating and preparation of warm water at the assumption of 15 years of exploitation.
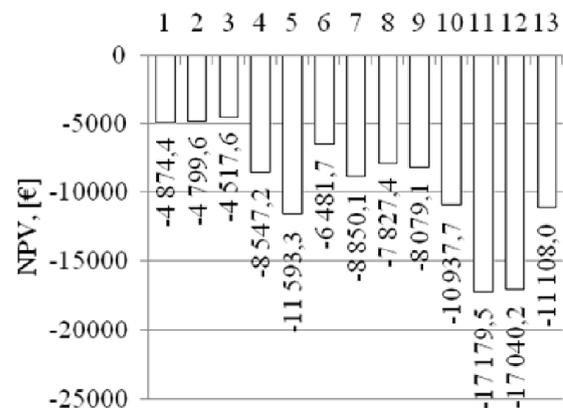


**Fig.1.** Discounted expenditures of heating system after 15 years of exploitation. **1**- firewood (15% of moisture), **2**- willow chips **3**-wood briquettes, **4**-wheat straw, **5**-wood pellets, **6**- sunflower husks pellets, **7**- pea-ecocoal, **8**- hard coal, **9**- fine coal, **10**- natural gas, **11**-light fuel oil, **12**-electric heating G11(24-h tariff ), **13** - electric heating G12 ( the night tariff)

It follows from calculations that discounted expenditures of heating system after 15 years of exploitation are the most advantageous for heating systems fired with firewood, then willow chips, wheat straw, wood briquettes, wood pellets, sunflowers husks pellets, pea-ecocoal hard coal and fine coal. The highest discounted expenditures of

heating system after 15 years of exploitation were estimated for electric heating for G11 (24-h tariff ) and G12 ( the night tariff)), light fuel oil and natural gas E.

## ECOLOGICAL EFFECTS

Emissisons arising from combustion of biomass (firewood, willow chips, wood briquetts, wheat straw , wood pellets, sunflowers pellets) and fossil fuels ( hard coal, pea-ecocoal, fine coal, natural gas E, light fuel oil) in the different types of the boilers were determined using emission factors presented in [30] for the boilers of thermal power < 5 MW.

Indirect emissions, resulting from electricity consumed for house heating and preparation of warm water were determined using emission factors presented in [1,31] for public electricity and power production. Contents of sulphur and ash in the fuels used in house heating systems [15, 16, 17, 32] are presented in Table 4.

**Table 4.** Contents of sulphur (S) and ash (A) in the fuels

| Type of the fuel | A ,[%] | S,[%] |
|---|---|---|
| Firewood(15% of moisture) | 1,1 | 0 |
| Willow chips | 1,1 | 0,005 |
| Wooden briquettes | 1,1 | 0 |
| Wheat straw | 3,0 | 0,2 |
| Wooden pellets | 1,1 | 0 |
| Sunflower pellets | 4,0 | 0 |
| Pea-ecocoal | 6,0 | 0,36 |
| Hard coal | 10,0 | 1,5 |
| Fine coal | 10 | 1,5 |
| Natural gas E | 0 | 0,942 |
| Light fuel oil | 0,01 | 0,1 |

Estimates for emissions from combustion of the different fuels are presented in Table 5.1 and Table 5.2.

**Table 5.1.** Emissions of gases in combustion process

| Heating system | Emission, [kg/year] | | |
|---|---|---|---|
| | $CO_2$ | CO | $SO_2/SO_x$ |
| Firewood (15% of moisture) | 9060,7 | 196,3 | 0,8 |
| Willow chips | 11099,4 | 240,5 | 1,0 |
| Wood briquettes | 9314,2 | 201,8 | 0,9 |
| Wheat straw | 7482,7 | 162,1 | 0,7 |
| Wood pellets | 7199,6 | 156,0 | 0,7 |
| Sunflowers husks pellets | 6659,6 | 144,3 | 0,6 |
| Pea-ecocoal | 7897,6 | 192,1 | 24,6 |
| Hard coal | 8927,8 | 217,2 | 115,8 |
| Fine coal | 10807,3 | 262,9 | 140,2 |
| Natural gas E | 5240,4 | 0,79 | 0,0025 |
| Light fuel oil | 7488,8 | 1,6 | 4,7 |
| Electric heating G11 | 10208,8 | 9,2 | 36,3 |
| Electric heating G12 | 41151,3 | 37,3 | 146,2 |

**Table 5.2.** Emissions of pollutants in combustion process

| Heating system | Emission, [kg/year] | | |
|---|---|---|---|
| | $NO_2/NO_X$ | BAP | TSP |
| Firewood (15% of moisture) | 7,6 | 0 | 12,5 |
| Willow chips | 9,2 | 0 | 15,3 |
| Wood briquettes | 7,8 | 0 | 12,8 |
| Wheat straw | 6,2 | 0 | 28,1 |
| Wood pellets | 6,0 | 0 | 9,9 |
| Sunflowers husks pellets | 5,5 | 0 | 33,3 |
| Pea-ecocoal | 9,4 | 5,98E-02 | 38,4 |
| Hard coal | 10,6 | 6,76E-02 | 72,4 |
| Fine coal | 12,9 | 8,18E-02 | 87,6 |
| Natural gas E | 4,0 | 0 | 0 |
| Light fuel oil | 5,5 | 0 | 0,9 |
| Electric heating G11 | 9,2 | 3,10E-08 | 5,0 |
| Electric heating G12 | 37,3 | 1,25E-07 | 20,3 |

As it follows from Table 5.1 and Table 5.2 heating systems with the boilers fired with biomass are characterized with the low emissions of sulphur and nitrogen oxides and zero emission of bezo (alfa) pyren (BAP). In case of biomass combustion carbon monoxide emissions are realtively high. TSP (Total Suspended Particulate) emissions are relatively high for biomass combustion, however lower than in case of hard coal, fine coal or pea-ecocoal.

The combustion of biomass and fossil fuels to produce heat and electricity is the largest source of $CO_2$ emissions. Carbon dioxide emissions resulting from combustion of biomass is considered neutral as long as carbon dioxide is sequestrated by living biomass. As it follows from [33] mean emission for EU countries is $E_{EU28}$= 7721,2 kg $CO_2$/capita, for Bulgaria $E_{BG}$ = 5985,3 $CO_2$/capita and for Poland $E_{PL}$ = 8437,5 kg $CO_2$/capita.

## RESULTS

Economic and ecological analysis of the conventional and alternative fuels use for heating purposes of an individual house was performed. Unit costs of heating system are influenced by the quality and the unit price of the fuel and efficiency of the boiler. As it follows from analysis biomass and hard coal are the most cost effective for energy production in an individual house, however combustion of hard coal is not environmentally friendly as emissions of pollutants are high. Performed study shows that the highest costs of heat production refer to electrical heating and combustion of light fuel oil, natural gas E and wood

pellets. Discounted expenditures of heating system after 15 years of exploitation are the most advantageous for combustion of firewood, then for willow chips, wheat straw, wood briquetts, wood pellets and sunflowers husks pellets.

It would be also interesting to compare obtained results with available data from the literature. Comparison of the results is difficult as the annual costs of heating depends on costs of the fuels and appliances and their efficiency. For households the end-user price comprises of the following components: fuels and electricity price as traded on the markets, fuel transport and transmission of electricity to local distribution centres, local distribution to households, administrative costs, different taxes (green taxes, VAT etc.).

Paper [34] presents calculator based on USA national averages that enables to estimate and compare fuel costs. In order to compare the results obtained from equation (2) two series of calculations were performed by means of calculator presented in [34]. To compare fuel costs current fuel prices given in [34] and in Poland were entered at the assumption that appliance efficiency for solid fuels is $\eta = 0,8$, for natural gas and light oil fuel $\eta =0,9$, for electricity $\eta=1$. Estimated comparison of the results is presented in Fig.3.
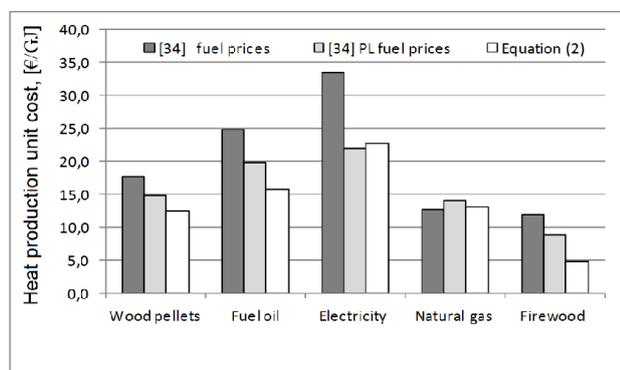


**Fig.2.** Comparison of heat production unit costs

As it follows from Fig.2 the results are different due to the different prices of the fuels. Heat production unit cost (equation 2) depends upon unit cost of energy delivered in the fuel. The differences in the obtained results may be considered also as the consequence of the different net calorific of the fuels given in Table 2 and included in the algorithm of calculator [34].

Papers [35, 36] present comparing heating costs of heating and cooling systems for different variants of the fuels and appliances, electric heating, kerosene heating and heat pump. Comparison of estimated costs of wood heating and pellet heating costs is given in Table 6.

**Table 6.** Comparison of heating costs

| Fuel price [€/t] | Appliance | Heating cost [€/GJ] | Source |
|---|---|---|---|
| 181,8 | Typical pellet stove | 14,8 | [35,36] |
| 185,0 | Farmer Bio | 12,5 | |
| 54,4 | EPA Certified wood stoves $\eta=70\%$ | 11,5 | [35,36] |
| 57,9 | Boiler Warmet 200 Ceramic $\eta=80\%$ | 4,9 | |

As it follows from calculations performed for boiler Farmer Bio [19] of efficiency $\eta=0,8$ fixed for combustion of pellets heating cost equals 12,5€/GJ. Data taken from the literature [35,36] shows that combustion of pellets of comparable pellet prices in typical pellet stove gives heating cost 14,8€/GJ. Calculations performed for combustion of firewood in boiler Warmet 200 Ceramic [19] of efficiency $\eta=80\%$ give the lower heating costs 4,9€/ GJ compared to combustion in EPA Certified wood stoves of efficiency $\eta=70\%$ [35,36].

Comparison of determined annual cost of heat production with available data from the literature [37] is shown in Fig.3. Comparison was performed for the different fuels and their prices and appliances of different efficiency, therefore it should be treated approximately.
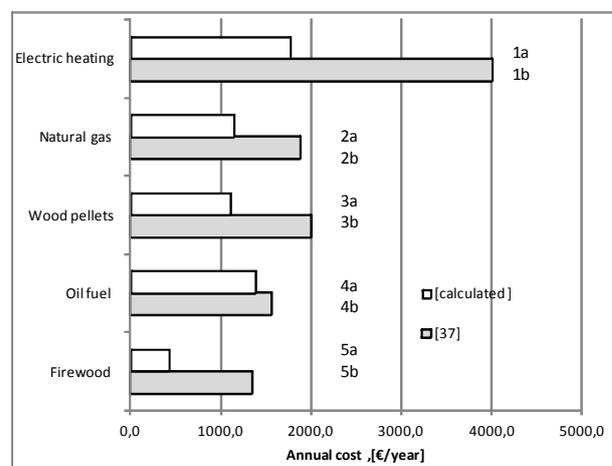


**1a-** accumulative heaters ZP DGN[20]; **1b-** baseboard [37]; **2a-** gas boiler Junkers Ceropur Midi ZWB24 1AR [18]; **2b-**energy star boiler [37]; **3a-**boiler Farmer Bio [19]; **3b-** EPA certified wood stove [37]; **4a-**boiler Vitoladens 300-C/300-T, Viessmann, [26]; **4b-**energy star boiler [37]; **5a-**boiler Farmer Bio [19]; **5b-**EPA certified wood stove [37]

**Fig.3.** Comparison of annual cost of heat production

CONCLUSIONS

Heating sytems fired with biomass (sunflowers husks pellets, willow chips, wood briquettes,

firewood ) except wheat straw and wood pellets are characterized with the lowest unit costs of heat. Recently, current purchase prices of straw and wood pellets increased very much. In case of pellets the range of the purchase price is variable and depends upon quality. The highest heat production unit costs were estimated for electric heating ( both tariffs G11 and G12) , then for light oil fuel heating, natural gas E and pellet heating systems. In case of the systems fuelled with: hard coal, pea-ecocoal or fine coal unit heating costs are between biomass systems and natural gas, light oil fuel and electric heating (both tariffs). In case of stationary combustion of fine coal , hard coal, pea-ecocoal TSP emissions are higher than for sunflowes husks pellets, wheat straw , willow chips, wood briquetts, and pellets. Combustion of light fuel oil is connected with very low TSP emission.

Analysis that has been carried out can be useful for comparison of the different heating systems. The results obtained for heating systems based on combustion of biomass might be interesting for households in the rural region of high potential in biomass.

The combustion and conversion technologies of biomass are increasingly relevant for countries to meet the targets of climate and energy package for 2020.

## REFERENCES

1    www.eea.europe.eu [29.04.2016].
2    www.ec.europa.eu [29.04.2016].
3    Energia /energy 2015, GUS – Central Statistical Office, Warsaw, (2015).
4    L. Janowicz, Biomasa w Polsce, *Energetyka i ekologia*, www.e-energetyka.pl, 601 (2006).
5    Praca zbiorowa, Ogrzewanie budynków za pomocą biopaliw stałych. Bałtycka Agencja Poszanowania Energii S.A.,Gdańsk, (2005).
6    Racjonalizacja przetwarzania i użytkowania energii. Wskaźniki techniczno- ekonomiczne i środowiskowe. Holendersko- polski pogram współpracy poszanowania energii SCORE, Gdańsk, (1999).
7    J. Zawistowski, Biomasa w ogrzewnictwie indywidualnym i komunalnym , *Rynek Instalacyjny* (11), 53,(2004).
8    J. Zawistowski, Biomasa w ogrzewnictwie indywidualnym i komunalnym, *Rynek Instalacyjny* (1/2), 30,(2005).
9    Praca zbiorowa, Kogeneracja z biomasy. Europejskie Centrum Energii Odnawialnej, IBMER, Gdańsk, 1-43, (2002).
10   PN-EN 12831:2006 Obliczenie zapotrzebowania na ciepło pomieszczeń o kubaturze do 600 m$^2$.
11   PN-EN ISO 6946:1999. Komponenty budowlane i elementy budynku. Opór cieplny i współczynnik przenikania ciepła. Metoda obliczania.
12   Komunikat Prezesa Głównego Urzędu Statystycznego z dnia 20 października 2015 w sprawie średniej ceny d sprzedaży drewna, obliczonej według średniej ceny drewna uzyskanej przez nadleśnictwa za pierwsze trzy kwartały 2015 r.
13   Taryfa PGNIG Obrót detaliczny. Spółka z.o.o. w zakresie obrotu detalicznego paliwami gazowymi Nr 3, Warszawa, marzec, (2016).
14   www.cenypaliw.eu [29.04.2016].
15   www.drewnoopalowe.com.pl [25.04.2016].
16   www.drewnoopalowe.suwalki.pl [25.04.20166].
17   www.drewno.pl [27.04.2016].
18   www.junkers.com.pl [29.04.2016].
19   www.kostrzewa.com.pl [29.04.2016].
20   www.leroymerlin.pl [29.04.2016].
21   www.lotos.pl [29.04.2016].
22   www.odnawialnezrodlaenergii.pl [25.04.2016].
23   www.twojaenergia.pl [24.04.2016].
24   www.enea.pl [25.04.2016].
25   www.instalacjebudowlane.pl [25.04.2016].
26   www.viessmann.pl [25.04.2016].
27   M.Rubik Współpraca sprężarkowych pomp ciepła z instalacjami odbiorczymi. *COW*, (7), (1997).
28   J.Górzyński, Audyting energetyczny, Warszawa, (2000).
29   J.Skorek, R.Kruppa, Analiza ekonomiczna zastosowania pompy ciepła w typowym budynku jednorodzinnym, *Gospodarka paliwami i energią* (4), 9,(2000).
30   Wskaźniki emisji zanieczyszczenia ze spalania paliw, kotły o nominalnej mocy do 5 MW, Warszawa, Krajowy Ośrodek Bilansowania I Zarządzania emisjami, Warszawa , styczeń (2015).
31   www.audytorenerg.pl [29.04.2016].
32   www.mpec.olsztyn [28.04.2016].
33   www.energy.eu [7.07.2016].
34   www.pelletheat.org [7.07.2016]].
35   Comparing fuel costs of heating and cooling systems, Engineering Extension, June (2003), www.engext.ksu.edu [7.07.2016].
36   Sidney M. Levy-Construction calculations manual, Elsevier, (2012).
37   Compare heating costs, www.efficiency.com [7.07.2016].

# 'Clean energy' vs. 'Green energy': Quantifying the online interest in USA & Australia

A. Mavragani, K. P. Tsagarakis*

*Business and Environmental Technology Economics Lab, Environmental Engineering Department, Democritus University of Thrace, Vas. Sofias 12, Xanthi, Greece*

This study examines the different modes that users of the World Wide Web employ to search for Renewable Energy. Up to this point, both terms –'Clean Energy' and 'Green Energy'- have been used. Our aim is to compare the terms' Google searches from January 2007 to December 2015 using data from Google Trends, a popular and powerful open tool for providing data on online search traffic. We calculate the ratios between the 'Clean Energy' and 'Green Energy' hits' normalized search volumes in the US and Australia, and analyze the quantified percentized hits. The results show that the 'Clean Energy' search volumes are higher in Australia, while, in the case of the US, 'Green Energy' is searched for more, consistent with the Worldwide trend. As is evident, the term 'Green Energy' is significantly more popular than 'Clean Energy' in online searches, contrary to the scientific community that uses the term 'Clean Energy' more often, judging by the number of documents in the Scopus database containing these terms in the titles. Results are further analyzed and compared with how these countries perform in terms of Renewable Energy consumption, in order to contribute to the discussion of choosing the term that best represents Renewable Energy.

**Keywords:** big data, clean energy, green energy, google trends, renewable energy

## INTRODUCTION

According to the Australian Renewable Energy Agency (ARENA), Renewable Energy is defined as *"energy which can be obtained from natural resources that can be constantly replenished",* implementing technologies that use *"one or more renewable energy sources",* such as bioenergy, geothermal energy, hydropower, ocean energy, solar energy and wind energy [1].

USA's Environmental Protection Agency (EPA) defines Clean Energy as including *"renewable energy, energy efficiency and efficient combined heat and power"* [2]. Though Green Energy as a concept is not defined by EPA, the term 'Green Power' is defined as a subset of Clean Energy [3]. Based on the above, it is safe to assume that defining these terms is quite ambiguous, especially for those that have no special experience in the subject.

But how and in what volumes do researchers use these two terms? A search in the Scopus database shows that the number of documents containing the term 'Clean Energy' in the title is significantly higher than the ones containing 'Green Energy'. Table 1 consists of the two terms' total number of documents and their combinations in "Article Title" and "Article Title -Abstract- Keywords" as search fields until March 2016, and Table 2 consists of the number of documents for each year from 2007 to 2015 for the same combinations. It is evident that

the academic community uses the term 'Clean Energy' more often.

**Table 1.** Scopus Total Number of Documents in Clean and Green Energy until March 2016

| Search Term | 2016 | 2015 | 2014 | 2013 | 2012 | 2011 | 2010 | 2009 | 2008 | 2007 | Field |
|---|---|---|---|---|---|---|---|---|---|---|---|
| Clean Energy | 904 | 893 | 815 | 721 | 641 | 529 | 425 | 367 | 317 | 271 | T |
| Green Energy | 630 | 624 | 555 | 461 | 382 | 302 | 247 | 195 | 156 | 123 | T |
| Clean Energy + Green Energy | 85 | 83 | 69 | 59 | 47 | 39 | 31 | 27 | 19 | 15 | TAK |
| Clean Energy + Green Energy | 0 | 0 | 0 | 0 | 0 | 0 | 0 | 0 | 0 | 0 | T |
| Green + Clean + Energy | 30 | 27 | 24 | 19 | 13 | 12 | 9 | 7 | 3 | 3 | T |
| Green +Clean + Energy | 1785 | 1754 | 1568 | 1364 | 1206 | 1011 | 858 | 701 | 547 | 423 | TAK |

T: Title, TAK: Title Abstract Keywords

**Table 2.** Scopus Number of Documents in Clean and Green Energy from 2007 to 2015

| Search Term | 2015 | 2014 | 2013 | 2012 | 2011 | 2010 | 2009 | 2008 | 2007 | Field |
|---|---|---|---|---|---|---|---|---|---|---|
| Clean Energy | 79 | 95 | 80 | 112 | 104 | 58 | 50 | 46 | 43 | T |
| Green Energy | 72 | 93 | 79 | 80 | 55 | 52 | 39 | 33 | 36 | T |
| Clean Energy + Green Energy | 15 | 10 | 12 | 8 | 8 | 4 | 8 | 4 | 1 | TAK |
| Clean Energy + Green Energy | 0 | 0 | 0 | 0 | 0 | 0 | 0 | 0 | 0 | T |
| Green + Clean + Energy | 3 | 5 | 6 | 1 | 3 | 2 | 4 | 0 | 1 | T |
| Green +Clean + Energy | 195 | 207 | 158 | 195 | 153 | 157 | 154 | 124 | 97 | TAK |

T: Title, TAK: Title Abstract Keywords

As definitions seem to differ, is the respective term attributed to the more suitable meaning? Why do people use the term 'Green Energy' when referring to 'Renewable Energy'? Is 'Clean Energy' the correct term? Keramitsoglou et al. [4] argue that the term 'Clean' is better than 'Green' when describing Renewable Energy Sources (RES).

As the interest in Renewable Energy is growing, what kind of information does the public has easy

---

* To whom all correspondence should be sent:
  ktsagar@env.duth.gr

access to when searching for these terms in Google? The first result for both 'Clean Energy' and 'Green Energy' is Wikipedia's page for Renewable Energy [5]. For 'Green Energy', the second result is the section "Green Energy and Green Power" in Wikipedia's "Sustainable Energy" page [6]. In the respective Wiki pages, 'Clean Energy' is defined as *"electricity or nuclear power, that does not pollute the atmosphere when used, as opposed to coal and oil, that do"* [5], while 'Green Energy' is defined as the energy *"that can be produced in a way that protects the natural environment, for example by using wind, water, or the sun"* [6]. Do these definitions bring even more confusion over which one is used for which term?

To address these questions, and in order to examine how the public views these two terms, large amount of information is needed. Handling such volumes of data requires new innovative tools. But in what way is it possible to obtain and analyze these vast amounts of data on online behaviour? A possible answer is Big Data; characterized by the three V's: 'Volume', 'Variety', Velocity', i.e. exponentially-increasing volumes [7], wide range of datasets, and high processing speed, respectively [8]. A trending Big Data tool is Google Trends [9], becoming all the more popular in academic research in several fields, such as medicine [10-11], economics and finance [12-14], politics [15-16], behaviour [17-19], and the environment [20-21].

We aim at quantifying and analyzing the public's online interest in the US and Australia in Clean and Green Energy, using data from Google Trends. Following this introduction, the rest of the paper is structured as follows: the next section covers the data collection and methodology, followed by the results and discussion of our analysis, and, finally, the overall conclusions are presented.

## DATA AND METHOD

We analyze the normalized in the 'Clean Energy' and 'Green Energy' hits data provided by Google Trends in the US and Australia from 2007 to 2015; search volumes before 2007 are not large enough to be evaluated.

In our initial search, we observed that Australia was the only major English-speaking country where Google hits were more in 'Clean Energy' than 'Green Energy'. We chose USA to perform a comparative analysis, as they perform similarly in economic, social, and environmental issues.

Google Trends' data are downloaded online in '.csv' format and are normalized over the selected

period: *"each data point is divided by the total searches of the geography and time range it represents, to compare relative popularity. The resulting numbers are then scaled to a range of 0 to 100"* [22].

For our search, Google Trends provide weekly data for the two terms, normalized over the selected period. We denote $C_{t_i}$ and $G_{t_i}$ as the weekly hits of the downloaded Google Trends' data for the search terms 'Clean Energy' and 'Green Energy' of the *i*-th week, respectively. For each week of our data, we percentize the hits in the two terms, and define $C_{t_{pi}}$ and $G_{t_{pi}}$ as the percentized weekly values of the normalized 'Clean Energy' and 'Green Energy' searches of the *i*-th week, respectively, with $C_{t_{pi}}+G_{t_{pi}}=1$ for each week. The percentized values are calculated using Equations (1) and (2).

$$C_{t_{pi}} = \frac{C_{t_i}}{C_{t_i}+G_{t_i}} \tag{1}$$

$$G_{t_{pi}} = \frac{G_{t_i}}{C_{t_i}+G_{t_i}} \tag{2}$$

For each year, we calculate the average of the weekly percentized hits for USA and Australia. Furthermore, we compare how the two countries perform in terms of production and use of Renewable Energy, in order to determine which term is used the most in the country performing better in Renewable Energy consumption. In addition, we examine if a relation exists between the number of documents in Scopus containing the terms 'Clean Energy' and 'Green Energy' in their titles and their affiliations, and the searches in Google for 'Clean Energy' and 'Green Energy' from 2007 to 2015.

## RESULTS AND DISCUSSION

The first step is to examine how the Worldwide trend is changing in the use of the terms 'Clean Energy' and 'Green Energy'. Over the period 2007-2015, we see that the searches for the term 'Green Energy' are constantly and with significant difference above the ones for the term 'Clean Energy' (Fig.1). The weekly ratios of the 'Clean Energy' over the 'Green Energy' searches are always below the value '1', showing that search volumes for 'Clean Energy' are at no point above the ones for 'Green Energy' over the examined period. What is observed is that there are two peaks in 2009 and 2011 with a ratio over 0.8, meaning

that at those specific times, the use of the term 'Clean Energy' showed a sudden, but short-in-time, boost (Fig.2).

Overall, we observe that the internet users worldwide search for the term 'Green Energy' in significant higher volumes than the term 'Clean Energy', which is in contrast to the scientific community, as shown in Table 1, i.e. the published papers containing the term 'Clean Energy' in their title over the last 30 years are about 40% more than the ones containing 'Green Energy'. Furthermore, we observe a periodic decrease in searches for both terms during Christmas vacations, which is an expected finding.
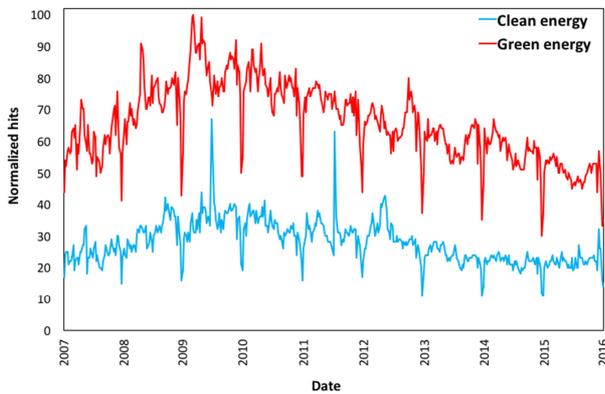


**Fig.1.** Worldwide Hits in Clean & Green Energy
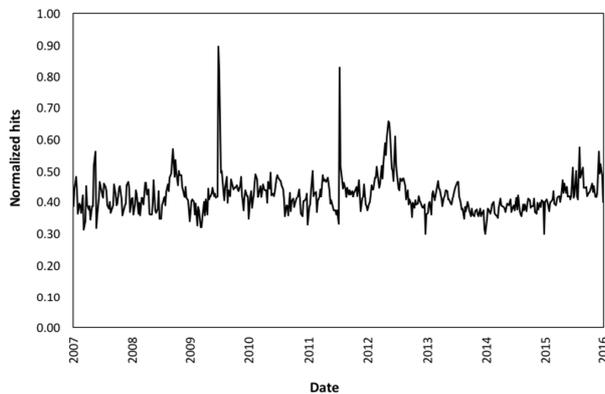


**Fig.2.** 'Clean Energy' per 'Green Energy' hits Worldwide

We proceed to analyze the online interest in Clean Energy and Green Energy in the US and Australia; Figures 3 and 4, respectively. In Google Trends, we select the period from January 2007 to December 2015 and search for the weekly hits in the terms 'Clean Energy' and 'Green Energy'.

For the US (Fig.3), the term that is mostly used is 'Green Energy'. In Australia, though up to 2010 the term 'Green Energy' was used more than

'Clean Energy', there is a shift in volumes (Fig.4), that reverses the percentages of the hits of 2009 and 2012. Up to this point, i.e. March 2016, the term 'Clean Energy' is searched for more in Google than 'Green Energy' in Australia.
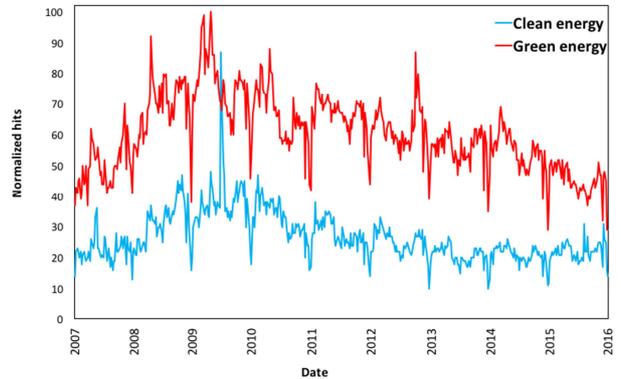


**Fig.3.** Hits in "Clean Energy" & "Green Energy" in USA
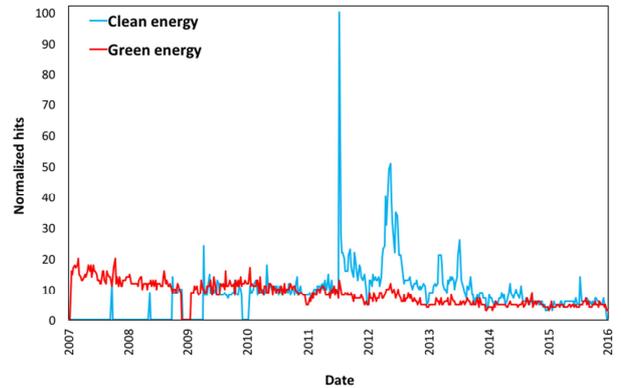


**Fig.4.** Hits in "Clean Energy" & "Green Energy" in Australia

Fig.5 and Fig.6 consist of the ratios of the 'Clean Energy' over 'Green Energy' hits in the US and Australia, respectively.
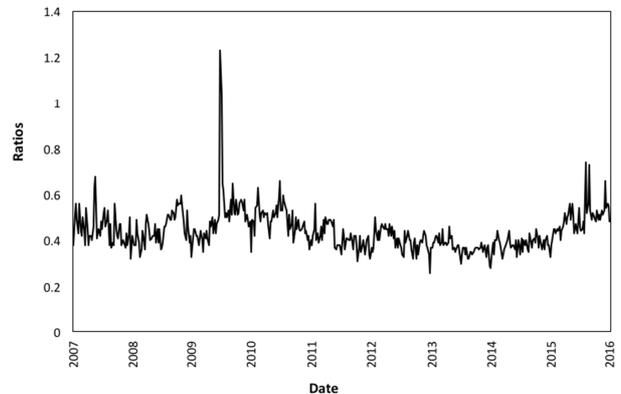


**Fig.5.** 'Clean Energy' per 'Green Energy' hits in USA
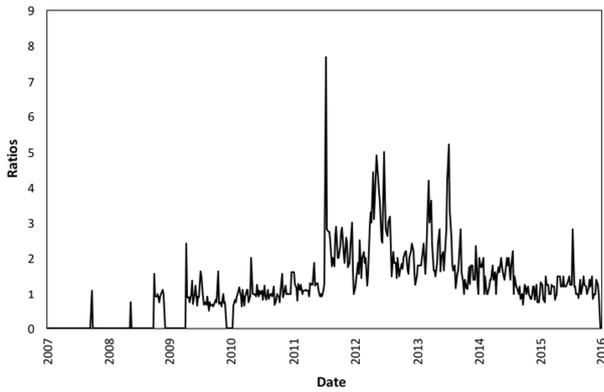
**Fig.6.** 'Clean Energy' per 'Green Energy' hits in Australia

In the case of the US, there is only one peak in 2009 with values above '1', for a two-week period (June 21th to July 4th), showing that the hits in 'Clean Energy' are over the ones in 'Green Energy'. Apart from this, all other weeks from 2007 to 2015 show that 'Green Energy' is searched for significantly more than 'Clean Energy'.

The analysis of the peaks is significant, as they could be attributed to important national or international incidents. We observe that the peak in the hits in the term 'Clean Energy' in the US in 2009 (Fig.5) influences the worldwide recording in the terms' hits. Google Trends can be useful in examining the reasons of this boost.

We see in the 'Region' field in Google Trends that the most searches occur in 3 countries, i.e. Australia (with a 100 score), USA (with a 74 score) and Canada (with a score of 50). There is a boost in the term's hits with the top searches in the 'Related Searches' field including *'clean energy act'* (100 score), *'American clean energy'* (90 score), *'clean energy power'* (50 score), *'green energy'* (45 score), *'clean energy council'* (35 score), and *'clean energy fund'* (35 score), suggesting that the aforementioned boost is attributed to the 'American Clean Energy and Security Act' of 2009.

In Australia, all ratios after 2010 are above '1', showing that the hits in 'Clean Energy' are more than the hits in 'Green Energy' at all times from 2010 to 2015.

Similarly, there is a peak in Australia in 2011 in 'Clean Energy'. An in-depth worldwide search for this year shows that the countries with the most hits on the term, in the 'Region' field in Google Trends, are Australia (100 score), and, with lower contribution, USA (26 score) and Canada (24 score). The top searches in the 'Related Searches' field include: *'clean energy council'* (100 score),

that could be attributed to the 'Clean Energy Council' in Australia, *'clean energy solar'* (85 score), *'clean renewable energy'* (60 score), *'clean energy future'* (55 score), *'clean green energy'* (55 score), *'green energy'* (55 score), and *'clean energy act'* (40).

Table 3 consists of the yearly averages of the weekly percentized hits in 'Clean Energy' and 'Green Energy' in the US, Australia and Worldwide from 2007 to 2015.

**Table 3.** Yearly Averages of the Percentized Hits: 'Clean Energy' & 'Green Energy' Hits

| | Worldwide | | USA | | Australia | |
|---|---|---|---|---|---|---|
| Year | Clean(%) | Green(%) | Clean(%) | Green(%) | Clean(%) | Green(%) |
| 2007 | 28.90 | 71.10 | 30.96 | 69.04 | 1.00 | 95.15 |
| 2008 | 29.68 | 70.32 | 30.97 | 69.03 | 10.41 | 79.97 |
| 2009 | 29.96 | 70.04 | 33.28 | 66.72 | 30.23 | 65.93 |
| 2010 | 29.67 | 70.33 | 32.87 | 67.13 | 48.69 | 51.31 |
| 2011 | 30.11 | 69.89 | 28.98 | 71.02 | 61.17 | 38.83 |
| 2012 | 31.19 | 68.81 | 28.53 | 71.47 | 68.38 | 31.62 |
| 2013 | 28.29 | 71.71 | 26.96 | 73.04 | 65.47 | 34.53 |
| 2014 | 27.56 | 72.44 | 27.68 | 72.32 | 56.18 | 43.82 |
| 2015 | 30.44 | 69.56 | 33.12 | 66.88 | 52.37 | 47.63 |

We observe that USA closely follows the percentages of the Worldwide trend, with the hits in 'Green Energy' being above the ones in 'Clean Energy' with a percentage around 70% for all examined years. Australia, though starting with a percentage of 1% in 2007 for the 'Clean Energy' hits, interest in this term rises continuously till the peak in 2012, with almost reversed percentages of the hits in 'Clean Energy' over the ones in 'Green Energy'. Hits in 'Clean Energy' start declining afterwards, with a percentage of 52.37% in 2015. From 2010 to 2015, the average online interest in Australia in 'Clean Energy' is 58.71%, while in 'Green Energy' it is 41.29%.

Fig.7 consists of the chart pies of the Google Trends' hits in 'Clean Energy' and 'Green Energy' compared to the Scopus' publications with the two terms in their titles from 2207 to 2015. While in the scientific community the term 'Clean Energy' is used in larger volumes (55%) compared to 'Clean Energy' (45%), the public prefers the term 'Green Energy' (70%) over 'Clean Energy' (30%), with statistically significant difference ($Z$=3.576, $p$<0.001).



**Fig.7.** Google Trends' hits vs. Scopus Publications terms for 'Green Energy' and 'Clean Energy'

251

A possible reason for the difference between Google Trends (public) and Scopus (scientific community) is the way that RES are communicated to the general public by the media, politicians, and other organizations, private or public. Since 'green' is mostly a 'folksy' word for the clean environment and all drivers related to it (e.g. green funds, green economy, green development etc), it is generally more 'trendy'. On the other hand, scientists and engineers are more orthological on average, thus refer to energy with more real or clear adjectives. In sense, energy is not 'green'; actually it is colorless, thus the term 'clean' is more rational than the term 'green', as the former is related to the production technology rather than a color of nature.

But how do researchers from Australian and USA report energy in their publications? To address this question, we ran two *scopus* searches with the terms 'Clean energy' and 'Green energy' in the title of the published hits. We included an additional term for the affiliation of the authors to be from Australia or USA. The comparison is shown in Fig.8. Though the portion of papers published in Australia with the term 'Clean energy' in their title is considerably higher, this is not statistically significant compared to those published in USA ($X^2$=2.3943, $p$=0.1218).

What is observed is that Australia's public's interest in the two terms agrees with what the scientific community suggests, i.e. 'Clean Energy' is used in larger volumes than 'Green Energy'. This could be attributed to the overall wording that is used in the country, that could be influenced by several factors, such as important political statements or events.
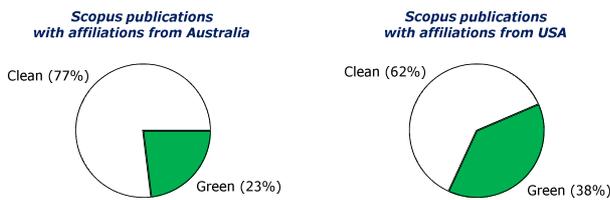


**Fig.8.** USA and Australia affiliations in Scopus Publications containing the terms 'Green Energy' and 'Clean Energy' in the title

Fig.9 shows the yearly percentages in Renewable Energy Consumption (% of total final energy consumption) in the US and Australia from 1990 to 2013 (data obtained from the World Bank [23]). Apart from the years between 2008 to 2011, Australia's percentages in Renewable Energy

consumption are higher than USA's from 1990 to 2013. A Z-test calculated per year (Fig.9) shows that Australia was better performing up to 2002. From that point on, including our selected study period i.e. from 2007 on, we cannot claim statistically significant better performance of one over the other country.
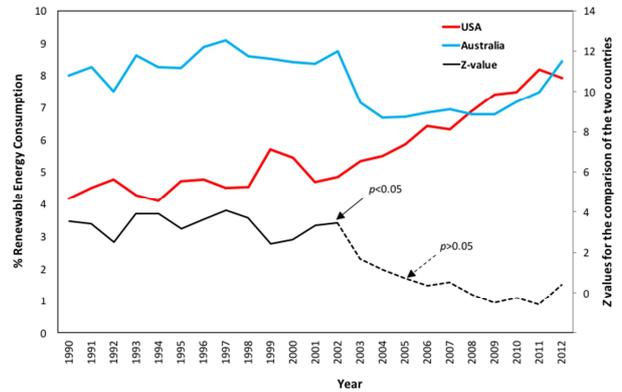


**Fig.9.** Yearly Percentages of Renewable Energy Consumption from 1990 to 2013 in USA and Australia

Based on the above, it is evident that both countries are actively concerned about environmental issues and promote the production and use of Renewable Energy. In the US, apart from the Environmental Protection Agency that is responsible for all environmental issues and legislation, there are the 'National Renewable Energy Laboratory' [24] and the 'Department of Energy' [25]. The most important Renewable Energy policy is the "US Climate Action Plan" (2013) [26]. In Australia, though the Department of the Environment by the Australian Government is the main agency responsible for environmental issues, there is also the 'Australian Renewable Energy Agency' [27]. The key Renewable Energy policies in force are the 'Australian Renewable Energy Agency' (2012) and the 'Renewable Energy Target' (2010) [26]. A key policy that has ended is the 'Clean Energy Future Plan' (2012) [26].

## CONCLUSIONS

This study aimed at examining the online interest in the terms 'Clean Energy' and 'Green Energy' for the US and Australia from 2007-2015. Using data from Google Trends, we quantify the normalized search volumes over the selected period and explore each country's selection in terminology for Renewable Energy. We find that, though USA follows the worldwide trend, i.e. uses the term 'Green Energy' in higher volumes, Australia shows

an increasing use of the term 'Clean Energy' from 2007 to 2010, and the percentages in 'Clean Energy' searches are dominant over the 'Green Energy' ones from 2010-2015, with significant difference.

Comparing the performances of the two countries in terms of Renewable Energy, as long as the implementation of policies and projects are concerned, it is evident that both countries are actively concerned for and promote Renewable Energy. This could be attributed to the fact that USA and Australia have been integrating all the more Renewable Energy issues in their way of governance. In addition, we observed that the scientific community uses the term 'Clean Energy' significantly more than 'Green Energy' in terms of containing these terms in the title of the published papers.

Google Trends as a tool has been shown to be useful and effective in assisting us to elaborate on the different use of the terms 'Clean Energy' and 'Green Energy'. This, compared to the use of these terms in published papers, shows a different approach from academics compared to the public, thus contributing to the discussion of redefining Renewable Energy, as 'Clean Energy' could be a more suitable term for describing it.

This paper provides ground for further research on redefining Renewable Energy, as the same methodology could be applied to other countries of interest. Further research could be especially applied to developing countries, so as to examine the relation between the public's change in online interest in Renewable Energy with other economic and social factors, like per capita income, industry levels, human development, social progress, and environmental performance.

## REFERENCES

1  Renewable Energy Definition. ARENA http://arena.gov.au/about-renewable-energy/ Accessed on March 3rd, 2016.

2  Clean Energy Definition. EPA https://www.epa.gov/energy/learn-about-energy-and-environment Accessed on March 3rd, 2016.

3  Green Power Definition. EPA. http://www3.epa.gov/greenpower/gpmarket/ Accessed on March 3rd, 2016.

4  K. Keramitsoglou, R.C. Mellon, M. I. Tsagkaraki, K. P. Tsagarakis, *Renewable and Sustainable Energy Reviews,* 59, 1332, (2016).

5  Renewable Energy. Wikipedia https://en.wikipedia.org/wiki/Renewable_energy Accessed on March 3rd, 2016.

6  Green Energy and Green Power. Wikipedia. https://en.wikipedia.org/wiki/Sustainable_energy#Green_energy_and_green_power Accessed on March 3rd, 2016.

7  M. Hilbert, P. Lopez, *Science*, 332, 60, (2011).

8  C. L. Chen, C. Y. Zhang, *Information Sciences*, 275, 314, (2014).

9  Google Trends. http://www.google.com/trends Accessed on March 3rd, 2016.

10  M. W. Davidson, D. A. Haim, J. M. Radin, *Scientific Reports,* 5, (2015).

11  V. Dukic, H. F. Lopes, N. G. Polson, *Journal of the American Statistical Association,* 170, No 500, 1410, (2012).

12  Y. Carriere-Swallow, F. Labbe, *Journal of Forecasting,* 32, 289, (2013).

13  L. Kristoufek, *Scientific Reports*, 3, 2713, (2013).

14  M. Alanyali, H. S. Moat, T. Preis, *Scientific reports*, 3, 3578, (2013).

15  Polykalas, S. E., Prezerakos, G. N. & Konidaris, A. in IEEE International Symposium on Signal Processing and Information Technology, IEEE ISSPIT 2013. 69-73.

16  Polykalas, S. E. (2013). A general purpose model for future prediction based on web search data: Predicting Greek and Spanish election. 27th International Conference on Advanced Information Networking and Applications Workshops.

17  T. Preis, H. S. Moat, H. E. Stanley, *Scientific reports*, 3, 1684, (2013).

18  L. Kristoufek, *Scientific reports*, 3, 3451, (2013).

19  T. Preis, H. S. Moat, H.E. Stanley, S. R. Bishop, *Scientific Reports,* 2, 350, (2012).

20  M. L. McCallum, G. W. Bury, *Biodivers Conserv,* 22, 1355, (2013).

21  G. F. Ficetola, *Biodivers. Conserv.,* 22, No 12, 2983, (2013).

22  Google Trends (2016). Data Normalization. https://support.google.com/trends/answer/4365533 Accessed on February 8th, 2016.

23  Renewable Energy Consumption. http://data.worldbank.org/indicator/EG.FEC.RNEW.ZS Accessed on March 29th, 2016.

24  National Renewable Energy Laboratory http://www.nrel.gov

25  Department of Energy, USA. http://energy.gov

26  Countries Statistics in Total Renewable Energy. http://www.iea.org/policiesandmeasures/renewableenergy Accessed on March 3rd, 2016.

27  Australian Renewable Energy Agency, Australia. http://arena.gov.au Accessed on March 3rd, 2016

# 'Clean' vs. 'Green': redefining renewable energy (evidence from Bulgaria)

A. Mavragani[1], R. Popov[2], A. Georgiev[3,5], C. Kamenova[4], K. P. Tsagarakis[1*]

[1]*Business and Environmental Technology Economics Lab, Environmental Engineering Department, Democritus University of Thrace, Vas. Sofias 12, Xanthi, Greece*
[2]*Department of Electronics, Communications and Information Technologies, Faculty of Physics, Plovdiv University "Paisii Hilendarski", 24 Tzar Assen Str., 4000 Plovdiv, Bulgaria*
[3]*Technical University of Sofia, Plovdiv Branch, Dept. of Mechanics,25 Tsanko Diustabanov Str, 4000 Plovdiv, Bulgaria*
[4]*Secondary School "Bratia Miladinovi", 14 Todor Aleksandrov Str., 4004 Plovdiv, Bulgaria*
[5]*European Polytechnic University, Dept. of "Green Energy", 23 Kiril and Metodiy str., 2300 Pernik, Bulgaria*

Renewable Energy Sources. Are they 'Clean' or are they 'Green'? What do those with no previous or biased experience think? This study examines how the term "Renewable Energy" is viewed by primary school students in Bulgaria. For this purpose, a face-to-face survey was applied, aiming at the elicitation of the students' preferences for the naming and the colour that best represents Renewable Energy Sources. This was done with an in-class information project, followed by the completion of a questionnaire. Findings contradict what is, so far, established, i.e. that Renewable Energy Sources are 'Green' and that Renewable Energy is 'Green Energy'.

**Keywords:** clean energy, education, green energy, public awareness, renewable energy sources

## INTRODUCTION

Over the last decade, the terms 'Renewable Energy', 'Clean Energy' and 'Green Energy' are becoming all the more popular in academic research and the public. But are their definitions clear? Are 'Green Energy' and 'Clean Energy' just other terms for Renewable Energy? If this is the case, which term is more suitable to define Renewable Energy? The various different definitions that exist have led to the confusion about the meanings that each term is attributed.

For example, in the USA's Environmental Protection Agency's (EPA) website, Clean Energy is defined as including "renewable energy, energy efficiency and efficient combined heat and power" [1], suggesting that Renewable Energy is a subset of Clean Energy. Green Energy is not defined by EPA; the closest term is 'Green Power', defined as "electricity produced from solar, wind, geothermal, biogas, eligible biomass, and low-impact small hydroelectric sources"; a subset of Renewable Energy [2]. The combining of these two definitions merely suggest that Green Power is a subset of Clean Energy.

As far as the academic community is concerned, is it 'Clean Energy' or 'Green Energy' the term that is used in larger volumes? Extracting information from the Scopus database [3] from 1990 to 2016, we observe that the number of studies containing the term "Clean Energy" in their title are 901, while the ones containing the term "Green Energy" are 625. Interestingly enough, there is not one study containing both terms in the title, and only 16 containing both terms in their keywords.

In addition, there are several academic Journals with reference to Renewable, Clean, or Green Energy. For example, Springer, in its category-search field, it includes the category "Renewable and Green Energy" [4]. Table 1 consists of examples of Journals that make references to Renewable Energy, Green Energy, or Clean Energy in their titles or Aims and Scope.

The *'International Journal of Renewable Energy Research'* [8] merely equates Renewable Energy to Green Energy: *".... the various topics and technologies of renewable (green) energy resources", "Green (Renewable) Energy Sources",* while it refers to Clean Energy as a different subject: *"Sustainable and Clean Energy Issues".*

How informed is the public about subjects related to Renewable Energy? On Google, a hit on the terms 'Green Energy' or 'Clean Energy' gives Wikipedia's page on *'Renewable Energy'* [17] as the first result. In addition, the *'Green Energy Institute'* [18] states that "Our policy program and projects promote renewable energy development". These are examples indicating that Green Energy is regarded as having the same meaning as Renewable Energy. Could it be that these three terms are regarded as synonyms by the public?

* To whom all correspondence should be sent:
ktsagar@env.duth.gr

**Table 1.** Journals Referencing to Renewable, Green or Clean Energy

| Journal | With reference to: | | |
|---|---|---|---|
| | **Renewable Energy** | **Green Energy** | **Clean Energy** |
| Renewable Energy [5] | ✓ | ✗ | ✗ |
| International Journal of Green Energy [6] | ✗ | ✓ | ✗ |
| Journal of Modern Power Systems and Clean Energy [7] | ✗ | ✗ | ✓ |
| International Journal of Renewable Energy Research [8] | ✓ | ✓ | ✓ |
| International Journal of Sustainable Energy [9] | ✓ | ✗ | ✗ |
| International Energy Journal [10] | ✓ | ✗ | ✗ |
| Journal of Technology Innovations in Renewable Energy | ✓ | ✗ | ✗ |
| International Journal of Smart Grid and Clean Energy [12] | ✗ | ✗ | ✓ |
| Journal of Clean Energy Technologies [13] | ✗ | ✗ | ✓ |
| International Journal of Sustainable and Green Energy [14] | ✓ | ✓ | ✗ |
| Current Sustainable/Renewable Energy Reports [15] | ✓ | ✗ | ✗ |
| Renewable and Sustainable Energy Reviews [16] | ✓ | ✗ | ✗ |

On the contrary, Google's page on *'Renewable Energy'* [19] makes no reference to the term 'Green Energy'. It only uses the term 'Green Power'; the same as EPA. The page's section in 'Investing in a Clean Energy Future Investments', contains the following sentences: *"We're investing in clean energy"* and *"... agreements to fund nearly $2.5 billion in renewable energy projects"*. Is Google equating Clean Energy to Renewable Energy?

As defining Renewable Energy is a quite complex issue, we aim at examining the term and colour preference of primary school students, as they are less biased by previous formal or informal education. Keramitzoglou et al. [20] conducted face-to-face interviews with students and adults in Greece, in order for them to choose their preference in the naming and colour that best represent Renewable Energy Sources (RES). We conduct a similar experiment in Plovdiv, Bulgaria, over a sample of 203 primary school students, aged 7-10, with face-to-face interviews and the completion of questionnaires.

We focus on introducing a method that could be applied to other regions and countries, so as to extract information on how the untrained eye views the subject, aiming at redefining Renewable Energy. What is important is the integration of the analysis of behavioural patterns in environmental issues, so as to examine the ways with which resources could be better managed. The rest of the paper is structured as follows: Section 2 consists of the detailed method of the data collection, Section 3 consists of the results and discussion of our analysis, and Section 4 of the overall conclusions and further research suggestions.

## DATA AND METHOD

In this section, the education system in Bulgaria is presented, followed by the description of the school where the survey took place, and the discussion of the questionnaire used to conduct our research. We describe how we reach an answer to the hypothesis that the choice of the colour Green for best representing RES results from the way energy is represented in nature textbooks, in addition to education in and out of school.

### *Curriculum*

School education in Bulgaria is mandatory for all children aged between 7 and 16. Grades 1 to 4 form the primary school education, with pupils of ages from 7 to 10. One of the main subjects taught in Bulgarian Primary Schools is 'Natural sciences and ecology', with energy related subjects appearing for the first time at the end of the first semester in the 3rd grade in the course called "Man and Nature" [21]. The students are taught the basics in water and air purity, as well as introductory references to sources of electricity. In the 4th grade, the subject "Bodies and substances" covers several topics, such as types of energy, energy sources and clean water protection [22].

### *Sample*

The students participating in the face-to-face interviews and the completion of the questionnaire are all from 1st to 4th grade; 7 to 10 years old. The survey was conducted at the Secondary School Bratia Miladinovi in Plovdiv, Bulgaria, established in 1935 and covering the school districts "Ear" and

"Brickworks" in the Ist urban area Kuchuk-Paris. The school area consists of two well-preserved and maintained school buildings, with two computer laboratories with internet access, and a well-established library. Sufficient infrastructure is available, so as to allow one-shift learning mode. "Brothers Miladinovi" is the only school in Plovdiv that implements the project "Inclusive Education" BG051PO00-4.1.07, funded by the European Social Fund of The European Union, with its overall objective being to provide a supportive environment for opening up education and providing equal access, aiming at detecting learning difficulties, promoting successful socialization and integration, and quality education tailored to the individual students' needs.

### *Questionnaire*

The school teacher conducting the survey was given a 4-Step instruction quide on how to brief the students before the interviews. The teacher had strict instructions as not to make any reference to pollution or clean energy throughout the process. The steps are as follows:

1. Explaining of the definition/ notion of Energy. For example, humans, in order to move, they need energy, which is covered by daily intakes of food.

2. What do electrical equipment, such as lamps, need in order to function? Electricity. How is it produced in Bulgaria?

3. If we constantly consume our sources from which electricity is produced, are they ever going to end? Explaining of "Renewable Energy Sources" and "Non-Renewable Energy Sources".

4. Provide examples of RES. Sun, wind, waterfalls, waves, biomass, etc. Utilization technologies of RES. Solar panels, windmills, watermills etc.

The questionnaire, apart from demographics such as age, grade etc, consisted of two main questions: 1) Which of the following definitions best describes, to your opinion, «Renewable Energy Sources»?, with the options being 'Clean Energy' or 'Green Energy', and 2) Select the colour that, to your opinion, best describes «Renewable Energy Sources», with the options being a green box, a yellow one, and a white one. We prepared six variations of the questionnaire, with the order or the answers being changed, so as to avoid order bias. They were given out in the order shown in Table 2.

The teacher interviewed each student one by one, in a quite space, where the students could not communicate with one another while responding to

the questions. The interview was the first time that the terms Clean Energy and Green Energy were mentioned to the students. The above mentioned research protocol was the same as the one used by Keramitsoglou et al. [20].

**Table 2.** Variations in the order of options in the questions

| Variation | 1st Question | 2nd Question |
|---|---|---|
| I | Green - Clean | Green White Yellow |
| II | Clean - Green | White Yellow Green |
| III | Green - Clean | Yellow Green White |
| IV | Clean - Green | Green White Yellow |
| V | Green - Clean | White Yellow Green |
| VI | Clean - Green | Yellow Green White |

### RESULTS AND DISCUSSION

During the experiment, a total of 203 students participated; 46 students are in 1st grade (about 7 years old), 59 in the 2nd grade (about 8 years old), 50 in the 3rd grade (about 9 years old), and 48 in the 4th grade (about 10 years old). Out of 203, 111 were girls and 92 were boys. This experiment took place during February 2016. In all four grades, the preferred term for representing Renewable Energy is 'Clean Energy'. Fig.1 shows the percentages in the selection of 'Clean Energy' and 'Green' Energy, and the colour for the better representation of Renewable Energy per grade level.

In the 1st, 2nd and 3rd grade, 'Clean' got scores of 76%, 80% and 70%, respectively. In the 4th grade, though 'Clean' was again the students' choice, it got a score of 56%; significantly lower than the other grades ($X^2$=6.5764, $p$<0.05, if 1st to 3rd grade are compared as a group with the 4th grade). These figures complement the findings of Keramitsoglou et al. [20], showing that, for students of the same age in Greece, about 78% of the 1st and 2nd grade chose the term 'Clean' for best describing RES.

Table 3 consists of the Chi2 figures for the comparisons among grades for selecting Green as the term of choice (compared to 'clean') for naming RES. Statistical differences are not observed among students attending the 1st, 2nd and 3rd grade. On the other hand, students attending the 4th grade report statistically significant higher rates for 'Green' compared to 'Clean' as their preferred term for naming RES, compared to those attending the 1st and 2nd grade ($X^2$=4.117, $p$<0.05 and $X^2$=6.801, $p$<0.01, respectively). Students attending the 3rd grade provided responses close to the first two grades, but this was not statistically different compared to the responses of the 4th grade.
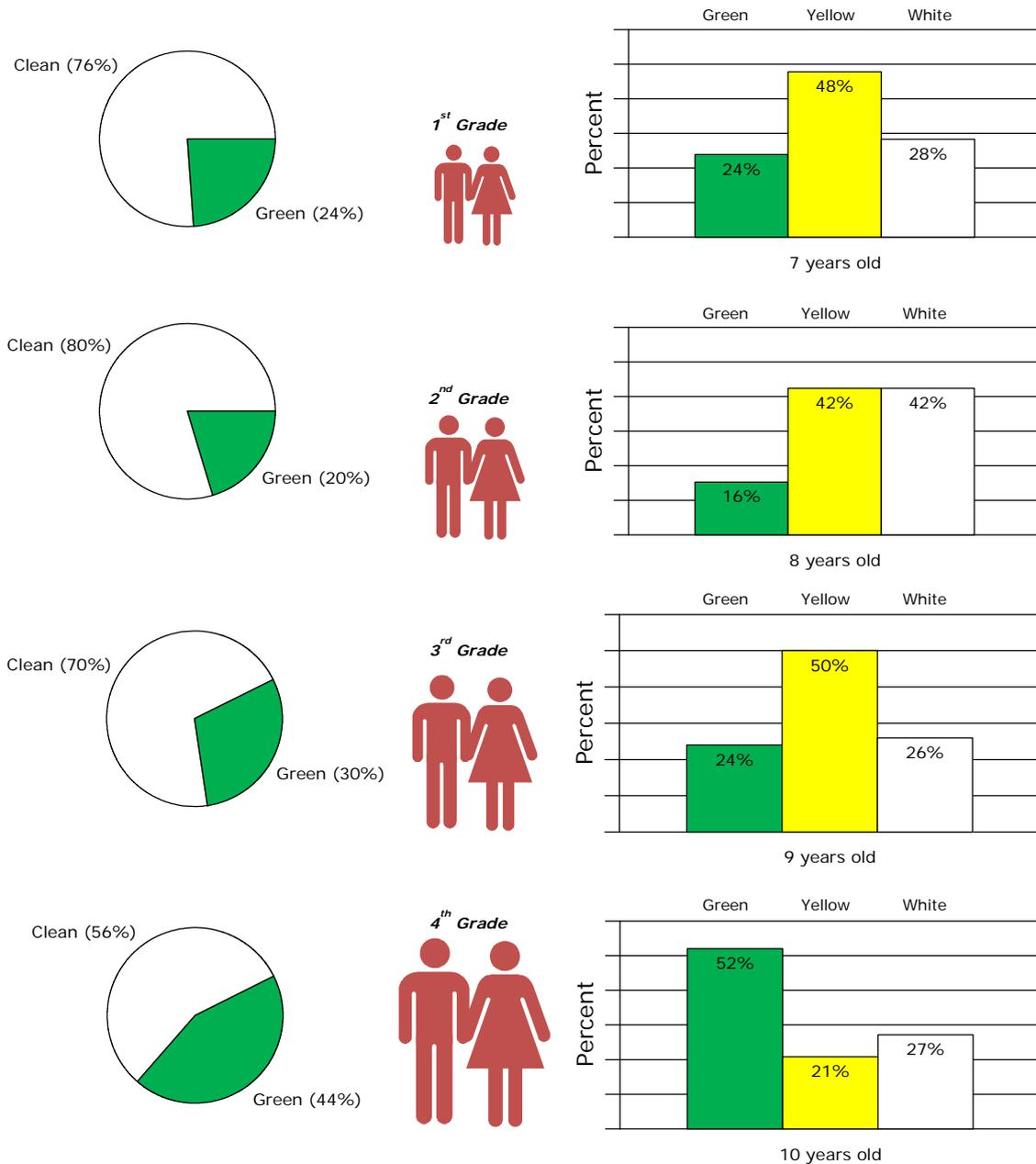
**Fig.1.** Percentages in the naming and colour selection for representing Renewable Energy per grade level

**Table 3.** Chi2 figures for selecting 'Green' for naming RES

| Grade | G1 | G2 | G3 | G4 |
|-------|------|------|------|------|
| G1 | 0 | | | |
| G2 | 0.1930 | 0 | | |
| G3 | 0.4495 | 1.3556 | 0 | |
| G4 | 4.1166* | 6.801** | 1.9923 | 0 |

*$p<0.05$, **$p<0.01$

As far as the preference in colour is concerned, in the 1st and 3rd grades 'Yellow' is the colour achieving the highest scores, with 48% and 50% respectively, with 'White' being the second choice. Yellow was also the most preferred colour in representing RES in the 1st and 2nd grade students in Greece [20]. In the 2nd grade, yellow and white each received 42%. In all three grades, 'Green' achieved the lowest scores. In the 4th grade, though, 'Green' got the highest percentage (52%), supporting our hypothesis that the choice of 'Green' for the colour best representing RES results from the way energy is represented in nature textbooks, in addition to

education in and out of school. Table 4 consists of the Chi2 figures for the comparisons among grades for selecting Green (instead of yellow or white) as the colour of choice for labelling RES.

Statistical differences are not observed among students attending the 1st, 2nd and 3rd grade about their preference in the green colour as their choice in representing RES. On the other hand, the preference of the students attending the 4th grade for 'Green' was significantly higher than those of the students attending the 1st, 2nd and 3rd grade ($X^2$=7.888, $p$<0.05, $X^2$=16.560, $p$<0.001, and $X^2$=8.219, $p$<0.01, respectively).

**Table 4.** Chi2 figures for selecting 'Green' as the colour of choice for labelling RES

| Grade | G1 | G2 | G3 | G4 |
|-------|------|---------|--------|----|
| **G1** | 0 | | | |
| **G2** | 1.2568 | 0 | | |
| **G3** | 0.0001 | 1.3309 | 0 | |
| **G4** | 7.8882* | 16.5599*** | 8.2187** | 0 |

*$p$<0.05, **$p$<0.01, ***$p$<0.001

Based on the above, we suggest that very young students with little or no exposure to the concept of Renewable Energy in Bulgaria are most likely to choose 'Clean' as the term for labelling RES and (not Green but) Yellow as the colour for best representing it. As students receive formal (followed by informal) education, their preferences start to shift, and they choose Green Energy and Green as the term for labelling and the colour for representing RES, respectively. These findings support those of Keramitzoglou et al. [20], who reached the same conclusions for students attending primary schools in Greece. While the implementation of energy education projects increase awareness in energy issues [23-24], it is important to elicit the students' preferences and adjust the findings in behavioural patterns, so as to contribute to the efficient use of RES and, consequently, natural resources.

## CONCLUSIONS

This study examined the preferences in naming and colour for the best representation of RES of primary school students, by conducting face-to-face interviews to 203 primary school students aged 7-10, in Plovdiv, Bulgaria. We aimed at introducing the methodology to be also applied in other regions and countries, so as to contribute to the discussion of defining Renewable Energy as 'Clean' instead of 'Green'.

The results show that, for describing Renewable Energy, the preferred term is 'Clean' for all grades, but with significantly lower percentage in the 4th grade. In selecting the colour that best describes Renewable Energy, in the first three grades the first choice was yellow, followed by white, but in the 4th grade the students selected Green with significantly higher percentages than the other three grades.

Overall, though 'Green' seems to be the term and colour that most select as the one describing RES, we see evidence that, for children not yet exposed to formal or informal education on the subject, the term 'Clean Energy' is the first choice for describing Renewable Energy, while for the colour, yellow and white are clearly the choice for representing RES. Similar research on the subject should be applied to other regions, so as to further explore the name and colour that is the most suitable to represent Renewable Energy.

## REFERENCES

1 Clean Energy Definition. Environmental Protection Agency. https://www.epa.gov/energy/learn-about-energy-and-environment Accessed on March 14th, 2016.
2 Green Power Definition. Environmental Protection Agency. http://www3.epa.gov/greenpower/gpmarket/ Accessed on March 14th, 2016.
3 Scopus database http://www.scopus.com Accessed on March 14th, 2016.
4 Renewable and Green Energy http://www.springer.com/energy/renewable+and+green+energy?SGWID=0-1721214-12-812104-0 Accessed on March 14th, 2016.
5 Renewable Energy http://www.journals.elsevier.com/renewable-energy/ Accessed on March 14th, 2016.
6 International Journal of Green Energy http://www.tandfonline.com/toc/ljge20/current Accessed on March 14th, 2016.
7 Journal of Modern Power Systems and Clean Energy http://www.springer.com/energy/systems%2C+storage+and+harvesting/journal/40565 Accessed on March 14th, 2016.
8 International Journal of Renewable Energy Research http://www.ijrer.org/ijrer/index.php/ijrer Accessed on March 14th, 2016.
9 International Journal of Sustainable Energy http://www.tandfonline.com/action/journalInformation

?show=aimsScope&journalCode=gsol20#.VuWyxMe YVFI Accessed on March 14th, 2016.

10  International Energy Journal http://www.rericjournal.ait.ac.th/index.php/reric Accessed on March 14th, 2016.

11  Journal of Technology Innovations in Renewable Energy. http://www.lifescienceglobal.com/journals/journal-of-technology-innovations-in-renewable-energy Accessed on March 14th, 2016.

12  International Journal of Smart Grid and Clean Energy http://www.ijsgce.com Accessed on March 14th, 2016.

13  Journal of Clean Energy Technologies http://www.jocet.org Accessed on March 14th, 2016.

14  International Journal of Sustainable and Green Energy. www.sciencepublishinggroup.com/journal/archive.aspx?journalid=169&issueid=-1 Accessed on March 14th, 2016.

15  Current Sustainable/ Renewable Energy Reports. http://www.springer.com/energy/renewable+and+green+energy/journal/40518 Accessed on March 14th, 2016.

16  Renewable and Sustainable Energy Reviews http://www.journals.elsevier.com/renewable-and-sustainable-energy-reviews/ Accessed on March 21st, 2016.

17  Renewable Energy. Wikipedia https://en.wikipedia.org/wiki/Renewable_energy Accessed on March 14th, 2016.

18  Green Energy Institute https://law.lclark.edu/centers/green_energy_institute/ Accessed on March 14th, 2016.

19  Renewable Energy, Google. https://www.google.com/green/energy/ Accessed on March 14th, 2016.

20  K. Keramitsoglou, R.C., Mellon, M.I. Tsagkaraki, K.P. Tsagarakis, Renewable and Sustainable Energy Reviews, **59**, 1332-1337, (2013).

21  3rd Grade Textbook in 'Man and Nature', Bulgaria. http://www.ciela.com/chovek-t-i-prirodata-za-3-klas-najdenova-todorova.html Accessed on March 14th, 2016.

22  4th Grade Textbook in 'Bodies and substances', Bulgaria. http://www.e-uchebnik.bg/book/viewBook/29 Accessed on March 14th, 2016.

23  N. Zografakis, A.N. Menegaki, K.P. Tsagarakis, Energy Policy, **36**, 3216-3222 (2008)

24  D. Çelikler, Renewable Energy, **60**, 343-348, (2013).

# CFD study of harmful substances production in coal-fired power plant of Kazakhstan

A. S. Askarova[1], E. I. Heierle[2], S. A. Bolegenova[3], R. Manatbayev[3*], V. Ju. Maximov[1], S. A. Bolegenova[3], M. T. Beketayeva[1], A. B. Yergaliyeva[3]

[1] *SRI of Experimental and theoretical physic, Al-Farabi Kazakh National University, 71, al-Farabi ave., 050040, Almaty, Kazakhstan*
[2] *Institute of Energy and Process Systems Engineering, 35, Franz-Liszt-Strasse, D-38106 Braunschweig, Germany*
[3] *Faculty of Physics and Technology, Al-Farabi Kazakh National University, 71, al-Farabi ave., 050040, Almaty, Kazakhstan*

In this paper a study of physical and technological processes that occur during combustion of high-dust fuel in the combustion chamber of Kazakhstan's boiler unit. Computational experiments were obtained the distribution of concentrations of harmful dust and gas emissions during the combustion of high-ash coal in the combustion chamber. The main purpose of the present work is to study different possibilities to improve the performance of the coal-fired furnace. Different influences which lead to decrease in pollutant emissions have been analysed.

**Keywords:** coal-dust torch, combustion, thermal power plant, heat and mass transfer, pollution

## INTRODUCTION

It is fair to say that the ability to use fire is an important factor in ushering the dawn of civilization. Today our dependence on the service of fire is almost total, from heating and lighting our homes to powering the various modes of transportation vehicles. Useful as it is, fire can also be menacing and sometimes deadly. Wild land and urban fires cause tremendous loss of property and lives every year; the noxious pollutants from automotive and industrial power plants poison the very environment in which we live; and the use of chemical weapons continues to be an agent of destruction with ever greater efficiency. Combustion is certainly one branch of science that affects almost every aspect of human activities [1].

Heat transfer problems pertaining to the combustion in industrial furnaces are of great importance to the engineering designer of boilers and steam generators. In most industrial flame applications, the achievement of high heat transfer rates is a main target and is desirable.

Pulverized coal combustion is the most commonly used method in the coal-fired power plants and it will continue to be important way for electricity production due to large stocks of coal worldwide. Since coal is a natural resource that depends on many factors, parameters and conditions it has variable properties and composition.

Pulverized coal combustion in industrial furnaces is a quite complex process and involves many physical and chemical sub-processes. Hence a proper description for the dynamic, thermal and reactive behaviors of pulverized air-coal flows is essential for a better prediction of combustion and pollutant emission formation in a coal-fired furnace.

Using of different types of coals combined with some modifications of the combustion furnaces and equipment can be a cost-effective way of improving combustion behavior and lowering pollutant emissions from power plant. Comprehensive modeling of pulverized coal combustion has become a commonly used tool for designing and optimization.

The purpose of the presented research was to investigate numerically the characteristics of reacting flows and heat transfer due to oil and coal turbulent combustion in large-scale boiler furnaces.

## EXPERIMENTAL DETAILS

### Description of furnace

The computer simulation is performed for furnace chambers of Kazakhstan Power Plants. The case-study boiler PK-39 with swirl burners in boxer-firing system is installed at Aksu Thermal Power Plant (Fig.1). The unit generates a nominal steam capacity of 475 t/h and electrical output of 160 MWe. Twelve swirl burners are placed in two layers: three in each layer on the front and rear wall of the furnace. The nominal-load operating

conditions (all burners operating) of the furnace are given in Table 1. Existing distribution of coal particle sizes is represented by using five different size classes of pulverized coal.

**Table 1.** Summary of the furnace operation parameters

| Steam generating capacity, | Total air, | Coal flow rate, | Excess air | Load, |
|---|---|---|---|---|
| t/h | kg/s | kg/s | | MWe |
| 475 | 157 | 24.32 | 1.18 | 390 |
| Coal composition | | | | | | |

| W | Ash | C | H | O | N | S |
|---|---|---|---|---|---|---|
| 0.07 | 0.41 | 0.79 | 0.05 | 0.13 | 0.015 | 0.015 |
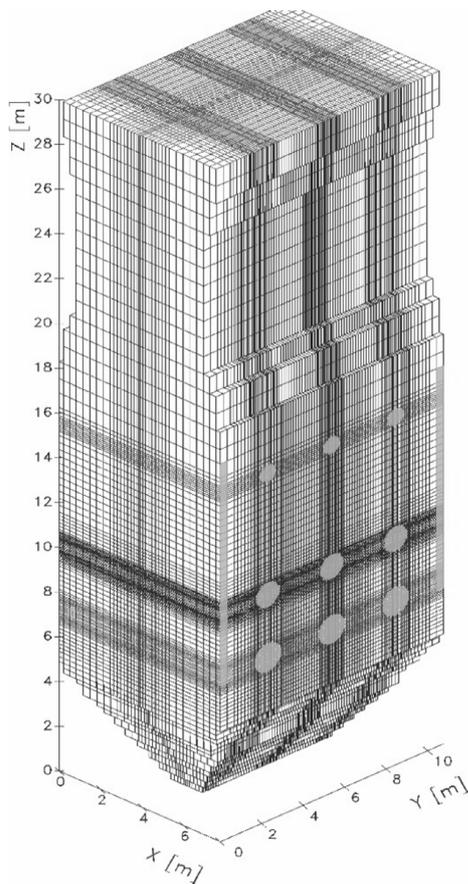


**Fig.1.** Scheme of the furnace PK-39

*Mathematical model*

Program FLOREAN is based on the numerical solution of the Reynolds averaged balance equations for mass, species, energy and momentum [1-3]. It predicts gas flows, species concentrations, temperature fields due to combustion, radiation and convective heat transfer and the pollutant formation and destruction in furnace chambers.

The transport by diffusion of each value is calculated by an effective exchange coefficient, based on the effective viscosity and the empirical Prandtl-Schmidt number. The mean flow equations are closed by the k-ε turbulence model.

The changes of the concentrations of the flue gas components and the fuel due to the combustion are taken into account in the source/sink terms by appropriate sub-models. In addition, in the source/sink term the heat balance takes into account the energy release due to the combustion reactions and the significant heat transfer due to radiation using a six flux radiation model by Lockwood etc. [4]. The energy balance equation is written in terms of the enthalpy.

In many practical combustion processes the fuels are liquids or solids, which have to be evaporated, and/or gasified usually prior combustion. The additional consideration of a phase change leads to more complex heterogeneous combustion processes than combustion processes in the gas phase.

*Coal Combustion Model*

The coal particle size distribution is modeled through different mean diameters. During the combustion process the coal particle diameters changes. The change depends on the coal type e. g. swelling coal. At the end ash and unburnt carbon is left.

The coal combustion model is divided into five submodels for drying, pyrolysis, combustion of volatiles, carbon monoxide and residual char. The drying model considers the heat necessary for evaporating the moisture content. The pyrolysis model is usually a first order reaction model; more detailed models are available. Three different reactions between char and flue gas are considered. The oxidation of the char to carbon monoxide or carbon dioxide and the reduction of carbon dioxide at the surface of the char particle to carbon monoxide. The model incorporates the different effects of oxygen and carbon dioxide diffusion to the particle surface and in the pores and the kinetics of the chemical reaction at the surface as a function of temperature and particle diameter. The Eddy Dissipation Model according to Magnusson et al. [5] is used to predict the combustion of the volatiles and the carbon monoxide formed during char combustion. Gaseous fuels are treated like volatiles.

In the case of coal combustion the two phase flow can be treated using the Eulerian or the Lagrangian approach to calculate the flow pattern of the solid phase.

*Fuel Oil Combustion Model*

Three phases of droplet combustion are considered:

Heating phase: heat from the gas phase causes the droplet surface to heat up. Much of the energy

is convected into the droplet until the entire droplet is approaching the boiling temperature.

Fuel evaporation stage: Fuel evaporates into the gas phase and a combustible mixture is formed; the droplet diameter decreases in time. The droplet evaporation model includes heat and mass transfer. Usually the continuous gas phase is at a higher temperature than the fuel droplets.

Combustion phase. The oil combustion model uses the Eddy Dissipation Model for the combustion of evaporated combustible species in the gas phase. The changes of the concentrations of the flue gas components and the fuel due to the combustion are taken into account in the source/sink terms.

### NOx formation model

Within the combustion of fossil fuels, nitric oxide is built up through different reaction paths. The main reactions are the oxidation of molecular nitrogen (thermal NO–formation) and the oxidation of the fuel bounded nitrogen (fuel–NO).

Detailed kinetic models for predicting fuel NO with 29 elementary reactions are used, for example, by Lendt [6]. In the case of three–dimensional simulation, such models consume too much CPU–time. Therefore global mechanisms are used. For simulation of nitrogen oxides formation the Zel'dovich mechanism for thermal $NO_x$, De Soete [7] or the Mitchell-Tarbell [8] mechanisms for fuel $NO_x$ formation are applied.

Depending on the coal type, fuel-bound nitrogen is released during pyrolysis and char burnout. It is supposed that the main gas species containing nitrogen produced during coal combustion are HCN and $NH_3$. In some modeling approach, volatile and char nitrogen is released only as HCN proportional to the char burnout rate [9-13].

### De Soete mechanism

Recognizing the importance of HCN as a precursor to the subsequent nitrogen compound intermediates, De Soete correlated the rate of NO formation and decay with a pair of competitive parallel reactions, each first order in HCN and $NH_3$. HCN and $NH_3$ are competitively oxidized and reduced according to the following generic scheme involving four reactions:

$$R_1 = 1.0 \cdot 10^{10} \cdot X_{HCN} \cdot X_{O_2}^o \cdot \exp\left(\frac{-33732.5}{T}\right),$$

$$R_2 = 4.0 \cdot 10^6 \cdot X_{NH_3} \cdot X_{O_2}^o \cdot \exp\left(\frac{-16111.0}{T}\right),$$

$$R_3 = -3.0 \cdot 10^{12} \cdot X_{HCN} \cdot X_{NO} \cdot \exp\left(\frac{-30208.2}{T}\right),$$

$$R_4 = -1.8 \cdot 10^8 \cdot X_{NH_3} \cdot X_{NO} \cdot \exp\left(\frac{-13593.7}{T}\right).$$

Where $R_1 \ldots R_4$, – reaction rate, 1/s; $X_{HCN}$, $X_{NO}$, $X_{O_2}^0$ – mole fraction, mol/mol; $T$ – temperature, K.

This model describes the gas phase reaction of HCN and $NH_3$ with an oxidation rate to NO and a reduction rate to $N_2$.

### Mitchell and Tarbell model

A global model has been proposed by Mitchell and Tarbell [8], involving $NH_3$, HCN, NO and $N_2$ as N-containing species. The first reaction step is the conversion of HCN to $NH_3$ by an attack of an oxidizing agent.

The $NH_3$ forms and destructs NO within a pair of competitive parallel reactions. In their global model, Mitchell and Tarbell propose the recycling of NO back to HCN through hydrocarbons $C_xH_y$.

The postulated reaction rate of the NO recycling is not temperature dependent [14-17]. The suggested value of the C atom number x in the hydrocarbons is eight; the value of y is calculated from coal analysis. The $H_2$ − concentration is calculated from equilibrium. In addition NO is reduced by a heterogeneous reaction between NO and char particles [18].

## RESULTS OF SIMULATION

Computer simulations were carried out with the aim to investigate different possibilities to improve the boiler performance, to decrease pollutant emissions and analyze different influences.

Thermal wall conductivity is dependent on several factors including accumulation of ash on the walls [19-23]. Hence, it also has significant impact to overall heat pick up of the furnace walls and thermal performance of the boiler (Fig.2).
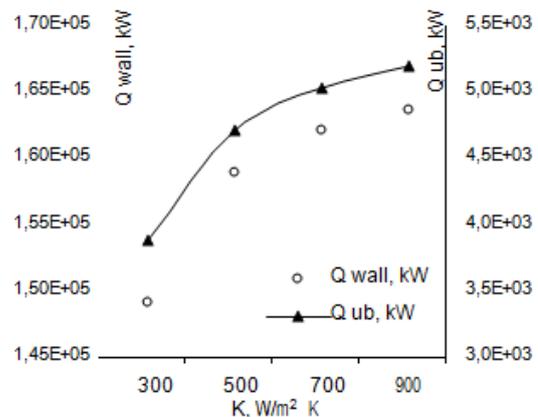


**Fig.2.** Influence of the wall conductivity on heat pick up of the walls and heat losses by unburned species at the furnace outlet

Fig.3 shows dependence of NO and CO emissions on the wall conductivity. It predicts that both emissions increase with increases in wall conductance.

Fig.4 shows predicted NO and CO concentrations at the furnace outlet as a function of swirling. Studies have shown that swirling of the incoming air stream which surrounds the coal stream can significantly influence the NO and CO concentrations.
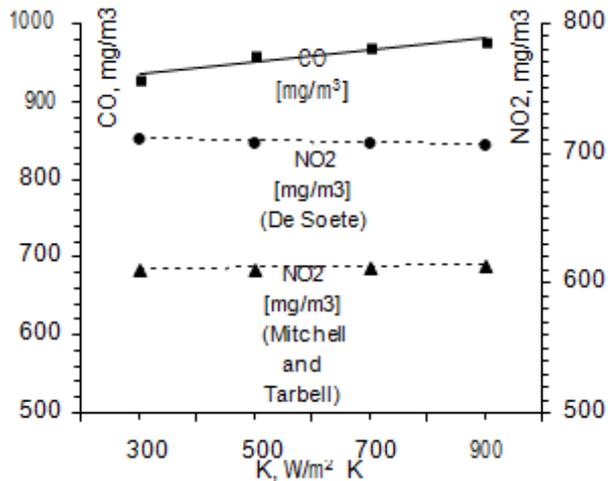


**Fig.3.** Influence of the wall conductivity on $NO_2$ and CO concentration at the furnace outlet

These variations in NO and CO result principally from difference in mixing process, when the swirling incoming air results in sufficient mixing to promote earlier ignition, hence the extent of mixing of the coal and air has a significant impact on the volatile N-containing species conversion to NO.
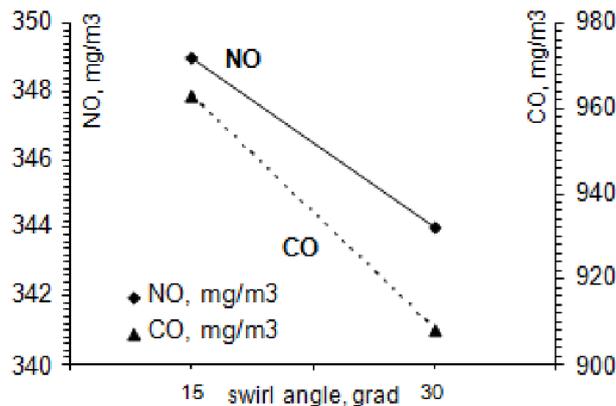


**Fig.4.** Influence of the incoming air stream swirling on NO and CO concentration at the outlet

To reduce NO emissions air staging was used. The penetration of the over fire air jets into the furnace can be seen in the velocity distribution

(Fig.5). A significant increase of the flue gas temperature arises along the jets induced by the carbon monoxide combustion.

Temperature distributions in the furnace for full load operation (with coal and oil combustion) are presented in the Fig.6 and Fig.7. It's seen that the zone of maximum temperatures is concentrated in the center of the fire-chamber on the level of the burners.

The minima in the presented temperature field are caused by the low temperatures of fuel and transporting gas supplied to the furnace through the burner nozzles. Calculated data show good agreement with experimental data (Fig.6) [24].
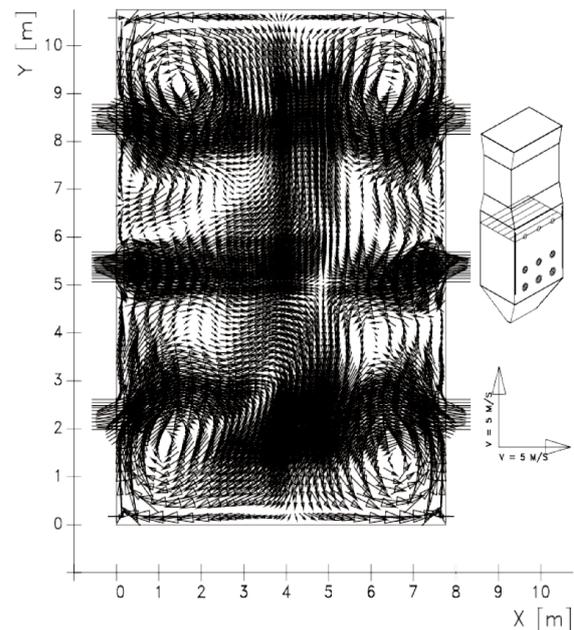


**Fig.5.** Velocity distribution in the level of the OFA jets during coal combustion at 100% load
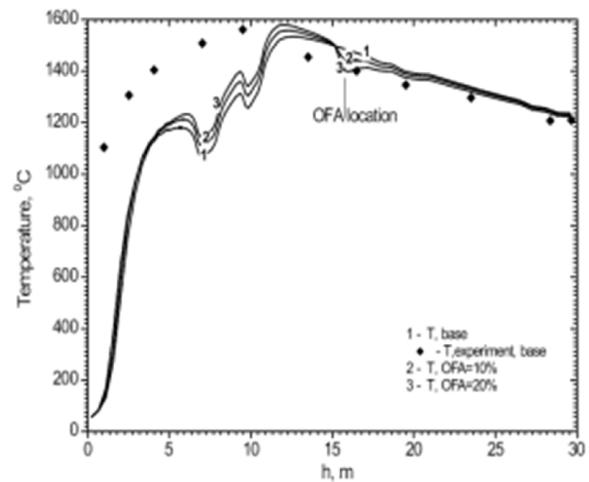


**Fig.6.** Simulated temperature distribution over furnace height during coal combustion at 100% load compared with experiment [24]
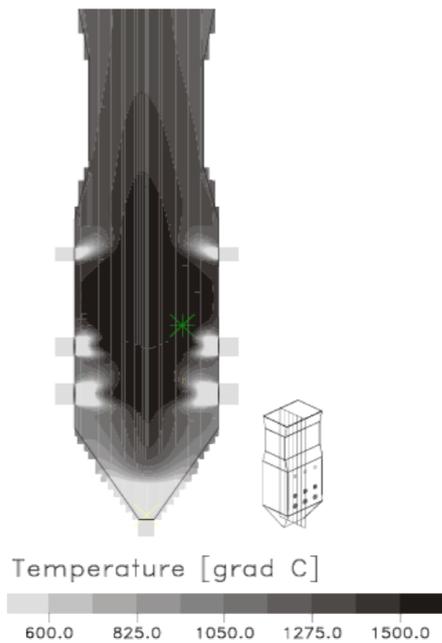
**Fig.7.** Temperature distribution in the middle vertical section during coal combustion at 100% load

Fig.8 shows predicted $NO_2$ and CO concentrations at the furnace outlet as a function of different air distribution between main burners, over fire air (OFA) and curtain air (CA) nozzles.
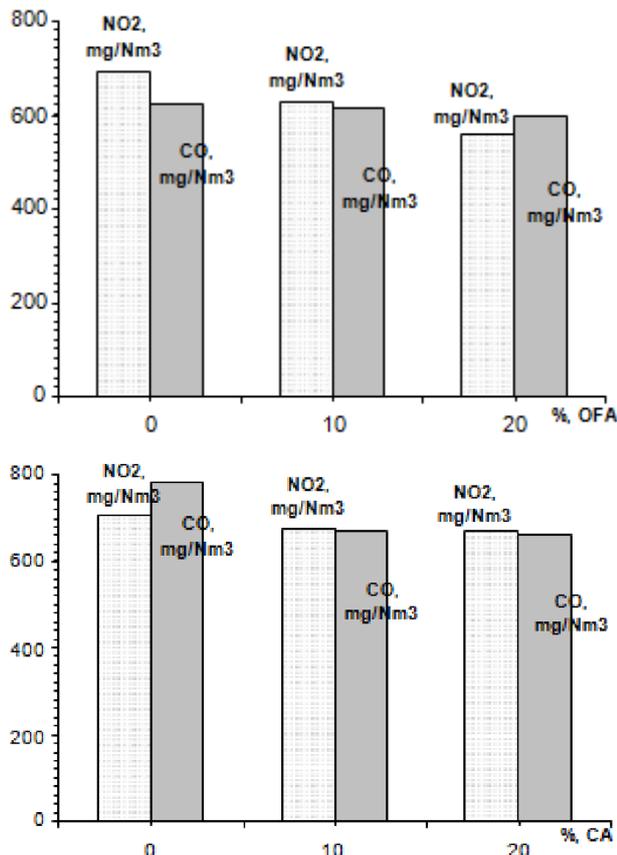


**Fig.8.** Influence of OFA and additional curtain air on CO and $NO_2$ concentrations at the outlet of the furnace PK-39-steam generator

Fig.8 shows that using the OFA-technology at the outlet of the combustion chamber observed a clear reduction in nitrogen dioxide ($NO_2$). However, the concentration of carbon monoxide (CO) is the same. When using a curtain air, conversely, decreasing the concentration of carbon monoxide (CO) and the concentration of nitrogen dioxide ($NO_2$) almost does not change.

Studies have shown that these parameters of the incoming air streams redistribution can significantly influence on the $NO_x$ and CO concentrations. These variation in $NO_x$ and CO emissions result principally from difference in mixing process staging of combustion in furnace and results in a significant impact on the nitrogen conversion to NO and CO formation.

## ACKNOWLEGEMENT

## CONCLUSION

The present paper is showing the dependence of NO and CO emissions on the wall conductivity and the prediction of NO and CO concentrations at the furnace outlet as a function of swirling. Moreover, to reduce NO emissions air staging was used. It shows the effect of OFA-Technology for distribution of velocity, temperature, and concentration characteristics ($NO_x$ and CO).

The data resulting from the present study allow an improved understanding of combustion processes and provide detailed description of furnace performance. Results from CFD simulation can be useful for engineers to choose an appropriate burner and furnace design, to reduce pollutant emissions, as well as to optimize furnace operation.

## REFERENCES

1  Ye. Heierle, R. Leithner, H. Müller, A. Askarova CFD Code FLOREAN for Furnaces Simulations in Environmental and Engineering Study, *J. Energy, Environment, Ecosystems, Development And Landscape Architecture*, 300 (2009).

2  A. Askarova, A. Bekmukhamet, S. Bolegenova, S. Ospanova, B. Symbat, V. Maximov, M. Beketayeva and A. Ergalieva 3-D Modeling of Heat and Mass Transfer during Combustion of Solid Fuel in Bkz-420-140-7C Combustion Chamber of Kazakhstan, *J. Applied Fluid Mechanics,* 9, 699 (2016).

3  H. Müller Numerische Berechnung Dreidimensionaler Turbulenter Strömungen in Dampferzeugern mit Wärmeübergang und

Chemischen Reaktionen am Beispiel des SNCR-Verfahrens und der Kohleverbrennung, vol. 6, VDI-Verlag, 1992, 158 p.

4  F.G. Lockwood An improved flux model for the calculation of radiation heat transfer in combustion chambers, *ASME Paper*, 55 (1976).

5  B. Magnussen, et al. On the mathematical modeling of turbulent combustion with special emphasis on soot formation and combustion, 16th Symposium of Combustion, 1976, pp. 719-729.

6  B. Lendt Numerische Berechnung der Stickoxid-konzentration in Kohlenstaubflammen – Ein Vergleich unterschiedlicher Reaktionsmodelle, VDI–Verlag, vol.254, 1991, 195 p.

7  G. De Soete Overall reaction rates of NO and $N_2$ formation from fuel nitrogen, 15th international symposium on combustion, Pittsburgh, USA, The Combustion Institute, 1975, p.1093.

8  J. Mitchell, J. Tarbell A kinetic model of nitric oxide formation during pulverized coal combustion, *AIChE J.*, 28, 302 (1982).

9  A.S. Askarova, E.I. Karpenko, V.E. Messerle Plasma enhancement of combustion of solid fuels, *J. High Energy Chemistry,* 40, 111 (2006).

10  Yu.E. Karpenko, E.I. Karpenko, A.S. Askarova Mathematical modeling of the processes of solid fuel ignition and combustion at combustors of the power boilers, 7-th International Fall Seminar on Propellants, Explosives and Pyrotechnics. Theory and Practice of Energetic Materials, China, vol. 7, 2007, p.672.

11  A.S. Askarova, V.E. Messerle, A.B. Ustimenko, S.A. Bolegenova, S.A. Bolegenova, V.Yu. Maximov, and A. Ergalieva Reduction of noxious substance emissions at the pulverized fuel combustion in the combustor of the BKZ-160 boiler of the Almaty heat electropower station using the "Overfire Air" technology, *J. Thermophysics and aeromechanics*, 23, 134 (2016).

12  A.S. Askarova, M.A. Gorokhovski, A. Chtab-Desportes, I. Voloshina Stochastic simulation of the spray formation assisted by a high pressure, 6-th International Symposium on Multiphase Flow, Heat Mass Transfer and Energy Conversion, vol. 1207, 2010, p. 66.

13  A.B. Ustimenko, A.S. Askarova, V.E. Messerle, A. Nagibin Pulverized coal torch combustion in a furnace with plasma-coal system, *J. Thermophysics and Aeromechanics*, 7, 435 (2010).

14  A.S. Askarova, S.A. Bolegenova, V.E. Messerle, A.B. Ustimenko, V.Yu. Maksimov Numerical

Simulation of the Coal Combustion Process Initiated by a Plasma Source, *J. Thermophysics and Aeromechanics*, 21, 747 (2014).

15  S.A. Bolegenova, A.S. Askarova, V.E. Messerle, V.Yu. Maksimov, Z. Gabitova Numerical simulation of pulverized coal combustion in a power boiler furnace, *J. High Temperature*, 53, 445 (2015).

16  P. Safarik, M. Beketayeva, S. Bolegenova, V. Maksimov Numerical Modeling of Pulverized Coal Combustion at Thermal Power Plant Boilers, *J. Thermal Science*, 24, 275 (2015).

17  S.A. Bolegenova, A.S. Askarova, V.Yu. Maksimov, M. Beketayeva, A. Bekmuhamet, Z. Gabitova Computational method for investigation of solid fuel combustion in combustion chambers of a heat power plant, *J. High Temperature*, 53, 751 (2015).

18  I.V. Loktionova, V.E. Messerle, A.B. Ustimenko 3D modeling of the two-stage combustion of Ekibastuz coal in the furnace chamber of a PK-39 boiler at the Ermakovo district power station, *J. Thermal engineering*, 50, 633 (2003).

19  I.V. Loktionova, E.I. Karpenko, A.S. Askarova, V.E. Messerle, A.B. Ustimenko Optimization of the combustion of power station coals using plasma technologies, *J. Thermal Engineering*, 51, 488 (2004).

20  A. Askarowa, M.A. Buchmann Structure of the flame of fluidized-bed burners and combustion processes of high-ash coal, VDI Berichte, Combustion and incineration, vol. 1313, 1997, p. 241.

21  A.S. Askarova, Ye.I. Lavrichsheva, M.Zh. Ryspayeva Numerical investigation of influence of coal particles sizes on the process of turbulent combustion in the furnace chambers, 17-th International Congress of Chemical and Process Engineering, 2006, p.5.

22  R. Leithner, H. Müller, A. Askarova, Ye. Lavrichsheva, A. Magda Combustion of low-rank coals in furnaces of Kazakhstan coal-firing power plants, VDI, vol. 1988, 2007, p.497.

23  S. Vockrodt, R. Leithner, A. Schiller Firing technique measures for increased efficiency and minimization of toxic emissions in Kasakh coal firing, VDI Berichte, vol. 1492, 1999, p. 93.

24  B.K. Aliarov, B.P. Ustimenko, M.A. Buhman Development and inculcation vertical three-channels burners on the boilers P-39-2 Ermnakovskaja Power Plant, Report № 01910010550, Almaty, 1991, 59 p.

# Application of Concentrated Solar Power for elaborating wear resistant hardfacing surface layers

A.G. Mourlas, P.P. Psyllaki[*]

*Piraeus University of Applied Sciences, Mechanical Engineering Department, 250 Thivon ave, 122 44 Egaleo, Greece*

The present study investigates the exploitation of Concentrated Solar Power (CSP) for the in-situ production of wear resistant carbide-based surface layers onto steel base metal. The use of alternative thermal sources, such as laser or solar, for remelting or cladding pre-deposited powder layers has been implemented in order to achieve continuous, non-porous coatings, well-adhered to the substrates. Compared to laser sources, concentrated solar energy is mainly characterized by its renewable nature and, in addition, by higher efficiency. For this purpose, "solar" experiments were carried out at the installations of *Plataforma Solar de Almería* (Spain). Carbide-based powders (TiC and WC) were pre-deposited onto carbon steel and subsequently exposed to concentrated solar irradiation for various dwell time values. The temperature field developed during solar exposure was recorded in real-time by the aid of an optical pyrometer that allowed monitoring the temperature evolution of the irradiated surface, as well as by the aid of a thermocouples' set placed at different loci within the base metal that allowed determining the progress of thermal fields within the steel. Microscopic observations of the obtained surface layers allowed the correlation between the treatment parameters and the microstructure achieved. Subsequently, preliminary sliding tests against an alumina ball and a cutting insert with a cBN-coated tip were performed using a pin-on-disc apparatus, in order to evaluate in-service performance and machinability of the elaborated hardfacings, respectively. Based on these experimental results, the proposed technique was compared to Flux Cored Arc Welding (FCAW), to which it exhibits many fundamental commonalities.

**Keywords:** Concentrated Solar Power, surface modification process, carbide-based hardfacing, microstructure, tribological performance

## INTRODUCTION

"Cemented carbides" are two-phase, ceramic-metal (CerMet) materials, consisting of hard carbide particles such as WC, TiC, $Cr_3C_2$ etc. bound together by a metal binder phase. They are the primary materials of choice in harsh applications, like hard metal cutting, rock drilling, excavation [1], due to their high hardness and wear resistance under non-lubricated conditions. Besides their use as sintered monolithic wear resistant components, they are also applied as coatings of metallic parts operating under sliding, abrasion and erosion conditions in high temperature and corrosive atmospheres [2, 3]. The principal deposition technique to obtain such coatings, with thickness in the range of 200-400 μm, is High Velocity Oxy-Fuel thermal spraying, which, like all thermal spraying techniques, requires specially pre-treated feedstock powders having a suitable particle size distribution to be sprayable. In addition, the coatings obtained are prone to decarburization/dissociation of the carbide particles during in-flight towards the substrate, due to the high temperatures developed.

In an effort to mitigate such high processing temperature problems, non- conventional thermal sources, such as laser, or alternative ones, like concentrated solar power (CSP) have been implemented. Compared to laser sources, concentrated solar energy is mainly characterized by its renewable nature and, in addition, by higher efficiency [4] and lower capital costs [5]. Previous works have already formed a solid background on the feasibility of creating metallic, oxide- or carbide-based coatings [6,7] onto metallic substrates via CSP. In particular with respect to carbide coatings, preliminary experiments on solar-aided surface alloying of steels, demonstrated that the obtained treated zones were thick, hard and free of pores and cracks [8,9].

The present study is part of an integrated research project targeted to investigate the feasibility of optimising the "solar surface treatment" process and obtaining carbide-based hardfacing layers with acceptable microstructure features and tribological performance. In this perspective, a first preliminary study by the present authors involved TiC-based surface layers as a case study [10]. The present work is a follow-up including in the one hand additional solar experiments with TiC powder to validate the first results. In the other hand, further experiments with WC-based powder were performed to demonstrate the feasibility of elaborating diverse carbide-based wear resistant surface layers by the proposed solar process.

* To whom all correspondence should be sent:
  psyllaki@teipir.gr

## EXPERIMENTAL DETAILS

The surface treatments using concentrated solar irradiation were carried out at the installations of *Plataforma Solar de Almería, PSA* (Spain). A schematic illustrating the operation principle of such facilities is presented in Fig.1, while the plant of Almeria has been previously described [6-9]. The present study took place in the new horizontal SF40 solar furnace, specifically designed for high temperature materials treatment under controlled atmosphere. The facility is of 40 kW power and reaches a peak concentration exceeding 7000 suns. An extensive description of this particular installation has been recently published [11], providing technical details of the concentrator system, the flux regulation modes and flux measurements.

The surface-modified base metal was a common carbon steel grade (DIN St 37-2), containing less than 0.17 wt. % C and exhibiting a liquidus temperature of ~1540 °C. Specimens of dimensions $70\times35\times15$ mm$^3$ were polished and the surface to be irradiated was covered by the respective carbide powder to form a disk-like, 1 mm-thick layer, with a diameter of 3.5 cm, since the radiation spots have a diameter of 3.0 cm. Two series of solar campaigns were performed applying TiC and WC powders. During solar exposure, the temperature of the specimen surface was recorded in real-time by the aid of an optical pyrometer, in order to determine the operational conditions and correlate them to their effects on the material. In all cases, treatment was taking place within a quartz bell jar, under inert atmosphere with the aid of Ar gas flow.

The optimization of process parameters comprised post-treatment macroscopic and stereoscopic observations of the exposed surfaces, using a Leica MS 5 and a Nikon SMZ 1500 stereomicroscope, as well as microscopic observations of the relevant cross-sections, conducted using a Nikon Epiphot 300 inverted metallographic microscope. Vickers microhardness measurements on characteristic areas of the specimens' cross-sections were carried out using an Instron-Wolpert tester, applying a 0.3 kg load. The tribological performance of hardfacing layers, obtained under the optimum conditions, was estimated using a pin-on-disk apparatus (Centre Suiss d' Electronique et de Microtechnique, CSEM). Preliminary sliding friction tests were performed in dry air (25%RH, 20 °C), using as counterbodies a cutting insert with a cBN-coated tip and an $Al_2O_3$ ball ($\varnothing$ 6), in order to estimate the machinability and the in-service performance of the obtained layers, respectively.
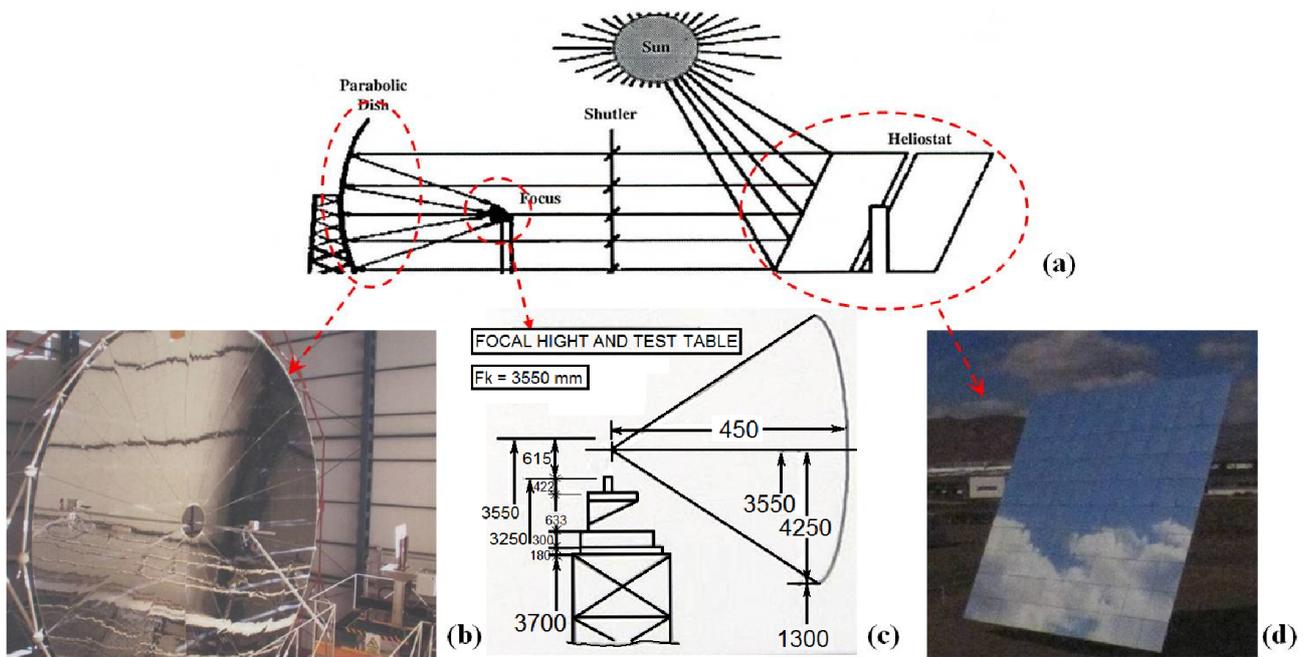


**Fig.1.** Solar furnace installation at *Plataforma Solar de Almeria, PSA* (Spain): (a) Schematic presentation of operation principle, (b) Actual stationary parabolic concentrator, (c) Schematic of arrangement ensuring a 3810 kW.m$^{-2}$ peak flux at the focal point, normalised to 1000 W.m$^{-2}$ insolation and (d) Photograph of heliostat consisting of 100 plane facets, each one of 1 m$^2$ reflecting surface

The specimens were tested applying normal loads (*N*) in the range of 1-10 N and for a linear velocity of 0.20 m.s$^{-1}$. After testing, the wear volume (*v*) was measured using a mechanical Taylor-Hobson stylus profilometer and the wear coefficient (*k*) was calculated, using the formula:

$$k = \frac{v}{N.s} \quad (1)$$

where (s) denotes the total sliding distance, in m

The tribological results for the solar-modified layers were compared to results concerning respective hardfacing deposits obtained by Flux Cored Arc Welding (FCAW) technique.

RESULTS AND DISCUSSION

Fundamental aspects on the proposed "solar" surface modification process were presented in a previous study [10], involving only TiC powder. This study was employed as a first test exploratory case aiming at identifying the crucial operational parameters leading to successful surface hardfaced layers. It was found therein that the crucial parameter inducing hardfacing was not the overall solar irradiation exposure time but the actual dwell time of the base metal at temperatures above its liquidus; thus this dwell time should be considered as the effective solar treatment duration. In fact, a linear relationship between the maximum hardfacing thickness and this time was observed.

The present study, involving a new campaign with TiC powder as well as a first-of-its-kind campaign with WC powder, corroborated further these observations. Fig.2 shows for each carbide, three representative in-situ measurements of the specimens' surface temperature via an optical pyrometer, demonstrating the temperature evolution as a function of the total exposure time. The relevant dwell times, in the particular experiments, for TiC span between 300-500 s and those for WC between 250-300 s. Both these intervals were within the optimum time ranges for hardfacing. Analytical details on the calculation of the surface treatment duration have been provided previously [10]. A dwell time below a critical threshold value was not sufficient to induce melting of the base metal up to a depth adequate to achieve incorporation of the carbide particles within the melting pool. On the other hand, excessive dwell above the liquidus temperature resulted in high porosity of the re-solidified metallic matrix.

A typical WC-hardfaced specimen obtained is presented in Fig.3a. It can be clearly distinguished that solar irradiation has affected only the area to be treated, leaving the rest of the specimen's volume intact. A visual result of solar surface modification is demonstrated in Fig.3b, showing achievement of immersion and entrapment of non-molten carbide particles within a surface pool of molten and re-solidified base metal.
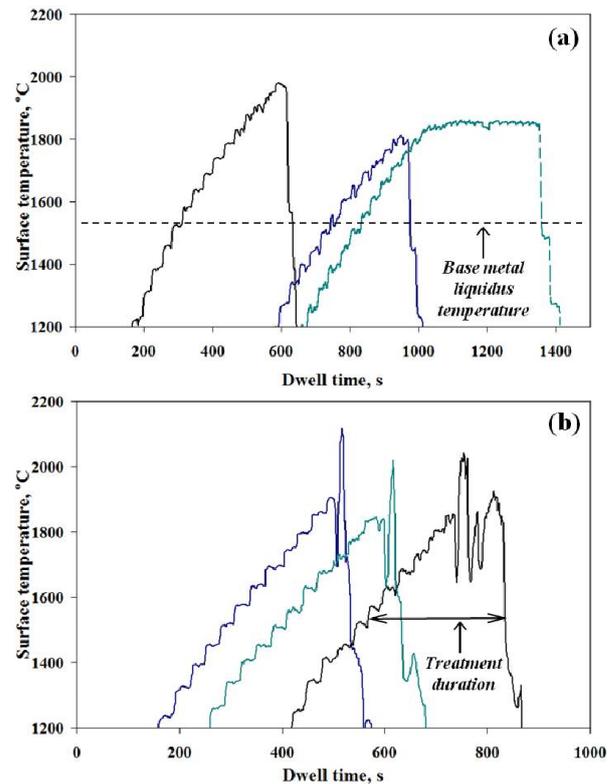


**Fig.2.** Surface temperature evolution during solar irradiation exposure of three different: (a) TiC- and (b) WC-covered specimens

Metallurgical processes involving metals' melting and re-solidification are frequently accompanied by the appearance of residual porosity and micro-cracking of the treated volume. A successful solar treatment should result in surface layers free of such microstructural defects as well as homogeneous distribution of the reinforcement particles within the base material in order for the surface layer to have uniform performance during application. An exemplary case of such a continuous, uniform surface layer obtained via solar irradiation is presented in Fig.4a, for TiC hardfacing. SEM observations at the neighbourhood of the solar-treated layer/ unmolten base metal interface (Fig.4b) demonstrated further the validity of the previous findings throughout the entire depth of the treated zone.

However, the specific type of the carbide, TiC or WC, had a significant influence on the micro-phenomena taking place during the effective solar treatment (dwell at temperatures above 1540 °C). TiC particles immersed within the ferrous pool seem not to be attacked by the liquid metal during treatment. As shown in Fig.5a, the carbide particles boundaries remained intact and totally unaffected by the surrounding metal. On the contrary, in the case of WC (Fig.5b), the contact of carbides with the liquid metal led to partial dissolution of the particles directed from the outer to their inner region. Thus, longer effective solar treatment duration and/ or smaller particles' size could result in total dissolution of WC particles within the metallic matrix.

relevance with the microstructure observations above. These values ranged from 2500 up to 2900 HV0.3 in the case of TiC-harfaced layers and from 1000 up to 1500 HV0.3 in the case of WC ones. The magnitude and the span of these values could be attributed to:

- The relevant inter-carbide spacing, imposing constraints to the plastic deformation of the metal [12], in the case of intact TiC particles.
- The enrichment of the metallic matrix in carbon around the semi-dissolved particles, in the case of WC-hardfaced layers.



**Fig.3.** (a) Macrograph of a typical WC-covered specimen, exposed to solar irradiation and (b) Typical cross-section view of a successfully TiC-hardfaced specimen (stereo-graph)
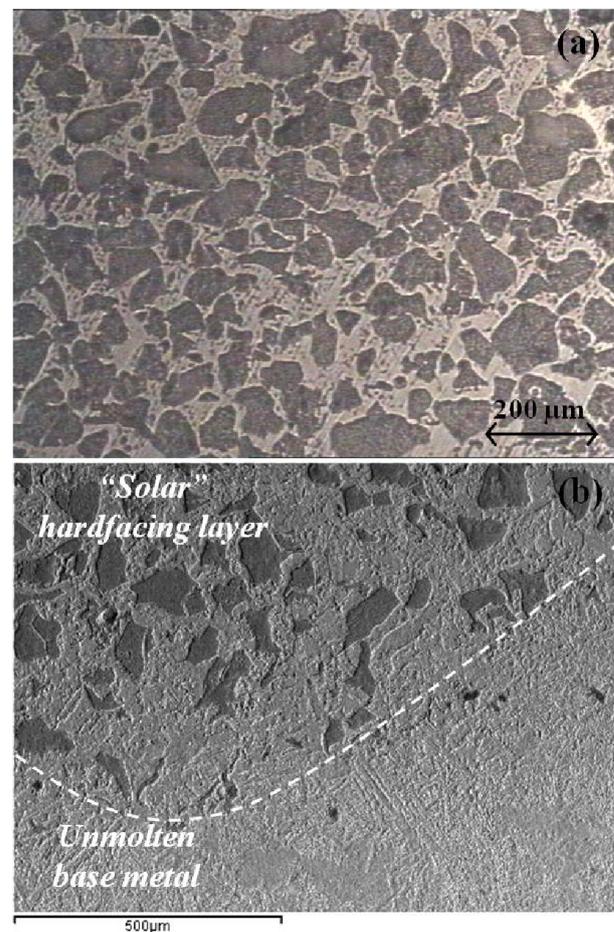


**Fig.4.** Cross-section of a microstructural-defects-free TiC-hardfaced layer: (a) Optical micrograph demonstrating the homogeneous distribution of carbide particles within the metallic matrix and (b) SEM photograph of the hardfacing / base metal interface

Microhardness values obtained at selected areas of the hardfacing layers demonstrated different trends for the two carbides that could be of

Preliminary dry sliding tests demonstrated the suitability of the solar hardfaced layers obtained for severe tribological applications, where high wear resistance is a requirement.

The evolution of the wear coefficient was estimated by interupted testing up to 200.000 sliding revolutions. Steady-state wear of the treated

layers was achieved above 20.000 sliding revolutions; thereafter, the wear coefficient values remained practically constant. As shown in Table 1, both TiC- and WC-hardfaced layers exhibited comparable machinability and in-service performance with respective hardfacing deposits obtained by conventional FCAW technique.
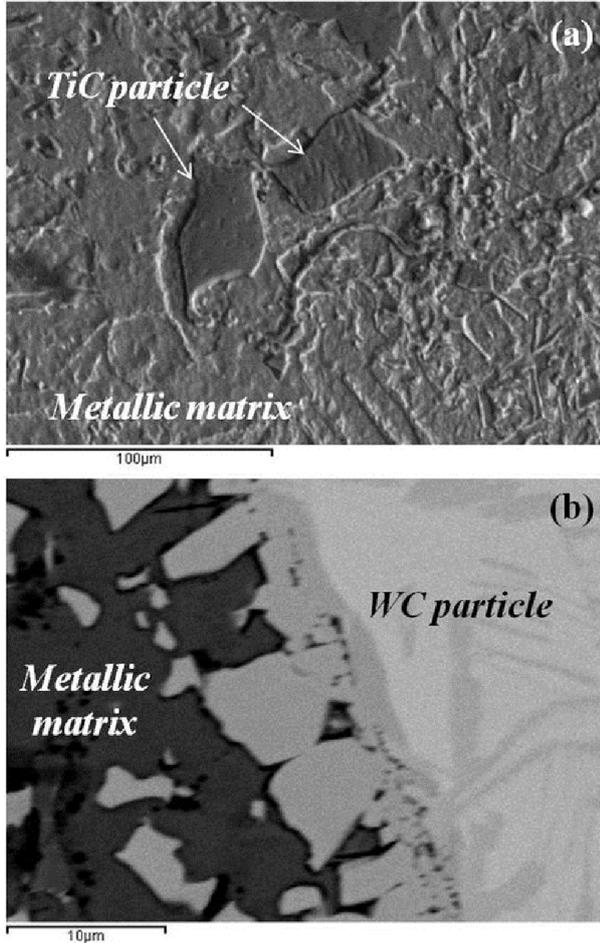




**Fig.5.** SEM micrographs of: (a) Non-dissolved TiC particles and (b) Partially dissolved WC particles, within the ferrous metallic matrix

**Table 1.** Comparison of the steady-state wear coefficient ($mm^3.N^{-1}.m^{-1}$) between "solar" and FCAW TiC- and WC-hardfaced surface layers, tested under the highest load (10 N)

| Surface layer | Sliding against cBN-coated pin | Sliding against $Al_2O_3$ ball |
|---|---|---|
| "Solar" TiC | $5.11\times10^{-5}$ | $4.64\times10^{-6}$ |
| FCAW TiC | $2.11\times10^{-5}$ | $7.64\times10^{-6}$ |
| "Solar" WC | $7.83\times10^{-6}$ | $4.35\times10^{-7}$ |
| FCAW WC | $7.90\times10^{-7}$ | $6.96\times10^{-7}$ |

For comparison purposes, Fig.6 depicts the dependence of wear coefficient on the normal load applied for ball-on-disk experiments performed on the base metal of this study (red curve), as well as on a ferrous alloy typically used for hard

tribological applications (blue curve). Both alloys exhibited wear coefficient values in the range of $1.12$-$2.09\times10^{-4}$ $mm.N^{-1}.m^{-1}$, when tested under the most severe conditions (10 N), whilst the relevant values for TiC- and WC-hardfaced layers were respectively 2 and 3 orders of magnitude lower (Table 1, last column).

A typical top-view of a wear track of the solar WC-hardfaced layers obtained is presented in Fig.7. Polishing and ploughing wear mechanisms of the metallic matrix that led to revealing of the carbide particles were clearly seen.
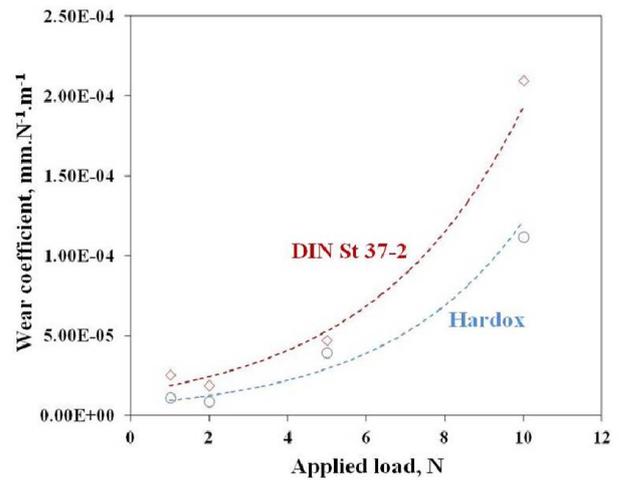


**Fig.6.** Wear coefficient evolution as a function of the normal load applied for the un-treated base metal employed in the present study (red curve) and for a typical wear resistant steel (blue curve)
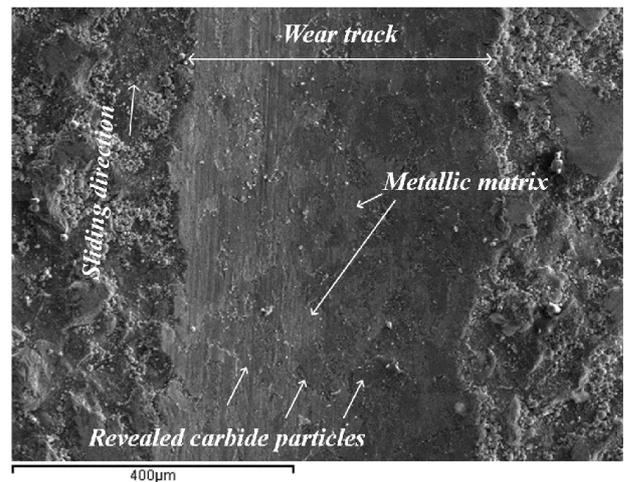


**Fig.7.** SEM top-view micrograph of the worn surface of WC-hardfaced specimen

## CONCLUSION

Concentrated Solar Power (CSP) was exploited for the in-situ production of TiC- and WC- wear

resistant surface layers onto steel base metal. The solar process parameters were optimised using as criterion the elaboration of layers without mictostructural defects. The kind of the carbide particles affected the micro-phenomena taking place during the melting stage of the process and consequently the microstructural features and the microhardness values of the obtained surface layers. The in-service tribological behaviour of both carbide layers was found superior to that of the base metal and comparable to that of relevant hardface deposits elaborated by Flux Cored Arc Welding (FCAW) technique.

## ACKNOWLEDGEMENTS

## REFERENCES

1  B. Basu, M. Kalin, Tribology of ceramics and composites. Hoboken, New Jersey: John Wiley & Sons, (2011).
2  A.M.Venter, O.P. Oladijo, V. Luzin, L.A. Cornish, N. Sacks, Thin Solid Films, 549, 330, (2013).
3  M. Heydarzadeh Sohi, F. Ghadami, Tribology International, 43, 882 (2010).
4  A. Ferriere, C. Sanchez Bautista, G.P. Rodrigues, A.J. Vazquez, Solar Energy, 80, 1338, (2006).
5  G. Flamant, A. Ferriere, D. Laplaze, C. Monty, Solar Energy, 66, 117, (1999).
6  D.I. Pantelis, A. Griniari, Ch. Sarafoglou, Solar Energy Materials & Solar Cells, 89, 1 (2005).
7  D.I. Pantelis, Ch. Sarafoglou, A. Griniari, P. Assimidis, Proc. 3rd Inter. Conf. "The Coatings" in Manufacturing Engineering, 461 (2002).
8  D.I. Pantelis, P. Psyllaki, Ch. Sarafoglou, Fonderie–Fondeur d' Aujourd'hui, 211, 23 (2002).
9  D.I. Pantelis, A. Griniari, Surface Modification Technologies XVIII, 159 (2006).
10 A. Mourlas, P. Psyllaki, D. Pantelis, Key Engineering Materials, 674, 296, (2016).
11 J. Rodriguez, I. Caňadas, E. Zarza, AIP Conference Proceedings, 1734, 070028, (2016).
12 H.C. Lee, J. Gurland, Materials Science and Engineering, 33, 125, (1978).

# Mathematical modeling of heat and mass transfer in the presence of physical-chemical processes

A.S. Askarova[1], S.A. Bolegenova[2], Symbat Bolegenova[2], V.Yu.Maximov[1], R. Manatbayev[2*], Zh.K. Shortanbayeva[2], A.M. Maksutkhanova[2], A.N. Aldiyarova[2], A.E.Boranbayeva[2]

[1] *SRI of Experimental and theoretical physic, Al-Farabi Kazakh National University, 71, al-Farabi ave., 050040, Almaty, Kazakhstan*

[2] *Faculty of Physics and Technology, Al-Farabi Kazakh National University, 71, al-Farabi ave., 050040, Almaty, Kazakhstan*

At the present time there is an increased interest to the study of heat-and-mass transfer in high temperature environments in the presence of burning. These processes occur in strong turbulent and non-isothermal flows, multiphase fluids, in the conditions of significant impact of nonlinear effects of thermal radiation, interfacial interactions and multistage chemical reactions. To solve the problems of modern power engineering and ecology it is especially important to study the processes of heat-and-mass transfer in the high-temperature reacting media and to simulate physical and chemical processes that occur during the combustion of pulverized coal. These problems are related, on the one hand, to the concept of "energy safety" of the country and, on the other hand, to the development of processes of "clean" fuel combustion under strict standards of emission of harmful substances into the environment. Consider development and application the numerical model for solution of processes at combustion chamber of the thermal power plant boiler. Mathematical simulation is based on solution of physical and chemical processes occurring at burning pulverized coal in the furnace model. Three-dimensional flows, heat and mass transfer, chemical kinetics of the processes, effects of thermal radiation are considered. Obtained results give quantitative information on velocity distributions, temperature and concentration profiles of the components, the amount of combustion products including harmful substances. The numerical model becomes a tool for investigation and design of combustion chambers with high-efficiency and reliable operation of boiler at thermal power plants.

**Keywords:** combustion, heat and mass transfer, emission, modeling, thermal powerplant

## INTRODUCTION

The power system of Kazakhstan is presented mostly by thermal power stations more than 70 % of total amount of the electric power are generated. Thermal power stations work on solid fuel when pulverized coal combustion is predominant. Also natural gas and black oil can be used. Tendency of low grade coals usage to increase in domestic industry, it becomes especially important to develop and introduce new energy-saving technologies of solid fuel consumption and reduction in pollutant substance emissions. Applied technology of direct burning of low-grade coals in furnaces does not provide demanded reliability of working equipment and protection of environment from harmful combustion products due to approximately 50 % of pollutant emissions from stationary sources comes from thermal power enterprises and about 33 % are emitted by ferrios and non-ferrious metallurgy and mining.

Industrial implementation of any new technology is not possible without preliminary analysis of advantages and disadvantages of suggested method. The rapid development in computer sciences gives the advance to computational techniques to be used for simulation of complex combustion processes in industrial furnaces.

Products of combustion contain different harmful substances and the emission of this components grows in to a great problem. Industrial development causes an increase in hydro carbonaceous fuels' consumption. These fuels contain harmful and poisonous components such as carbonic oxide (CO), nitric oxide (NO), sulphur dioxide, acid sulphate, lead combinations and different hydrocarbons etc.

To decrease emissions of harmful substances various methods are applied, including special fire regimes (organization of combustion process), which suppresses the formation of harmful substances in flame and two-stage burning, when the burners work with low air surplus. In this way numerical experiments became one of the most effective and suitable means for detail analysis and in-depth study of physical and chemical phenomena.

In contrast to construction of an operating reduced model of the chamber, the three-dimensional modeling with the application of modern computer technology enables to carry out deep analysis of all chamber's parameters and save

* To whom all correspondence should be sent:
  rustem1977@mail.ru

time and finances. At the same time, without additional inputs, it is possible to obtain the full set of characteristics of a convective heat and mass transfer process in reactive media, intervene flexibly in the process at any stage and reproduce separate technical solutions (the configuration of the fire chamber and assembly and construction burners), to model the formation of harmful dust and gaseous emissions and to investigate the influence of previous preparation of coal on its ignition and combustion stabilization.

Thus the development of "clean" combustion process when the discharge of harmful substances is minimal is extremely important. That is why all constructive and regime parameters of such process must be optimized both in way of maximal effective energy production and high ecological safety. In this relation usage of computed aided complex for modeling of combustion process and prediction of main characteristics behavior in furnace volume and on the furnace outlet is of great interest for research.

## MATHEMATICAL MODEL

The computer simulation experiment was fulfilled with the help of the computer code FLOREAN [1-3] valid for the three-dimensional simulation of coal fired furnaces. This code is based on the solution of the conservative equations of the flue gas mixture by finite volume method. It includes a submodels of momentum and energy balances, SIMPLE-method for pressure corrections, k-ε turbulence model, six-flow model for radiation heat transfer calculations and balance equation for the components of substance. This computer code allows to extract the velocity components $\{u,v,w\}$, the temperature T, the pressure P, the concentration of combustion products and other characteristics of the process.

Pulverized coal flames are turbulent reacting two–phase flows. In pulverized coal flames, the volumetric fraction of the particle phase is typically less than 0.001. Therefore, the particle cloud is approximated as continuum and the mean particle velocity is assumed to be approximately equal to the gas phase velocity. Additional transport equations for the oxidant, coal, volatiles, char and combustion products are solved. The pollutant formation is calculated de- coupled from the calculation of the flow and temperature field. Using a global model, the NOx–concentrations are post– calculated by means of the previously predicted values (velocity, temperature, species concentration) in the furnace chamber.

For description of chemistry simplified models were used. They account only chemical reactions of the main components and integral reactions of fuel components oxidizing up to stable end-products of the reactions. At that intermediate reactions and also the formation and alteration of unstable intermediate products are not taken into consideration.

The formation of nitrogen oxides from the nitrogen-containing fuel can be approximately calculated by a simplified process scheme. According to this scheme these substances are mainly decomposed during the combustion of the volatile matters down to active atomic nitrogen which partially recombines into molecular nitrogen ($N+N \rightarrow N_2$) and partially oxidizing to the mixture of nitrogen oxides ($mN+O_2 \rightarrow mNO_X$). The concentration of resulting molecular nitrogen and mixture of nitric oxides in the combustion gas is found by the solution of the equation of homogeneous kinetics. Different combinations of possible reaction ways serve as a basis of various models. The choice of one of them is associated with capabilities of the available computer [4-7].

For simulation of nitrogen oxides formation in combustion it is assumed that the main re- action are the oxidation of molecular nitrogen (thermal $NO_X$) and the oxidation of the fuel bounded nitrogen (fuel $NO_X$). The detailed kinetic models for fuel NO prediction with 29 elementary reactions are used [8-11].

At the same time selection criteria of a model are the minimum number of reactions and participating components with simultaneous precision of carrying calculations and their satisfactory agreement with experimental data.

## RESULTS

Computational experiments have been carried out for low-rank Kuuchekinskij bitumi- nous coal incinerated at the boiler BKZ-160 with steam capacity of 160 t/h. This furnace has jet type burners in tangential firing system The boiler is installed in Almaty Thermal Power Plant (Kazakhstan). The cross section of the furnace is 7,1 m x 6,5 m and the height is 21 m (Fig.1). Eight jet burners are placed in the corners, 4 burners on two levels, directed to a fictive combustion cycle (Fig.2).
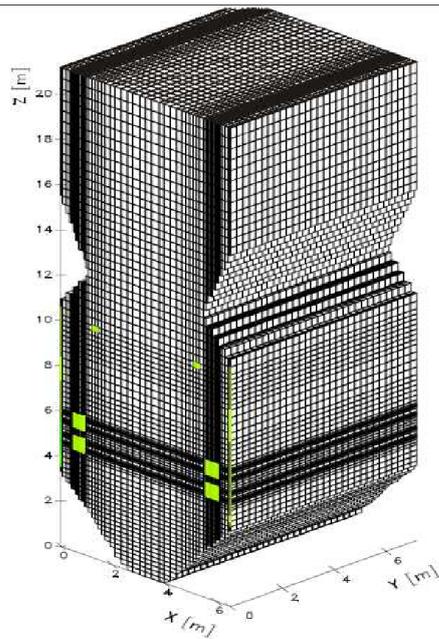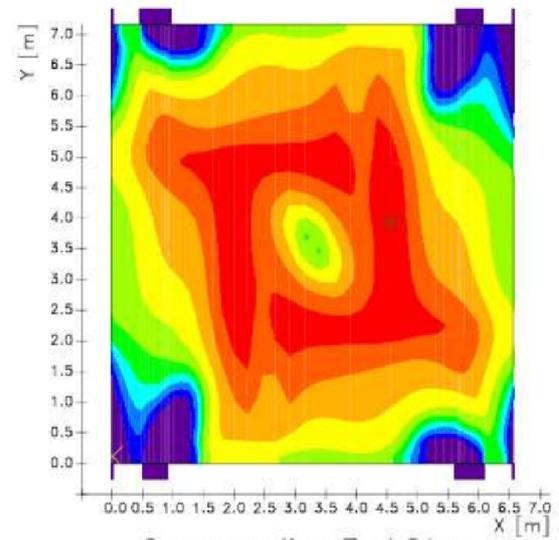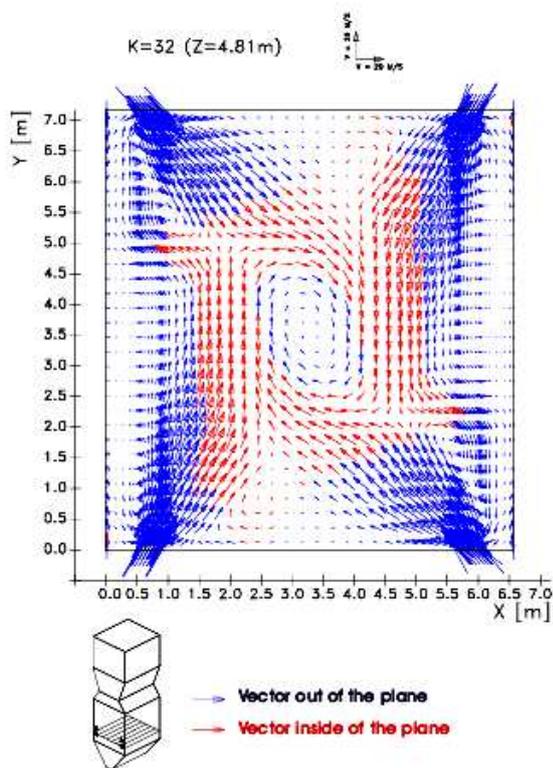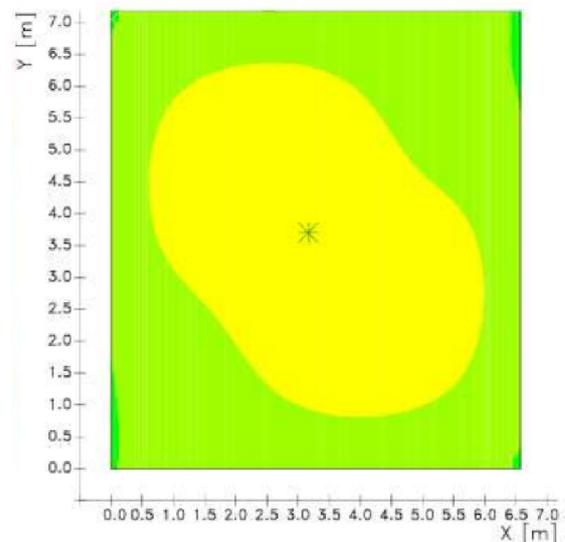
**Fig.1.** Scheme of the furnace BKZ160

the level of the burners. Here the intensive combustion took place.

The existing of minima in presented temperature field caused by low temperature of fuel and transporting gas supplied to furnace through the burners nozzles.



Cross–section Z=4.81m

✳ Maximum: 1597.5    Mittelwert: 1206.7
✕ Minimum:  41.61



Cross–section Z=20.96m

✳ Maximum: 1169.6    Mittelwert: 1113.7
✕ Minimum:  905.6
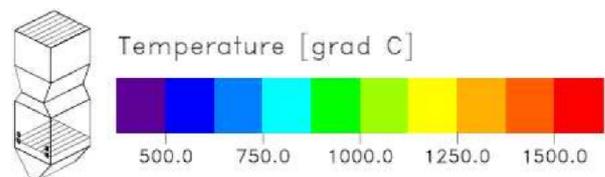
Temperature [grad C]



**Fig.2.** Scheme of burners location

Fig.3 and Fig.4 shows the temperature distribution in cross section of the furnace in the lower level of the burners and furnace outlet and temperature distribution in the middle vertical sections of the furnace. It's seen that maximum temperatures is in the center of the fire-chamber on

**Fig.3.** Temperature distribution in cross section of the furnace in the level of the burners and furnace outlet
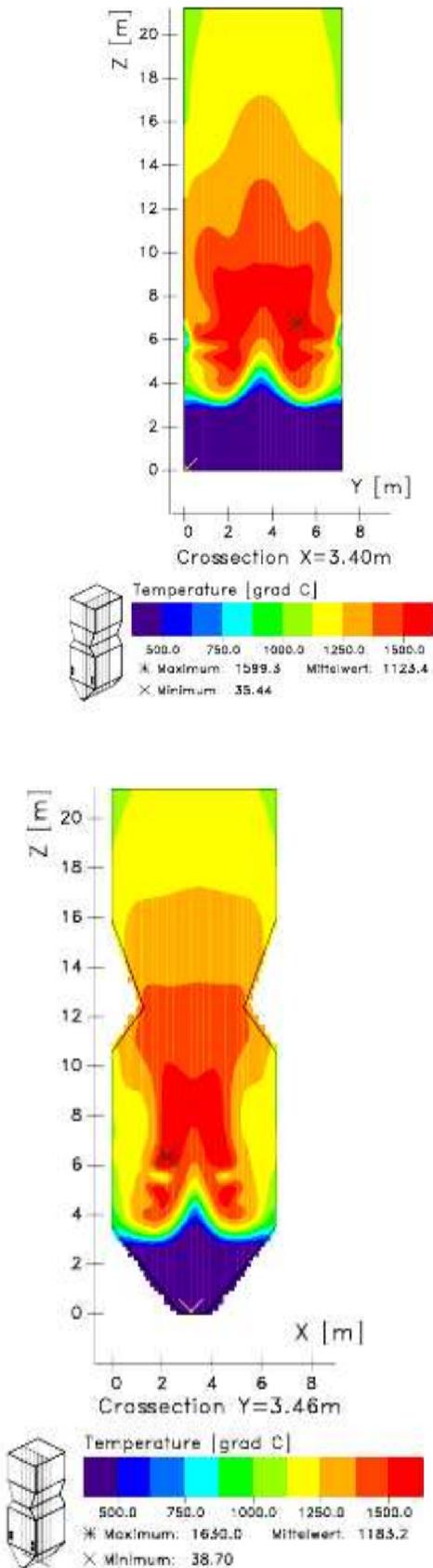
**Fig.4.** Temperature distribution in the middle vertical sections of the furnace
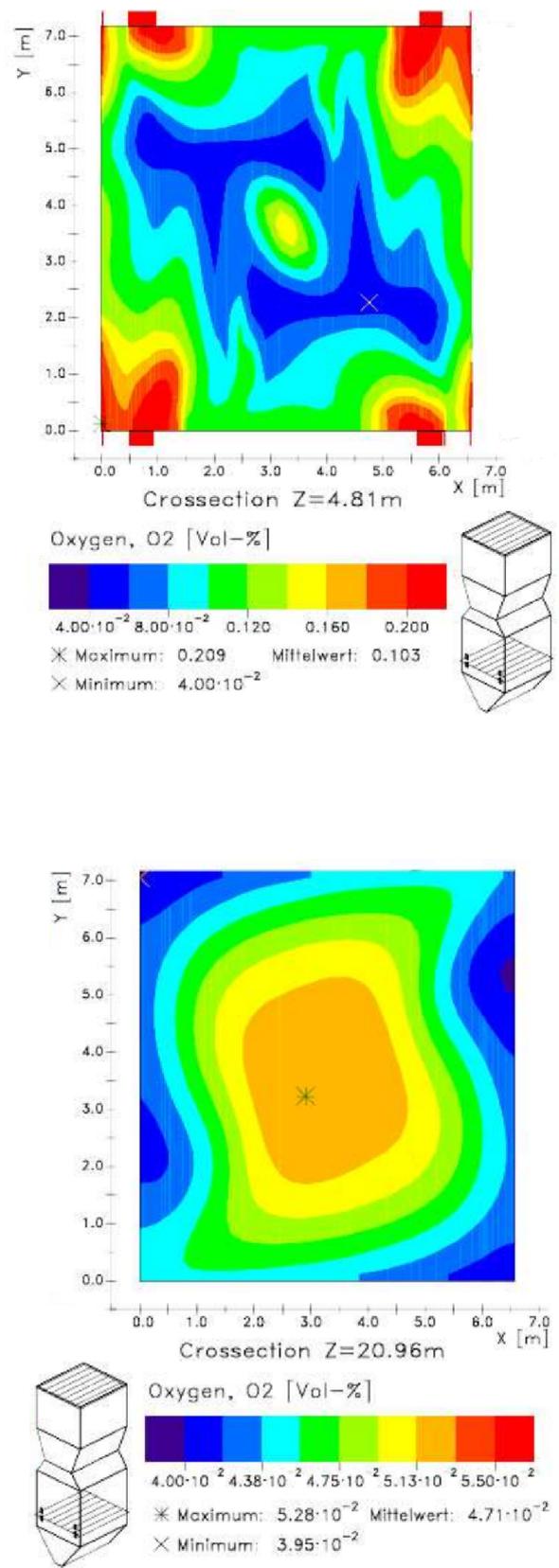


**Fig.5.** Oxygen distribution in cross section of the furnace in the level of the burners and furnace outlet
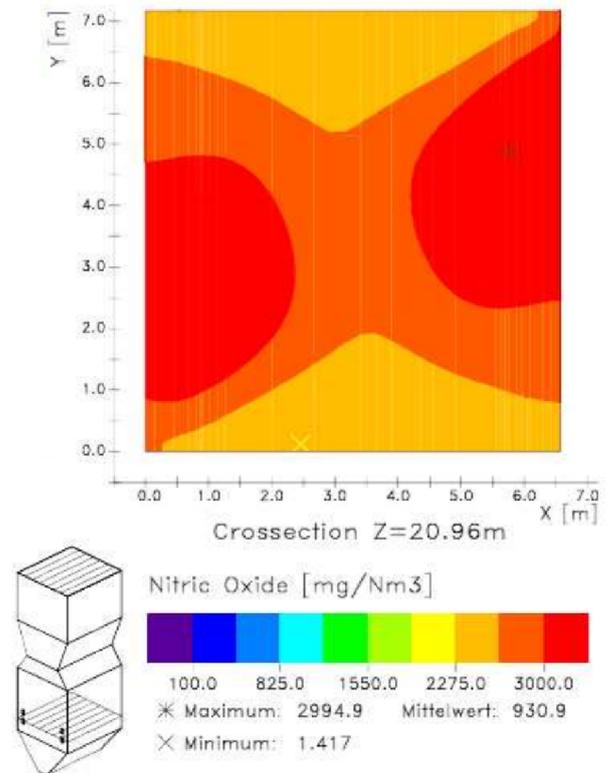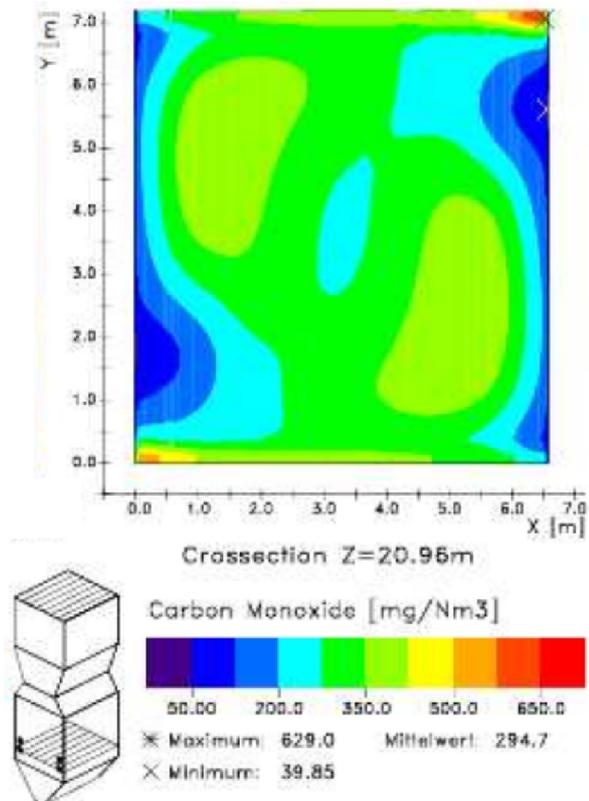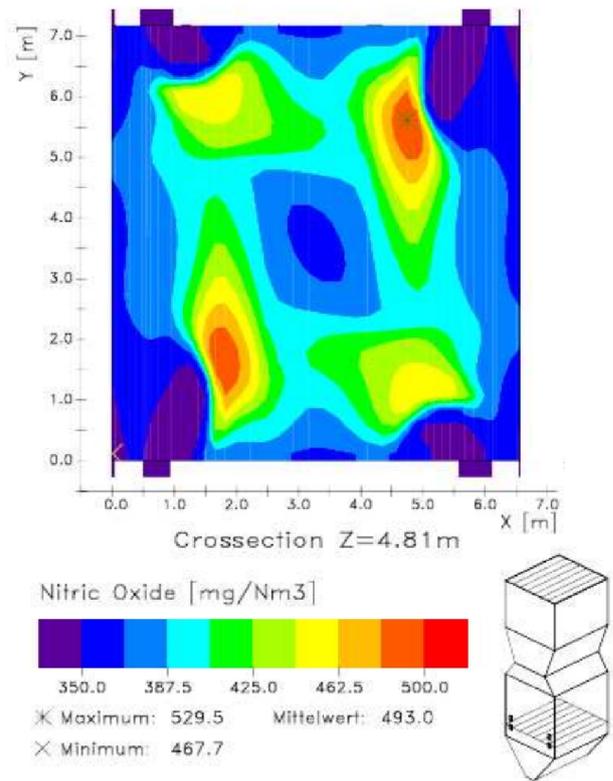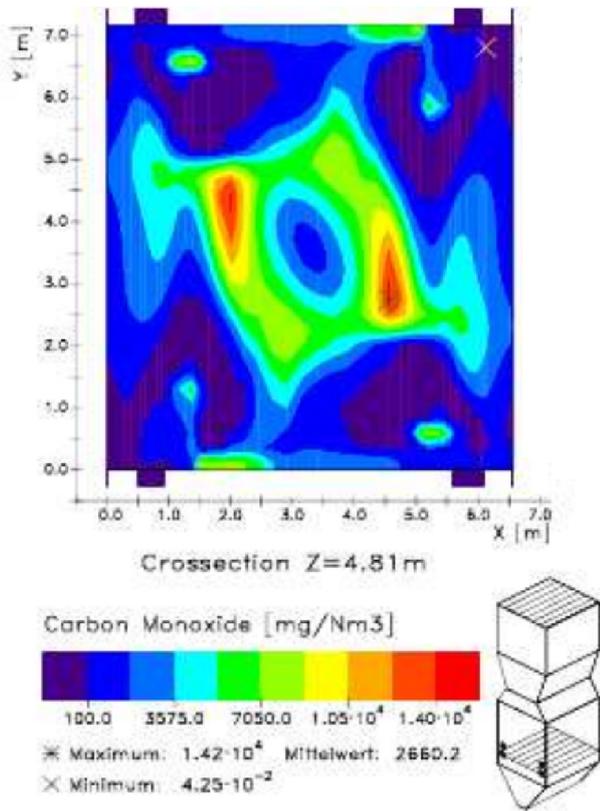
**Fig.6.** Carbon monoxide distribution in cross section of the furnace in the level of the burners and furnace outlet

**Fig.7.** Nitric oxide distribution in cross section of the furnace in the level of the burners and furnace outlet

The picture of fuel burning out is shown in Fig.5 to Fig.7 by fields of concentration change of oxygen $O_2$ (Fig.5), carbon monoxide CO (Fig.6) and nitric oxide NO (Fig.7) in cross section of the furnace in the level of the burners and furnace outlet. The analysis of these figures shows, that main gas formation in a torch occurs in a zone of burners, and in general it is typical for all kinds of combustion chambers.

Fig.5 and Fig.6 show the oxygen and carbon monoxide distributions in cross section of the furnace in the lower level of the burners.

The carbon monoxide (Fig.6) is concentrated mainly in a zone of jets collision of fuel from opposite torches, i.e. there, where carbon exists. Let's note that the zone of its formation begins and comes to an end before exothermic zone of torch. Concentration of $O_2$ and CO at the outlet of the furnace (Fig.6 and Fig.7) depends not only on the transport phenomena but also on kinetics. In the upper space of the combustion chamber rate of burning out decreases.

Nitrogen oxide distribution in cross section of the furnace in the lower level of the burners and furnace outlet is displayed in the Fig.7.

## ACKNOWLEGEMENT

## CONCLUSION

Results obtained by means of computer modeling of gas flows behavior, species concentrations, temperature fields due to combustion, radiation and convective heat transfer and the pollutant formation and destruction in furnace of real boiler BKZ-160 can be used to predict main characteristic of combustion process and to provide recommendations for effective boiler performance. Results from CFD simulation can be useful for engineers to choose an appropriate boiler performance for successful furnace and overall combustion process optimization.

## REFERENCES

1 A. Askarova, E. Karpenko, Yu. Karpenko, E. Messerle, A. Ustimenko Mathematical modelling of the processes of solid fuel ignition and combustion at combustors of the power boilers 7th International Fall Seminar on Propellants, Explosives and Pyrotechnics. Xian, Vol. 7, 672, (2007).

2 A. Askarova, V Messerle, A Ustimenko, S Bolegenova, V Maximov, Z Gabitova Numerical simulation of pulverized coal combustion in a power boiler furnace, High temperature, Vol. 53, issue 3, 445, (2015).

3 V. Maximov, S. Bolegenova, M. Beketayeva, P. Safarik et al. Numerical Modeling of Pulverized Coal Combustion at Thermal Power Plant Boilers, Journal of thermal science, Vol. 24, issue 3, 275 (2015).

4 V. Messerle, A. Ustimenko, A. Askarova A. Nagibin Pulverized coal torch combustion in a furnace with plasma-coal system, Thermophysics and aeromechanics, Vol. 17, issue 3, 435, (2010).

5 E. Karpenko, V. Messerle et al. Plasma enhancement of combustion of solid fuels, Journal of High Energy Chemistry, Vol. 40, Issue: 2, 111, (2006).

**6** V. Messerle, Ye. Lavrishcheva, E. Karpenko, A. Ustimenko et al. Plasma-supported coal combustion in boiler furnace, **IEEE Transactions on Plasma Science,** Vol. **35,** Issue **6, 1607, (**2007).

7 A. Askarova, V Messerle, A. Ustimenko, S. Bolegenova, V. Maksimov Numerical simulation of the coal combustion process initiated by a plasma source, Thermophysics and aeromechanics, Vol. 21, issue 6, 747, (2014).

8 S. Bolegenova, V. Maximov, A. Bekmukhamet, M. Beketayeva, Z. Gabitova etc. Computational method for investigation of solid fuel combustion in combustion chambers of a heat power plant, High temperature, Vol. 5, issue 5, 751, (2015).

9 A. Askarowa, M. Buchmann Structure of the flame of fluidized-bed burners and combustion processes of high-ash coal, Gesell Energietech, Combustion and incineration - eighteenth dutch-german conference on flames, VDI Berichte, v. 1313, 241, (1997).

10 S. Vockrodt, R. Leithner, A. Schiller et al. Firing technique measures for increased efficiency and minimization of toxic emissions in Kasakh coal firing, VDI, 19th German Conference on Flames, Germany, VDI Gesell Energietechn; Verein Deutsch Ingn., Combustion And Incineration, VDI Berichte, v. 1492, 93, (1999).

11 M. Gorokhovski, A. Chtab-Desportes, I. Voloshina, A. Askarova Stochastic simulation of the spray formation assisted by a high pressure, AIP Conference Proceedings, Xian, Vol. 1207, 66, (2010).

# Towards developing numerical methods for the modelling of oil slick behaviour on the vegetated coastal areas of Caspian Sea in western Kazakhstan

B. E. Bekmukhamedov[1], A. Sattarova[2*], I. V. Kaipov[1], Zh. Sh. Zhantayev[1]

[1]*National Center of Space Research and Technology, Almaty, 050010, Kazakhstan*
[2]*M. Auezov South Kazakhstan State University, Shymkent, 160012, Kazakhstan*

In case of emergency oil spills, we must be ready to understand how and in which direction oil slicks will move. Since remote sensing or tracking these spills from satellite at every hour is expensive, most reliable tool becomes mathematical modeling. The current paper, considers mathematical modeling of advection-diffusion of oil slicks within the vegetated water zones, which also takes into account significant chemical and physical processes that change the properties and the behavior of the oil slick in marine environment.

**Keywords:** oil spill, vegetation, wetlands, Caspian Sea, modelling, numerical simulation

## INTRODUCTION

While extracting crude oil from offshore reserves or transporting it from one place to another though water by tankers or by underwater pipelines, there is a risk of oil spills to the marine environment. There is also risk of natural seepage of oil or gas from reservoirs to the environment. However, the latter is usually less harmful and is at small scales compared to the first one, which is caused by human interference. If marine oil spill is at large scale and is close to a shoreline, it affects ecosystem of coastal wetlands. Pollution of coastal wetlands by oil spills is considered as serious environmental disaster since wetlands are important for the ecosystem by storm and flood protection, good water quality, faunal support, recharge groundwater, carbon sequestration and stabilize climate conditions and control pests [1, 2].

Not all types of crude oil are buoyant. Whether spilled oil floats or not is defined by a scale developed by the American Petroleum Institute (API scale). The scale is inversely proportional to the specific gravity of the oil at 15.60°C. API of freshwater is 10 and most of the crude oil has higher API than 10, therefore, they float in freshwater. But, there are also some heavier refined products which have lower API. Such types of products are referred also as Group V oils. Oils of Group V are not dangerous to vegetation unless oil spill occurred very close to coastal wetlands. Once this type of oil is spilled it starts to sink immediately, thus, presenting different clean up challenges. In the current paper we consider buoyant oil, and how air and water flow influence

to its movement in vegetated wetlands [3]. The study was carried out using numerical analysis. Such studies are very important, since they help to predict oil slick behavior near shorelines with vegetation or plants. One of the potential places for applications of the numerical modeling techniques is the coastal areas of Caspian Sea in western Kazakhstan where oil contamination takes place as a result of emergency situations such as crude oil discharge from abandoned oil wells, damaged underwater pipelines, or the transportation of crude oil by tankers or ships.



**Fig.1.** Consequence of the oil spill in the Gulf of Mexico. *Photo by Lee Celano*

* To whom all correspondence should be sent:
  aigul_01_09@mail.ru

Fig.2 shows the oilfields in the Caspian Sea, the western part of [4, 5] Kazakhstan. Some of the oil places are very close to the shoreline. Therefore, there is a risk of oil spills to the coastal flora and fauna.



**Fig.2.** Oilfields in western Kazakhstan: Kashagan, Kalamkas, and Kairan

Although, results in this paper does not completely describe the process, it is considered as the first step towards developing efficient numerical tool for prediction of oil slick advection in vegetated coastal areas. The model also takes into account physical and chemical processes affecting to oil slick properties which are different from the open-air case.

## MODEL FORMULATOIN

Once oil spilled to a marine environment, it is influenced by physical and chemical processes caused by the environment. They are spreading, advection, evaporation, dissolution, natural dispersion, emulsification, photo-oxidation, sedimentation, and biodegradation [6, 7]. Most of the previous studies related to oil slick advection with above listed physical and chemical processes taken into account, were carried out without considering any hydrodynamic interaction between oil slicks and vegetation in coastal areas, but only in an open sea.

We decided to study this process in a simple way with the purpose of developing complex mathematical model later which describes oil slick movement in vegetated coastal areas. Therefore, it is assumed that there is vegetation established in a channel with flow direction as described in Fig.3. The leaves and shoots of the vegetation are not fully submerged to the water. Therefore, it is assumed that air flow also takes place together with water flow through the vegetation. If oil slicks are presented in the channel flow, the physics of the process become similar to Fig.1. In order to numerically model this process, two dimensional modelling approach is considered to be enough to evaluate the process of oil slick movement through the vegetated water, otherwise, three dimensional modelling is computationally expensive for such processes.
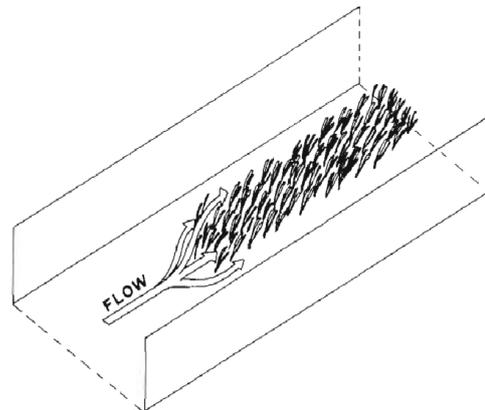


**Fig.3.** Visualization of the physics of the problem

Fig.4 illustrates the computational domain, where flow direction is along positive *x* direction. The vegetation is located in the center of the domain in $1m^2$ area and the cross section of the vegetation is considered as a circular shape with the diameter of 1 cm. The number of the circles are 256 which are evenly distributed in the $1m^2$ area and the oil slick will flow through the vegetation with the velocity determined from the water flow velocity.
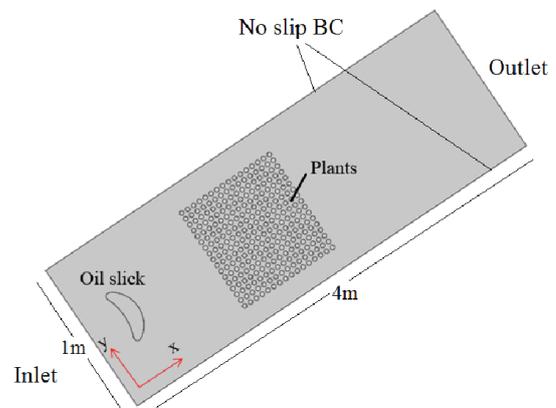


**Fig.4.** Visualization of the computational domain

Water flow is described using Navier-Stokes equations:

$$\frac{\partial u}{\partial t} + u\frac{\partial u}{\partial x} + v\frac{\partial u}{\partial y} = \nu\left(\frac{\partial^2 u}{\partial x^2} + \frac{\partial^2 u}{\partial y^2}\right) \quad (1)$$

$$\frac{\partial v}{\partial t} + u\frac{\partial v}{\partial x} + v\frac{\partial v}{\partial y} = \nu\left(\frac{\partial^2 v}{\partial x^2} + \frac{\partial^2 v}{\partial y^2}\right)$$

where *u, v*- velocity components, m/s; *V* - kinematic viscosity, $m^2$/s; *x, y*- coordinates, m and *t*- time, s. Eqn. (1) is solved numerically using non-slip boundary conditions (BC) at the side walls of

the channel, and inlet velocity is 1 m/sec. Moreover, BC at the outlet is set up in terms of the pressure. Thus, based on the solution of Eqn. (1) velocity field is determined. Velocity field, in its turn, is used to calculate advection-diffusion process of the oil slick:

$$\frac{\partial C}{\partial t} + u\frac{\partial C}{\partial x} + v\frac{\partial C}{\partial y} = D\left(\frac{\partial^2 C}{\partial x^2} + \frac{\partial^2 C}{\partial y^2}\right) \quad (2)$$

where $C$ is oil concentration which equals to 100 mol/m$^3$ at initial time and $D$ is the diffusion coefficient (m$^2$/sec). Boundary conditions for oil concentration along sidewalls are Neumann type:

$$\frac{\partial C}{\partial n} = 0 \quad (3)$$

where $n$ - normal vector to the side wall, m. At the inlet there is no entering oil concentration, and at the outlet, outflow boundary condition is set up for the oil slick movement.

## RESULTS AND DISCUSSIONS

### *Modelling results*

Once water starts to flow, vortices are formed after the vegetations. Such vortices can be seen from Fig.5 based on velocity streamlines.
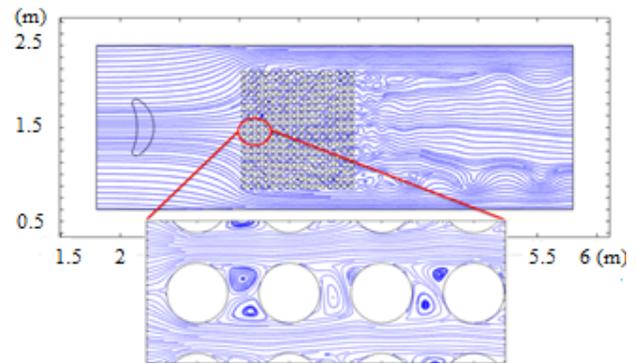


**Fig.5.** Velocity streamlines and vortices around the vegetations

The oil concentration movement is calculated after finding the velocity field. The resulting oil slick spread thought the vegetations after 1 sec is shown in Fig.6. It can be noticed that oil slick consternation spreads over large area while passing thought the vegetations. The spreading area depends on the density of the vegetations. Such behaviour of the oil slick thought the vegetations directly influence to physical and chemical processes that affect to the oil slick composition and properties. Indeed, these processes dominate at different times following the oil spill and thus leading to the loss of the oil mass.
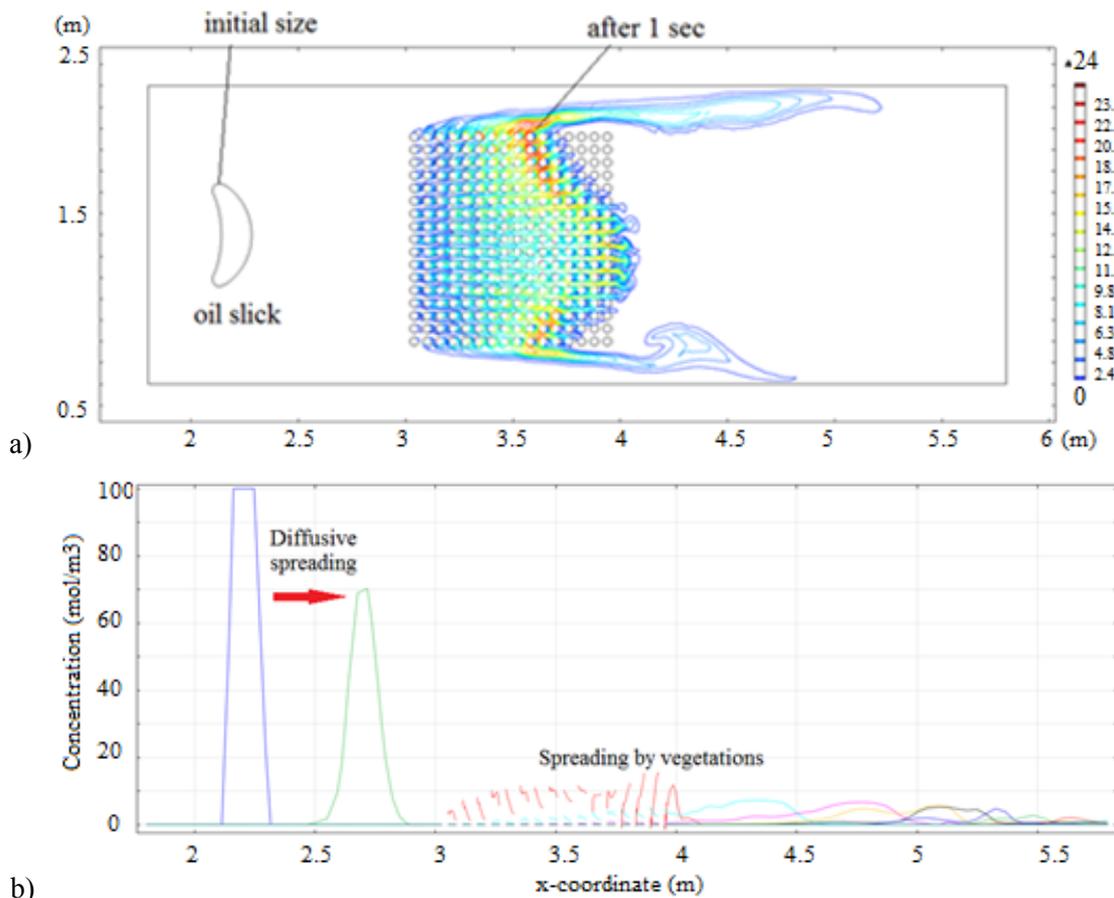


**Fig.6.** Oil slick spreading: a) after 1 sec; and b) oil slick spreading with time interval 0.2 s

It can be seen from Fig.7 that processes such as evaporation, dispersion, emulsification and spreading affect to the oil slick right after it spilled to the sea, and have more influence to change the oil properties than dissolution, oxidation, biodegradation and sedimentation.
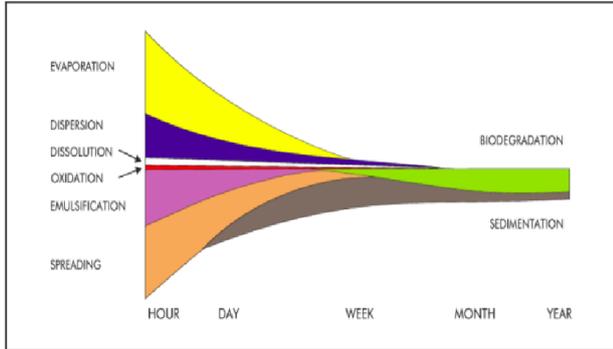


**Fig.7.** Time dependence of the physical and chemical processes that affect to oil slick properties

*Spreading*

Once oil spilled, it spreads while floating over the water surface. The rate of surface area change of the oil slicks has been studied by Fay [7], Hault [8], and later modified by Mackay at al. [12]. Thus, the rate of surface area change of the oil slick is calculated by the following formula:

$$\frac{dA_S}{dt} = K_{Spread} \cdot A_S^{\frac{1}{3}} \cdot \left[\frac{V}{A}\right]^{\frac{4}{3}} \quad (4)$$

where $A_S$ - area of the slick, m$^2$; $K_{Spread} = 150$ - constant, 1/s; $V$ - volume of the spilled oil, m$^3$. But, in case of the absence of vegetation not fully submerged to the water, it influences to the rate of the surface area of the oil slick. Thus, it is concluded that surface area change of the oil slick should be proportional to the density of the vegetation. For instance, when vegetation density increases, surface area of the oil slick also increases. Therefore, eqn. (4) should be modified to the following form:

$$\frac{dA_S}{dt} = K_{Spread} \cdot A_S^{\frac{1}{3}} \cdot \left[\frac{V}{A}\right]^{\frac{4}{3}} \cdot \rho_{vegetation} \quad (5)$$

*Evaporation*

It is one of the early time processes that causes significant mass loss in all kinds of oil which has API>10. Moreover, it can significantly change density, viscosity and other properties. Most of the time, evaporation is responsible up to 60 percent of spilled oil mass loss. As the lighter components of the oil slick evaporates faster than heavier components, chemical composition of the slick changes. There are two famous methods applied to calculate an evaporation rate: a) the pseudo-component method [9, 10], and b) the analytical approach [11]. The pseudo-component approach uses oil as a set of fractions grouped by boiling point and molecular weight. Consequently, for different components, there are different evaporation rates. On the other hand, in the analytical approach vapor pressure is a function of evaporated fraction. The analytical method developed by Stiver and Mackay [10] is applied to calculate volume fraction evaporated:

$$F_E = \ln[1 + B(T_G/T_E)(K_E \cdot A_S \cdot t/V_0) \\ \cdot \exp(A - B(T_0/T_E))] \cdot [T_E/(BT_G)] \quad (6)$$

where $F_E$ - evaporated volume fraction, %; $K_E = 2.5 \cdot 10^{-3} \cdot U_{wind}^{0.78}$ mass transfer coefficient for evaporation, m/s; $U_{wind}$ - wind speed, m/s; $V_0$ - initial volume of oil spill, m$^3$; $T_0$ - initial boiling point, $K$ when $F_E$ is zero I, $T_E$ - environmental temperature, K; $T_G$ - gradient of the boiling point, K/m; $T_B$ и $T_E$ line, $K$, $A$ and $B$ are constants which can be chosen from distillation data. According to Stiver and Makay's calculations where they used distillation data for five different types of crude oils, magnitude of $A$ and $B$ are 6.3 and 10.3 respectively.

It can be seen from Eqn. (6) that evaporated volume fraction $F_E$ is the function of surface are of the slick which depends on the vegetation density. Moreover, $U_{wind}$ - wind velocity, m/s and temperature profile inside the vegetation also depends on, $\rho_{vegetation}$ number of vegetation/m$^2$. Therefore, Eqn. (6) also must be modified in the way that it accounts for the presence of the vegetation and its height emerged from the water surface which influences to the temperature inside the vegetation, consequently, evaporation rate.

*Emulsification*

The process of emulsification is the inverse of dispersion where instead of oil droplets dispersing into the water column, water enters into the oil [13]. As a consequence of the emulsification, volume, density and especially viscosity of oil slick changes. Mackey et al. suggested the following formula to calculate the incorporation of water into oil slick:

$$\frac{dF_{wc}}{dt} = K_{wc}(U_{wind} + 1)^2(1 - F_{wc})/OC \quad (7)$$

where $F_{wc}$ - fraction of water in oil, %; $OC$ - final fraction of water content, % and $K_{wc}$ is taken as 2x10$^{-6}$, ms/m$^2$. Here, Eqn. (7) also needs to be modified because if oil slick is located in vegetated

area, the rate of fraction of water in oil $F_{wc}$ changes differently. It can be seen from the last formula that $U_{wind}$ is different in case of vegetated area than the one where open water surface because inside vegetation wind speed changes depending on the density of the vegetation.

### *Density and viscosity*

As already mentioned above, evaporation and emulsification are the main processes that change the density and viscosity of the oil slick, and they must be modified taking into account the presence of the vegetation and its density. The following formulas are broadly used to calculate density $\rho$, kg/m³ and viscosity changes $\mu$ Pa/s [14]:

$$\rho = F_{wc}\rho_w + (1 - F_{wc})(\rho_{ref} + C_{E2}F_E) \qquad (8)$$

$$\mu = \mu_{ref}\exp(C_{E1}F_E + (C_{wc1}F_{wc})/(1 - C_{wc2}F_{wc}))$$

where $\rho_{ref}$ and $\mu_{ref}$ are the viscosity and density of fresh oil at reference temperature, $C_{E1}$, $C_{E2}$, $C_{wc1}$ and $C_{wc2}$ are assigned values by the user based on the general oil type. Thus, from the formulas, it can be noticed that once evaporation and emulsification equations are modified in order to take into account the vegetation, Eqns. (8) will describe density and viscosity changes of the oil slicks inside the vegetation zones.

### CONCLUSION

Oil contamination of water is hazardous to the environment. It happens naturally as well as with the interaction of humans. It is very important to predict how spilled oil behaves itself in the marine environment and what kind of environmental processes influence to the change of the oil properties.

The fluid and thermal properties of oil slicks change differently in vegetated coastal areas than the case where slicks are on an open sea. Therefore, in the current paper, we studies the hydrodynamics of oil slick in vegetated areas, using two dimensional modelling and the channel flow parameters. Results showed that the oil slick spreads faster while flowing thought the vegetated zone. Such behaviour of the oil slick assists in the changes of physical and chemical processes such as evaporation, emulsification, surface area change, density and viscosity changes which influence to the oil property. It was discussed that formulas used to describe these processes should be modified by taking into account the presence of the vegetation and its density. Our purpose in the future, is to

carefully study the appropriate modification of these formulas based on experimental and numerical methods which will describe the changes of oil slick properties and its hydrodynamic behaviour in vegetated coastal areas.

### REFERENCES

1  Irving A. Mendelssohn, Gary L. Andersen, Donald M. Baltz, Rex H. Caffey, Kevin R. Carman, John W. Fleeger, Samantha B. Joye, Qianxin Lin, Edwa rd Maltby, Edwa rd B. Overton, and Law rence P. Rozas. Oil Impacts on Coastal Wetlands: Implications for the Mississippi River Delta Ecosystem after the Deepwater Horizon Oil Spill. *BioScience*, 62 (6), 562-574, (2012).

2  ITOPF, Fate of marine oil spills, Technical information letter.

3  C. H. Peterson, R. A. Luettich Jr., F. Micheli, G. Skillete Attenuation of water flow inside seagrass canopies of differing structure, *Mar Ecol Prog Ser*, 268, 81-92 (2004).

4  D. Urbaniak, E. Gerebizza, G. Wasse, M. Kochladze, Kashagan oil field development, Kazakhstan, *Report of European Union*, 2007.

5  T. K. Akhmetzhanov, A. S. Abd elmaksoud, D. K. Baiseit, and I. B. Igembaev, Chemical properties of reservoirs, oil and gas of Kashagan field, southern part of pre-caspian depression, Kazakhstan, *International Journal of Chemical Science*, 10 (1), 568-578, (2012).

6  W. J. Lehr, Review of modeling procedures for oil spill weathering behavior. HAZMAT Division, NOAA. USA.

7  J.A. Fay, The spread of oil slicks on a calm sea, *Oil on the Sea*,. NY: Plenum Press ,53-63 (1969).

8  D.P. Hoult, Oil Spreading on the sea. *Annual Review of Fluid Mechanics*, Van Dyke (ed.), 341-368 (1972).

9  W.C. Yang, and H. Wang, Modelling of oil evaporation in aqueous environment, *Water Res*, 11, 879-887 (1977).

10  P. Sebastiao, and C.G. Soares, Weathering of oil spills accounting for oil components, *Transactions on Ecology and the Environment*, 20, 63-72 (1998).

11  In R. Garacia-Martinez & C. A. Brebbia, Oil and Hydrocarbon Spills III: Modelling, Analysis and Control, Southampton, UK: WIT Press, 63–72 (2002).

12  D. Mackay, I. Buist, R. Mascarenhas, and S. Paterson, Oil Spill Processes and Models. *Environmental Protection Service, Environment Canada*, (1980).

13  M. Reed, The physical fates component of the natural resource damage assessment model system, *Oil Chem Pollut*, 5 (2-3), 99-123 (1989).

14  T. Stocker, Introduction to Climate Modelling, Springer (2011).

# Analysis of results after implementation of energy saving measures in public buildings

G. I. Valtchev[1], N. G. Kalojanov[2], V. D. Rasheva[1*], M. St. Minchev[1], S. Ts. Tasheva[1]

*[1]University of Food Technologies, Address 26, Maritza Blvd. 4000, Plovdiv, Bulgaria*
*[2]Technical University of Sofia, Address 8, St. Kliment Ohridski Blvd., 1756, Sofia, Bulgaria*

Energy audit of educational buildings of the University of Food Technologies (UFT) is performed. A project for renovation of these buildings has been developed and accomplished in this view. The data from the invoices for heating of these buildings for more than three full heating seasons after the project accomplishment have been collected and analysed. The results show 25.56% reducing of energy consumption for heating of Block 1, respectively 46.73% for heating of Block 3 and 60% for heating of Block 4. The energy savings for all three blocks is 40.4%.

**Keywords:** energy efficiency, energy savings, UFT

## INTRODUCTION

Climate change and security of energy supply are two major challenges needing urgent action. They have common causes and common solutions. Except of that, the future seems marked by permanently rising price of energy, which we use in our life.

Analyses based on Eurostat data show retardation of Bulgaria in basic energy-economical indicators for sustainable development. Bulgaria is the most energy-intensive country - respectively 7.46; 6.81; 6.37; 6.81; 7.41; 6.12; 2.62 and 4.7 times more energy intensive than Austria, Denmark, France, Germany, Italy, Greece, Hungary and Turkey. Except of that, Bulgaria is one of the most dependent countries with regard to imports of energy resources in Europe – 71.6 %. Heating in buildings is the largest consumer of energy and generator of $CO_2$ emissions, released into the environment. The new EU member countries use more than 40% of their energy in buildings. In fact up to 80% of this energy can be saved by renovating the existing buildings and implementation of cost-effective energy conservation measures (ECMs) [1, 2, 3, 4, 5].

The aim of this paper is to report the results of ECMs implementation in educational buildings of University of Food Technologies (UFT) according to the project "Energy efficiency, improve access for people with disabilities in UFT and modernization of information services", realized with the financial support of OP "Regional Development", co-financed by European Union through European Regional Development Fund.

## MATERIALS AND METHODS

The above mentioned project has been developed and won on the basis of energy audits of the educational building blocks 1, 3 and 4 of the UFT carried out in 2010. Details of their geometric, structural and energy characteristics are presented in our previous publication [6].

The building of Block 1 was put into operation in 1962. It is a building with monolithic structure of 4 floors, built up area of 2520 $m^2$ and heated area of 10138 $m^2$. The exterior walls have a global heat transfer coefficient of 1.48 W/(m$^2$K). The windows were in poor condition – with deformed frames and unsealed. The floor is mainly floor of a heated basement above the ground and only 132.9 $m^2$ are exposed to outdoor air. The roof of the main building is cold roof with ventilating airspace and over the tower is a cold roof. The heating system is "Tichelman" type with upper distribution and forced circulation. The heating station is common to the blocks 1, 2 and 3 and is equipped with all measurement. Losses in the distribution network are estimated at 5.6%.

Based on the available funding for the project, only 1 ECM (replacement of old windows by new ones with aluminium frame, thermal bridge and double glazing with 1 "K" glass) was provided and realized.

The building of Block 3 is composed of two bodies - monolithic and sectional with a hot link between them. The build up area is 2130 $m^2$ and the heated area is 5580 $m^2$. The monolithic body is a sequel of Block 1 with three floors and a heated basement with exterior walls of grid bricks. The roof is a cold roof with ventilating airspace. The sectional body consists of a heated basement and two floors. The walls are built of grid bricks. The roof is made

of reinforced concrete slab with waterproofing. The windows were in poor conditions – with deformed frames and unsealed. The two-pipe heating system has lower distribution and forced circulation. The horizontal piping is well insulated. Vertical pipes are not insulated, but are in good condition. Losses in the distribution network are estimated at 6.1%.

The following ECMs were provided and implemented as a result of the energy audit:

1. Thermal insulation of all outside walls: with 7 cm fiber.

2. Replacement of old windows with new ones with aluminium frames, interrupted thermal bridge and double glass package having 1 "K" glass.

3. Thermal insulation of the roof with 10 cm mineral wool (for the monolithic body over the ceiling plate in the roof space and for the sectional body - externally).

The building of Block 4 is a monolithic building with 4 flours. In adjacent to main building one-store buildings are situated: a Teaching laboratory and a Boiler room. The built area is 1740 m$^2$ and the heated area is 5044 m$^2$ (boiler room is not heated). The heating system type «Tichelman» was in bad condition. Supply and return lines were located in a technical channel below the ground floor and were in very bad condition, with compromised insulation. There were difficulties with the correct maintenance of supply and return lines. Losses in the distribution network were estimated at 12.4 %. Internal heating system was amortized with glider cast iron radiators. In premises with a North exposure it could not maintain the required temperature. The lack of thermostatic room temperature control did not allow the regulating the heat supply in the two branches of the installation – North and South. The windows were in poor condition – with deformed frames and unsealed. The fourth floor belonged many years to another organization and after being released it was found that some of the windows have been left open for a long time. The science laboratory (former gymnasium) had the heating system switched off because of the many leakages.

As a result of the energy audit, and then of the project implementation, the following ECMs have been put into practice:

1. Thermal insulation of all outside walls: with 7 cm fibre.

2. Replacement of old windows by windows with aluminium frames, interrupted thermal bridge and double glass package having 1 "K" glass.

3. Thermal insulation of the roof: for the main building - inside of the ceiling plate with 10 cm mineral wool and gypsum-paper wall, and for the

two adjacent one-stored buildings - outside with 12 cm mineral wool.

4. Thermal insulation of the floor exposed to outdoor air: outside with 7 cm fibre.

5. Replacement of the horizontal distribution network of heating system (removing over level 0). Installation of three horizontal circles: one northern and two southern circles (for the ground floor and the other floors).

6. Replacement of vertical pipes and radiators with aluminium ones.

7. Installation of energy-efficient variable-speed pumps in the boiler room.

8. Replacing the heat source – passing from central heating towards a condensing boiler of a new generation, operating on natural gas.

The project was implemented from September 2011 until the end of April 2012.

## RESULTS

More than three full heating seasons after implementing the ECMs have analysed. Data from the invoices for heating of Blocks 1, 3 and 4 for the period before the implementation of ECMs (2009, 2010 and 2011) and for the period beyond implementation of ECMs (from November 2012 to the end of 2015) in the natural and financial terms were collected and processed. These data are presented in Table 1. Heat consumption during the project implementation (from September 2011 to April 2012) is not subject to this study.

**Table 1.** Energy consumption for heating of Blocks 1, 3 and 4 before and after ECMs implementation

| Years | Month | I | II | III | IV | Total for I, II, III и IV | X | XI | XII | Total for X, XI и XII | Total for the year |
|---|---|---|---|---|---|---|---|---|---|---|---|
| 2015 | MWh | 199 | 194 | 86 | 24 | 502 | - | 48 | 117 | 166 | 668 |
| 2015 | BGN | 18526 | 18024 | 7916 | 2036 | 46503 | - | 3948 | 9503 | 13451 | 59954 |
| 2014 | MWh | 182 | 138 | 58 | - | 378 | 32 | 125 | 105 | 263 | 640 |
| 2014 | BGN | 16426 | 12517 | 5173 | - | 34115 | 3007 | 11632 | 9736 | 24375 | 58490 |
| 2013 | MWh | 230 | 182 | 120 | 23 | 555 | - | 63 | 135 | 199 | 754 |
| 2013 | BGN | 21531 | 17034 | 11139 | 2005 | 51710 | | 5259 | 12159 | 17419 | 69128 |
| 2012 | MWh | - | - | - | - | - | - | 63 | 161 | 224 | - |
| 2012 | BGN | - | - | - | - | - | - | 6250 | 16041 | 22291 | - |
| 2011 | MWh | 293 | 354 | 263 | - | 909 | - | - | - | - | - |
| 2011 | BGN | 29076 | 35251 | 26185 | - | 90512 | - | - | - | - | - |
| 2010 | MWh | 259 | 400 | 227 | - | 886 | - | 58 | 215 | 273 | 1159 |
| 2010 | BGN | 23128 | 35671 | 20136 | - | 78935 | - | 6053 | 22647 | 28701 | 107635 |
| 2009 | MWh | 214 | 276 | 246 | - | 736 | - | 149 | 242 | 390 | 1126 |
| 2009 | BGN | 22426 | 29160 | 25844 | - | 77430 | - | 12538 | 20386 | 32923 | 110353 |

The results of the Table 1 show that the total energy consumption for heating of Blocks 1, 3 and 4 is 1126.37 MWh for 2009 and 1159.51 MWh for

2010. The average thermal energy consumption for these 2 years is 1142.94MWh. The total energy for heating is 754 MWh for 2013, 640.4 MWh for 2014 and 667.61 MWh for 2015. The average consumption of thermal energy of these 3 years is 2061.04 MWh. The decrease in the heat energy consumed for heating after the ECMs implementation is 40.04%. The results of the Table 1 are presented in Fig.1.
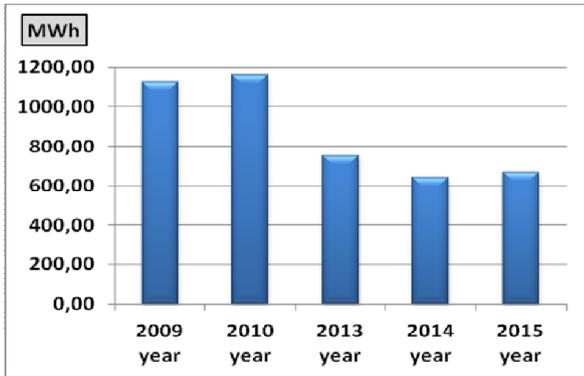


**Fig.1.** Energy consumption for heating of Blocks 1, 3 and 4 before and after ECMs implementation

The same data, but considered for the first half of years (months I, II, III and IV) show that the total consumption of energy for heating for I, II, III and IV months of 2009 is 735.75 MWh, 886.51 MWh for 2010, 909.3MWh for 2011, and the average of this three years for the same months is 843.7 MWh. The monthly energy consumption in total for the months I, II, III and IV is 555 MWh in 2013, respectively 377.53 MWh in 2014, 502.1 MWh in 2015 and the average of these 3 years for the same months is 477.9 MWh. The decrease in the energy consumed for heating after ECMs implementation is 43.36%. The results are presented in Fig.2.
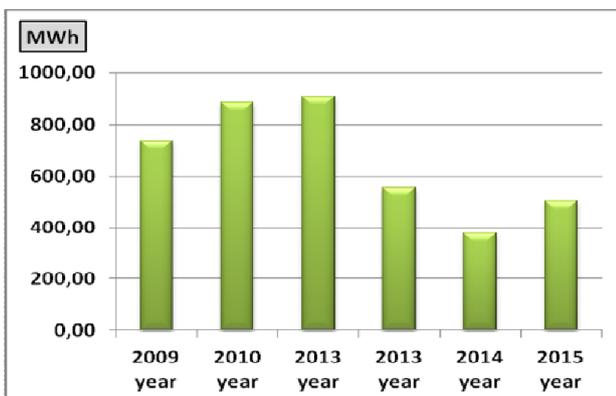


**Fig.2.** Average monthly energy consumption per years for months I, II, III and IV

For the period of the second half of years (months X, XI and XII) the total energy consumption after

ECMs implementation (2012, 2013, 2014 and 2015) is 851.4 MWh and the average annual energy consumption is 212.8 MWh. The total energy consumption before ECMs implementation (2010 and 2011) is 6636 MWh and the average annual energy consumption is 331.3MWh. The average annual decrease in the heat energy consumed after the ECMs implementation is 35.8%. The results are presented in Fig.3.
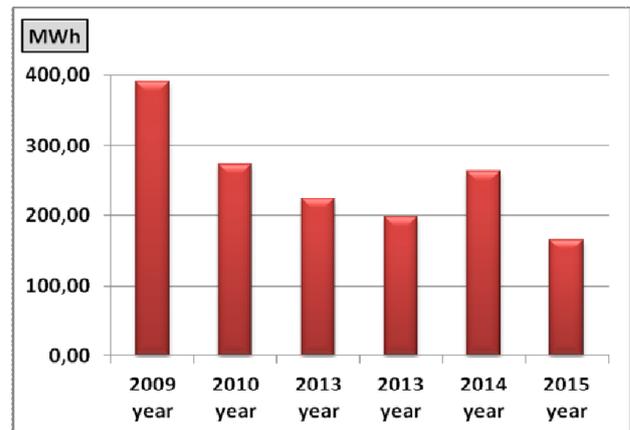


**Fig.3.** Average monthly energy consumption per year for month X, XI and XII

The data of energy consumption only for heating of Block 1 before and after implementation of the ECMs are presented in Table 2.

**Table 2.** Energy consumption for heating of Block 1 before and after ECM implementation

| Years | Month | I | II | III | IV | Total for I, II, III и IV | X | XI | XII | Total for X, XI и XII | Total for the year |
|---|---|---|---|---|---|---|---|---|---|---|---|
| 2015 | MWh | 122 | 123 | 83 | 14 | 342 | - | 33 | 71 | 104 | 445 |
| | BGN | 11067 | 11190 | 7519 | 1138 | 30913 | - | 2687 | 5882 | 8569 | 39482 |
| 2014 | MWh | 110 | 83 | 36 | - | 228 | 21 | 66 | 78 | 164 | 393 |
| | BGN | 9460 | 7194 | 3073 | - | 19727 | 1862 | 6003 | 7045 | 14910 | 34638 |
| 2013 | MWh | 145 | 112 | 80 | 16 | 353 | - | 39 | 82 | 121 | 475 |
| | BGN | 13200 | 10199 | 7302 | 1404 | 32105 | - | 3114 | 7102 | 10215 | 42320 |
| 2012 | MWh | - | - | - | - | - | - | 39 | 100 | 139 | - |
| | BGN | - | - | - | - | - | - | 3810 | 9661 | 13472 | - |
| 2011 | MWh | 151 | 184 | 135 | - | 470 | - | - | - | - | - |
| | BGN | 14983 | 18343 | 13418 | - | 46743 | - | - | - | - | - |
| 2010 | MWh | 134 | 215 | 114 | - | 463 | - | - | 115 | 115 | 578 |
| | BGN | 11971 | 19159 | 10129 | - | 41259 | - | - | 12085 | 12085 | 53344 |
| 2009 | MWh | 113 | 145 | 132 | - | 390 | - | 78 | 130 | 208 | 598 |
| | BGN | 11911 | 15370 | 13883 | - | 41164 | - | 6558 | 10988 | 17546 | 58710 |

The results of the Table 2 show that the total energy consumption for heating of Block 1 for the three full years after the ECMs implementation (2013, 2014 and 2015) is 1312.6 MWh and the average annual energy consumption for the same period is 437.5 MWh per year. The heating energy

consumption for the two full years before the ECMs implementation (2009 and 2010) is 1175.6 MWh and the average annual energy consumption for the same period is 587.8 MWh per year. The average annual decrease in heat energy consumption after the ECMs is 25.56%. The results in Table 2 are presented in Fig.4.
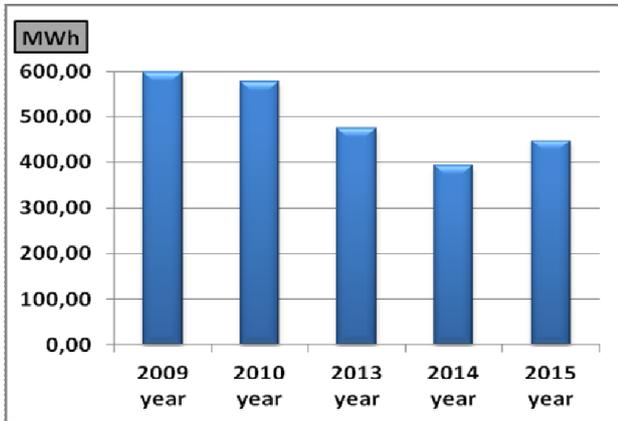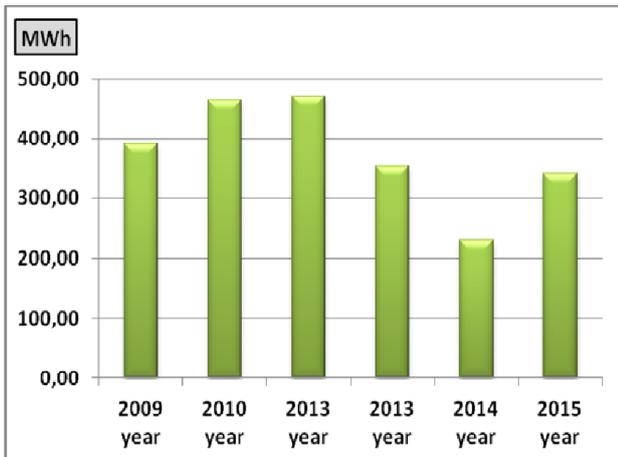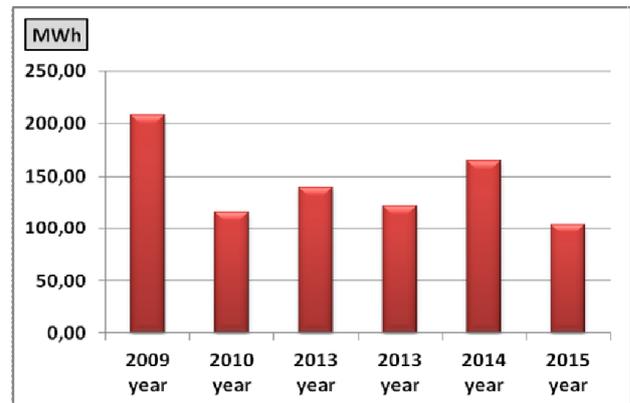


**Fig.4.** Energy consumption for heating of Block 1

The results in Table 2 show that the total consumption of thermal energy for heating of Block 1 for months I, II, III and IV is 390.4 MWh in 2009, 462.7 MWh in 2010 and 469.30 MWh in 2011. The average of these three years for the same months is 440.9 MWh. The monthly consumption of thermal energy for heating in the months I, II, III and IV of 2013 is 353.2 MWh, respectively for 2014 is 228.37 MWh, for 2015 is 341.63 MWh and the average of these 3 years for the same months is 307.73 MWh. The decrease in the heat energy consumption for heating after the implementation of ECMs is 30.6%. The results are presented in Fig.5.



**Fig.5.** Average monthly energy consumption (Block 1) per years for month I, II, III and IV

Similarly the total consumption of thermal energy for heating of Block 1 during the months X, XI and XII of 2009 is 207.6 MWh, respectively for 2010 year is 114.9 MWh (as there was no heating for November this year) and the average of these 2 years is 132.16 MWh. The consumption of thermal energy for heating in total for the months X, XI and XII of 2012 is 139.2 MWh, respectively for 2013 is 121.44 MWh, for 2014 is 164.31 MWh, for 2015 is 103.71 MWh, and the average consumption of these 4 years for the same months is 132.16 MWh. The decrease in the heat energy consumed for heating after the ECMs implementation is 18%. The results are presented in Fig.6.



**Fig.6.** Average monthly energy consumption (Block 1) per years for month X, XI and XII

The data on energy consumption for heating of Block 3 before and after implementation of the ECMs are presented in Table 3.

**Table 3.** Energy consumption for heating of Block 3 before and after ECMs implementation

| Years | Month | I | II | III | IV | Total for I, II, III и IV | X | XI | XII | Total for X, XI и XII | Total for the year |
|---|---|---|---|---|---|---|---|---|---|---|---|
| 2015 | MWh | 48 | 49 | 33 | 5 | 134 | - | 13 | 28 | 41 | 175 |
| | BGN | 4355 | 4403 | 2958 | 447 | 12163 | - | 1057 | 2314 | 3371 | 15535 |
| 2014 | MWh | 43 | 33 | 14 | - | 90 | 8 | 26 | 31 | 65 | 155 |
| | BGN | 3722 | 2830 | 1209 | - | 7762 | 733 | 2772 | 2362 | 5867 | 13628 |
| 2013 | MWh | 57 | 44 | 32 | 6 | 139 | - | 15 | 32 | 48 | 187 |
| | BGN | 5194 | 4013 | 2873 | 553 | 12632 | - | 1225 | 2794 | 4020 | 16652 |
| 2012 | MWh | - | - | - | - | - | - | 16 | 40 | 56 | - |
| | BGN | - | - | - | - | - | - | 1499 | 3801 | 5301 | - |
| 2011 | MWh | 76 | 92 | 68 | - | 235 | - | - | - | - | |
| | BGN | 7505 | 9188 | 6721 | - | 23415 | - | - | - | - | |
| 2010 | MWh | 67 | 108 | 57 | - | 232 | - | 58 | 58 | 115 | 347 |
| | BGN | 5996 | 9597 | 5074 | - | 20667 | - | 6053 | 6053 | 12107 | 32774 |
| 2009 | MWh | 57 | 73 | 66 | - | 196 | - | 39 | 65 | 104 | 300 |
| | BGN | 5966 | 7699 | 6954 | - | 20620 | - | 3285 | 5504 | 8789 | 29409 |

The results in Table 3 show that the total energy consumption for heating of Block 3 for the three full years after the ECMs (2013, 2014 and 2015) is 516.5 MWh and the average annual energy

consumption for the same period is 172.2 MWh per year. The heating energy consumption for the two full years before the ECMs (2009 and 2010) is 646.5 MWh and the average annual energy consumption for the same period is 323.3 MWh per year. The average annual decrease in the heat energy consumed after the ECMs is 46.73%. The results in Table 3 are presented in Fig.7.
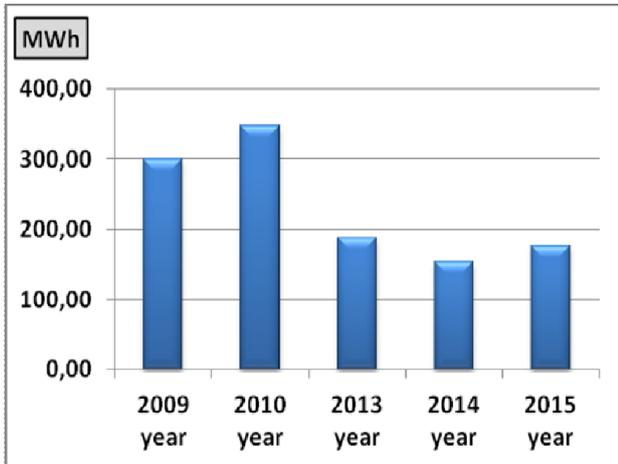


**Fig.7.** Energy consumption for heating of Block 3

The results in Table 3 show that the total consumption of thermal energy for heating of Block 3 for the months I, II, III and IV of 2009 is 195.5 MWh, for 2010 is 231.8 MWh and for 2011 is 235.3 MWh, and the average consumption of this three years for the same months is 220.7 MWh. The monthly consumption of thermal energy for heating in total for I, II, III and IV months of 2013 is 138.96 MWh, for 2014 – 89.9 MWh, for 2015 – 134.45 MWh and the average of these 3 years for the same months is 121.1 MWh. The decrease in the heat energy consumed for heating after the implementation of ECMs is 45.17%. The results are presented in Fig.8.
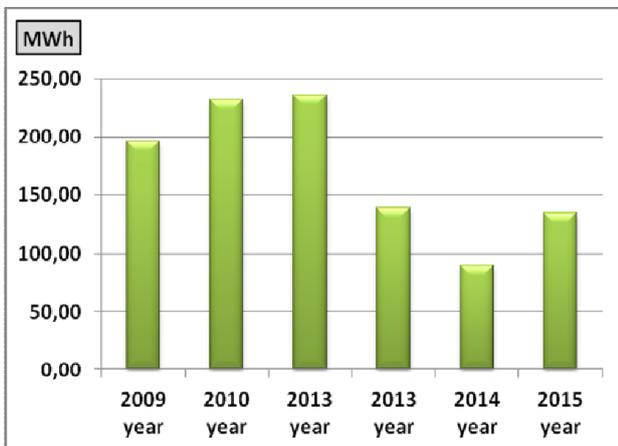


**Fig.8.** Average monthly energy consumption (Block 3) per years for months I, II, III and IV

Similarly the total energy consumption during X, XI and XII months of 2009 is 104.0 MWh, for 2010 – 115.2 MWh and the average of these 2 years – 109.8 MWh. The energy consumption for X, XI and XII months of 2012 is 55.6 MWh, for 2013 – 47.8 MWh, for 2014 – 64.6 MWh, for 2015 – 40.81 MWh, and the average consumption for these 4 years for the same months is 52.2 MWh. The decrease in the heat energy consumption after the ECMs is 52%. The results are presented in Fig.9.
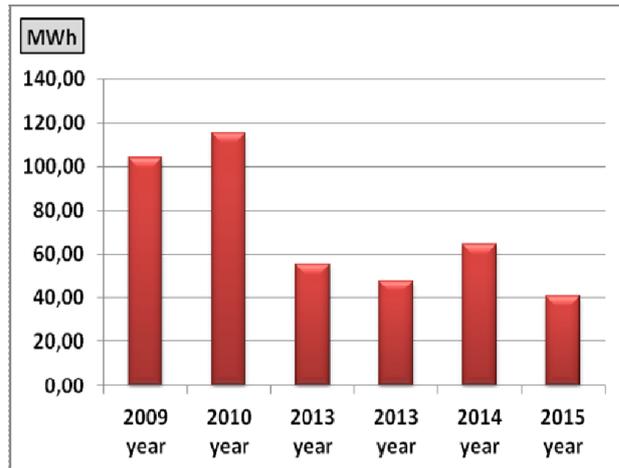


**Fig.9.** Average monthly energy consumption (Block 3) per years for month X, XI and XII

The data on energy consumption of Block 4 before and after the ECMs are presented in Table 4.

**Table 4.** Energy consumption of Block 4

| Years | Month | I | II | III | IV | Total for I, II, III и IV | X | XI | XII | Total for X, XI и XII | Total for the year |
|---|---|---|---|---|---|---|---|---|---|---|---|
| 2015 | Nm³.10³ | 3,087 | 2,418 | 1,874 | 0,495 | 7,874 | 0,001 | 0,305 | 1,951 | 2,257 | 10,131 |
| | MWh | 28,7 | 22,5 | 17,4 | 4,6 | 73,2 | 0,0 | 2,8 | 18,2 | 21,0 | 94,2 |
| | BGN | 3104 | 2432 | 1885 | 7 | 7871 | 1 | 204 | 1307 | 1511 | 9383 |
| 2014 | Nm³.10³ | 3,113 | 2,400 | 0,858 | - | 6,371 | 0,419 | 1,845 | 1,395 | 3,659 | 10,03 |
| | MWh | 29,0 | 22,3 | 8,0 | - | 59,3 | 3,8 | 17,2 | 13,0 | 33,9 | 93,3 |
| | BGN | 3243 | 2493 | 893 | - | 6629 | 411 | 1815 | 1371 | 3598 | 10224 |
| 2013 | Nm³.10³ | 3,015 | 2,711 | 0,926 | 0,048 | 6,700 | - | 0,912 | 2,243 | 3,155 | 9,855 |
| | MWh | 28,1 | 25,2 | 8,6 | 0,4 | 62,3 | - | 8,5 | 20,9 | 29,3 | 91,7 |
| | BGN | 3138 | 2822 | 964 | 48 | 6972 | | 920 | 2263 | 3184 | 10156 |
| 2012 | Nm³.10³ | - | - | - | - | - | - | 0,834 | 2,287 | 3,121 | - |
| | MWh | - | - | - | - | - | - | 7,8 | 21,3 | 29,0 | - |
| | BGN | - | - | - | - | - | - | 940 | 2578 | 3518 | - |
| 2011 | MWh | 66,1 | 77,5 | 60,7 | - | 204,3 | - | - | - | - | - |
| | BGN | 6588 | 7720 | 6047 | - | 20355 | - | - | - | - | - |
| 2010 | MWh | 57,8 | 77,5 | 56,3 | - | 191,5 | - | - | 42,9 | 42,9 | 234,4 |
| | BGN | 5161 | 6914 | 4933 | - | 17008 | - | - | 4509 | 4509 | 21517 |
| 2009 | MWh | 44,0 | 57,6 | 48,3 | - | 150,0 | - | 32,2 | 46,8 | 79,5 | 229,5 |
| | BGN | 4549 | 6092 | 5006 | - | 15647 | - | 2694 | 3894 | 6588 | 22235 |

The results of the Table 4 show that the total energy consumption for heating of Blocks 4 for the

three full years after the ECMs (2013, 2014 and 2015) is 279.22 MWh and the average annual energy consumption for the same period is 93.1 MWh per year. The heating energy consumption for the two full years before the ECMs (2009 and 2010) is 463.9 MWh and the average annual energy consumption for the same period is 231.2 MWh per year. The decrease in the heat energy consumed after the ECMs is 60%. The results of the Table 4 are presented in Fig.10.
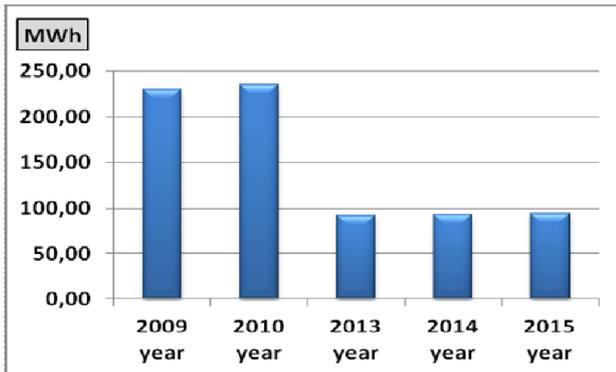


**Fig.10.** Energy consumption for heating of Block 4

The results of the Table 4 show that the total consumption of thermal energy for heating of Block 4 for I, II, III and IV months of 2009 is 149.95 MWh, for 2010 year – 191.51 MWh and for 2011 – 204.3 MWh. The average of these three years for the same months is 181.92 MWh. The monthly consumption of thermal energy for heating in total for I, II, III and IV months of 2013 is 62.33 MWh, for 2014 – 59.26 MWh, for 2015 – 73.24 MWh and the average of these 3 years for the same months is 65.1 MWh. The decrease in the energy consumed for heating after the implementation of ECMs is 64.27%. The results are presented in Fig.11.
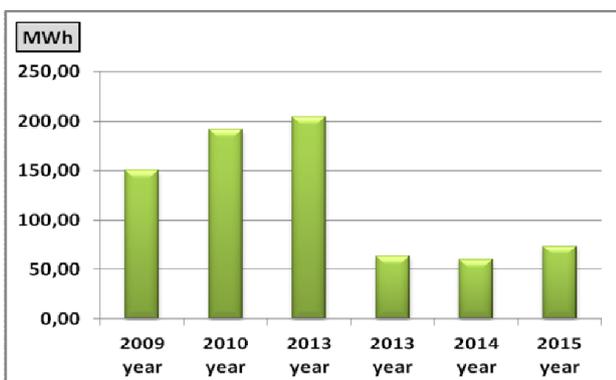


**Fig.11.** Average monthly energy consumption (Block 4) per years for months I, II, III and IV

Similarly the total consumption of thermal energy for heating of Block 4 during the months X, XI and XII of 2009 is 79.54 MWh, for 2010 year –

42.9 MWh (as there was no heating for November this year) and the average of these 2 years – 61.22 MWh. The consumption of thermal energy for heating in total for months X, XI and XII of 2012 is 29.02 MWh, for 2013 – 29.34 MWh, for 2014 – 33.94 MWh, for 2015 – 20.99 MWh, and the average consumption of these 4 years for the same months is 28.32 MWh. The decrease in the heat energy consumed for heating after the ECMs implementation is 53.74%. The results are presented in Fig.12.
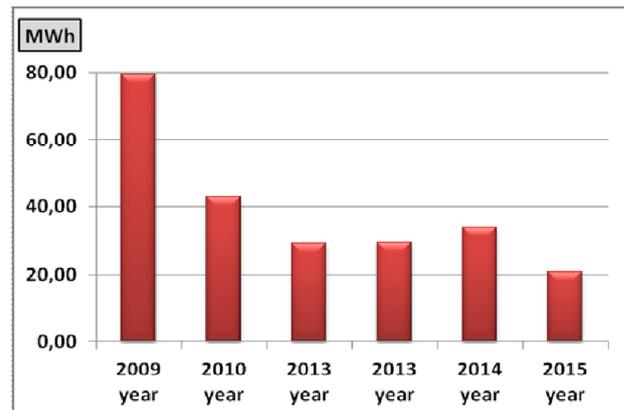


**Fig.12.** Average monthly energy consumption (Block 4) per years for month X, XI and XII

This paper presents data on energy savings compared to the actual energy consumption before implementation of the ECMs.

ECONOMIC ANALYSIS OF THE ECMs

Economic analysis of the rehabilitation must be performed in comparison to the baseline energy consumption, which ensures living comfort of the building (according to the legislation in this field). The baseline energy consumption in Block 1 is 918 034 kWh/y, in Block 3 - 595 222 kWh/y; in Block 4 - 600 734 kWh/y and in all three Blocks of UFT is 2 113 990 kWh/y.

The average energy consumption for heating of the three Blocks after ECMs implementation is 687 330 kWh/y, while the average annual energy savings are 1 426 660 kWh/y.

Investments for the ECMs implementation are: for Block 1 - 330 560 BGN, for Block 3 - 350 207 BGN, for Block 4 - 374 409 BGN and total for all 3 Blocks are 1 055 176 BGN.

Under these conditions, the payback period (PB) of all ECMs is 8.9 years, the inner return ratio (IRR) is 11.1% and the net present value (NPV) is 3 586 323 BGN. Therefore the ECMs are cost effective. The economic analysis has been performed with software ENSI Economy.

## CONCLUSIONS

1. University of Food Technologies (UFT) in Plovdiv implemented the project **"Energy efficiency, improving access for people with disabilities at the University of Food Technologies - Plovdiv and modernization of information services",** BG161PO001/1.1-07/2009/010 within which being implemented the prescribed energy saving measures.

2. The data on energy consumption for heating of 3 educational buildings of UFT before and after the implementation of ECMs were collected and processed on the basis of energy invoices.

3. As result of project ECMs implementation in Blocks 1, 3 and 4 the heat energy consumption has been reduced with 40.04% yearly. The really saved energy for the whole studied period is 1571.3 MWh compared to the average consumption for 2009 and 2010. The saved $CO_2$ emissions, emitted in the environment represent 456 tons.

4. Reduction of heat energy consumption for Block 1 is 25.56% per year. The saved heat energy for the whole studied period is 515.87 MWh and the saved $CO_2$ emissions are 149.60 tons.

5. Reduction of heat energy consumption for Block 3 is 46.73% per year. The saved heat energy for the whole studied period is 528.88 MWh and the saved $CO_2$ emissions are 153.38 tons.

6. Reduction of heat energy consumption for Block 4 is 60.0% per year. The saved heat energy for the whole studied period is 482.39 MWh and the saved $CO_2$ emissions are 139.89 tons.

7. The economic analysis shows that the performed ECMs are cost effective with a PB of 8.9 years, a IRR of 11.1% and a NPV of 3 586 323 BGN.

## REFERENCES

1 Valtchev, G. Energy Efficiency and Protection of the Environment. Scientific Conference 2010, University in Town of Chanak Kale, Turkey, (2010).

2 Valtchev, G., N. Kalojanov, M. Minchev, V. Rasheva, S. Tasheva. Analysis of the Potential of Energy Consumption in Student Hostel "Maritza 3" of University of Food Technologies – Plovdiv, Scientific Conference with International Participation «Food Science, Equipment and Technologies» UFT – Plovdiv, 2010, pp. 509-514, (2010).

3 Kalojanov, N., G. Hristov and others. Analysis of the Alternative Possibilities for Energy Saving in 142nd Secondary School "St. Methodij" – Sofia. TU – Sofia, Proceedings of Scientific Conference with International Participation EMF'2000, Volume II, 25 – 28 June, Varna, pp. 15 – 23, (2000).

4 Kalojanov, N. and others. Utilization of Geothermal Water for Heating of Administrative Buildings in Town of Kyustendil. TU – София, Proceedings of Scientific Conference with International Participation EMF'2002, Volume II, 18 – 20 септември, 2002, pp. 84 – 92, (2002).

5 Kalojanov, N., V. Sharankov and others. Guide for Energy Efficiency Audit and Certification of Buildings. TU – Sofia, (2006).

6 Valtchev, G., N. Kalojanov, V. Rasheva, M. Minchev, S. Tasheva. Study of Energy Efficiency of Educational Buildings of University of Food Technologies – Plovdiv, Scientific Conference with International Participation «Food Science, Equipment and Technologies» UFT – Plovdiv, 2010, pp. 499-508, (2010).

# Energy storage solutions for small and medium-sized self-sufficient alternative energy objects

J.Kleperis[1*], V.V.Fylenko[2], M.Vanags[1], A.Volkovs[1], P.Lesnicenoks[1], L.Grinberga[1], V.V.Solovey[2]

[1]*Institute of Solid State Physics, University of Latvia, 8 Kengaraga str, Riga, LV-1063, Latvia*
[2]*A.N. Podgorny Institute for Mechanical Engineering Problems, NAS, 2/10 Pogarskogo str, Kharkiv, 61000, Ukraine*

Energy storage becomes more important as mankind switch to renewable energy, away from fossil resources. Traditional way – batteries - offer a limited number of cycles, require regular maintenance; nevertheless gravitational storage, flywheels, compressed air are mainly large scale and expensive methods. The hydrogen as energy carrier and hydrogen fuel cells are possible option to store different amounts of energy for relatively long times with low losses. Different solutions for self-sufficient sun/wind energy objects are analysed - the solar radiation collecting systems, wind power generators, and high pressure electrolysis technologies for hydrogen production and the metal-hydride energy storage. This article describes the development of a versatile technology that can be used to provide continuous power for small and medium-sized self-sufficient objects or their micro-grids using alternative energy and energy storage. The technology uses advanced electrolysis and fuel cells to efficiently store excess energy from sun/wind generation as hydrogen for later use in fuel cells.

**Keywords:** Energy storage, metal-hydride, electrolysis technologies

## INTRODUCTION

In order to reduce greenhouse gas emissions within the European Community and reduce its dependence on energy imports, the development of energy from renewable sources should be actively supported. The Renewable Energy Directive [1] establishes an overall policy for the production and promotion of energy from renewable sources and requires the EU to fulfil at least 20% of its total energy needs with renewables by 2020 – to be achieved through the attainment of individual national targets. Improvement the efficiency of wind energy infrastructure and solar energy sector using hydrogen as energy carrier storage technologies will significantly reduce the consumption of hydrocarbon fuels and will improve the environment in the most environmentally stressed urban areas and industrial regions.

Implementation of renewable energy solutions is essential in Latvia and Ukraine too. Latvia is depending on energy imports –deficit of electricity (12-33%); shortages in heat production resources (55-70%) and the lack of 99% of local fuel for transport [2]. For production of electricity and heat in Latvia, imported (natural gas, coal, fuel oil) and local (vegetable oil, alcohol, wood) resources are used after business interests of neighbourhood big companies. Energy resources for district heating in Latvian cities are mainly imported (coal, coke, petroleum products, natural gas) and only 30% are

local (used tires, waste, peat, wood, charcoal, straw, wood, biogas, bioethanol, biodiesel, hydropower, wind energy). It is possible to reduce the energy sector's dependence on import in Latvia by switching to local renewable energy resources - sun, wind, rivers, biomass, geothermal, but the transport sector by promoting the transition to electric, electric / hydrogen cars.

The Ukraine is going through an economic crisis caused by Russian aggression in 2014. The resulting massive attack on Ukraine's energy sector is one of the most important elements of Russia's hybrid war against its neighbour. More than half of the Ukraine's primary energy supply comes from local uranium and coal resources, although natural gas also plays an important role in its energy mix. Ukraine consumed about 1.5 trillion cubic feet of natural gas in 2014, with domestic production accounting for 47% of the total at about 700 billion cubic feet. The remainder of supply is made up by Russian natural gas, imported through the Bratstvo and Soyuz pipelines. Switching to renewables and increased energy efficiency are priorities especially important for Ukraine because it is one of the biggest energy consumers in the world [3]. The usage of fossil energy resources must be decreased – there are real concerns over the exhaustion of them and global climate changes due to consuming them. Other concern is that local energy markets indicates increased dependency on energy imports. These factors make the development of alternative energy sources and usage of renewable resources an

* To whom all correspondence should be sent:
  janis.kleperis@h2lv.eu

urgent matter for Ukraine researchers and policy makers to strengthen independence [4].

Ukrainian and especially Latvian energy balance of solar energy share is growing slowly and one reason is necessity for energy accumulation. Energy storage capacity is an important value and must be planned for each solar/wind grid separately, depending on availability of local energy systems and actual geographic location. This article summarises experience of Ukrainian and Latvian researchers in scaling hydrogen energy technologies to facilitate energy storage in power systems operating from renewable resources. A planned theme in joint future collaboration project is dealing with the possibility of using solar energy in two countries - Latvia and Ukraine on the basis of particular application of distributed energy micro-grids in urban environment – attractive and functional lighting poles connected in micro-grids with a common energy storage option. Planned experiments and the expected benefits are addressed in this publication.

ENERGY STORAGE METHODS

A proper energy (electricity) storage can enhance the value of wind energy acquisition by dispatching that energy when it is needed rather than when it was originally generated. Multiple solutions are available and both fundamental as well as applied research in this field is still ongoing. The landscape of energy storage is extensive. The review of Sabihuddin et al., 2015 [5] has discussed 27 types of storage technologies. Some storage technologies are strongly coupled to particular generation technologies. Storage technologies have been compared numerically and qualitatively on the basis of such parameters as specific energy, energy density, lifespan, cycle life, self-discharge rate, capital costs of energy and power etc. (see Luo et al., 2015 [6]). For instance, pumped hydro storage (PHS) systems show strong similarities with hydro-electric plants and are often used in conjunction with nuclear facilities. Compressed air electricity storage systems (CAES) are much like peaking gas turbine plants. Thermal storage systems are integral parts of thermal (and solar thermal) plants and are often used in the context of steam generation and waste heat recovery for subsequent power plant cycles. Flywheel systems (FWS), in comparison to CAES, are fairly mature and commercially tested [5, 6]. They exhibit many advantages over both PHS and CAES solutions.

Most chemical energy storage systems have a number of common features, for instance: the electrodes, the electrolyte and the separators or membranes. Improvements have largely focused on materials [5]. A shift has occurred towards more reactive electrodes. These more reactive variants have shown the promise of increasing energy and power densities - the use of lithium (e.g., Li-Ion batteries) and oxygen/air based chemistries (i.e., metal-air batteries) reflects this trend. Nevertheless, virtually every chemical battery type has seen the utilization in different electricity storage systems.

Energy can be stored also using hydrogen as energy carrier, transforming electricity from renewables to hydrogen through electrolysis of water and storing this hydrogen in high pressure vessels, liquid form or as hydrides of specific materials [7]. Fuel cell (FC) is indispensable part in hydrogen storage system, as it increases in scale, operates much like traditional thermal generation plants, albeit converting fuel (hydrogen) directly to electricity. Fuel cells offer an alternative to burning, have high energy and power performance and have seen some commercial applications to large scale grid level storage/generation (Fig.1).
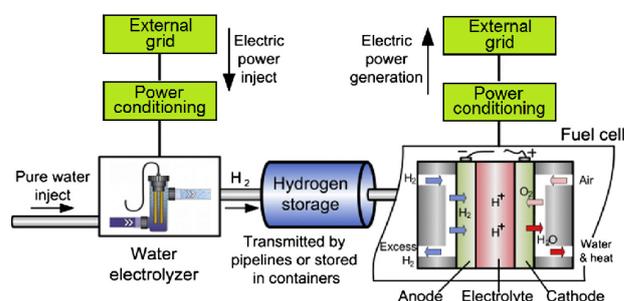


**Fig.1.** Topology of hydrogen storage system (electrolyser, storage vessel and fuel cell - after Luo et al, 2015)

However, there is a need, to reduce costs of hydrogen energy storage *systems even further in order to be com*petitive with other energy storage solutions. Traditional chemical batteries are likely to be strong contenders for small/middle scale storage at this point, though with additional research metal-air chemistries may hold future promise [6, 7]. FC and FWS are tested in large and small scale applications; therefore, these systems may be more relevant to deployment for distributed grid infrastructure [6]. For long-term storage (months, years) the hydrogen energy storage is competing not so much with overall efficiency (below 60%) but costs, ease of installation and

multipurpose usage (electricity, heat and fuel for transport), see [5-7].

Despite the search for new ways to produce environmental friendly fuels, the focus of research is still concentrated on the possibility of producing hydrogen from water [7, 8]. Technology of hydrogen production based on the processes of decomposition of water by electrolysis, are widely used in various fields of modern industry. Compared with other methods of producing hydrogen, electrolysis systems are easily scalable and usable in various power applications. Therefore, urgent problem is the development of electrochemical technologies to generate hydrogen from water with minimal cost of electricity, especially in light of the expansion of the use this hydrogen as resource for environment-friendly energy in advanced technologies.

EXPERIMENTAL DETAILS

Micro-grid of 5 solar lighting poles (PV 200W and LED 100W each – see Fig.2) as prototype of renewable energy power plant and consumer simultaneously, self-made 2 different electrolysers (high pressure and pulse powered) connected with hydrogen storage in compressed gas cylinder and metal hydride tank accordingly is used as potential long-period energy storage facilities.
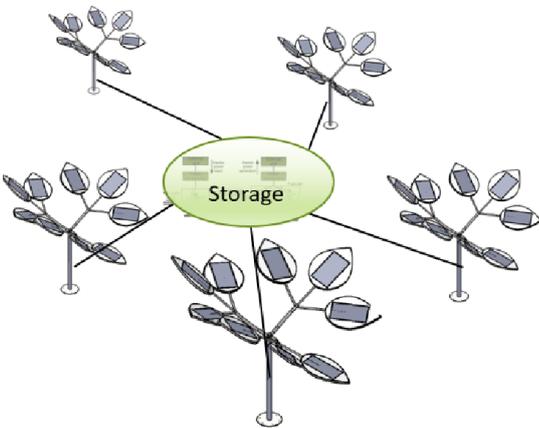


**Fig.2.** Principal scheme of micro-grid from 5 solar trees (light poles)

*Energy excess transformation into hydrogen via water electrolysis*

In industry, widely used conventional liquid alkaline electrolyte is chosen to ensure the generation of gases at pressure of 0.05 - 1.6 MPa in the temperature range from 333 K to 353 K and current density of 1200-2500 A/m$^2$ [8]. Thus the

energy consumption (depending on the process temperature, pressure, quality of the electrode cell design, and other factors) varies in the range from 4.3 kWh/m$^3$ to 5.2 kWh/m$^3$ of hydrogen (H$_2$).

*High pressure electrolysis*

At AN Podgorny Institute of Mechanical Engineering Problems of NAS Ukraine has developed a technology of electrochemical production of hydrogen and oxygen at high pressure using a getter electrode and diaphragm-less cell design [9,10]. Operating temperatures are in the range of 280 K to 423 K, pressure range is from 0.1 to 70 MPa, electrolyte - 25% aqueous solution of alkali. Designed electrochemical method for the decomposition of water is a cyclic and consist of alternating in time processes of hydrogen and oxygen evolution. It means that comparing with traditional electrolysis were the reaction of water decomposition takes place continuously with simultaneous evolution of hydrogen and oxygen on electrodes in an electrochemical cell, in the proposed technology proceeds cyclic distribution of gases H$_2$ and O$_2$ to the consumer. In the first half-cycle, hydrogen is released at the passive electrode in a gaseous form and fed to the high pressure line, but oxygen is chemically bonded to the active electrode forming a chemical compound. In the subsequent half-cycle the hydrogen is carried out reduction of previously formed chemical compound on the active electrode, but oxygen is released at the passive electrode in gaseous form and fed to the high pressure line (Fig.3).
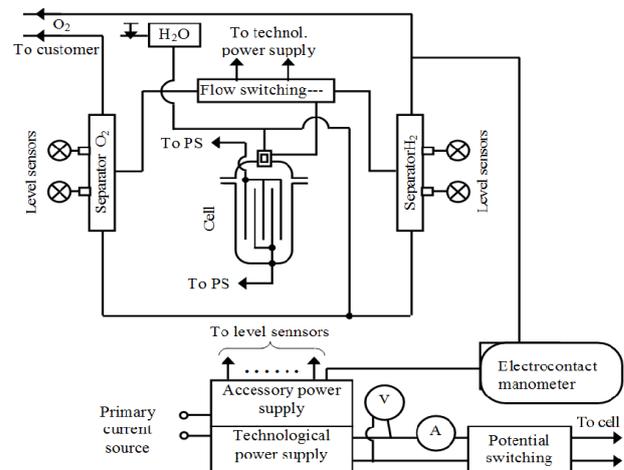


**Fig.3.** Schematic of an installation with an electrochemical cell using a gas-absorbing electrode

*Pulse electrolysis*

Typically direct current (DC) power is used in electrolysis; nevertheless, pulse DC voltage also can be used [11-13]. Bockris et al. [11] found that applying voltage pulses on an electrolysis cell, the long current tail is observed just after end of voltage pulse. Shimizu et al. [12] used inductive voltage pulses (200 ns) to power electrolysis cell and found that efficiency of electrolysis does not change by varying applied power. Researchers from Institute of Solid State Physics, University of Latvia [12] used inductive voltage pulses to compare different metals as cathode and found that concentration of dissolved hydrogen grows faster on metals with higher hydrogen evolution overvoltage and lower hydrogen solubility. In this work [12] we prove the fact that using inductive voltage pulses to power electrolysis cell, it is possible effectively reduce applied potential thanks to the possibility to separate both the charging current from the charge transition (Faradic) current in hydrogen evolution reaction.

Inductive voltage pulses were generated with an electric circuit (Fig.4) consisting from pulse generator, DC power source, field transistor and blocking diode.
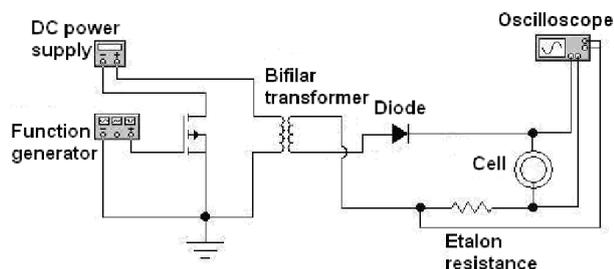


**Fig.4.** Experimental circuit for generation of inductive reverse voltage pulses

Special transformer is wound as bifilar from two wires twisted together. Obtained inductive reverse voltage pulses powers the primary winding in bifilar transformer and is directed through blocking diode. Resulting high voltage pulses with width $1 \cdot 10^{-6}$ s are obtained and used to power electrolysis cell. Two beam oscilloscope GWinstek GDS-2204 is used to register voltage and current (voltage drop on an etalon resistance) in circuit powering electrolysis cell.

*Energy Storage*

Battery, hydrogen and hybrid energy storage will be analysed for particular case - 5 small solar lighting poles (200W each) are connected in micro-grid with total installed power 1 kW (Fig.2). LED lights for each pole has maximum 100 W, electric system is designed to 12V and nominal current – 1 A. With smart power regulation (motion sensors in every pole) it is possible to reduce consumed power five times, accounting to micro-grid of 5 poles - from 0.1 to 0.5 kW. Volumes of energy necessary to be stored are calculated from actual amount of electricity to be consumed. In our case two consumption scenarios – one for particular day and second for average year should be combined. Daily amounts of harvested energy from the sun and the consumed in dark time is highly variable through year and for latitudes of Riga (Latvia): 56°57'0" N/24°6'0" E and Kharkiv (Ukraine): 49°55'0" N/36°19'0" E varies between 0.53 - 12.23 kWh/m$^2$ (Riga) and 1.67 – 12.12 kWh/m$^2$ (Kharkiv) [14].

The number of hours the sun is shining each day (that is the number of hours between sunrise and sunset) when averaged over the year are 12 hours multiplied by number of days in year everywhere in the world. It differs only in the maximum height of the sun above the horizon and an angle of the Earth's rotation axis with respect to the sun. Therefore in the Northern latitudes the average intensity is lower than at the Southern latitudes. Harvested energy from 5 poles is surplus from spring to autumn and deficit in winter time (Fig.5, calculated from [15]), that is 1/4$^{th}$ from year .
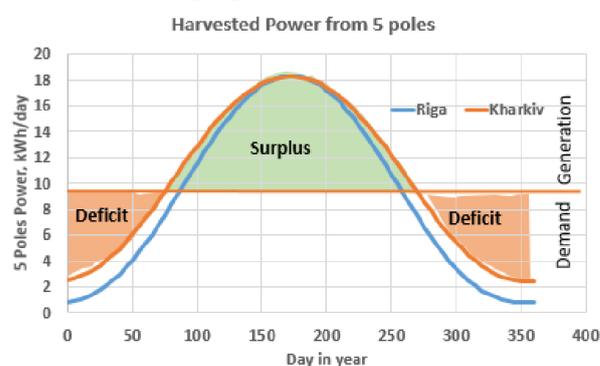


**Fig.5**. Annual solar generation versus demand for a solar system at latitudes of Riga (57N) and Kharkiv (50N)

Hydrogen is produced in water electrolysis using two different electrolysers. When high pressure electrolysis is used, typical gas vessels up to 200 bar can be connected directly to store hydrogen for winter time. The second option to produce hydrogen from water is low pressure electrolysis, and such hydrogen can be easily stored in metal hydride tank for utilization in winter time. Low temperature can decrease pressure of stored

hydrogen in both cases (pressed and bind in crystal lattice). Therefore, the storage at least 1 meter below the ground, where constant temperature is maintained during the year, is desired.

*Electricity generation*

Proton electrolyte membrane fuel cell stack (PEMFC) 1 kW is used to generate electricity from stored hydrogen. As it could be understood from Fig.5, the need for additional electricity will arise of the dark and cold season only (November – February).

RESULTS AND DISCUSSION

*High pressure electrolysis*

The proposed technology of electrolysis for producing hydrogen and oxygen at high pressure eliminates the cost of electric energy transfer resistance separation membranes due to their absence [9,10]. This ensures the generation of $H_2$

($O_2$) under high pressure, up to 200 bars without necessity for additional compressor. The advantage of the described method for obtaining hydrogen includes the ability to relatively simple (adjusting current) control of the reaction rate and thus the energy consumption, which is especially important when electricity from renewable energy sources of differing volatility (solar, wind) is used.

The process of hydrogen generation begins with applying negative potential to the passive electrode (Fig.6). The gas-absorbing active electrode operates as an anode at this stage. The water-dissociation reaction produces hydrogen and oxygen simultaneously. The hydrogen is isolated at the passive electrode in the gaseous state, and the oxygen is chemically combined at the active electrode (i.e., it is accumulated as an oxide). This operational sequence is provided by automatic switching of electrodes to act as anode/cathode electrodes.
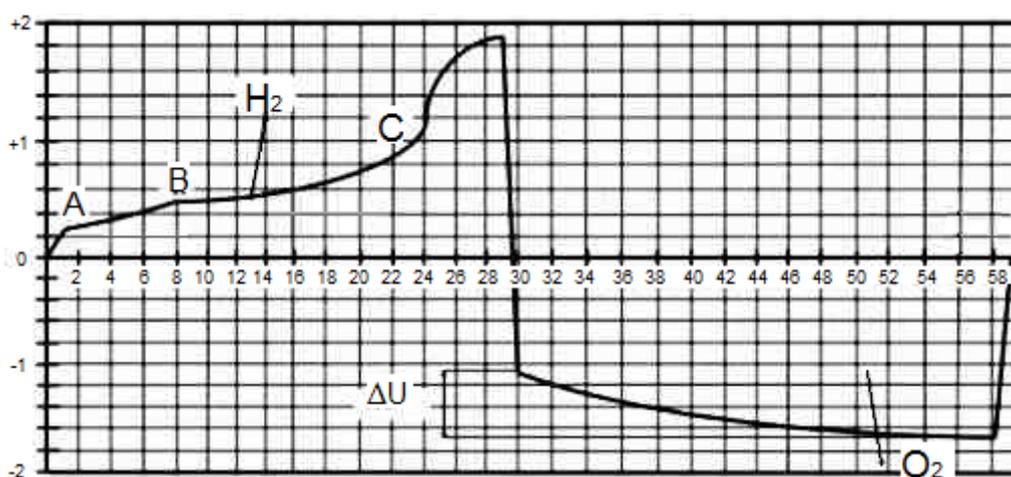


**Fig.6.** Change of voltage for hydrogen and oxygen isolation in the electrolysis process (Y-axis in Volts, X-axis in Minutes, from [9, 10]). Current density I = 200 A/m²; (A – B) – working area of the hemicycle; (B – C) – area of operation when there are the additional power inputs; ΔU – overvoltage under reduction of the active mass

Supplying the electrolysis cell with electric power is synchronized with an electromagnetic switch that controls the gas flow. As a result, hydrogen is isolated under high pressure and only fills a hydrogen pipeline. In the same manner, oxygen is fed to a separate pipeline. The water-dissociation reaction is initiated by increasing the voltage at the electrodes during the gas-generation process. Automatic control of the gas-generation process is based on the process's voltage-current characteristics, which were determined experimentally.

Pulse electrolysis is developed for efficient low-pressure electrolysis. The voltage to split water in practical electrolysis devices is higher than thermo-neutral cell voltage due transformation into heat, which heats up the cell. Therefore industrial electrolyser requires additional cooling and the value of DC voltage is defined [15]:

$$E = E_{rev} + loss, \qquad (1)$$

where the loss is:

$$loss = E_{anode} + E_{cathode} + E_{mt} + IR, \qquad (2)$$

where $E_{anode}$ – activation overvoltage of the anode, $E_{cathode}$ – activation overvoltage of the cathode, $E_{mt}$ – overvoltage of the mass transfer, $IR$ – ohmic overvoltage (includes resistance in an electrolyte, on electrodes, leads). Current density is higher in industrial DC electrolysers, therefore applied voltage partly transforms into the heat, becoming typical loss in DC water electrolysis [16].

Inductive voltage and current pulse kinetics of water electrolysis cell (Fig.7) can be divided into two fundamentally distinct parts: a rapidly growing charging (1μs) and slowly descending discharge tail (about 20μs).
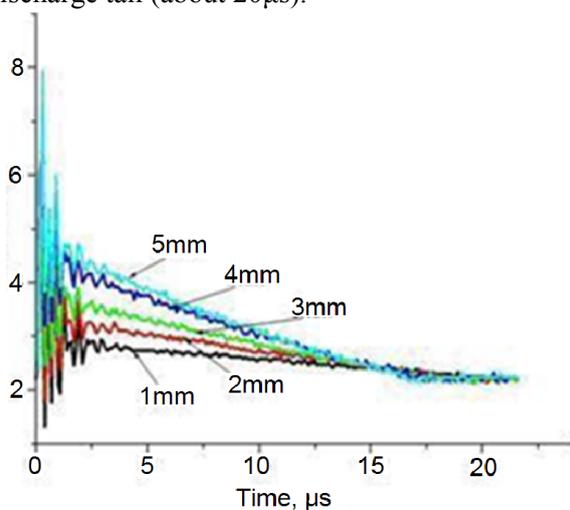


**Fig.7.** Voltage pulses registered with oscilloscope in 0.1 M KOH

The transition from the rapid charge to slow discharge tail happens through the breakpoint. By changing spacing between electrodes, the charging amplitude voltage pulse changes (Fig.7) – at 5mm distance the rapid charging ends at about 5V, while reducing the distance between the electrodes to 3mm and 1mm, the voltage value at the end of the charge drops to 4,2V and 3,8V respectively. To find the effective value of voltage taking into account the possible charge separation between cell's geometric capacitance and the electric double-layer charging with following Faraday reactions, the voltage oscillograms are modified to be compared with DC electrolysis. Comparison of volt-ampere curves shows that in the weak and also in 0.1 M KOH solution pulse electrolysis is more intense as the DC mode - slope is almost twice steeper. By contrast, in 0.3 and 0.5 M KOH solutions the steepness of pulse electrolysis volt-ampere curve is almost the same as the DC mode. This confirms previously discussed hypothesis that

the inductive voltage pulse in rapid growing phase is charging only geometric capacity of electrolysis cell, and only then the charging of the electric double-layer capacity and parallel starting charge transfer (electrolysis) process. High power short pulse generator is elaborated to power 1 kW electrolysis unit with efficiency close to 67%.

*Energy production, consumption and storage*

In Latvia the sun shines average 1,790 hours per year, which is around half of the possible sunshine duration (clear weather). The sunniest days are from May to August, when the sun shines an average of 8-10 hours per day, but in contrast, from November to February the sun shines an average of only 2-3 hours a day [18]. From installed power of solar PV – 1 kW in micro-grid, it can be calculated maximal annual harvested energy in sunny hours – 1kW*1790h=1790 kWh, in case all modules are perpendicular to Sun. Let us assume that the rest 2590 day-light cloudy hours will 600 kWh more. In our case it means, that around 2400 kWh can be harvested from PV panels in an average year. The maximal consumed power for lighting in average year is calculated from equation 0.5kW*1/2 year (4380 h) = 2190 kWh which can be reduced 3-5 times with smart power management system. Let us assume that the 1/4th from 2190 kWh or 538 kWh will be energy shortages in winter and our storage facility should be with same energy capacity that is 538 kWh. If we want to store this energy amount in batteries, then the battery packs from 6 Tesla electric vehicles (85 kWh each) would be necessary. The Tesla Motors (Company producing most powerful electric vehicles) has just announced [20], that it will sell a battery pack for home use that will cost approximately $3500 for 10 kWh of power.

Hydrogen has one of the highest energy density values per mass. Its energy density is between 120 and 142 MJ/kg or 33-39 kWh/kg [19]. Assuming that the fuel cell can recover electricity from hydrogen with 70% efficiency, we obtain that for storage of 538 kWh is necessary about 20 kg of hydrogen or 21 reservoirs each 50 l with pressure 200 bar, or 212 Nm$^3$ gas at normal conditions. To produce such amount of hydrogen in summer time, in average 605 sunny hours are necessary, if electrolyser with capacity around 350 l/h is used.

CONCLUSIONS

In this paper innovative methods of water electrolysis are described – high pressure hydrogen

gas generation up to 200 bar, and short pulse electrolysis of hydrogen gas at low pressure up to 3 bar. Both hydrogen-generation systems allow the chemical reaction rate to be controlled by controlling the current intensity (high pressure electrolysis) or pulse sequence rate (pulse electrolysis). This is especially important when the primary energy source for the electrolysis device is Sun or Wind with unpredictable and variable power affected by seasons, night/day changes, and climatic factors. Both investigated electrolysis technologies have shown high promise for use in the small and medium-sized self-sufficient objects or their micro-grids in combination with high-pressure or metal hydride hydrogen storage facilities.

It is calculated in case of 1 kW solar PV/0.5 kW LED lights micro-grid, the storage facility with capacity of 538 kWh is necessary. This amount of electricity can be recovered from 21 kg or 212 $Nm^3$ hydrogen gas, and to produce such amount of gas with electrolysis system having capacity 350 l/h, the 605 sunny hours in summer time are necessary.

## ACKNOWLEDGEMENTS

## REFERENCES

1 Directive 2009/28/EC of the European Parliament and of the Council of 23 April 2009 on the promotion of the use of energy from renewable sources: http://eur-lex.europa.eu/legal-content/EN/ALL/?uri=CELEX:32009L0028

2 Consumption of energy resources in Latvia. The Central Statistical Bureau of Latvia (CSB). Viewed 02.03.2016: http://www.csb.gov.lv/en

3 Ukraine: Energy Sector Highlights. The U.S. Energy Information Administration (EIA). Viewed 02.03.2016: https://www.eia.gov/beta/international/analysis.cfm?iso=UKR

4 S. Romanko. Alternative Energy in Ukraine: Challenges, Prospects and Incentive Mechanisms. Country Report: Ukraine. Viewed 28.02.2016: www.iucnael.org/en/documents/1248-ukraine-1

5 S. Sabihuddin, A.E. Kiprakis, M. Mueller, *Energies* 2015, 8, 172-216.

6 X. Luo, J. Wang, M. Dooner, J. Clarke, *Applied Energy,* vol. 137 (2015) 511–536.

7 Decourt, B, Lajoie, B, Debarre, R, & Soupa, O 2014, The hydrogen-based energy conversion FactBook, The SBC Energy Institute.

8 Millet, P & Grigoriev, S 2013, "Water electrolysis technologies", in: Gandia, L, Arzamendi, G, & Diéguez, P (eds.), Renewable hydrogen technologies, Elsevier, Amsterdam.

9 V.V. Solovey; A. Shevchenko; A. Kotenko; O. Makarov. 3013. The Device for Generation High-pressure Hydrogen. *Patent of Ukraine № 103681* МПК С25В 1/12, С25В 1/03. Made public on November 11, 2013, Bulletin № 21.

10 V.V.Solovey, A.A. Shevcenko, I.A. Vorobjeva, V.M.Semikin, C.A. Koversun, *Scientific Journal of Kharkiv National Auto-Road University,* Kharkiv, 2008, No 43, p. 69-72 (In Russian).

11 J. O'M. Bockris, T.N. Veziroglu, *Int. J.of Hydrogen Energy*, vol.32 (12) 2007, p.

12 N. Shimizu, S. Hotta, T. Sekiya, O. Oda, *J. of Applied Electrochemistry* (2006) 36: 419–423.

13 M.Vanags, J.Kleperis, G.Bajars. *J. of Hydrogen Energy*, Vol 36, issue 2, (2011), p.

14 A.Roger, How Much Battery Storage Does a Solar PV System Need? 2015, on http://euanmearns.com/how-much-battery-storage-does-a-solar-pv-system-need/;

15 Calculation of Solar Insolation: http://pveducation.org/pvcdrom/properties-of-sunlight/calculation-of-solar-insolation

16 M. Vanags, J. Kleperis and G. Bajars. Water Electrolysis with Inductive Voltage Pulses. Chapter 2 in Book: Electrolysis, Editors J. Kleperis and V. Linkov, InTech (2012), pp.19-44, doi.org/10.5772/52453

17 R.R. Salem, Chemical Thermodynamics, Fizmatlit, 2004, 352 p, ISBN 5-9221-0078-5

18 Latvian Environment Geological and Meteorological Centre: https://www.meteo.lv/lapas/laika-apstakli/klimatiska-informacija/latvijas-klimats/latvijas-klimats?id=1199&nid=562

19 Thomas, George. Overview of Storage Development DOE Hydrogen Program [pdf]. Sandia National Laboratories, 9 May 2000.

20 Schneider Electric Promising Battery At Lower Cost Than Tesla. News from Forbes.com, Jan 13, 2016.

# Effect of reservoir on controllable loop thermosyphon

Jingyu Cao[1], Gang Pei[*,1], Yuehong Su[2], Anjum Munir[3], Jing li[*,1], Wang Yunyun[4]

[1] *Department of Thermal Science and Energy Engineering, University of Science and Technology of China, Hefei 230027, China*
[2] *Departments of Architecture and Built Environment, Engineering, University of Nottingham, Nottingham*
[3] *Department of Energy Systems Engineering, University of Agriculture, Faisalabad-Pakistan*
[4] *Key Laboratory of Optoelectronic Devices and Systems of Ministry of Education and Guangdong Province, College of Optoelectronic Engineering, Shenzhen University, Shenzhen 518060, China*

The controllable loop thermosyphon (CLT) has the potential to be utilized in various applications, including cool-storage refrigerators powered by solar energy and electricity with the time-of-use price policy. An active control method can be achieved by interrupting the two-phase natural circulation flow of CLTs. However, the precise temperature control performance of CLTs under active control depends on the system design and should be optimized. In this study, CLTs with and without a reservoir were designed and tested. Valves were added to the vapor and liquid lines. Therefore, three control modes were available to start and stop the heat transfer process of the CLTs. A series of experiments was conducted to compare the start–stop and heat transfer performances of the two CLTs at various R134a fill ratios and heat sink temperatures. The heat transfer performance of the CLT with a reservoir was more stable than that of the CLT without a reservoir. The reservoir degraded the start–stop performance of CLT in control mode A. The start–stop performances of the two CLTs were similar in control mode C. The CLTs in control mode C started up in approximately 20–25 s and stopped in about 70–80 s. Results revealed that an optimal system design could be selected under different application backgrounds.

**Keywords:** refrigerator, loop thermosyphon, reservoir, start–stop performance

## INTRODUCTION

Phase-change materials (PCMs) are widely used in refrigerators to save energy, reduce cost, and protect the environment. Cool-storage refrigerators present significant advantages and promising prospects.

The solar photovoltaic (PV) vapor compression refrigerator is the most common solar-powered refrigerator [1–3]. In traditional PV refrigerators, storage batteries are adopted widely because of the unstable solar energy. High-priced batteries cause considerable energy wastage in the charge–discharge process [4]. Siaka Toure and Foster et al. designed and investigated battery-free cool-storage refrigerators. Their results showed that the cooling capacity of ice is completely adequate for a few days of operation without a power input [5, 6]. PV cool-storage refrigerators provide significant advantages in terms of cost and efficiency; however, they cannot control the temperature of fresh food precisely when their compressors stop working. This disadvantage is caused by the low heat transfer rate between PCM and the air in fresh food compartments.

Cool-storage refrigerators are more efficient than traditional direct-cooling refrigerators [7–10]. Moreover, the time-of-use price policy has been implemented worldwide because of the significant difference between peak and valley power demands [11]. Cool-storage refrigerators are a major energy-consuming home appliance and demonstrate the potential to stabilize electric grids and reduce electricity costs [12]. However, similar to PV cool-storage refrigerators, they have the disadvantage of imprecise temperature control.

The fresh food compartment temperatures of cool-storage refrigerators are controlled by the start–stop mechanism of compressors when powered by electricity. This temperature control mechanism is similar to that of traditional direct-cooling refrigerators without frequency conversion functions [13–15]. The start–stop frequency increase of a compressor can decrease the coefficient of performance of refrigeration systems directly. Thus, the temperature control performance of traditional and cool-storage refrigerators is difficult to improve.

A novel cool-storage refrigerator was proposed in this study to overcome these shortcomings. A loop thermosyphon, which is also referred to two-phase thermosyphon loop, was employed to control the temperature of fresh food. Fig.1 shows that the fresh food compartment is located at the bottom of the refrigerator, and the evaporator is located in the freezer only. The compressor in this novel cool-storage refrigerator can operate continuously for half a day to cool the freezer and store cold energy.

---

The temperature of the fresh food compartment is controlled only by the intermittent heat transfer of the loop thermosyphon. With the long-running compressor and frequent start–stop loop thermosyphon, the efficiency of the refrigeration system and the precision of temperature control improved significantly. Active control of the loop thermosyphon in this novel cool-storage refrigerator was achieved by artificially interrupting its two-phase natural circulation flow. The performance of the precise temperature control of the loop thermosyphon under active control is highly important and requires further investigation.
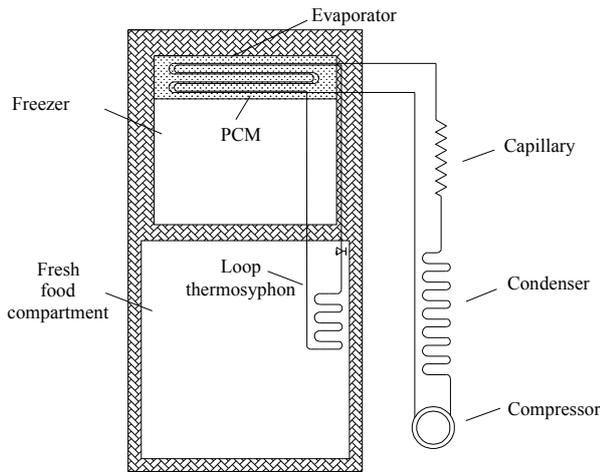


**Fig.1.** Simplified sample configuration of the novel cool-storage refrigerator

Various characteristics of the loop thermosyphon have been studied since the 1980s [16]. Rahmatollah Khodabandeh and Richard Furberg analyzed the two-phase flow instabilities of a loop thermosyphon with R134a as a refrigerant and found that copper nano- and micro-porous structures decrease the oscillations and enhance the heat transfer coefficient [17]. Yu Song et al. focused on nucleate boiling heat transfer in a helium loop thermosyphon coupled with a cryocooler. The error of the proposed correlation was within 30% in the regime of two-phase nucleate boiling [18]. Jiang He et al. investigated the effect of non-condensable gas on the startup of a loop thermosyphon. No failed startups occurred during any of the tests [19]. Chehade et al. investigated the performance of a loop thermosyphon with water as a working fluid. Their results showed that the optimal fill ratio is between 7% and 10% [20]. Ali Chehade et al. performed experimental and simulative research on a loop thermosyphon for cooling with zero electrical consumption. A new model was proposed and

confirmed by experimental data [21]. Ji Li et al. investigated the performance of an insert-type loop thermosyphon for split-type solar water heaters. The experimental system displayed an improvement of 100% in water heating speed [22]. Penglei Zhang et al. studied the performance of a loop thermosyphon with a partially liquid-filled downcomer. A visual test bench was established, and a partially liquid-filled phenomenon was discovered in the downcomer [23]. Zhen Tong et al. investigated an R744 loop thermosyphon used to cool a data center. The R744 loop thermosyphon functioned under a small driving temperature difference of 5 °C, and a theoretical model was utilized to calculate thermal resistance [24]. These experimental and theoretical studies revealed the attractive and comprehensive performance of loop thermosyphons. Thus, loop thermosyphons have been utilized widely in solar applications, electronic equipment cooling, air conditioning, nuclear reactors, waste heat recovery, and other heat transfer fields [25]. However, precise temperature control ability under active control has been neglected. A cool-storage refrigerator combined with a loop thermosyphon remains an unexplored but attractive field.

The performance of the precise temperature control of a controllable loop thermosyphon (CLT) under active control depends largely on the system design. The effect of a reservoir on the precise temperature control performance of CLT within a known range has not been reported. In our previous study, we evaluated the performance of a CLT without a reservoir [26]. On this basis, we designed and tested CLTs with and without a reservoir in the current study. Two valves for each CLT were added to the vapor and liquid lines. Therefore, three control modes were available to start and stop the heat transfer process of the CLTs. A series of experiments was conducted to compare the start–stop and heat transfer performances of the two CLTs at various R134a fill ratios and test conditions.

EXPERIMENTAL SETUP

*Operating principle of CLT*

The two-phase natural circulation flow in a CLT is presented in Fig.2. The liquid working fluid evaporates in the evaporator and flows to the condenser through the vapor line. The vapor working fluid condenses to the liquid phase in the condenser and flows back through the liquid line to

the evaporator again. The working fluid flows automatically with the assistance of gravity.
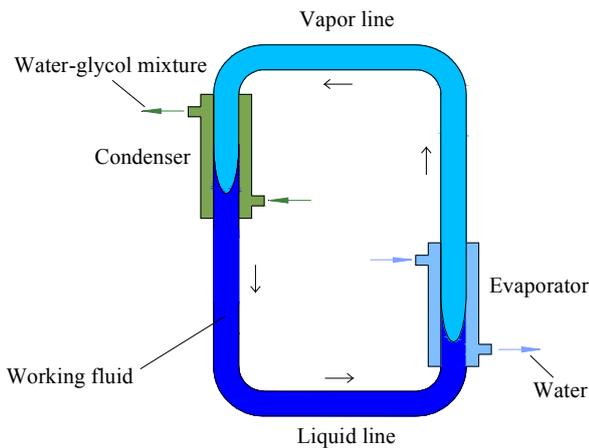


**Fig.2.** Operating principle of a CLT

The automatic movement of the working fluid is accompanied by heat transfer and can be controlled actively by one or two valves. The two-phase natural circulation flow transfers heat steadily from the evaporator to the condenser when the valves are open. The two-phase natural circulation flow and the heat transfer of CLT cease immediately when the valves are closed. Given that the two-phase natural circulation flow in CLT starts and stops rapidly, CLT can operate intermittently to control heat transfer and the loading temperature. A high start–stop frequency can improve the temperature control precision of CLT significantly.

## *Experimental facility description*

Fig.3 shows the two CLTs designed. The only difference between the two CLTs is the reservoir in the liquid line. R134a was used as the working fluid, and copper was used as the pipe material. The condenser is located above the evaporator, and the vapor line is located between the evaporator outlet and the condenser inlet. The liquid line, which contains a reservoir, connects the condenser outlet to the evaporator inlet. The evaporator and condenser consist of inner tubes with two tube-in-tube helical heat exchangers. A shell inlet and a shell outlet exist in the tube-in-tube helical heat exchanger. Valves 1 and 2 are located on the top of the vapor line and on the bottom of the liquid line, respectively. The geometrical parameters of the CLTs are listed in Table 1.

Fig.3 shows the primary components of the test rig. DC-0515 and DC-3015 were set as the water hot bath and cold bath, respectively. The temperature control range of DC-0515 is from −5 °C to 100 °C and that of DC-3015 is from

−30 °C to 100 °C. Their common characteristics of accuracy, maximum flow rate, and total power are 0.1 °C, 10 L/min, and 2.5 kW, respectively. Water was supplied to the evaporator as a heat source, whereas a water–glycol mixture was supplied as the heat sink for the condenser. The temperatures of the supplied water and water–glycol mixture can be varied. The evaporator and condenser heat exchangers were in counter flow. A heat insulation layer was utilized to minimize the cooling loss.

**Table 1.** Geometrical characteristics of CLT

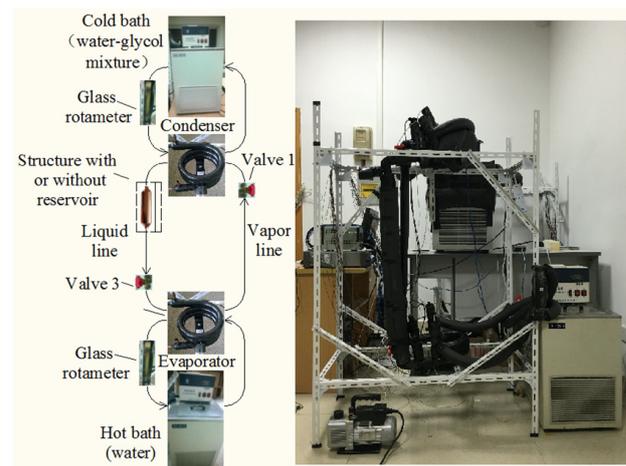| Component | Inner diameter (mm) | Outer diameter (mm) | Length (m) |
|---|---|---|---|
| Vapor line | 10 | 12 | 1.3 |
| Liquid line | 10 | 12 | 1.5 |
| Evaporator | 10 | 12 | 1.34 |
| Shell of evaporator | 23 | 25 | 1.34 |
| Condenser | 10 | 12 | 1.34 |
| Shell of condenser | 23 | 25 | 1.34 |
| Helical heat exchanger | 147 | 172 | 1.34 |
| Reservoir (if present) | 33 | 35 | 0.25 |



**Fig.3.** Test rig

## *Measurements*

The measurement points of the CLTs are shown in Fig.4, and a list of experimental testing and monitoring devices is provided in Table 2. The inlet and outlet temperatures of the water–glycol mixture and water were measured with WZP-291 Pt100 platinum resistances. The wall temperatures of the vapor and liquid lines were monitored through numerous T-type thermocouples. The pressures of R134a at the evaporator and condenser inlets were measured with two JT-131 pressure sensors. These measurements were recorded with an Agilent data acquisition instrument every 5 s. The flow rates of the water–glycol mixture and water were measured

with two glass rotameters. An electronic scale was used to measure the mass of R134a filled in CLT.
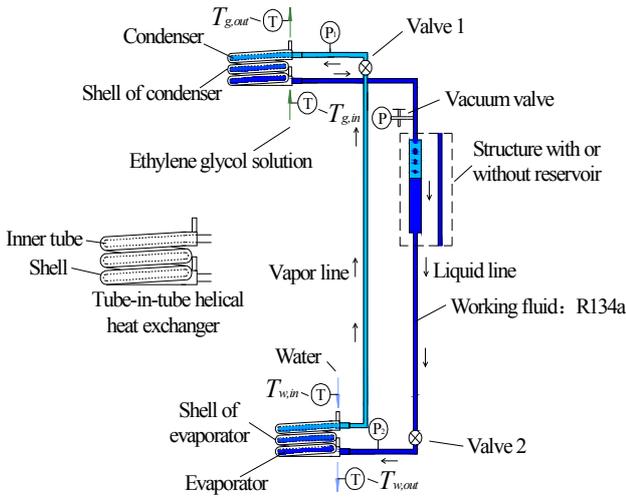


**Fig.4.** Structure and measurement points of CLTs

**Table 2.** Experimental testing and monitoring devices

| Name | Specification | Accuracy |
|------|---------------|----------|
| Pressure sensor | JT-131 | 0.5% |
| Platinum resistance | WZP-291 Pt100 | ±0.1 °C |
| Thermocouple | T-type | ±0.5 °C |
| Flow meter | Glass rotameter | 2.5% |
| Scale | Electronic | ±0.5 g |
| Data acquisition unit | Agilent 34970 | / |

## EXPERIMENTAL METHODS AND CALCULATION

The water and water–glycol mixture were supplied stably when the valve (or two valves) was closed to simulate the internal environment of a cool-storage refrigerator. When CLT was completely stopped, its heat transfer rate reached zero, and the pressure was constant. The CLT without a reservoir and that with a reservoir were named CLT1 and CLT2, respectively. The time for the heat transfer rate to decrease from 100% to 5% in the stopping process was selected to represent the stopping performance of CLT. The time consumed to reach the maximum heat transfer rate in the start-up process was selected to represent the start-up performance.

Normal test conditions were adopted unless mentioned otherwise and were set as follows. The temperature of the water–glycol mixture supplied from the cold bath was −25 °C, and the temperature of water flowing from the hot bath was 5 °C. The flow rates of the water–glycol mixture and water were set to 80 and 100 L/H, respectively.

Two valves were added to the vapor and liquid lines, so three control modes were available to start and stop the heat transfer process of the CLTs.

(1) Control mode A: The valve located on the vapor line functions as the only switch.

(2) Control mode B: The valve located on the liquid line functions as the only switch.

(3) Control mode C: The two valves function as switches.

The experiment was performed as follows. The R134a fill ratio was verified, and the inlet temperature of the water–glycol mixture was verified from −25 °C to −17 °C. The steady-state heat transfer and start–stop performances of the CLTs with and without a reservoir were tested under different test conditions. Optimal fill ratios were selected for further investigation. The start–stop performance of CLT was then investigated under different experimental conditions.

During the course of the experiment, the transient heat transfer capability of CLT was represented by the heat transfer rate of the evaporator. At any time, the transient heat transfer rate of evaporator can be calculated as follows:

$$Q = \rho V C p (t_{w,in} - t_{w,out}), \qquad (1)$$

where $V$ is the transient measured volume flow rate of water and $t_{w,in}$ and $t_{w,out}$ are the transient measured inlet and outlet water temperatures of the evaporator, respectively.

## RESULTS AND DISCUSSION

### Effect of reservoir on steady-state performance

Experiments were performed on CLT1 and CLT2 at different fill ratios of R134a to analyze the effect of the reservoir on the steady-state working performance of CLT. At each fill ratio, the inlet water–glycol mixture temperature, $t_{g,in}$, varied from −25 °C to −17 °C. The heat transfer rate of stably operating CLT1 at different R134a fill ratios and $t_{g,in}$ values is shown in Fig.5. The heat transfer rate of CLT1 for each $t_{g,in}$ value increased initially and then decreased with an increasing fill ratio. This variation trend was evident when fitted by a cubic spline interpolation curve. The maximum heat transfer point of each curve was defined as the optimal operating point. The fill ratios of optimal working points for different heat sink temperatures varied from 34.74% to 38.9%. In the normal test condition, the maximum heat transfer capability was obtained at a fill ratio of approximately 38.9%. Excessive or insufficient R134a restricted the heat

transfer capability of CLT1. Moreover, the fill ratios of optimal operating points varied with $t_{g,in}$. In the practical application of cool-storage refrigerators, the fill ratio of CLT1 cannot be changed, and this defect would cause a deviation from the ideal working condition if the heat sink temperature is varied.
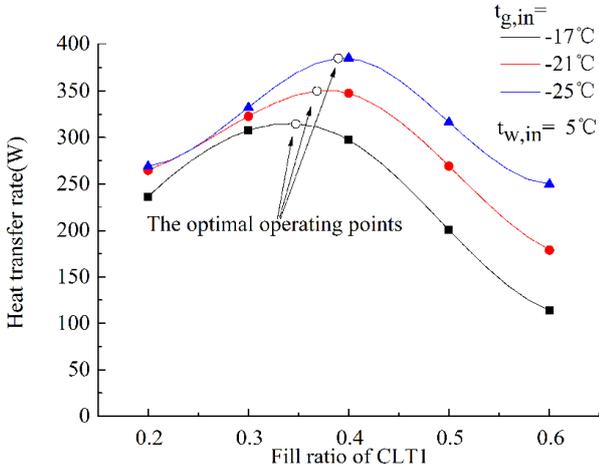


**Fig.5.** Heat transfer performance of CLT1

Fig.6 shows that using an additional reservoir exerts a remarkable effect on the steady-state heat transfer performance of CLT. The heat transfer rate of CLT2 in normal test conditions was almost unchanged when the R134a fill ratio changed from 32% to 67%. The heat transfer rate of CLT2 decreased when the fill ratio exceeded this suitable range. This suitable range was still valid when $t_{g,in}$ increased. Thus, CLT2 could operate in its optimal working condition even if the heat sink temperature was varied.
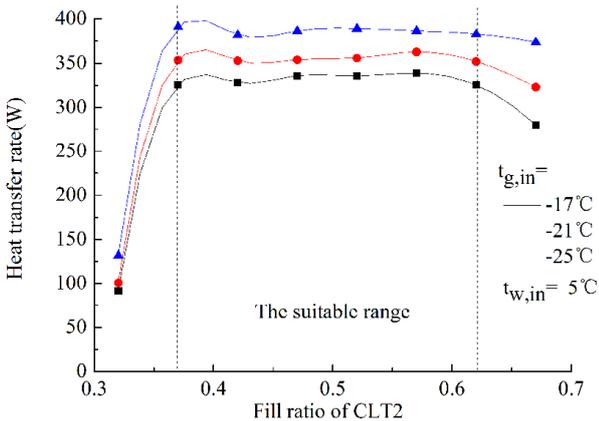


**Fig.6.** Heat transfer performance of CLT2

Comparison of the heat transfer performance of CLT1 and CLT2 showed that the reservoir can improve the steady-state performance of CLT. The heat transfer stability improvement can be explained as follows. The optimal R134a distribution in the evaporator and condenser

changed when the heat sink temperature of CLT without a reservoir varied. Thus, the optimal R134a fill ratio varied with the working environment. CLT1 experienced difficulty reaching and maintaining its optimal working condition. By contrast, in CLT2, the R134a storage function of the reservoir could adjust the R134a distribution in the evaporator and condenser at any time. The CLT with a reservoir could maintain the ideal steady-state heat transfer status because of the wide range of suitable R134a fill ratio.

### Effect of reservoir on control stability

The control stability of CLT was tested by starting up and stopping CLT at various R134a fill ratios, control modes, and $t_{g,in}$ values. CLT1 never failed to start or stop during the dozens of tests, and it started and stopped steadily even when the fill ratio deviated from its optimal value and the steady-state heat transfer of CLT1 was degraded seriously. By contrast, several adverse phenomena occurred in the starting process of CLT2. CLT2 could start and stop steadily under different test conditions when the R134a fill ratio varied from 57% to 67%. However, CLT2 could not start up normally under various test conditions when the fill ratio was lower than 57%. The three typical start-up failures are as follows.

1. Fig.7 shows that high-frequency heat transfer and pressure oscillation occurred when CLT2 was initialized in control mode A with a 47% fill ratio. The steady-state heat transfer rate of CLT2 under normal test conditions was approximately 380 W; however, the highest heat transfer rate in this oscillation process was less than 100 W. When CLT2 entered the oscillation state, the oscillation continued for hours, and the circulation flow could not return to normal automatically.
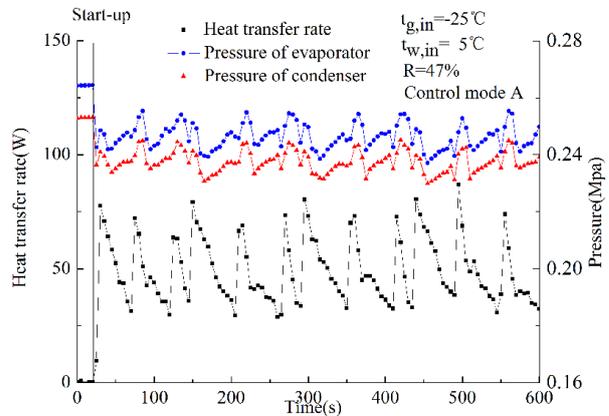


**Fig.7.** First typical start-up failure of CLT2

2. The second typical start-up failure is shown in Fig.8. CLT2 failed to start up in control mode A again when $t_{g,in}$ was −21 °C and the R134a fill ratio was 52%. No heat transfer and pressure oscillation occurred during this start-up process. However, CLT2 could only maintain a stable low heat transfer. This heat transfer deterioration was unable to recover without artificial interference.
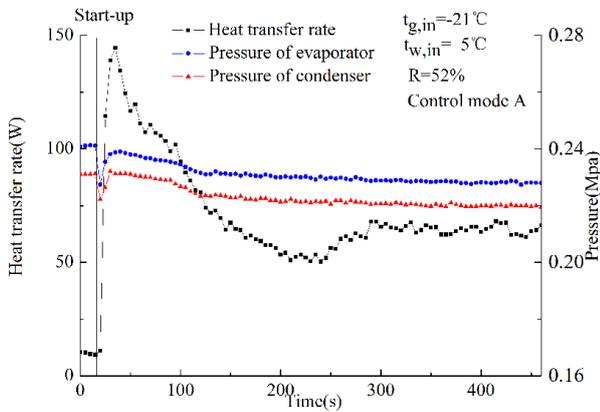


**Fig.8.** Second typical start-up failure of CLT2

3. Fig.9 shows that the third typical start-up failure appeared in control mode C. The heat transfer rate increased rapidly with pressure when CLT2 was initialized and almost reached stability in approximately 200 s. This period of start-up process was similar to other normal start-up processes of control mode C. However, temporary heat transfer deterioration appeared in about 250 s. This temporary heat transfer deterioration only lasted for 200 s and disappeared after pressure fluctuation within a narrow range. The recovery process was similar to a normal start-up process and did not require artificial interference. CLT2 reached its stable operating state after this temporary heat transfer deterioration in the start-up process.
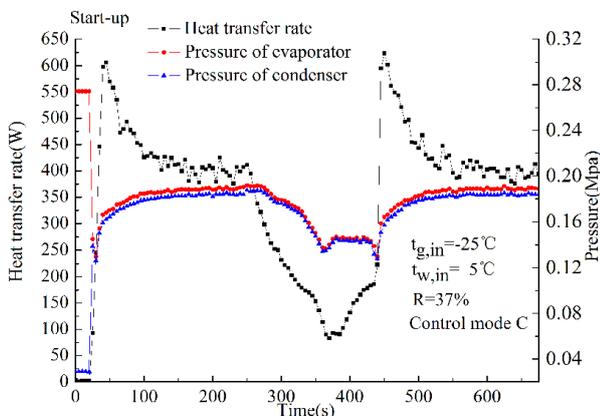


**Fig.9.** Third typical start-up failure of CLT2

The abovementioned typical cases show the unstable control performance of CLT2. Such unstable phenomena may be caused by a reservoir with a low liquid level height. We recommend that CLT2 be operated at an R134a fill ratio of 57% to 67% to avoid start-up failure. By contrast, CLT1 showed better active control stability than CLT2.

The optimal fill ratio of CLT2 was approximately 62% because of its excellent start–stop performance and good steady-state heat transfer capability. The optimal fill ratio of CLT1 under normal test conditions was determined in our previous study, and the value is 38.9% [26]. The following start–stop performance comparison between CLT1 and CLT2 was based on their optimal fill ratios.

*Effect of reservoir on start–stop performance*

The three control modes of CLT were well investigated in our previous work. The results showed that the start–stop performance of control mode C is the best, that of control mode A is acceptable, and that of control mode B is not recommended [26]. Thus, in the present study, control modes A and C were tested to compare the start–stop performances of CLT1 and CLT2.

We performed experiments with different $t_{g,in}$ values. CLT1 and CLT2 were tested to analyze the effect of the reservoir on the start–stop performance of control mode A. A comparison of the results is shown in Fig.10. For convenience, heat transfer rate and pressure are denoted by $Q$ and $P$, respectively. In control mode A, the start-up of CLT1 and CLT2 was quite rapid, and the time consumed to reach the maximum heat transfer rate was approximately 15–20 s. The heat transfer rates of CLT1 and CLT2 were also similar after a stable working status was reached. However, the time consumed for heat transfer stabilization differed.
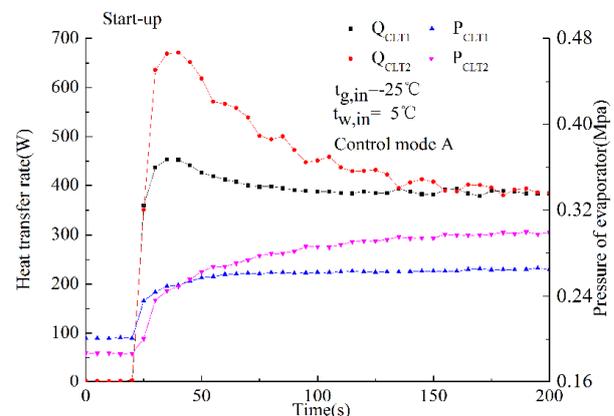


**Fig.10.** Comparison of start-up processes in control mode A

The heat transfer rate and pressure of CLT1 in the start-up process stabilized in 100 s, whereas

those of CLT2 required twice as much time. Temporary heat transfer enhancements appeared in the early start-up processes, and that of CLT2 was much stronger than that of CLT1. Fig.11 shows the stopping processes in control mode A at normal test conditions. The heat transfer of CLT1 stopped in approximately 100 s and was faster than that of CLT2. The evaporator pressure of CLT1 increased temporarily before it steadily declined and reached stability in 400 s. Fig.10 and Fig.11 show that the stable operating and stopping pressures of CLT1 differed from those of CLT2.
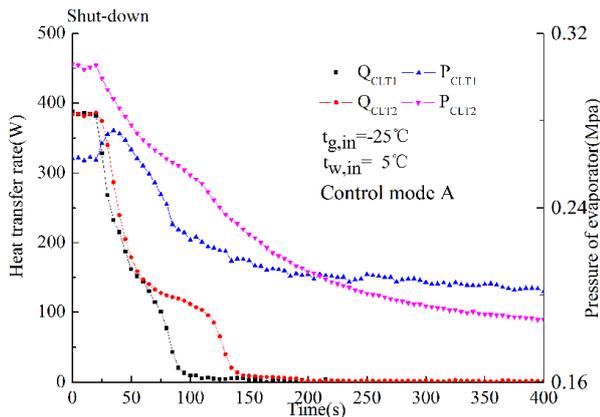


**Fig.11.** Comparison of stopping processes in control mode A

$t_{g,in}$ was varied from −25 °C to −17 °C to analyze the start–stop performance difference between CLT1 and CLT2 in control mode A. The start-up time stabilized within 15–25 s. However, various differences were observed in control mode A. Table 3 shows that the steady-operating and steady-stopping evaporator pressures and the heat transfer stopping time increased gradually with $t_{g,in}$. Moreover, the operating pressures of CLT1 at various $t_{g,in}$ values were higher than those of CLT2, contrary to the stopping pressures. These phenomena in the start–stop process of control mode A can be explained as follows.

**Table 3.** Stopping time of CLT1 and CLT2 at various $t_{g,in}$ values in control mode A

| $t_{g,in}$ (°C) | Stopping time (s) | | Operating pressure (Mpa) | | Stopping pressure (Mpa) | |
|---|---|---|---|---|---|---|
| | CLT1 | CLT2 | CLT1 | CLT2 | CLT1 | CLT2 |
| −25 | 75 | 120 | 0.263 | 0.302 | 0.202 | 0.187 |
| −23 | 75 | 125 | 0.267 | 0.305 | 0.211 | 0.197 |
| −21 | 80 | 130 | 0.270 | 0.306 | 0.222 | 0.207 |
| −19 | 85 | 145 | 0.276 | 0.308 | 0.233 | 0.218 |
| −17 | 95 | 155 | 0.279 | 0.310 | 0.245 | 0.230 |

The additional reservoir stored much R134a. Thus, R134a needed more time to reach stability in the stopping process. The reservoir also decreased the R134a liquid level. Hence, the degrees of overheating in the evaporator and overcooling in the condenser decreased, and the average temperature of R134a increased with pressure. In the steady-state operating process, more liquid R134a extruded from the evaporator by hot vapor in CLT2, and more liquid R134a was affected by the low temperature of the condenser.

The active control abilities of CLT1 and CLT2 in control mode C were tested under normal test conditions. The results were compared. Fig.12 shows that the heat transfer variations of the CLTs in the start-up process were similar to those in control mode A. Their heat transfer began quickly, and CLT2 required more time than CLT1 to reach stability. The evaporator pressures in control mode C decreased rapidly at first and then increased slowly. The time wasted for CLT2 to reach a stable operating status was approximately 150 s, which is triple the time consumed by CLT1.
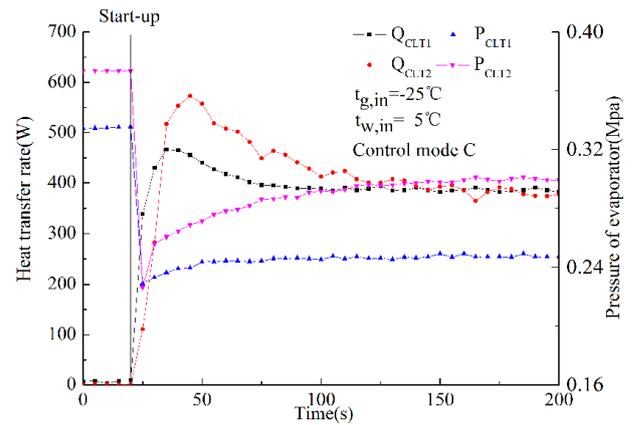


**Fig.12.** Comparison of start-up processes in control mode C

The stopping processes of CLT1 and CLT2 are shown in Fig.13. The heat transfer and pressure variations are similar. The stopping time of CLT1 and CLT2 is approximately 70–80 s. Their evaporator pressures increased slowly and reached stability in approximately 100 s. The above similarity was retained even when the test conditions were varied. The start–stop performance of control mode C was hardly affected by the reservoir structure unlike that of control mode A primarily because of the unique control method of control mode C. The evaporator in control mode C was isolated from the condenser and reservoir completely when CLT was stopped; thus, the

variations in R134a state in the start-up and stopping processes were unrelated to the reservoir.
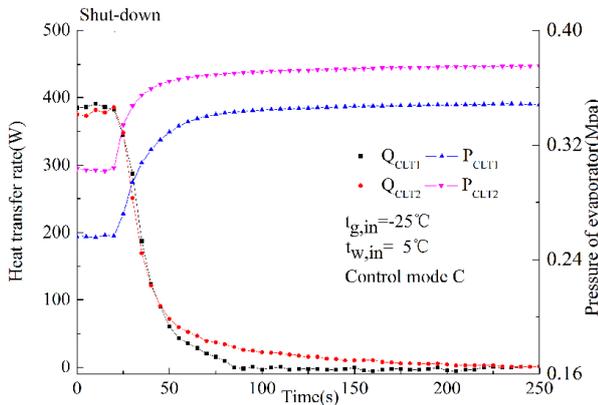


**Fig.13.** Comparison of stopping processes in control mode C

## CONCLUSIONS

We designed and arranged two test rigs to investigate the effect of a reservoir on CLT. Tests were conducted with various R134a fill ratios under normal test conditions to compare the steady-state heat transfer and start–stop performances of the two CLTs. The CLT1 and CLT2 were studied at their optimal R134a fill ratios. The heat sink temperature varied. The following conclusions were obtained.

1. The optimal heat transfer performance of CLT1 was obtained at a fill ratio of 38.9% under normal test conditions. The fill ratios of the optimal working points varied from 38.9% to 34.74% at different $t_{g,in}$ values. CLT2 could operate well at any fill ratios within the range of 32%–67% at each $t_{g,in}$ value. The results showed that a reservoir can remarkably improve the steady-state heat transfer stability of CLT.

2. The CLT without a reservoir displayed a significant advantage in control stability. CLT1 never failed to start or stop even when the fill ratio deviated from its optimal value and the steady-state heat transfer performance was degraded seriously. CLT2 could start steadily under different test conditions when the R134a fill ratio varied in the range of 57%–67%. Several unstable start-ups occurred in the starting process of CLT2 at a fill ratio of less than 57%.

3. The effect of the reservoir on the start–stop performance of CLT revealed clear distinctions among the control modes, which were evident in the stopping process. In control mode A, the additional reservoir increased the stopping time obviously at each $t_{g,in}$ value. Thus, the reservoir could degrade the active control performance of

control mode A. By contrast, the start–stop time of CLT1 and CLT2 in control mode C was similar. This result indicates that the active control performance of control mode C was hardly affected by the reservoir structure.

The optimal system design can be selected under different application backgrounds. To obtain good steady-state heat transfer and start–stop performances, the CLT without a reservoir needs to be operated with its optimal R134a fill ratio. The CLT with a reservoir should be operated in control mode C with an R134a fill ratio of 57%–67%.

## NOMENCLATURE

$C_p$: Specific heat capacity of water (J/(kg·K))
$P$: Pressure of the evaporator (Mpa)
$Q$: Heat transfer capability of CLT (W)
$R$: R134a fill ratio
$t_{g,in}$: Inlet water–glycol mixture temperature of the condenser (°C)
$t_{w,in}$: Inlet water temperature of the evaporator (°C)
$t_{w,out}$: Outlet water temperature of the evaporator (°C)
$V$: Measured volume flow rate of water (m$^3$/s)
$\rho$: Density of water (kg/m$^3$)

## REFERENCES

1 Kim D. S., Ferreira .C A. I., Solar refrigeration options–a state-of-the-art review, International Journal of refrigeration, Elsevier, 31, (2008).

2 El Tom, O. M. M., et al., Performance of a photovoltaic solar refrigerator in tropical climate conditions, Renewable energy, Elsevier, 1 (1991).

3 Long, Rui, et al., Performance analysis of a solar-powered electrochemical refrigerator, Chemical Engineering Journal, Elsevier, 284 (2016).

4 Kattakayam T. A. and Srinivasan K., Lead acid batteries in solar refrigeration systems, Renewable energy, Elsevier, 29 (2004).

5 Siaka Toure and Fassinou W. F., Technical note Cold storage and autonomy in a three compartments photovoltaic solar refrigerator: experimental and thermodynamic study, Renewable energy, Elsevier, 17, (1999).

6 R.E. Foster, D. Bergeron, Photovoltaic Direct Drive Refrigerator with Ice Storage: Preliminary

Monitoring Results, in: ISES 2001 Solar World Congress, 2001.

7 Azzouz K., Leducq D. and Gobin D., Enhancing the performance of household refrigerators with latent heat storage: An experimental investigation, international Journal of Refrigeration, Elsevier, 32, (2009).

8 Subramaniam P, Tulapurkar C, Thiyagarajan R, et al., Phase change materials for domestic refrigerators to improve food quality and prolong compressor off time, International refrigeration and air conditioning conference, Purdue, USA, (2010).

9 MD. Imran Hossen Khan and Hasan M. M. Afroz, Experimental investigation of performance improvement of household refrigerator using phase change material, International journal of air-conditioning and refrigeration, Elsevier, 21, (2013).

10 C. Del Pero, F.M. Butera et al., Feasibility study of a Solar Photovoltaic Adaptable Refrigeration Kit for remote areas in developing countries, 2015 International Conference on. IEEE, 2015.

11 Torriti, J., Price-based demand side management: Assessing the impacts of time-of-use tariffs on residential electricity demand and peak shifting in Northern Italy, Energy, Elsevier, 44, (2012).

12 Barzin R., Chen J. J. Chen, Young B. R., et al, Peak load shifting with energy storage and price-based control system, Energy, Elsevier, 92, (2015).

13 Sekhar, S. Joseph, D. Mohan Lal, and S. Renganarayanan, Improved energy efficiency for CFC domestic refrigerators retrofitted with ozone-friendly HFC134a/HC refrigerant mixture, International journal of thermal sciences, Elsevier, 43, (2004).

14 Jung D, Kim C B, Song K, et al., Testing of propane/isobutane mixture in domestic refrigerators, International journal of refrigeration, Elsevier, 23, (2000).

15 James S. J. and Evans J., The temperature performance of domestic refrigerators, International Journal of Refrigeration, Elsevier, 15, (1992).

16 Amir Faghri, Heat Pipe Science and Technology, Global Digital Press, Washington, 1995.

17 Rahmatollah Khodabandeh, Richard Furberg, Heat transfer, flow regime and instability of a nano- and micro-porous structure evaporator in a two-phase thermosyphon loop, International Journal of Thermal Sciences, Elsevier, 49, (2010).

18 Yu Song, Aurélien Four and Bertrand Baudouy, Nucleate boiling heat transfer in a helium natural circulation loop coupled with a cryocooler, International Journal of Heat and Mass Transfer, Elsevier, 66, (2013).

19 Jiang He, Guiping Lin et al., Effect of non-condensable gas on startup of a loop thermosyphon, International Journal of Thermal Sciences, Elsevier, 72, (2013).

20 A.A. Chehadea, H. Louahlia-Gualous et al., Experimental investigation of thermosyphon loop thermal performance, Energy Conversion and Management, Elsevier, 84, (2014).

21 Ali Chehadea, Hasna Louahlia-Gualous et al., Experimental investigations and modeling of a loop thermosyphon for cooling with zero electrical consumption, Applied Thermal Engineering, Elsevier, 87, (2015).

22 Ji Lia, Feng Linb, Gengwen Niu, An insert-type two-phase closed loop thermosyphon for split-type solar water heaters, Applied Thermal Engineering, Elsevier, 70, (2014).

23 Penglei Zhang, Baolong Wang, Wenxing Shi, Xianting Li, Experimental investigation on two-phase thermosyphon loop with partially liquid-filled downcomer, Applied Energy, Elsevier, 160, (2015).

24 Zhen Tong, Tao Ding, Zhen Li, Xiao-Hua Liu, An experimental investigation of an R744 two-phase thermosyphon loop used to cool a data center, Applied Thermal Engineering, Elsevier, 90, (2015).

25 Alessandro Franco and Sauro Filippeschi, Closed Loop Two Phase Thermosyphon of Small Dimensions: a Review of the Experimental Results, Microgravity Sci. Technol., Elsevier, 24 (2012).

26 Jingyu Cao, Jing Li and Gang Pei, Performance Evaluation of Controllable Loop thermosyphons, Applied Thermal Engineering, Elsevier, 100 (2016).

# Adsorption characteristics evaluation of R134A and R404A on different adsorbents

M. Kılıç[*], E. Gönül

*Uludağ University, Engineering Faculty, Department of Mechanical Engineering, Bursa, Turkey*

In order to design adsorption employed cooling or refrigeration system, it is inevitably required the knowledge of the adsorption isotherms and the isosteric adsorption heat for the assorted adsorbent/adsorbate pair. The physical adsorption phenomena occurs mainly within the pores and on the surface of the adsorbent. Since, the characteristics of each adsorbent-adsorbate pair is different than others. The knowledge of adsorption characteristics with the variation of temperature and pressure is necessary for the evaluation. However, these data are usually unavailable from the manufacturers of adsorbents. The objective of this study is to evaluate adsorption characteristics of R134A (HFC-134A) and R404A (HFC-404A) on different adsorbents experimentally by a constant volume variable pressure method at different adsorption temperatures ranging from 20 to 50 C and for pressures up to 5 bar. The forms of the isotherms obtained from the experimental measurements are similar in all cases and comparable to those reported in the literature for commercially available different adsorbents. Adsorption parameters are evaluated from the isotherms using the Dubinin-Astakhov (DA) equation. The concentration dependence of the isosteric enthalpies of adsorption is extracted from the obtained data. Further, the enthalpy of adsorption data are extracted, and correlations are provided for the different specimens investigated. These data are essential for the design of a thermally driven adsorption chiller employed the assorted pair.

**Keywords:** adsorbent, adsorbate, adsorption cooling, R134A, R404A

## INTRODUCTION

Adsorption refrigeration and cooling research has attracted attention in view of the pressing need for combating ozone depletion and global warming [1, 2]. The main heat sources for adsorption systems are waste heat and solar energy. Physical adsorption working pairs are usually preferred when solar energy is the heat source [3]. It provides an alternative to conventional vapor compressor refrigeration, because the systems based on adsorption can be driven by low grade heat sources such as solar energy and industrial waste heat. In addition, they have minimal moving parts. In contrast to vapor absorption cycles, adsorption cycles dispense with the heat exchangers [4]. The properties of adsorbent/adsorbate pairs as well as the operating conditions have significant effects on the system performance [5]. The isosteric heat of adsorption is a specific combined property of an adsorbent/adsorbate combination. The equilibrium adsorption properties at several adsorbent temperatures and adsorption chamber adsorbate pressures were studied for a wide range of pairs [6]. Meanwhile, on the refrigerant field considerable motivation already exists to use natural and/or ozone friendly refrigerants. If the need is to use refrigerants that result in system pressures above atmospheric pressures, that are also non-flammable, non-toxic and ozone friendly, the choice narrows down to partly halogenated hydro fluorocarbon refrigerants such as R134A (tetrafluoroetan

CF$_3$CH$_2$F) and R404A (CHF$_2$CF$_3$ / CH$_3$CF$_3$ / CF$_3$CH$_2$F) which is near a zeotropic blend of HFC-125/HFC-143A/HFC-134A. R134A is the one of the very well-known and widely used refrigerants in both domestic and commercial medium and high temperature refrigeration, residential and vehicle air conditioning as well as several industrial applications. A number of HFC refrigerant blends are also composed by the use of R134A. R404A is an HFC blend that is also employed a wide range of low and medium temperature refrigeration applications. R404A is a quite common refrigerant used in commercial refrigeration applications such as those used in the both chilled and frozen food refrigeration. Although, the Ozone Depletion Potential (ODP) of R404A and R134A is zero, the Global Warming Potential (GWP) of R404A and R134A are high and medium level with the value of 3943 and 1300, respectively. However, the safety classifications of R404A and R134A according to the ASHRAE Standard 34 are in the lowest rank (A1) to the hazard involved in their use [7].

Thus, R134A and R404A based adsorption refrigeration cycles provide a very well match for the current aspirations and expectations from adsorption cooling systems. The design of these refrigeration systems requires data on isotherms and the heats of adsorption for indenting heating inventories. Detailed literature review on adsorption working pairs for refrigeration is given by Wang et.al. [8,9].

Isosteric heat of adsorption is traditionally expressed as a function of concentration due to its dependence on temperature is relatively weaker

---
\* To whom all correspondence should be sent:
mkilic@uludag.edu.tr

[10,11,12]. For adsorption of fluids below their thermodynamic critical point, its magnitude is larger than the heat of vaporization of the adsorbate, which has a strong temperature dependence [12]. As a result, the difference between the two is a property of relevance in the design of adsorption refrigeration systems.

It is a matter of regret that adsorption data are unavailable from the manufacturers of adsorbents. The characteristics of a new adsorbent like a kind of silica gel or activated alumina may show differently than the known ones. In order to design adsorption based cooling cycle it is inevitable to evaluate adsorption isotherms of the assorted adsorbent/adsorbate pair as well as the isosteric heat of adsorption.

From the above mentioned perspectives, the present paper reports an experimental study to obtain isotherm data for commercially available activated carbon (AC), silica gel (SG) and activated alumina (AA). Adsorption isotherms of R134A and R404A on the different materials were measured over a temperature range of 20–50 °C and pressures up to 5 bar using constant volume variable pressure (CVVP) method. Moreover, the isosteric heat of adsorption data is extracted from the data of the present experiments.

## MATERIAL AND METHOD

The CVVP experimental setup comprises: (i) a charging tank with a volume of 3000 cc, (ii) an adsorption tank with a volume of 3000 cc, (iii) temperatures of the both the charging and adsorption tanks are controlled independently by the separate circulating water systems, (iv) a pressure transducer with an uncertainty of 0.15% of full scale and a pressure ranging from 0 to 1.6 MPa, (v) Pt 100 type thermometers with an uncertainty of 0.2% for temperature measurement, (vi) separate sensors with an uncertainty of 0.2% used with the adsorbent species for direct temperature measurement, (vii) a vacuum pump that achieves vacuum level of 0.5mbar, and (viii) a computer used to control the test system and record the data. The volume of both charging and adsorption tanks are inclusive of the volumes of related piping and valves.

### *Procedure*

Prior to adsorption process, the specimen of the adsorbent is placed in an oven for 24 h to desorb any residual gas. The oven temperature is kept constant at 120˚C. Before starting adsorption measurements the system was evacuated to take out any gases and moisture from the system using a vacuum pump to 0.5 mbar. The tanks were heated by using hot water circulation at 60˚C during 6 h, while the vacuum process is still running. At the end of regeneration process, the test system is purged with helium gas and evacuated further to achieve low vacuum conditions. The evacuation and helium purging are continued several times to ensure that there is no residual gas left in the system. It is observed from the performed measurements that there is not any measurable interaction between the inert gas and the adsorbent. After evacuation, the charging cell is pressurized with the assorted refrigerant and left until it reaches an equilibrium state. During charging process, it is necessary to keep the charging pressure lower than the saturation pressure of the refrigerant to ensure no condensation is occurred. At this state the initial pressure and temperature in the charging cell are measured before adsorption. Once thermal equilibrium is achieved, the needle valve between the charging and adsorption tank is opened. The pressure and temperature in the adsorption tank are recorded to calculate the uptake of the assorted refrigerant by ensuring thermal equilibrium present. This process was repeated for the each charging step until the high pressure reached. By the use of a specimen, each isotherm was measured at a constant temperature over a range of pressure from 0 to 5 bar.

Experimental study was performed by the use of commercially available adsorbents as activated carbon (AC), silica gel (SG) and activated alumina (AA) specimens. Phyiscal characteristics of the adsorbents used in the tests are presented in Table 1.

**Table 1.** Physical characteristics of the adsorbents used in the tests.

|  | Activated Carbon | Silica Gel | Activated Alumina |
|---|---|---|---|
| Size (mm) | 0.6-2.6 | 2-5 | 1.4-2.8 |
| Density (kg/m³) | 470 | 720 | 753 |
| Micro Pore Specific Volume (cm³/g) | 0.472 | 0.276 | 0.166 |
| Specific Surface Area (m²/g) | 949 | 556 | 350 |
| Color | Black | Blue | White |
| Shape | Granulated | Spherical | Spherical |

For each specimen with the known initial dry mass, experiments were performed at constant temperatures chosen as 20, 30 and 50 ºC for pressures up to 5 bar.

*Assessment of overall uncertainty*

There are some uncertainties associated with instrumentation, average adsorption cell temperature during adsorption and the void correction. Moreover, certain errors introduced due to the mathematical calculations. It is expected that the overall uncertainty will be within 3%.

## ANALYTIC TREATMENT

The starting point for this analysis is the use of Dubinin–Astakhov (D–A) model of adsorption isotherm in the following form [8,9]:

$$W = W_0 \exp\left\{-\left[\frac{RT}{E} ln\left(\frac{p_s}{p}\right)\right]^n\right\} \quad (1)$$

with

$$W = Cv_a \quad \text{and} \quad W_0 = C_0 v_0 \quad (2)$$

Here $E$ is the characteristic energy of the assorted adsorbent/adsorbate pair which can be evaluated experimentally. The parameter $n$ is an exponential constant which gives the best fitting of the experimental isotherms. The quantity $C$ denotes the specific mass of adsorption (kg of adsorbate per unit mass of adsorbent), and $v_a$ is the specific volume of the adsorbed phase, which is given by

$$v_a = v_b \exp(\Omega(T - T_b)) \quad (3)$$

where

$$\Omega = \ln(b/v_b)/ (T_c - T_b) \quad (4)$$

The quantity $b$ denotes the van der Waals volume, $v_b$ is the saturated liquid specific volume at the normal boiling point [11,12,13]. T is the temperature with suffixes $c$ and $b$ referring to critical and normal boiling points, respectively. The parameter $v_0$ can be obtained by using Eq. (3) at T = 0. Table 2 shows the properties and parameters of the adsorbates used in the present experimental study. Eq. (1) can be rewritten as follows:

$$\ln p = \ln p_s - E/(RT)[ln(C_0 v_0/Cv_a)]^{1/n} \quad (5)$$

Differentiating Eq. (5) with respect to 1/T for the isosteric conditions (i.e. C is constant). Noting that $v_a$ is also a function of temperature, one can get the following equation:

$$\frac{\partial \ln p}{\partial(1/T)} = \frac{\partial \ln p_s}{\partial(1/T)} - \left(\frac{E}{R}\right)[ln(C_0 v_0/Cv_a)]^{\frac{1}{n}}$$

$$-(ET\Omega/(nR))[ln(C_0 v_0/Cv_a)]^{((1-n))/n} \quad (6)$$

Isosteric heat of adsorption is defined by the Clausius–Clapeyron relation at constant consantrations as

$$Q_{ads}|_{CC} = -R(\partial \ln p)/\partial(1/T) \quad (7)$$

and for the heat of vaporization defined as

$$h_{fg} = -R(\partial \ln p_s)/\partial(1/T) \quad (8)$$

Substituting Eq.7 and 8 into Eq.6, the following equation for the heat of adsorption can be derived.

$$Q_{ads} = h_{fg} + (E)[ln(C_0 v_0/Cv_a)]^{1/n}$$

$$+(ET\Omega/n)[ln(C_0 v_0/Cv_a)]^{((1-n))/n} \quad (9)$$

**Table 2.** Properties and parameters of the adsorbates.

|  | **R134A** | **R404A** |
|---|---|---|
| Molecular Weight (MW) | 102.03 | 97.60 |
| Boiling Point at 1 atm ($T_b$) | -26.06 °C | -46.45 °C |
| Critical Temperature ($T_c$) | 101.08 °C | 72.07 °C |
| Critical Pressure ($P_c$ ) | 4059 kPa | 3729 kPa |
| Critical Density | 515.3 kg/m$^3$ | 484.5 kg/m$^3$ |
| $b$ | 0.0009390 | 0.0009857 |
| $v_b$ (m$^3$/kg) | 0.0007260 | 0.0007655 |
| $v_0$ (m$^3$/kg) | 0.0007657 | 0.0008445 |
| $\Omega$ | 0.002018 | 0.002125 |

The standard procedure for evaluation of isosteric heat of adsorption as described by Eq.7, is to plot the isosters on *ln p* versus *1/T* plane. Normally, a constancy of slope is observed at temperatures well over the critical point of the adsorbate. As a result the classical treatment of isosteric heat of adsorption being shown as a function of relative uptake is a good approximation for adsorbent–adsorbate combinations which broadly follow the Dubinin's isotherms [14, 15]. Due to non-ideality of the gas phase, during an adsorbate molecule uptake to the assorted adsorbent is affected by the pressure and temperature changes [5, 8]. In order to consider the effect of pressure and temperature changes, heat of adsorption can be calculated by using the Eq.9.

## RESULTS AND DISCUSSIONS

The experimental data was used to evaluate the adsorption parameters for the activated carbon (AC)-R134A, silica gel (SG)-R134A, activated alumina (AA)-R134A, activated carbon (AC)-R404A, silica gel (SG)-R404A pairs. By the use of Eqs. 1-4, an objection function can be derived as follow:

$$F = \sum_{i=1}^{N}\left[C_i - \frac{C_0 v_0}{v_a}\exp\left\{-\left[\frac{RT_i}{E} ln\left(\frac{p_s}{p_i}\right)\right]^n\right\}\right]^2 \quad (10)$$

Where $N$ is the number of data sets, $C_i$, $p_i$ and $T_i$ are known variables obtained from the

experimental measurements. $C_0$, $E$ and $n$ are unknown constants. To obtain the unknown parameters, the objection function must be minimized. Derived objection function is optimized by the use of a homemade code based on a genetic algorithm. Table 3 shows that computed values of the adsorption parameters ($W_0$, $C_0$, $E$ and $n$) for the AC-R134A, SG-R134A, AA-R134A, AC-R404A and SG-R404A pairs.

**Table 3.** Computed adsorption parameters of the different adsorbent-adsorbate pairs.

| Pairs | $W_0$ (m³/kg) | $C_0$ (kg/kg) | $E$ (kJ/kmol) | n |
|---|---|---|---|---|
| AC-R134A | 0.3728x10⁻³ | 0.487 | 8874.9 | 1.725 |
| SG-R134A | 0.3629x10⁻³ | 0.474 | 5120.9 | 1.034 |
| AA-R134A | 0.2412x10⁻³ | 0.315 | 5509.4 | 1.318 |
| AC-R404A | 0.3379x10⁻³ | 0.400 | 11090 | 1.734 |
| SG-R404A | 0.3268x10⁻³ | 0.387 | 6130.7 | 1.300 |

Comparison of the experimental and the computed isotherms of the adsorbent-adsorbate pairs at 20 °C are given in Fig.1. It can be seen from the Fig.1 that the measured results and the computed data obtained from D-A equation (Eq.1) with the parameters given in Table 2 are in a very good agreement.
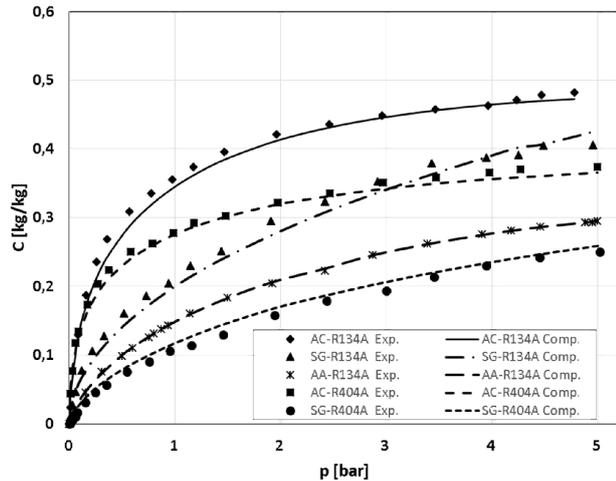


**Fig.1.** Comparison of the experimental and the computed isotherms of R134A and R404A on different adsorbents at 20 °C

The shapes of the isotherms obtained from the experimental data were similar in all cases and comparable to those reported in the literature for commercially available different adsorbents [3, 5,6,11,12]. Then, Eq.5 and Eq.9 with the parameters provided in Table 3 were used to evaluate isosters and isosteric heat of adsorption of the adsorbent-adsorbate pairs. Fig.2 shows the

isosters of adsorption of R134A and R404A on activated carbon, silica gel and activated alumina for $C/C_0 = 0.6$ It can be seen from the Fig.2 that the variation of ln(p) with 1/T presents linear variation for each adsorbent-adsorbate pairs. It is interesting to see that the isosters of the adsorbates of R134A and R404A with activated carbon is overlap each other, while the slopes of the lines are different for each adsorbent-adsorbate pairs.
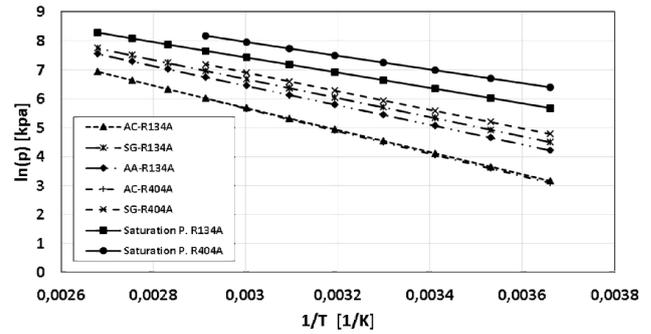


**Fig.2.** Obtained isosters of adsorption of R134A and R404A on activated carbon, silica gel and activated alumina for $C/C_0 = 0.6$
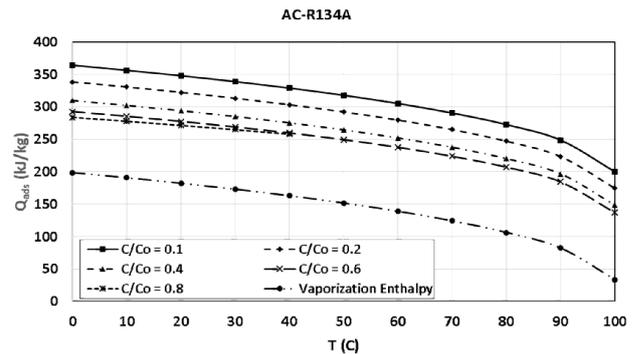


**Fig.3.** Obtained isosteric heat of adsorption of R134A on activated carbon

A careful inspection on the Fig.3 to Fig.7, it can be seen that the isosteric heat of adsorption decreases with increasing adsorbate uptake for all the cases. In addition, the temperature has more effect on isosteric heat, where the maximum value of isosteric heat obtained with low temperature at 0˚C. The adsorbate molecules first penetrate into narrow pores of adsorbent, where a stronger interaction between adsorbate and adsorbent exists. As a result of this a higher isosteric heat value of adsorption at lower loading occurs. After completely filling the smaller pores, adsorbate molecules are gradually accommodated in larger pores, in which the adsorption affinity becomes weaker. Therefore a monotonic decrease in isosteric heat of adsorption as a function of adsorbate uptake.
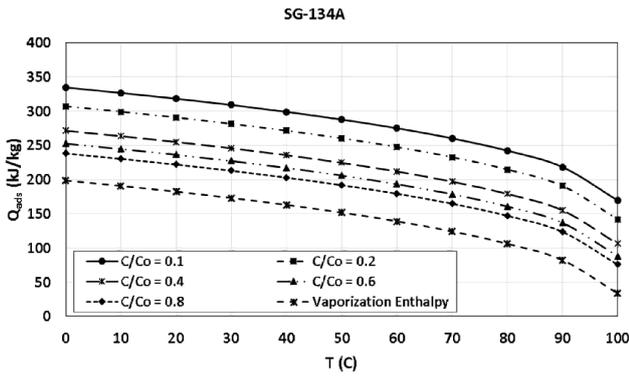
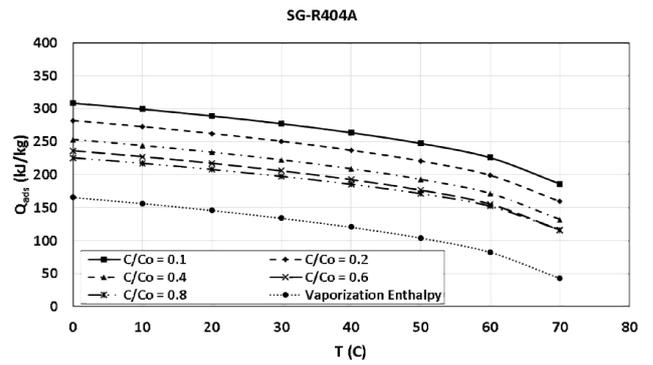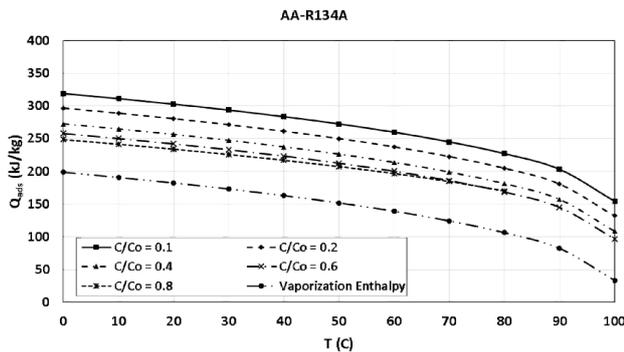**Fig.4.** Obtained isosteric heat of adsorption of R134A on silica gel



**Fig.5.** Obtained isosteric heat of adsorption of R134a on activated alumina

Comparing the magnitude of the isosteric adsorption heat, AC-R134A pair has the greatest one among the pairs tested in this study. Meanwhile, SG-R134A and AA-R134A pairs have the comparable magnitude of the isosteric adsorption heat. It is also observed that replacing R134A with R404A do not significant effect on the magnitude of the isosteric adsorption heat on the same adsorbent as seen Fig.4 and Fig.6 for AC, and also Fig.5 and Fig.7 for SG.

In addition to all, the magnitude of the heat of adsorption is greater than that of the enthalpy of vaporization of R134A and R404A in the all range of the experimental tests performed.
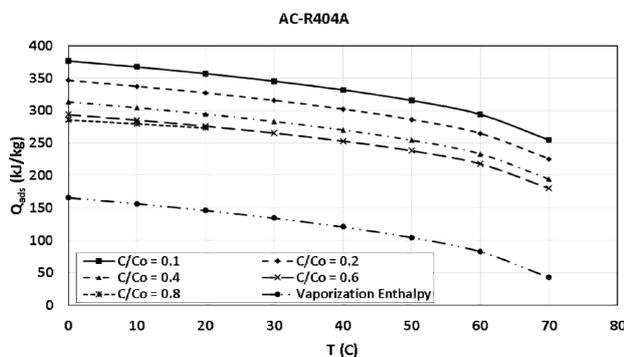


**Fig.6.** Obtained isosteric heat of adsorption of R404A on activated carbon



**Fig.7.** Obtained isosteric heat of adsorption of R404A on silica gel

CONCLUSIONS

In this study, the adsorption properties of R134A and R404A on commercially available specimens of activated carbon, silica gel and activated alumina for adsorption process has been experimentally studied. The measurements were performed over a temperature range from 20°C to 50°C and pressure up to 5 bar. The data were correlated with Dubinin-Astakhov (D-A) equation for corresponding adsorption process. Adsorption parameters were evaluated from the isotherms using the D-A equation. Further, the isosteric heat of adsorption were obtained, and correlation parameters were provided for the specimens investigated. Comparisons between the correlated results and the experimental data show very good agreement. It is observed that the adsorption capacity per kg of adsorbent increases rapidly with rising relative pressure at the starting period of the adsorption process. The maximum value of adsorption capacity decreases with the rising temperature of adsorbent . The isosteric heat of adsorption varied with the temperature and the maximum value of isosteric heat obtained at the lowest temperature. In addition, it is also observed that the magnitude of the heat of adsorption is higher than that the vaporization enthalpy of R134A and R404A in the range of experimental studies performed. This aspect is important for the design of thermal compressors in which the amount of coolant requirements to remove the heat of adsorption process have to be estimated.

310

## REFERENCES

1  M. Pons, Y. Feng, *Appl Therm Eng*, 17 (3), 289 (1997).

2  R.Z. Wang, R.G. Oliveira, *Prog Energy Combust Sci*, 32 (4), 424 (2006).

3  B.S. Akkimaradi, M. Prasad, P.Dutta, K. Srinivasan, *J. Chem. Eng. Data*, 46, 417, (2001).

4  S.B. Riffat, M.D. Williams, S. Corr, *Int. J. Energy Res.*, 21, 481, (1997).

5  A. Chakraborty, B.B. Saha, S. Koyama, K.C. Ng, *Appl. Phys. Lett.*, 89, 171901, (2006).

6  B. B. Saha, K. Habib, I.I. El-Sharakawy and S. Koyama, *International Journal of Refrigeration*, 32(7), 1563, (2009).

7  ASHRAE, Number designation and safety classification of refrigerants, ANSI/ASHRAE Standard 34-2013, ASHRAE, 2013.

8  R. Z. Wang, J. P. Jia, Y. H. Zhu, Y. Teng, J. Y. Wu, J. Cheng and Q. B. Wang, *Transactions on ASME*, 119 (3), 214, (1997)

9  L.W. Wang, R.Z. Wang, R.G. Oliveira, *Renewable and Sustainable Energy Reviews*, 13, 518, (2009).

10  D.C. Wang, Y.H. Li, D. Li, Y.Z. Xia, J.P. Zhang, *Renewable and Sustainable Energy Reviews*, 14, 344, (2010).

11  C.K. Chan, E. Tward, K.I. Boudale, *Cryogenics*, 24, 451, (1984).

12  I Solmuş, C. Yamalı, B. Kaftanoğlu, D. Baker, A. Çağlar, *Applied Energy*, 87, 2062 (2010).

13  I.I. El-Sharkawy, K. Kuwahara, B.B. Saha, S. Koyama, K.C. Ng, *Appl. Therm. Eng.*, 26, 859, (2006).

14  S.H. Lin, R.C. Lin, *J. Environ. Sci. Health*, 34 (1), 183, (1999).

15  M. Prakash, A. Mattern, M. Prasad, R. Sant, P. Subramanya, K. Srinivasan, *Carbon*, 38 (8), 1163, (2000).

# Energy and exergy analysis of a double effect LiBr-H₂O and LiCl-H₂O chillers

M. Kılıç*, H. B. Ravul

*Uludağ University, Faculty of Engineering ,Department of Mechanical Engineering, 16059 Bursa, Turkey*

Absorption refrigeration systems (ARS) is a type of environmental friendly technology with zero ozone depletion and global warming potential that can utilize industrial waste heat and renewable energy sources such as solar and geothermal. Therefore, there is an ongoing effort and many research for further improvements. A comparative study between single effect and double effect absorption refrigeration systems using lithium bromide/water and lithium chloride/water as working fluid solutions is presented in this paper. The coefficient of performance (COP) and the second law efficiency (exergetic efficiency) of absorption system under different operating conditions are calculated. Simulation results are used to evaluate the influence of the various operating parameters on the performance coefficient, the thermal loads of the system components, exergetic efficiency and the total change in exergy of the systems. It is observed that operation temperatures of the overall system and its components have a major effect on their performance and functionality. In this regard, a parametric study conducted here to investigate this effect on heat capacity and exergy destruction of the system components. Also, a comparative analysis for the working fluids is carried out. It is observed that the COP of double effect system is considerably higher than the COP of single effect system, however, the exergetic efficiency of double effect system is slightly higher than the exergetic efficiency of single effect system.

**Keywords*:* absorption cooling, coefficient of performance (COP), exergy, lithium bromide/ water, lithium chloride/ water, refrigeration

## INTRODUCTION

In recent years, interest in absorption refrigeration technology has been growing because these systems use such pairs of refrigerant and absorbent which do not deplete the ozone layer. Absorption refrigeration systems [1] are therefore essentially powered by heat, which not only minimizes exergy depredations, but it also allows for the use of free thermal energy resources such as low-grade industrial heat, solar energy, geothermal energy, etc., helping in control of global warming.

Performance of an absorption cycle is critically dependent on the thermodynamic properties of working fluids. A survey of absorption fluids provided by Marcriss [2] suggested that there are 40 refrigerant compounds and 200 absorbent compounds available. However, two common absorbent-refrigerant pairs widely used in absorption chillers are $LiBr - H_2O$ and $NH_3 - H_2O$. The use of $LiBr - H_2O$ chillers in air conditioning systems is more common since not only the refrigerant of these systems ($H_2O$) is available everywhere, inexpensive and not toxic, but also its latent heat of evaporation is high which makes it possible to produce considerable amount of cooling [3]. The $LiCL - H_2O$ system is one of the working pair for absorption cycles is studied as an alternative to the most common working fluids which can work under relatively lower heat source temperature [4].

Many experimental studies have been reported in the current literature. Kaushik and Arora [1] developed a computational model for single effect and series flow double effect water–lithium bromide absorption systems. The analysis involves the determination of generator, absorber and evaporator temperatures effects on the energetic and exergetic performance of these systems. Kaynakli [5] investigated the exergy analysis of a coil absorber using $LiBr - H_2O$. The results show that the exergy destruction increases with increasing coolant flow rate, inlet concentration of solution, absorber vapor pressure, total coil turn and dead state temperature but decreases with increasing inlet temperatures of coolant and vapor. Gebreslassie et al. [6] analysed COP, the exergetic efficiencies and the exergy destruction rates for multi-effect $LiCL - H_2O$ absorption. The results show, COP increases significantly from double lift to triple effect cycles. The variation of the exergetic efficiency is quite small among the different cycle configurations. In all cycles the effect of the heat source temperature on the exergy destruction rates is similar for the same type of components, while the quantitative contributions depend on cycle type and flow configuration. Largest exergy destruction occurs in the absorbers and generators, especially at higher heat source temperatures. Talbi and Agnew [7] and Kilic and Kaynakli [8] calculated the system performance, exergy loss of each component and total exergy loss of all the system components of single effect $LiBr - H_2O$ ARS.

---

* To whom all correspondence should be sent:
  mkilic@uludag.edu.tr

Gomri [9] investigated COP, thermal loads of all components, exergetic efficiency and the change in exergy that occurs between the entrances of each component, total change in exergy of all components of single effect and double effect absorption refrigeration systems. The results show that while the efficiency of the first law increases or remain constant, the efficiency of the second law may decrease.

## NOMENCLATURE

| | |
|---|---|
| *ARS* | absorption refrigeration system |
| *COP* | coefficient of performance [-] |
| *e* | specific exergy [kJ/kg] |
| $e_{ph}$ | Specific physical exergy [kJ/kg] |
| $\dot{E}$ | exergy [kW] |
| $\dot{E}_F$ | energy input (Fuel F) [kW] |
| $\dot{E}_P$ | energy output (Product P) [kW] |
| *h* | enthalpy [kJ/kg] |
| $\dot{m}$ | mass flow rate [kg/s] |
| *s* | specific entropy [kJ/kg K] |
| *shx* | solution heat exchanger |
| $\dot{Q}$ | heat transfer rate [kW] |
| $\dot{W}$ | mechanical power  [kW] |
| *T* | temperature [˚C or K] |
| *UA* | product of overall heat transfer coefficient and heat exchanger area [kW/K] |

*Greek letters*

| | |
|---|---|
| $\psi$ | exergetic efficiency |
| $\varepsilon$ | heat exchanger efficiency |
| $\Delta$ | total |

*Subscripts*

| | |
|---|---|
| *i* | inlet |
| *a* | absorber |
| *c* | condenser |
| *d* | desorber (generator) |
| *cd* | condenser-desorber |
| *e* | exit |
| *p* | pump |
| *o* | thermodynamic environment |

Gogoi [10] performed a comparison between $LiCl - H_2O$ and $LiBr - H_2O$ systems under identical conditions. Results show that coefficient of performance (COP) increases with evaporator temperature while the exergy efficiency decreases and the total system irreversibility increases. COP also rises at lower condenser and absorber temperature, however the exergy efficiency drops and total system irreversibility increases. $LiCl - H_2O$ system is found superior to the $LiBr - H_2O$ for

single effect system. Borge et al. [11] analysed a $LiCl - H_2O$ thermally driven heat pump with integral energy storage that uses outdoor swimming pools as heat sink. The results shows, in solar cooling systems, ARS with $LiCl - H_2O$ as working fluid provide a powerful solution in comparison with $LiBr - H_2O$ due to its internal energy storage capacity which allows cooling when no solar radiation is available. Gunhan et al. [12] studied on the exergy destruction rate, the exergy efficiency in various forms, the relative irreversibility and sustainability index in both charging and discharging processes of a novel solar assisted $LiCl - H_2O$ absorption cooling system. She et al. [13] has recently proposed a novel low grade heat-driven ARS using $LiCl - H_2O$ both in the high-pressure cycle and the low pressure cycle. In their work, three different heat source utilization modes are considered to provide performance comparison among them and also with a traditional double-stage $LiBr - H_2O$ ARS. The effect of heat source temperature, intermediate pressure and the component temperatures on system performance has also been analysed in this paper. Saravanan and Maiya [14] also provided a thermodynamic analysis of a water based ARS with four binary mixtures including that of $LiCl - H_2O$. Exergy analysis overcomes the limitations of the first law of Thermodynamics; as it is based on both the first and second laws. It is capable of introducing meaningful efficiencies and identifying the locations, causes and true magnitudes of available energy losses which leads to improved operation or technology [3].

In so far considering the current literature, exergy analysis of a double effect $LiCl - H_2O$ ARS is neither available nor it has been attempted to compare with $LiBr - H_2O$ ARS. The main objective of the present study, a detailed comparative energy and exergy analysis of $LiBr - H_2O$ and $LiCl - H_2O$ ARS is performed with both single and double effect cycles.

## MATERIALS AND METHODS

### *Description of the absorption cycles*

The operation and the configuration of absorption cycles already have been described in detail elsewhere [15]. Therefore, only the schematics of the single and series double effect configurations will be presented (Fig.1 and Fig.2).

The cycles are presented in the pressure–temperature diagrams as shown in Fig.1 and Fig.2. The solution flow between absorber and generator

can be achieved in series, parallel of reverse flow. Compared to the single-effect cycle with the double effect cycle, an additional internal heat exchanger takes place on the condenser-generator assembly. Here the heat released on the hot side of the heat exchanger (condenser) by the condensing vapor is producing more vapor in the solution on the cold side (desorber). Thus the generation of refrigerant vapor is distributed among more generators. The difference between series, parallel and reverse flow is in the way the solution is distributed.
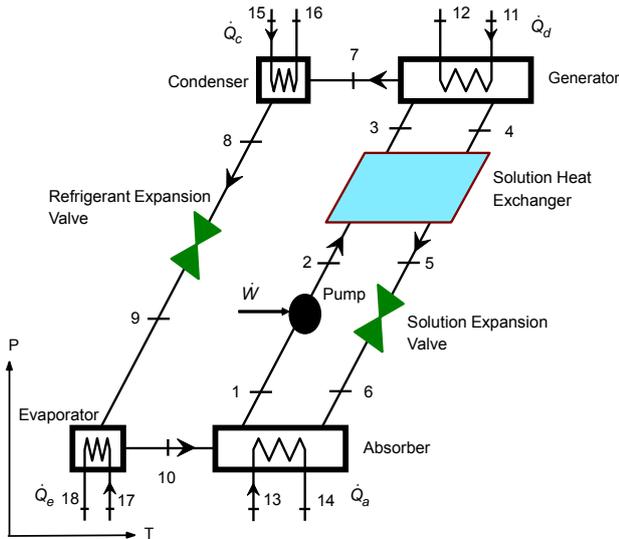


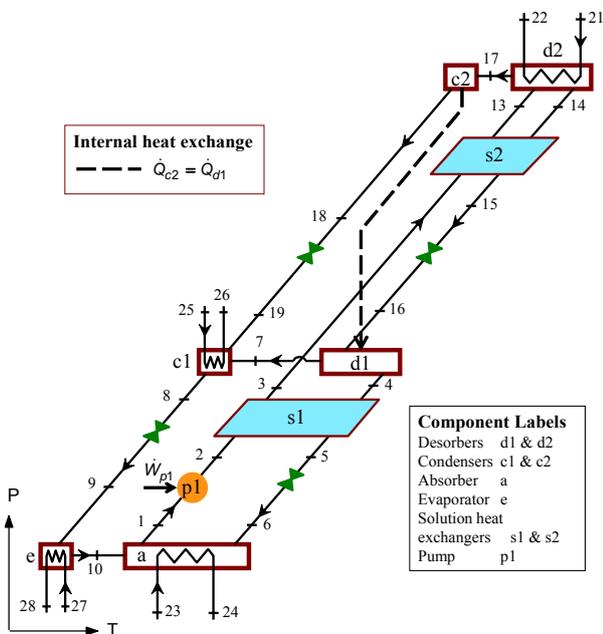**Fig.1.** Schematic diagram of water cooled single effect absorption chiller



**Fig.2.** Schematic diagram of water cooled double effect series cycle

A computer code for simulating the cycles has been established using the Engineering Equation Solver Software [16]. Property correlations for $LiBr - H_2O$ systems are provided from Yuan and Herold [17]. The correlations for $LiCl - H_2O$ system are developed by Patek and Klomfar [4]. The correlations are valid for temperatures between 273 K and 400 K for mole fractions up to 0.5. Properties for all state points have been evaluated.

The absorption systems are simulated considering the following assumptions:
1. The analysis is done considering steady state conditions.
2. Refrigerant leaving the condenser is saturated liquid at condenser pressure.
3. Refrigerant leaving the evaporator is saturated vapor at evaporator pressure.
4. Solution leaving the absorber, the generator of the single-effect chiller, and the high and low pressure generators of the double-effect chiller is assumed to be saturated in equilibrium conditions at its respective temperature and pressure.
5. Pressure drop due to friction is negligible in heat exchangers and the piping system.
6. Direct heat transfer from the components of the system to the surroundings is negligible.
7. The solution and refrigerant valves are isenthalpic
8. Refrigerant vapour leaving the generator is considered to be superheated.

Non-equilibrium states at the inlet to generator and absorber, and states at outlet to the solution pump and solution heat exchanger are taken to be at their actual conditions.

Various heat exchanger models exist in the literature that are useful when modelling absorption machines. These include 1) pinch point specification, 2) UA models, and 3) effectiveness models [15]. In this work, UA type model for four heat exchangers (D, C, E, A), and effectiveness type for solution heat exchanger were employed. ARS simulation models were modified from the Klein model and input parameters in both of models are that $UA_d = 20$ [kW/K] , $UA_c = 65$ [kW/K] , $UA_e = 85$ [kW/K] , $UA_a = 50$ [kW/K] , $UA_{cd} = 10$ [kW/K] , $\dot{m}[11] = 8$ [kg/s] , $\dot{m}[13] = 12$ [kg/s] , $\dot{m}[15] = 12$ [kg/s] , $\dot{m}[17] = 20$ [kg/s] and $\dot{m}[1] = 0.5$ [kg/s] (single effect system) , $\dot{m}[1] = 1$ [kg/s] (double effect system). External water temperatures are various to see how effect on COP and exergetic efficiency.

### Thermodynamic Analysis

The energy and exergy analysis of absorption systems involve the application of principles of mass conservation, species conservation, first and

second law of thermodynamics. The general equations of these principles are specified below [1-3]:

Mass conservation :

$$\sum \dot{m}_\iota = \sum \dot{m}_e \qquad (1)$$

Species conservation:

$$\sum \dot{m}_\iota X_i = \sum \dot{m}_e X_e \qquad (2)$$

Energy conservation :

$$\sum \dot{Q} - \sum \dot{W} = \sum \dot{m}_e h_e - \sum \dot{m}_\iota h_i \qquad (3)$$

where $\dot{Q}$ is the heat transfer rate between the control volume and environment and $\dot{W}$ is the work transfer rate. The COP of the system is defined by the equation (4).

$$COP = \frac{\dot{Q}_e}{\dot{Q}_g + \dot{W}_p} \qquad (4)$$

According to Bejan et al. [18] the exergetic balance applied to fixed volume is given by the following equation [5],

$$0 = \sum \dot{m}_\iota e_i - \sum \dot{m}_o e_o + \dot{Q}\left(1 - \frac{T_o}{T}\right) - \dot{W} - \Delta\dot{E} \quad (5)$$

The first two terms are the sum of the exergy input and output rates of the flow, respectively. The third term is the exergy of heat, which is positive if it is to system. $\dot{W}$ is the mechanical work rate transfer to or from the system and the last term $(\Delta\dot{E})$ is exergy destruction rate because of the internal irreversibilities. When the kinetic and potential energies are neglected, specific exergy (e) can be evaluated as given in Eq.(6):

$$e = (h - h_o) - T_o(s - s_o) \qquad (6)$$

The exergetic efficiency of a cycle $\Psi$ is defined as the useful exergy output rate (Product P) $\dot{E}_p$ divided by the required exergy input rate (Fuel F) $\dot{E}_F$. The input is given by the reduction of the exergy steam in the generator and the pump power. Solution pump power is very small according to whole system capacity and can be ignored in calculation for simplicty. The product is represented by the increase in the exergy rate of the chilled water (7).

$$\Psi = \frac{\dot{E}_p}{\dot{E}_F} = \frac{[\dot{m}(e_{ph,o} - e_{ph,i})]_{chilled\,water}}{[\dot{m}(e_{ph,o} - e_{ph,i})]_{steam/hot\,water} + \dot{W}_p} \qquad (7)$$

## RESULTS AND DISCUSSION

Fig.3 and Fig.4 shows the effect of generator temperature on the coefficient of performance (COP) and exergetic efficiency (ψ) for the single and double effect cycles of $LiCl - H_2O$ and $LiBr -$

$H_2O$ systems. It can be seen from Fig.3 that the COP of $LiCl - H_2O$ ARS increases initially with increase in generator temperature tends to level off rather than continue to increase and with a further increase in generator temperature even drops somehow. ψ decreases for both of the two pairs with increase in generator temperature. $LiCl - H_2O$ system can work under low generator temperature instead of $LiBr - H_2O$ system. At the same working temperatures $LiBr - H_2O$ system shows slightly better performance with respect to COP value but ψ is higher for $LiCl - H_2O$ system. For example at 90 ˚C generator inlet temperature, COP and ψ for $LiBr - H_2O$ are 0.806 and 0.236, respectively, meanwhile COP and ψ for $LiCl - H_2O$ are 0.795 and 0.237, respectively. On the other hand, in different generator inlet temperatures performances of two pairs are not the same. At 110 ˚C generator inlet temperature, COP is 0.784, ψ is 0.191 for $LiBr - H_2O$ and at 80˚C generator inlet temperature, COP is 0.797, ψ is 0.266 for $LiCl - H_2O$ .

Fig.4 shows that the double effect system performance is quite different than the single effect cycle for both solution pairs. First thing is that the difference between two systems COP values is high. The values of the COP of the systems increase to 1.284 (59 %) and 1.191 (49 %) for $LiBr - H_2O$ and $LiCl - H_2O$ (T[21]=145 ˚C), respectively. Second thing is that exergy performance increases with generator inlet temperature and $LiCl - H_2O$ is higher than $LiBr - H_2O$ system unlike single effect system. Against the increase in COP, in exergy efficiency similar reduction is realized which are 0.226 (9 %) and 0.212 (9 %) for $LiBr - H_2O$ and $LiCl - H_2O$ systems respectively.
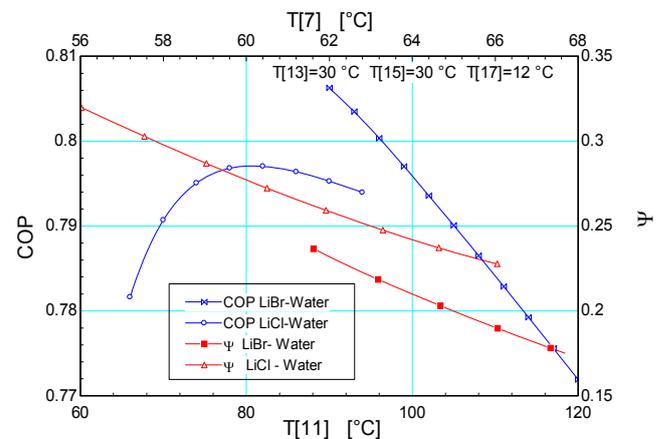


**Fig.3.** Comparisons of single effect $LiBr - H_2O$ and $LiCl - H_2O$ cycles with generator inlet temperature
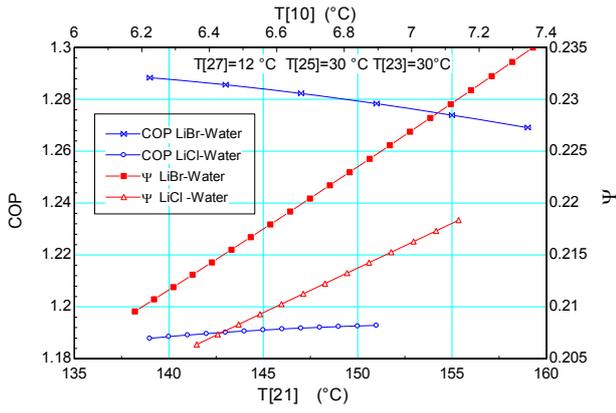
315

**Fig.4.** Comparisons of double effect LiBr − H$_2$O and LiCl − H$_2$O cycles with generator inlet temperature
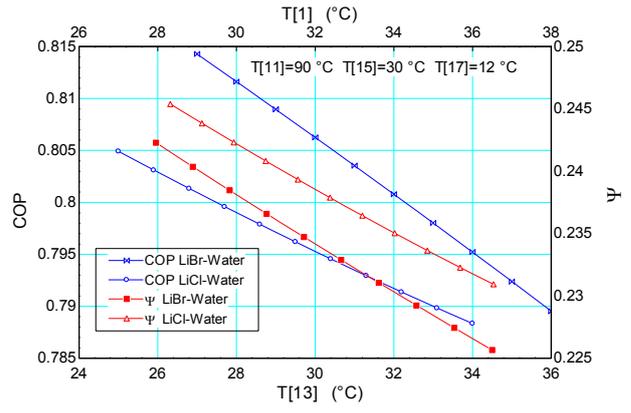


**Fig.7.** Comparisons of single effect LiBr − H$_2$O and LiCl − H$_2$O cycles with absorber inlet temperature
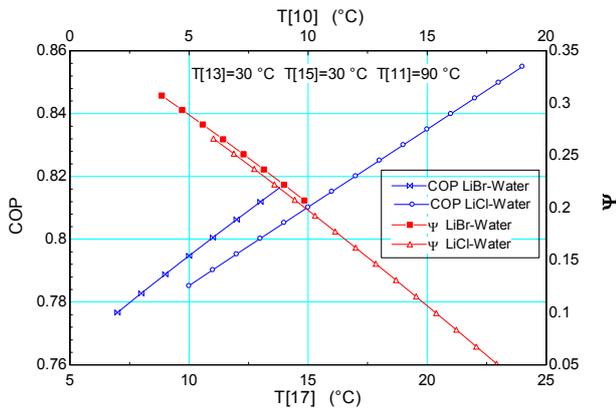


**Fig.5.** Comparisons of single effect LiBr − H$_2$O and LiCl − H$_2$O cycles with evaporator inlet temperature
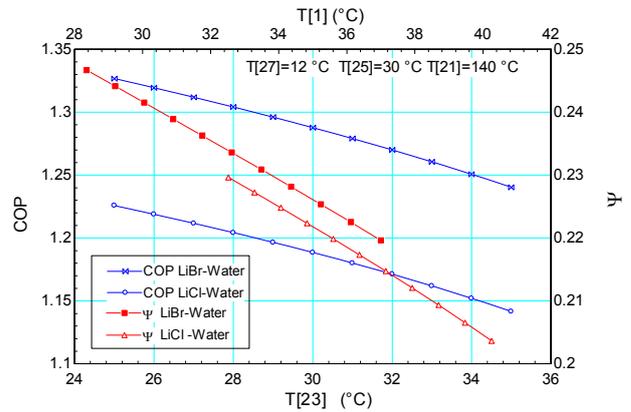


**Fig.8.** Comparisons of double effect LiBr − H$_2$O and LiCl − H$_2$O cycles with absorber inlet temperature

As shown in Fig.5, with increasing evaporator temperature COP increases linearly for both of systems. However, ψ decreases for both of two pairs with increase in evaporator temperature . The important point is that ψ is very variable depending on the temperature rise at the evaporator. It decreases from 0.307-0.207 (T[17]=7-14 ˚C) for LiBr-Water and 0.266-0.051 (T[17]=10-24 ˚C) for LiCl-Water systems. With increasing evaporator inlet temperature the same effect is observed on COP and ψ in Fig.6.
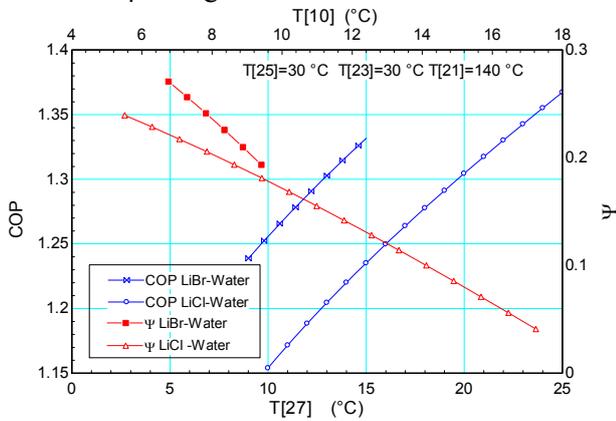


**Fig.6.** Comparisons of double effect LiBr − H$_2$O and LiCl − H$_2$O cycles with evaporator inlet temperature

Fig.7 represents the effect of absorber inlet temperature on the COP and ψ efficiency of single effect system. Performances are close to each other, COP is 0.814 and 0.801, ψ is 0.241 and 0.243 at the low cooling water inlet temperature (T[13]=27 ˚C). It decreases slightly with increasing absorber temperature to 0.795 and 0.788, 0.229 and 0.231 for LiBr − H$_2$O and LiCl − H$_2$O systems respectively. Similar situation in performance shows in double effect system in Fig.8. The only difference, exergy efficiency is slightly higher of LiCl − H$_2$O system than LiBr − H$_2$O system.

In order to validate the simulation results of the present work have been compared with the available numerical data reported by other authors' results. Briefly ,Kaushik and Arora [1] gives the COP values for single and series flow double effect systems for LiBr-Water are up to 0.78 and 1.35 , ψ are up to 0.21 and 0.20 respectively. Gebreslassie at al. [6] give the maximum COP values as 0.88 and 1.655, and the values of ψ are 0.438 and 0.473 for the single and the series flow double effect systems for LiBr-Water, respectively. Gomri [9] shows that COP values are 0.80 and 1.30 for single

and series flow double effect systems using LiBr-Water, $\psi$ values are up to 0.24 and 0.26, respectively. Gogoi ve Konwar [10] give the COP value up to 0.85, and $\psi$ value is 0.27 for single effect LiCl-Water ARS. In the present study, COP values and exergetic efficiencies are evaluated for the both single and double effect cycles with given UA values of the components. The obtained results are valid for these designs, but may change for other design specifications. Besides, it can be seen that the obtained theoretical results for COP and $\psi$ have a good agreement with other works.

## CONCLUSION

In this study, two mathematical models have been developed to compare the performance of single and series flow double systems for $LiBr-H_2O$ and $LiCl-H_2O$ solutions by using EES. The effects of various inlet temperatures on COP and exergetic efficiency for the both systems are analysed. The key findings can be summarized as follows.

An increase in the generator temperature increases the COP and exergetic efficiency in both single and series flow double effect systems up to an optimum generator temperature. $LiCl-H_2O$ ARS can work lower generator inlet temperature instead of $LiBr-H_2O$ system. They show close performance in single effect cycle. Besides, with increasing temperature in double effect cycle $LiBr-H_2O$ is superior against to $LiCl-H_2O$ system. The exergetic efficiency in single system decreases with increasing generator temperature, on the other hand it increases with generator inlet temperature.

The increase in evaporator temperature increases the COP but reduces exergetic efficiency. $LiBr-H_2O$ system performance is higher than $LiCl-H_2O$ at various evaporator temperature for single and double effect cycles.

It is also shown that increasing the absorber temperature reduces the system performance influentially. COP of the $LiBr-H_2O$ system is higher for the single and the double effect systems at various absorber temperature. The exergetic efficieny ($\psi$) of $LiCl-H_2O$ is better for single system, but double effect $LiBr-H_2O$ ARS has higher exergetic efficiency for the cases considered in this study.

According to the results presented in this study, $LiCl-H_2O$ system is more suitable to work at low temperature and could be an alternative to $LiBr-H_2O$ system. Besides with increasing temperature, especially for double effect system, $LiBr-H_2O$ solution pair system has better COP and $\psi$. Exergy loss of every system element is needed to be investigated to maximize $\psi$.

## REFERENCES

1 S.C. Kaushik ,A. Arora , *International Journal of Refrigeration* ,32 , 1247 (2009).
2 R.A. Macriss , J.M. Gutraj , T.S. Zawacki , Absorption fluid data survey: final report on worldwide data , ORLN/sub/8447989/3, Inst. Gas Tech., 1998.
3 T. Avanessian , M. Ameri , *Energy and Buildings,* 73, 26-36, (2014).
4 J. Patek, J. Klomfar, *International Journal of Regrigeration* , 31 , 287 (2008).
5 O. Kaynakli, *Heat Mass Transfer* , 44 , 1089 (2008).
6 B.H. Gebreslassie ,M. Medrano, D. Boer, *Renewable Energy*, 35, 1773 (2010).
7 M.M. Talbi, B. Agnew, *Applied Thermal Engineering*, 20, 619 (2000).
8 M.Kilic, O.Kaynakli, *Energy*, 32, 1505 (2007).
9 R. Gomri, *Energy Conversion and Management*, 50, 1279 (2009).
10 T.K. Gogoi , D. Konwar, *Energy Conversion and Management,* 110, 436 (2016).
11 D. Borge, A. Colmenar, M. Castro ,S. Martin,E. Sancristobal, *Energy and Buildings*, 43, 3161 (2011).
12 T. Gunhan ,O. Ekren, V. Demir,A. Hepbasli, A.Erek, A.S.Sahin, *Energy and Buildings*, 68, 138 (2014).
13 X. She, Y. Yin, M. Xu, X. Zhang, *International Journal of Regrigeration,* 58, 219 (2015).
14 R. Saravanan, M.P. Maiya, *Applied Thermal Engineering* , 18, 553 (1988).
15 K. E. Herold, R. Radermacher , S. A. Klein , Absorption Chillers and Heat Pumps ,CRC Press , 1996.
16 S. A. Klein , Engineering Equation Solver , Professional V.9.948, F-Chart software ,Middleton ,WI.
17 Z. Yuan, K.E. Herold, *HVAC&R Research*, 11, 377 (2005).
18 A. Bejan, G. Tsatsaranis , M. Moran ,Thermal Design and Optimization ,John Wiley and Sons, Newyork , 1996.

# A novel design of a compressed air storage system with liquid pistons

## M. Kılıç[1*], M. Mutlu[2]

[1]*Uludağ University, Engineering Faculty, Department of Mechanical Engineering, Bursa, Turkey*
[2]*Ermetal Otomotiv ve Eşya Sanayi Tic. A.Ş., Bursa, Turkey*

Renewable energy systems (RES) require more efficient, reliable and cost effective energy storage systems to benefit more from these kind of environmentally friendly energy sources and reduce $CO_2$ emissions. Compressed air energy storage (CAES) is one of the mechanical energy storage technologies that uses pressurized air to store and generate power when needed. Small scale CAES systems has been developed for RES application due to its advantages like easy installation, low maintaining costs, modular structure and running up time. In this study, a new small scale CAES system, which is running with liquid pistons to obtain isothermal compression and expansion, and a pressure regulator to compensate pressures between liquid pistons and air, is suggested. A detailed description of the novel CAES system design is given and effect of the components' specifications of the system are explained. Experimental results showed that, designed CAES system is a promising technology for RES, standalone and mobile applications. Specific components compatible with operating conditions of the system need to be designed in order to improve effectiveness and reliability.

Keywords: compressed air energy storage, liquid pistons, air compression, experimental setup, component performance

## INTRODUCTION

After huge progresses in renewable energy sources, they gained an important role for energy demand and energy storage systems took a significant part in these sources for providing feasibility and quality of the produced energy. Energy storage systems are also a major component of the stand-alone renewable energy systems for home applications. Energy storage systems are stores electrical energy in a different form like chemical energy or potential energy, and convert them to electrical energy when needed. Main energy storage forms of these systems are electrical, mechanical, chemical and thermal energy storage systems [1]. In electrical energy storage systems, energy is stored in a form of electric field where capacitors, super capacitors and superconducting magnetic energy storage (SMES) systems store energy in this form. Pumped hydro energy storage (PHES), flywheel and compressed air energy storage (CAES) systems are mechanical storage systems that store energy in kinetic or potential energy forms. Chemical storage systems are based on electron transmission between two materials during charging and discharging processes. Most of the storage devices used in our daily life like batteries and accumulators store energy in chemical form. In thermal energy storage systems (TES), energy is stored in heat form where special materials are required. CAES systems possesses several practical advantages such as freely available "storage media", no storage time

limit in sealed storage without self-discharge, high life cycle, no harmful waste and no emissions etc. However, further research and studies on CAES systems are required to guarantee the reliability, optimal efficiency and flexible operations for the commercial usage.

CAES systems are one of the commercial plants with PHES for large scale applications. There are two operating CAES plants in the world, one is Huntorf CAES in Germany and the other one is McIntosh CAES in Alabama, USA [1, 2]. The air is compressed in an electrical motor driven compressor and stored in large salt caverns. During electricity generation, pressurized air is expanded in a conventional gas turbine. During expansion, air temperature decreases considerably which can damage the blades of the turbine. Therefore, air is warmed in natural gas heaters during expansion [3]. Adiabatic CAES (ACAES) systems are introduced to avoid this fuel requirement during expansion stage of the conventional CAES system. In ACAES systems, generated heat during compression stage is stored and then used to warm up the air during expansion stage, so the fuel input requirement is eliminated [4]. European Union is focused on this concept to develop this technology for commercial use within the AACAES (Advanced Adiabatic CAES) project [5, 6]. Another concept that eliminates the fuel input is the isothermal CAES (I-CAES) where air is compressed and expanded at a constant temperature [7, 8]. One of the options to achieve isothermal compression and expansion is to use liquid pistons (LP) [8,9,10]. Various CAES designs with LP are under research for renewable

* To whom all correspondence should be sent:
mkilic@uludag.edu.tr

energy sources and other applications [8, 9]. Kilic et. al. made a mathematical model of a CAES with LP and they calculated the temperature and the pressure in LP and storage tanks [11]. Mutlu and Kiliç focused on the LP by simulating the compression process using computational fluid dynamics and determined the main parameters affecting the performance of the LP [12].

Although, a large number of study about the CAES is reported in the current literature, there is not too much study and applications present in the context of a standalone renewable energy storage with the CAES system for small scale applications. The aim of this study to present a prototype of the new small scale CAES system using liquid pistons for the compression and expansion processes. The new CAES system with LP is described in details and its performance is experimentally investigated. The system has a 1.5 kWh storage capacity and all system components are purchased from the market. Commercially available common hydraulic oil is used in the pistons and a pressure regulator (PR) which was constructed to adjust pressure between liquid side and air side of the system. Pressure and temperature changes are investigated during compression and component efficiencies are calculated.

## CAES WITH LIQUID PISTONS AND EXPERIMENTAL SET UP

LP are similar to conventional pistons that are used in many applications like engines and compressors but in LP systems a fluid which water and oil are commonly preferred is used unlike other pistons. The fluid which is generally forced by a pump goes in to the piston chamber thus air volume decreases and pressure rises. The interface between the air and the fluid provides compression and prevents air leakages. The fluid pressure is related to air pressure, as air pressure increases, fluid pressure rises as well. Hence it can be said that a CAES system with LP has two main components which affect the performance and power of the system: one is the fluid pump and the other is LP. Schematic view of the experimental design is given in Fig.1.

As seen in figure there are two parts which are essential for proper working of the system addition to pump and LP. Air storage tanks are the environment where the compressed air is stored after compression and the pressurized air source of the expansion process. The working pressure of hydraulic systems are higher than pneumatic systems thus a PR is designed in order to

compensate the pressure difference between fluid and air and the PR takes an important role for the system. Some auxiliary equipment which are electrical motor, hydraulic unit and a computer are needed to control and ensure proper working of the system. The AC Electrical motor drives the hydraulic pump which pressurized the working fluid and its technical specifications are crucial to obtain efficient compression. The hydraulic unit consists of several hydraulic valves controlled by a PLC program for propose of directing the fluid flow to desired pipe or component. The computer controls the whole systems' components and stores the collected data from sensors.
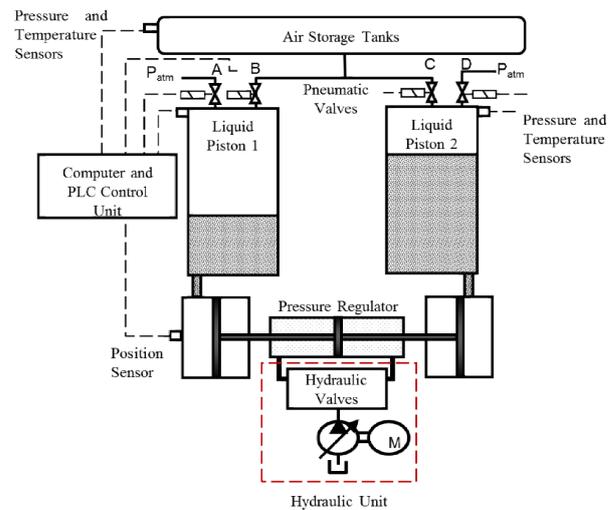


**Fig.1.** Experimental setup and main components of the system

The working principle of the system is based on pumping the fluid which was hydraulic oil in experiments though in the pistons and reducing the air volume in the piston camber therefore air pressure rises according to ideal gas law (Eq.1).

$$PV = mRT \qquad (1)$$

In this equation $P$ is the air pressure in the piston chamber, $V$ is the air volume, $m$ is the mass of the air inside piston, $R$ is the gas constant whose value is 287 Pa·m$^3$/kg·K and $T$ is the temperature of the air. According to critical temperature and pressure, gases behave as an ideal gas at high temperatures unless pressure is too high. Working range of the system is far from the critical values in the experiments thus ideal gas law approach is quite acceptable to calculate air properties. After the fluid is pumped hydraulic valves direct the flow through the piston which one is time for compression. When the air pressure which is measured by sensors that placed above of the piston reaches a previously defined value, valves (Valve C in Fig.1) that provide connection between piston and air tanks is

opened to allow air flow though in the tanks. In that stage of the compression the air pressure in tanks and piston is equalized and compression continues until fluid level reaches predefined upper limit which is similar to top dead center (TDC). Therefore the air mass and pressure rise in storage tanks and the compression process for this piston ends at this time. Then, valve C is closed and valve D connecting the piston to its environment is opened hereby air pressure decreases to atmospheric pressure and piston is able to vacuum air from ambient conditions, meanwhile fluid level in other piston reaches the bottom dead center (BDC) and the process is ready for compression. Using two pistons aims to ensure continuity by operating them simultaneously during compression and expansion. While one piston compresses the air other one vacuums the fresh air from ambient at atmospheric pressure. The energy input to the system is supplied by electrical motor driving the pump. The work which is done by pump increases when air is compressing because pump work is highly related to fluid pressure therefore the required work varies during compression process.

Operating of the system during expansion is fairly similar to compression process. Considering Fig.1, high pressure air enters the piston 2 where the fluid level is at TDC by opening valve C then it is closed in a few seconds therefore the piston 2 is filled up with pressurized air that can cause fluid flow thorough the hydraulic motor which is coupled with a generator to produce electricity. When the air expands in piston 2, valve A is open and fluid level rises up to TDC. Then valve A is closed and valve B is opened to preparing the next expansion step. The produced energy varies according to air pressure in the pistons so it alters during expansion and is needed to control smoothly.

The hydraulic systems operate at high pressures which is more than 250 bar, much as the pressure of the pneumatic systems is less than 10 bar. Therefore a device allowing these two systems to cooperate with each other is required. This issue is solved by designing the PR of which consists three hydraulic cylinders. Diameters of the two cylinders connecting to LP are three times greater than other ones. The main advantage of the PR is establishing a convenient coupling between two systems with different pressure. Moreover the fluid level in pistons can be determined by calculating the fluid flow rate that can be specified by volume difference using cylinder diameter and position measured by a sensor located in cylinders. On the other hand using an additional component in the system causes

energy losses thus the efficiency is influenced negatively.

## COMPONENTS OF THE SYSTEM AND EXPERIMENTS

The key parts of the designed CAES system is mentioned above are purchased from the market. Since the compression and the expansion cycles are reverse each other, the components of the compression is given in this study. In expansion process hydraulic pump and electrical motor are substituted with hydraulic motor and generator respectively.

An asynchronous three phase electrical motor which consumes the electrical energy stored in the system was chosen. A 4 kW AC motor, whose speed is 1425 rpm with four pole, is used in experiments and its efficiency is 85.1%. The electrical motor is mounted to pump by using a coupling. As the electrical motor is the only device consuming electricity, it is substantial to measure the amount of the electrical energy which is used for compression in order to evaluate performance of the system. An energy analyzer is used to measure the voltage, current and energy values to determine the energy need of the system. The energy input through the system is measured then transferred energy to the pump is calculated by taking account the efficiency of the electrical motor and the coupling whose efficiency is assumed 90%.

In the designed system a variable displacement axial piston pump is employed by the reason of pressure altering which causes energy demand to vary in the pump during compression. The displacement of the pump is controlled by a load sensing control device according to pressures occurred in pump which is highly related to air pressure in LP. The pump supplied from the market is selected by considering oil mass flow rate which was needed to obtain desired compression time and needed power for the process but as it was designed for hydraulic systems which are commonly industrial application specifications of the pump (Table 1) is inadequate to meet the demands required for a special application like CAES. Hence it can be said that designing more suitable pumps for CAES systems can improve the performance of the system.

**Table 1.** Characteristics of the hydraulic pump

| | |
|---|---|
| Nominal Pressure (MPa) | 28 |
| Maximum Pressure (MPa) | 35 |
| Maximum Displacement (cm$^3$/rpm) | 32 |
| Maximum Flow Rate (litre/min) | 100 |
| Maximum Power (kW) | 46 |

The input energy of the pump ($E_{p,in}$) is assumed being equal to energy transferred from the motor. The work done by pump is calculated by using oil volume and pressure difference which is between pump inlet and outlet (Eq. 2). The data recording interval is 2 seconds, thus the work done by pump was calculated in every 2 seconds and then all of them added in order to obtain total pump energy output.

$$E_{p,out} = \sum V \Delta P \qquad (2)$$

In this equation $V$ is the volume of the oil injected through in the PR and was calculated by determining the displacement in cylinders of the PR using position sensor. The energy efficiency of the pump is defined by ratio of output ($E_{p,out}$) and input energy amount (Eq.3).

$$\eta_p = \frac{E_{p,out}}{E_{p,in}} \qquad (3)$$

The PR made up of three cylinders which are connected to one another in order (Fig.2). The diameter ratio between cylinder 2 and 1 is chosen 3 which means oil pressure in the LP reduces by three times while the oil flow rate increases with the same rate. The output energy of the device is calculated with the same approach as pump energy calculations and the output pressure of the PR is equal to the air pressure in LP.
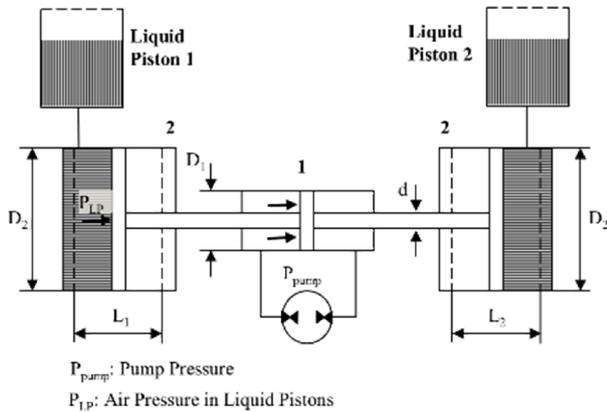


P$_{pump}$: Pump Pressure
P$_{LP}$: Air Pressure in Liquid Pistons

**Fig.2.** Schematic view of the pressure regulator

The LP whose length and diameter are 1.2 m and 0.2 m respectively were designed to compress air as slowly as possible to obtain isothermal compression that the minimum energy is needed. As a known phenomenon the air temperature increases when it is compressed thus energy transfer from the air is necessary for isothermal conditions. The hydraulic oil plays an important role with the purpose of transferring energy from the air which is in the piston chamber during compression process in the system. The energy required for isothermal compression ($E_{LP,ideal}$) is

calculated by Eq.4 and used in efficiency (Eq.5) calculations of the LP.

$$E_{LP,ideal} = P_1 V_1 \ln \frac{V_2}{V_1} \qquad (4)$$

$$\eta_{LP} = \frac{E_{LP,ideal}}{E_{p,in}} \qquad (5)$$

In this equations $P_1$ and $V_1$ are the air pressure and volume in the beginning of the compression stage respectively. $V_2$ is the final air volume after compression finishes. $E_{p,in}$ is assumed that it is equal to pump output energy value.

Dimensions of the air storage tanks are the same as LP. The storage capacity can be improved by mounting extra tanks to the system. In the experiments two storage tanks whose volume is around 62 l are used. The illustration of the whole designed system are given in Fig.3.

Temperature, pressure and power measurements are given in dimensionless form derived by dividing the initial values at the beginning of the compression stage on the purpose of comparing the results due to initial values affect the process remarkably and could not be controlled during experiments.
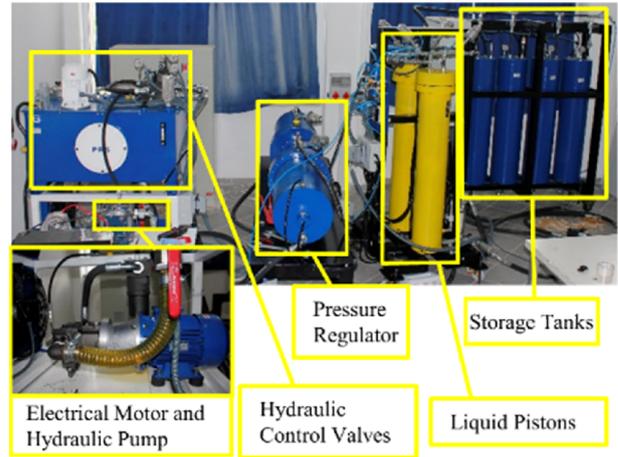


**Fig.3.** CAES with liquid pistons

*Assessment of overall uncertainty*

There are some uncertainties associated with instrumentation, the measurements of the temperature and pressure values due to the dynamics of the system cycle. Moreover, certain errors introduced due to the mathematical calculations. Considering a general case in which an experimental result, $S$ is a function of $k$ measured variables $x$ as

$$S = S(x_1, x_2, x_3, \ldots, x_k,) \qquad (6)$$

Eq.6 is the data reduction equation used for determining $S$ from the measured values of the variable $x$. The uncertainty of the result ($U_S$) is then given by

$$U_S = \left[ \left( \frac{\partial S}{\partial x_1} w_1 \right)^2 + \left( \frac{\partial S}{\partial x_2} w_2 \right)^2 + \cdots + \left( \frac{\partial S}{\partial x_k} w_k \right)^2 \right]^{1/2} \quad (7)$$

where the $w_k$ are the uncertainties in the measured variable $x_k$. It is assumed that the relationship given by Eq.7 is continuous and has continuous derivatives in the domain of interest, that the measured variables $x$ are independent of one another, and that the uncertainties in the measurable variable are independent of one another. It is expected that the overall uncertainty will be within 5%.

## RESULTS AND DISCUSSION

The air pressure, temperature occurred in LP and motor power are examined in experiments during compression stage. Additionally, the effect of the compression speed which can be controlled by adjusting a variable hydraulic valve that is located after the pump in the system is investigated. Although the pump is variable, an addition valve is used to specify the desired oil mass flow rate because the aim of using a variable pump is to achieve more efficient system. Thus the oil flow rate can be defined according to valve opening which means that if the valve is fully open the oil flow rate becomes its maximum and if the valve is fully closed the oil flow rate equals to zero. The oil flow rates obtained from experiments are given in Fig.4. As seen in the Fig.4 there is a linear relationship between valve opening rates and oil flow rate.
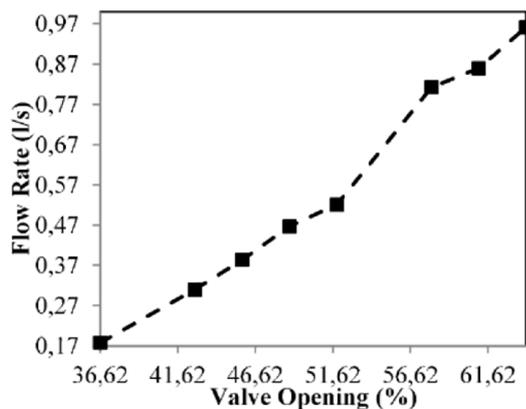


**Fig.4.** Oil flow rate according to valve opening

When the air pressure and temperature variation according to various valve openings in the liquid piston is examined in a single stroke it can be easily realized that compression takes more time at low

valve openings (Fig.5) and temperature (Fig.6) is highly related to compression speed which affects the heat transfer through the piston surfaces and required compression power (Fig.7).

Fast compression reduces the process time, hence, final air temperature increases inside the LP because sufficient heat transfer rates which are necessary to obtain isothermal conditions cannot be achieved (Fig.6). However, a 15 °C difference in air temperature which can be assumed as an isothermal process between initial and final conditions of the fastest compression stage.
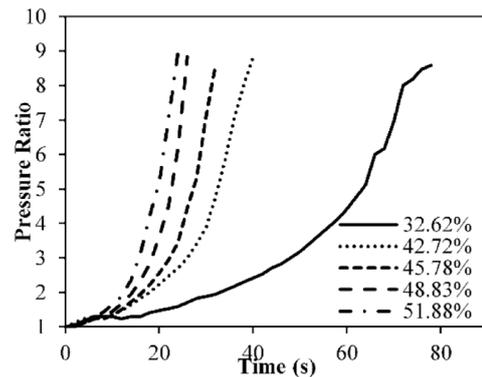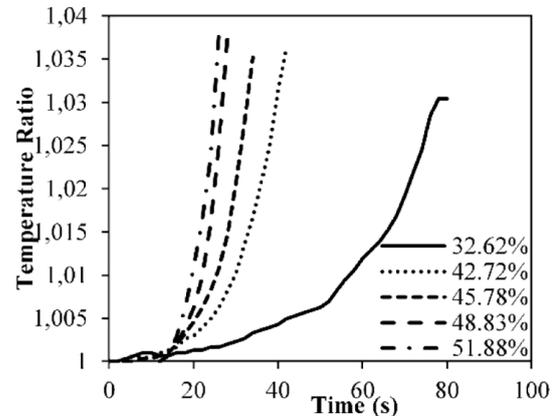


**Fig.5.** Pressure variation in a single compression stage



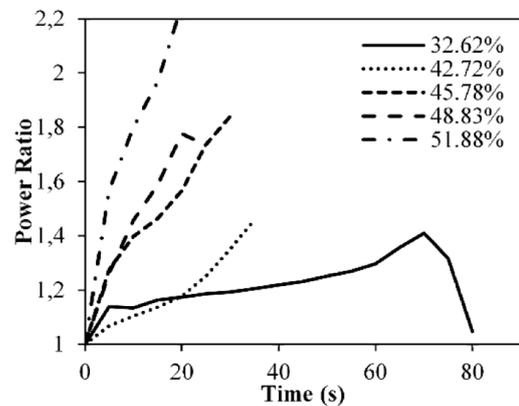**Fig.6.** Temperature variation in a single compression stage



**Fig.7.** Power consumption of the electrical motor during a single compression stage

Because of minor deviations from isothermal conditions, the only factor affecting the power of the electrical motor is compression time as a result more power is required for faster process (Fig.7). Additionally, fast compression speeds make the system components like pump and PR work faster and increase the frictional energy losses. During compression process required power decreases when the valve between LP and storage tanks opens (Valve B and C in Fig.1 depends on compression stage) because of pressure drop occurred as soon as the valve opens.
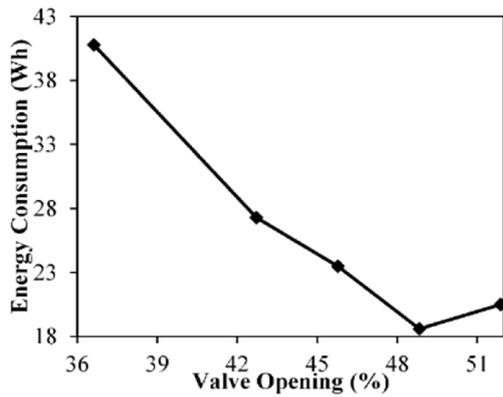


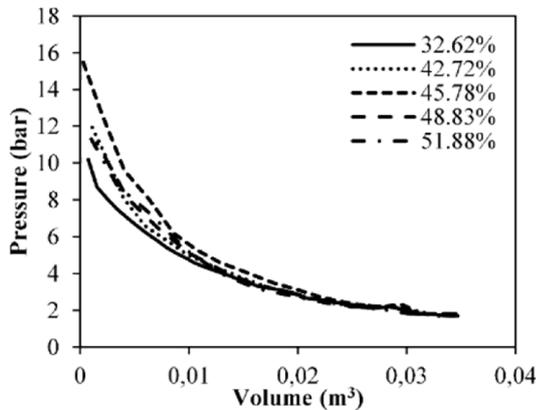**Fig.8.** Energy consumption according to valve opening rates



**Fig.9.** P-V curves with different compression speeds
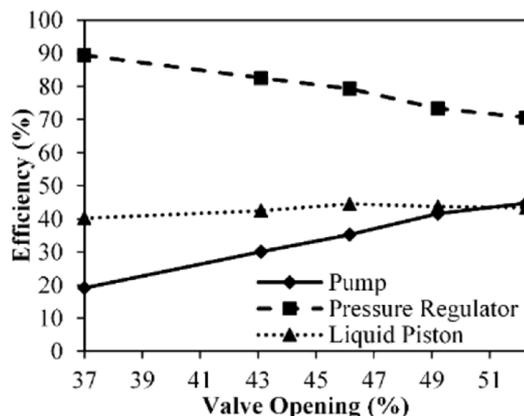


**Fig.10.** Efficiencies of the system components

Requiring less power does not mean to consume less energy because it is needed more time for compress air to desired pressure. As seen in Fig.8 consumed energy in a single stroke decreases till the valve opening is 48.83%. After that point the required power increases due to high flow rate and the consumed energy increases even the compression time decreases.

Tank pressure rises during the compression process therefore it is necessary to reach higher pressure than previous one which is needed more energy in every single compression stage.

The effect of the isothermal compression can be easily understood by P-V diagrams which explain the whole process. The P-V diagrams with various speed is given in Fig.9 presenting that higher compression speeds has a negative influence on isothermal conditions.

The efficiency of the system components is given in Fig.10. As seen in the figure faster compressions speeds considerably influence the PR efficiency which decreases from 90% to 70% because of increasing the frictional losses and inertia forces in PR. It is observed that compression speed slightly affect the efficiency of the LP much as the efficiency of the pump alters dramatically.

CONCLUSION

Energy storage systems will play an important role in feasibility of the renewable energy systems in near future. Conventional CAES systems are the only proved technology for large scale energy storage requirements. On the other hand renewable energy sources demands more compact and economic storage systems. In this study a new CAES system with liquid pistons is proposed and the experimental results from the prototype of the system are presented. It is observed that the compression speed is the key factor influencing the system performance for the isothermal compression and expansion cycles. Hence, it can be said that the control strategies with a dynamic speed control should have to be planned to consider the dynamic compression process. During the experimental study, the CAES system is run to achieve the isothermal compression which is supposed to be the most efficient process. Despite succeeding the isothermal conditions which the air temperature increases by only 4% of its initial value, the minimum energy consumption does not occurred in minimum speed because of the performances of the system components change with speed and uncontrollable behaviors are observed during the cycle processes. After all, P-V diagrams shows that

compressing slowly the process approaches the isothermal conditions. Unsurprisingly increasing the storage pressure needs more energy for a single compression stage. Since the system is assembled with components commercially available in the market, the efficiencies of the components such as electric motor, hydraulic pumps etc, are highly affected when they work at off design conditions. Therefore, it is concluded that special pump and motor designs must be used for a better system performance. Although, the results presented in this study is promising, further improvements and developments are required for fully reliable and commercially available small scale CAES systems.

## ACKNOWLEDGEMENTS

## REFERENCES

1  H. Chen, T. N. Cong, W. Yang, C. Tan, Y. Li, Y. Ding, *Progress in Natural Science*, **19**, 291 (2009).
2  F. Crotogino, K. U. Mohmeyer, R. Scharf, in: Huntorf CAES: More than 20 years of successful operation, SMRI Spring Meeting, 15-18 April 2001, Orlando, Florida, USA.
3  F. S. Barnes, J. G. Levine, Large Energy Storage Systems Handbook, CRC Press, 2011.
4  N. M. Jubeh, Y. S. Najjar, Applied Thermal Engineering, 44, 85 (2012).
5  S. Zunft, C. Jakiel, M. Koller, C. Bullough, in: Adiabatic Compressed Air Energy Storage for the Grid Integration of Wind Power, Sixth International Workshop on Large-Scale Integration of Wind Power and Transmission Networks for Offshore Windfarms, 26-28 October 2006, Delft, Netherlands.
6  C. Bullough, C. Gatzen, C. Jakiel, M. Koller, A. Nowi, S. Zunft, in Advanced Adiabatic Compressed Air Energy Storage for the Integration of Wind Energy, Proceedings of the European Wind Energy Conference, EWEC 2004, 22-25 November 2004, London, UK.
7  Y. M. Kim, J. H. Lee, S. J. Kim, D. Favrat, Entropy, 14, 1501 (2012).
8  P. Y. Li, E. Loth, T. W. Simon, J. D. Van de Ven, S. E. Crane, in: Compressed air energy storage for offshore wind turbines. In International Fluid Power Exposition, 2011, Las Vegas, NV.
9  S. Lemofouet, A. Rufer, in: Hybrid energy storage systems based on compressed air and supercapacitors with maximum efficiency point tracking, In Power Electronics and Applications, 2005 European Conference on IEEE.
10  J. D. Van de Ven, P. Y. Li, Applied Energy, 86, 2183 (2009).
11  M. Kiliç, Z. K. Kocabiçak, E. E. Topçu, M. Mutlu, in: Progress in Exergy Energy and the Environment, I. Dinçer, A. Midilli and A. Küçük (eds.), Springer, Switzerland, 2014, p.477.
12  M. Mutlu, M. Kiliç, Thermal Science, doi: 10.2298/TSCI140926146M , (2014).

# MATERIALS SCIENCE

# Polypropylene electrets films stored between two plate electrodes at low pressures

A. P. Viraneva[*], T. A. Yovcheva, I. P. Bodurov, M. G. Marudova

*Plovdiv University "Paisii Hilendarski", Faculty of Physics 24 Tsar Asen str., 4000 Plovdiv, Bulgaria*

The electrets are dielectric materials of specific type which are able to create an external quasi static electric field. In many modern devices, built on electret effects, electrets are placed as active elements between two electrodes with an air gap. In these cases, if the device is under low pressure, one can expect a decrease in the electric charge. In the present paper we investigated the low pressure ($p$ from 1013 mbar to 0.1 mbar) influence on the surface potential decay of polypropylene electrets films, placed between two short circuited plate electrodes at various air gaps ($d$ values could be from 0.1 mm to 3.00 mm) between the charged surface of electrets and the upper electrode. For all ranges of the $pd$ values the main process responsible for the surface potential decay can be associated with the desorption of charged species from the electret surface. In addition it was established that only for some relevant ranges of $pd$ values the breakdown voltage following the Paschen's law was reached in the initial moment of the period for which the sample had been situated in the vacuum chamber and a spark breakdown in the air gap could be observed. The results obtained have both phenomenological character and great practical use as the investigated electrets were in similar conditions to those under which the electret elements of various sensors and signal transducers, dosimeters, air filters, generators, focusing systems of the electret optics, etc. operate.

**Keywords:** electrets, low pressure, Paschen's law, dielectric materials

## INTRODUCTION

Polymer dielectric materials, which are able to retain electric charges over a long period of time and create an external quasistatic electric field, are known as electrets. Many kinds of electret devices are widely used in various industrial applications owing to their electric field [1]. The surface potential values and the lifetime of electrets are the most important parameters giving rise to the possibility of practical usage. A number of factors which influence charge storage and charge transport in electrets have been investigated. But there are only a several publications on the influence of low pressure on electret behaviour [2-5].

The investigation of the pressure effect on the surface charge decay was first reported in [2]. The carnauba wax electrets have been studied and the method of dissectible capacitor has been used to measure the equivalent surface charge. It was shown that the surface charge decay became different when the electrets were placed under different pressures, lower than atmospheric. The authors have assumed that surface charge decay is due to discharges in the air gap between the samples and the measuring electrode in accordance with the Paschen's law. The effect of low pressure on surface charge decay of polystyrene and mylar electrets has been studied by Catlin et al. in [3, 4].

The results obtained in [3] have shown that the decrease of effective surface charge observed when electrets are exposed to low pressure is not the result of a spark breakdown between the electret surface and the nearby conductors. It has been supposed that the charge drops are due to ion desorption.

Two years later the electret behaviour at low pressures was studied again in [4]. The results observed have been explained by the spark breakdown theory. Furthermore, the authors have explained the experimental results in [3] in terms of the spark breakdown mechanism by calculating the amount of surface which had been active in the spark breakdown process.

The effect of low pressure on the surface potential decay has also been studied in [5]. It has been supposed when the pressure under which the electrets have been kept decreases ions desorption from the electret surface was most likely to occur.

In [6] polymer foams and void-containing polymer-film systems with internally charged voids combine large piezoelectricity with mechanical flexibility and elastic compliance were investigated. It has been found that the voids can be internally charged by means of dielectric barrier discharges (DBDs) under high electric fields. It was established that the threshold behaviour can be explained with the Paschen's law which describes the breakdown voltage between parallel plate electrodes in a gas as a function of pressure and the gap height.

* To whom all correspondence should be sent.
  asia83@abv.bg

In [7] Paschen's curves in air and different gases are obtained by measuring the gas breakdown voltage. It was shown that the Paschen's curve has a different minimum value of *pd* at different gases and it depends on the composition of the gas.

The purpose of the paper is to investigate the low pressure influence on the surface potential decay of the PP electrets stored at different low pressures between two short circuited plate electrodes at various air gaps between the charged surface of the electrets and the upper electrode. The main task is to compare the calculated voltages in the electret surface-electrode gap with breakdown voltages according to the Paschen's law and analyse the results.

## EXPERIMENTAL DETAILS

### *Used material and sample preparation*

Isotactic polypropylene (PP) films with thickness of 20 μm produced by "Assenova Krepost" LTD – Bulgaria were investigated. Initially, the PP films were cleaned in an ultrasonic bath with alcohol for 4 minutes then washed in distilled water and dried on filter paper under room conditions. Samples of 30 mm diameter were cut from the films. Each of the samples was put on a metal pad with the same diameter.

### *Corona charging and surface potential measurement*

Electret charging was carried out in corona discharge by corona triode system consisting of a corona electrode, a plate grounded electrode and a grid placed between them (Fig.1).
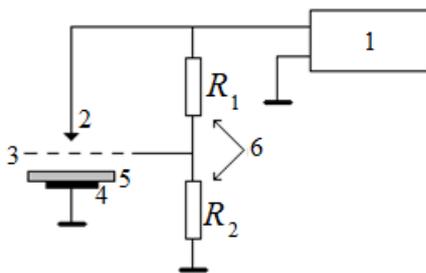


**Fig.1.** Scheme for obtaining electrets: 1. high voltage source; 2. corona electrode; 3. grid; 4. plate grounded electrode; 5. sample on a metal pad; 6. voltage divider

Charging of the electrets was performed under relative humidity of (45% - 50%), atmospheric pressure and temperature of 23 ℃ for 1 minute. Positive or negative 5 kV voltage was applied to the corona electrode. A voltage of 500 V, 700 V or 950 V of the same polarity as that of the corona

electrode was applied to the grid. After charging, the initial surface potential of the samples $V_0$ was measured. Electrets' surface potential was measured by the method of the vibrating electrode with compensation [8] and the estimated error was less than 5%.

### *Low pressure measurement*

After charging to the initial surface potential, the samples, together with their metal pads, were placed into a vacuum chamber, consisting of isolated bases and a jar bell, under a low pressure for 1 hour. Dry air (RH = 0%) is provided with silica gel put in the chamber. The humidity is measured continuously with an electronic mini hygrometer placed in the chamber. The pressures created in the vacuum chamber were 0.1 mbar, 1 mbar, 10 mbar, 20 mbar, 66 mbar, 132 mbar, and 1013 mbar. In the vacuum chamber the electrets were placed between two short circuited plate electrodes at various air gaps between the charged surface of electrets and the upper electrode (Fig.2).
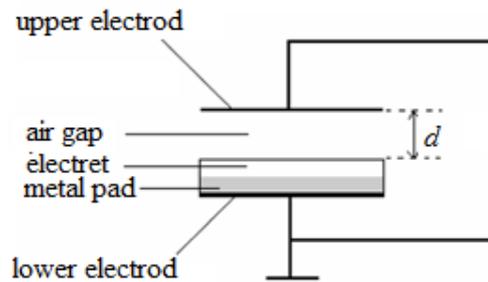


**Fig.2.** Schematic diagram of the electret stored in the vacuum chamber between two short circuited plate electrodes (*d* is the air gap thickness)

After that the samples on the metal pads were removed from the vacuum chamber, the surface potential *V* was measured again and the normalized surface potential $V/V_0$ was calculated.

## RESULTS AND DISCUSSION

All electret samples were divided into five groups according to the air gap thickness values (0.10 mm, 0.28 mm, 0.84 mm, 1.69 mm and 3.00 mm). Each group was divided into three sets according to the grid potential values (500 V, 700 V, or 950 V).

The dependences of the normalized surface potential $V/V_0$ on the air gap thicknesses at the 0.1 mbar pressure for positively charged PP and negatively charged PP samples are illustrated in Fig.3 and Fig.4, respectively. Each column value corresponds to an average value obtained by the

measurement of 6 samples. The maximum deviation from the average value determined at confidence level 95% is 5%.
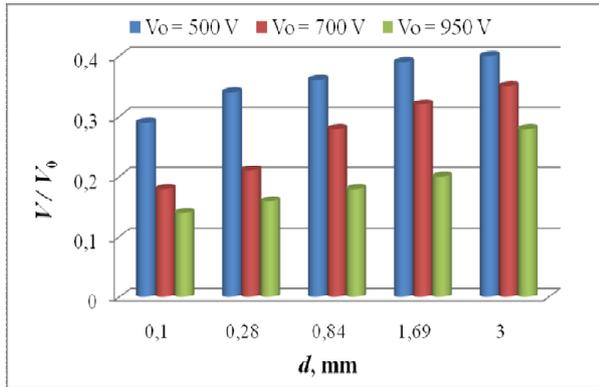


**Fig.3.** Dependence of the normalized surface potential on air gap thicknesses for PP electrets charged in a positive corona to different values of the initial surface potential and stored at pressure 0.1 mbar
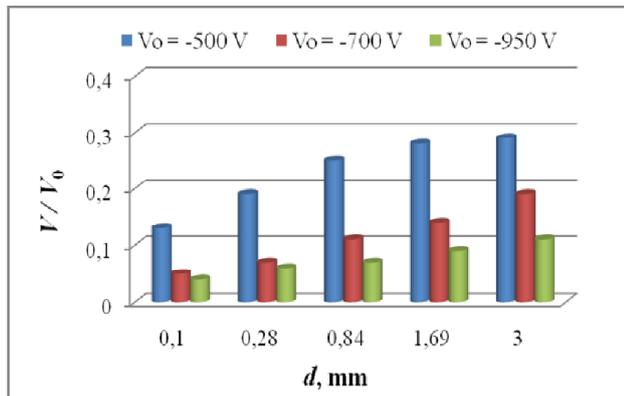


**Fig.4.** Dependence of the normalized surface potential on air gap thicknesses for PP electrets charged in a negative corona to different values of the initial surface potential and stored at pressure 0.1 mbar

The results obtained show that:

➢ The normalized surface potential values at 0.1 mbar decrease with the increase of the initial surface potential;
➢ The normalized surface potential values at 0.1 mbar grow with the increase of the air gap thickness.
➢ The final values of the normalized surface potential for positively charged PP films are higher than those for negatively charged ones independently of the air gaps thicknesses and the initial surface potential values.

Analogous results have been obtained for the other pressures used in our experiments.

In the papers [8, 9] it is assumed that the electrets charge decay is due to breakdown voltage between parallel plate electrodes in a gas as a function of pressure ($p$) and the thickness ($d$) of the gap itself according to the Paschen's law. For dry air the Paschen's curve has a minimum value of $pd$ = 6.65 mbar.mm corresponding to a breakdown voltage of 360 V as shown in Fig.5 [9].
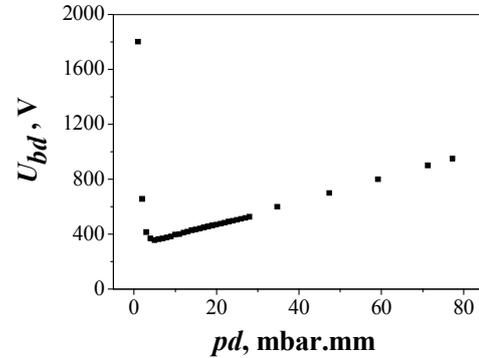


**Fig.5.** Paschen's curve for dry air and parallel plate electrodes

If the air gap field creates a voltage less than the breakdown voltage for the particular gas, gas discharges will not occur in the gap. When the air gap field creates a voltage equal or higher than the breakdown voltage, a discharge will occur and the electret charge will consequently decrease. The discharge will continue until the voltage across the air gap is reduced to a value below the minimum breakdown voltage for the respective value of the product $pd$ and will depend on neither the size nor the polarity of the initial electret surface potential as well as on the air gap thickness. Therefore, the minimal voltage value in the gap at our experiments at which a discharge can be initiated is 360 V [9].

For each value of the pressure at which the samples were stored for 1 hour, the electric field in the electret surface-electrode gap is changed from the initial value $E_0$ determined by the electret surface potential $V_0$ measured before placing the sample in the chamber to the final value $E$ determined by the electret surface potential $V$ measured immediately after removing the electret from the vacuum chamber.

The values of the electric fields in the electret surface-electrode gap for PP samples stored between two short-circuited electrodes with air gap thickness of 0.10 mm, 0.84 mm and 3.00 mm are calculated by equation:

$$E' = \frac{\varepsilon V'}{\varepsilon d + \varepsilon_1 L},\qquad(1)$$

where $E'$ is the air gap field ( $E' = E_0$ or $E' = E$ ), $\varepsilon = 2,2$ is the relative dielectric permeability of PP, $\varepsilon_1 = 1$ is the relative dielectric permeability of the

air, $d$ is the air gap thickness, $L$ is the electret thickness, $V'$ is the electret surface potential ($V' = V_0$ or $V' = V$).

The values of the voltages in the electret surface-electrode gap for PP samples stored between two short-circuited electrodes with air gap thickness of 0.10 mm, 0.84 mm and 3.00 mm are calculated by equation:

$$U' = E'd , \qquad (2)$$

where $U' = U_0$ is the voltage in the initial moment of the period for which the sample has been situated in the vacuum chamber, $U' = U$ is the voltage in the end of the same period.

The calculated values of the electric fields and the voltages for three air gap thicknesses of 0.10 mm, 0.84 mm and 3.00 mm at pressure 1013 mbar are presented in Table 1 to Table 3 respectively.

**Table 1.** Electric fields and voltages in a 0.10 mm air gap at pressure 1013 mbar and different grid voltages values

| $V_0$, V | 492 | 693 | 941 |
|---|---|---|---|
| $E_0$, kV/cm | 45.10 | 63.50 | 86.30 |
| $U_0$, V | 451 | 635 | 863 |
| $V$, V | 490 | 685 | 937 |
| $E$, kV/cm | 44.90 | 62,80 | 85,90 |
| $U$, V | 449 | 628 | 859 |

**Table 2.** Electric fields and voltages in a 0.84 mm air gap at pressure 1013 mbar and different grid voltages values

| $V_0$, V | 500 | 687 | 950 |
|---|---|---|---|
| $E_0$, kV/cm | 5.89 | 8,10 | 11.19 |
| $U_0$, V | 495 | 680 | 940 |
| $V$, V | 500 | 679 | 950 |
| $E$, kV/cm | 5.91 | 8.00 | 11.20 |
| $U$, V | 496 | 672 | 941 |

**Table 3.** Electric fields and voltages in a 3.00 mm air gap at pressure 1013 mbar and different grid voltages values

| $V_0$, V | 500 | 680 | 944 |
|---|---|---|---|
| $E_0$, kV/cm | 1.66 | 2.26 | 3.14 |
| $U_0$, V | 498 | 678 | 941 |
| $V$, V | 500 | 664 | 933 |
| $E$, kV/cm | 1.60 | 2.20 | 3.10 |
| $U$, V | 480 | 660 | 930 |

The calculated values of the electric fields and the voltages for three air gap thickness of 0.10 mm, 0.84 mm and 3.00 mm at pressure 0.1 mbar are presented in Table 4 to Table 6 respectively.

**Table 4.** Electric fields and voltages in a 0.10 mm air gap at pressure 0.1 mbar and different grid voltages values.

| $V_0$, V | 492 | 677 | 925 |
|---|---|---|---|
| $E_0$, kV/cm | 45.10 | 62.10 | 84.80 |
| $U_0$, V | 451 | 621 | 848 |
| $V$, V | 72 | 30 | 34 |
| $E$, kV/cm | 6.60 | 2.80 | 3.10 |
| $U$, V | 66 | 28 | 31 |

**Table 5.** Electric fields and voltages in a 0.84 mm air gap at pressure 0.1 mbar and different grid voltages values

| $V_0$, V | 485 | 685 | 933 |
|---|---|---|---|
| $E_0$, kV/cm | 5.71 | 8.07 | 1.10 |
| $U_0$, V | 480 | 678 | 923 |
| $V$, V | 136 | 77 | 62 |
| $E$, kV/cm | 1.60 | 0.91 | 0.70 |
| $U$, V | 134 | 76 | 59 |

**Table 6.** Electric fields and voltages in a 3.00 mm air gap at pressure 0.1 mbar and different grid voltages values

| $V_0$, V | 493 | 691 | 946 |
|---|---|---|---|
| $E_0$, kV/cm | 1.64 | 2.30 | 3.14 |
| $U_0$, V | 492 | 689 | 943 |
| $V$, V | 154 | 124 | 96 |
| $E$, kV/cm | 0.50 | 0.40 | 0.30 |
| $U$, V | 150 | 120 | 90 |

Analogous calculations have been made for the other gaps and pressures used in our experiments. At atmospheric pressure and various thicknesses of the air gap used in our experiments the $pd$ values change from $pd_{min}$ ($d = 0.1$ mm) = 101.3 mbar.mm to $pd_{max}$ ($d = 3$ mm) = 3039 mbar.mm, which corresponds to breakdown voltages according to the Paschen's curve higher than 950 V (Fig.5). At pressure of 0.1 mbar and air gap thicknesses from 0.10 mm to 3.00 mm, the $pd$ product values lay in the range (0.01 - 0.30) mbar.mm, which corresponds to breakdown voltages according to the Paschen's curve higher than 1800 V. The calculated $pd$ values for different pressures and air gap thicknesses obtained of our experiments are presented in Table 7.

It can be found that the Paschen breakdown voltage is reached at certain $pd$ product values in the initial moment of the period for which the sample has been situated in the vacuum chamber (Table 7):

- (3 - 16.80) mbar.mm for samples charged at grid voltage 500 V;
- (2 – 30.00) mbar.mm for samples charged at grid voltage 700 V;
- (2 – 60.00) mbar.mm for samples charged at grid voltage 950 V.

**Table 7.** Experimental and breakdown voltages at different values of *pd*.

| $pd$, nbar.mm | $p$, mbar | $d$, mm | $V_g = 500$ V | | | | $V_g = 700$ V | | | | $V_g = 950$ V | | | | $U_{bd}$, V |
|---|---|---|---|---|---|---|---|---|---|---|---|---|---|---|---|
| | | | $V_0$, V | $U_0$, V | $V$, V | $U$, V | $V_0$, V | $U_0$, V | $V$, V | $U$, V | $V_0$, V | $U_0$, V | $V$, V | $U$, V | |
| 0.01 | 0.1 | 0.10 | 492 | 451 | 72 | 66 | 677 | 621 | 30 | 28 | 925 | 848 | 34 | 31 | >1800 |
| 0.08 | 0.1 | 0.84 | 485 | 480 | 136 | 134 | 685 | 678 | 77 | 76 | 933 | 923 | 62 | 59 | >1800 |
| 0.10 | 1 | 0.10 | 487 | 446 | 86 | 79 | 687 | 630 | 50 | 46 | 928 | 851 | 72 | 66 | >1800 |
| 0.30 | 0.1 | 3.00 | 493 | 492 | 154 | 150 | 691 | 689 | 124 | 120 | 946 | 943 | 96 | 90 | >1800 |
| 0.84 | 1 | 0.84 | 494 | 489 | 130 | 129 | 695 | 688 | 65 | 64 | 950 | 940 | 75 | 74 | >1800 |
| 1.00 | 10 | 0.10 | 496 | 455 | 60 | 55 | 693 | 635 | 42 | 39 | 938 | 860 | 47 | 43 | 1800 |
| 2.00 | 20 | 0.10 | 495 | 454 | 140 | 128 | 696 | 638 | 32 | 29 | 949 | 870 | 45 | 41 | 656 |
| 3.00 | 1 | 3.00 | 486 | 485 | 170 | 170 | 686 | 684 | 137 | 137 | 945 | 942 | 120 | 120 | 414 |
| 6.60 | 66 | 0.10 | 489 | 448 | 194 | 178 | 683 | 626 | 50 | 46 | 938 | 860 | 38 | 35 | 365 |
| 8.40 | 10 | 0.84 | 480 | 475 | 139 | 138 | 684 | 677 | 73 | 72 | 922 | 912 | 70 | 69 | 380 |
| 13.20 | 132 | 0.10 | 499 | 457 | 169 | 155 | 673 | 617 | 38 | 35 | 929 | 852 | 40 | 37 | 418 |
| 16.80 | 20 | 0.84 | 484 | 479 | 182 | 180 | 682 | 675 | 73 | 72 | 937 | 927 | 65 | 64 | 448 |
| 30.00 | 10 | 3.00 | 483 | 482 | 164 | 164 | 679 | 677 | 150 | 150 | 936 | 933 | 90 | 90 | 550 |
| 55.44 | 66 | 0.84 | 497 | 492 | 496 | 491 | 690 | 683 | 91 | 90 | 942 | 932 | 70 | 69 | 767 |
| 60.00 | 20 | 3.00 | 491 | 490 | 491 | 490 | 671 | 669 | 132 | 132 | 921 | 918 | 110 | 110 | 800 |
| 101.30 | 1013 | 0.10 | 492 | 451 | 490 | 449 | 693 | 635 | 685 | 628 | 941 | 863 | 937 | 859 | >950 |
| 110.88 | 132 | 0.84 | 494 | 489 | 479 | 474 | 699 | 692 | 270 | 267 | 938 | 928 | 70 | 69 | >950 |
| 198.00 | 66 | 3.00 | 488 | 487 | 485 | 484 | 695 | 693 | 685 | 683 | 948 | 945 | 935 | 932 | >950 |
| 396.00 | 132 | 3.00 | 487 | 486 | 481 | 479 | 679 | 677 | 675 | 673 | 945 | 942 | 932 | 929 | >950 |
| 850.92 | 1013 | 0.84 | 500 | 495 | 500 | 496 | 687 | 680 | 679 | 672 | 950 | 940 | 950 | 941 | >950 |
| 3039.00 | 1013 | 3.00 | 500 | 498 | 500 | 480 | 680 | 678 | 664 | 660 | 944 | 941 | 933 | 930 | >950 |

Therefore in the conditions of our experiments for the relevant range of *pd* in the initial moment of the period for which the sample has been situated in the vacuum chamber a spark breakdown in the air gap can occur. For other ranges of *pd* in the end of the same period a spark breakdown in the air gap cannot be observed.

For all ranges of the *pd* values it can be seen from Table 7 that the calculated voltages in the end of the period for which the sample has been situated in the vacuum chamber decreases to a value lower than the breakdown voltages according to the Paschen's law. Therefore, it is assumed that the different oxygen content in the various cases because of different air pressure is in consequence of various sorption processes on the sample surface. These results make us suppose that the main process responsible for the surface potential decay in all our experiments can be associated with desorption of charged species from the electret surface under the influence of its own electric field. These might be ions deposited on the surface or groups in which the ions have given their charge away. The results obtained are in a good agreement with the results observed and described earlier [10, 11].

## CONCLUSION

Our experimental investigations show that the low pressure influence on the surface potential decay of PP electrets films, placed between two short circuited plate electrodes at various air gaps between the charged surface of electrets and the upper electrode. Charging of the electrets was performed in a positive or in a negative corona at 5 kV voltage to the corona electrode. Voltage of 500 V, 700 V or 950 V of the same polarity as that of the corona electrode was applied to the grid. The experimental results obtained show a significant change in the electret behaviour of the PP films after stored at low pressures.

It was established that for all ranges of the *pd* values the main process responsible for the surface potential decay can be associated with desorption of charged species from the electret surface. In addition, it was established that the breakdown voltage following the Paschen's law was reached in the initial moment of the period for which the sample has been situated in the vacuum chamber and a spark breakdown in the air gap can be observed only for some relevant ranges of *pd* values.

## REFERENCES

1 G. M. Sessler, and R. Gerhard-Multhaupt, *Electrets* 3rd edition, Laplacian Press, Morgan Hill, California (1999).

2 J. Wild, and J. Stranathan, *Journal of Chemical Physics* 27(5), 1055-1059 (1957).

3 R. Draughn, and A. Catlin, *Journal of Electrochemical Society* 115(4), 391-394 (1968).

4 F. Palaia, and A. Catlin, *Journal of Chemical Physics* 52(7), 3651-3654 (1970).

5 G. Mekishev, T. Yovcheva, E. Gentcheva, and S. Nedev, *Journal of Electrostatics* 63(11), 1009-1015 (2005).

6 X. Qiu, R. Gerhard, A. Mellinger, *IEEE Transactions on Dielectrics and Electrical Insulation* 18(1), 34-42 (2011).

7 M. A. Lieberman, and A. J. Lichtenberg, *Principles of plasma discharges and materials processing* 2nd edition Wiley Interscience Hoboken, N.J.: Wiley (2005).

8 M. Knoll, F. Ollendorff, and R. Rompe, *Gasentladungstabelen*, Springer-Verlag, Berlin, 84 (1935).

9 R. Schaffert, *Electrophotography*, The Focal Press, London, New York (1965).

10 T Yovcheva, A Viraneva, and M Galikhanov, *Journal of Physics: Conference Series* 558, 1-7 (2014).

11 A. Viraneva, T. Yovcheva, and G. Mekishev, *Polypropylene*, ed. by Fatih Doğan, InTech - Open Access Publisher, Rijeka Croatia, 161-184 (2012).

# Influence of refining process for the eco-friendly industrial lubricants on their rheological properties

A. V. Radulescu[1*], I. Radulescu[1], C. Georgescu[2], L. Deleanu[2]

[1]*University POLITEHNICA Bucharest, 313 Spl. Independentei, Romania*
[2]*"Dunarea de Jos" University of Galati, 111 Str. Domneasca, Romania*

Today, there is an increased interest in studying the eco-friendly industrial lubricants as possible replacers of mineral oils. And this interest obliged the researchers to test the different grades of vegetable oils in order to evaluate their rheological behaviour. The paper presents the influence of shear rate and temperature on the rheological properties (viscosity, flow index and consistency index) of the rapeseed oil, in three different stage of refining process: crude, degummed and refined. Tests were done on a Brookfield cone and plate viscometer CAP 2000+, having the following test parameters: test type - shear rate imposed, shear rate (100...2000 $s^{-1}$) and temperature range of 20...75°C. The results of the tests highlight the better rheological and tribological behaviour of the rapeseed oil, thus it could be recommended in tribological applications.

**Keywords:** biodegradable lubricants, rheology, rapeseed oil

## INTRODUCTION

Because of they have relatively weaker properties, biodegradable oils have not yet an important presence in technical systems that require intensive operating regimes. To compete with petroleum based lubricants or synthetic ones, research studies should provide a viable alternative in performance and price for vegetable oils. In recent years, the regional level (such as the European Union), but also at national level they were created policies that encourage the use of lubricants based on renewable resources, but there are still problems to solve [1].

The process of replacing of "classic" lubricants can only be a gradual process, because it depends on many factors: focus research on making new performant recipes of bio lubricants, availability of farmers to produce such crops, the existence of cost-effective facilities for processing raw materials and support of big consumers in using these lubricants [2], [3].

Today, there is a growing interest in the study of rapeseed oil as potential substitute for mineral or synthetic oils. Some of the last ones are relatively expensive or more polluting to the environment. This interest compels researchers to evaluate a function of oil refining process - the rheological and tribological behaviour [4], [5], [6]. The refining process involves degumming, neutralization, drying, bleaching and deodorization. Crude oil

from extraction has to be refined to obtain high quality oil. Natural impurities of crude rapeseed oil include water, dirt, phosphatide gums, free fatty acids, colour matter, odoriferous and flavorous substances, natural breakdown and oxidation products of the oil itself [7], [8].

The paper presents the influence of shear rate and temperature on the rheological properties (viscosity, flow index and consistency index) of the rapeseed oil, in three different stage of refining process: crude, degummed and refined.

## RAPESEED OIL PROPERTIES

The biodegradable oils were supplied by the Romanian company "Prutul" from Galati. The degumming and refining processes were performed at the firm.

The degumming process extract components (phospholipids and non-triglycerides) that, if they were left in the vegetable oil, they would favor the fermentation and the generation of gum deposits [9]. The refining process includes degumming, neutralization and washing for removing some radicals of the fat acids, metallic traces and other water-soluble substances [10].

The chemical composition of the vegetable oils is given in Table 1 and was done with the aid of gas cromatography, according to the standards PN-EN ISO 5508:1996 and PN-EN ISO 12966-2:2011, at J.S. Hamilton from Poland for the company Prutul S.A from Romania.

Characteristics in Table 2 were determined in the laboratory of Prutul S.A.

**Table 1.** Composition of fat acids for the tested oils

| Fat acid, g/100 g | Crude rapeseed oil | Refined rapeseed oil |
|---|---|---|
| Myristic acid | 0.05 | < 0.1 |
| Palmitic acid | 4.84 | 5.1 |
| Palmitoleic acid | 0.06 | 0.2 |
| Margaric acid | 0.14 | < 0.1 |
| Heptadecenoic acid | - | < 0.1 |
| Stearic acid | 0.14 | 1.8 |
| Oleic acid | 62.73 | 57.1 |
| Linoleic acid | 22.4 | 27.9 |
| Linolenic acid | 7.50 | 5.9 |
| Arachidic acid | 0.50 | 0.4 |
| Eicosenoic acid | 1.25 | 1.0 |
| Behenic acid | 0.30 | 0.3 |
| Erucic acid | - | < 0.1 |
| Lignoceric acid | - | < 0.1 |

**Table 2.** Characteristics for the rapeseed oil

| Characteristic | Crude rapeseed oil | Degummed rapeseed oil | Refined rapeseed oil |
|---|---|---|---|
| Free fatty acids (% oleic acid) | 1.2 | 1.2 | 0.09 |
| Water and volatiles (%) | 0.13 | 0.13 | 0.035 |
| Impurities insoluble in ethyl ether (%) | 0.1 | 0.1 | 0.008 |
| Phosphorus (%) | 0.05 | 0.028 | - |
| Total fat (%) | | 99 | - |
| Energetic value (kcal) | - | 891 | - |
| Erucic acid (%) | - | 0 | 0 |
| Iodine value (mg.I/ 100 cm³) | - | - | 2 |
| Soap (sodium oleate) (%) | - | - | 0.004 |
| Peroxide (meq/ kg) | - | - | 0.5 |

## EXPERIMENTAL METHODOLOGY

The rheological tests were done on a cone and plate rotational viscometer "Brookfield Cap 2000+". This is suitable for the complete characterization of Newtonian and non-Newtonian fluids including the measurement of yield points or thixotropy. The built-in display shows all relevant results and the flow-/viscosity curve could be plotted using CAPCALC32 software.

Using the cone-plate viscometer, highly viscous liquids and pastes from many differing fields of industry can be characterized according to ISO 3219. Flow curves deliver a rheological determination of Newtonian and non-Newtonian behaviour. The features of the viscometer are:
- Automatic recording of flow curves;

- Time measurements;
- Temperature programs;
- Viscosity measurements according to ISO 3219.

To determine the lubricant rheological model for rapeseed oil, in all three states, it was used an "imposed velocity gradient" test, with the variation limits 100 ... 2000 s$^{-1}$ and temperature range of 20...75°C. The tests were carried out by loading to 2000 s$^{-1}$ and downloading to 100 s$^{-1}$, in order to highlight the effects of lubricant thixotropy.

There were tested the three samples of fluid and were calculated the lubricant rheological parameters, using the rheometer software, beyond the non-Newtonian fluids model, for the power law:

$$\tau = m\left(\frac{du}{dy}\right)^n, \qquad (1)$$

where:

$\tau$ - shear stress, Pa;

$\dfrac{du}{dy}$ - shear rate, 1/s;

$m$ - consistency index (which is equivalent to the Newtonian fluid viscosity), Pa.s$^n$;

$n$ - flow index (equal to 1 if the fluid is Newtonian).

To determine the apparent viscosity variation of law versus temperature for analyzed lubricants, there were made tests for four imposed velocity gradients: 500 s$^{-1}$, 1000 s$^{-1}$, 1500 s$^{-1}$ and 2000 s$^{-1}$ and for a temperature range of 20 ... 75$^0$C. The law of variation which has been assumed was Reynolds law:

$$\eta = \eta_{50} e^{m(t-50)}, \qquad (2)$$

where:

$\eta$ – viscosity, Pa.s;

$\eta_{50}$ – viscosity at 50 $^0$C, Pa.s;

$m$ – temperature parameter, 1/$^0$C;

$t$ – temperature, $^0$C.

The parameters values of the variation laws were determined using the regression analysis method, using MathCAD software.

## RESULTS AND DISCUSSION

Lubricant rheograms for rapeseed oil, in crude, degummed and refined state, are presented in Fig.1, Fig.2 and Fig.3. The results for lubricant rheological parameters for all three states are directly obtained by using the rheometer software (Capcalc V3.0), being centralized in Table 3.

**Table 3.** The lubricant rheological parameters for rapeseed oil, in different states

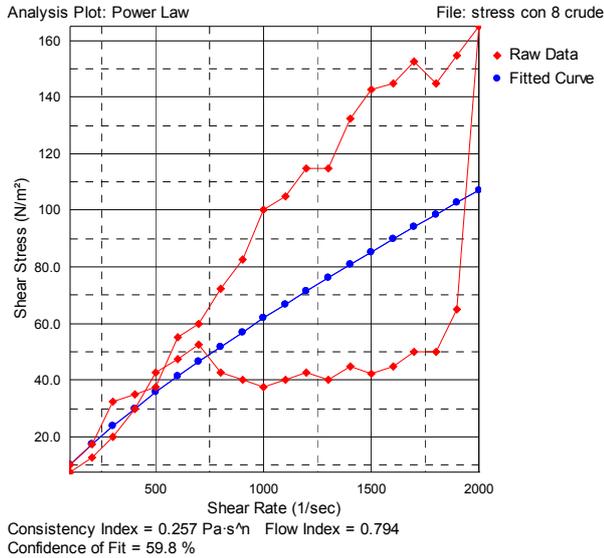| States of rapeseed oil | Consistency index ($m$), Pa·s$^n$ | Flow index ($n$) | Correlation coefficient - |
|---|---|---|---|
| Crude | 0.257 | 0.794 | 59.8% |
| Degummed | 0.291 | 0.767 | 52.7% |
| Refined | 0.521 | 0.672 | 49.6% |



Consistency Index = 0.257 Pa·s^n   Flow Index = 0.794
Confidence of Fit = 59.8 %

**Fig.1.** Lubricant rheogram for crude rapeseed oil



Consistency Index = 0.291 Pa·s^n   Flow Index = 0.767
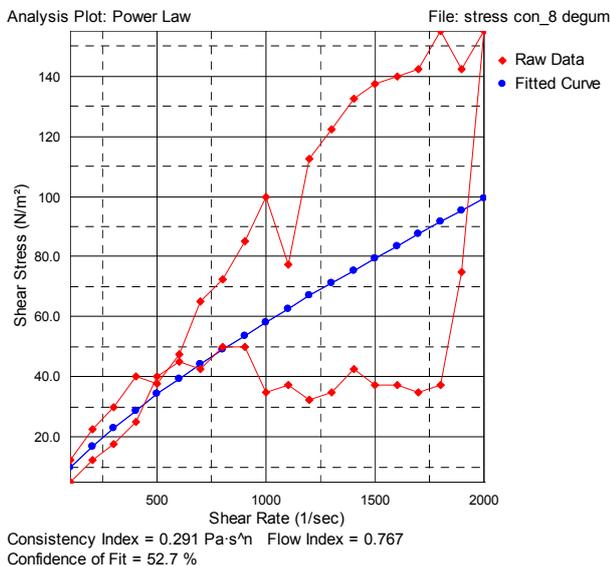Confidence of Fit = 52.7 %

**Fig.2.** Lubricant rheogram for degummed rapeseed oil

Analysing the values of the the rheological parameters, it can observe that the characteristic rheological model for all three states of rapeseed oil (crude, degummed and refined) is the power law model, but with a low correlation coefficient. This is due to the pronounced thixotropy phenomenon, which occurs regardless the refining degree of the lubricant.
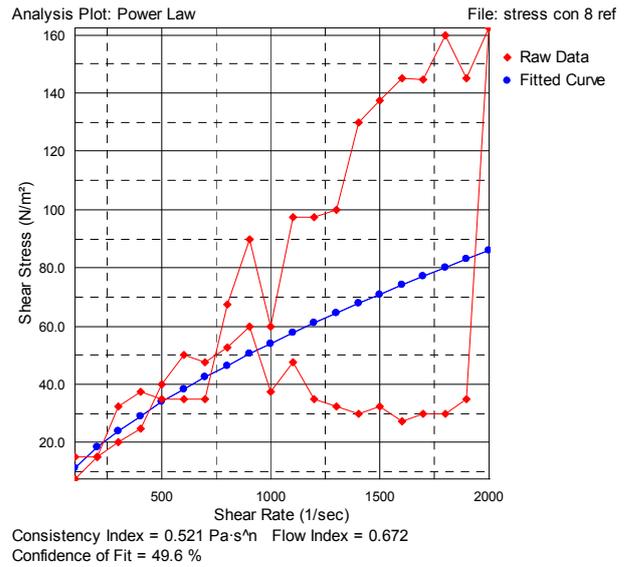


Consistency Index = 0.521 Pa·s^n   Flow Index = 0.672
Confidence of Fit = 49.6 %

**Fig.3.** Lubricant rheogram for refined rapeseed oil

In the case of crude, degummed and refined rapeseed oils, pronounced oscillations of tangential stresses were observed, which means that their structure is relatively unstable and heterogeneous.

The results concerning the variation of apparent viscosity versus temperature, for all three states of rapeseed oil, are presented in Fig.4, Fig.5 and Fig.6.
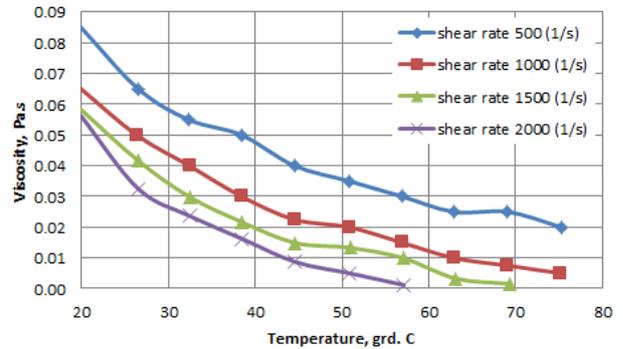


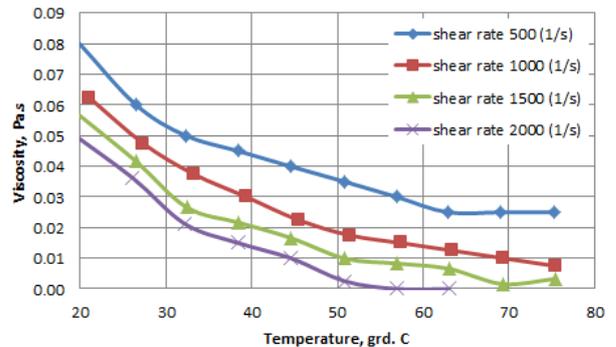**Fig.4.** Variation of apparent viscosity versus temperature for crude rapeseed oil



**Fig.5.** Variation of apparent viscosity versus temperature for degummed rapeseed oil
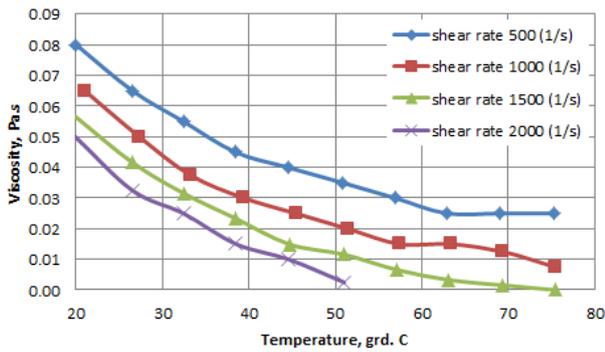
335

**Fig.6.** Variation of apparent viscosity versus temperature for refined rapeseed oil

The characteristic parameters for the Reynolds model corresponding to all three states of rapeseed oils (eq. 2) are presented in Table 4.

**Table 4.** Characteristic parameters for the variation of the apparent viscosity versus temperature, according to Reynolds model, for rapeseed oil in different states

| Parameter Shear rate, 1/s | Crude rapeseed oil | | |
|---|---|---|---|
| | $\eta_{50}$, Pa·s | m, 1/$^0$C | Correlation coefficient |
| 500 | 0.0367 | -0.025 | 98.62% |
| 1000 | 0.0179 | -0.045 | 98.99% |
| 1500 | 0.0095 | -0.067 | 93.07% |
| 2000 | 0.0040 | -0.095 | 93.88% |
| Parameter Shear rate, 1/s | Degummed rapeseed oil | | |
| | $\eta_{50}$, Pa·s | m, 1/$^0$C | Correlation coefficient |
| 500 | 0.0366 | -0.021 | 95.41% |
| 1000 | 0.0194 | -0.037 | 99.65% |
| 1500 | 0.0105 | -0.058 | 92.58% |
| 2000 | 0.0042 | -0.090 | 92.43% |
| Parameter Shear rate, 1/s | Refined rapeseed oil | | |
| | $\eta_{50}$, Pa·s | m, 1/$^0$C | Correlation coefficient |
| 500 | 0.0372 | -0.022 | 96.01% |
| 1000 | 0.0210 | -0.036 | 98.08% |
| 1500 | 0.0089 | -0.070 | 96.44% |
| 2000 | 0.0043 | -0.089 | 91.45% |

Analysing Table 4, it can be observed that the Reynolds model for the variation of apparent viscosity with temperature is valid for all states of the oil, with values of correlation coefficients higher than 90%.

## CONCLUSIONS

At present, the eco-friendly industrial lubricants could be serious possible replacers of mineral and synthetic oils. In this category, an important place is taken by the vegetable oils, because of the fact that they are biodegradable, generally less toxic and renewable. Rapeseed oil production occupies third place in the world production of vegetable and marine oils. This oil is characterized by excellent lubricity, a very high viscosity index (VI) and high flash point.

On the negative side, rapeseed oil in crude state has a lack of sufficient oxidative stability for lubricant use. Low oxidative stability means the oil oxidizes rather quickly during use, if it is untreated, becoming thick and polymerizing to a plastic-like consistency.

The solution for this problem is chemical modification by refining and adding antioxidant additives. The presence of additives could reduce the phenomenon of thixotropy and increase the structural stability of the lubricant. Anyway, the thixotropy of rapeseed oil disappears at low shear rates (less than 500 s$^{-1}$), regardless the refining degree of the lubricant.

Regarding the thermal behaviour of the rapeseed oils, it can be observed a strong decrease of apparent viscosity with increasing of shear rate, for all three states of lubricant. This shows an important pseudo plastic behaviour of the rapeseed oil.

## REFERENCES

1  S. C. Cermak, G. Biresaw, T. A. Isbell, R. L. Evangelista, S. F. Vaughn, R. Murray, *Ind. Crops Prod.*, 44, 232, (2013).
2  N. J. Fox, G. W. Stachowiak, *Tribol. Int.*, 40, 1035, (2007).
3  B. Krzan, J. Vizintin, *Tribol. Int.*, 36, No. 11, 827, (2003).
4  F. M. T. Luna, B. S. Rocha, Jr. E. M. Rola, M. C. G. Albuquerque, D. C. S. Azevedo, Jr. C. L. Cavalcante, *Ind. Crops Prod.,* 33, 579, (2011).
5  B. Lyu, X. B. Duan, D. G. Gao, J. Z. Ma, X. Y. Hou, J. Zhang, *Ind. Crops Prod.,* 70, 292, (2015).
6  H. M. Mobarak, M. Chowdhury, *Tribology in Industry*, 36, No. 2, 163 (2014).
7  E. M. J. Deffense, *Ol., Corps Gras, Lipides*, 16, 14, (2009).
8  I. Pirna, C. Lica, M. Nicolescu, E. Voicu, M. Radu, G. Gageanu, Ch. Fürll, *INMATEH - Agricultural Engineering*, 32, No. 3, 84, (2010).
9  X. Ji, Y. Chen, X. Wang, W. Liu, *Ind. Lubr. Tribol.,* 64, No. 6, 315, (2012).
10  R. M. Mortier, M. F. Fox, S. T. Orszulik, Chemistry and Technology of Lubricants, Springer, Third Edition, 209, (2010).

# Supercapacitor electrodes from activated wood charcoal

Aleksandrs Volperts[1,2]*, Galina Dobele[1], Aivars Zhurinsh[1], Zane Zalane[1,2], Jurijs Ozolinsh[2], Janis Kleperis[3], Darya Vervikishko[4], Evgeny Shkolnikov[4]

[1] *Latvian State Institute of Wood Chemistry, Riga, Latvia*
[2] *Riga Technical University, Faculty of Material Science and Applied Chemistry, Riga, Latvia*
[3] *Latvian University Institute of Solid State Physics, 8 Kengaraga Street, Riga, LV-1063, Latvia*
[4] *Scientific Association for High Temperatures, Russian Academy of Science, Moscow, Russia*

Influence of main stages of wood thermochemical activation parameters on activated carbons porous structure formation were elucidated with for sodium hydroxide as activating agent. The main factors governing the properties of carbon materials, such as specific surface area, volume and pore size distribution, surface oxygen content, as well as their influence on capacitance and working properties of supercapacitor electrodes are demonstrated.

**Keywords:** wood, activated carbon, alkali activation, porous structure, supercapacitors

## INTRODUCTION

The traditional way of biomass conversion is production of wood chars and carbon materials with developed porous structure, activated carbons (AC), which are used as sorbents in many areas. Nowadays elucidation of AC structure is of scientific and practical interest since areas of these materials application are constantly widening: membrane technologies for rare earth metals separation, metallurgy, electronics, electrochemistry, aerospace technologies, and nuclear energy. This broad spectrum of AC application is justified by diversity of their structures with completely different physical and chemical properties, which can be achieved by various physical-chemical treatment of carbonaceous precursors. One of distinctive features of plant biomass based AC is the fact that they can be obtained in various conditions of pyrolysis and activation from extremely wide choice of precursors: wood chips, cellulose and lignin, lignocellulosics, nut shells, straw, peat, husks, etc. As the result properties of AC will be different depending on precursor and synthesis conditions.

Wood based carbonizates have low porosity and their structure consists of elementary crystallites divided by multiple slit-like pores [1]. These pores are filled with pyrolysis products – pyrolytic tar. In the process of activation closed pores open up and the porous structure is being formed. Varying carbon materials and activation conditions (temperature, time, atmosphere) it is possible to control total porosity, pore size distribution and nature of inner space.

Chemical activation is a widely used method for production of AC with developed porosity. The most important advantage of chemical activation is a possibility to synthesize carbonaceous materials with very high specific surface which is close to theoretical limits for carbon materials.

Alkali metal hydroxides are one of the most effective activating agents allowing in certain cases to synthesize microporous carbon sorbents with specific surface more than 3000 m² g$^{-1}$ [2].

There are numerous examples of application of AC as electrodes for storage and transmission of electrical energy. The main goals of ongoing researches are high specific surface and low electric resistance of carbon matrix with low costs of production. AC synthesized with the use of alkali metals hydroxides meet the above mentioned demands [3-4].

Sorption methods and Raman spectroscopy are the most popular non-destructive techniques for the characterization of carbon-containing materials. The intensity ratio of the G and D bands as well as their wavenumbers and widths are useful quantitative criteria for comparing the degree of structural order of different carbon forms [5, 6].

In the development of new systems for the modern electric-power industry one of the important problems is the research devoted to application of electric double layer capacitors or supercapacitors (SC) where porous AC are used as the main material for electrodes. It is known that energy capacity of carbon electrode is influenced by the following AC properties: precursor origin, dispersity and elemental composition, conditions of

---

carbonization and activation, porous structure characteristics, etc. [8].

This work is devoted to the study of influence of wood based carbon material porous structure characteristics for the use in electric double layer capacitors (supercapacitors) with sulfuric acid as electrolyte.

## MATERIALS AND METHODS

Birch wood chips (0.2 – 0.4 mm fraction) were used as a raw material. It was carbonized in the argon atmosphere at $400^{o}C$ for 150 minutes. Then the carbonizate was impregnated with NaOH water solution (50 wt%). Ratio of carbonizate to activator was varied from 1:2 to 1:4. The mixture was activated at the temperatures $600-800^{o}C$ for 120 minutes in Nabertherm L-40 muffle oven in argon flow ($150 \, l \, h^{-1}$). Pyrolysis product was washed with deionized water, demineralized with hydrochloric acid and washed with deionized water again up to filtrate pH 5. The obtained AC was dried overnight at $105^{o}C$. Ash content in the AC was found to be 0.1-0.4%. The main variables in the experiment were activation temperature and carbonizate/activator ratio.

Porous structure was assessed by $N_2$ sorption at 77 K (Nova – 4200e, Quantachrome). Pores volumes were calculated using, Brunauer–Emmet–Teller(BET) and in case of micropores Dubinin-Radushkevich theories from $N_2$ sorption isotherms [9].

Raman spectra of carbon material were taken in back-scattering geometry at room temperature through 50 x microscope objective using micro-Raman spectrometer equipped with argon laser (514.5 nm, max cw power Pex=10 mW). The spectral signal was dispersed by the 2400 grooves/mm grating onto Peltier-cooled ($-60^{o}C$) CCD detector. Frequency shifts in the Raman spectra were calibrated using $CaWO_4$ as a reference.

Immersion calorimtery was performed using Setaram C-80 device in water and benzene. Samples were outgassed at $300^{o}C$ and sealed under vacuum in glass ampules.

For supercapacitor assembly AC was first mixed with ethanol, then a binder - water suspension of PTFE F-4D (10 wt% on dry electrode mass) was added, and the resulting mixture was treated in calender press. Electrodes were dried and then impregnated with 4.9M water solution of $H_2SO_4$. Cellulosic separator NKK TF 4030 (10 μm) was used to make a supercapacitor (SC). The electrode area was 4.15 cm². Foil from thermally expanded graphite (200 μm) was used as a current collector. Assembled SC were pressed under 10 atm in a dry box. SC capacity was assessed using potentiostate Elins 30-S at 1 V for 5 minutes. Inner resistance was calculated by voltage drop at current transient in the beginning of SC discharge. Capacities shown are calculated on a dry mass of electrode, without electrolyte.

## RESULTS

Raman spectroscopy was used to compare structures of charcoal and activated carbon (AC) synthesized at $700^{o}C$ and carbonizate to activator ratio 2.
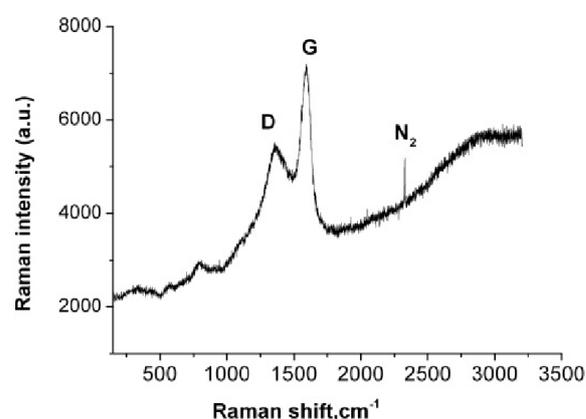


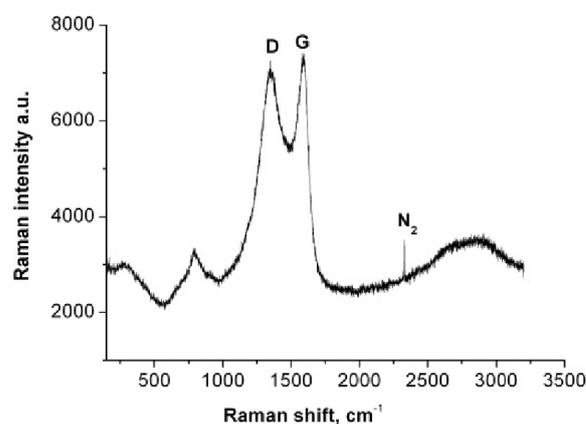**Fig.1.** Micro-Raman scattering spectrum of wood charcoal



**Fig.2.** Micro-Raman scattering spectrum of activated carbon (activation temperature $700^{o}C$, carbonizate to activator ratio 1:2)

The Raman-active vibration numbering for natural single-crystal graphite exhibits a single Raman peak at around 1580 cm$^{-1}$, called the G peak.

This peak is associated with the in-plane C−C stretching mode of the sp$^2$ hybridized carbon atoms. For polycrystalline graphite, depending on the size of the crystallites, a second peak at 1350 cm$^{-1}$

appears namely the disorder or D peak. If the long-range order of the crystalline material is lost and the carbon phase becomes glassy, both the G and the D peaks broaden [7]. Three Raman scattering peaks at around 1364, 1596 and 2325 cm$^{-1}$ are observed. The peak at 1580 cm$^{-1}$ (G band) is attributed to an $E_{2g}$ mode of graphite and is related to the vibration of sp$^2$ – bonded carbon atoms. For polycrystalline graphite, depending on the size of the crystallites a second peak at 1350 cm$^{-1}$ appears, namely the disorder or D peak [10]. Note that in a perfect graphite crystal the first-order vibrational mode of the D band is forbidden because of the selection rules. Decreasing particle size or bending of the lattice fringes may activate this band [11]. We can see this phenomenon: after carbon activation the intensity of Raman scattering D band increases with decreasing of particle size of carbon (Fig.1 and Fig.2.). Stretch vibrations of $N_2$ in the ambient might have caused sharp (narrow) peak at 2325cm$^{-1}$ [10].
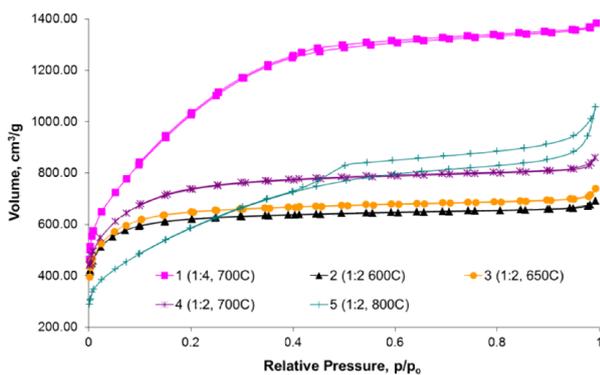


**Fig.3.** AC nitrogen adsorption isotherms at 77K with alteration of carbonizate to activator ratio and activation temperature

AC porous structure characteristic for use as electrodes in supercapacitors were evaluated using nitrogen sorption isotherms (Fig.3). The samples under study were first carbonized at 400$^{o}$C and then activated at carbonizate to NaOH ratio 1:2 (Fig.3, isotherms 2-5) and 1:4 (Fig.3, isotherm 1) in the isothermal conditions at the temperatures 600, 650, 700 and 800$^{o}$C. Judging by the shape of isotherms samples obtained at temperatures 600, 650 and 700$^{o}$C (Fig.4, isotherms 2-4) are microporous. With increase of activation temperature volume of adsorbed nitrogen increases as well. At the activation temperature 800$^{o}$C (Fig.3, isotherm 5) the shape of isotherm changes. The appearance of hysteresis is an indication of capillary condensation of sorbate, which also points at increase of mesopores number. With the increase of carbonizate to activator ratio to 1:4 (activation

temperature 700$^{o}$C) volumes of adsorbed nitrogen, as well as number of mesopores in AC structure, increase (Fig.3, isotherm 1).

Total pore volume increases with the increase of carbonizate to activator ratio (1:2 and 1:3) and activation temperature in the range 600 – 750$^{o}$C, but micropores (0.8 – 1.5 nm) volumes were increasing only until 700$^{o}$ (Fig.4). At the same time specific surface area increased with increase of NaOH addition ratio and activation temperature in the whole range (Fig.5).
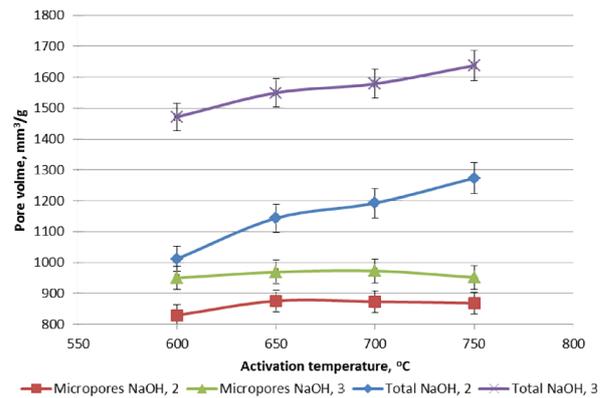


**Fig.4.** Dependence of total and micropores (Dubinin-Radushkevich) volumes from activation temperature and NaOH addition ratio
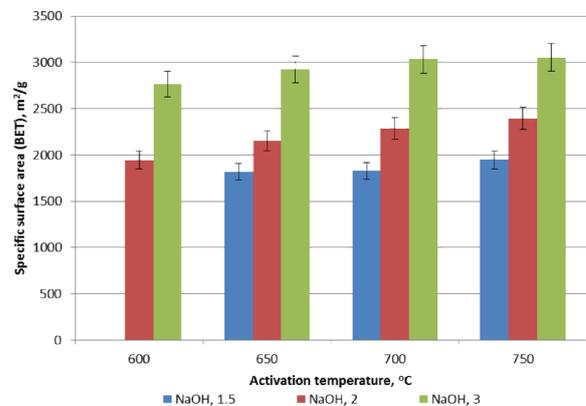


**Fig.5.** Dependence of specific surface from activation temperature and NaOH addition ratio

Immersion calorimetry can be used to determine content of oxygen-containing surface groups in the carbonaceous materials by immersion into polar (water) and nonpolar (benzene) liquids [12]. This method allowed establishing correlation between heats of immersion, specific surface area and surface oxygen content which are important parameters for supercapacitor stability in charge-discharge cycles and double electric layer formation.

It was shown that the lowest oxygen content was found for the samples obtained at 650-700$^{o}$C

(Fig.6). For these samples the highest specific capacitance (~330 F/g) and electric resistance (~250 mOhm) was found. This proves that comparison of porosity and immersion enthalpies allows forecasting supercapacitor electrical properties.
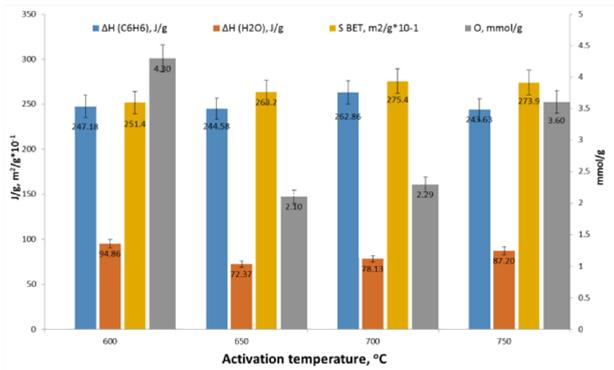


**Fig.6.** Influence of activation temperature on surface oxygen content (carbonizate to NaOH 1:2)

Characteristics of supercapacitor cells made with electrodes from AC prepared at different activation temperatures and carbonizate/activator ratio 1:2 are illustrated in the Fig.7. At the lower carbonization temperatures – 600 to 700°C capacitance was around ~330 F g$^{-1}$. Increase of carbonization temperature negatively influences on electrochemical properties - at the activation temperature 800°C capacitance decreased to 220 F g$^{-1}$.
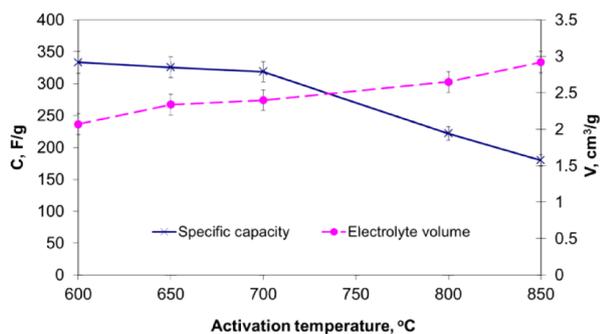


**Fig.7.** Dependence of supercapacitor cell capacitance and volume of electrolyte retained by AC from the activation temperature (carbonizate to activator ratio 1:2)

As it is shown in the Fig.7 total volume of electrolyte retained by electrode considerably increases with the increase of activation temperature. This parameter is important when evaluating efficiency of the device under development, namely for the calculation of specific characteristics to the mass of elementary capacitor cell. This behavior can be explained basing on

literature data [13]. Decreasing the pore size to a value approaching the crystallographic diameter of the ion leads to a 100% increase in normalized capacitance. It was shown that under a potential, there is substantial ion motion and diminished dielectric permittivity in pores less than the size of their solvation shells. The solvation shell becomes highly distorted as the ion is squeezed through the pore in much the same way a balloon distorts when squeezed through an opening smaller than its equilibrium size.

The distortion of solvation shells in small pores of carbon nanostructures was also reported recently. Such distortion would allow closer approach of the ion center to the electrode surface which leads to improved capacitance [13].

Thus electrode pores should provide transport and availability of ions in the process of double electric layer charge and discharge. Obviously there are an optimal micropores volume and size required to effectively form double electric layer, while meso- and macropores provide transport function for electrolyte ions. These pores do not contribute into electric double layer formation, and additional electrolyte mass negatively influences on the SC specific characteristics calculating on cell or whole device.
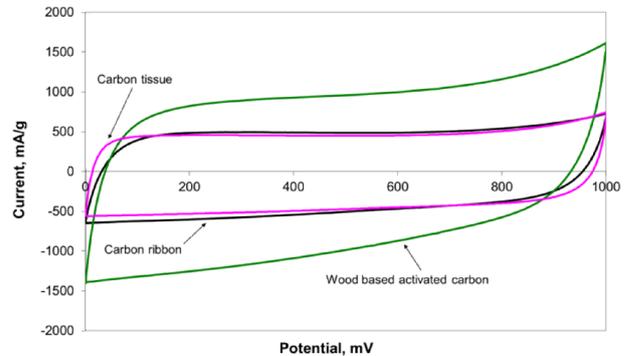


**Fig.8.** Cyclic voltammograms (two electrode cells) of the capacitors with electrodes built from wood based activated carbons (carbonizate to activator ratio 1:2, activation temperature 600 °C), commercial carbon tissue electrodes and commercial carbon ribbon electrodes ($H_2SO_4$ aqueous solution)

To illustrate properties of the obtained nanoporous activated carbons they were tested in two electrode system. Charge/discharge cyclic voltammograms were recorded and compared to vomtammograms obtained for electrodes based on commercial carbon materials (Fig.8). All three materials exhibit a regular box-like shape with a steep current change at the switching potential, which is a characteristic of the behavior of an ideal

capacitor. It is clear that nanoporous activated carbons show higher specific capacitance. The other benefit of disperse carbon material is the ability to control thickness of carbon layer.

Further research of the carbon porous structure and synthesis of materials with optimal volume of pores with sizes tailored for the specific electrolyte may allow both energy and power characteristics of supercapacitors to be improved.

## CONCLUSIONS

Microporous wood based carbon materials were obtained using thermochemical synthesis, which includes carbonization and consequent alkali activation. The synthesized carbon materials have good electrode characteristics for the capacitors with double electric layer. Maximal capacity of supercapacitor ~330 F g$^{-1}$ is achieved at the activation temperatures 650$^{\circ}$C and carbonizate to activator ratio 1:2 for sulphuric acid electrolyte. Capacity decreases with activation temperature increase, which corresponds to decrease of micropores proportion in activated carbons porous structure.

## ACKNOWLEDGEMENTS

## REFERENCES

1 Tsyganova, S., Korolkova, I., Bondarenko, G., Chesnokov, N., Kuznetsov, B. Synthesis of Active Carbons from Birch Wood modified by phosphoric Acid and Potassium Hydroxide. J. Siberian Fed University Chemistry, 2009, vol. 2, N 3, p. 275-281.

2 Torne-Fernandez, V., Mateo-Sanz, J.M., Montane, D., Fierro, V. Statistical Optimization of the Synthesis of Highly Microporus Carbons by Chemical Activation of Kraft Lignin with NaOH. J. Chem. Eng. Data. 2009, N 54, p. 2216–2221.

3 Marsh, H., Rodriguez-Reinoso, F. Activated Carbon. Amsterdam : Elsevier, 2006, 536 p.

4 Dobele, G., Dizhbite, T., Gil, M.,V., Volperts, A..Centeno,T.,A. Production of Nanoporous Carbons from Wood Processing Wastes and their use in Supercapacitors and CO2 Capture. Biomass and Bioenergy, 2012, N 46, p. 145-154.

5 Bansal, R, Goyal, M. Activated carbons Adsorption, Boca Raton : CRP Press, 2005. 472 p.

6 Cheng, Y. H., Tay, B.K., Lau, S.P., Shi, X., Qiao, X.L., Chen J.G., Wu, Y.P., Xie, C.S. Raman spectroscopy of carbon nitride films deposited using the filtered cathodic vacuum-arc combined with a radio-frequency nitrogen-ion beam. Appl. Phys. 2001, A 73, p. 341–34.

7 Zickler, G. A., Smarsly, B, Gierlinger, N., Peterlik, H., Paris, O. A reconsideration of the relationship between the crystallite size of carbons determined by X-ray diffraction and Raman spectroscopy. Carbon, 2006, N 44, p. 3239–3246.

8 Inagaki, M., Konno, H., Tanaike, O. Carbon Materials for Electrochemical Capacitors. J. Power Sources, 2010, N 195, p. 7880-7903.

9 Rouquerol, J., Rouquerol, F., Sing K. Adsorption by Powders and Porous Solids Principles, Methodology and Applications. San Diego : Academic Press, 1998. 467 p.

10 Ferrari A. C., Meyer J.C., Scardaci, V., Casiraghi, C., Lazzeri, S., Mauri, F., Piscanec, S., Jiang, D., Novoselov, A. K., Roth, S., Geim, A. K. Raman Spectrum of Graphene and Graphene Layers. Phys. Rev. Lett., 2006, N 97, p. 187401.

11 Klinke, C., Kurt, R., Bonard, J.M. Raman Spectroscopy and Field Emission Measurements on Catalytically Grown Carbon Nanotubes. J. Phys. Chem. B, 2002, N 106, p. 11191-11195.

12 Centeno, T.A., Fernandez, J.A.,. Stoeckli F. Correlation between heats of immersion and limiting capacitances in porous carbons. Carbon 46, 2008, p. 1025-1030.

13 Chmiola, J., Yushin, G., Gogotsi, Y., Portet, C., Simon, P., Taberna P.L. Anomalous Increase in Carbon Capacitance at Pore Sizes Less Than 1 Nanometer. Science, 2006, N 313, p.1760-1763.

# Soliton regime of propagation of optical pulses in isotropic medium under the influence of third order of linear dispersion and dispersion of nonlinearity

D. Y. Dakova[1, *], A. M. Dakova[1, 2], V. I. Slavchev[2, 3], L. M. Kovachev[2]

[1]*Faculty of Physics, University of Plovdiv "Paisii Hilendarski", 24 Tsar Asen Str., 4000 Plovdiv, Bulgaria*
[2]*Institute of Electronics, Bulgarian Academy of Sciences,72 Tzarigradsko shossee,1784 Sofia, Bulgaria*
[3]*Faculty of Pharmacy, Medical University - Plovdiv, Bul. Vasil Aprilov 15-A, 4002 Plovdiv, Bulgaria*

In the recent years the evolution of ultrashort broad-band optical pulses in nonlinear dispersive media attracts a considerable attention. For attosecond and phase-modulated femtosecond laser pulses the following condition is satisfied: $\Delta\omega \approx \omega_0$. One of the most commonly used equation in optics, to describe the propagation of optical pulses in planar and one-dimensional waveguides, is the nonlinear Schrodinger equation (NSE). It is derived for narrow-band pulses ($\Delta\omega << \omega_0$) and works very well for nanosecond and picosecond laser pulses. As a result of different linear and nonlinear mechanisms, in femtosecond and attosecond region it is easy to obtain broad-band pulses where $\Delta\omega \approx \omega_0$. In this case, it is more convenient to use the general nonlinear amplitude equation (NAE) which works properly for narrow-band as well as broad-band light pulses. In the present work a theoretical model of the evolution of broad-band optical pulses in single-mode silica ($SiO_2$) fibers is presented. In the frames of ultrashort optics the influence of effects of dispersion and nonlinearity of the medium are significant. This requires the inclusion of additional terms in NAE that govern the third order of linear dispersion and dispersion of nonlinearity. In present paper we found a new exact analytical soliton solution of NAE. It is shown that it is possible to observe a soliton as a result of the dynamic balance between the effects of higher order of dispersion and nonlinearity of optical $SiO_2$ fibers. Obtained results are important for better understanding of the evolution of broad-band optical pulses, propagating in medium under the influence of third order of linear dispersion and dispersion of nonlinearity.

**Keywords:** $SiO_2$ single-mode fibers, third order of linear dispersion, the dispersion of nonlinearity, nonlinear amplitude equation, soliton solution, broad-band optical pulses

## INTRODUCTION

In the last two decades the evolution of femto-second and attosecond optical pulses with broad-band spectrum in nonlinear dispersive medium is of a considerable interest for the scientific community [1-3]. Its study is a result of the growing needs of ultrafast high intensity optics. One of the most commonly used equations to describe the propagation of laser pulses in one-dimensional structures and planar waveguides is the nonlinear Schrodinger equation [4-9]. In the frames of ultrashort optics ($T_0 < 1ps$) it is usually modified by adding terms that govern the third order of the linear dispersion (TOD) and the dispersion of nonlinearity [4,10]:

$$i\frac{\partial A}{\partial \xi} + \frac{1}{2}\frac{\partial^2 A}{\partial \tau^2} + i\delta\frac{\partial^3 A}{\partial \tau^3} + k_0 n_2 L_D\left[\left|A\right|^2 A + is\frac{\partial}{\partial \tau}\left(\left|A\right|^2 A\right)\right] = 0 \quad (1)$$

where $\delta = k'''/(6T_0 |k''|)$, $s \approx 1/(T_0\omega_0)$, $L_D = T_0^2/|k''|$.

It is well known that, for such pulses, it is necessary TOD ($k'''$) to be taken into account even when group velocity dispersion (GVD) is nonzero $k'' \neq 0$. As a result of that, the shape of the pulse becomes asymmetric with an oscillatory structure on one of its edges, depending on the sign of $k'''$ (Fig.1) [4].
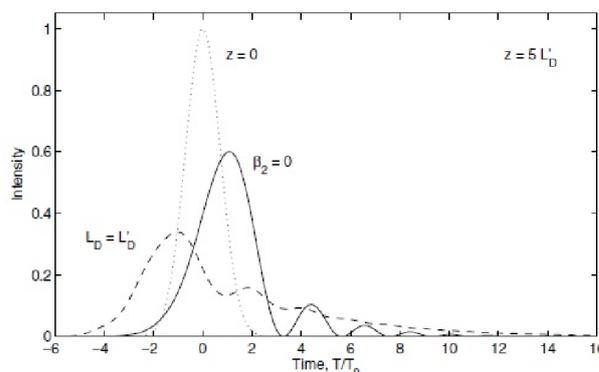


**Fig.1.** Gaussian pulse in the presence of TOD, $L'_D = T_0^3/|k'''|$, [4]

If pulses propagate at the zero-dispersion wavelength, the effects of TOD are dominant and lead to deep oscillations with intensity dropping to zero at the leading edge of the pulse when $k''' < 0$ and at its trailing edge when $k''' > 0$, respectively. In soliton regime of propagation, the main effect of TOD, on the evolution of laser pulses, is to shift theirs peak position linearly with distance $z$ [4]. When $k''' > 0$ the soliton peak is slowed down and when $k''' < 0$ it speeds up. The shift is considerable in attosecond and femtosecond region. Effects of TOD on the propagation of optical solitons are widely discussed in [11-16].

Self-steepening (dispersion of nonlinearity)

---

$(s=1/\omega_0 T_0)$ is a higher-order nonlinear effect that results from the intensity dependence of group velocity and leads to an asymmetry in the shape and spectrum of ultrashort pulses. Their peaks shift toward the trailing edges, moving at lower speed than wings (Fig.2) [4].
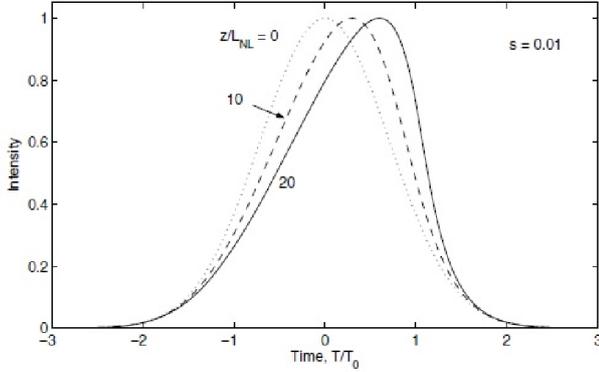


**Fig.2.** Dispersionless case of self-steepening of Gaussian pulse, $z=10L_{NL}$ and $20L_{NL}$, $s=1/\omega_0 T_0$ [4]

Self-steepening could create an optical shock wave, which formation is delayed in dispersionless case as a result of fiber losses. In soliton regime of propagation self-steepening leads to a spectral and temporal shift of pulses. These effects have been studied extensively in [17-21].

It is important to mention that the separate influence of third order of linear dispersion and dispersion of nonlinearity alter the pulses parameters and breakup higher-order solitons into their constituents [4]. Thus, it was interesting to ask the question: *Is it possible a soliton to be formed in such a medium as a result of the compensation of the simultaneous influence of these two effects*?

Our quick review shows that the dynamics of optical solitons in different nonlinear dispersive media is well studied, based on the nonlinear Schrodinger equation [10,22-26]. Authors in [10] investigated the standard and modified NSE numerically. It is shown that for broad-band femtosecond optical pulses, under certain conditions, it is possible a soliton to be observed. It maintains its shape even in the presence of self-steepening and third order of dispersion as a result of the balance between the higher-order nonlinear and dispersive effects (Fig.3) [10].

The NSE very well describes the propagation of slowly varying amplitude function of the envelope of narrow-band pulses in optical fibers but in the frames of broad-band optics (phase-modulated femtosecond and attosecond laser pulses) it is necessary to work with the more general nonlinear

amplitude equation NAE [27,28] which differs from NSE (1) with two additional terms. The biggest advantage of NAE is that it can be applied in both cases – for pulses with broad-band and narrow-band spectrum.
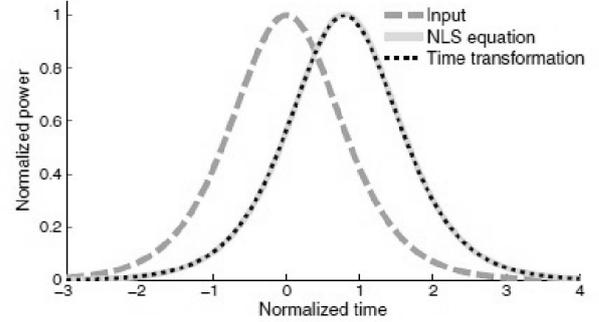


**Fig.3.** Intensity profile of *sech* input pulse (dashed line) $z=0$ and $z=10L_D$, $s=1/4\pi$, $T_0=10fs$, $\delta=0.02$. Predictions of modified NSE are shown by the solid curve [10]

In present paper we propose a theoretical model based on the evolution of light pulses with a broad-band spectrum in optical fibers under the effects of third order of linear dispersion and dispersion of nonlinearity. In our work losses and Raman scattering of the medium are neglected. New exact analytical soliton solution of NAE is found by using mathematical method described in [28].

BASIC EQUATION

The 3D vector amplitude equation that describes the evolution of short optical pulses in Kerr-type nonlinear dispersive isotropic medium has the form [27]:

$$\Delta \vec{A} + 2ik_0 \left[ \frac{\partial \vec{A}}{\partial z} + \frac{1}{v_{gr}} \frac{\partial \vec{A}}{\partial t} + \left( \frac{2n_2 k_0}{\omega_0} + k_0 \frac{\partial n_2}{\partial \omega} \right) \frac{\partial}{\partial t} \left( \left| \vec{A} \right|^2 \vec{A} \right) \right] +$$
$$\frac{2i}{v_{gr}} \hat{\Theta} \frac{\partial \vec{A}}{\partial t} + 2k_0 \hat{\Theta} \vec{A} - \frac{1}{v_{gr}^2} \frac{\partial^2 \vec{A}}{\partial t^2} + 2n_2 k_0^2 \left| \vec{A} \right|^2 \vec{A} = 0 \quad (2)$$

where:

$$\hat{\Theta} = \sum_{n=2}^{\infty} \frac{1}{n!} k^{(n)} (i \frac{\partial}{\partial t})^n = -\frac{1}{2} k'' \frac{\partial^2}{\partial t^2} - i \frac{k'''}{3!} \frac{\partial^3}{\partial t^3} + ... \quad (3)$$

$$k_0 = k(\omega), \ n = n(\omega_0), \ k' = \frac{\partial k}{\partial \omega},$$
$$k'' = \frac{\partial^2 k}{\partial \omega^2}, \ k''' = \frac{\partial^3 k}{\partial \omega^3}, \ v_{gr} = \frac{1}{k'} \quad (4)$$

In the equation above (2) $\vec{A}$ is the vector amplitude function of the pulse envelope; $t$ is time; $\omega_0$, $k$, $v_{gr}$, $n$ and $n_2$ are the carrier frequency, wave number, group velocity, linear and nonlinear refractive index of the medium, respectively; $\Delta$ is the operator of Laplace.

- It is assumed that:

$$\vec{A} = A\vec{n} \quad , \qquad (5)$$

where $\vec{n}$ is the single constant vector and $A = \left|\vec{A}\right|$ is the magnitude of the amplitude function. Thus:

$$\Delta\vec{A} = \vec{n}\Delta A \qquad (6)$$

By the substitutions above equation (2) can be presented in scalar form.

- The evolution of one-dimensional pulses in SiO$_2$ single-mode fiber is examined. So, we are not interested in their transverse size. It is assumed that the axis $Oz$ coincides with the axis of symmetry of the medium. Therefore, the magnitude of the amplitude function $A$ is presented as a function of only two variables $t$ and $z$, i.e.:

$$A = A(t,z) \qquad (7)$$

- We work in local time coordinate system:

$$T = t - z/v_{gr} \quad . \qquad (8)$$

By these assumptions equation (2) can be written in scalar form:

$$i\frac{\partial A'}{\partial\xi} + \frac{1}{2\alpha}\left[\frac{\partial^2 A'}{\partial\xi^2} - 2\frac{\partial^2 A'}{\partial\xi\partial\tau}\right] + \frac{|\beta_2|}{2\alpha}\frac{\partial^2 A'}{\partial\tau^2} +$$

$$\frac{iC}{2\alpha}\frac{\partial^3 A'}{\partial\tau^3} + \gamma|A'|^2 A' + i\gamma s\frac{\partial}{\partial\tau}(|A'|^2 A') = 0, \qquad (9)$$

where

$$A = A'\sqrt{A_0}, \quad \xi = \frac{z}{z_0}, \quad \tau = \frac{T}{T_0}, \quad z_0 = v_{gr}T_0,$$

$$\alpha = k_0 z_0, \quad |\beta_2| = k_0|k''|v_{gr}^2, \quad |\beta_3| = \frac{k_0|k'''|v_{gr}^2}{3T_0},$$

$$\gamma = \alpha_0 n_2 |A_0|^2, \quad s = \left[\frac{2}{\omega_0 T_0} + \frac{1}{\chi^{(3)}T_0}\frac{\partial\chi^{(3)}}{\partial\omega}\right],$$

$$C = \frac{|\beta_2|}{\alpha}(1+\theta), \quad \theta = \frac{k_0 c}{n_0}\frac{|k'''|}{|k''|} = \frac{\alpha}{3}\frac{L_D}{L_D'}$$

Using the substitutions above the amplitude equation (2) is presented in dimensionless form. The parameters $z_0$ and $T_0$ represent the initial longitudinal length and pulse duration; $A_0$ is its initial amplitude. The constant $\alpha$ ($\alpha > 1$) characterizes the number of harmonic oscillations at level $1/e$ from the maximum of the pulse amplitude. The coefficients $\beta_2$ and $\beta_3$ are connected with second and third order of the linear dispersion. It is assumed that higher orders of linear dispersion are negligible compared to the second and third ones, characterized by $k''$ and $k'''$. Therefore, we consider only the first two terms of the differential operator (3). The GVD of the medium is anomalous, i.e. $k'' < 0$ and $\beta_2 < 0$: $\beta_2 = -|\beta_2|$. The parameter $\gamma$ depends on the nonlinear refractive index $n_2$.

Equation (9) is a nonlinear partial differential equation that describes the change in the magnitude of the amplitude function of pulses, propagating in SiO$_2$ single-mode fibers. It presents the effects of linear and nonlinear dispersion of the medium and describes the evolution of the amplitude function of the electric field even when the laser pulse admits few optical cycles inside. Here, it is important to mention that for nanosecond and picosecond light pulses, the coefficient $1/2\alpha$ in front of the brackets in equation (9) is quite small and it can be neglected. In this case, NAE tends to the modified NSE. That is the reason why, NSE describes very well the evolution of narrow-band laser pulses in single-mode fibers. Obviously, in femtosecond and attosecond regions, the coefficient $1/2\alpha$ is significant and the two additional terms - the second derivative ($\partial^2 A'/\partial\xi^2$) and the mixed derivative ($\partial^2 A'/\partial\xi\partial\tau$), must be taken into account [29,30].

## SOLITON SOLUTION OF THE NONLINEAR AMPLITUDE EQUATION

We search for a solution of the scalar nonlinear amplitude equation (9) of the form:

$$A'(\xi,\tau) = \Phi(x)\exp(ia\tau + ib\xi),$$
$$x = \tau + u\xi \qquad (10)$$

where $a$, $b$ and $u$ are constants which are due to be defined, $\Phi(x)$ is a real function. It is important to mention that constant $u$ has a meaning of velocity which shifts the peak of pulses.

As a first step, the expression (10) is substituted in equation (9). A complex nonlinear ordinary differential equation of third order and third degree with respect to the unknown function $\Phi(x)$ is obtained. In the next step, the real and imaginary parts on both sides of the equation are equalized. Thus, the following two differential equations are obtained:

$$Re: \begin{array}{l} \Phi''\left[u^2 - 2u + |\beta_2| - 3aC\right] - \\ \Phi\left[2ab + b^2 - 2ab + a^2|\beta_2| - Ca^3\right] + \Phi^3 2\alpha\gamma[1 - as] = 0 \end{array} \qquad (11)$$

$$Im: \begin{array}{l} \Phi'''C + 3\Phi^2\Phi'2\alpha\gamma s - \\ \Phi'\left[2b + 2au + 3Ca^2 - 2a|\beta_2| - 2bu - 2\alpha u\right] = 0 \end{array} \qquad (12)$$

The coefficients in front of the corresponding derivatives and degrees of the function $\Phi$ in equations (11) and (12) are dimensionless. Equation (12) is integrated with respect to the variable $x$ to lower its order. Thus, it takes the following form:

$$\Phi''C - \Phi\left[2b + 2au + 3Ca^2 - 2a|\beta_2| - 2bu - 2\alpha u\right] + \tag{13}$$
$$\Phi^3 2\alpha\gamma s = B = const$$

As it can be noticed, equations (11) and (13) are of the same type and are referred to the same unknown function. In that sense, they should match. Moreover, the coefficients in front of the corresponding derivatives and degrees of $\Phi$ must be the same. Thus, the integration constant $B$ is zero [28,31]. By equalizing these coefficients constants $a$, $b$ and $u$ are obtained:

$$a = \frac{\alpha}{2} - 1,$$

$$b_{1,2} = -\left(1 + \frac{\alpha}{2}\right) \mp \sqrt{1 - |\beta_2|\left[1 - (1+\theta)\left(\frac{3}{2} - \frac{2}{\alpha}\right)\right]} \pm \tag{14}$$
$$\frac{\alpha}{2}\sqrt{1 - |\beta_2|\left(1 - \left(\frac{1+\theta}{2}\right)\right)},$$

$$u = 1 \pm \sqrt{1 - |\beta_2|\left[1 - (1+\theta)\left(\frac{3}{2} - \frac{2}{\alpha}\right)\right]}$$

Once the three constants are defined in a way that equations (11) and (13) match, for the unknown real function $\Phi = \Phi(x)$ the following ordinary nonlinear differential equation of second order is obtained:

$$\Phi'' - \eta^2\Phi + 2N^2\Phi^3 = 0 \quad, \tag{15}$$

where

$$\eta^2 = \frac{3\alpha^2}{4} - 1 - \tag{16}$$
$$\frac{\alpha^2}{|\beta_2|(1+\theta)}\left[1 + |\beta_2| \pm \sqrt{1 - 2|\beta_2|\left[1 - (1+\theta)\left(1 - \frac{1}{\alpha}\right)\right] + |\beta_2|^2\left[1 - 2(1+\theta)\left(1 - \frac{1}{\alpha}\right) + (1+\theta)^2\left(\frac{3}{4} - \frac{1}{\alpha}\right)\right]}\right]$$

The number of the soliton is given as follow:

$$N^2 = \frac{\alpha s}{C}\gamma \tag{17}$$

The soliton solution of equation (15) has a well-known form [4-7]:

$$\Phi = \eta\sqrt{\frac{C}{\alpha\gamma s}} \operatorname{sech}(\eta x) \tag{18}$$

The constant $\eta$ has a meaning of amplitude. The solution (18) has a physical meaning when $\eta$ is real and $\eta > 0$. This condition can be satisfied by the appropriate selection of the parameters of optical pulses and SiO$_2$ fibers.

Having in mind the expressions (14) and substituting (18) in (10), a new exact analytical soliton solution of NAE (9), including the effects of self-steepening and TOD, is obtained:

$$A'(\xi,\tau) = \eta\sqrt{\frac{C}{\alpha\gamma s}} \operatorname{sech}[\eta(\tau + u\xi)] e^{i[a\tau + b\xi]} \tag{19}$$

This result differs from the standard soliton solution of NSE. The additional phase term found in solution (19) leads to a significant temporal shift of the soliton peak position. Constants (14) depend on the number of optical cycles inside the pulse and the parameters of the medium. The biggest advantage of the soliton solution (19) is that, it can be used for more accurate description of the propagation of narrow-band as well as broad-band optical pulses in isotropic one-dimensional nonlinear dispersive media.

## NUMERICAL CALCULATIONS

For laser pulse with $\lambda = 1,55\mu m$ propagating in fused silica ($n_0 \approx 1,47$; $|k''| \approx 1,8.10^{-26}s^2/m$; $|k'''| \approx 10^{-40}s^3/m$) [4] it is defined that $k_0 = 4,05.10^6 \ m^{-1}$, $|\beta_2| \approx 3.10^{-3}$ and $\theta \approx 1,53$. In that case, it is assumed that $\partial\chi^{(3)}/\partial\omega \approx 0$.

Thus, the following approximate solution of equation (9) is obtained:

$$\Phi \approx \eta \operatorname{sech}(\eta x), \quad \eta \approx \alpha, \quad u \approx |\beta_2|\left(\frac{5,2}{\alpha} - 3,4\right)$$
$$a = \frac{\alpha}{2} - 1, \quad b \approx -\left(1 + \frac{\alpha}{2}\right) + |\beta_2|\left(3,9 - \frac{7,8}{\alpha}\right), \quad s \approx 2/\alpha \tag{20}$$

On Fig.4 and Fig.5 numerical calculations of expression (20) are shown. It is observed a soliton with amplitude proportional to the parameter $\alpha$, characterizing the number of harmonic oscillations under the pulse envelope. In Fig.4 the amplitude of initial *sech* pulse with time duration $T_0 = 10fs$ at $z = 0$ is presented.
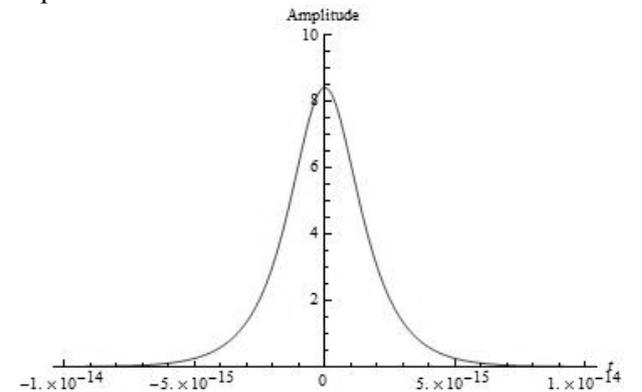


**Fig.4.** Amplitude of the *sech* pulse with $T_0 = 10fs$ and $z = 0$

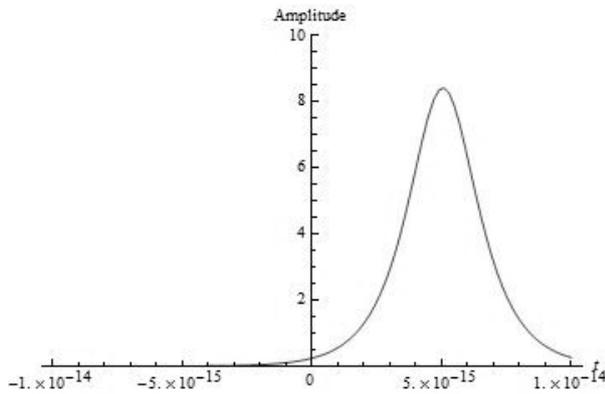In Fig.5 is shown the same femtosecond *sech* pulse at distance $z=z_0$.



**Fig.5.** Amplitude of the *sech* pulse with $T_0=10fs$ and $z=z_0$

The shift in the temporal position of the soliton peak can be clearly seen. Nevertheless, the pulse keeps its shape as a result of the dynamic balance between the effects of third order of linear dispersion and dispersion of nonlinearity. As it was mentioned before, this shift is significant in attosecond and femtosecond regions [4,10]. For laser pulses with many oscillations under the envelope, two additional terms in equation (9) do not impact the soliton evolution and do not lead to a noticeable temporal shift. Decreasing the number of oscillations, the effect becomes important. This phenomena is explained in the frames of the applied mathematical model [29,32] and the influence of higher-order nonlinear and dispersive effects [4,10].

## CONCLUSION

In the present paper, the evolution of optical pulses with broad-band spectrum in nonlinear dispersive $SiO_2$ medium is reviewed. A new exact analytical soliton solution of NAE (9) is found, in which the effects up to third order of linear dispersion and dispersion of nonlinearity are included. The expression (19) differs significantly from the standard soliton solution of NSE – the constants $\eta$ and $u$, connected with the amplitude and the velocity of the temporal shift, respectively, depend on the coefficients, characterizing the second and third order of the linear dispersion and the nonlinearity of the medium, as well as the number of harmonic oscillations at level *1/e* of maximum of the amplitude.

The analytical solution (19) and the numerical calculations of expression (20) answer to our question: *Is it possible a soliton in single-mode fibers to be formed under the simultaneous influence of TOD and self-steepening effects*? Fig.4 and Fig.5 show that in such media it is possible a soliton to be observed. The pulse is stable and keeps its shape as a result of the dynamic balance between the higher-order nonlinear and dispersive effects.

## REFERENCES

1 P. Gibbon, Short Pulse Laser Interactions with Matter, London: Imperial College Press, (2007).
2 P. Tchofo Dinda, A. B. Moubissi, and K. Nakkeeran, *Phys. Rev. E* 64, 016608, (2001).
3 J. Santhanam and G. P. Agrawal, *IEEE J. Sel. Topics Quantum Electron.* 8, 632, (2002).
4 G. P. Agrawal, Nonlinear fiber optics, Academic Press, INC, New York, (2007).
5 Y. S. Kivshar and G. P. Agrawal, Optical Solitons: From Fibers to Photonic Crystals, San Diego: Academic Press, (2003).
6 F. Abdullaev, S. A. Darmanian, P. Khabibullaev, Optical solitons, London: Springer-Verlag, Berlin, (1993).
7 A. Hasegawa, F. Tappert, Transmission of stationary nonlinear optical pulses in dispersive dielectric fibers. I. Anomalous dispersion*, Appl. Phys. Lett.*, 23, 142, (1973).
8 J. S. Aitchison et al., *J. Opt. Soc. Am. B*, 8 1290, (1991).
9 A. Barthelemy, S. Maneuf and C. Froehly, *Opt. Commun*, 55 201, (1985).
10 Y. Xiao, D. N. Maywar, G. P. Agrawal, New approach to pulse propagation in nonlinear dispersive optical media, *JOSA B*, Vol. 29, Issue 10, pp. 2958-2963, (2012).
11 P. K. Wai, C. R. Menyuk, H. H. Chen, and Y. C. Lee, *Opt. Lett.* 12, 628 (1987).
12 M. Desaix, D. Anderson, and M. Lisak, *Opt. Lett.* 15, 18, (1990).
13 V. K. Mezentsev and S. K. Turitsyn, *Sov. Lightwave Commun.* 1, 263, (1991).
14 Y. S. Kivshar, *Phys. Rev. A* 43, 1677, (1981); Opt. Lett. 16, 892, (1991).
15 V. I. Karpman, Phys. Rev. E 47, 2073, (1993); *Phys. Lett. A* 181, 211, (1993).
16 A. Peleg and Y. Chung, J. Phys. A 26, 10029, (2003).
17 N. Tzoar and M. Jain, *Phys. Rev.* A 23, 1266, (1981).
18 E. A. Golovchenko, E. M. Dianov, A. M. Prokhorov, and V. N. Serkin, *JETP Lett.* 42, 87, (1985).

19 K. Ohkuma, Y. H. Ichikawa, and Y. Abe, *Opt. Lett.* 12, 516, (1987).

20 A. M. Kamchatnov, S. A. Darmanyan, and F. Lederer, *Phys. Lett. A* 245, 259, (1998).

21 W. P. Zhong and H. J. Luo, *Chinese Phys. Lett.* 17, 577, (2000).

22 M. Mirzazadeh et al., *Journal of Nonlinear Optical Physics and Materials*, 24 1 1550006, (2015).

23 Q. Zhou et al., *Laser Physics*, 25 2 025402, (2015).

24 A. Sardar et al., *Journal of Nanoelectronics and Optoelectronics*, 11 3 382-387, (2016).

25 H. M. Li, J. Q. Zhao and L. Y. You, Indian Journal of Physics, 89 10 1065-1075, (2015).

26 Vivek K. Sharma, *Indian Journal of Physics*, 1-6, (2016).

27 R. W. Boyd, Nonlinear optics, Third Edition, Academic Press, Orlando, (2003).

28 A. M. Dakova, D. Y. Dakova, Evolution of optical pulses with broadband spectrum in a nonlinear dispersive media, *Bulg. J. Phys.* 40, 182–185, PACS codes: 42.81.-I, (2013).

29 A. M. Dakova, D. Y. Dakova, L. M. Kovachev and V. I. Slavchev, Comparison between the solutions of the general nonlinear amplitude equation and the modified Schrödinger equation, *Journal of Russian Laser Research*, Volume 37, Number 2, March (2016), p. 103-111.

30 D. Dakova, A. Dakova, V. Slavchev, L. Kovachev, Solitons in non-paraxial optics, *Journal of Optoelectronics and Advanced Materials*, Vol. 18, Iss. 5-6, May – June (2016), p. 435-439.

31 S. Krasteva and D. Dakova, *University of Plovdiv „Paisii Hilendarski" Scientific studies Physics*, 37 4, (2012).

32 A. Dakova, D. Dakova, L. Kovachev, Comparison of soliton solutions of the nonlinear Schrödinger equation and the nonlinear amplitude equation, *Proc. SPIE 9447, 18th International School on Quantum Electronics: Laser Physics and Applications*, 94471A (January 8, 2015); doi:10.1117/12.2177906, (2015).

# On the low-temperature critical behaviour of a quantum model of structural phase transitions

E. S. Pisanova[1*], Kr. T. Nikolova[2]

*[1]Faculty of Physics, University of Plovdiv "P. Hilendarski", 24 Tzar Assen Str., Plovdiv, Bulgaria*
*[2]Department of Mathematics and Physics, University of Food Technologies, 26 Maritza Blvd., Plovdiv, Bulgaria*

A quantum model describing structural phase transitions in an anharmonic crystal with long-range interaction (decreasing at large distances $r$ as $r^{-d-\sigma}$, where $d$ is the space dimensionality and $0 < \sigma \le 2$) is studied at low temperatures. A general expression for the specific heat capacity is derived in the low-temperature region of the $T$, $\lambda$ - phase diagram, where $T$ is the temperature and $\lambda$ is a quantum parameter, associated with the external pressure or the amount of doping. It is shown that in the vicinity of the quantum critical point ($T = 0$, $\lambda = \lambda_c$) this expression has a scaling form. The temperature dependence of the critical specific heat capacity $c(T)$ is established in the three regions of the phase diagram (renormalized classical region, quantum critical region and quantum disordered region). From the results obtained one can see that $c(T) \sim T^{2d/\sigma}$ in the renormalized classical region and in the quantum critical region, and $c(T)$ exponentially tends to zero in the quantum disordered region. The applicability of the results obtained to other models is discussed.

Keywords: bulk critical behaviour, low-temperature effects, specific heat capacity, long–range interaction

## INTRODUCTION

Over the past few decades the theory of zero-temperature quantum phase transitions, initiated in 1976 by Hertz, continues to be a subject of great interest [1-4]. These phase transitions, caused by quantum fluctuations rather than thermal ones, appear at zero temperature $(T = 0)$ as a function of some non-thermal control parameter (associated with pressure, doping concentration or magnetic fields) or a competition between different parameters describing the basic interaction of the system. Most importantly, the zero-temperature quantum phase transitions can have great impact on the leading $T$ dependence of all observables for a relatively large region of rather low temperatures, compared to characteristic excitation in the system. The low-temperature effects can be explored in the framework of the theory of finite-size scaling (FSS) [5-10]. The most famous model for discussing these properties is the quantum nonlinear $O(n)$ sigma model (QNLσM) [5-7], [11-13]. Its equivalence (in the limit $n \to \infty$) with a quantum version of the spherical model, known as the spherical quantum rotors model (SQRM), has been given in [14]. The SQRM is suitable for a joint description of the quantum and classical fluctuations in dependence on the dimensionality and the geometry of the system [8, 9], [15, 16].

Here we consider a more realistic quantum model with long-range interaction (decreasing at large distances $r$ as $r^{-d-\sigma}$, where $d$ is the space dimensionality and $0 < \sigma \le 2$), intended to describe structural phase transitions [17]. The main feature of this model is that the real anharmonic interaction is substituted by its quantum mean spherical approximation reducing the problem to an exactly solvable one. Its exact solvability has been proven in [18]. The relation of this model with the SQRM has been commented in [8]. A rigorous proof of the effect of its quantum fluctuations has been given in [19]. The bulk critical behaviour of the model on the whole $(T, \lambda)$-phase diagram, where $\lambda$ is a quantum parameter, has been studied in [20]. In real systems a phase transition driven by $\lambda$ can be observed by changing the external pressure or the amount of doping. The finite-size corrections to the free energy for the pure quantum version $(T = 0)$ of the model have been derived in [21]. For a more complete discussion of the bulk critical behaviour and the finite-size properties of the model and its generalizations, see Chapter 3 of [16]. In the context of this model it has been shown [22-24] that the Lambert W-function can be applied for a more exact computation of non-universal critical properties with leading logarithmic behaviour at the upper critical dimension of the system.

In this paper we study the low-temperature behaviour of the bulk specific heat capacity in the vicinity of the quantum critical point $(T = 0, \lambda = \lambda_c)$ for different space dimensionalities

* To whom all correspondence should be sent:
   katia_pisanova@abv.bg

$(\sigma/2 < d < 3\sigma/2)$ of the system and in different regions of the $(T, \lambda)$-phase diagram.

Let us note that results for the bulk critical specific heat capacity of classical systems $(\lambda = 0)$ for $d = 2\sigma$ [24] and of quantum systems in the low-temperature region for $d = \sigma$ [25] are available.

## THE MODEL

The Hamiltonian of the model is [16, 17]

$$H = \frac{1}{2}\sum_{\mathbf{r}}\left(\frac{P_{\mathbf{r}}^2}{m} - AQ_{\mathbf{r}}^2\right) + \frac{1}{4}\sum_{\mathbf{r},\mathbf{r}'}\varphi(\mathbf{r}-\mathbf{r}')(Q_{\mathbf{r}} - Q_{\mathbf{r}'})^2$$
$$+ \frac{B}{4N}\left(\sum_{\mathbf{r}}Q_{\mathbf{r}}^2\right)^2, \qquad (1)$$

where $P_{\mathbf{r}}$ and $Q_{\mathbf{r}}$ are the operators of the momentum and displacement, respectively, of the particle of mass $m$ at the site $\mathbf{r}$ of a $d$-dimensional hypercubic lattice. The parameter $A = mv_0^2 > 0$ determines the frequency of a mode which is unstable in the harmonic approximation and the parameter $B > 0$ introduces an anharmonic interaction which is inversely proportional of the particle number $N$. The harmonic force constants $\varphi(\mathbf{r}-\mathbf{r}')$, which are assumed to decrease at large distances $r = |\mathbf{r}-\mathbf{r}'|$ as $r^{-d-\sigma}$, describe a short-range $(\sigma = 2)$ or a long-range $(0 < \sigma < 2)$ interaction.

The free energy density of the model (1), obtained by using the Approximating Hamiltonian Method, is [18]

$$f = \frac{A^2}{B}f_0 = \frac{A^2}{2B}\left[I_{d,\sigma}(\lambda, t, \overline{\Delta}) - \frac{1}{2}(1+\overline{\Delta})^2\right], \quad (2)$$

where $\overline{\Delta}$ is the solution of the self-consistent equation

$$\frac{\partial I_{d,\sigma}(\lambda, t, \Delta)}{\partial \Delta} = 1 + \Delta. \qquad (3)$$

In the thermodynamic limit $N \to \infty$ the function $I_{d,\sigma}(\lambda, t, \overline{\Delta})$ is defined by

$$I_{d,\sigma}(\lambda, t, \Delta) = 2k_d t\int_0^{x_D} x^{d-1}\ln\left(2\sinh\left(\frac{\lambda}{2t}\sqrt{\Delta + x^\sigma}\right)\right)dx,$$
$$\qquad (4)$$

where $t = T/(4E_0)$ is the dimensionless temperature and $\lambda = \hbar v_0/(4E_0)$ is a quantum parameter which is a function of the external pressure or the amount of doping, $E_0 = A^2/(4B)$ is the barrier height of the double well potential in Eq.(1), $x_D = 2\pi(d/S_d)^{1/d}$ is the radius of the effective sphere replacing the Brillouin zone and $k_d = 2(4\pi)^{-d/2}/\Gamma(d/2)$ ($\Gamma(x)$ is the Euler gamma function).

In the disordered phase $(t > t_c)$ $\overline{\Delta}$ is finite and the susceptibility of the system is $\chi = \overline{\Delta}^{-1}$. Setting $\overline{\Delta} = 0$ into Eq. (3) one obtains the critical temperature $t_c(\lambda)$. At the critical value $\lambda_c = (2 - \sigma/d)x_D^{\sigma/2}$ of the quantum parameter the critical temperature is reduced to zero, $t_c(\lambda_c) = 0$.

Eqns. (2) and (3) provide the basis for studying the critical behaviour of the model. For the specific heat capacity $c(T) \equiv -T(\partial^2 f/\partial T^2)$, taking into account Eq. (3), one obtains

$$c(t) = -t\frac{\partial^2 f_0}{\partial t^2} = -\frac{t}{2}\left[\frac{\partial^2 I_{d,\sigma}(\lambda, t, \overline{\Delta})}{\partial t^2}\right.$$
$$\left. + \frac{\partial^2 I_{d,\sigma}(\lambda, t, \overline{\Delta})}{\partial \overline{\Delta}\partial t}\left(\frac{\partial \overline{\Delta}}{\partial t}\right)\right]. \qquad (5)$$

Let us note that Eq. (3) is similar to the mean-spherical constraint in the SQRM up to the linear $\Delta$-term in the right side of Eq. (3) [8, 9]. This term appears to be essential only above the upper critical dimension.

## A GENERAL EXPRESSION FOR THE SPECIFIC HEAT AT LOW TEMPERATURES

At low temperatures the integral, given by Eq. (4), has been studied in the framework of the SQRM for $\sigma = 2$ [8, 9] and $0 < \sigma \le 2$ [15]. In the low-temperature region $(\lambda/t \gg 1)$ it can be presented in the form

$$I_{d,\sigma}(\lambda,t,\Delta) = 2\lambda A_{d,\sigma}(\Delta) - 2t B_{d,\sigma}\left(\frac{2t}{\lambda}, \frac{\lambda}{2t}\sqrt{\Delta}\right). \quad (6)$$

In Eq. (6) the function $A_{d,\sigma}(\Delta)$, expressed in terms of the hypergeometric function $_2F_1(a,b;c;z)$, has the form

$$A_{d,\sigma}(\Delta) = \frac{k_d x_D^d}{2d}\sqrt{x_D^\sigma + \Delta}\,_2F_1\left(-\frac{1}{2},1;1+\frac{d}{\sigma};\frac{x_D^\sigma}{x_D^\sigma + \Delta}\right), \quad (7)$$

and the function $B_{d,\sigma}(x,y)$ is

$$B_{d,\sigma}\left(\frac{2t}{\lambda},\frac{\lambda}{2t}\sqrt{\Delta}\right) = \frac{k_d}{\sqrt{\pi}\sigma}\Gamma\left(\frac{d}{\sigma}\right)\left(\frac{2t}{\lambda}\right)^{2\frac{d}{\sigma}}$$

$$\times \tilde{K}\left(\frac{d}{\sigma}+\frac{1}{2},\frac{\lambda}{2t}\sqrt{\Delta}\right), \quad (8)$$

where the function

$$\tilde{K}(\nu,y) \equiv y^{2\nu} K(\nu,y) \quad (9)$$

is introduced. The function $K(\nu,y)$ in Eq. (9) has been defined and studied in [8, 9]:

$$K(\nu,y) \equiv 2\sum_{m=1}^{\infty}(my)^{-\nu}K_\nu(2my)$$

$$= \frac{\sqrt{\pi}}{2}\Gamma\left(\frac{1}{2}-\nu\right)y^{-1}+\Gamma(\nu)\varsigma(2\nu)y^{-2\nu}-\frac{1}{2}\Gamma(-\nu)$$

$$+\pi^{2\nu-\frac{1}{2}}\Gamma\left(\frac{1}{2}-\nu\right)y^{-2\nu}\sum_{m=1}^{\infty}\left[\left(m^2+\frac{y^2}{\pi^2}\right)^{\nu-\frac{1}{2}}-m^{2\nu-1}\right], \quad (10)$$

where $K_\nu(x)$ is the MacDonald function (second modified Bessel function) and $\varsigma(x)$ is the Riemann zeta function. The asymptotic form of the function $\tilde{K}(\nu,y)$ at $y \ll 1$, obtained by using the asymptotic form of the function $K(\nu,y)$ [8, 9], for $1 < \nu < 3/2$ and $3/2 < \nu < 2$ is

$$\tilde{K}(\nu,y) \approx \frac{\pi^{1/2}}{2}\Gamma\left(\frac{1}{2}-\nu\right)y^{2\nu-1}+\Gamma(\nu)\varsigma(2\nu)$$

$$+\pi^{2\nu-5/2}\left(\nu-\frac{1}{2}\right)\Gamma\left(\frac{1}{2}-\nu\right)\zeta(3-2\nu)y^2$$

$$-\frac{1}{2}\Gamma(-\nu)y^{2\nu}. \quad (11)$$

For the specific heat capacity at low temperatures, from Eqns. (5)-(8), we obtain the following expression

$$c(t) = \frac{k_d}{\sqrt{\pi}\sigma}\Gamma\left(\frac{d}{\sigma}\right)\left[\Phi_1\left(\frac{d}{\sigma}+\frac{1}{2},\frac{\lambda}{2t}\sqrt{\overline{\Delta}}\right)\right.$$

$$\left.+\frac{1}{2}\Phi_2\left(\frac{d}{\sigma}+\frac{1}{2},\frac{\lambda}{2t}\sqrt{\overline{\Delta}}\right)\left(\frac{t}{\overline{\Delta}}\frac{\partial\overline{\Delta}}{\partial t}\right)\right]\left(\frac{2t}{\lambda}\right)^{2d/\sigma}, \quad (12)$$

in which the functions

$$\Phi_1(\nu,y) \equiv 2\nu(2\nu-1)\tilde{K}(\nu,y)$$

$$+2(4\nu-3)y^2\tilde{K}(\nu-1,y)+4y^4\tilde{K}(\nu-2,y) \quad (13)$$

and

$$\Phi_2(\nu,y) \equiv -4(\nu-1)y^2\tilde{K}(\nu-1,y)-4y^4\tilde{K}(\nu-2,y) \quad (14)$$

are introduced and $\overline{\Delta} = \chi^{-1}$ is the solution of the equation for the inverse susceptibility, Eq. (3), in the low-temperature region.

In the next section we present results for the low-temperature critical inverse susceptibility of the model for systems with different space dimensionalities $d$ in different regions of the $(t,\lambda)$-phase diagram. These results (see also [16] and [20]) will be used in obtaining the corresponding expressions for the critical specific heat capacity.

## THE LOW-TEMPERATURE CRITICAL INVERSE SUSCEPTIBILITY

In the low-temperature region close to the quantum critical point $(\Delta \ll 1)$ for $1/2 < d/\sigma < 3/2$ Eq. (3) has the form

$$\frac{k_d}{2\sqrt{\pi}\sigma}\Gamma\left(\frac{d}{\sigma}\right)\Delta^{\frac{d}{\sigma}-\frac{1}{2}}\left[2K\left(\frac{d}{\sigma}-\frac{1}{2},\frac{\lambda}{2t}\sqrt{\Delta}\right)\right.$$

$$-\left|\Gamma\left(\frac{1}{2}-\frac{d}{\sigma}\right)\right|\right] = \frac{1}{\lambda} - \frac{1}{\lambda_c}, \qquad (15)$$

where $\lambda_c$ is the quantum critical point and the function $\mathrm{K}(v, y)$ is given by Eq. (10).

On the line $\lambda = \lambda_c$ $(t \to 0^+)$ the solution of Eq. (15) is given by

$$\overline{\Delta} = D_1 t^{\gamma_T^q}, \qquad (16)$$

where the critical exponent $\gamma_T^q = 2$, $D_1 = 4y_0^2/\lambda_c^2$ and $y_0$ is the solution of the equation $\left|\Gamma(1/2 - d/\sigma)\right| = 2\mathrm{K}(d/\sigma - 1/2, y)$. The behaviour of the universal constant $y_0$ as a function of the dimensionality $d$ of the system in the case of short-range $(\sigma = 2)$ interaction is graphically represented in [8, 9].

By using the critical exponent $\gamma_\lambda = \sigma/(d - \sigma)$, the solution of Eq. (15) can be presented in the form (see [16])

$$\overline{\Delta} \approx D_2 \varepsilon^{\gamma_\lambda} t^{-\gamma_\lambda}, \qquad (17)$$

where $D_2 = \left[\sigma\left|\sin(\pi d/\sigma)\right|/(k_d \pi)\right]^{\gamma_\lambda}$, in the two cases: (i) for $1/2 < d/\sigma < 1$ at $\lambda < \lambda_c$, in Eq. (17) $\varepsilon = 1 - \lambda/\lambda_c$, i.e. in the system there is a phase transition driven by $t$ $(t \to 0^+)$ and (ii) for $1 < d/\sigma < 3/2$ at $\lambda_c(t) < \lambda < \lambda_c$, in Eq. (17) $\varepsilon = \lambda/\lambda_c(t) - 1$, i.e. at finite temperatures in the system there is a phase transition driven by $\lambda$ for very close values of $\lambda$ to the "shifted" critical value $\lambda_c(t)$.

For $1/2 < d/\sigma < 3/2$ at $\lambda > \lambda_c$ sufficiently close to the quantum critical point by using the critical exponents $\gamma_\lambda^q = 2\sigma/(2d - \sigma)$ and $\phi_T = \sigma/(2d - \sigma)$ the solution of Eq. (15) can be written as (see [16])

$$\overline{\Delta} \approx D_3 \varepsilon^{\gamma_\lambda^q} \left(\frac{t}{\varepsilon^{\phi_T}}\right)^{(\gamma_\lambda^q - \gamma_\lambda)/\phi_T}, \qquad (18)$$

where $D_3 = \left\{2\sigma\sqrt{\pi}/\left[k_d \Gamma(d/\sigma)\left|\Gamma(1/2 - d/\sigma)\right|\right]\right\}^{\gamma_\lambda^q}$ and $\varepsilon = 1/\lambda_c - 1/\lambda$.

In the important case $d = \sigma$ Eq. (15) is simplified considerably and has the form

$$2\sinh\left(\frac{\lambda}{2t}\sqrt{\overline{\Delta}}\right) = \exp\left[-\frac{\sigma}{2k_\sigma t}\left(1 - \frac{\lambda}{\lambda_c}\right)\right], \qquad (19)$$

where $k_\sigma = 2(4\pi)^{-\sigma/2}/\Gamma(\sigma/2 + 1)$. Its solutions are as follows: (i) on the line $\lambda = \lambda_c$ and $t \to 0^+$, i.e. in the quantum critical region,

$$\overline{\Delta} = \Theta^2 t^2/\lambda_c^2, \qquad (20)$$

where $\Theta = 2y_0 = 2\ln\left[\left(1 + \sqrt{5}\right)/2\right] = 0.962424...$ is a universal constant [8, 9]; (ii) in the region where $(1 - \lambda/\lambda_c)/t \gg 1$ and $\lambda < \lambda_c$, i.e. in the renormalized classical region,

$$\overline{\Delta} \approx \frac{t^2}{\lambda^2}\exp\left[-\frac{\sigma(1 - \lambda/\lambda_c)}{k_\sigma t}\right]; \qquad (21)$$

(iii) for $(\lambda/\lambda_c - 1)/t \gg 1$ and $\lambda > \lambda_c$, i.e. in the quantum disordered region,

$$\overline{\Delta} \approx \frac{\sigma^2(\delta\lambda)^2}{k_\sigma^2}\left[1 + \frac{4k_\sigma t}{\sigma\lambda\delta\lambda}\exp\left(-\frac{\lambda\delta\lambda}{k_\sigma t}\right)\right], \qquad (22)$$

where $\delta\lambda = 1/\lambda_c - 1/\lambda$. The first term in Eq. (22) is a particular case of Eq. (18) for $d = \sigma$.

Let us note that Eqns. (16)-(18) have been obtained in [20] (see also [16]) in another way. At $\sigma = 2$ Eqns. (16)-(22) coincide with the corresponding ones for the spherical field obtained in [8, 9] for the SQRM with short-range interaction.

## THE LOW-TEMPERATURE CRITICAL SPECIFIC HEAT CAPACITY

In the vicinity of the quantum critical point for $1/2 < d/\sigma < 3/2$, taking into account the temperature dependence of $\overline{\Delta}$, it is easy to see that Eq. (12) has a scaling form, where $\lambda\sqrt{\overline{\Delta}}/2t$ and $2t/\lambda$ are the scaling variables.

For $1/2 < d/\sigma < 3/2$ at $\lambda = \lambda_c$ and $t \to 0^+$, i.e. *in the quantum critical region*, substituting Eq. (16) in Eq. (12), for the critical specific heat capacity we have

$$c(t) = \frac{k_d}{\sqrt{\pi}\sigma}\Gamma\left(\frac{d}{\sigma}\right)\left[\Phi_1\left(\frac{d}{\sigma}+\frac{1}{2},y_0\right)\right.$$

$$\left.+\Phi_2\left(\frac{d}{\sigma}+\frac{1}{2},y_0\right)\right]\left(\frac{2t}{\lambda}\right)^{2d/\sigma}. \qquad (23)$$

For $1/2 < d/\sigma < 1$ at $(1-\lambda/\lambda_c)/t \gg 1$, i.e. *in the renormalized classical region*, and for $1 < d/\sigma < 3/2$ in the region where $(\lambda/\lambda_c(t)-1)/t \ll 1$ and $\lambda_c(t) < \lambda < \lambda_c$, from Eq. (12) and Eq. (17), by using the asymptotic forms of the functions $\Phi_1(\nu,y)$ and $\Phi_2(\nu,y)$ at $y \ll 1$, we obtain

$$c(t) \approx \left[\frac{4k_d}{\sigma\sqrt{\pi}}\Gamma\left(\frac{d}{\sigma}+1\right)\Gamma\left(\frac{d}{\sigma}+\frac{3}{2}\right)\right.$$

$$\left.\times\varsigma\left(\frac{2d}{\sigma}+1\right)\right]\left(\frac{2t}{\lambda}\right)^{\frac{2d}{\sigma}}. \qquad (24)$$

For $1/2 < d/\sigma < 3/2$ when $(\lambda/\lambda_c-1)/t \gg 1$, i.e. *in the quantum disordered region*,

$$c(t) \approx \frac{k_d}{\sqrt{\pi}\sigma}\Gamma\left(\frac{d}{\sigma}\right)\Phi_{1\infty}\left(\frac{d}{\sigma}+\frac{1}{2},\frac{\lambda}{2t}\sqrt{\bar{\Delta}}\right)\left(\frac{2t}{\lambda}\right)^{\frac{2d}{\sigma}}, \qquad (25)$$

where $\bar{\Delta}$ is given by Eq. (18) and by $\Phi_{1\infty}(\nu,y)$ is denoted the asymptotic form of the function $\Phi_1(\nu,y)$, defined by Eq. (13), for $y \gg 1$.

In the particular case $d = \sigma$ the functions $\Phi_1(3/2,y)$ and $\Phi_2(3/2,y)$ in Eq. (12) are expressed in terms of the polylogarithmic function $Li_s(x)$,

$$\Phi_1\left(\frac{3}{2},y\right) = \sqrt{\pi}\left[3Li_3\left(e^{-2y}\right)+6yLi_2\left(e^{-2y}\right)\right.$$

$$\left.+6y^2Li_1\left(e^{-2y}\right)+4y^3Li_0\left(e^{-2y}\right)\right] \qquad (26)$$

and

$$\Phi_2\left(\frac{3}{2},y\right) = -2\sqrt{\pi}\left[y^2Li_1\left(e^{-2y}\right)+2y^3Li_0\left(e^{-2y}\right)\right]. \qquad (27)$$

By using Eqns. (20)-(22) we obtain the critical specific heat capacity in the tree regions: (i) for $\lambda = \lambda_c$ and $t \to 0^+$, i.e. *in the quantum critical region*,

$$c(t) = \frac{k_\sigma}{\sigma}\left[3Li_3\left(e^{-\Theta}\right)+3\Theta Li_2\left(e^{-\Theta}\right)\right.$$

$$\left.+\Theta^2Li_1\left(e^{-\Theta}\right)\right]\left(\frac{2t}{\lambda_c}\right)^2; \qquad (28)$$

(ii) for $(1-\lambda/\lambda_c)/t \gg 1$, i.e. *in the renormalized classical region*,

$$c(t) \approx \frac{3\varsigma(3)k_\sigma}{\sigma}\left(\frac{2t}{\lambda}\right)^2; \qquad (29)$$

(iii) for $(\lambda/\lambda_c-1)/t \gg 1$ and $\lambda > \lambda_c$, i.e. *in the quantum disordered region*,

$$c(t) \approx \frac{2\sigma^2\lambda_c(\delta\lambda)^3}{k_\sigma^2 t}\exp\left[-\frac{\sigma\lambda_c}{k_\sigma}\left(\frac{\delta\lambda}{t}\right)\right]. \qquad (30)$$

In obtaining Eq. (29) and Eq. (30) the asymptotic forms of the functions $\Phi_1(3/2,y)$ and $\Phi_2(3/2,y)$ for $y \ll 1$ and $y \gg 1$ are used, respectively. Let us note that Eq. (30) is a particular case of Eq. (25).

The results for $d = \sigma$ have been obtained in [25].

## CONCLUSIONS

In the present study we are interested in the low-temperature behaviour of the critical specific heat capacity of a quantum model with long-range interaction, intended to describe structural phase transitions, Eq. (1).

A general expression for the specific heat capacity in the low-temperature region $(\lambda/t \gg 1)$ of the $(t,\lambda)$-phase diagram, Eq. (12), is derived. Taking into account the temperature dependence of the inverse susceptibility, Eqns. (16)-(18), it is easy to see that in the vicinity of the quantum critical point $(t=0,\lambda=\lambda_c)$ for $1/2 < d/\sigma < 3/2$ Eq. (12) has a scaling form.

The temperature dependence of the critical specific heat capacity $c(t)$ is obtained in the three

regions of phase diagram (renormalized classical region, quantum critical region and quantum disordered region). From Eqns. (23), (24), (28)-(30) one can see that $c(t)$ is going to zero as $t$ raised to the power $2d/\sigma$ in the renormalized classical region and in the quantum critical region, and $c(t)$ exponentially tends to zero as $t \to +0$ in the quantum disordered region.

Finally, the results obtained here for the low-temperature specific heat capacity are directly applicable to the more popular SQRM.

## ACKNOWLEDGEMENTS

## REFERENCES

1  D. Belitz, T. R. Kirkpatrick, *Rev. Mod. Phys.* 66, 261 (1994).
2  S. L. Sondhi, S. M. Girvin, J. P. Carini, D. Shahar, *Rev. Mod. Phys.* 69, 315 (1997).
3  P. Coleman, A. J. Schofield, *Nature* 433, 226 (2005).
4  S. Sachdev, B. Keimer, *Phys. Today* 64, No. 2, 29 (2011).
5  S. Chakravarty, B. I. Halperin, D. R. Nelson, *Phys. Rev. B* 39, 2344 (1989).
6  A. V. Chubukov, S. Sachdev, J. Ye, *Phys. Rev. B* 49, 11919 (1994).
7  S. Sachdev, *Z. Phys. B* 94, 469 (1994).
8  H. Chamati, D. M. Danchev, E. S. Pisanova, N. S. Tonchev, Low-temperature regimes and finite-size scaling in a quantum spherical model, Preprint IC/97/82, ICTP, Trieste (1997).
9  H. Chamati, E. S. Pisanova, N. S. Tonchev, *Phys. Rev. B* 57, 5798 (1998).
10 H. Chamati, N. S. Tonchev, *J. Phys. A: Math. Gen.* 33, 873 (2000).
11 B. Rosenstein, J. Warr, S. H. Park, *Nucl. Phys. B* 336, 13336, 435 (1990).
12 A. H. Castro Neto, E. Fradkin, *Nucl. Phys. B* 400, 525 (1990).
13 A. Fujii, T. Inami, *Prog. Theor. Phys.* 118, 229 (1995).
14 T. Vojta, *Phys. Rev. B* 53, 710 (1996).
15 H. Chamati, D. M. Danchev, N. S. Tonchev, *Eur. Phys. J. B* 14, 307 (2000).
16 J. G. Brankov, D. M. Danchev, N. S. Tonchev, in: *Series in Modern Condensed Matter Physics* 9 (World Scientific, Singapore, 2000).
17 T. Schneider, E. Stoll, H. Beck, *Physica A* 79, 201 (1975).
18 N. M. Plakida, N. S. Tonchev, *Physica A* 136, 176 (1986).
19 A. Verbeure, V. A. Zagrebnov, *J. Stat. Phys.* 79 377 (1995).
20 E. S. Pisanova, N. S. Tonchev, *Physica A* 197, 301 (1993).
21 H. Chamati, *Physica A* 212, 357 (1994).
22 E. S. Pisanova, N. S. Tonchev, *J. Phys.: Conf. Ser.* 253, 012020 (2010).
23 E. S. Pisanova, S. Ivanov, *Bulg. J. Phys.* 40, 159 (2013).
24 E. S. Pisanova, S. Ivanov, *J. Phys.: Conf. Ser.* 558, 012019 (2014).
25 E. S. Pisanova and A. Y. Krushkov, *AIP Conf. Proc.* 1722, 220016 (2016).

# Kinetic studies of β-galactosidase immobilized in chitosan/xanthan multilayers

I. N. Iliev[1], M. G. Marudova[2], D. S. Cholev[1], T. A. Vasileva[1], V. P. Bivolarski[1], A. P. Viraneva[2], I. P. Bodurov[2], T. A. Yovcheva[2*]

*[1]Department of Biochemistry & Microbiology, Plovdiv University, 24, Tzar Assen, str, 4000, Plovdiv, Bulgaria*
*[2]Department of Experimental Physics, Plovdiv University, 24, Tzar Assen, str, 4000, Plovdiv, Bulgaria*

A study of the kinetic parameters of β-galactosidase produced from *Aspergillus niger* was carried out in the present work. This enzyme was immobilized in chitosan and xanthan polyelectrolyte multilayers (PEMs) deposited by dip coating method on corona charged polylactic acid pads. The enzyme activity showed a temperature optimum at 50 °C and a pH optimum at 5.0. The effects of lactose concentrations on the initial velocity of the enzyme reaction were also compared and Michaelis-Menten constans were calculated at 53.4 mmol of lactose. These results gave insights for further optimization of transgalactosydase reactions in order to obtain lactulose and other specific galactooligosaccharides having pronounced bioactive properties.

**Keywords:** β-galactosidase, lactose, kinetics, transgalactosylation, multilayers

## INTRODUCTION

β-Galactosidases (EC 3.2.1.23) also known as lactases are enzymes belonging to glycoside hydrolase families 1, 2, 35, 42 and 59 (GH1, GH2, GH35, GH42 and GH59) [1]. These enzymes catalyze the hydrolysis of terminal non-reducing β-D-galactose residues in β-D-galactoside substrates. In the case of lactose as a substrate the products of hydrolysis – namely glucose and galactose are transferred to water. When the initial concentration of lactose is more that 15%, acceptor of galactose residue can be another carbohydrate presents in the reaction mixture – for example lactose, fructose or lactulose, and an transgalactosylation reaction is observed, resulting in production of galactooligosaccharides (GalOSs) with a different degree of polymerization (DP) [2, 3]. Known microbial sources of β-galactosidases are bacteria (*Bacillus*, *Lactobacillus*, *Bifidobacterium*, *Escherichia*), yeasts (*Kluyveromyces*, *Sterigmatomyces*) and fungal producers (*Aspergillus*) [3, 4]. Among these producers, the commercial preparations from *Kluyveromyces lactis* (Lactozym 3000L and Maxilact LGX 5000), *Aspergillus oryzae* (Enzeco® Fungal Lactase) and *Bacillus circulans* (Biolacta – Daiwa Kasei and Biolactase) are applied mainly for the hydrolysis of lactose in dairy industry concerning lactose intolerance in significant part of human populations [5]. On the other hand the GalOSs synthesized by β-galactosidases contain variety of bonds including β-(1→4), β-(1→6) and β-(1→3), which

determines their application as food additives with significant prebiotic potential and other beneficial effects [3, 4]. The amount and structure of the synthesized GalOSs are significantly affected by the enzyme source, the acceptor molecules and the reaction conditions (substrate concentration, pH and temperature) [6-8].

The review [9] sheded light on the strategic advantages of the microscale promising technology for the development and realization of biocatalytic processes and subsequent product recovery steps.

The immobilization of enzymes into polymer matrices is widely used in biotechnology. This technique makes it possible to increase the functional efficiency of enzyme, enhance the reproducibility of the processes, improve the process control and ensure stable supply of the products in the market [10]. The basic idea of enzyme immobilization is to entrap the protein in a semi-permeable support material, which prevents the enzyme from leaving while allowing substrates, products, and co-factors to pass through [11]. The main requirements for the immobilizing matrix are that the material should be non-degradable and compatible with the enzymes. The immobilization process should be mild enough and not to denature the enzyme during preparation [12].

One of the suitable and mostly used natural polymers for enzyme immobilization is chitosan. It is characterized as biocompatible, nontoxic, physiologically inert, and hydrophilic, offers the unique characteristic of a remarkable affinity to proteins and has been widely applied in medicine and biological research. Furthermore, chitosan is positively charged in acidic aqueous solutions and its charge density is high [13].

---

* To whom all correspondence should be sent:
  yovchevat@gmail.com

The effect of the support size on the properties of enzyme immobilization was investigated by using chitosan macroparticles and nanoparticles in [14]. β-Galactosidase was used as a model enzyme. It was found that the different sizes and porosities of the particles modify the enzymatic load, activity, and thermal stability of the immobilized biocatalysts. The biocatalysts thermal stability was improved for macroparticles, especially under reactive conditions (presence of lactose) in comparison with the free enzyme. Besides, both preparations could be reused for 50 repeated batches in the lactose hydrolysis without any outstanding loss of enzyme activity.

In [15] the suitability of spray drying as a method for the preparation of cross-linked chitosan microparticles with immobilizes laccase, and the influence of process parameters, composition and cross-linking method on the properties of the resulting microparticles and the activity of the immobilized enzyme were investigated.

Alginate–chitosan core-shell microcapsules were prepared in order to develop a biocompatible matrix for enzyme immobilization, where the protein is retained either in a liquid or solid core and the shell allows permeability control over substrates and products. In [16] alginate–chitosan core-shell microcapsules were prepared as a novel biocompatible matrix system for β-galactosidase enzyme immobilization where the catalyst is confined to either a liquid or solid core and the transport properties of the substrate and product are dictated by the permeability of the shell. Thus the biological agent is protected in the inner biocompatible alginate core and the outer chitosan shell dictates the transport properties.

The method of surface modification by layer-by-layer (LbL) polyelectrolyte multilayers allows very precise control and changes in a wide range of the carrier's physicochemical properties — thickness, charge, hydrophilic–hydrophobic balance [17]. Such multilayer coatings with included functional components (nanoparticles, enzymes, and dyes) may be used in microelectronics, optics, biotechnology, and pharmacy [18]. The LbL technique is based on a sequential deposition of oppositely charged polyelectrolytes from their solutions via electrostatic interactions. The assembly is based on spontaneous adsorptions, no stoichiometric control is necessary to maintain surface functionality, and the assembled films have good thermal and mechanical stability [19]. In [20] the immobilization of α-chymotrypsin on the surface of boron silicate glass microspheres is conducted via the technique of multilayer adsorption of polyelectrolytes. It is shown that the enzyme is adsorbed on both positively and negatively charged surfaces and its activity is partially preserved relative to that in solution. It was established that the activity of the enzyme depends on the number of polyectrolyte layers preliminarily adsorbed on glass microspheres and on the charge of the surface. The activity of α-chymotrypsin adsorbed on the negatively charged surface is four times higher than the activity of this enzyme adsorbed on a positively charged surface.

The aim of the present work is to describe the immobilization of the β-galactosidase enzym in chitosan/xanthan multylayers deposited on corona charged polylactic acid pads. Emphasis was focused on the effect of the number and the sequence of the multilayers on the immobilized enzyme functional properties.

## MATERIALS AND METHODS

### Enzyme activity

A commercial fungal β-galactosidase (from *Aspergillus niger*) was used in the current kinetic studies. One unit of β-galactosidase activity is defined as the amount of enzyme catalyzing the release of 1 μmol min$^{-1}$ ortho-nitrophenol at 37 °C and pH 5.0. The influence of the substrate concentration on the initial velocity of the enzyme reaction was studied at a range 0.01 M – 1.30 M lactose. β-Galactosidase activity was studied in the presence of lactose – 1%, 5%, and 10% and mixtures of chitosan (0.1%) and lactose (1%, 5%, and 10%). One unit of β-galactosidase activity is defined as the amount of enzyme catalyzing the release of 1 μmol min$^{-1}$ glucose or fructose at 37 °C and pH 5.0. The concentrations of the released glucose and fructose were determined enzymatically [21]. Protein concentration was assayed by the method of Bradford [22]. All the analyses were performed at least in triplicate. Programmable scientific calculation "CITIZEN" SRP-45N and SigmaPlot 12.0 (Systat Software, Inc) were used for data analysis.

### Samples preparation

Biodegradable pads were prepared from polylactic acid (PLA) with ester end groups and intrinsic viscosity 0.55 - 0.75 dL/g purchased from Lactel Absorbable Polymers (USA). The PLA pads were cast from 2% w/v PLA solution in chloroform and dried at 35 °C for 48 hours. Then the PLA pads were kept for 24 hours in an exicator, at room

temperature, and 54% relative humidity (RH). Before the deposition process, the pads were charged in a corona discharge system, consisting of a corona electrode (needle), a grounded plate electrode, and a metal grid placed between them. Positive or negative 5 kV voltage was applied to the corona electrode. 1 kV voltage of the same polarity as that of the corona electrode was applied to the grid. The samples were charged under standard room conditions (T = 21÷23 °C and RH = 50-60%) for one minute. The polylactic acid electret properties are described in [23].

### Polyelectrolyte multilayers deposition

Xanthan gum and chitosan (low molecular weight) were purchased from Sigma-Aldrich. They were used without further purification or characterization. The layer-by-layer (LbL) deposition technique was applied for multilayer build-up. For the LbL assembly 0.1% w/v chitosan and 0.05% w/v xanthan solutions in acetate buffer (pH 5 and ionic strength 0.1 M) were prepared. 1 g/L β-galactosidase was dissolved in the chitosan solution just before the deposition process. The deposition was done by the dip-coating process. The first built-up layer always possesses opposite to the pad electric charge. A slide stainer (Poly Stainer IUL, Spain) was used with the following program: 15 min dipping process – adsorption from the first polyelectrolyte solution, 5 min washing step in the acetate buffer (pH 5 and ionic strength 0.1 M), 15 min dipping process - adsorption from the second polyelectrolyte molecules of opposite charge; 5 min washing in the same acetate buffer. The procedure was repeated until obtaining the desired numbers of even layers (8, 14 or 20 xanthan/chitosan or chito-san/xanthan). After the deposition of the last layer the film was dried in hot air. The produced PEMs structures were stored in an exicator at 55% RH.

## RESULTS AND DISCUSSION

### Effect of type of PEMs on immobilization and enzyme activity

The effect of the initial concentration of lactose on the enzyme activity of β-galactosidase was studied. Enzyme activity was measured under various immobilization procedures in different types of PEMs. Chitosan was selected as a material for polyelectrolyte multilayer preparation for several reasons - cationic biopolymer with intra- and intermolecular hydrogen bonding ability; unique approach to modify the surface of chitosan by anionic biopolymer xanthan to improve biocompatibility; and the possibility to prepare chitosan membranes with controlled pore size and density. The results of the enzyme activity measuring are shown in Table 1. The enzyme activity of immobilized β-galactosidase was compared with that of free enzyme using o-nitrophenol-β-D-galactopyranoside (ONPG) as a substrate. As it is shown in Table 1, the highest activity was determined for positively charged PLA pad with 14 multilayers. The immobilization efficiency indicated that significant amount of the enzyme was bond to the positively charged PLA pad with 14 multilayers of xanthan/chitosan. On the contrary, immobilization efficiency is almost 3 times less in negatively charged PLA pad with 14 multilayers of chitosan/xanthan. Obviously, in order to achieve a good enzyme activity the optimal configuration is 14 multilayers with consecutive xanthan/chitosan layer deposition. We have to note that the order of layer deposition is important. For the PEMs with 8 layers and with 14 layers we observed better enzyme activities with consecutive deposition of xanthan/chitosan layers. The enzyme activity was very low for the 20-layer PEMs.

**Table 1.** β-Galactosidase activity in different types of PEMs.

| Type of PEMs | Enzyme activity (U/ml) |
|---|---|
| Positively charged PLA pad with 8 multilayers | 0.0191 |
| Negatively charged PLA pad with 8 multilayers | 0.0104 |
| Positively charged PLA pad with 14 multilayers | 0.0557 |
| Negatively charged PLA pad with 14 multilayers | 0.0194 |
| Positively charged PLA pad with 20 multilayers | 0.0010 |
| Negatively charged PLA pad with 20 multilayers | 0.0011 |

### Effect of lactose concentration in 0.1% chitosan solution on enzyme activity

The operational stability of the studied enzyme was evaluated by the hydrolysis of buffered lactose solutions (1%; 5%; 10% w/v; pH 5.0) at 37 °C.

Lactose hydrolysis was performed at varying concentrations of lactose and with an enzyme concentration of 1 U/ml. As illustrated in Table 2, there is not any inhibition effect of 0.1% chitosan in 1% lactose.

**Table 2.** Lactose hydrolysis preformed with β-galactosidase

a) Concentration of lactose – 1%

| Time (h) | Glucose (mg/ml) | |
|---|---|---|
| | **1.0% Lactose** | **1.0% Lactose in 0.1% Chitosan** |
| 0 | 0.00 | 0.00 |
| 0.5 | 0.00 | 0.00 |
| 1.0 | 0.06 | 0.74 |
| 1.5 | 0.26 | 1.01 |
| 2.0 | 0.66 | 1.33 |
| 2.5 | 1.28 | 1.52 |
| 3.0 | 1.33 | 1.86 |

b) Concentration of lactose – 5 %

| Time (h) | Glucose (mg/ml) | |
|---|---|---|
| | **5.0% Lactose** | **5.0% Lactose in 0.1% Chitosan** |
| 0 | 0.00 | 0.00 |
| 0.5 | 0.38 | 0.28 |
| 1.0 | 1.63 | 1.85 |
| 1.5 | 1.84 | 1.93 |
| 2.0 | 3.12 | 2.29 |
| 2.5 | 4.09 | 2.66 |
| 3.0 | 4.19 | 3.67 |

c) Concentration of lactose – 10%

| Time (h) | Glucose (mg/ml) | |
|---|---|---|
| | **10.0% Lactose** | **10.0% Lactose in 0.1% Chitosan** |
| 0 | 0.00 | 0.00 |
| 0.5 | 0.79 | 1.40 |
| 1.0 | 1.77 | 2.06 |
| 1.5 | 2.68 | 2.98 |
| 2.0 | 4.09 | 4.47 |
| 2.5 | 4.76 | 5.01 |
| 3.0 | 5.68 | 5.50 |

The highest value of enzyme hydrolysis from the tested concentrations of lactose was measured in the presence of 1% of this sugar (19% of initial concentration). When the enzyme reactions were performed in the presence of increasing concentration of lactose (from 5% to 10%) a light decrease of hydrolyzing reaction was observed in the presence of 0.1% chitosan (88% of total substrate by 5% lactose and 96% of total substrate by 10% lactose).

*Effect of type of multilayer on lactose hydrolysis with immobilized β-galactosidase*

On the other hand lactose hydrolysis performed with 1 U/ml β-galactosidase in the presence of 0.1

% chitosan resulted in 19% of lactose conversion in 3h reaction time by 1% lactose concentration. When the lactose concentration was increased, its conversion was decreased to 7.3% by 5% initial lactose concentration and 5.5% by 10% initial lactose concentration. From these results, it can be concluded that the β-galactosidase studied shows good operational stability in the hydrolysis of lactose in presence of 0.1% chitosan and under the conditions stated above. It was necessary to set the experimental conditions at which the diffusion of substrates in the PEMs of the support does not modify the rate of the hydrolysis reaction. The immobilization of β-galactosidase on PEMs was based mainly on absorption. It has been reported that protein adsorption on a surface follows a three step diffusion, attachment and reconfirmation regime.

Lactose hydrolysis was performed at different types of PEMs and with different enzyme activity. From the results in Table 3, the maximum of glucose concentration was detected for the positively charged PLA pads with 20 multilayers at 3h of incubation.

**Table 3.** Lactose hydrolysis preformed with immobilized β-galactosidase in PEMs

| Type of PEMs | Glucose (mg/ml) | | |
|---|---|---|---|
| | **1 h** | **2 h** | **3 h** |
| Positively charged PLA pad with 8 multilayers | 0.1 | 0.1 | 0.21 |
| Negatively charged PLA pad with 8 multilayers | 0 | 0.21 | 0.21 |
| Positively charged PLA pad with 14 multilayers | 0.1 | 0.21 | 0.39 |
| Negatively charged PLA pad with 14 multilayers | 0 | 0.20 | 0.28 |
| Positively charged PLA pad with 20 multilayers | 0 | 0.11 | 0.80 |
| Negatively charged PLA pad with 20 multilayers | 0.1 | 0.28 | 0.36 |

For the tested PEMs, the highest value of enzyme hydrolysis was measured for the ones with 14 and 20 multilayers with xanthan/chitosan consecutive deposition. Obviously, the order of layer deposition is significant.

When comparing the activity of the immobilized enzyme with that of the free enzyme, a similar inhibition has been observed due to galactose in the activity of the immobilized enzyme and a decrease in the activation energy of Michaelis–Menten constant of the immobilized enzyme compared to that of the free enzyme at 37 °C. The activity of the

enzyme after immobilization was in all cases equal or higher than 50% of the activity of the free enzyme (data not show).

In the present work, we have studied the influence of different concentrations of lactose on the initial velocity of β-galactosidase reaction. Such kind of kinetic information for lactose hydrolysis by β-galactosidases is scarce in the literature, despite of the fact that this disaccharide can use by transgalactosylation reaction or used in many studies as a donor / acceptor of galactose / glucose units during the synthesis of GalOSs having specific structures and bioactive properties [24-26].

From studies performed by other authors it is known that the galactosyltransferase reaction for synthesis of GalOSs is favored when the lactose concentration in the reaction mixture is more than 15%. Under these conditions the content of free water is low and the transfer of galactose moiety of lactose to suitable acceptor molecules is more likely to occur [27, 28]. It is necessary to perform additional studies concerning the distribution, composition and yield of the obtained transgalactosylation products during the reactions with increasing concentrations of lactose and fructose molecules.

## CONCLUSION

The current study is the first time when the influence of chitosan on the initial velocities of reaction catalyzed by β-galactosidase is investigated. The studied immobilizing enzyme in PEMs showed substantial differences in its affinity to the lactose concentration. The obtained results will be further applied and extended in experiments dealing with the direction and optimization of the GalOSs production.

## REFERENCES

1  B. Cantarel, P. Coutinho, C. Rancurel, T. Bernard, V. Lombard, and B. Henrissat, *Nucleic Acid Research* 37, 233–238 (2008).
2  C. Martinez-Villaluenga, A. Cardelle-Cobas, N. Corzo, A. Olano, and M. Villamiel *Food Chem.*, 107(1), 258–264 (2008).
3  D. Otieno, *Compr. Rev. Food Sci. F.*, 9(5), 471–482 (2010).
4  B. Rodriguez-Colinas, L. Fernandez-Arrojo, M. De Abreu, P. Urrutia, M. Fernandez-Lobato, A. Ballesteros, and F. Plou, In: *Advances in Enzyme Biotechnology* ed. P. Shukla, B. Pletschke, Springer, New Delhi 23–39 (2013).
5  N. Scrimshaw, and E. Murray, *Am. J. Clin. Nutr.*, 48(4), 1079–1159 (1988).
6  R. Mahoney, *Food Chem.*, 63(2), 147–154 (1998).
7  C. Kim, E. Ji, and D. Oh, *Biochem. Bioph. Res. Co.*, 316(3), 738–743 (2004).
8  R. Gaur, H. Pant, R. Jain, and S. Khare, *Food Chem.*, 97(3), 426–430 (2006).
9  R. Wohlgemuth, I. Plazl, P. Znidarsic-Plazl, K. Gernaey, and J. Woodley, *Trends in Biotech.*, 33(5), 304-314 (2015).
10  S. Datta, L. Christena, and Y. Rajaram, *Biotech.*, 3(1), 1-9 (2013).
11  P. Gemeiner, *Enzyme engineering: immobilized biosystems* Chichester, UK: Ellis Horwood, Ltd; (1992).
12  J. Liang, Y. Li, and V. Yang, *J Pharm Sci*, 89, 979–790 (2000).
13  J. Suh, and H. Matthew, *Biomaterials*, 21, 2589-2598 (2000).
14  M. Klein, M. Nunes, R. Rodrigues, E. Benvenutti, T. Costa, P. Hertz, and J. Ninow, *Biomacromolecules*, 13(8), 2456-2464 (2012).
15  O. Kaspara, V. Tokarova, G. Nyanhongo, G. Gubitz, and F. Stepaneka, *Food and bioproducts processing*, 91, 525–533 (2013).
16  E. Taqieddin, and M. Amiji, *Biomaterials*, 25, 1937-1945 (2004).
17  E. Decher, J. Schlenoff, *Multilayer Thin Films*, WileyVCH, Weinheim (2002).
18  C. Picart, F. Caruso, and J.-C. Voegel, *Layer-by-Layer Films for Biomedical Applications*, John Wiley & Sons (2014).
19  X. Zhou, L. Wu, and J. Zhou, *Langmuir*, 20, 8877-8885 (2004).
20  A. Malinin, A. Rakhnyanskaya, A. Bacheva, and A. Yaroslavov, *Polymer Science Series A*, 53(1), 52-56 (2011).
21  V. Bivolarski, T. Vasileva, B. Dzhambazov, A. Momchilova, J.-M. Chobert, I. Ivanova, and I. Iliev, *Biotechnol. Biotec. Eq.*, 27(3), 3811–3820 (2013).
22  M. Bradford, *Anal. Biochem.*, 72(1–2), 248–254 (1976).
23  A. Guzhova, M. Galikhanov, Yu. Gorokhovatsky, D. Temnov, E. Fomicheva, E. Karulina, and T. Yovcheva, *J. Electrostat.*, 79, 1-6 (2016).
24  C. Guerrero, C. Vera, F. Plou, A. Illanes, *J. Mol. Catal. B: Enzymatic*, 72, No 3-4, 206-212, (2011).
25  B. Padilla, A. I. Ruiz-Matute, C. Belloch, A. Cardelle-Cobas, N. Corzo, P. Manzanares, *J. Agr. Food Chem.*, 60, No 20, 5134–5141, (2012).
26  Q. Shen, R. Yang, X. Hua, F. Ye, H. Wang, W. Zhao, and K. Wang, *Food Chem.*, 135(3), 1547-1554 (2012).
27  P. Monsan, F. Paul, M. Remaud, and A. Lopez, *Food Biotechnology*, 3(1), 11–29 (1989).
28  R. Mahoney, *Food Chemistry*, 63, 147-154 (1998).

# Analytic nonlinear elasto-viscosity of two types of BN and PI rubbers at large deformations

K. B. Hadjov, A. S. Aleksandrov, M. P. Milenova, V. A. Aleksandrova[*]

*University of Chemical Technology and Metallurgy, 8 Kl.Ohridski Blvd., Sofia 1756, Bulgaria*

In this work, in analytical form, are derived instantaneous stress-strain and vice-versa relations using the Neo-Hookean and the Mooney-Rivlin models. These relations are obtained resolving algebraic equations of third and fourth degree respectively. The above mentioned analytical solutions are incorporated in the hereditary integral equations of Volterra to predict the creep and relaxation of such as materials at large deformations. One takes into account the non-linearity of the viscous behaviour in the presence of similarity in the isochrone stress-strain curves. Our theoretical results are compared with experimental data for two kinds of rubbers and demonstrate very good coincidence.

**Keywords:** rubber, mechanical properties, rheology, large deformations

## INTRODUCTION

Rubbers are increasingly used in modern industry [1-4]. Resinous materials and rubbers are elastoviscous solids. They are very deformable and possess non-linear behaviour. Their creep is also non-linear according to the applied stresses. The last non-linearity can be observed excluding the time from the creep curves (the so-called isochrones). Thus, rubbers require identification and description of two different kinds of nonlinearities. Here we examine two compositions: the first one is the Butadiennitril rubber (BN) and the other one - the Polyisoprene rubber (PI) [5]. In the first rubber composition is used rubber with 40% acrylonitril in the macromolecule [5]. In the second composition is used polyisoprene rubber - an analogue of the natural rubber. The microstructure conciste of 1,4 cispolyisoprene with content of these units almost 98% [5]. Both elastomeric compositions include fillers (cinders) with a developed surface respectively 75 and 50 m²/ g.

## THEORETICAL

### *Nonlinear elasto-viscosity at small deformations*

The hereditary linear equations can be generalized to account the nonlinear mechanical behaviour using the Rabotnov-Rzanitzin approach [6, 7]. This approach requires similarity in the stress‑strain curves for different moments

$$\varepsilon(t) = \frac{\sigma}{E}\Big[1 + f(\sigma)\int_0^t K(t-\tau)d\tau\Big], \qquad (1)$$

---
\* To whom all correspondence should be sent:
  aleksandrovassuctm@gmail.com

where $\varepsilon(t)$ is the strain, $\sigma$ - the applied stress, $f(\sigma)$ - the nonlinearity function, $K(t\text{-}\tau)$ - the creep kernel, $t$ - the current time and $0 \le \tau \le t$. Concerning the creep kernel we can say the following. It is the resolving kernel of the relaxation one. As kernels in the integral equations of Volterra like eq. (1) it is recommended to take singular kernels which better describe the enhanced creep and relaxation rate at the beginning. In this work we assume the singular relaxation kernel of Koltunov [7]

$$R(t) = A\frac{e^{-\beta t}}{t^{\alpha}} \quad , \qquad (2a)$$

whose resolving kernel (the creep kernel) looks like [7].

$$K(t) = \frac{e^{-\beta t}}{t}\sum_{n=1}^{\infty} A\Gamma(\alpha)^n t^{\alpha n}/\Gamma(\alpha n) \ , \qquad (2b)$$

The function of the nonlinearity $f(\sigma)$ is determined from the isochrone curves. This presentation of the nonlinearity involves a coincidence of the initial points at the strain scale and requires a similarity of the isochrones. If at low stresses (up to the limit axial stress of the linearity $\sigma_o$) the behaviour is linear, equation (1) can be generalized as follows:

$$\varepsilon(t) = \frac{\sigma}{E}\Big[1 + (\sigma/\sigma_o)^n \int_0^t K(t-\tau)d\tau\Big] \qquad (3)$$

In equation (3) $n$ is the potency which can be determined from the isochrones. Eq. (3) remains valid if $\sigma \ge \sigma_o$. In the opposite case the behaviour is linear and $\sigma/\sigma_o = 1$. Such a presentation of the viscous nonlinearity is used in many practical problems [8].

*Nonlinear elasticity at large deformations*

Rubbers are very deformable and their elastic behaviour cannot be described by the Hooke's law. Here as elastic behaviour it is mean the instantaneous elasticity of equation (3) given by the ratio before the brackets. This expression should be changed to be able to account the large elastic deformations of the rubbers.

Here it is used the theory of the large deformations described in [9]. The material is considered as isotropic and incompressible. To describe the mechanical behaviour of rubbers and other resinous materials as successful models are accepted the neo-Hookean and the Mooney-Rivlin ones [9]. According to the above models the following thermodynamic potentials are introduced

$$W = \frac{G}{2}(\lambda_1^2 + \lambda_2^2 + \lambda_3^2 - 3) \ , \tag{4a}$$

$$W = \frac{1}{2}(\varsigma - \chi)(\lambda_1^2 + \lambda_2^2 + \lambda_3^2 - 3)$$
$$+ \frac{\chi}{4}(\lambda_1^2 \lambda_2^2 + \lambda_2^2 \lambda_3^2 + \lambda_3^2 \lambda_1^2 - 3) \tag{4b}$$

where $G$ is the second module of Young, $\varsigma$ and $\chi$ are experimentally determined parameters based on the instantaneous force-extension curves and $\lambda_i$ are the large relative extensions in the main directions

$$\lambda_i = 1 + \varepsilon_i . \tag{5a}$$

Here $i = 1, 2, 3$ and $\varepsilon_i$ are the main Cauchy's strains (the classic ones in the case of small displacements).

In the case of incompressible materials $\lambda_1 \lambda_2 \lambda_3 = 1$ and by traction it follows

$$\lambda_1 = \lambda, \quad \lambda_2 = \lambda_3 = \lambda^{-1/2} . \tag{5b}$$

Therefore, to the potentials (4a) and (4b) follows

$$W = \frac{G}{2}(\lambda^2 + 2\lambda^{-1/2} - 3) , \tag{6a}$$

$$W = \frac{1}{2}(\varsigma - \chi)(\lambda^2 + 2/\lambda - 3) + \frac{\chi}{4}(1/\lambda^2 + 2\lambda - 3) \tag{6b}$$

In the theory of large deformations [9] the axial tensile force is given by the expression

$$Q(\lambda) = S_o \frac{dW}{d\lambda}, \tag{7}$$

where $S_o$ is the initial section of the sample associated with the current section $S(\lambda)$ as

$$S(\lambda) = \frac{S_o}{\lambda} . \tag{8}$$

So, based on equations (6a), (6b) and (7) to the axial tensile force of highly deformable materials are obtained the following expressions (depending on the relative extension) concerning both models respectively

$$Q(\lambda) = S_o G \frac{\lambda^3 - 1}{\lambda^2}, \tag{9a}$$

$$Q(\lambda) = S_o G \frac{\lambda^3 - 1}{\lambda^2}(\varsigma - \chi(\frac{1}{2\lambda} - 1)) \tag{9b}$$

Relations (9) must be expressed through the deformations of Cauchy and replaced in (3) in order to take into account the large deformations. This can be done as follows. Based on eq.(9) is deduced the relationships instantaneous stress-strain concerning both models which give the non-linearity in the elastic part of the hereditary equation (3). In the case of incompressible materials between the instantaneous Young modules one has the following relation

$$G = \frac{E}{2(1 + \nu)} = \frac{E}{3} \tag{10}$$

This is because the Poisson ratio is $\nu = 0.5$. Moreover, from equations (7), (8) there is the relationship

$$\sigma(\lambda) = \frac{Q(\lambda)}{S(\lambda)} = \frac{Q(\lambda)}{S_o}\lambda . \tag{11}$$

Then from equations (9), (10) and (11) it is obtained the following relations stress-elongation

$$\sigma(\lambda) = \frac{E}{3}\frac{\lambda^3 - 1}{\lambda} \tag{12a}$$

$$\sigma(\lambda) = \frac{E}{3}\frac{\lambda^3 - 1}{\lambda}(\varsigma - \chi(\frac{1}{2\lambda} - 1)) \tag{12b}$$

Equations (12) may also be represented as a relation stress-strain according to eq. (5a). These expressions have the form

$$\sigma(\varepsilon) = \frac{E}{3}\frac{(1 + \varepsilon)^3 - 1}{1 + \varepsilon} \tag{13a}$$

$$\sigma(\varepsilon) = \frac{E}{3}\frac{(1 + \varepsilon)^3 - 1}{1 + \varepsilon}(\varsigma - \chi(\frac{1}{2(1 + \varepsilon)} - 1)) \tag{13b}$$

Equations (13) should be resolved about the strains in order to obtain the non-linear stress-strain relation for highly deformable materials. These equations are of third and fourth degree respectively and can be represented in the following form using equations (12)

$$\lambda^3 - \frac{3\sigma}{E}\lambda - 1 = 0 , \tag{14a}$$

$$(\varsigma+\chi)\lambda^4 -0.5\chi\lambda^3 -\frac{3\sigma}{E}\lambda^2 -(\varsigma+\chi)\lambda+0.5\chi=0 \quad (14b)$$

The solution of equation (14a) using the Cardano's formula [10] taking into account (5a) looks like

$$\varepsilon=\varepsilon(\sigma)=\sqrt[3]{0.5+\sqrt{0.25-(\sigma/E)^3}}+\sqrt[3]{0.5-\sqrt{0.25-(\sigma/E)^3}}-1 \quad (15a)$$

The solution of equation (14b) using the Ferrari's formula [10] taking into account (5a) looks like

$$\varepsilon=\varepsilon(\sigma)=\frac{-0.5\chi}{4(\varsigma-\chi)}+\frac{W(\sigma)+\sqrt{-(3\alpha(\sigma)+2y(\sigma)+2\beta(\sigma)/W(\sigma))}}{2}-1,$$

$$(15b)$$

where:

$$\alpha(\sigma)=\frac{-3(0.5\chi)^2}{8(\varsigma+\chi)^2}-\frac{3\sigma/E}{\varsigma+\chi},$$

$$\beta(\sigma)=\frac{-(0.5\chi)^3}{8(\varsigma+\chi)^3}+\frac{3\sigma\chi/E}{4(\varsigma+\chi)^2}-1$$

$$\gamma(\sigma)=\frac{-3(0.5\chi)^4}{256(\varsigma+\chi)^4}-\frac{3\sigma(0.5\chi)^2/E}{16(\varsigma+\chi)^3}+\frac{3\chi}{8(\varsigma+\chi)}$$

$$Q(\sigma)=-\frac{1}{108}\alpha^3(\sigma)+\frac{1}{3}\alpha(\sigma)\gamma(\sigma)-\frac{1}{8}\beta^2(\sigma),$$

$$P(\sigma)=-\frac{1}{12}\alpha(\sigma)-\gamma(\sigma)$$

$$R(\sigma)=-\frac{1}{2}Q(\sigma)-\sqrt{\frac{Q^2(\sigma)}{4}+\frac{P^3(\sigma)}{27}},$$

$$y(\sigma)=\frac{5}{6}\alpha(\sigma)+\sqrt[3]{R(\sigma)}-\frac{P(\sigma)}{3\sqrt[3]{R(\sigma)}},$$

$$W(\sigma)+\sqrt{\alpha(\sigma)+2y(\sigma)}.$$

*Nonlinear elastoviscosity at large deformations*

The relationship of the Cauchy's deformations with the stresses in the form (15) is used as instantaneous nonlinearity in the hereditary equation (2). Equation (2) based on (15) looks like

$$\varepsilon(t)=\varepsilon_o(\sigma)\left[1+(\sigma/\sigma_o)^n\int_0^t K(t-\tau)d\tau\right] \quad (16)$$

The creep law (16) contains parameters that need to be experimentally identified. The necessary experimentations are as follows:
- Instantaneous (with constant strain rate or otherwise) identified from (15). Note that eq. (15a) is a very successful equation containing only one parameter to describe the complex nonlinear elasticity and this is the elastic module $E$.
- Tests based on the curves of stress relaxation (or creep) in the linear region at small imposed strains.

These parameters are identifiable from (3) at low stresses $\sigma \le \sigma_0$.
- Tests based on the isochrone curves of creep (or relaxation). These parameters are identifiable from equation (3) at high stresses $\sigma > \sigma_0$.

EXPERIMENTAL

Fig.1 and Fig.2 show the instantaneous nonlinearity of the butadienenitril (BN) and polyizoprene (PI) rubbers.
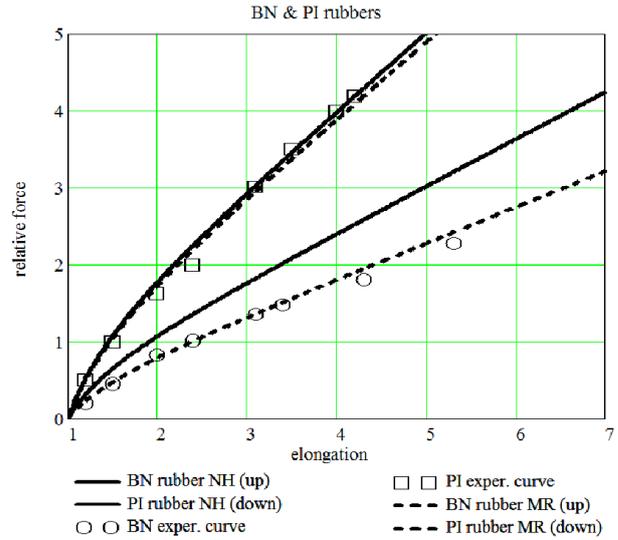


**Fig.1.** Relative tensile force - relative elongation according to the Neo-Hookean and according to the Mooney-Rivlin law for both rubbers

Both rubbers are produced on open mixer with dimensions 400x150 [mm] at T=50$^0$C. Time of vulcanization is determined on oscillating rheometer type "Moncanto". Vulcanization of tested specimens is done at hydraulic press with automatic control of pressure and temperature.
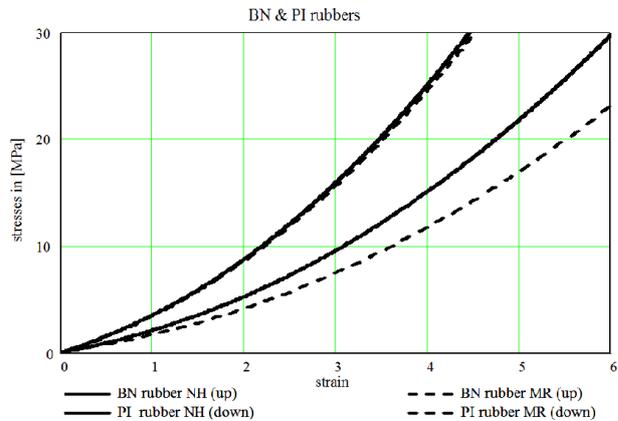


**Fig.2.** Tensile stress - strain according to the Neo-Hookean - equation (14a) and to the Mooney-Rivlin law - equation (14 b) for both rubbers. Solid lines - the Neo-Hookean, dashed lines - the M. Rivlin model, above - PI rubber, below - BN rubber

Fig.3 and Fig.4 illustrate the identification of the above parameters concerning both rubbers. Figure 3 shows the stress relaxation of the BN by constant strain. Fig.4 shows the corresponding creep curve for BN at stresses on the limit of the nonlinearity (see Table 1a and Table 1b). The same is done in Fig.5 and Fig.6 for the PI rubber.
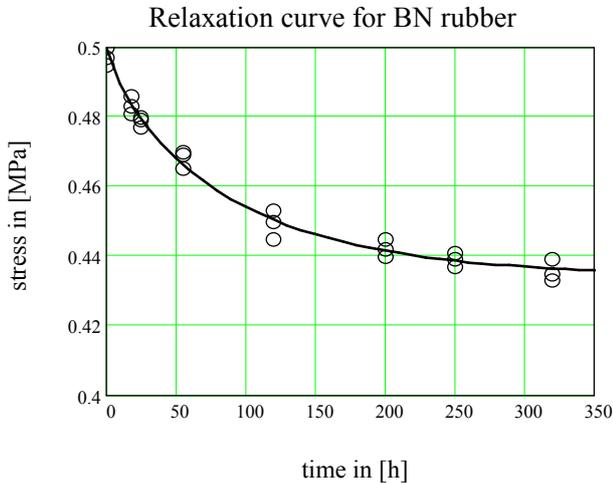


**Fig.3.** Stress relaxation of BN rubber
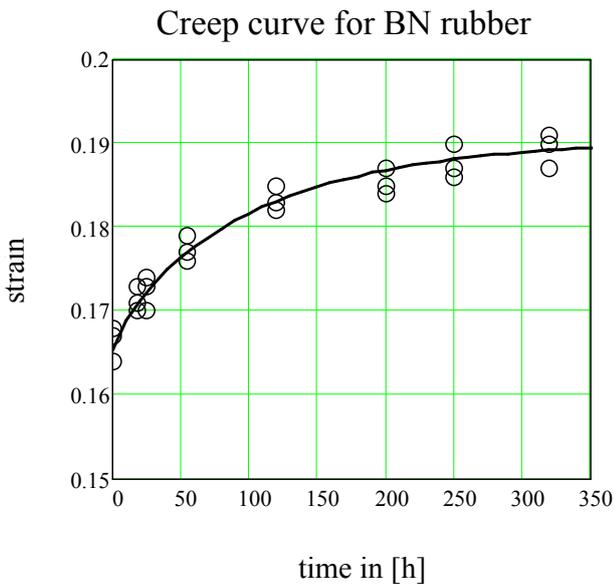


**Fig.4.** Creep curve of BN rubber

Note: In Fig,3 and Fig.4 are shown all the experimental points. In the next figures - just the averaged values.

Creep curves are not necessary to predict the behaviour and can be used only for verification. In practice, the parameters in the Koltunov's kernel can be identified from the relaxation curves, which can be obtained much easily than the creep curves.
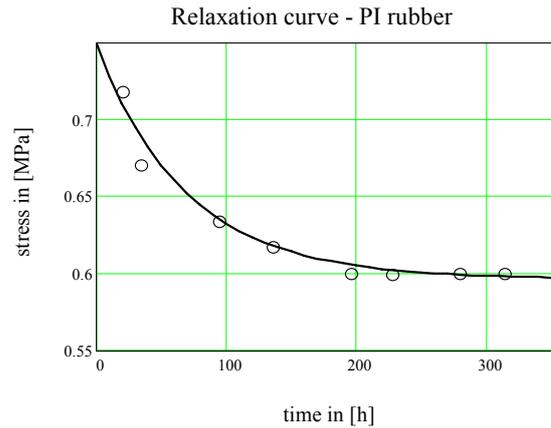


**Fig.5.** Stress relaxation of PI rubber
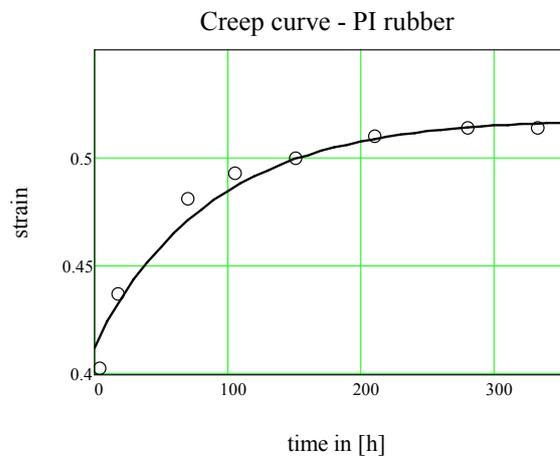


**Fig.6.** Creep curve of PI rubber

In the next two Fig.7 and Fig.8 are shown the nonlinear isochrone curves stress-strains at stresses greater than the limit of non-linearity.
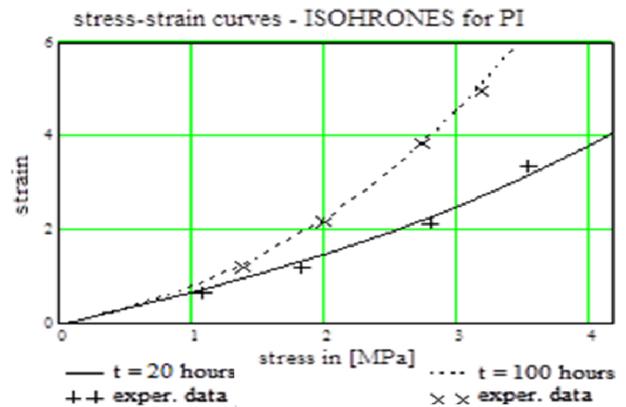


**Fig.7.** Rubber nonlinearity of PI rubber (isochrones at 20 and 100 hours)

Fig.9 and Fig.10 show the creep of the PI and BN rubbers at two stress levels according to equation (16).
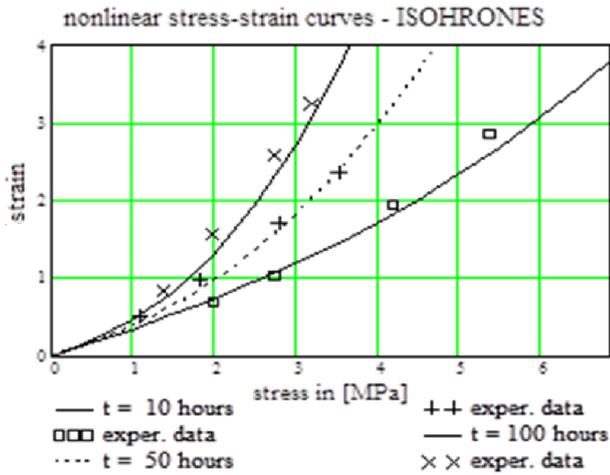
**Fig.8.** Rubber nonlinearity of BN rubber (isochrones at 10, 50 and 100 hours)
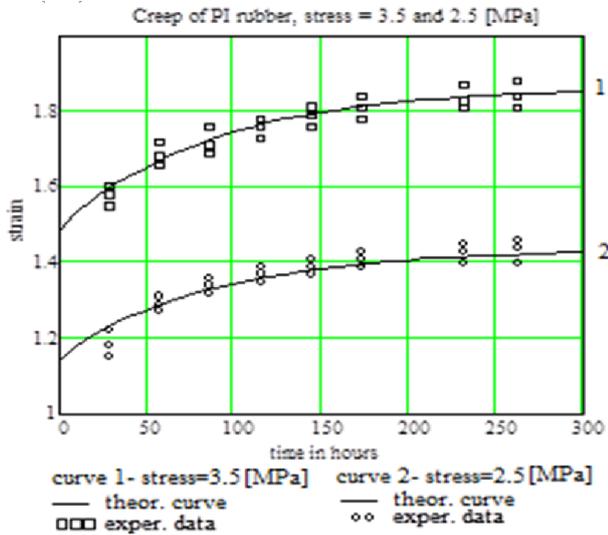


**Fig.9.** Creep at large deformation of PI
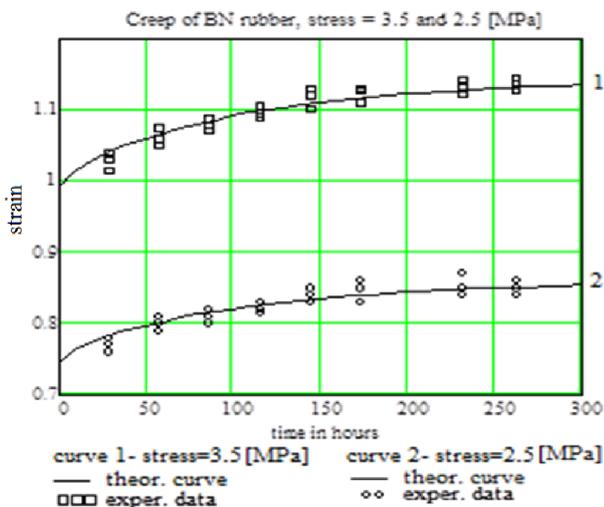


**Fig.10.** Creep at large deformation of BN

From both figures we can see that under bigger stress for studied time interval creep has unidentified character.

Finally, in Table 1(a and b) are systematized all the parameters obtained from the experimental curves above.

**Table 1.** (a and b) Elastoviscous characteristics of the investigated rubbers

**Table 1a.** Instantaneous (elastic) characteristics

| Character | Elastoviscous instantaneous (elastic) | | | | |
|---|---|---|---|---|---|
| Parameters | $E$ | $\sigma_o$ | $N$ | $\chi$ | $\varsigma$ |
| Dimension | [MPa] | [MPa] | - | - | - |
| PI rubber | 1.820 | 0.75 | 1.71 | 0.124 | 0.642 |
| BN rubber | 3.025 | 0.50 | 1.55 | 0.018 | 0.960 |

**Table 1b**. Hereditary (viscous) characteristics

| Character | elastoviscous hereditary (viscous) | | |
|---|---|---|---|
| Parameters | $A$ | α | β |
| Dimension | - | - | - |
| PI rubber | 0.0032 | 00.97 | 0.0140 |
| BN rubber | 0.0029 | 00.77 | 0.0089 |

### RESULTS AND DISCUSSION

For the BN rubber both models give good results. Therefore for BN rubbers it is used the neo-Hookean model. It has the advantage that it does not require the entire force-displacement curve to determine the parameters (the elastic module is sufficient). The PI rubber however, requires the use of the 3-parameter model of Mooney-Rivlin.

Stress-strain curves according to equations (12a, b) or also to (15a, b) appear as shown in Fig.2. The experimental results in figure 1 show that the neo-Hookean law well describes the instantaneous behaviour of the BN rubber but to the PI rubber should be applied the more flexible model of Mooney-Rivlin.

The assumption of incompressibility for the rubbers is perfectly acceptable. For our materials the Poisson's ratio values are 0.485 to the BN rubber and 0.49 to the PI rubber.

The hereditary theory with kernel of Koltunov well describes the temporary effects due to the viscosity.

## CONCLUSION

Using the integral equations of Volterra to describe the nonlinear elastoviscous behaviour are obtained equations predicting the time dependent behaviour taking into account the stress-strain nonlinearity. On the basis of the Neo-Hookean and Mooney-Rivlin models concerning the instantaneous nonlinearity at large deformations are derived the respective strain-stress constitutive relations in analytical form. Both Neo-Hookean and Mooney-Rivlin models well describe the instan-taneous mechanical behaviour at large deformations for the BN rubber. Concerning the PI rubber, only the Mooney-Rivlin model is able to well predict the stress-strain instantaneous constitutive relation. These strain-stress constitutive relations are incorporated in the hereditary theory of Volterra to obtain the complex time dependent mechanical behaviour of rubbers at large deformations. The theoretical predictions show very good coincidence with the experimental data for PI and BN rubbers.

## REFERENCES

1 N. R. Legge, G. Holden, H. E. Schroeders, Thermoplastic elastomers: A comprehensive review, Hanser, Munich, (1987).
2 S. Ilisch, H. Menge, H-J. Radusch, Kautschuk und Gummi Kunststoffe, 53, 206-212, (2000).
3 K. Naskar, Rubber Chemistry and Technology, 80, 504–510, (2007).
4 A. Alexandrov, Z. Tzolov, 6th European Polymer Federation Symposium on Polymeric Materials, Thesaloniki, Creece, 79-83, (1996).
5 A. Alexandrov, Z. Tzolov, International Journal of Differential Equations and Applications, 3 (4), 359-363, (2001).
6 N. Rabotnov, Elements of the hereditary mechanics of solids, Moskow, Nauka, 1977.
7 M. A. Koltunov, Creep and relaxation, Moskow, Nauka, (1976).
8 A. Alexandrov, Z. Tzolov, International Journal of Differential Equations and Applications, 5 (3), 147-154, (2002).
9 J. Salençon, Mécanique du Continu, Tomes 1, 2, 3, Ellipses, (1995).
10 M. Abramowitz, I. A. Stegun, (Eds.). Handbook of Mathematical Functions with Formulas, Graphs and Mathematical Tables, 9th printing. New York, Dover, (1972).

# Nanostructured carbon materials as promoters of energy storage

P. Lesnicenoks[1,2], M. Zvine[3], A. Januskevica[3], V.L. Muzikants[3], M.K. Jurjans[3], K. Kaprans[1], A. Volperts[4], G. Kucinskis[1], G. Bajars[1], G. Dobele[4], J. Kleperis[1*]

[1]*Institute of Solid State Physics, University of Latvia, 8 Kengaraga str, Riga, LV-1063, Latvia;*
[2]*Faculty of Materials Science and Applied Chemistry, Riga TU; 14/24 Azenes str, Riga, LV-1048, Latvia;*
[3]*Riga French Lyceum, 8 Meness str, Riga, LV-1013, Latvia;*
[4]*Latvian State Institute of Wood Chemistry; 27 Dzerbenes str, Riga, LV-1006, Latvia*

Nanostructured carbon materials in recent years have proved to be promoters of energy storage in different technologies – electricity storage in lithium ion batteries and supercapacitors, and hydrogen storage in solid state materials. Our research results on nanostructured carbon materials in lithium ion batteries, electrodes for supercapacitors and hydrogen storage vessels, confirms the indispensable role of it. The commercial and self-made nanostructured carbon materials (black carbon, graphite flakes, graphene oxide, wood-based activated carbons, few layer graphene stacks) are used as additives and selected results reported. $LiFePO_4/C$ composite material as cathode for lithium ion battery is prepared and electrochemical tests are performed to determine the charge capacity and analyse the role of additives. Research on activated wood-based carbon for electrodes of supercapacitors with organic electrolyte showed that specific capacity and ohmic losses of electrode is influenced by the properties of the pores in carbon structures. The ratio of raw material to activator and appropriate activation temperature are most important factors to obtain optimal pore dimensions. Few layer graphene stacks (FLGS) without and with different interlayer ion additives are synthesized and tested for electrodes in supercapacitors as well as solid state sorption media for hydrogen storage. It is found that non-reduced FLG is able to realize sorption on defects mostly at cryogenic temperatures, and this is also true for non-intercalated graphene at low hydrogen pressures. Nevertheless, Li intercalation allows to reach higher values of bind hydrogen (around 1 wt%) at higher temperatures.

**Key words:** carbon, nanoporous, few layer graphene stacks, energy storage, hydrogen storage

## INTRODUCTION

In order to reduce global climate change by limiting $CO_2$ emissions, it is necessary to switch from continuous power (electricity) production by burning fossil fuels (coal, oil, gas) to the unsteady energy generation from local renewable energy sources (sun, wind, water in rivers). Therefore nowadays reliable energy storage systems are critically needed to store and supply power in continuous manner. Electricity and hydrogen are two comparable energy carriers, and in order to be able to meet humanity's demand for energy, electricity storage and hydrogen storage methods are researched.

Already for years electricity is stored in large quantities pumping water in basins of hydro-electric power stations, in flywheels, in vessels with compressed air etc. [1]. Low scale electrochemical energy storage systems are electrochemical capacitors (also supercapacitors), rechargeable batteries, and fuel cells [2]. Pristine and intercalated carbon nanostructures have attracted significant research interest for electrochemical energy storage systems – supercapacitors – as electrode materials due to their developed structures with large specific surface area, excellent electrical conductivity and electro-catalytic activity [2, 3]. Carbon nanostructured materials such as fullerenes, nanotubes, nanowires, graphene are most researched materials in this field in the last decades [4, 5]. Smaller attention is given to organic nanoporous charcoals [5].

After the commercialization of the Li-ion battery with metallic lithium anode and numerous self-ignition cases in hands of consumers, carbon-based anode for rechargeable batteries have gained extensive attention [6]. Here carbon porous/layered structures are reversibly absorbing/desorbing lithium ions at low electrochemical potentials. Graphite can intercalate one Li atom per carbon ring: $Li^+ + e^- + C_6 \leftrightarrow LiC_6$ corresponding to 372 mAh/g theoretically (comparing to about 3800 mAh/g for Li metal). With some amorphous carbons Li can intercalate at even higher capacity, corresponding to an obtainable stoichiometry of $LiC_3$. Therefore, by replacing Li metal anodes with carbon nanomaterials in Li batteries, there is 90% decrease of anode capacity, but the advantages are increased stability and prolonged cycle life [2]. The most important cathode materials for commercially available Li-ion batteries are layered oxides having potential 3.5–4 V (versus Li electrode) $LiCoO_2$, as well as $LiMn_2O_4$ [7], $LiFePO_4$ [8] and $LiMn_xLi_yCo_zO_2$ [9] with capacities of 150, 120, 155

* To whom all correspondence should be sent:
  janis.kleperis@h2lv.eu

and 160 mAh/g, respectively. As a rule, the electrodes from oxide nanocrystals are formed by mixing them with various carbon nanostructured materials to improve the electrical and heat conductivities and mechanical strength [10].

Activated carbons are produced from wood charcoal with developed porous structure and previously used as sorbents in many areas, but nowadays also in membrane technologies for separation of rare earth metals, in metallurgy, in electronics, in electrochemistry, aerospace, nuclear energy. Pyrolysis and activation are two basic technologies to obtain activated carbons from extremely wide range of precursors: wood chips, cellulose and lignin, lignocelluloses, nut shells, straw, peat, husks, etc. The chemical activation is a widely used method to produce activated carbons with developed porosity for electrodes in electric double layer capacitors or supercapacitors [11]. The chemical activation allows possibility to synthesize carbonaceous materials with very high specific surface, close to the theoretical limits for carbon materials.

Hydrogen is important energy carrier for mobile as well as stationary applications and storage is important consideration in all applications of hydrogen energy technologies. High pressure (up to 70 MPa) vessels are used to store 5-6 kg of hydrogen in passenger car – enough for 500-600 km travel [12]. Liquid hydrogen has a very low temperature (20 K) and mostly is stored for space applications. Hydrogen can also be stored in solid materials: metal hydrides, chemical hydrides, porous materials are the most known ones [12]. Only high density alloys forms hydrides at room temperature (LaNi$_5$, Ti$_2$Fe), but lighter metals Mg, Li form hydrides at high temperatures and/or high pressure [12]. In metal hydrides hydrogen atom is incorporated in crystal lattice structure, but in microporous materials molecular hydrogen is absorbed in pores leading to an increase in the density of hydrogen compared to the hydrogen compressed in the gas phase [12]. Adsorption on surfaces and in pores occurs primarily at relatively low temperatures ($\approx$100 K) and in micropores (below 2 nm). The porous materials being considered for physisorbed molecular hydrogen storage are predominantly microporous [12,13] with pore dimensions less than 0.7 nm (close to the size of a single hydrogen molecule).

Carbonaceous materials are attractive candidates for hydrogen storage because of a combination of adsorption ability, high specific surface area,

layered or pore microstructures, and low mass density. In spite of extensive results available on hydrogen uptake by carbonaceous materials, the actual mechanism of storage still remains a mystery [13]. Hydrogen molecule can interact with carbon surface through van der Waals attractive forces (physisorption), or dissociate in atoms and are chemisorbed. The physisorption of hydrogen limits the hydrogen-to-carbon ratio to less than one hydrogen atom per two carbon atoms (i.e., 4.2 wt. %), while in chemisorption, the ratio of two hydrogen atoms per one carbon atom (8.4 wt. %) is reported in the case of polyethylene [13–15]. Physisorbed hydrogen normally has a binding energy on the order of 0.1 eV, while chemisorbed hydrogen has C–H covalent bonding, with a binding energy of more than 2-3 eV [13]. The graphene has some advantages for hydrogen storage because the sp$^2$ covalent-bonding arrangement of the carbon atoms in the honeycomb structure allows efficient binding to hydrogen atoms [16]. Graphene is stable, light, with high theoretical surface; it is mechanically flexible, and it is possible to charge/discharge it at room conditions through hydrogen-carbon binding on local curvatures [16].

In this article our research results on the role and properties of nanostructured carbon materials in lithium ion batteries, electrodes for supercapacitors and hydrogen storage materials have been summarized.

## EXPERIMENTAL SYNTHESIS OF MATERIALS AND SAMPLES

Two types of nanostructured carbons are synthesized – activated carbon (AC) from Latvian alder wood [17] and few layer graphene stacks (FLGS) [18]. AC synthesis consists of two stages of thermal treatment [17] – carbonization of raw material in Ar atmosphere (400 °C, 150 min) at the first stage, and carbonization with activator (NaOH in Ar flow (600-800 °C, 120 min) at the second stage. The pyrolysis product was washed with deionized water, demineralized with hydrochloric acid, washed with deionized water until neutral pH and dried overnight at 105 °C. In order to obtain few layer graphene (FLG), the electrochemical exfoliation was performed, using graphite industrial waste rod as working electrode 18]. Different pulse sequences, amplitudes and filling factors were used to find optimal parameters of exfoliation process. Important step is purification of processed raw material – single sheets are lightest and can be easy

separated with centrifuge or sedimentation. To guaranty higher degree of reduction of FLGS, filtered material was annealed in $Ar/H_2$ (95:5) gas flow at 300°C for 3 hours.

### Carbon in battery electrodes

To design cathode from $LiFePO_4$, different carbon additives are used. $LiFePO_4$ was obtained in a two-step solution reaction of lithium dihydrogen phosphate $LiH_2PO_4$ and iron oxalate $FeC_2O_4 \cdot 2H_2O$ (all from Sigma-Aldrich, ≥99.9%) in de-ionized water. Graphene oxide was added to the synthesis at various steps and then thermally reduced in order to study the influence that the grain structure of $LiFePO_4$/reduced graphene oxide (rGO) has on the electrochemical properties of the composite.

Thick films of $LiFePO_4$/C cathode are made from $LiFePO_4$, conducting additive (carbon black or acetylene black, graphite flakes, Latvian wood charcoal, few layer graphene stacks) and binder (polyvinylidene difluoride PVDF and n-methyl-2-pyrrolidone NMP 50%:50%) in proportions 75:15:10 and grounded 30 min in ball mill (RETSCH Mixer Mill MM 200) then casted on aluminium foil and dried 24 h at 60 °C in air and 3h at 100 °C in an argon atmosphere.

Water suspension of graphene oxide was used for electrophoretic deposition (EDP) of thick graphene films for anode in lithium ion battery [19]. Before the EPD process the graphene oxide suspension was sonicated for 1 h in order to ensure homogenous dispersion. Electrodes used for EPD process were 316 stainless steel plates and the distance between the two electrodes was 10 mm; electric field 30 $V \cdot cm^{-1}$ was applied using DC power supply Agilent Technologies N5772A). Thermal reduction of as-deposited graphene oxide (GO) films was performed by heating at 700 ºC in argon atmosphere. The measurements of synthesized electrodes (area 0.8 $cm^2$) were performed in Swagelok type two electrode cells with metallic lithium as a reference and a counter electrode, and $LiPF_6$ in ethylene carbonate and dimethyl carbonate mixture (volume ratio 1:1) as an electrolyte. The cell was assembled in an argon filled glove box.

### Carbon in supercapacitors

Two methods were used to prepare electrodes from nanostructured carbons for supercapacitor research [17, 20]. *In one of them* the AC was first mixed with ethanol, then a binder – a water suspension of PTFE F-4D powder (10 % from mass of dry electrode) was added. The resulting mixture was treated in rollers, electrode was prepared on thermally expanded graphite sheet (200 μm), than it was dried and impregnated with 4.9 M $H_2SO_4$ water solution. Cellulosic separator NKK TF 4030 (10 μm) was used to make a supercapacitor with electrode area 4.15 $cm^2$. The assembled supercapacitor was pressed under 10 atm pressure in a dry box. **Second method** uses aluminium foil plate as current collector and substrate, which is first treated with $CuSO_45H_2O$ and NaCl etching solution in order to remove oxides [20]. Different FLGS powders (pristine and intercalated with Na and Li) as well as AC powder were mixed with poly-vinyl acetate (PVAc) and the obtained paste gently was applied to etched aluminium electrode using small tungsten blade and left to dry for 1-2 days. Capacitor was made from two equal electrodes, one from three tested separators (Celgard-2400 membrane, Rossmann rayon/cellulose fabric and Whatman glass fibre filter) and one from following electrolytes – 1 M water solutions of $NH_4Cl$, NaCl, $LiPF_6$, $KOH$, and $Na_2SO_4$. Cut electrodes with an area of 1 $cm^2$ and separator soaked with electrolyte were put in plastic pocket and laminated directly with a laminator or on a hotplate.

### Carbon for hydrogen storage

Two different nanostructured carbon materials were tested – activated carbon AC from Latvian alder wood [17] and few layer graphene stacks FLGS – pristine and intercalated with Na, Mg and Li [18].

## METHODS USED IN RESEARCH

The crystal structure was examined by x-ray diffraction (XRD) using a Philips X'Pert Pro MPD diffractometer with CuKα radiation. Molecular structure was investigated by Raman spectroscopy, using an Advantage-785 spectrometer with a laser wavelength of λ=785nm and InVia Renishaw micro-Raman spectrometer equipped with argon laser (514.5 nm, 10 mW). Surface morphology of synthesized samples was characterized by scanning electron microscopes (SEM) - Carl Zeiss EVO 50 XVP, Hitachi S-400N, Tescan Lyra and table-top SEM Phenom Pro.

Pore structure was assessed by $N_2$ adsorption at 77 K (Kelvin 1042, Costech Instruments). Pore volume was calculated by using Dubinin-Radushkevich and Brunauer– Emmet–Teller (BET) theories and $N_2$ sorption isotherms [17]. Carbon

content in LiFePO$_4$/C samples was determined via thermogravimetric analysis (TGA).

Electrochemical measurements were carried out with potentiostat Voltalab PGZ-301 (and partly with potentiostat ELLINS 30-S) using open circuit potential scanning, electrochemical impedance, cyclic voltammetry and chronopotentiometry methods. Charge-discharge measurements of electrodes for batteries and supercapacitors were done with various current densities in a range of 1-100 μA/cm$^2$. Capacities shown were calculated ether using the dry mass of an electrode without the electrolyte or normalized per 1 cm$^2$ area.

Hydrogen adsorption measurements were performed with Sievert's type device, attached to Mass spectrometer RGA-100, in which cryogenic cooling as well external heating is possible in temperature range +/- 200$^o$ C. Two gases, hydrogen and helium, are applied to the sample, firstly with He calibrating sample volume, then measuring H$_2$ adsorption-desorption values in powdered samples. The volume of camera is 94 cm$^3$, both gases are filled with pressure 3.2 ±0.1 bar at room temperature (20$^o$ C). Pressure sensor is situated outside from camera to be heated/cooled therefore pressure values measured at higher and lower temperatures are relative. When absolute values of hydrogen adsorbed in sample are calculated, temperature correction in differential pressure values are taken into account.

## RESULTS AND DISCUSSION

### *Carbon in battery electrodes*

XRD analysis displays all peaks characteristic to the orthorhombic LiFePO$_4$ crystal lattice and Pnma space group, no impurities have been observed [21, 22]. Raman spectroscopy shows carbon D and G bands located at 1350 cm$^{-1}$ and 1600 cm$^{-1}$ respectively. No significant differences in Raman spectra can be observed between samples with and without reduced graphene oxide (rGO), therefore it can be concluded that rGO sheets coated on LiFePO$_4$ are very thin. TGA shows that LiFePO$_4$/C consists of 1.1 % carbon and confirms that LiFePO$_4$/C/rGO additionally contains almost 3 % rGO. SEM image of LiFePO$_4$/C/rGO is shown in Fig.1.

The observation of single and few layer graphene in SEM is complicated, and often advanced SEM equipment is necessary, as one or few layer graphene can be nearly transparent for

high energy electron beams [21]. Nevertheless, rGO sheets have been observed in all prepared LiFePO$_4$/C samples. The grain sizes are approximately 100 – 700 nm, the obtained powders are noticeably porous - the average pore volume is 56 mm$^3$/g. The BET surface area is not sensitive to additive rGO, therefore it is similar to all prepared LiFePO$_4$/C samples – ~30 m$^2$/g. The presence of rGO in LiFePO$_4$/C/rGO composite has caused an increase of the already high rate capability of LiFePO$_4$/C – up to 163.5 mAh/g at 0.1 C (here 1 C = 170 mA/g). The rGO-wrapped LiFePO$_4$/C grains in sample LiFePO$_4$/C/rGO have also provided significant rate capability improvements (Fig.2).
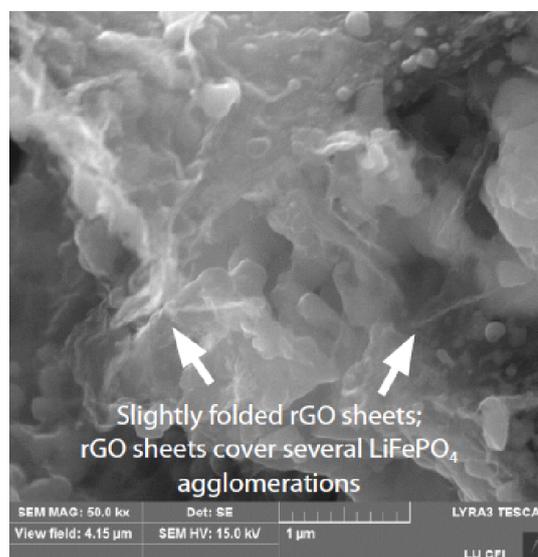


**Fig.1.** SEM image of LiFePO$_4$/C/rGO [22].
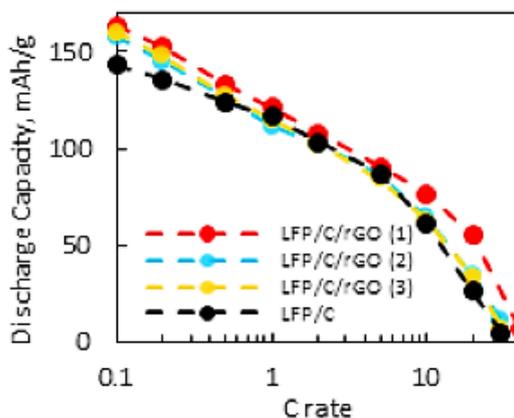


**Fig.2.** The rate capabilities of the obtained composites [22].

The increase of the galvanostatically measured charge capacities above 5 C rate for rGO containing cathodes is seen due to the electron – conducting network created by rGO in LiFePO$_4$/C improving

the electron transport in the cathode. It seems that the rate capability is improved more if the graphene oxide (GO, rGO precursor) is added to the synthesis at the earliest possible stage (sample LFP/C/rGO (1)). It is also worth noting that the capacity is increased not only at the higher charge and discharge rates, but also lower rates. The increase of the amount of the stored lithium in $LiFePO_4/C/rGO$ and other obtained $LiFePO_4$ – rGO composites is most likely also due to the increased fraction of the electrochemically active $LiFePO_4$ particles as a result of the rGO electron-conducting network. It is worth noting that recently an additional Li storage capacity due to the newly formed $LiFePO_4$ – rGO composite has been observed by Hu et al. [23], and such contributions also cannot be ruled out in this work.

Other nanostructured carbon additives (commercial carbon black and AC [17]) were tested [24]. From the charge – discharge graphs it can be concluded that the model battery in which carbon black has been used as an electron conducting additive for the $LiFePO_4$ electrode displays a higher charge capacity - 109.5 mAh/g) as compared with model battery where AC is used as additive to $LiFePO_4$ – 97 mAh/g [24]. This result can be explained with differences in microstructures of both carbon forms - carbon black is like a sponge capable of covering the $LiFePO_4$ grains and providing better electrical conductivity between them, whereas AC mostly consists of large grains with rather sharp edges (Fig.3).
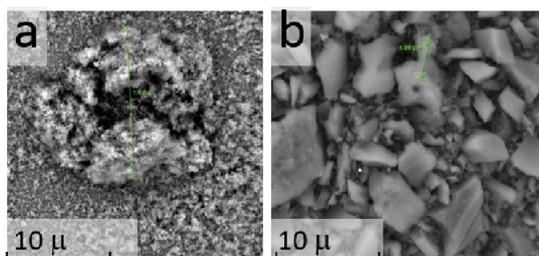


**Fig.3**. SEM image of carbon black (a) and activated carbon (b) materials [24].

Electrophoretically coated GO films can be used as anodes in lithium ion batteries. XRD analysis of electrophoretically prepared rGO film (Fig.4) exhibits a characteristic peak of graphene at 26.5° (002), which was not observed for GO [19]. The characteristic peak of GO powder at 11° was not observed for electrophoretically coated and reduced film on steel substrate (upper curve, Fig.4). It means that most of the GO was successfully converted to graphene by thermal reduction of the

electrophoretically deposited GO films. The gravimetric charge capacity at slow discharge rate (I = 0.8 mA) reaches high value ~ 1120 mAh/g, but increasing of discharge rate causes the gradual decrease of capacity.
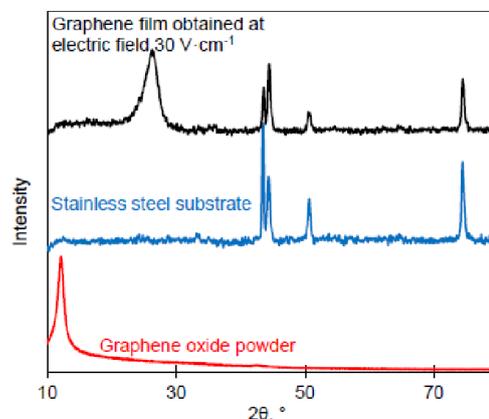


**Fig.4.** XRD patterns for GO, steel substrate and rGO or graphene film [19].

At much higher discharge rate (I = 2 mA) capacity falls to ~ 620 mAh/g and after 50 cycles stabilizes at ~ 530 mAh/g [19]. The Coulombic efficiency for first 50 cycles of rGO electrode exceeded over 85 % and further decrease of capacity during the cycling is negligible. Much lower capacities are measured for anode made from commercial graphite flakes - 135.6 mAh/g, and even less is determined for anode made from FLGS - 111.5 mAh/g [24]. The results show that electrophoretic deposition compares favourably with the classical thick film technology in the case of lithium ion battery anode preparation.

*Carbon in supercapacitors*

Results of capacitor electrodes made from AC according to methodology developed by Volperts et al. [17, 25] showed that highest values of specific capacitance is achieved for materials obtained at low carbonization temperatures – 600 °C and 700 °C – the capacitance is 330 F/g and 320 F/g correspondingly. With increase of activation temperature, specific capacity decreases, although total volume of pores increases. This capacity decrease with increase of activation temperature corresponds to decrease of micropore volume (0.8 nm – 1.5 nm) proportion in porous structure of activated carbons. Few layer graphene stacks (FLGS) is a different nanostructured carbon material made according to the methodology developed by Lesnicenoks et al. [18]. The presence of graphene is confirmed by Raman spectroscopy

(Fig.5). This spectroscopy is the most commonly used method in the characterization of the quality of graphene, as well as separation of graphite from graphene. A single Raman peak at 1580 cm$^{-1}$, called the G peak is characteristic to natural single-crystal graphite. It is formed by in-plane C−C bond stretching ($E_{2g}$) mode of sp$^2$ hybridized carbon atoms.
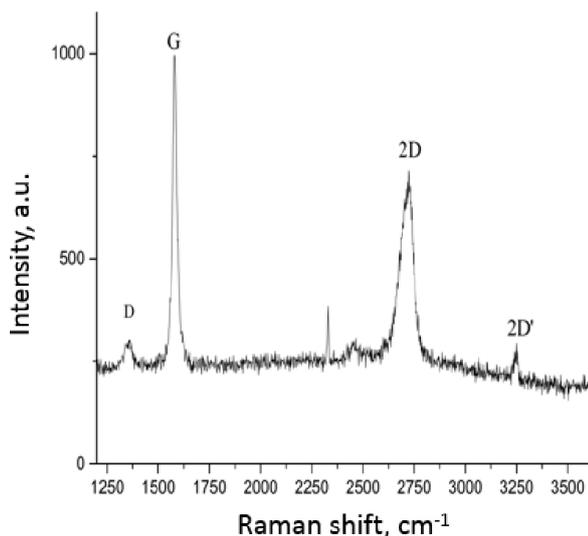


**Fig.5.** Raman spectra of FLGS powder material.

In a perfect graphite crystal the first-order vibrational mode of the D band is forbidden because of selection rules, but if the long range order of the crystalline material is lost and the graphite becomes polycrystalline (splits in sheets), D peak appears at 1358 cm$^{-1}$. The relation between width and intensities of G and 2D peaks is characterized with the number of graphene layers and sample quality. High number of layers in stacks is responsible for the width of 2D peak at 2685 cm$^{-1}$.
Cyclic voltammetry results (Fig.6) confirms that from the tested separators – "Celgard 2400" membrane, "Rossmann" rayon/cellulose fabric and "Whatman" glass fibre filter - the last two show higher current values 1 M solution of NH$_4$Cl is used as electrolyte [20] in all cases). The dependence from membrane material could indicate insufficient ionic transport through the separator. The role of separator in a perfect case is to only separate both electrodes [26]. However, in real life different separators might lead to different amounts of electrolyte being used, therefore not allowing a proper wetting of the electrodes. It should also be noted that all three of the membranes have different thicknesses; in addition, samples were encapsulated using a commercial laminating device (temperature

+110 $^{o}$C) and plastic covers, which can influence materials more sensitive to temperature, as the Celgard 2400 membrane is made of polypropylene.
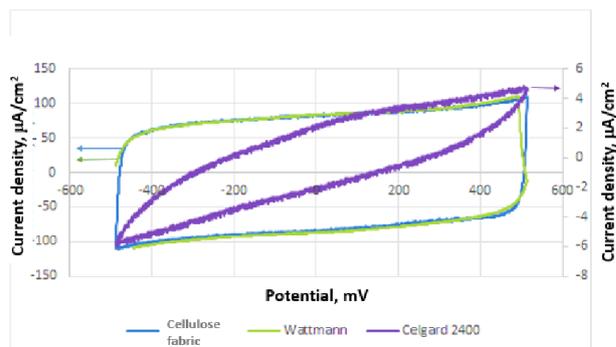


**Fig.6.** Volt-amperic characteristics (scan rate of potential – 50 mV/s) of capacitors with FLGS electrodes and different separators.

FLGS were tested as electrodes in capacitors with difference in formation of active material as described above (using PVAc as binder instead of PTFE), and several measurements were made.
From charge-discharge curves the capacity values are calculated for all measured samples (Table 1).

**Table 1.** The values of measured capacities.

| Electrode material | Electrolyte | Capacity ± 0.01 mF/cm$^2$ |
|---|---|---|
| AC | KOH | 0.37 |
| AC | NH$_4$Cl | 0.86 |
| FLG, | NaCl | 0.26 |
| FLG isolated | NaCl | 0.95 |
| Na FLG | NaSO$_4$ | 4.47 |
| Li FLG | LiPF$_6$ | $2.28 \cdot 10^3$ |

From capacitor volt-amperic (Fi.6) and charge-discharge curves (not shown here) it can be seen that they are partly reminiscent to batteries and partly to capacitors. Since the graphene electrodes can be used in lithium-ion batteries as the anode and cathode, apparently we have obtained a hybrid battery-supercapacitor, especially in case using LiPF$_6$ electrolyte; this sample also has the largest capacity (Table 1). The hybrid battery is combination of different types of energy storage in one source [27].
The reason of such remarkable difference between capacitors with inorganic and organic electrolytes may be caused by the applied binder (PVAc).

## Carbon for hydrogen storage

Comparing the hydrogen adsorption performance of activated carbon (AC) from Latvian alder wood with few layer graphene stacks FLGS intercalated with Li (Fig.7) it can be seen that activated carbon (brown line) starts to adsorb hydrogen at temperature of approx. 230 K.
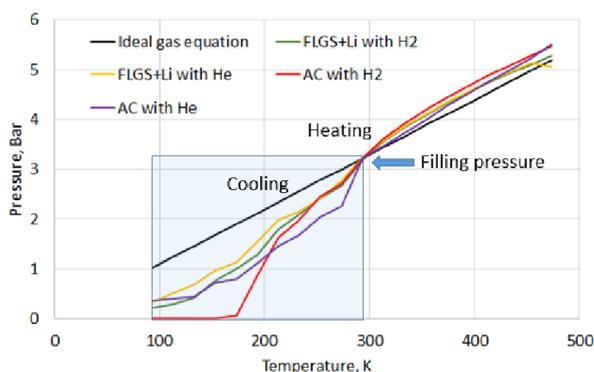


**Fig.7.** Pressure – Temperature characteristics of two samples (AC and FLGS+Li) in two different atmospheres – helium and hydrogen.

Calculated value of absorbed hydrogen mass in AC sample approaches 1.3 wt% and is promising value for further research and potential applications. Detailed analysis of the pressure and temperature output data for this sample (Fig.8) shows pronounced hydrogen absorption region (coloured circle) with temperature and pressure oscillations, which indicate an exothermic reaction (heat is released).
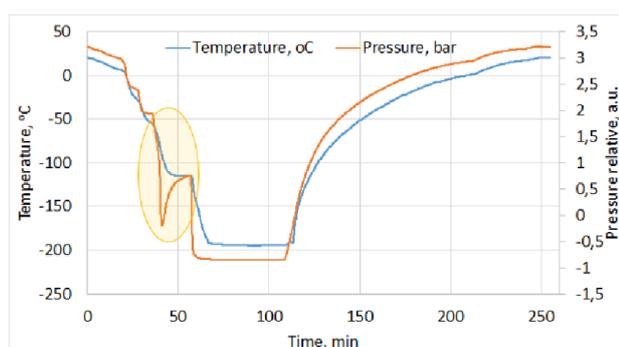


**Fig.8.** Pressure and Temperature as function of time during cooling and heating sample AC in hydrogen atmosphere.

If we consider mechanisms such as metal hydride formation, Li should not be favourable as low temperature hydride, but in our system – intercalated graphene surfaces, we are more concerned with stabilisation of defects in FLGS plates, thus Li FLGS is still considered because preliminary results (Fig.7) show small but positive

value – 0.1 wt% of adsorbed hydrogen starting from 170 K.

## CONCLUSIONS

### Carbon in battery electrodes

From the charge – discharge graphs it can be concluded that the cathode material $LiFePO_4$/carbon black has a higher charge capacity as cathode material with active carbon additive (109.5 and 97 mAh/g accordingly). The presence of rGO in $LiFePO_4$/C/rGO composite has caused an increase of the already high rate capability of $LiFePO_4$/C – up to 163.5 mAh/g at 0.1 C (here 1 C = 170 mA/g). The rGO-wrapped $LiFePO_4$/C grains in sample $LiFePO_4$/C/rGO have also provided significant rate capability improvements. Electrophoretically deposited GO films can be used as anodes in lithium ion batteries. The gravimetric charge capacity at slow discharge rate (I = 0.8 mA) reaches high value ∼ 1120 mAh/g, but at higher discharge rate (I = 2 mA) capacity falls to ∼ 620 mAh/g and after 50 cycles stabilizes at ∼ 530 mAh/g. Much lower capacities are measured for anode made for commercial graphite flakes - 135.6 mAh/g, and even less is determined for anode made from FLGS - 111.5 mAh/g.

### Carbon in supercapacitors

Results of capacitor electrodes made from activated carbon showed that highest values of specific capacitance 330 F/g and 320 F/g are achieved for materials obtained at low carbonization temperatures – 600 °C and 700 °C – correspondingly. From the tested separators - "Celgard 2400" membrane, "Rossmann" rayon/cellulose fabric and "Whatman" glass fibre filter - the last two show higher current values, when 1 M solution of $NH_4Cl$ is used as electrolyte.

### Carbon for hydrogen storage

Comparing hydrogen adsorption performance of activated carbon from Latvian alder wood with few layer graphene stacks FLGS intercalated with Li it can be seen that activated carbon starts to adsorb hydrogen at temperatures of approx. 230 K and reach value 1.3 wt%.

REFERENCES

1 H. Ibrahim, A. Ilinca, J. Perron, *Renew. Sustain. Energy Rev.*, 12, 1221 (2008).

2 H.D. Yoo, E. Markevich, G. Salitra, D. Sharon, D. Aurbach, *Materials Today*, 17, No 3, 110 (2014).

3 Y. Wang, H. Wei, Y. Lu, S. Wei, E.K. Wujcik, Z. Guo, *Nanomaterials*, 5. No 2, 755 (2015).

4 M.D. Stoller, S. Park, Y. Zhu, J. An, R.S. Ruoff, *Nano Lett.* 8, 3498 (2008).

5 D. Saha, Y. Li, Z. Bi, J. Chen, J.K. Keum, D.K. Hensley, H.A. Grappe, H.M. MeyerI, S. Dai, M.P. Paranthaman, A. K. Naskar, *Langmuir*, 30, No 3, 900 (2014).

6 C. De las Casas, W. Li, *J. Power Sources*, 208, 74 (2012).

7 M.S. Whittingham, *Chem. Rev.*, 104, 4271 (2004).

8 J.B. Goodenough, *J. Power Sources*, 174, 996 (2007).

9 J.W. Fergus, *J. Power Sources*, 195, 939 (2010).

10 G. Kucinskis, G. Bajars, J. Kleperis, *J. Power Sources,* 240, 66 (2013.

11 M. Inagaki, H. Konno, O Tanaike, *J. Power Sources*, 195, 7880 (2010).

12 D. P. Broom, Hydrogen Storage Materials: Green Energy and Technology, Springer-Verlag London Limited, 2011.

13 M.U. Niemann, S.S. Srinivasan, A.R. Phani, A. Kumar, D.Y. Goswami, E.K. Stefanakos, *J. Nanomaterials*, 2008, 9 pages (2008).

14 B. Viswanathan, M. Sankaran, and M. A. Schibioh, *Bulletin of the Catalysis Society of India*, 2, 12 (2003).

15 M. G. Nijkamp, J. E. M. J. Raaymakers, A. J. van Dillen, and K. P. de Jong, *Applied Physics*, 72A, No 5, 619 (2001).

16 V. Tozzini and V. Pellegrini, *Phys. Chem. Chem. Phys.*, 15, 80 (2013).

17 A. Volperts, G. Dobele, J. Ozolins, N. Mironova-Ulmane, *Material Science and Applied Chemistry*, 31, 16 (2015).

18 P. Lesnicenoks, J. Zemitis, J. Kleperis, G. Chikvaidze, R. Ignatans, *Material Science and Applied Chemistry*, 31, 21 (2015).

19 K. Kaprans, G. Bajars, G. Kucinskis, A. Dorondo, J. Mateuss, J. Gabrusenoks, J. Kleperis, A. Lusis, *IOP Conf. Series: Materials Science and Engineering*, 77, 5 pages (2015).

20 M. Zvine, A. Januskevica, P. Lesnicenoks, G. Taurins, J. Kleperis. Abstracts of the 32nd Scientific Conference of Institute of Solid State Physics, University of Latvia, Febr 17–19, 2016, Riga, p. 65.

21 G. Kucinskis, G. Bajārs, J. Kleperis, J. Smits, *Environmental and Climate Technologies*, No 4, 53 (2010).

22 G.Kucinskis, The study of nanostructured bulk and thin film LiFePO$_4$ cathode materials for lithium-ion batteries. Summary of Doctoral Thesis, University of Latvia, 2015.

23 L.-H. Hu, F.-Y. Wu, C.-T. Lin, A. N. Khlobystov, L.-J. Li, *Nature Communications*, 4, 1687 (2013).

24 V.L. Muzikants, G. Kucinskis, M.K. Jurjans, G. Bajars, *Abstracts of the 32nd Scientific Conference of Institute of Solid State Physics*, University of Latvia, Febr 17–19, 2016, Riga, p. 66.

25 G. Dobele, D. Vervikishko, A. Volperts, N. Bogdanovich, E. Shkolnikov, *Holzforschung,* 67, No 5, 587 (2013).

26 A.C. Forse, C. Merlet, J.M. Griffin, C.P. Grey. J. Am. Chem. Soc. 2016, 138, 5731−5744.

27 A. Vlad, N. Singh, J. Rolland, S. Melinte, P.M. Ajayan & J.-F. Gohy. NATURE, SCIENTIFIC REPORTS, 2014, 4: 4315.

# Study of the properties of multilayered gradient TiAlSiN nanocomposite coating deposited on 1.2343 steel

S. I. Dishliev[1], G. A. Mishev[2], V. S. Rupetsov[2], L. P. Kolaklieva[3], Ch. O. Pashinski[3,4*], R. A. Minchev[2]

[1]*Department of Machinery for the Food Industry, University of Food Technologies, 26 Maritza Blvd, 4000 Plovdiv, Bulgaria*
[2]*Technical College of Smolyan, Paisii Hilendarski University of Plovdiv, 28 Dicho Petrov St., 4700 Smolyan, Bulgaria*
[3]*Central Laboratory of Applied Physics, Bulgarian Academy of Sciences, 61 St. Petersburg Blvd., 4000 Plovdiv, Bulgaria*
[4]*Department of Mechanics, Technical University - Sofia, Br. Plovdiv, 25 Tsanko Diustabanov St., 4000 Plovdiv, Bulgaria*

The application of hard coatings in the machining industry has rapidly grown recently. Their variety is huge and each of them has advantages and disadvantages. The latter makes them suitable for certain and relatively limited purposes. Although one universal coating which is suitable for almost all kind of machining does not still exist, a coating which is close to this definition is discussed in this work: nc-$(Al_{1-x}Ti_x)N$/a-$Si_3N_4$. Its properties which are important from a practical point of view are studied and an analysis of its wide application is performed here.

**Keywords:** nanocomposites, physical vapour deposition (PVD), superhard coatings, tool wear

## INTRODUCTION

The advantages of the composite materials have long been known and they have found application in the nanotechnologies reasonably. In respect to the hard and superhard coatings, one of the major contemporary trends is exactly the creation of nanocomposite coatings. Nowadays, their use in industry is extensive and their diversity is increased [1-5].

The advanced technology for obtaining of superhard nanocomposite coatings is aimed at a creation of small crystallites in size of several nm which are surrounded by an amorphous tissue with thickness of several tenths of nm. Practically, such one construction ensures a lack of columnar structure and the propagation of dislocations is strongly hampered respectively [6, 7]. This, along with the Hall-Petch effect [2, 7, 8], greatly increases the hardness which is the most important mechanical property of these coatings. Thus it reaches and even exceeds the hardness of the diamond [3, 7, 8, 9]. The practical absence of an internal stress in such coatings ensures good adhesion and permanent mechanical properties for an unlimited time period [8, 9].

As far as the above description is common to the modern nanocomposite coatings, the multilayered gradient coating nc-$(Al_{1-x}Ti_x)N$/a-$Si_3N_4$ possess some specific characteristics which make it notably suited for various machining processes. Its excellent adhesion due to a smooth transition from the substrate material to the main layers ensures its strength even in incontinuous processing (e. g. milling, punching). The solid solution of the nc-$(Al_{1-x}Ti_x)N$ nanocrystallites allows relatively easily to control the formation of their small sizes. Even if other than optimum for a high hardness grain sizes have been prepared, they can change during the work operations and one such high hardness can be reached: this is one unique "self-hardening" effect [3, 8, 9, 10]. The a-$Si_3N_4$ amorphous phase gives a good oxidation resistance [9, 10] and prevents the change of the face centered cubic lattice of the nc-$(Al_{1-x}Ti_x)N$ into a hexagonal at a high-temperature [9, 10] which would lead to a hardness decrease. The top layer which is enriched with Al, ensures the passivation of the coating surface thus increasing the oxidation resistance significantly [11, 12]. Because of above mentioned facts, this coating can be used at a very high temperature: up to ca. 1200 °C [3, 8, 10, 11], when the Co (when used WC/Co tool) begins to diffuse in

---

the layers which worsens the properties of the coating [1, 10]. As a result, this allows a machining without a coolant [1], as the low thermal conductivity of this coating protects the cutting tool [1, 13].

One superhard nc-$(Al_{1-x}Ti_x)N/a$-$Si_3N_4$ gradient nanocomposite coating deposited by Vacuum (Cathodic) Arc Deposition (VAD, CAD) on steel 1.2343 (4X5МФС, X37CrMoV5-1) is discussed below. Most of the mechanical and tribological parameters are studied. One analysis of its practical implementation is performed.

EXPERIMENTAL DETAILS

The used samples of 1.2343 steel have a rectangular parallelepiped shape: 25 x 8 x 5 mm (Length x Breadth x Height). This steel is often applied as material for injection molds, punches, conveyor screws, etc. They were hardened to 52 HRC (at the highest temperature attained during the deposition process: 485 °C, this steel does not change its hardness), then polished to Ra = 0,033 μm. Immediately before the deposition, they were mechanically cleaned and then treated in an ultrasonic bath with a solvent of deconex HT 1170.

The completely cleaned samples were loaded into the vacuum chamber of a VAD system π80+ (manufactured by PLATIT, Switzerland), in which a LAteral Rotating Cathodes (LARC® technology) [1, 3, 4, 14] are used. An initial pressure of $1,0.10^{-4}$ mbar was reached in the chamber, then the samples were heated in an environment of Ar (a flow rate of 6 sccm) up to 485 °C for 90 min. During this period the pressure was risen, but after its end the Ar and heaters were stopped and the pressure was waited to fall back again to $1,0.10^{-4}$ mbar.

Next, one etching in Ar+ glow discharge for 5 min was done at a gradually increase of the flow rate of Ar from 55 to 130 sccm and a bias pulsed voltage to the samples $U_{bias}$ = -760 V, while the temperature in the chamber was stabilized at 470 °C to the end of the whole deposition. Then, a pre-cleaning of the cathodes was carried out for 1 min. This is done by a rotation of their magnetic system and evaporation in the opposite direction from that of the deposition, i. e. to the door where they are mounted - Virtual Shutter® technology [1, 14]. The last ensures the production of unpolluted layers with guaranteed quality. Through the already cleaned cathodes one bombardment of the samples with metal Ti+ ions was done for 4 min at a flow rate of Ar of 20 sccm and a bias voltage $U_{bias}$ which was changed from -850 to -1000 V. During this

cleaning, the Ti cathode worked only at arc current of ca. 65 A. With that the actual coating deposition was ready to begin.

The deposition was performed in a pure $N_2$ atmosphere. The process was regulated by pressure, not flow rate, in order to achieve higher accuracy and repeatability. It was carried out at a bias voltage $U_{bias}$ = -110 ÷ -40 V (being varied according to the respective steps of the coating recipe), while the maximum ion current to the samples $I_{bias}$ (two working cathodes of Ti and AlSi) reached 5,0 ÷ 5,5 A. Initially, the deposition begun with the interface TiN layer, passed through gradient layers to the nc-$(Al_{1-x}Ti_x)N/a$-$Si_3N_4$ base layer and finally reached gradiently to the outermost layer which has an increased content of Al for a greater oxidation resistance of the surface. The structure of the obtained coating is partially described in [7]. The total duration of the deposition was about 2 h, a three-axial rotation of samples was used.

After that, the samples were cooled down (the pumps and gas flow were turned off), as when temperature dropped to 380 °C, the chamber was inflated with $N_2$ at a flow rate of 200 sccm for 5 min. Finally, a temperature drop to 200 °C was waited, after which samples were unloaded from the chamber.

The coating thickness which is an important complex characteristic was measured using calo tester developed by CLAP-Plovdiv [15]. A ball with a diameter of 30 mm was used and the formed calotte section (ball crater) was observed and geometrically dimensioned through the optical system of a Compact Platform CPX (MHT/NHT) CSM Instruments in CLAP-Plovdiv.

The nanohardness and elastic modulus of the coating were studied using Compact Platform CPX (MHT/NHT) CSM Instruments in CLAP-Plovdiv. A Berkovich type diamond indenter was used and the measurements were processed by the Oliver and Pharr method.

The adhesion was evaluated using Micro Scratch Tester (MST) module of the last equipment. A Rockwell type diamond indenter rounded on top (radius of 200 μm) was applied. The coefficient of friction was additionally observed during the scratch test.

The wear resistance of the coating was investigated by the pin-on-flat test using a stand which is developed at Technical University - Sofia, Branch Plovdiv [16]. The counter-part was a pin of $Al_2O_3$ rounded on top (radius of 2,45 mm). The width of the tracks was found using a microscope:

contactless PC based measuring system TESA VISIO-300 at 100x magnification (resolution: 0,001 mm).

## RESULTS AND DISCUSSION

An image of a calotte section made by the calotest is displayed in Fig.1. The interface TiN layer and outermost layer with increased content of Al could be outlined. Also, droplets could be seen there which are occurred unavoidably in VAD processes, but here they are relatively a few and do not make the overall behaviour of the deposited coating worse.
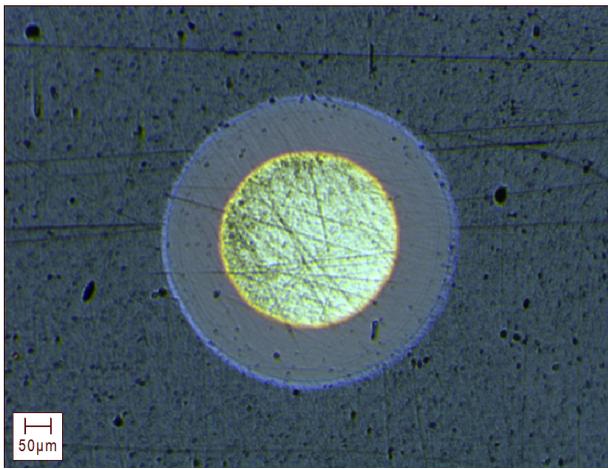


**Fig.1.** Image of the calotte section

Despite this section was designed for the coating thickness measurement, it indirectly demonstrates a good adhesion. In coatings with a poor adhesion, a partial delamination/spallation after such a test could be met frequently.

The coating thickness *h* was calculated using the equation [15]:

$$h = \frac{D^2 - d^2}{8R}.10^3 \left[\mu m\right] \qquad (1)$$

where $D$ – the external section diameter (mm), $d$ – the internal section diameter (mm), $R$ – the grinding ball radius (here: 15 mm). It was evaluated that the coating thickness is 1,960 μm. This is a standard value for deposition on machining tools (2 μm).

Fig.2 shows a load/unload curve caused by the nanoindentation. It is very smooth and this an evidence for no significant damages on the coating during this test [2]. The latter implies good mechanical properties, especially an improved adhesion. The high hardness of the substrate has less influence on the measured coating nanohardness and its smooth surface allows more precise carrying out of such a test.
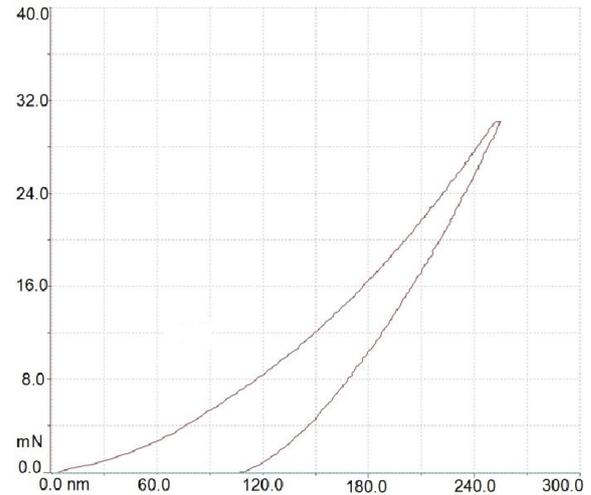


**Fig.2.** Load/unload curve

The following parameters were derived: nanohardness H = 38 GPa; elastic modulus E = 370 GPa; maximum penetration depth $h_m$ = 253 nm (at maximum load of 30 mN). This penetration depth is less than 15 % of the coating thickness (1,960 μm) and implies that the measured nanohardness is related mostly to the coating, i. e. the influence of the substrate is almost completely reduced [9]. This nanohardness is close to the limit for superhard coatings (40 GPa). It could be assumed, that when less penetration (down to 10 %) is used [9], this limit will be exceeded. But, then one has to take the indentation size effect (ISE) in consideration [8, 9]

The results by the scratch test (sliding distance of 3 mm) are shown in Fig.3.
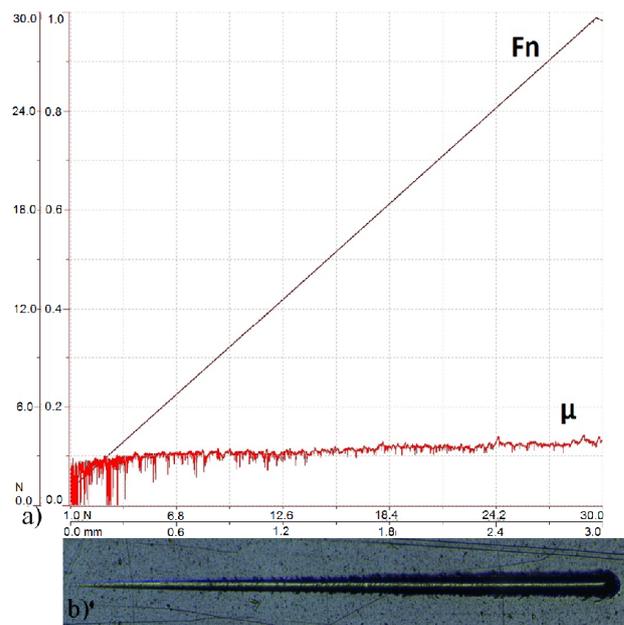


**Fig.3.** Scratch test: a) diagram; b) trace

The load Fn (Fig.3a) which presses the indenter, is changed linearly to its maximum value of 30 N (the maximum load which the used apparatus can create). The coefficient of sliding friction µ is measured along the trace. Its value is almost constant (especially within the boundaries from concatenation to the first damages), which could be explained by a very little stress in the coating due to the nanocomposite structure. Also, the last predetermines a predominantly smooth trace (Fig.3b). It should be pointed out that the measured low values of the friction coefficient are due to the use of a diamond indenter.

Images of the trace at different load on the indenter are shown in Fig.4. In the beginning, a relatively smooth track without destructions could be seen (Fig.4a and 4b). The first apparent damages in the coating are detected under compressive load of ca. 24 N (Fig.4c). Their insignificance causes a very slight leap in the graph of the coefficient of friction (Fig.3a) - this is the first critical load $L_{C1}$. Since an evident delamination, i. e. substrate exposure, could not be seen in the track, it is acceptable that the second critical load $L_{C2}$ is not reached up to the maximum applied load of 30 N. Also, here could be observed a small amount of droplets which was smashed during the test.
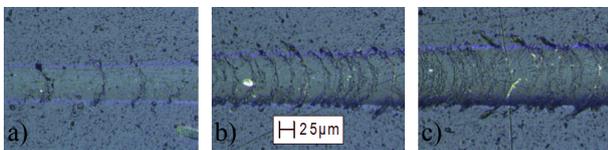


**Fig.4.** View of the trace at different load: a) 9 N; b) 17 N; c) 24 N

A survey of the wear rate was carried out at a room temperature with the following parameters: sliding speed = 6,78 mm/s, stroke of the sample (length of the track) = 11 mm, normal load = 0,65 N. Two test series with different duration t (respectively sliding distance L) were done: t = 30 min (L = 12,21 m) and t = 60 min (L = 24,42 m).

The wear rate $I_w$ was computed by the following equation [17, 18]:

$$I_w = \frac{V}{FL}\left[\frac{mm^3}{Nm}\right] \qquad (2)$$

where $V$ - wear volume (mm³), $F$ - normal load (N), $L$ - sliding distance (m).

After the width of the track was measured initially using a microscope, the wear volume was determined by geometric calculations. For more convenience, one program for the calculation of

this volume and wear rate was made using a MS Excel software. Also, using a SolidWorks software, one 3D-model of the track end sections was generated which confirmed the accuracy of these calculations [17].

Table 1 shows the experimental data received by the test for the wear rate assessment. The obtained results prove that under identical conditions, the coated sample is much more wear resistant than the uncoated one. The values for the wear rate are ordinary, but rather to the upper limit for similar coatings. This could be explained by the occurrence of one tribochemical interaction between the counterpart and coating [18]. Also, it could be assumed that the relatively small coating thickness contributes to the higher values of the wear rate (the bottom gradient layers which possess lower wear resistance are affected earlier by the indenter).

**Table 1.** Values of the wear rate under different experimental conditions (mm³/Nm)

| sample type | t, min | V, mm³ | $I_w$, mm³/Nm |
|---|---|---|---|
| without coating | 30 | 39,457.10⁻³ | 4,971.10⁻³ |
| | 60 | 68,848.10⁻³ | 4,337.10⁻³ |
| after the deposition | 30 | 16,345.10⁻³ | 2,059.10⁻³ |
| | 60 | 43,615.10⁻³ | 2,747.10⁻³ |

Additional details about the wear resistance test could be found in [17].

CONCLUSIONS

The studied nc-$(Al_{1-x}Ti_x)N$/a-$Si_3N_4$ coating demonstrates high hardness, excellent adhesion, low friction coefficient and obviously good wear resistance. Assuredly, these good tribomechanical properties are mainly due to its two-phase nanocomposite structure.

The results of the presented studies are fully proven by the practical application of this coating. According to the data (despite they are unsystematic) received from the partners of CLAP-Plovdiv, it works well when deposited on a variety of cold working machining tools: end mills, drill bits, gear cutters, etc. Also, good results are achieved when it is implemented on injection molds, punches, bed dies, etc., but in such cases, depending on the particular situation, it is successfully competed by other coatings: TiCN, TiN/CrN-ml, nc-$(Al_{1-x}Cr_x)N$/a-$Si_3N_4$, etc. Among its other properties, this coating allows multiple overlapping (re-coating) after a re-sharpening of the tool without removal of the old coating (stripping) [7].

The nanocomposite superhard coatings are one relatively new phenomenon which has become widespread quickly. Described here coating nc-$(Al_{1-x}Ti_x)N$/a-$Si_3N_4$ is already proven in practice and now being worked mostly on its improvement [4, 14]. The presented analysis shows that in the near future this and similar coatings going to become even more relevant to the machining industry.

## REFERENCES

1 S. Veprek, M.J.G. Veprek-Heijman, *Surface & Coatings Technology*, 202(21), 5063 (2008).

2 S. Zhang, D. Sun, Y. Fu, H. Du, *Surface and Coatings Technology*, 167(2-3), 113 (2003).

3 E.N. Reshetnyak, V.E. Strel'nitskij, *Problems of Atomic Science and Technology* (in Russian), 2, 119 (2008).

4 T. Cselle, O. Coddet, C. Galamand, P. Holubar, M. Jilek, J. Jilek, A. Luemkemann, M. Morstein, *Journal of Machine Manufacturing*, XLIX(E1), 19 (2009).

5 B. Sovilj, J. Javorova, P. Kovac, I. Sovilj-Nikic, Proceedings of the XXVI International Science Conference in honour of 65 anniversary of MTF of TU-Sofia and 100 birth anniversary of Acad. Angel Balevski, Sozopol, Bulgaria, 515 (2010).

6 K. Su, D.M. Liu, T.M. Shao, *Science China Technological Sciences*, 58(10), 1682 (2015).

7 Ch. Pashinski, R. Kakanakov, L. Kolaklieva, *Fundamental Sciences and Applications*, 19(2), 71 (2013).

8 A.D. Pogrebnjak, A.P. Shpak, N.A. Azarenkov, V.M. Beresnev, *Uspekhi Fizicheskikh Nauk* (in Russian), 179(1), 35 (2009).

9 S. Veprek, M.G.J. Veprek-Heijman, P. Karvankova, J. Prochazka, *Thin Solid Films*, 476(1), 1 (2005).

10 S. Veprek, H.-D. Männling, M. Jilek, P. Holubar, *Materials Science and Engineering A*, 366(1), 202 (2004).

11 Y. Tanaka, N. Ichimiya, Y. Onishi, Y. Yamada, *Surface and Coatings Technology*, 146–147, 215 (2001).

12 Y.Y. Chang, S.M. Yang, *Thin Solid Films*, 518(21), S34 (2010)

13 L. Chen, S.Q. Wang, Y. Du, S.Z. Zhou, T. Gang, J.C. Fen, K.K. Chang, Y.W. Li, X. Xiong, *Surface & Coatings Technology*, 205(2), 582 (2010).

14 PLATIT AG Compendium 2012, 49th Edition, available through http://www.platit.com (accessed October 24, 2012).

15 V. Kopanov, L. Kolaklieva, *Fundamental Sciences and Applications* (in Bulgarian), 21(2), 37 (2015).

16 S. Dishliev, *Fundamental Sciences and Applications* (in Bulgarian), 14(2), 153 (2009).

17 G. Mishev, S. Dishliev, V. Rupetsov, *Tribological Journal BULTRIB* (in Bulgarian), IV, 147 (2014).

18 D. Philippon, V. Godinho, P.M. Nagy, M.P. Delplancke-Ogletree, A. Fernández, *Wear*, 270(7-8), 541 (2011).

# Mathematical modelling concerning the influence of chemical composition upon hardness of cadmium telluride crystal
## - Part 1-

T.L. Severin[1*], A. Potorac[2]

[1,2] *University Stefan cel Mare, Suceava, Faculty of Mechanical Engineering, Mechatronics and Management, Department of Mechanics and Technologies, 13 University St., 720229 Suceava, Romania*

Cadmium telluride is an alloy with semiconductor properties obtained by melting on furnaces of cadmium and tellurium, and is currently the basic material for manufacturing photovoltaic cells. The mathematical model developed in this paper expresses the hardness values of cadmium telluride crystal, depending on the micro-alloying elements. This material has been studied in the literature only in terms of properties defining characteristics of semiconductors, without presenting any data concerning the influence of micro-alloying elements upon hardness values. Micro-alloying elements concentration was determined using laser ablation technique with New Wave Research UP213 coupled to an ICP-MS Agilent 7500 and hardness values were determined with DUH-211S Shimadzu ultra-micro hardness tester, the Martens method. The mathematical model is aimed to determine hardness of cadmium telluride crystals depending on the chemical composition.

**Keywords:** hardness, laser ablation, alloy, hardness tester

## INTRODUCTION

Cadmium telluride is an alloy with semiconductor properties, obtained through melting in special furnaces tellurium and cadmium semimetals and is currently the base material for manufacturing photovoltaic cells. Furthermore, through micro-alloying (crystal doping) with mercury, the base material for high performance infrared detectors used in spectrometry and remote sensing is manufactured, whereas through micro-alloying with zinc is obtained the base material for manufacturing Röntgen and Gamma detectors [1, 2].

Cadmium telluride is characterized through a crystal, hence fragile structure. In the process of manufacturing large areas solar panels, the cadmium telluride, as base material, should provide corresponding mechanical characteristics depending on operating conditions. That is why a thorough study and an advanced characterization of the mechanical behavior of cadmium telluride crystal could be extremely useful.

The paper proposes a mathematical model which provides the hardness values of cadmium telluride crystal depending on the micro alloying elements. This material has been studied in the literature only in terms of defining the characteristics of semiconductor properties [3, 4, 5,

6, 7], without presenting any data concerning the influence of micro-alloying elements upon hardness values. That is why, providing a model and, consequently, having the possibility to predict the mechanical behavior and especially the hardness of cadmium telluride is of the last importance for practical issues depending on operating particularities.

## EQUIPMENT USED FOR THE ACQUISITION OF EXPERIMENTAL DATA

LA-ICP-MS technique is particularly useful for in situ samples analyzes, that is, for applications that require understanding of elementary spatial variation for the sample.

Laser ablation (*LA*) coupled to an ICP-MS equipment (mass spectrometry with inductively coupled plasma) may perform direct analysis on almost all materials.

This technology was used in determining the composition of cadmium telluride crystal, by the instrumentality of a LA model UP213 of New Wave Research Company, coupled with a model Agilent 7500 ICP-MS, Agilent Technologies, from the laboratory of Instrumental Analysis of the Faculty of Food Engineering, University of Suceava Romania (Fig.1). The UP 213 (213 nm laser ablation) releases atomic vapors of the material absorbed in the ICP MS to quantitatively determine its elements.

---

* To whom all correspondence should be sent:
  severin.traian@fim.usv.ro
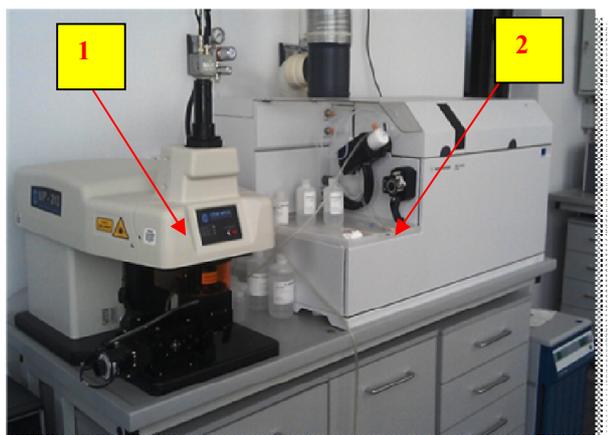
**Fig.1.** Laser ablation system UP-213 New Wave (1) – ICP-MS Agilent 7500 (2)

The UP series of laser ablation equipment manufactured by New Wave Research Company is specially designed to work with *ICP-MS* and *ICP-OE* systems. The *YAG* laser of *UP213* ablation equipment is operating in *213 nm UV* region, Fig.2.
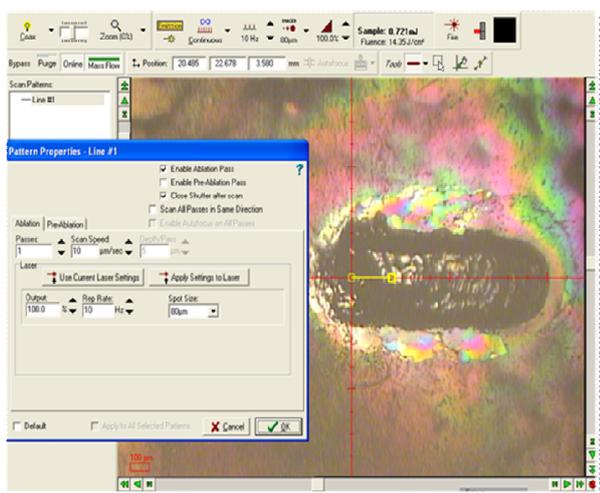


**Fig.2.** Ablation zone on surface CdTe crystal after a qualitative and quantitative analysis performed with NewWave UP213 spectrometer coupled to an Agilent 7500 ICP-MS; laser continuously 10Hz rate, scan speed 10 μm/s, working energy 0.721 mJ channel length 1 mm

Using ICP MS type spectroscopy to study hardness allows highlighting the influence of micro alloying elements traces upon the hardness.

Micro hardness of cadmium telluride crystal was investigated and evaluated using the Shimadzu DUH-211S micro hardness tester (Fig.3).

## RESULTS

In this experimental research, cadmium telluride single crystal has the composition, concentrations of components and mechanical characteristics consistent with those presented in Tables 1 and 2

and determined by ICP-MS-LA technique. Moreover, the research was focused also on the distribution of the segregation of chemical elements of micro alloying with respect to the geometrical position of a point down the axis of the crystal, distribution enabling further correlation of the composition and concentration with the semiconductor, mechanical and thermal properties of cadmium telluride. To this end cadmium telluride crystal was mechanically cut lengthwise and on the symmetry axis have been marked distances of 5 mm on 5 mm (17 areas,), Fig.4.
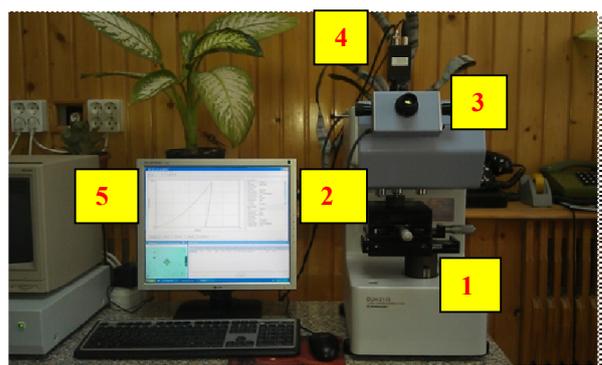


**Fig.3.** Shimadzu DUH-211S micro hardness tester (1), sample manual positioning system (2), footprint optical viewing system (3) image pickup video system CCD (4), hardness measurement and footprint inspection software (5)
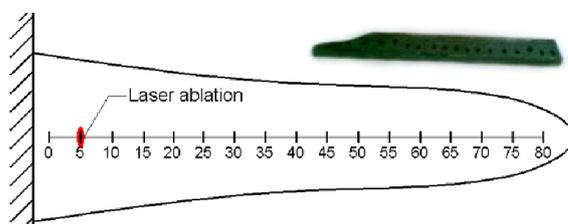


**Fig.4.** Analysis scheme on areas of cadmium telluride crystal, [8], [11]

The analysis of the distribution of micro alloying elements of cadmium telluride crystal on was extended to all ten chemical elements, whose average concentration (mean concentrations of all the seventeen measurement areas) is shown in Table 1.

Determination of the mechanical characteristics (HMV, HM - Martens hardness), indentation elasticity modulus ($E_{IT}$), tendency of creep indentation ($C_{IT}$) and depth of indentation for cadmium telluride crystal depending on the micro alloying elements for the 17 analyzed areas (S1-S16) was instrumented through the Martens method for determining hardness, using an automatic hardness testing device Shimadzu DUH-211S, ($n_{it}$=plastic and elastic portions of indentation work).

**Table 1.** Average concentrations of micro alloying elements in a cadmium tellurium single crystal (ppb=parts per billion)

| Test no. | V(ppb) | Cr(ppb) | Co(ppb) | Ni(ppb) | Cu(ppb) |
|---|---|---|---|---|---|
| 0 | 120 | 334 | 29 | 37 | 31 |
| 1 | 120 | 250 | 28 | 36 | 30 |
| 2 | 130 | 220 | 27 | 33 | 33 |
| 3 | 150 | 210 | 25 | 25 | 35 |
| 4 | 154 | 180 | 24 | 25 | 36 |
| 5 | 154 | 168 | 24 | 24 | 37 |
| 6 | 159 | 165 | 25 | 24 | 38 |
| 7 | 161 | 163 | 24 | 24 | 40 |
| 8 | 161 | 155 | 24 | 23 | 42 |
| 9 | 168 | 148 | 25 | 22 | 44 |
| 10 | 170 | 134 | 26 | 21 | 48 |
| 11 | 171 | 132 | 25 | 20 | 49 |
| 12 | 173 | 129 | 25 | 19 | 50 |
| 13 | 180 | 127 | 24 | 19 | 53 |
| 14 | 220 | 125 | 24 | 19 | 58 |
| 15 | 221 | 125 | 23 | 18 | 60 |
| 16 | 229 | 124 | 22 | 18 | 61 |
| $\bar{x}$ | 167,117 | 169,941 | 24,941 | 23,941 | 43,823 |
| stdev | 31,966 | 56,302 | 1,748 | 5,984 | 10,107 |

**Table 1.** Continuation

| Test no | Zn(ppb) | Sn(ppb) | W(ppb) | Tl(ppb) | Pb(ppb) |
|---|---|---|---|---|---|
| 0 | 5100 | 3,4 | 46 | 0,21 | 0,57 |
| 1 | 3800 | 3,8 | 33 | 0,21 | 0,51 |
| 2 | 2500 | 3,9 | 25 | 0,18 | 0,35 |
| 3 | 1800 | 5 | 19 | 0,19 | 0,41 |
| 4 | 1660 | 9,5 | 17 | 0,21 | 0,37 |
| 5 | 1610 | 9,4 | 18 | 0,22 | 0,44 |
| 6 | 1590 | 8,6 | 20 | 0,2 | 0,45 |
| 7 | 1580 | 9,2 | 18 | 0,25 | 0,43 |
| 8 | 1570 | 9,6 | 17 | 0,17 | 0,54 |
| 9 | 1550 | 9,6 | 20 | 0,16 | 0,42 |
| 10 | 1420 | 9,5 | 17 | 0,2 | 0,41 |
| 11 | 1419 | 9,5 | 15 | 0,15 | 0,46 |
| 12 | 1411 | 9,4 | 13 | 0,19 | 0,71 |
| 13 | 1405 | 9,4 | 12 | 0,16 | 0,57 |
| 14 | 1400 | 9,3 | 11 | 0,18 | 0,44 |
| 15 | 1398 | 9,2 | 11 | 0,18 | 0,33 |
| 16 | 1398 | 9,4 | 11 | 0,14 | 0,47 |
| $\bar{x}$ | 1918,294 | 8,10 | 19,00 | 0,188 | 0,463 |
| stdev | 1015,069 | 2,359 | 8,909 | 0,027 | 0,093 |

**Table 2.** Mechanical characteristics of CdTe Crystal depending on the micro alloying elements of the 17 areas of analysis

| Cr. no. | $F_{max}$ [mN] | $h_{max}$ [μm] | HMV [N/mm²] | $HM_s$ [N/mm²] | Analyzed area |
|---|---|---|---|---|---|
| 1 | 500.50 | 51.985 | 697.33 | 538.897 | S 0 |
| 2 | 500.12 | 52.587 | 681.33 | 526.533 | S 1 |
| 3 | 500.71 | 52.850 | 679.33 | 524.987 | S 2 |
| 4 | 500.50 | 53.046 | 674.33 | 521.123 | S 3 |
| 5 | 500.91 | 53.431 | 667.66 | 515.97 | S 4 |
| 6 | 500.21 | 53.544 | 663.66 | 512.88 | S 5 |
| 7 | 500.50 | 53.554 | 662.66 | 512.10 | S 6 |
| 8 | 500.10 | 53.644 | 661.33 | 511.07 | S 7 |
| 9 | 500.50 | 53.731 | 660.66 | 510.56 | S 8 |
| 10 | 500.98 | 53.723 | 657.33 | 507.98 | S 9 |
| 11 | 500.00 | 53.750 | 649.33 | 501.80 | S 10 |
| 12 | 500.10 | 53.815 | 649.00 | 501.54 | S 11 |
| 13 | 500.50 | 53.809 | 644.33 | 497.93 | S 12 |
| 14 | 500.50 | 53.815 | 640.66 | 495.10 | S 13 |
| 15 | 500.50 | 54.001 | 639.66 | 494.33 | S 14 |
| 16 | 500.50 | 54.194 | 638.66 | 493.56 | S 15 |
| 17 | 500.03 | 54.256 | 635.00 | 490.72 | S 16 |

**Table 2.** Mechanical characteristics of CdTe Crystal depending on the micro alloying elements of the 17 areas of analysis (continuation)

| Cr no. | Hit [N/mm²] | Eit [N/mm²] | Cit [%] | nit [%] | Analyzed area |
|---|---|---|---|---|---|
| 1 | 898.167 | 3.096e+004* | 0.624 | 15.825 | S 0 |
| 2 | 881.805 | 3.032e+004* | 0.621 | 16.265 | S 1 |
| 3 | 872.484 | 2.982e+004* | 0.596 | 16.425 | S 2 |
| 4 | 864.408 | 2.640e+004* | 0.590 | 16.434 | S 3 |
| 5 | 860.234 | 2.617e+004* | 0.588 | 16.486 | S 4 |
| 6 | 860.758 | 2.601e+004* | 0.587 | 17.236 | S 5 |
| 7 | 854.355 | 2.504e+004* | 0.530 | 17.373 | S 6 |
| 8 | 853.564 | 2.500e+004* | 0.529 | 17.397 | S 7 |
| 9 | 848.605 | 2.499e+004* | 0.529 | 17.498 | S 8 |
| 10 | 837.764 | 2.498e+004* | 0.524 | 17.514 | S 9 |
| 11 | 837.764 | 2.489e+004* | 0.524 | 17.914 | S 10 |
| 12 | 827.154 | 2.489e+004* | 0.518 | 17.936 | S 11 |
| 13 | 824.842 | 2.487e+004* | 0.506 | 18.079 | S 12 |
| 14 | 823.154 | 2.484e+004* | 0.504 | 18.116 | S 13 |
| 15 | 821.792 | 2.483+004* | 0.504 | 18.129 | S 14 |
| 16 | 820.304 | 2.479e+004* | 0.503 | 18.257 | S 15 |
| 17 | 819.602 | 2.479e+004* | 0.502 | 18.568 | S 16 |
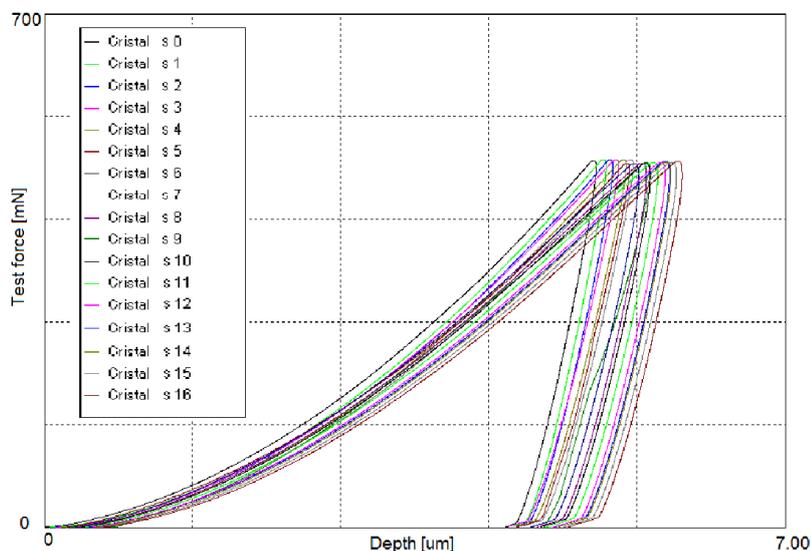


**Fig.5.** The graphical representation of the evolution of average hardness of cadmium telluride crystal depending on the micro alloying elements for the 17 analyzed areas: power (F) - indentation depth ($h_{max}$), Martens Hardness Test, using hardness testing device Shimadzu DUH-211S
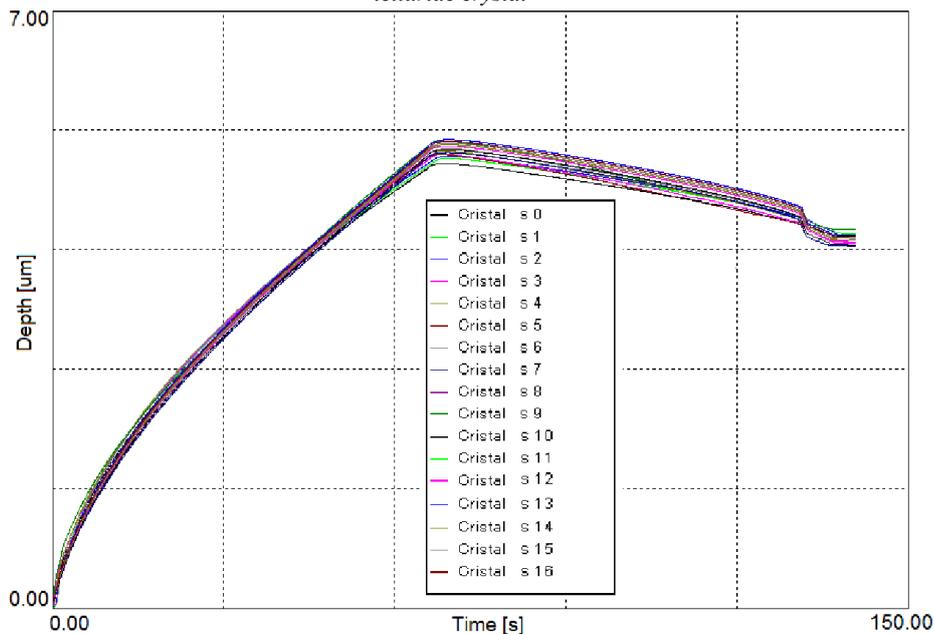
**Fig.6.** The graphical representation of the evolution of average hardness of cadmium telluride crystal depending on the micro alloying elements for the 17 analyzed areas: indentation depth ($h_{max}$) – time (t), Martens Hardness Test, using hardness testing device Shimadzu DUH-211S

Also plotted in Fig.5 it is shown the evolution of the indentation force (F) depending on the indentation depth (h) of the indenter, respectively in Fig.6 the variation of the indentation depth (h) of the indenter in time, for the cadmium telluride crystal.

## CHECKING THE HOMOGENEITY OF HARDNESS VALUES VARIANCES FOR CADMIUM TELLURIDE CRYSTAL

Checking the homogeneity of hardness values variances for cadmium telluride crystal is performed using Bartlett Test and finally verifying $\chi_B^2$ which should obey to the law $\chi^2$ with *k-1* degrees of freedom. The decision concerning $H_0$ *hypothesis* will be accepted if: $\chi_B^2 \leq \chi_{v;\alpha}^2 = \chi_{k-1;\alpha}^2$, and rejected if: $\chi_B^2 \rangle \chi_{v;\alpha}^2 = \chi_{k-1;\alpha}^2$ [9, 10].

**Table 3**. Bartlett test results for CdTe crystal hardness values

| Current no. | Bartlett parameters checking | Crystal area | | | | | | | | |
|---|---|---|---|---|---|---|---|---|---|---|
| | | Area 0 | Area 1 | Area 2 | Area 3 | Area 4 | Area 5 | Area 6 | Area 7 | Area 8 |
| 1 | k- area no. | | | | | 17 | | | | |
| 2 | $n_i$ – sample | 3 | 3 | 3 | 3 | 3 | 3 | 3 | 3 | 3 |
| 3 | $V_i = n_i - 1$ | 2 | 2 | 2 | 2 | 2 | 2 | 2 | 2 | 2 |
| 4 | $s^2$ ( variance ) | 0,33 | 12,33 | 20,33 | 9,33 | 6,33 | 20,33 | 2,33 | 6,33 | 4,33 |
| 5 | $v_i \cdot ln\, s^2$ | -2,217 | 5,024 | 6,024 | 4,466 | 3,690 | 6,024 | 1,691 | 3,690 | 2,931 |
| 6 | $v \cdot ln\, s^2$ | | | | | 68,59724 | | | | |
| 7 | $\sum_{i=1}^{k} v_i \cdot ln\, s_i^2$ | | | | | 47,96952 | | | | |
| 8 | $\dfrac{1}{3(k-1)}$ | | | | | 0,02083 | | | | |
| 9 | $\sum_{i=1}^{k}\left(\dfrac{1}{v_i} - \dfrac{1}{v}\right)$ | | | | | 8,00003 | | | | |
| 10 | $\chi_B^2$ - **calculated** | | | | | **17,68** | | | | |
| 11 | $\chi_B^2$ - **table** | | | | | **27,58** | | | | |

**Table 3.** Bartlett test results for CdTe crystal hardness values (continuation)

| Current no. | Bartlett parameters checking | Crystal area | | | | | | | |
|---|---|---|---|---|---|---|---|---|---|
| | | Area 9 | Area 10 | Area 11 | Area 12 | Area 13 | Area 14 | Area 15 | Area 16 |
| 1 | K- nr. area no. | | | | 17 | | | | |
| 2 | $n_i$ - sample | 3 | 3 | 3 | 3 | 3 | 3 | 3 | 3 |
| 3 | $V_i = n_i - 1$ | 2 | 2 | 2 | 2 | 2 | 2 | 2 | 2 |
| 4 | $s^2$ ( variance ) | 0,33 | 6,33 | 13 | 12,33 | 9,33 | 1,33 | 0,33 | 3 |
| 5 | $v_i \cdot ln\, s^2$ | -2,217 | 3,690 | 5,129 | 5,024 | 4,466 | 0,570 | -2,217 | 2,197 |
| 6 | $v \cdot ln\, s^2$ | | | | 68,59724 | | | | |
| 7 | $\sum_{i=1}^{k} v_i \cdot ln\, s_i^2$ | | | | 47,96952 | | | | |
| 8 | $\dfrac{1}{3(k-1)}$ | | | | 0,02083 | | | | |
| 9 | $\sum_{i=1}^{k} \left( \dfrac{1}{v_i} - \dfrac{1}{v} \right)$ | | | | 8,00003 | | | | |
| 10 | $\chi_B^2$ **- calculated** | | | | **17,68** | | | | |
| 11 | $\chi_B^2$ **- table** | | | | **27,58** | | | | |

According to the results shown in Table 3 with respect to checking the homogeneity of variance for hardness values recorded for the CdTe crystal: $\chi^2_{B\text{-}calculated}$ = (**17,68**) < $\chi^2_{B\text{-}table}$ (**27,58**). Consequently the hypothesis of the homogeneity of hardness dispersions should be accepted, with a probability $P = 1 - \alpha = 1 - 0,05 = 0,95 = 95\%$.

It is clear that using Bartlett test, the results concerning the influence of micro alloying elements upon the hardness obtained for cadmium telluride crystal is confirmed by 95% confidence level.

## CONCLUSIONS

In order to establish a link between the micro alloying elements and cadmium telluride crystal hardness experimental researches were carried out using ablation laser equipment UP213 New Wave Research, coupled to ICP-MS 750 Agilent, respectively Martens method for hardness measuring with hardness testing device Shimadzu DUH-211S.

Moreover, using the method of homogeneity of hardness values variance (Bartlett test) was checked and validated by 95% confidence level, the influence of micro alloying elements upon cadmium telluride crystal hardness.

According to the theoretical and experimental research, as shown from both Figures 5, 6 and values in Tables 1, 2, it is obvious that the influence of micro alloying elements have a significant role on the mechanical characteristics of cadmium telluride crystals.

In order to extend the current research a mathematical model able to predict the value of cadmium telluride crystals hardness depending on the micro alloying elements should be developed. This model will be drawn up based on the values of the alloying elements in Table 1, with hardness values specific to the analysis of the crystal according to Table 2.

The results of Bartlett test on the values determinated and presented in this paper encourage us to continue the work through developing the mathematical model for predicting the influence of chemical composition upon hardness of cadmium telluride crystal.

## ACKNOWLEDGEMENTS

## REFERENCES

1  Capper, P. *Properties of narrow gap cadmium-based compounds*, IET. p. 39-40, ISBN 978-0-85296-880-2, 2012.

2   Brewer, P.D., Zinck, J.J., Olson, G.L., *Surface composition changes and ablation dynamics in excimer laser irradiated CdTe Laser ablation for materials synthesis,* Book Series, Materials Research Society Symposium Proceedings, p. 68-70, 1990.

3   Fochuk, P.; Nykonyuk, Ye, Verzhak, Ye, *Dopant content and thermal treatment of CdZnTe in effects on point-defect structures*, IEEE Nuclear Science Symposium and Medical Imaging Conference (2008 NSS/MIC), vol. 1-9, p. 4880-4882, 2009.

4   Fochuk, P., Grill, R. Kopach, O., *Elimination of Te inclusions in Cd1-xZnxTe crystals by short-term thermal annealing*, IEEE Transactions on Nuclear Science, vol. 59, Issue 2, p. 258-260, 2012.

5   Rzeszutek, J., Oszmaldowski, M., Savchuk, V, *Ablation of CdTe with 100 pulses from Nd:YAG laser: Velocity distribution of emitted particles*, Nuclear Instruments & Methods in Physics Research Section B-beam Interactions with Materials and Atoms, vol.: 266, Issue 21, p. 4766-4774, 2008.

6   Savchuk, Victor K.; Kotlyarchuk, Bohdan K.; Zaginey, Apollinary O.; et al.*Ablation species generated by high power laser pulses from Cd-Te target*, 70091M, Proceedings of the Society of Photo-Optical Instrumentation Engineers (SPIE) vol. 7009, p. M91-M91, 2008.

7   Semaltianos, N. G., Logothetidis, S., Perrie, W., et al. *CdTe nanoparticles synthesized by laser ablation*, Applied Physics Letters, vol. 95 Issue 3, no. 033302, 2009.

8   Gutt, S., Gutt, G., Severin, T. L., Vasilache, V., Poroch, M., *Contribution to design and carry out an universal dynamic hardness tester for metalic materials testing*, Annals of DAAAM for 2010 & Proceedings of 21 st International Symposium, ISBN 978-3-901509-73-5, ISSN 1726-9679, p. 0506, Vienna, Austria, 2010.

9   Iacob, D., *Statistica*, Ed. Universităţii Ştefan cel Mare Suceava, ISBN 973-9408-57-5, p.114-132, 2000.

10  Bulgaru, M., Bolboaca, L., *Ingineria calitatii. Mangementul calităţii, statistică şi control, măsurari în 3D*, Ed. Alma Mater, ISBN 973-85153-0-0, Cluj-Napoca, p.188-209, 2001.

11  Severin Traian Lucian, *Cercetări şi contribuţii la realizarea şi promovarea de noi metode şi aparate pentru încercarea de duritate*, teza de doctorat*, Research and contributions to the development and promotion of new methods and devices for hardness testing*, doctoral thesis 2012.

# Protective multilayer (Ti, Al) N coatings deposited at low temperature by closed-field unbalanced magnetron sputtering

T. M. Cholakova[1*], V. A. Chitanov[1], L. P. Kolaklieva[1], R. D. Kakanakov[1], D.G. Kovacheva[2], P. K. Stefanov[2], S. N. Rabadzhiyska[1], E. A. Korina[1], V. I. Kopanov[1]

[1]*Central Laboratory of Applied Physics, Bulgarian Academy of Sciences, 61 Sankt Petersburg Blvd., 4000 Plovdiv, Bulgaria*

[2] *Institute of General and Inorganic Chemistry, Bulgarian Academy of Sciences, 1113 Sofia, Bulgaria.*

This article reports the results of a study of the physical-mechanical properties of the multilayer Ti-Al-N coatings deposited onto two types of substrates: high-speed steel and carbon tool steel. The coatings were deposited at the temperatures of 150-200 ºC by closed-field reactive unbalanced magnetron sputtering, while the process parameters were optimized to achieve adherent good quality coatings. Nanoindentation, scratch tests, X-ray diffractometry (XRD) and X-ray photoelectron spectroscopy (XPS) were used to characterize structural, compositional and mechanical properties of the coatings. The obtained coatings exhibited nanohardness and elastic modulus in the range of 26-38 GPa and 320-418 GPa respectively. The results of the scratch tests showed that the state of adhesion of the coating to the substrate depends on the coating deposition conditions. The measured coefficient of friction for all of the coatings was in the range of 0,09-0,13. The XPS and XRD analyses revealed that the coatings have $Ti_{0.42}Al_{0.58}N$ composition with a lattice constant of 4.17Å. The findings are that the main process parameters defining the mechanical properties of the deposited at low temperature Ti-Al-N coatings are: reactive gas flow rate, sputtering temperature and plasma cleaning time.

**Keywords:** physical vapour deposition (PVD), unbalanced magnetron sputtering, Ti–Al–N layers, hardness, adhesion

## INTRODUCTION

Physical vapour deposition (PVD) processes are widely used for deposition of oxidation and corrosion resistant coatings on tools or machine components. The PVD transition metal nitrides such as Titanium Nitride (TiN) have been widely used as protective hard coatings to increase the lifetime and performance of cutting and forming tools [1-5]. However, the main drawback of TiN is its limited oxidation resistance (approximately $500^oC$). Later on, a light metal element such as aluminium was incorporated into the TiN forming Titanium Aluminium Nitride (TiAlN) to overcome its shortcoming of instability at high temperatures. Furthermore, TiAlN coatings have been developed as an alternative to TiN, because of their higher oxidation resistance (approximately 750–800ºC), enhanced hardness (30–35 GPa) and higher corrosion resistance [6-11].

TiAlN films have been widely developed in many application fields such as cutting, forming tools, semiconductor devices, optical instruments, diffusion and biocompatible barriers [8-10]. A fundamental advantage of TiAlN films is that during heating they form a highly adhesive, dense protective $Al_2O_3$ film on the surface preventing further inward diffusion of oxygen into the coated material [11]. Among the many materials that can be chemically modulated in a multilayer, TiAlN is a favourite since it has a reputation for being wear resistant and chemically stable at high working temperatures.

Many studies have been reported on the deposition and properties of TiAlN coating produced by various techniques [12]. Among PVD coating technologies, reactive magnetron sputtering is a very useful method for producing different types of coatings including TiAlN. Although the basic sputtering process has been known and used for many years, the developed unbalanced magnetron and its incorporation into multi-source "closed-field" systems is responsible for the rise in importance of this technique. Closed-field unbalanced magnetron sputtering (CFUBMS) is an exceptionally versatile technique for the deposition of high-quality, well-adhered films. The main advantages of this technique are as follows: possibility for deposition at low temperatures, including room temperature; use of non-toxic working gases; a high degree of smoothness, uniformity and density of the deposited coatings. In order to improve the efficiency of coating process several modifications of magnetron sputtering techniques have been developed [13-19].

It is known that protective hard coatings (Ti, Al) N are generally deposited at temperatures of 400-500 ºC which provide high adhesion of the coating to the substrate, but lead to structural changes and

---

* To whom all correspondence should be sent:
ipfban-dve@mbox.digsys.bg

could worsen the substrate material properties. However, some instrumental materials such as carbon tool steel (U12) have low thermal resistance (≤200ºC) which requires low-temperature deposition of the coatings to protect the instruments from overheating. The requirement to maintain a low temperature during deposition of the Ti-Al-N coatings complicates the preparation process. Hence, the establishment of optimal technological regimes providing stable and high functional properties of the system "tool-coating" is necessary. This task could be solved by developing a multilayer coating since each sub-layer has defined composition, structure, optimal adhesion, physical-mechanical, tribological and corrosion resistance properties. Notwithstanding, the fact that TiAlN coatings have been used for many years, there are few articles on their preparation at low temperatures [18-20].

The results of the study of the physical and mechanical properties of TiAlN coatings deposited via CFUBMS process at the low temperatures are presented in this article.

## EXPERIMENTAL DETAILS

The multilayer Ti-Al-N coatings were deposited in a temperature range of 150 - 200 ºC by reactive unbalanced magnetron sputtering (UDP 850-4, Teer Coatings Ltd.) from two titanium (99,99 %) and two aluminium (99,99%) rectangular targets in a closed-field configuration. The coatings were deposited onto two types of hardened substrates: high-speed steel (HSS) and carbon tool steel (U12). Prior to coating deposition, the substrates were cleaned in a special alkaline solution in an ultrasonic bath at 60 °C for 10 minutes to remove oils used for steel protection against corrosion, ten followed by a rinse in de-ionized water and drying at 140 °C. In general, after the cleaning procedure metal substrates contain an oxide layer which critically affects the adhesion of substrate-coating. Due to this, prior to the coating deposition, the substrates were cleaned in situ by ion etching in pure argon atmosphere under typical cleaning conditions: low magnetron power and a high negative pulsed DC bias potential on the substrate. Prior to the deposition, the vacuum chamber was evacuated to a base pressure of $2\times10^{-3}$ Pa. After the evacuation, Ar or Ar + N$_2$ mixture was introduced into the chamber. The Ar flow rate was controlled by mass flow controller and the flow rate of the reactive gas N$_2$ was controlled by Optical Emission Monitor (OEM).

In the deposition process, the substrates were rotated biaxially at a speed of 5 rpm in order to obtain homogenous film thickness and composition, and the distance between the substrates and the targets was 150 mm. In Table 1. are summarized the basic parameters for the TiAlN coatings deposition.

**Table 1.** Experimental conditions for the TiAlN coatings deposition

| Process | Parameter | Value |
|---|---|---|
| Chamber evacuation | Base pressure | $2 \times 10^{-3}$ Pa |
| Plasma cleaning | Negative substrate bias | 500 V |
| | Ti target current | 0.5 A |
| | Time | 5 – 20 min |
| | Ar flow rate | 25 sccm |
| Coating deposition | Substrate bias | -70 V |
| | Ti target current | 5.0 A |
| | Al target current | 0.3 - 3.0 A |
| | N$_2$ flow rate | 0.5 - 16 sccm |
| | Substrate temperature | 150 - 200°C |
| | Film thickness | 1.2 - 1.6 µm |

The deposition of the multilayer Ti-Al-N coatings starts with a Ti bond layer (~ 100 nm) followed by two TiN interlayers (graded and stoichiometric, ~ 250 nm), then the Al content is increased gradually to form a graded Ti-Al-N transition layer and the structure is then completed with a Ti-Al-N layer. Graded interfaces are routinely formed to ensure that stress induced in the coating is dissipated away from the coating-substrate interface. All the films were deposited at a bias voltage of -70V and a frequency of 150 kHz, in pulsed regime of the Al cathodes and DC regime of the Ti cathodes using a mixture of argon (99.9999%) and nitrogen (99.9999%) gases with different partial pressure ratio. The Ar flow rate was kept constant (25 sccm) in all of the experiments.

Measurements of the coating thickness were performed by a Calotest which is a suitable method for obtaining quick information about layer configuration, abrasion resistance and thickness. A stainless steel ball (~ 30 mm diameter) is used with diamond slurry with particles of 0.25 µm in diameter. The coating was abraded until the substrate was reached by the ball. After that, the coating was placed under an optical microscope where the circular crater shape was used to measure

the coating thickness by comparing the relative diameter of the exposed surface layers to the known diameter of the ball. The thickness was calculated using the CCD camera of the CPX Compact Platform of Anton Paar, CSM Instruments.

The mechanical properties of the deposited coatings were investigated using Compact Platform CPX (MHT/NHT) CSM Instruments equipment. Nanoindentation was performed by a triangular diamond Berkovich pyramid in the loading interval of 15 - 200 mN. The nanohardness and elastic modulus were determined by applying the Oliver & Phar method. The microscratch tests for coating adhesion and friction coefficient determination were performed using a spherical Rockwell indenter with a radius of 200 μm at normal force, progressively increasing from 1 N to 30 N.

Powder X-ray diffraction pattern of the sample was collected within the range from 5.3 to $80^{\circ}2\theta$ with a constant step $0.02^{\circ}2\theta$ and counting time 175 sec./step on Bruker D8 Advance diffractometer (Germany) with Cu Kα radiation and LynxEye detector. Diffraction patterns from the coating were obtained with a detector scan at fixed tube position with tube angle $10^{\circ}$ and $5^{\circ}$. Phase identification was performed with the Diffracplus EVA using ICDD-PDF2 (2014) Database. The unit cell parameters and mean crystallite size were determined with the Topas-4.2 software package using the fundamental parameters peak shape description, including appropriate corrections for the instrumental broadening and difractometer geometry.

XPS studies were carried out in an ESCALAB MkII (VG Scientific) electron spectrometer with an Al K, (1486.6 eV) X-ray source. In order to obtain information about chemical composition of the Ti-Al-N coatings, XPS measurements were taken.

## RESULTS AND DISCUSSION

### *Coating thickness*

A series of multilayer TiAlN coatings were deposited on commercially available 5 mm thick HSS (EN: 1.3343) and carbon tool steel (EN:CT 120) substrates with diameter of 20 mm and 12 mm accordingly. Coating thickness measurements were taken by applying a Calotest method. The thickness of the deposited coating was calculated from measurements of the diameters of the craters in the coating and substrate. Fig.1 shows a segment of the optical microscopy image of the TiAlN coating architecture, obtained by ball-cratering test. This technique can be easily adapted for the measuring of the thickness of the different layers in a

multilayered coating as long as the individual layers are easily distinguished and of sufficient thickness to be resolved by the microscope used to view and measure the crater diameters.

The calculated total thickness for all deposited coatings was in the range of 1.2 −1.6 μm.
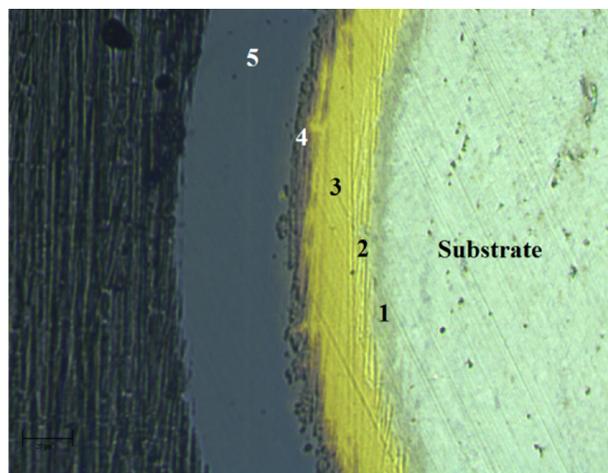


**Fig.1.** A segment of the optical microscopy image of the TiAlN coating architecture, obtained by ball-cratering test: (1)- Ti bond layer; (2)- TiN graded interlayer; (3)- TiN stoichiometric interlayer; (4)- TiAlN transition layer; (5)- TiAlN top layer

### *Mechanical properties*

The mechanical properties of the multilayer TiAlN coatings obtained at different deposition conditions are summarized in Table 2. The hardness (H) and elastic modulus (E) were determined from the indentation loading/unloading curves generated with a Berkovich indenter using the Oliver–Pharr method [22]. A maximum load of 15 mN was applied, which corresponded to maximum indentation depths of less than 15% of the coating thickness, to minimize the substrate influence on the measurement. In our experiments, all the films were deposited at a constant bias voltage of -70 V and a frequency of 150 kHz in pulsed regime of the Al cathodes and DC regime of the Ti cathodes. The substrate bias plays an important role in determining the mechanical properties of the coatings. The use of ion bombardment allows deposition of adherent coatings at low substrate temperatures. In general, the hardness increases with the substrate bias up to 100 V, and does not change significantly at higher bias values [21]. Nanoindentation measurements reveal that the TiN interlayers (see Table 2) have nanohardness of 24 GPa and elastic modulus of 297 GPa. The measured mechanical properties lead to a H/E ratio of 0.08. The TiAlN coatings deposited at

substrate temperature of 200°C presented maximum hardness H= 38 GPa and elasticity modulus E = 418 GPa. However, this temperature is not recommended for deposition onto carbon tool steel U12 substrate due to its low thermal resistance ($\geq$ 200 ºC). For this reason, the main deposition processes are developed at lower temperatures. The TiAlN coatings (Table 2) obtained at a temperature of 170 °C and nitrogen flow rate of 14.6 sccm possessed a good combination of mechanical properties- high coating hardness (26-31 GPa) and

high adhesion to the substrate material (> 30 N). G.S. Kim et al. [19] reported similar hardness (38 GPa) for TiAlN coatings with the same chemical composition obtained by CFUBMS at temperature of deposition of 100ºC. Good hardness value (31 Gpa) were achieved by Z.-J. Liu et al. [20] where deposition was done at room temperature for nanocristalline TiAlN films with a content of Al (x=0.41). But in these publications, no information on the adhesion of coatings are provided.

**Table 2.** Results of mechanical properties characterization of the selected TiAlN coatings

| Samples | Substrate temperature T [ºC] | Coating thickness [µm] | Hardness H [GPa] | Elastic modulus E [GPa] | Plasticity index H/E | OEM [%] | Cleaning time t [min] | COF µ | Critical load Lc [N] |
|---|---|---|---|---|---|---|---|---|---|
| TiN | 170 | 1.0 | 24 | 297 | 0.08 | 60 | 10 | 0.11 | > 30 |
| TiAlN- #26 | 200 | 1.2 | 38 | 418 | 0.09 | 45 | 10 | 0.09 | > 30 |
| TiAlN- #71 | 150 | 1.2 | 28 | 392 | 0.071 | 45 | 10 | 0.1 | 19.3 |
| TiAlN- #79 | 170 | 1.3 | 31 | 374 | 0.083 | 45 | 7 | 0.1 | 21.4 |
| TiAlN- #81 HSS substr, | 170 | 1.4 | 27 | 353 | 0.076 | 45 | 20 | 0.1 | > 30 |
| TiAlN- #81 U12 substr. | 170 | 1.4 | 29 | 367 | 0.079 | 45 | 20 | 0.1 | > 30 |
| TiAlN- #97 HSS substr. | 170 | 1.6 | 29 | 395 | 0.074 | 40 | 7 | 0.09 | 15.6 |
| TiAlN- #97 U12 substr. | 170 | 1.6 | 26 | 513 | 0.05 | 40 | 7 | 0.13 | 14.0 |
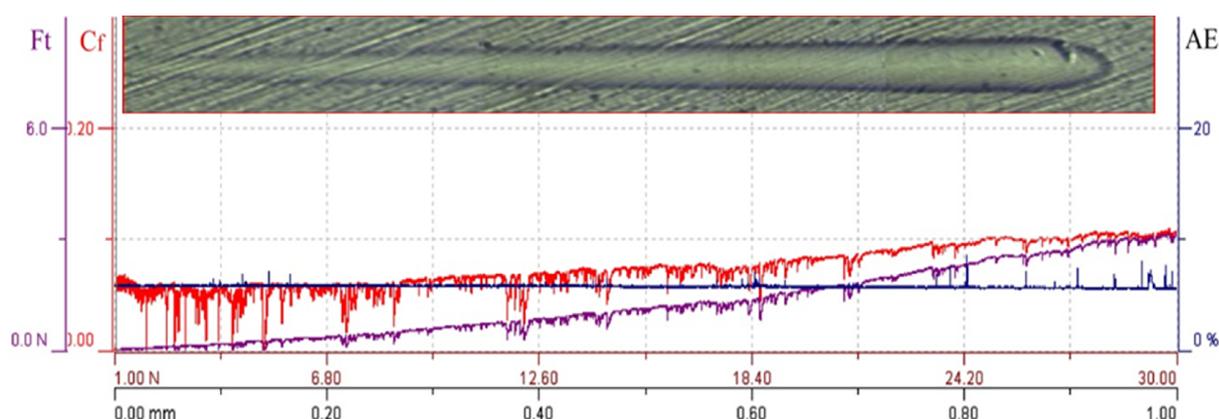


**Fig.2.** Optical micrograph of the scratch track in the TiAlN coating #81 and scratch test results of the acoustic emission (AE), friction force (Ft) and coefficient of friction (Cf)

The adhesion and toughness of the coatings were evaluated by a microscratch technique, using Rockwell diamond indenter with 200 µm tip radius. During the tests the load was progressively increased in linear mode from 1N to 30 N at scratch lengths of 1 mm and 3 mm at a constant scratching speed of 0.02 mm/min. The measurement device

registered the friction force, friction coefficient, indenter penetration depth and acoustic emission along the scratch track. Three scratches for each sample were done. Critical loads were determined after the test by optical microscopy observation of the damages formed in the scratch tracks and from the recorded acoustic emission (AE) and friction

force (Ft) signals. The critical load values Lc1 and Lc2 indicate the loads when first cohesive and adhesive cracks appeared, respectively [18, 26].
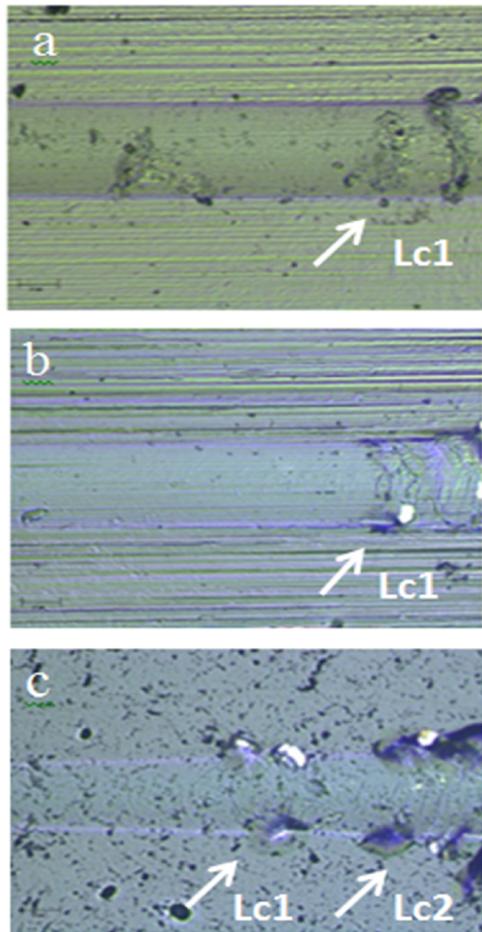


**Fig.3.** Main parts of scratch tracks with marked critical loads Lc1 and Lc2 in the TiAlN coatings: a) #71, b) #79 and c) #97 deposited at different deposition conditions

The critical loads corresponding to a load leading to the appearance of the first crack Lc1 for the selected coatings are presented in Table 2. It shows that the TiAlN coatings #26 and #81 have the best adhesion result without any visible damages within 30 N. An optical micrograph of the scratch track in the TiAlN coating #81 and scratch test results of the acoustic emission (AE), friction force (Ft) and coefficient of friction (Cf), are shown in Fig.2. As a result of the tests carried out, it was established that the critical load Lc1 for the coatings deposited at high $N_2$ flow rate (40% OEM) lies in the loading range 14 -16 N. presented The main parts of scratch tracks in the TiAlN coatings #71 (a), #79 (b) and #97 (c) are presented in Fig.3. The first symptoms of these coating damages (Lc1) are observed in the form of arch cracks (#71 and #79) and on scratch part of #97 there are small

chippings on the scratch edges. Along with the load increase, semicircles are leading to a local delamination of the coating. In general, the coatings deposited on the HSS substrate show better adherence to the substrate than coatings deposited on the carbon tool steel U12 substrate. Y. Pinot et al. [18] reported properties of hard TiAlN coatings with different Al content ($0.46 \leq x \leq 0.62$) deposited at room temperature by r.f magnetron reactive sputtering from TiAl alloy targets. Contrary to our results, on these coatings lower adhesion strength was observed (Lc1 $\leq 8.5$ N).
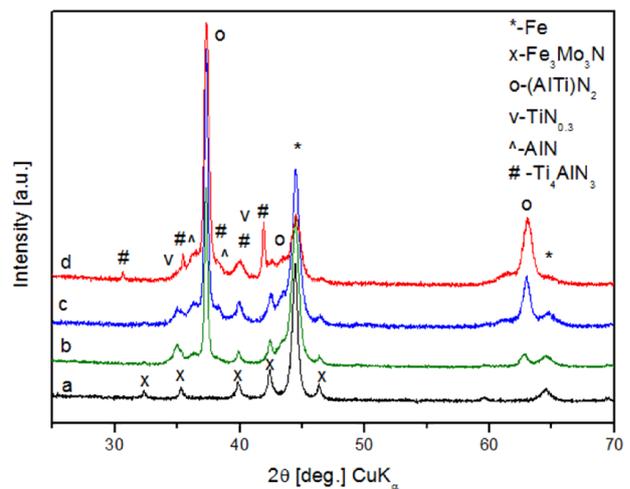


**Fig.4.** XRD patterns of a) substrate SS, b) substrate with coating at normal θ-2θ geometry, c) detector scan with fixed tube position at $10^o$, d) detector scan with fixed tube position at $5^o$

### XRD analysis

The X-ray diffraction patterns of the coatings in the hard metal-coating system are difficult to obtain due to overlapping of the coating peaks with those of the substrate. With the aim to reduce the substrate effect, the grazing incidence X-ray diffraction method with a constant incident angles beam was used. The results from XRD analyses are summarized in Fig.4. Spectrum (a) shows the diffraction pattern of the SS-substrate, spectrum (b) represents the XRD pattern of the coating over the substrate in normal (θ-2θ) geometry while spectra (c) and (d) represent the diffraction patterns collected with a fixed tube position with angle $10^o$ and $5^o$ respectively (the signal is obtained predominantly from the coating). The HSS substrate is represented by two sets of peaks – the main phase corresponds to the cubic Fe phase. Due to the high values of molybdenum and tungsten presented in the steel, a second set of lines is also presented in the diffraction pattern of the substrate

corresponding to composition $Fe_4W_2N$ and/or $Fe_3Mo_3N$ (the peaks of these two phases overlap).

The coating itself comprises mainly the phase $(AlTi)N_2$ which crystallizes in the cubic Fm-3m space group with unit cell parameter a = 4.175 Å close to the value 4.172 Å given in ICDD PDF2 #71-5864. Mean crystallite size of the $(AlTi)N_2$ phase is 44 (1) nm. The presence of small peaks of some impurity phases as $TiN_{0.3}$, AlN and $Ti_4AlN_3$ could be seen as indication of some local inhomogeneity of the coating layer.

*XPS analysis*

Fig.5 represents the high resolution XPS spectra results of the multilayer TiAlN coating of #81 before and after the sputter etching. It is observed that the peak associated with Ti metal (Fig.5a) consists of two peaks centred at 457.0 eV and 462.1 eV. These peaks originate from Ti 2p3/2 and Ti 2p1/2 electrons in titanium oxynitride [25, 26]. Fig.5(b) shows the XPS spectra for the corresponding Al 2p levels of #81. The contribution in Fig.5(b) with maximum binding energy at 73.7 eV is assigned to Al-N chemical bonding state within the coating [27]. The fact that after etching the N1s spectrum shows only one peak with binding energies of approximately 396.3 eV (Fig.5c) is attributed to the presence of nitride films (TiN and AlN) [25].

The concentrations of titanium, aluminium and nitrogen in the coating top layer (#81) as determined by XPS analysis are 24,3 at.%, 33,4 at.% and 42,3 at.%, respectively. As expected, when the Al target current increases, the relative Al content in the film also increases during the transition Ti-Al-N layer deposition, while the reverse trend is seen for the Ti content.
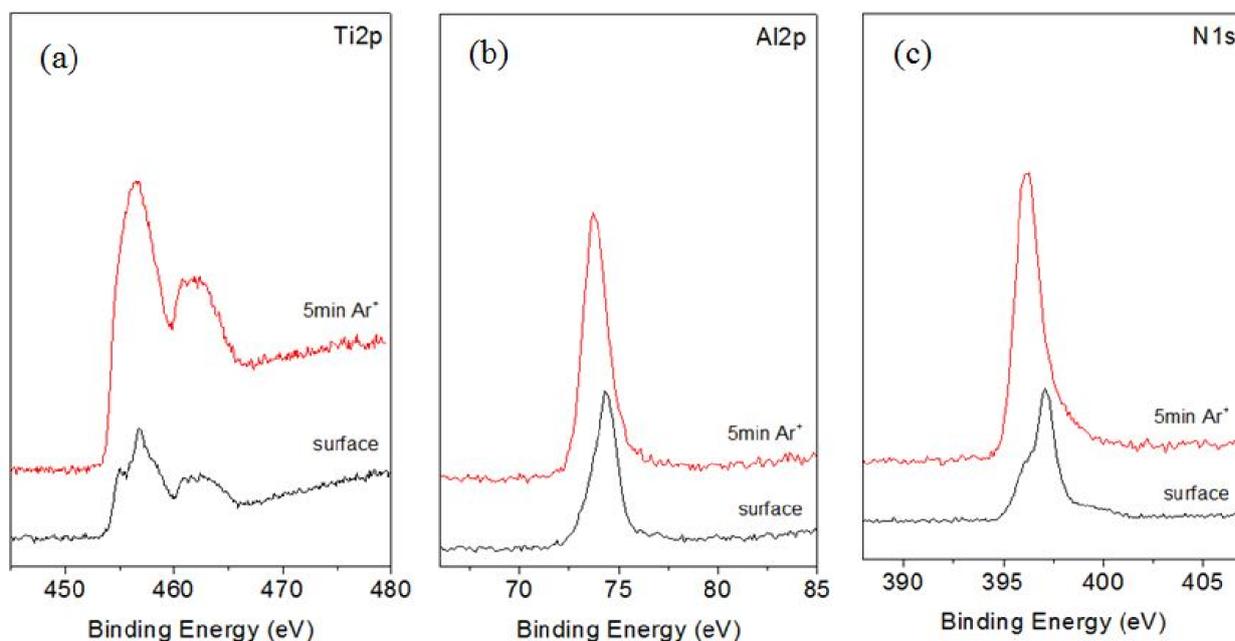


**Fig.5.** XPS spectra of (a)- Ti 2p, (b)- Al 2p and (c)- N 1s of the TiAlN sample (#81) before and after sputter etching in Ar$^+$ to remove the contaminated surface layer

The XPS results of the top layer show that the fraction (x) of Al atomic concentration [Al /(Ti + Al)] is approximately 0,58. This result is in line with the XRD results. The main AlTiN phase reveals the lattice constant to be approximately 4.17 Å which is significantly lower as compared to the reference value of 4.24 Å for pure TiN.

CONCLUSIONS

TiAlN coatings were prepared by closed-field reactive unbalanced magnetron sputtering on commercially available high speed steel and carbon tool steel with low thermal resistance. The coatings deposited at 200 ºC exhibit the greatest nanohardness and elastic modulus of 38 GPa and 418 GPa, respectively. Maximum value of the critical failure load (>30 N) was observed for the coating deposited at substrate temperature of 170ºC, nitrogen flow rate of 14,6 sccm and substrate cleaning time of 20 min. These coatings have very good adhesion strength. On the other hand, minimum critical failure load (Lc ≈15 N) was

observed for coatings deposited at substrate temperature of 170 ºC , nitrogen flow rate of 15,4 sccm and substrate cleaning time of 10 min. It can be concluded that the duration of plasma cleaning before deposition was mainly responsible for the adhesion strength of the coating to the substrate. The x-ray diffraction data shows formation mainly on the AlTiN phase with B1 NaCl structure and a mean crystallite size of 44 nm. The XPS analysis reveals that the coatings have $Ti_{0.42}Al_{0.58}N$ composition. It is evident, that the deposition of coatings with superior mechanical properties at low deposition temperatures needs to be controlled and balanced through careful selection of coating composition and development of processing conditions.

## REFERENCES

1  Y.I. Chen, J.G. Duh, Surf. Coat. Technol., Vol. 46, Iss. 3, 371–384 (1991).

2  S. Yamamoto and H. Ichimura, J. Mater. Res., Vol. 11, No.5 (1996).

3  Ph. Roquiny, F. Bodart, G. Terwagne, Surf. Coat. Technol., 116–119, 278–283 (1999).

4  V. Chawla, R. Jayaganthan, R. Chandra, Mater. Charact., 59, 1015-1020 (2008).

5  N. Saoula, K. Henda et R. Kesrij, Plasma Fusion Res. SERIES, Vol. 8, 1403-1407 (2009).

6  Munz W D, J. Vac. Sci. Technol., 4, 2717 (1986).

7  J.C. Oliveira, A. Manaia, A. Cavaleiro, Thin Solid Films, 516, 5032 (2008).

8  C. Chokwatvikul, S. Larpkiattaworn, S. Surinphong, C. Busabok, P. Termsuksawad, Journal of Metals, Materials and Minerals, 21, 115 (2011).

9  D.G. Park, T.H. Cha, S.H. Lee, I.S. Yeo, J. Vac. Sci. Technol,. 19 (6), 2289 (2001).

10  J.T. Chen, J. Wang, F. Zhang, G.A. Zhang, X.Y. Fan, Z.G. Wu, P.X. Yan, J. Alloys Compd., 472, 91 (2009).

11  A. K. Singh, N. Kumari, S. K. Mukherjee, P. K. Barhai, IJRRAS., 14(3), 603 (2013).

12  S. PalDey, S.C. Deevi, Mater. Sci. Eng., A342, 58-79 (2003).

13  P.J. Kelly, R.D. Arnell, Vacuum, 56, 159-172 (2000).

14  J. Weichart, M. Lechthaler, IOP Conf. Series: Mater. Sci. Eng., 39, 012001 (2012).

15  S.K. Wu, H.C. Lin, P.L. Liu, Surf. Coat. Technol. 124, 97–103 (2000).

16  Q. Yang, D.Y. Seo, L.R. Zhao, X.T. Zeng, Surf. Coat. Technol. 188–189, 168–173 (2004).

17  A. Z. Ait-Djafer, N. Saoula, H. Aknouche, B. Guedouar, N. Madaoui, Appl. Surf. Sci., 350, 6–9 (2015).

18  Y. Pinot, M.-J. Pac, P. Henry, C. Rousselot, Ya.I. Odarchenko, D.A. Ivanov, C. Ulhaq-Bouillet, O. Ersen, M.-H. Tuilier, Thin Solid Films, 577, 74–81 (2015).

19  G.S. Kim, S. Lee, J. Hagh, Surf. Coat. Technol., 193, 213– 218 (2005).

20  Z.-J. Liu, P.W. Shum, Y.G. Shen, Thin Solid Films, 468, 161–166 (2004).

21  21. H. C. Barshilia, N. Selvakumar, K.S. Rajam, A. Biswas, Sol. Energy Mater. Sol. Cells, 92, 1425–1433 (2008).

22  22.W.C. Oliver, G.M. Pharr, J. Mater. Res., Vol. 19, No.1, 3-20 (2004).

23  23.L. García-González, M. G. Garnica-Romo, J. Hernández-Torres and F. J. Espinoza-Beltrán, Braz. J. Chem. Eng., Vol. 24, No. 02, 249 – 257, (2007).

24  24.T.Weirather, K. Chladil, B. Sartory, D. Caliskanoglu, R. Cremer, W. Kölker, C. Mitterer, Surf. Coat. Technol., 257, 48–57 (2014).

25  25.H. C. Barshilia, K. Yogesh, K.S. Rajam, Vacuum, 83, 427–434 (2009).

26  26.P.W. Shum, Z.F. Zhou, K.Y. Li, Y.G. Shen, Mater. Sci. Eng., B100, 204–213 (2003).

27  27.Yi , L. Peng , J. Huang, Mater. Sci. Eng., C59, 669–676 (2016).

# Structural defects in gallium arsenide

T. P. Mihailova[*], D. K. Gospodinov, E. G. Marekova

*University of Plovdiv "Paisii Hilendarski" 4000 Plovdiv, 24 Tzar Asen St., Bulgaria*

Structural defects in monocrystal GaAs, obtained by Czochralski method, have been studied. Two methods of chemical etching in KOH and eutectic melt KOH- NaOH were used. The distribution of dislocations in doped with tellurium and indium, tellurium and undoped crystals were compared. Doping with tellurium and indium changes the radial distribution of dislocations, decreases its density, but increases the concentration of microdefects. The obtained results may be used for optimization of the semiconductor technological processes.

**Keywords:** structural defects, gallium arsenide, etching

## INTRODUCTION

Gallium arsenide is a semiconductor, widely used in modern microelectronics and optoelectronics. The combination of direct energy structure, optimal band gap, high mobility of the charge carriers, well-developed technological methods for growing a single crystal, homo and hetero-epitaxial structures, make it a promising material for multijunction solar cells [1-5]. The basic requirements in terms of single crystals are orientation, diameter, dislocations density and electrophysical parameters.

In conventional production the average density of dislocations is being controlled, although most parameters of semiconductor materials are "structure-sensitive" [6]. Except dislocations in the crystals, other defects are formed like native and impurity point defects or their complexes, clusters, twins, stacking faults etc. These defects manifest themselves by the solution, offered by Abrahams and Bujocci, which is composed of 2 ml $H_2O$, 8 mg $AgNO_3$, 1 g $CrO_3$ and 1 ml HF [7]. A variant of the method is presented by the diluted modification (DS method) or diluted Sirtl - like solution with a light - DS (L) etching [8, 9]. Through these methods it has been studied the growth and multiplication of dislocations from the substrate in the epitaxial layer, the formation of misfit dislocations and the influence of point defects. This method is suitable for low density of dislocations [9].

Another method that displays both dislocations and point defects is proposed by Lessoff and Gorman and contains equal number of mols of KOH and NaOH [10, 11]. The authors consider the lower temperature and speed of the etching to be

advantages of the method. Miyari and co-authors call it eutectic etching and use it to identify micro defects in undoped and In-, B- or Si-doped monocrystals [12]. This method has been used by us to study the low-dislocation parts of monocrystalline GaAs, doped with Zn, In, or Zn + In [13]. The doping with Te, In or In + Te is an effective method of reducing dislocations, but there is no evidence of their impact on the type and the distribution of microdefects, developed by eutectic etching [6, 14, 15].

The aim of this study is to compare the distribution of structural defects after development first in KOH and second in KOH-NaOH, and to study the possibilities of using eutectic etching in control of the basic parameters of monocrystalline gallium arsenide.

## EXPERIMENTAL PART

Substrates were tested with orientation (001) of monocrystalline GaAs, doped with Te, In, In + Te and undoped. All crystals were prepared by the liquid encapsulated Czochralski. The information about the quantity and type of dopant are known in advance. All crystals are grown at the same temperature conditions, growth rates and crystal and crucible rotation.

The concentration and mobility of the carriers was measured by the Hall effect method under constant electrical and magnetic fields on samples with alloyed indium ohmic contacts.

The preparation of the wafers for the development of dislocations includes mechanical grinding, polishing, chemical polishing in a mixture of $H_2SO_4$: $H_2O_2$: $H_2O$ in a ratio of 3: 1: 1 for 5 minutes, rinsing with deionized water and drying. The defects development is done in a resistivity furnace with automatic temperature control. Etching in KOH is at a temperature and time 470°C

---
* To whom all correspondence should be sent:
  tsmihail@uni-plovdiv.bg

for 10-15 minutes and for the eutectic etching - 380°C temperature and for a 30 minutes period. Wafers in both cases are placed in a silver crucible with pre-melted base. After the process the crucible is removed, cooled and the remainder of the base was dissolved in tap water.

The morphology of the defects and the stoichiometry of a portion of the resulting crystals and of the used polycrystalline material were measured with a scanning electron microscope Philips SEM 515 in a back reflected electrons mode (BS) and energy-dispersive X-ray analysis (EDAX).

## RESULTS AND DISCUSSION

The results of the electro-parameters, the type of the doping elements and the average dislocations density are shown in Table 1. The density of dislocations is determined by metallographic microscope after etching in KOH and averaging the values of nine fields.

**Table 1**. Electro-physical and structural parameters on the crystals where: N [cm$^{-3}$] is Hall concentration, $\mu$ [cm$^2$/V s] is Hall mobility and N$_D$ [cm$^{-2}$] - dislocation density

| Number of the crystal and doping element | N cm$^{-3}$ | $\mu$ cm$^2$/V s | N$_D$ cm$^{-2}$ |
|---|---|---|---|
| 1 GaAs | $2 \times 10^8$ | 2850 | $3 \times 10^4$ |
| 2 GaAs : Te | $5.5 \times 10^{17}$ | 3390 | $1 \times 10^4$ |
| 3 GaAs : Te | $1.1 \times 10^{18}$ | 1860 | $3 \times 10^4$ |
| 4 GaAs : Te | $1.2 \times 10^{18}$ | 2380 | $2 \times 10^4$ |
| 5 GaAs : Te | $2.6 \times 10^{18}$ | 1730 | $1.6 \times 10^4$ |
| 6 GaAs : Te | $3.1 \times 10^{18}$ | 1818 | $1.8 \times 10^4$ |
| 7 GaAs : In | $4 \times 10^8$ | 4000 | $6,8 \times 10^3$ |
| 8 GaAs : Te + In | $1.2 \times 10^{18}$ | 2500 | $4 \times 10^3$ |
| 9 GaAs : Te + In | $2 \times 10^{18}$ | 2450 | $1 \times 10^3$ |

All samples except for 2 are taken from the end of the grown crystals. The concentration of the dopant in the melt of the obtained crystals is respectively: Tellurium - 1.8 x 10$^{19}$ cm$^{-3}$, indium in a sample 7 – 1,28 x 10$^{20}$ cm$^{-3}$, in 8 – 1,7 x 10$^{20}$ cm$^{-3}$ and in 9 – 5 x 10$^{20}$ cm$^{-3}$. The table shows the measured concentrations of electrons and mobility of the charge carriers with the Hall effect.

The results of the table show that average density of dislocations ranges from 1 x 10$^4$ cm$^{-2}$ to 3 x 10$^4$ cm$^{-2}$ when doped with tellurium and is near to the dislocation density of the undoped sample. Adding In with a concentration of 1 x 10$^{20}$ cm$^{-3}$ in the melt slightly reduces the average density of dislocations and slightly increases the mobility of the charge carriers. The effect is enhanced in the sample 8, doped with two impurities, where the concentration of In is 1.7 x 10$^{20}$ cm$^{-3}$. A significant

reduction of the average dislocation density can be found in sample 9 at a concentration level of the isovalent impurity indium in the melt of 5 x 10$^{20}$ cm$^{-3}$. We assume that the reduction in the average dislocation density in samples 8 and 9 is mainly due to the isovalent impurity indium. Doping with tellurium also reduces the density of dislocations, but the required concentration of the impurity in the crystal is (5 – 9) x 10$^{18}$ cm$^{-3}$ [6].

The dislocations distribution in the cross section of the substrates reflects the distribution of thermal stresses and provides additional information about the causes of their nucleation. Fig.1 shows the effect of doping on the radial distribution of dislocations.
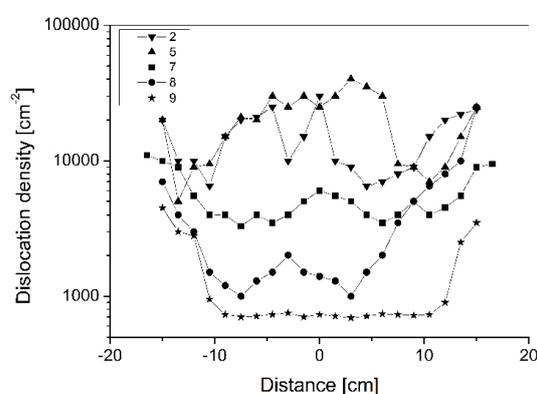


**Fig.1.** Radial distribution of the dislocations in the following crystals: 2 – GaAs: Te, 5 – GaAs;Te, 7 – GaAs: In, 8 – GaAs: Te+In, 9 – GaAs: Te+In

The distribution of the dislocations in samples 2 and 5 is "W" shaped with high density in the center and the periphery and lower density in the circular area between them. Increasing the concentration of indium change the macro-distribution from low "W" shaped to a "U" shape. The distributions of the dislocations depends on the distribution of thermal stresses [6].

The heat when cooling the crystal is discharged mainly through radiation from the side surface. The peripheral layers have a lower temperature than central ones and this leads to the occurrence of compressive stresses in the center, stretching stresses in the periphery and their compensation in the middle region. The influence of the electrically active impurity tellurium and the isovalent indium on the structural parameters is explained by the increase of the critical stresses for the formation of dislocations and modifying the type and concentration of the equilibrium point defects. [6, 15].

The eutectic etching develops simultaneously dislocations and various microdefects. Fig.2 reveals

SEM microphotographs of the central part of the samples of undoped and doped with tellurium and indium crystals.
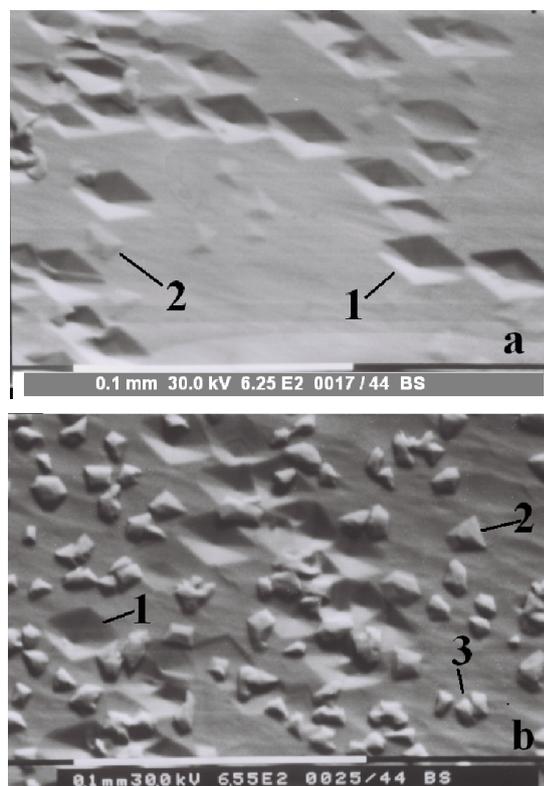


**Fig.2.** Microdefects observed after eutectic etching on: (a) undoped wafer 1 and (b) doped with Te + In wafer 8

To distinguish between defects the classification proposed by Tseng at al. [11] and supplemented by H. Miyairy at al [12], is used. Fig.2 shows: 1 – dislocations; 2 - raised structure and 3 - diamond shaped pit. There are also oval pits, surface roughness and rectangular pits. The dislocations are pits with a hexagonal shape and their size depends on the time of etching. The number of dislocations in the undoped sample is larger, but the concentration of microdefects is low. Alloying reduces the number of dislocations and increases the number of the microdefects. Like etching with KOH part of the dislocations have a flat bottom and are decorated with microdefects. Fig.2b shows that in the doped with In and Te crystal the prevalent types of defects are type 2 and 3, which we will call respectively A-defects, and T-defects. The size of A-defects ranges from 20 μm to 200 μm and they have an irregular shape. The T-defects have a triangular shape and relatively equal size. Part of the A and T-defects are combined in groups and form complexes with irregular shape. Alloying leads to the occurrence of surface roughness of small round pits and rectangular defects of larger size [11, 12]. In wafer 8 one can observe poorly

shaped rectangular pits, which are remnants of mechanical treatment. The measured values of dislocations, A and T defects after etching in KOH and eutectic etching are shown in Table 2.

**Table 2.** Structural parameters after etching with KOH and KOH – NaOH

| Number of the crystal | Dislocations KOH $N_D$ cm$^{-2}$ | Dislocations KOH-NaOH $N_{DE}$ cm$^{-2}$ | A-Defects $N_A$ cm$^{-2}$ | T-Defects $N_T$ cm$^{-2}$ |
|---|---|---|---|---|
| 1 | $2 \times 10^4$ | $2.1 \times 10^4$ | $6.3 \times 10^3$ | 0 |
| 2 | $1 \times 10^4$ | $1 \times 10^4$ | $1 \times 10^4$ | $3{,}1 \times 10^4$ |
| 7 | $9 \times 10^3$ | $8.5 \times 10^3$ | $1 \times 10^4$ | $1.1 \times 10^4$ |
| 8 | $3 \times 10^3$ | $2.8 \times 10^3$ | $2 \times 10^4$ | $5 \times 10^4$ |

The density of dislocations and microdefects is determined by counting by a metallographic microscope at a magnification of 800. The results were averaged from three measurements made in the center of the substrates. It can be seen in Table 2, that density of dislocations is not dependent on the method of etching and the dopant increases the concentration of microdefects. Fig.3 exposes the radial distribution of the dislocations, A- and T defects in sample 9 of Table 1 after eutectic etching.
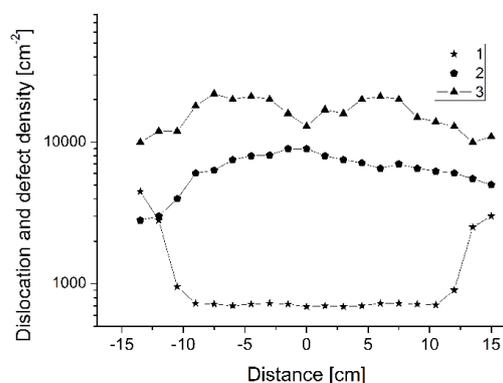


**Fig.3.** Radial distribution of the dislocations, A and T-microdefects (1 – dislocations, 2 – A-defects, 3 – T-defects)

The distribution of A-defects is reverse to the distribution of the dislocations and increases slightly from the periphery to the center of the crystal. A similar change is identified for the T defects, but the difference in concentrations there is much higher. The T-defects density sharply decreases around the periphery of the crystal and in the presence of Ga clusters (sample 5).

By other authors A-defects are formed with growing of As-enriched melts and the advent of T-defects is determined by the deviation of

stoichiometry to both components [12]. The origin of the A-defects is associated with antiphase domains [11]. The stoichiometry of the resulting crystals is dependent on the type of polycrystal, the growing conditions, the type and concentration of impurities and can be measured [13, 17]. Samples 1 to 7 were prepared by previously synthesized polycrystal with a composition Ga (51.59 - 51.75) at.% and As (48.05 - 48.25) at.%. The ratio between the main components when doping with Te (sample 4) is Ga (52.43 at.%) and As (47.57 at.%). The sample 8, doped with In has a composition of Ga (52.58 at.%) and As (47.42 at.%). In both cases, the stoichiometry changes, and the obtained crystals were enriched with Ga. Crystals 8 and 9 are derived from non-standard residues of semi-isolation GaAs with a residual concentration of In about $1 \times 10^{20}$ cm$^{-3}$ and further doped with InAs. The deviation from the stoichiometry of the resulting crystals was approximately identical to that of crystals 1-7.

The stoichiometry of the A-defects is approximately equal to that of the substrate. Part of defects in crystals 8 and 9 contain In with a concentration of less than 0.5 at.%. Similar types of defects are developed in crystals, doped with Zn or Zn + In [13]. In both cases there is no connection between the electro-parameters and the concentration of A-defects, showing that defects are electrically neutral. Both types of defects are formed by growing of crystals from a non-stoichiometric melt.

The electrically neutral anti-phase domains are complexes with a composition $As_{Ga} - Ga_{As}$. All crystals, examined by us, were obtained from Ga-enriched melt. The concentration of the $As_{Ga}$ is relatively low and this hinders the formation of antiphase domains.

Samples 8 and 9, studied by us, are from the end of the formed crystals before the onset of cell growth. There is a problem with heavily doped samples, which is constitutional supercooling. This leads to termination of the crystal growth in a relatively early stage of the process.

The initiating of cells growth is determined by the following relationship:

$$g_{cell} \approx \frac{G}{R} \qquad (1)$$

where the monocrystal portion is $g_{cell}$, G – the axial temperature gradient, and R - the growth rate [18].

Fujii et al. have shown that for an axial gradient 80$^o$C/cm and pulling speeds of 9, 5 and 3 mm/h the values of $g_{cell}$ are around 0.22, 0.45 and 0.7 [18].

We assume that te cause of A-defects is the high rate of crystals growth. The nonequilibrium conditions at the crystallization front lead to occurrence of microfluctuations that solidify in a defective structure. Depending on the stoichiometry and doping, it is possible that gallium or arsenic microclusters are formed, which will be impurity enriched or depleted [6,19]. The composition of the defects will be determined by the main point defects as gallium and arsenium interstials and is close to the composition of dislocation loops. It was found that the thermal annealing of the undoped crystals increases the size of the A-defects and reduces their density [13]. We assume that concentration of A and T defects can be reduced by annealing and this is the cause for the improvement of parameters in pre-epitaxial preparation of the substrates [20, 21].

## CONCLUSIONS

Structural defects were examined in this study by subsequent etching with KOH and eutectic mixture of KOH and NaOH. Both methods exhibit dislocations and the measured densities are close.

Doping with tellurium and indium significantly reduces the density of dislocations, but increases the microdefects concentration.

The concentration of maximum size defects (A and T defects) depends on the stoichiometry and is close to or greater than dislocation density. The concentration increases from the periphery to the center and sharply reduced in areas with gallium clusters.

A-defects have a composition similar to the base material and in some of them there is an increased concentration of indium.

The eutectic etching can be used to improve the processing conditions for the growth of low-dislocation gallium arsenide.

## ACKNOWLEDGEMENTS

## REFERENCES

1   GaAs Microelectronics, Ed. N. Einspruch and W. Wisseman, Moskva, Mir, (in Russian) (1988).
2   F. Dimroth, C, Baur, A. Bett, M. Meusel, G. Strobl, *IEEE,*525, (2005).

3   J. Vyskočil, P. Gladkov, O. Petriček, A. Hospodkova, J. Pangrac, *J. Cryst Growth,* 417, 172, (2015).

4   M. Milanova, P. Vitanov, P. Terziyska, G. Koleva, C. Barthov, B. Clerjand, *Bulg. Chem. Communication,* 47 B, 71, (2015).

5   J. Mullin, *J. Cryst Growth,* 264, 578, (2004).

6   M. Milvidski, V. Osvenski, Structur. Defekti v monokr. Poluprovodnikov, Moskva, Metallurgia, (in Russian), (1984).

7   M. Abrahams, C. Bujocci, *J. Appl. Phys., 36,* 2855, (1965).

8   J. Weyker, J. van de Ven, *J. Cryst. Growth,* 78,191, (1986).

9   Ts. Mhailova, N. Velchev, V. Krastev, Ts. Marinova, *Appl. Surface Science,* 120, 213, (1997).

10  H. Lessoff, R. Goman, Proc. Conf. on semi-insulating III-V materials, Ed. P. Lock and J. Blakemor, Kan-nee-ta, 83, (1984).

11  W. Tseng, H. Lessov, R. Gorman, *J. Electrochem. Soc.,* 132, 3067, (1985).

12  H. Miyairi, Sh. Ozawa, M. Eguchi, Ts. Fukuda, *J. Cryst. Growth*, 76, 388, (1986).

13  Ts. Mihailova, *J. Optoelectronics and Advanced Materials,* 7, 521, (2005).

14  H. Kimura, C. Afable, H. Olsen, A. Hunter, H.Winsten, *J. Cryst. Growth,* 70, 185, (1984).

15  I. Stepantsova, M. Mejeniy, V. Osvensciy, S. Shifrin, Y. Bolsheva, Y. Grigoriev, *Cristallografia,* 33, 938, (in Russian), (1988).

16  P. Hutchinson, P. Dobson, *J. Mater. Science,* 10, 1636, (1975).

17  Ts. Mihailova, S. Nedev, E. Toshkov, A. Stoyanov, *Bulg. Chem. Communications*, 47 B, 162, (2015).

18  T. Fujii, M. Makajima, Ts. Fukuda, *J. Cryst. Growth,* 87, 547, (1988).

19  A. Morozov, *J. Cryst. Growth,* 106, 258, (1990).

20  D. Wong, T. Schlesinger, A. Milnes, *J. Appl. Phys.,*68, 5588, (1990).

21  H. Valencia, Y. Kangawa, K. Kakimoto, *J. Cryst. Growth,* 432, 6, (2015).

# Modeling of ceramic products molding process

U.K. Zhapbasbayev[1], G.I. Ramazanova[1], B.K. Assilbekov[1, *], Z.K. Sattinova[2]

*[1]Kazakh-British Technical University, Laboratory of Mathematical modelling of technological processes in oil and gas industry, 050000, Almaty, Kazakhstan*
*[2]L.N. Gumilyov Eurasian National University, Department of Physics, 010008, Astana, Kazakhstan*

Results of experiments and calculations of the motion and heat exchange of the BeO slurry in the annular cavity are presented. The slurry is a highly concentrated structured system where the mineral phase is BeO powder and liquid phase is an organic binder. The obtained temperature field determines the transition of the slurry from liquid (viscous-plastic) to solid-plastic state. Calculated data of the isotherms of solidification zone of the beryllia thermoplastic slurry are in a good agreement with the experimental results.

**Keywords***: thermoplastic slurry, molding, solidification*

## INTRODUCTION

The development of new areas of science and directions of technology increases requirements for advanced properties and quality of ceramic fabrications. Products of complex configuration from new non-metallic materials (high thermal conductivity, oxygen-free, superconducting, etc.) are becoming more and more popular. In spite of using isostatic pressing technology of hot casting under pressure [1, 2] remains the basis for the obtaining long-length, multi-channel, complex shaped ceramic fabrications from non-plastic powders.

Nowadays technology of slurry molding (extrusion) is very relevant in connection with intensive development of Metal Injection Moulding (MIM) technology [3, 4], where same physical processes take place.

While a lot of attention has been paid to improving of the technology and the creation of the new equipment last years, up to now there remains an unsolved problem of obtaining fault free products by this method. As a result, in practice it does not often achieve the desired quality of moldings and obtaining of acceptable products, which makes this process less profitable. Obtaining of ceramic fabrications by hot molding from dispersion materials with anomalous physical properties, such as BeO is particularly complicated. In this case, the difficulties of obtaining the products of high quality are caused firstly by thermal properties of beryllium oxide, in particular, its unique thermal conductivity [5, 6]. Clearly, it is impossible to eliminate technological limitations

and problems without the development based on all experience and knowledge of theoretical representations about regularities and mechanisms of regulation of the thermal regime of the casting on the forming process of molding.

The results of experimental research and the generalization of them by calculations of mathematical model of the thermoplastic slurry of beryllium oxide molding process are presented in this paper.

## EXPERIMENTAL

Experimental research of the effect of casting regimes on the temperature field in the zone of solidification of the molding was made on the experimental bushing (Fig.1), by measuring the temperature using a thermocouple installed on the different levels by the height of crystallizer. Experimental bushing is structurally closed to the production plant and it is designed for casting of circular tube with the outer diameter 0.02 m and the inner diameter 0.012 m. Material of mandrel and crystallizer is steel of grade X18H10T. The total height of the cylindrical part of the annular cavity is H = 0.028 m, the height of the hot zone of the annular cavity is $h_1$=0.008 m, the height of the cold zone of the annular cavity is $h_2$=0.02 m. Water with the temperature $t_1$=80℃ fed to the upper (hot) contour of the crystallizer. Water with the temperature $t_2$=15-20℃ fed to the bottom (cold) contour. The maximum through put of the crystallizer contours in volume of water is 1500 l/hour.

Conical input of the bushing is connected with the working tank of casting installation where beryllia slurry is kept. BeO slurry is a high concentrated structured medium. Slurry flows from

* To whom all correspondence should be sent:
   assilbekov@mail.ru

the tank to the conical inlet of the annular cavity with an initial temperature $t_0=80^{\circ}$C. During its flow in result of heat exchange with the walls of mandrel and bushing slurry changes its aggregate state and solidifies.
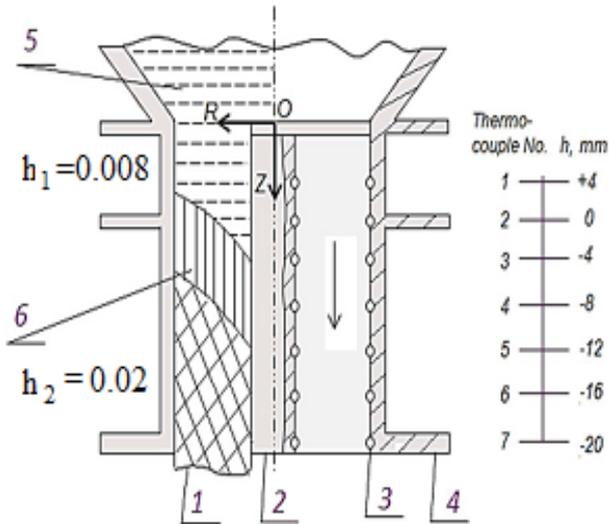


**Fig.1.** Scheme of molding solidification process and installation of thermocouple in the bushing: 1 – molding, 2 – mandrel, 3 – thermocouple, 4 – bushing, 5 – liquid slurry, 6 – zone of solidification

According to the obtained data, dependence of position of the boundary of solidification slurry from different parameters of casting was built. The shape of the curve of surface solidification, which is dependent on the casting parameter, is defined taking into account that the temperature changes linearly by the height and radius of crystallizer on the short segments.

The influence of molding velocity on the thermal regime of the casting was determined in the first series of experiments. The flow rate and temperature values of hot and cold water in the cooling contours are presented in Table 1. In the experiments molding velocity increases from 20 to 100 mm/min. Fig.2 shows positions of solidification zones depending on the molding velocity. Isotherm of the AB "solidus" corresponds to the temperature 54$^{\circ}$C and isotherm of the CD "solidus" to 40$^{\circ}$C (Fig.2).

As we see in Fig.2, the increase of the molding velocity leads to expansion of zone of solidification and its movement to the area of heat extraction of cold contour. It explains that with increasing of molding speed heat extraction on the walls of the annular cavity does not have time to cool the slurry, and zone of solidification extends, and it moves down towards the molding velocity.

**Table 1.** Regimes of experiments as a function of the molding velocity

| Refer to fig.2 | 1 | 2 | 3 | 4 | 5 |
|---|---|---|---|---|---|
| Hot water flow rate, l/hour | 500 | 500 | 500 | 500 | 500 |
| Cold water flow rate, l/hour | 1500 | 1500 | 1500 | 1500 | 1500 |
| Molding velocity, mm/min | 20 | 40 | 60 | 80 | 100 |
| Hot water temperature, $^{\circ}$C | 80 | 80 | 80 | 80 | 80 |
| Cold water temperature $^{\circ}$C | 20 | 20 | 20 | 20 | 20 |

As we see in Fig.2, the increase of the molding velocity leads to expansion of zone of solidification and its movement to the area of heat extraction of cold contour. It explains that with increasing of molding speed heat extraction on the walls of the annular cavity does not have time to cool the slurry, and zone of solidification extends, and it moves down towards the molding velocity.
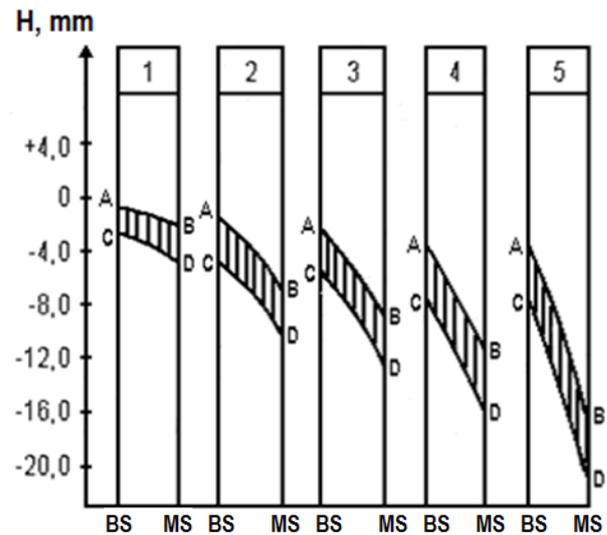


**Fig.2.** The position of solidification zone depending on the molding velocity: AB – isotherm "solidus" (54$^{\circ}$C), CD – isotherm "solidus" (40$^{\circ}$C), BS – the surface of the bushing, MS – the surface of the mandrel

In the second series of experiments the influence of cold water temperature and flow rate on the thermal regime of molding solidification was investigated (Table 2). In the experiments the molding velocity is 20 mm/min. Flow rate and temperature of hot water do not change, 500 l/hour and 80$^{\circ}$C. Flow rate of cold water changes from 250 to 1500 l/hour, and the temperature from 15 to 20$^{\circ}$C.

The results of the second series of experiments are shown in Fig.3. In the first three regimes cold water temperature is 15$^{\circ}$C, and the flow rates are

1000, 500 and 250 l/hour, respectively. Solidification zones of molding are located in the area of cold contour, and move downstream with reducing cold water flow rate. Reducing of cold water flow rate leads to reduction of the heat extraction on the wall of bushing (Fig.3). Therefore, solidification zone of molding is moving down the length of the cold contour.

**Table 2.** Regimes of experiments as a function of the cold water flow rate and temperature

| Refer to fig.3 | 1 | 2 | 3 | 4 | 5 |
|---|---|---|---|---|---|
| Hot water flow rate, l/hour | 500 | 500 | 500 | 500 | 500 |
| Cold water flow rate, l/hour | 1000 | 500 | 250 | 1500 | 250 |
| Molding velocity, mm/min | 20 | 20 | 20 | 20 | 20 |
| Hot water temperature, °C | 80 | 80 | 80 | 80 | 80 |
| Cold water temperature °C | 15 | 15 | 15 | 20 | 20 |
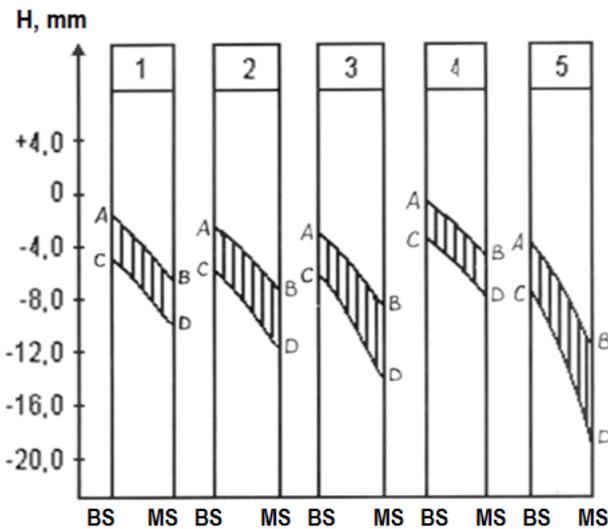


**Fig.3.** The position of solidification zone depending on the flow rate and the temperature of cold water

In the last two experiments of this series cold water temperature was 20°C, and its flow rate was changing from 1500 to 250 l/hour, respectively. In the fourth experiment, the beginning of solidification zone is located nearer to the hot contour area. Increase of cold water temperature from 15 to 20°C leads to reduction of temperature difference of the hot slurry and cold water. In the conditions of the fifth experiment except increase of cold water temperature takes place reduction of its flow rate from 1500 to 250 l/hour. Therefore, heat extraction reduces and solidification zone of molding moves down towards motion of the thermoplastic slurry (Fig.3).

Accordingly, the experimental data show that the thermal regime of molding of the beryllium oxide thermoplastic slurry is sensitive to change of the molding velocity, and to conditions of heat extraction on the walls of the annular cavity.

MATHEMATICAL MODEL OF THE SOLIDIFICATION PROCESS

Motion and heat exchange of the BeO thermoplastic slurry in the annular cavity are considered. The slurry flows into cavity with initial temperature of 80°C (Fig.1). As it moves the slurry is cooled and solidified, and on the output from the cavity it acquires structural form of the tube. The movement of slurry occurs in the laminar regime. Special feature of the slurry beryllium oxide is its high thermal conductivity; however due to high viscosity of thermoplastic slurry Prandtl number is much higher than one. Density of the slurry mass is function of temperature and increases as solidification.

The problem is studied in Cartesian coordinate system with axis *z* and *r*. OZ axis coincides with the cavity axis direction, and OR axis is radially directed to it. Molding velocity is directed vertically downward along the OZ axis. Radial component of the velocity originates due to the heat exchange of the slurry with the walls of annular cavity.

Rheological properties of the slurry change with temperature. The heat of phase transition is released during the change of state. Cooling of the slurry may lead to the irregularity of the temperature profile and rheological properties of the pressing molding. Solidification begins at the walls of the annular cavity, while in the central part slurry may be in liquid state. As a result, in-feeding of slurry for the compensation of internal shrinkage of volume in the cooling zone of the cavity may occur.

According to the experimental data the slurry solidification occurs at the temperature range from 54 to 40°C. Binder of the slurry is in the amorphous state and passes from the liquid amorphous state to the solid-plastic amorphous state in the zone of solidification [5, 7, 8]. The total amount of heat released per unit mass of the slurry mass is determined by the change of enthalpy $\Delta H$ at the phase transition zone.

Heat capacity of the slurry changes in the transition zone. Increase of the enthalpy during the phase transition can be determined by the apparent heat capacity method [9-14]. In this method, the latent heat is taken into account by increasing the

heat capacity in the phase transition zone. Changing of heat capacity can be represented as [16-18]:

$$c_p = \begin{cases} c_s, & t < t_s & \text{solid phase} \\ c_{in}, & t_s \leq t \leq t_l & \text{transition zone} \\ c_l, & t > t_l & \text{liquid phase} \end{cases} \quad (1)$$

where $c_{in} = \dfrac{\left\{\displaystyle\int_{t_s}^{t_l} c(t)dt + H_{1\to2}\right\}}{(t_l - t_s)}$, $H_{1\to2}$ – the phase transition specific enthalpy of beryllia slurry is determined by experimental data and is equal to $H_{1\to2}$ =7800 J/kg [15].

In [14] phase transition function $\alpha(\bar{t})$ is introduced to the transition zone to consider the latent heat, and changing of the slurry heat capacity is expressed by:

$$c_p = c_s \cdot (1 - \alpha(\bar{t})) + c_l \cdot \alpha(\bar{t}) + H_{1\to2}\frac{d\alpha}{dt} \quad (2)$$

where $c_s$ – specific heat of the slurry in the solid state, $c_l$ – specific heat of the slurry in the liquid state, $\alpha(\bar{t}) = 0$ for the pure solid slurry and $\alpha(\bar{t}) = 1$ for the pure liquid slurry, $\bar{t}$ – dimensionless temperature of slurry ($\bar{t} = t/t_0$, $t_0$-initial temperature of the slurry at the inlet of the cavity).

According to the experimental data of beryllium oxide slurry with binder mass fraction of $\omega = 0,117$ function $\alpha(\bar{t})$ takes a form:

$$\alpha(\bar{t}) = 5.712 \cdot \bar{t} - 2.8544 \quad (3)$$

The equations (1)-(2) of the method of apparent heat capacity include the latent heat of the phase transition, and are convenient for calculations. For convenience position of the transition zone is not known in advance and is determined as a result of the calculations.

The rheological properties of the slurry for binder mass content $\omega = 0,117$ depend on temperature, and expressed by empirical formulas [16]:

$$\mu(t) = 293.6259\exp(-0.05816t), \text{(Pa·s)} \quad (4)$$

$$\tau_0(t) = 11.4 + 11.41\exp(-\frac{t - 70.05}{5.47}), \text{(Pa)} \quad (5)$$

Density of the thermoplastic slurry is defined by the concentrations of the beryllium oxide powder and the binder:

$$\rho = \frac{\rho_{BeO}\rho_{bin}}{(1 - \omega)\rho_{bin} + \omega\rho_{BeO}}, \text{(g/cm}^3) \quad (6)$$

where $\rho_{BeO}$ is the density of the beryllium oxide powder, $\rho_{bin}$ is the density of the binder, $\omega$ is relative mass content of the binder in the fractions.

The density of the binder where $\omega = 0,117$ is determined by Eq. (7):

$$\rho_{bin}(t) = 0.852 + 0.0725\cos\beta(t), \text{(g/cm}^3) \quad (7)$$

where $\beta(t) = 0.0561(t + 273.15) - 16.7361$.

The density of the beryllium oxide is $\rho_{BeO} = 3.02\,g/cm^3$. The density of the binder $\rho_{bin}$ is in the range of temperature from $t = 80 - 40^0C$ changed within 0.7797 to 0.9010 g/cm³ and the density of the thermoplastic slurry during solidification increases from 2.2457 to 2.3553 g/cm³ for this fraction $\omega = 0,117$.

Thermal conductivity of the slurry depends on the temperature, and for $\omega = 0,117$ it has the following form [15]:

$$\lambda(t) = 1.6 + 4.8\exp(-0.017t), \text{(W/m·}^0\text{C)} \quad (8)$$

In the experiments [5, 8] beryllium oxide slurry shows thixotropic properties of non-Newtonian fluid, and is described by Shvedov-Bingham rheological model [17]. The motion of the slurry in annulus is considered to be steady-state and the system of equations in the narrow channel is used for its study [16, 18]:

$$\rho u\frac{\partial u}{\partial z} + \rho v\frac{\partial u}{\partial r} = -\frac{dp}{dz} + \frac{1}{r}\frac{\partial}{\partial r}\left(r\mu\frac{\partial u}{\partial r}\right) - \frac{1}{r}\frac{\partial}{\partial r}(r\tau_0) \quad (9)$$

$$\frac{\partial\rho u}{\partial z} + \frac{1}{r}\frac{\partial r\rho v}{\partial r} = 0 \quad (10)$$

In the limit of solid-plastic state of the slurry the motion equation (9) expresses the squeezing-out of the molding from the cavity and takes the form:

$$-\frac{dp}{dz} = \frac{1}{r}\frac{\partial}{\partial r}(r\tau_0)$$

In contrast to the motion equation (9) conduction heat transfer along the OZ axis is substantially due to solidification of the slurry, and heat of phase transition is determined by the apparent heat capacity method (2). In the steady-state solidification process of slurry energy equation can be written as [12-14]:

$$\rho u c_p \frac{\partial t}{\partial z} + \rho v c_p \frac{\partial t}{\partial r} = \frac{\partial}{\partial z}\left(\lambda \frac{\partial t}{\partial z}\right) + \frac{1}{r}\frac{\partial}{\partial r}\left(r\lambda \frac{\partial t}{\partial r}\right) \quad (11)$$

The following notes are used in the Eq. (9)-(11): $z, r$ – axial and radial coordinates; $u, v$ – components of the velocity vector; $p, \rho, T, \tau_0, c_p, \mu, \lambda$ – pressure, density, temperature, shear stress, coefficients of thermal capacity, viscosity and thermal conductivity of the slurry, respectively.

In the Eq. (11) temperature is calculated on the Celsius scale for convenience in comparison with experiment.

Condition of the mass flow rate conservation determines the pressure gradient for thermoplastic slurry extrude from the annular cavity [18]:

$$2\pi \int_{r_1}^{r_2} \rho u r \, dr = \pi(r_2^2 - r_1^2)\rho_0 u_0 \quad (12)$$

where $r_1, r_2$ – the radius of the mandrel and bushing, respectively.

Distributions of the velocity and the temperature at the inlet of the cylindrical portion are constant along the cross section of the annular cavity; respectively, all the thermo-physical properties of the slurry are constant:

$$u = u_0, \, v = 0, \, t = t_0 \text{ for } z = 0. \quad (13)$$

On the cavity walls in the area of the liquid slurry state for velocity are put conditions of sticking:

$$u_i = v_1 = 0 \text{ for } z > 0, \, r = r_i, \, i = 1, 2. \quad (14)$$

In solid-plastic state they are no flow and slip conditions:

$$v_1 = 0, \left(\frac{\partial u}{\partial r}\right)_{r_i} = 0 \text{ for } z > 0, \, r = r_i, \, i = 1, 2. \quad (15)$$

The assumption is that the heat from the hot slurry is transferred to the walls of bushing and mandrel. Then, condition of heat exchange can be applied to the surface of the mandrel [26]:

$$\lambda \frac{\partial t}{\partial r} = \alpha_d(t_c - t_d) \text{ for } z > 0, \, r = r_1, \quad (16)$$

where $\alpha_d$ – coefficient of heat exchange between the slurry and the wall of the mandrel, $t_d$ – the temperature of the wall of mandrel, $t_c$ – the average temperature of slurry in cross-section of the annular cavity.

If we mark temperature of the water in the hot and cold contours as $t_1, t_2$, we can put the boundary conditions on the wall of bushing as:

$$-\lambda \frac{\partial t}{\partial r} = k(t - t_i), \, i = 1, 2 \text{ for } z > 0, \, r = r_2, \quad (17)$$

where $k$ is the coefficient of heat transfer on the wall of *bushing*.

At the outlet section of the cavity for temperature are put the following condition:

$$\frac{\partial t}{\partial z} = 0 \text{ for } z = l. \quad (18)$$

Eq. (9)-(12) and boundary conditions (13)-(18) are presented in the dimensionless form for the convenience. Coordinates $z, r$ are divided by $r_1$, velocity components $u$ and $v$ – by $u_0$, pressure $p$ – by the value of dynamic head $\rho_0 u_0^2$, temperature $t$ – by $t_0$, density, yield point, coefficients of thermal capacity, viscosity, and thermal conductivity – by their values at the temperature $t_0$. The equations in the dimensionless form include Reynolds number *Re*, Prandtl number *Pr*, and Eckert number *Ec*.

Set of Eq. (2)-(12) is solved numerically at boundary conditions of Eq (13)-(18) [18]. The considered zone is divided into elementary cells with sides $\Delta z_i, \Delta r_j$. Different analogues of the motion equation (9) and energy (11) were obtained by the Crank-Nicolson method of the second order precision, but different analogue of Eq. (10) was obtained by two layer scheme of the second order precision [18]. Pressure gradient is defined by the splitting method [18] from the condition of conservation of mass flow rate (12).

The coefficients of heat exchange and heat transfer on the walls of the annular cavity were determined by comparison of experimental and calculation data.

## RESULTS OF CALCULATIONS AND COMPARISON WITH EXPERIMENTAL DATA

The calculation is performed under the same regime parameters and conditions as of the experiments. Calculated data by distribution of temperature in an annular cavity according to the conditions of the first series of experiments are demonstrated in Fig.4.

At the inlet of the cylindrical part of the annular cavity the temperature of the slurry is constant and equal to $t_0 = 80^0 C$. In the area of hot contour isolines (isotherms) of the temperature show the

zones of the constant values of the temperature and parameters of the slurry mass is in liquid state. In this part the temperature of the slurry and the hot

water is the same, heat transfer practically does not occur on the bushing wall.
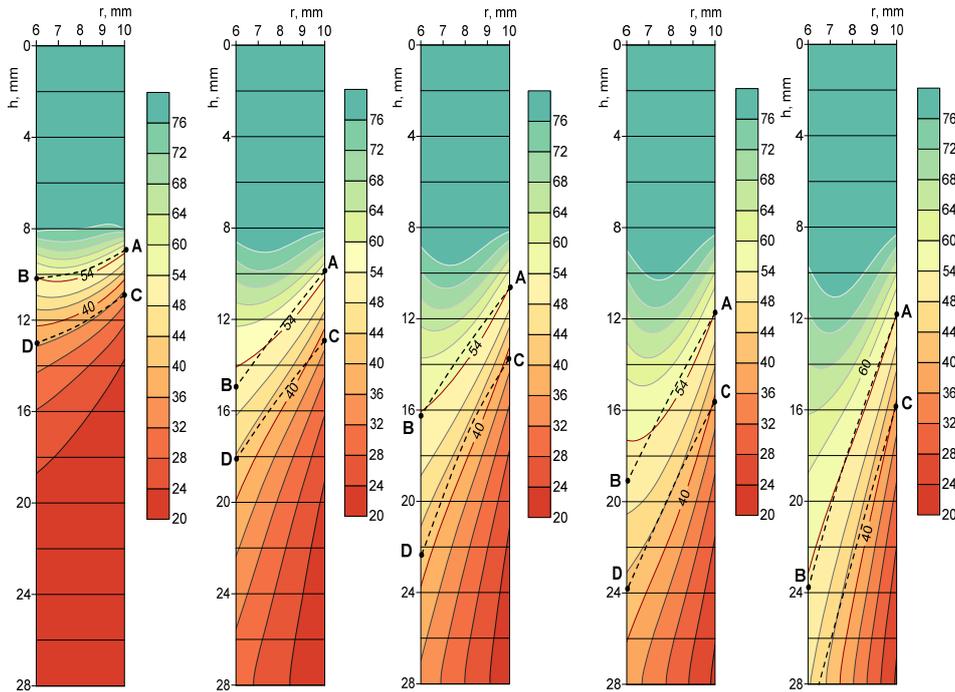


**Fig.4.** Comparison of the calculated and experimental data of distribution of the temperature depending on the molding velocity (the dashed line is the experimental, and the red line is the calculated)

Cooling of the slurry mass starts in the area of cold contour. Difference of the temperature of the slurry mass and cold water leads to an intensive heat transfer in the second cooling contour, and to reduction of the temperature and to change of rheological properties of the slurry.

The slurry temperature field is variable and changes from 80 to 54$^0$C in the beginning of the second contour.

Isotherm with the temperature 54$^0$C expresses upper bound of solidification zone of the slurry mass, and isotherm 40$^0$C expresses the lower bound of the solidification zone. In the area of solidification the slurry passes from the liquid (viscous-plastic) state to solid-plastic state. The experimental data of isotherms "solidus" AB and "solidus" CD are shown in Fig.2 and 3. It may be noticed an agreement between the calculated data and experiments of positions of isotherms *AB* and *CD*.

At the value of the molding velocity of 20 mm/min position of the transition zone of the slurry from the liquid (viscous-plastic) state to solid-plastic state is located closer to the beginning of the cold contour of cooling. With increasing molding velocity the position of the transition zone begins to pull down towards movement of the molding and takes extensive areas. It explains that

with increasing of molding rate convective component of heat flow of the slurry mass increases. The position of the transition zone increases and it covers all length of the mold cavity (Fig.4).

The effect of flow rate and temperature of cold water on the position of the transition zone of the molding by conditions of the experimental researches were determined in the second series of calculations (Table 2). Calculation data of the temperature distribution and the position of the transition zone of molding, limiting by isotherms *AB* and *CD* are shown in Fig.6. In the first three cases, the temperature of cold water is 15$^0$C, and its flow rate reduces from 1000 to 250 l/hour, respectively. Reducing the temperature of cold water increases the intensity of heat extraction and reducing of its flow rate and vice versa, it slows down the process of heat extraction. Increasing the temperature of cold water till 20$^0$C, as well as reducing of its flow rate leads to a reduction of heat extraction.

The calculated temperature data are in agreement with the experiment results (Fig.5).

The experimental and calculated data show that beryllia thermoplastic slurry solidification process can be controlled by adjusting the flow rate and temperature of the hot and cold water.
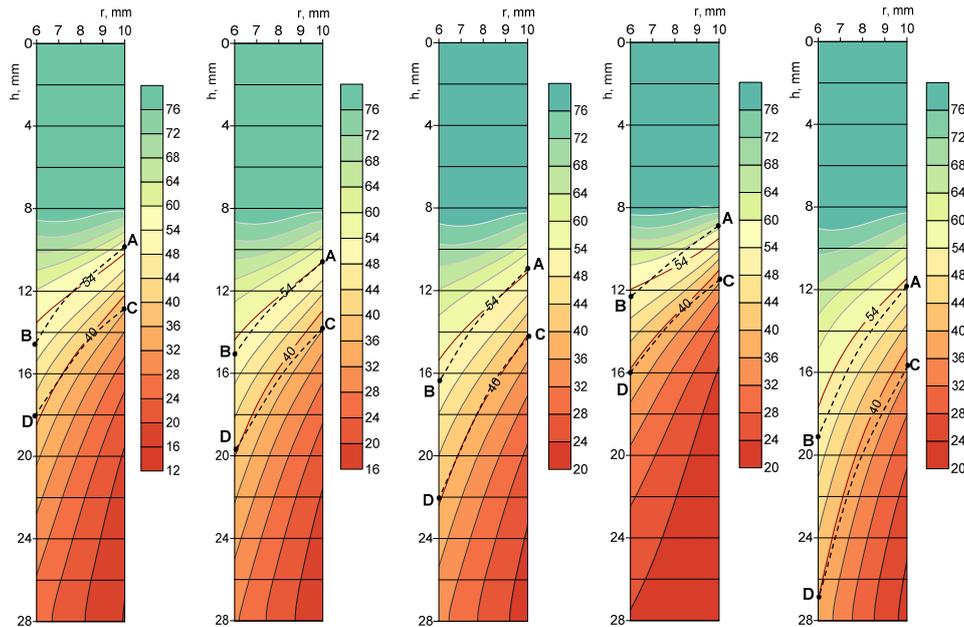
**Fig.5.** Comparison of the calculated and experimental data of distribution of the temperature depending on the flow rate and the temperature of cold water (the dashed line is the experimental, and the red line is the calculated)

One of the important parameters characterizing the solidification process of thermoplastic slurry is the change of its density in a formative cavity during cooling. The dynamics of changes of slurry density averaged over the cross section, and slurry density on the inside (mandrel) and outer (bushing) walls of the formative cavity for first mode of the experiment (Table 1) is shown in Fig 6. Significant sealing of thermoplastic slurry occurs in the second contour, where the temperature of cooling liquid is $20^0$C. The distribution of densities confirms that the cooling extends from the outer wall, since the slurry on the wall is solidified earlier than in other parts (Fig.6).
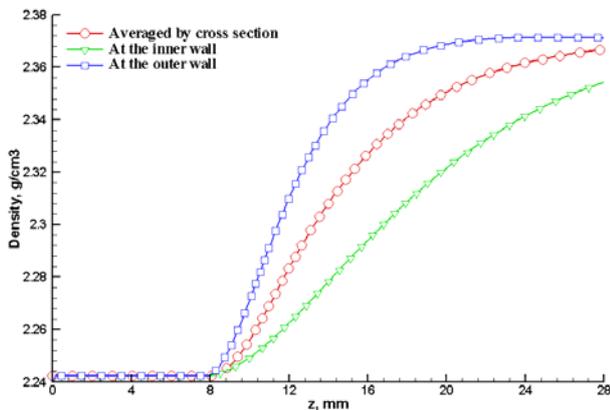


**Fig.6.** Change of the density of the slurry along the length of the cavity

The intensity of the hot slurry solidification by cooling is estimated by the heat amount transferred by slurry to the cooling liquid through the wall. The distribution of the dimensionless heat flux through

the outer wall of the cavity along its length is shown in Fig.7. The heat flow characterizes heat exchange between the hot slurry and the cooling liquid and it is defined as the gradient of the heat amount through the wall.
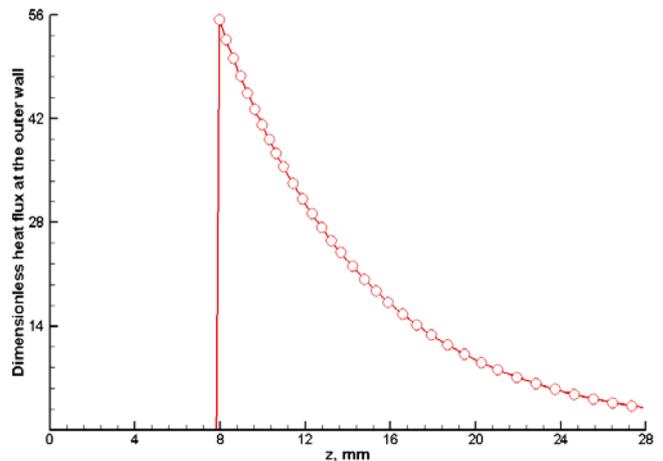


**Fig.7.** Change of the heat flux at the outer wall along the length of the cavity

As seen from Fig.7 the greatest heat flow comes to the beginning of the cold contour, where the temperature decreases sharply. Then, the heat flow is reduced to a minimum at the end of formative cavity. This is because the slurry temperature until the end of the cold contour approaches the temperature of cooling liquid.

CONCLUSION

During the experiments of the research on the effect of casting regimes on the temperature field in

the solidification zone of the molding were identified the followings:

- the position of solidification zone of the slurry mass when molding velocity changes from 20 to 100 mm/min;

- the position of solidification zone of the slurry mass in the form-building cavity depending on the water flow rate and the temperature in the cold contour of cooling.

The upper bound of the solidification zone was estimated by isotherm "solidus" $54^0$C, and the lower bound – by isotherm "solidus" $40^0$C.

Temperature distribution, estimated during the experiments, in the form-building cavity of bushing depending on the molding velocity and heat extraction conditions on the walls of form-building of annular cavity lets us determine the transition from liquid (viscous-plastic) state to solid-plastic one.

The experiment results were analysed and generalized using mathematical model of the thermoplastic slurry molding process. The latent heat of the phase change has been accounted by the apparent heat capacity.

The mathematical model includes the equations of the law of conservation of mass, momentum and energy of non-Newtonian fluid with the Shvedov-Bingham's rheological model. Rheological and thermo-physical properties of the slurry were found on the basis of experimental data and express dependence on the temperature. The temperature field of the slurry in liquid (viscous-plastic) and solid-plastic states were obtained in the calculations. The positions of isotherm "solidus" ($54^0$C) and "solidus" ($40^0$C), expressing the upper and lower boundaries of the solidification zone position were determined.

The results of calculation show physical validity of the proposed mathematical model of the molding process of the thermoplastic slurry beryllium oxide. The model of the process of forming ceramic fabrication is a flexible system, and it includes the rheological and thermal properties of other original materials.

## REFERENCES

1  P.O. Gribovsky. Hot casting of ceramic products, Energoizdat, Moscow-Leningrad, [in Russian], (1961).

2  A.G. Dobrovol'skii. Slurry Casting, Metallurgiya, Moscow, [in Russian], (1977).

3  R.M. German, A. Bose. Injection molding of metals and ceramics, Princeton, New Jersey, USA, (1997).

4  A.V. Parkhomenko, A.P. Amosov, A.R. Samboruk and et. al. Casting powder formation of Metal Parts. *Metallurgy Eng.*, Vol. 3, 39-42 [in Russian], (2012).

5  S.A. Shakhov, G.D. Bitsoev. Application of Ultrasound in the Manufacture of High Thermal Conductivity Ceramic Articles. Ust'-Kamenogorsk, [in Russian], (1999).

6  G.P. Akishin, S.K. Turnaev, V.Ya. Vaispapir and et. al. Thermal conductivity of beryllium oxide ceramic. *Refractories and Industrial Ceramics*, Vol. 50, 465-468, (2009).

7  S.A. Shakhov. Controlling the deformation behavior of thermoplastic slips with ultrasound. *Glass and Ceramics*, Vol. 64, 354-356, (2007).

8  S.A. Shakhov, A.E. Gagarin. Rheological characteristics of thermoplastic disperse systems treated with ultrasound. *Glass and Ceramics*, Vol. 65, 122-124, (2008).

9  V.R. Voller, C.A. Prakash. Fixed grid numerical modeling methodology for convection-diffusion mushy region phase-change problems. *Heat and Mass Transfer*, Vol. 30, No.8, 1709-1719, (1987).

10 V.R. Voller, C.R. Swaminathan, B.G. Thomas. Fixed grid techniques for phase change problems: a review. *Numerical Methods in Eng.*, Vol. 30, 875-898, (1990).

11 H. Hu, S.A. Argyropoulos. Mathematical modeling of solidification and melting: a review, Modelling Simul. Mater. Sci. Eng., Vol. 4, 371-396, (1996).

12 N.O. Moraga, M.A. Andrade, D.A. Vasco. Unsteady conjugated mixed convection phase change of power law non Newtonian fluid in a square cavity. *Heat and Mass Transfer*, Vol. 53, 3308-3318, (2010).

13 M. Carbona, C. Cortes. Numerical simulation of a secondary aluminum melting furnace heated by a plasma torch. *Materials Process. Tech.*, Vol. 214, 334-346, (2014).

14 N. Bannach. Phase Change: Cooling and Solidification of Metal, https://www.comsol.com/blogs/phase-change-cooling-solidification-metal/2014, accessed 12.08.14.

15 Yu.V. Dvinskikh, R.Ya. Popil'skii, L.I. Kostin, V.V. Kulagin. Thermophysical properties of thermoplastic casting slips of some high-refractory oxides. *Ogneupory*, Vol. 12, 37–40 [in Russian], (1979).

16 U.K. Zhapbasbayev, G.I. Ramazanova, Z.K. Sattinova, A.D. Shabdirova. Modeling of the beryllia ceramics formation process. *J. of the European Ceramic Society*, Vol. 33, 1403-1411, (2013).

17 W.L. Wilkinson. Non-Newtonian fluids. Mir, Moscow, [Russian translation], (1964).

18 J.D. Anderson, J.C. Tunnehill, R.H. Pletcher. Computational fluid mechanics and heat transfer, Mir, Moscow, [Russian translation], (1990).

19 T. Cebeci, P. Bradshaw. Physical and Computational Aspects of Convective heat transfer, Mir, Moscow, [Russian translation], (1987).

# FOOD ENGINEERING AND TECHNOLOGIES

# The effect of extrusion variables on the colour of bean-based extrudates

Iv. Y. Bakalov[1], T. V. Petrova[1], M. M. Ruskova[1*], K. D. Kalcheva – Karadzhova[1], N. D. Penov[2]

[1] *Food Research and Development Institute – Plovdiv, 154 Vassil Aprilov Blvd, 4000 Plovdiv, Bulgaria*
[2] *University of Food Technologies – Plovdiv, 26 Maritza Blvd, 4000 Plovdiv, Bulgaria*

A mixture of bean (50%), einkorn wheat (40%), and buckwheat (10%) was extruded in a laboratory single screw extruder, using die with 3 mm diameter. The effect of extrusion conditions, including moisture content, barrel temperature, screw speed, and screw compression ratio on colour of the extrudates was investigated. Response surface methodology with combinations of moisture content (16, 19, 22, 25, 28%), barrel temperature (120, 140, 160, 180, 200ºC), screw speed (120, 140, 160, 180, 200 rpm), and screw compression ratio (1:1, 2:1, 3:1, 4:1, 5:1) was applied. Feed screw speed was fixed at 50 rpm. Feed zone temperature and metering zone temperature were kept constant at 100 and 140ºC, respectively. The total colour differences between the extruded and non-extruded samples ($\Delta E$) were determined. The average $\Delta E$ values ranged from 11.92 to 21.15. Statistical analysis showed that the barrel temperature and moisture content had an effect on the total colour differences ($P < 0.05$) whereas the screw speed and screw compression ratio had no effect on the colour.

**Keywords:** colour, extrusion, bean-based extrudates

## INTRODUCTION

Extrusion is widely used as a high-temperature short-time process to produce commercially shelf stable extruded products. Many physical and chemical changes take place during the process, including the gelatinization of starch, denaturation of protein and even complete cooking. To fully understand changes during the process, evaluation of the effect of extrusion process variables on the extruded product is very important. There are many process and product-dependent variables associated with the extrusion process such as barrel temperature, screw speed, die diameter, and raw material composition [1-6].

Colour is an important component of the visual appearance of foods. It may also be related to the wholesomeness of foods. Along with flavour and texture, colour is often perceived as a valuable quality factor in the acceptability and marketability of food products. Colour is perceived three dimensionally, based on responses of three different receptors (red, green and blue) in the human eye [7], yet all three dimensions may not be of practical importance. The Judd–Hunter L, a, b and CIELAB L*, a*, b* are alternative colour scales used to measure the degree of lightness (L*), redness or greenness (±a*) and yellowness or blueness (±b*), with the CIELAB scale being most commonly used for the evaluation of colour in foods [8]. Conversion of a* and b* readings to hue and chroma values gives results more closely associated with human perception [9].

The purpose of this study was to evaluate the effect of extrusion variables on the colour characteristics of bean-based extrudates.

## MATERIALS AND METHODS

### *Raw materials and preparation*

The raw materials einkorn wheat and buckwheat are provided and delivered by village of Lomets, municipality of Troyan, Bulgaria. The bean is variety "Bivolare" and it is grown in the Rhodope Mountains, Bulgaria.

Bean seeds, einkorn wheat, and buckwheat were ground using a hammer mill and passed through standard sieves to be obtained homogenized meals. The bean meal, einkorn wheat meal, and buckwheat meal were blended at a ratio of 50:40:10 (w/w/w). Samples of prepared composite meal were mixed with distilled water to be obtained various moisture contents (Table 1). The wet materials were placed and kept in sealed plastic bags for 12 h in a refrigerator at 5ºC. The samples were tempered for 2 h at room temperature prior to extrusion.

### *Extrusion process*

The samples were extruded in a laboratory single screw extruder (Brabender 20 DN, Germany). The compression ratio of the screw was 1:1, 2:1, 3:1, 4:1, 5:1 according to the experimental design (Table 1). The extruder barrel (476.5 mm in length and 20 mm in diameter) contained three sections and independently controlled die assembly electric heaters. The screw speed was 120, 140, 160, 180, 200 rpm. Feed zone temperature and metering zone temperature were kept constant at 100 and 140ºC, respectively. The temperature of

* To whom all correspondence should be sent:
mmruskova@gmail.com

the extruder die was 120, 140, 160, 180, 200ºC. The feed screw speed was fixed at 50 rpm and the die

diameter was 3 mm.

**Table 1.** Experimental design for the extrusion experiments

| Run № | Coded levels | | | | Actual levels | | | |
|---|---|---|---|---|---|---|---|---|
| | $X_1$ | $X_2$ | $X_3$ | $X_4$ | Moisture content (*W*, %) | Barrel temperature (*T*, ºC) | Screw speed (*N*, rpm) | Screw compression ratio *(K)* |
| 1 | -1 | -1 | -1 | -1 | 19 | 140 | 140 | 2:1 |
| 2 | 1 | -1 | -1 | -1 | 25 | 140 | 140 | 2:1 |
| 3 | -1 | 1 | -1 | -1 | 19 | 180 | 140 | 2:1 |
| 4 | 1 | 1 | -1 | -1 | 25 | 180 | 140 | 2:1 |
| 5 | -1 | -1 | 1 | -1 | 19 | 140 | 180 | 2:1 |
| 6 | 1 | -1 | 1 | -1 | 25 | 140 | 180 | 2:1 |
| 7 | -1 | 1 | 1 | -1 | 19 | 180 | 180 | 2:1 |
| 8 | 1 | 1 | 1 | -1 | 25 | 180 | 180 | 2:1 |
| 9 | -1 | -1 | -1 | 1 | 19 | 140 | 140 | 4:1 |
| 10 | 1 | -1 | -1 | 1 | 25 | 140 | 140 | 4:1 |
| 11 | -1 | 1 | -1 | 1 | 19 | 180 | 140 | 4:1 |
| 12 | 1 | 1 | -1 | 1 | 25 | 180 | 140 | 4:1 |
| 13 | -1 | -1 | 1 | 1 | 19 | 140 | 180 | 4:1 |
| 14 | 1 | -1 | 1 | 1 | 25 | 140 | 180 | 4:1 |
| 15 | -1 | 1 | 1 | 1 | 19 | 180 | 180 | 4:1 |
| 16 | 1 | 1 | 1 | 1 | 25 | 180 | 180 | 4:1 |
| 17 | -2 | 0 | 0 | 0 | 16 | 160 | 160 | 3:1 |
| 18 | 2 | 0 | 0 | 0 | 28 | 160 | 160 | 3:1 |
| 19 | 0 | -2 | 0 | 0 | 22 | 120 | 160 | 3:1 |
| 20 | 0 | 2 | 0 | 0 | 22 | 200 | 160 | 3:1 |
| 21 | 0 | 0 | -2 | 0 | 22 | 160 | 120 | 3:1 |
| 22 | 0 | 0 | 2 | 0 | 22 | 160 | 200 | 3:1 |
| 23 | 0 | 0 | 0 | -2 | 22 | 160 | 160 | 1:1 |
| 24 | 0 | 0 | 0 | 2 | 22 | 160 | 160 | 5:1 |
| 25 | 0 | 0 | 0 | 0 | 22 | 160 | 160 | 3:1 |
| 26 | 0 | 0 | 0 | 0 | 22 | 160 | 160 | 3:1 |
| 27 | 0 | 0 | 0 | 0 | 22 | 160 | 160 | 3:1 |

*Total colour difference (ΔE)*

The extrudates were finely ground using a laboratory hammer mill. The colour parameters determined for the raw blends (non-extruded) and extruded samples included *L\**, *a\** and *b\** values (CIE Lab system) using a colorimeter Colorgard 2000, BYK – Gardner Inc., USA. Total colour difference (*ΔE*) was calculated applying the equation

$$\Delta E = \sqrt{(L - L_o)^2 + (a - a_o)^2 + (b - b_o)^2} \qquad (1)$$

where *L*, *a*, and *b* are the values for the extruded samples; $L_o$, $a_o$, and $b_o$ are the values for the raw mixture.

The colour parameters are the mean values of ten observations.

*Experimental design and data analysis*

A central composite rotatable design was used to investigate the effect of the moisture content ($X_1$), barrel temperature ($X_2$), screw speed ($X_3$), and screw compression ratio ($X_4$) on the total colour difference (response, y) in 27 runs of which 16

were for the factorial points, 8 were for axial points, and 3 were for centre points [10]. The outline of the experimental design is outlined in Table 1.

The levels of the independent variables were established according to literature information and preliminary trials.

A second order polynomial model for the dependent variable (total colour difference) was established to fit the experimental data:

$$y = b_0 + \sum_{i=1}^{n} b_i x_i + \sum_{i=1}^{n} b_{ii} x_i^2 + \sum_{i=1}^{n} \sum_{j=1}^{n} b_{ij} x_i x_j \qquad (2)$$

where $b_0$ = intercepts, $b_i$ are linear, $b_{ii}$ are quadratic, and $b_{ij}$ are interaction regression coefficient terms.

SYSTAT statistical software (SPSS Inc., Chicago, USA, version 7.1) and Excel were used to analyze the data results.

RESULTS AND DISCUSSION

The total colour differences between the extruded and non-extruded samples expressed by

$\Delta E$ are given in Table 2. Higher $\Delta E$ means darker products. The total colour change in extruded samples ranged between 11.92 and 21.15 (Table 2). The extrudates were darker in colour compared to their raw blends. $L^*$ values of the extruded samples (from 66.97 to 76.43) were lower than $L_o$ value of the raw mixture (87.59). A similar finding has been reported by Leonel et al. [11], Bhattacharya et al. [12]. This may be due to the formation of brown pigments through non-enzymatic Maillard reactions between proteins and reducing sugars that occur during the product processing [13, 14].

**Table 2.** Total colour differences of bean-based extrudates

| № | $L^*$ | $a^*$ | $b^*$ | $\Delta E$ |
|---|-------|-------|-------|------------|
| 1 | 71.33 | 5.78 | 15.11 | 16.92 |
| 2 | 66.97 | 5.99 | 14.96 | 21.15 |
| 3 | 73.53 | 6.15 | 15.45 | 14.98 |
| 4 | 71.45 | 6.20 | 14.67 | 16.79 |
| 5 | 71.52 | 6.41 | 15.96 | 17.06 |
| 6 | 69.15 | 6.45 | 14.79 | 19.08 |
| 7 | 73.67 | 6.47 | 16.09 | 15.11 |
| 8 | 71.73 | 6.74 | 16.24 | 17.01 |
| 9 | 67.80 | 6.98 | 16.19 | 20.76 |
| 10 | 68.24 | 5.78 | 13.45 | 19.67 |
| 11 | 76.43 | 3.99 | 15.47 | 11.92 |
| 12 | 71.53 | 4.51 | 15.65 | 16.69 |
| 13 | 71.49 | 4.99 | 16.05 | 16.88 |
| 14 | 69.58 | 4.78 | 15.53 | 18.56 |
| 15 | 72.34 | 4.60 | 16.73 | 16.24 |
| 16 | 69.69 | 4.52 | 15.31 | 18.38 |
| 17 | 71.49 | 4.83 | 16.84 | 17.09 |
| 18 | 68.08 | 4.39 | 15.23 | 19.93 |
| 19 | 67.46 | 6.29 | 16.11 | 20.95 |
| 20 | 75.73 | 3.57 | 16.22 | 12.81 |
| 21 | 72.15 | 4.09 | 16.67 | 16.34 |
| 22 | 69.85 | 4.12 | 16.21 | 18.41 |
| 23 | 69.78 | 4.71 | 16.71 | 18.66 |
| 24 | 68.82 | 3.94 | 18.18 | 19.97 |
| 25 | 70.82 | 4.06 | 16.89 | 17.67 |
| 26 | 71.10 | 3.83 | 16.48 | 17.27 |
| 27 | 70.51 | 4.01 | 16.95 | 17.98 |

Chroma a* (redness) values ranged from 3.57 to 6.98. There was little variability in this parameter during the extrusion, which indicates that the development of the red colouration is negligible. Similar results have been observed by Leonel et al. [11].

Responses of the b* colour parameter, which represents variation from blue to yellow, varied according to the treatment (from 13.45 to 18.18). The positive b* values indicate the yellowness of the sample. For all samples, the b* values were higher for the extrudates than for the raw mixture, which indicates more yellow products. The results

correspond with established from Leonel et al. [11] and Paes and Maga [15].

Studies were conducted using the response surface method. The independent and dependent variables were fitted to the second order model equation and examined for the goodness of fit. The analysis of variance were performed to evaluate the lack of fit and the significance of the linear, quadratic and interaction effects of the independent variables on the dependent variables. The R-squared is defined as the ratio of the explained variation to the total variation and is a measure of the degree of fit [16]. When $R^2$ approaches unity, the better the empirical model fits the actual data. The smaller is $R^2$, the less relevant the dependent variables in the model have in explaining the behavior of variation [10]. It is suggested that for good fit model, $R^2$ should be at least 80%.

The results of the statistical analysis of variance (ANOVA) for the colour show that 3 effects have P-values less than 0.05 indicating that they are significantly different from zero at the 95.0% confidence level. The R-squared statistic is 0.83; the standard error of the estimate - 1.35, the mean absolute error - 0.71. The regression equation describing the effect of extrusion variables on the total colour difference of bean-based extrudates is given in Table 3.

**Table 3.** Regression equation coefficients for total colour differences of bean-based extrudates in terms of coded variables

| Variables | Coefficients |
|-----------|--------------|
| Constant | 55.7281 |
| $X_1$ | -0.3219* |
| $X_2$ | -0.2334* |
| $X_3$ | -0.1579 |
| $X_4$ | -0.6792 |
| $X_1X_1$ | 0.0113 |
| $X_2X_2$ | -0.0008 |
| $X_3X_3$ | -0.0005 |
| $X_4X_4$ | 0.3029 |
| $X_1X_2$ | 0.0039 |
| $X_1X_3$ | -0.0021 |
| $X_1X_4$ | -0.0513 |
| $X_2X_3$ | 0.0021* |
| $X_2X_4$ | -0.0073 |
| $X_3X_4$ | 0.0081 |

$X_1$ - moisture content (%), $X_2$ - barrel temperature (°C), $X_3$ - screw speed (rpm), $X_4$ - screw compression ratio.
*Significant at 95% CI.

The coefficients in the regression equation can be used to examine the significance of each term relative to each other when used with coded values. Statistical analysis showed that the barrel temperature and moisture content had an effect on

the total colour differences (P<0.05) whereas the screw speed and screw compression ratio had no effect on the colour.

Each of the estimated effects and interactions are shown in the standardized diagram - the Pareto diagram (Fig.1). It consists of horizontal blocks with lengths proportional to the absolute values of the estimated effects, divided by their standard errors. The vertical line in the Pareto diagram represents the value of the Student criterion at 95 % confidence level and separates factors that are significant to those that are not. The Pareto diagram shows the predominance of the barrel temperature (factor B). Next in order of importance is the moisture content (factor A) and the less influential parameter is the interaction between the barrel temperature and screw speed (B × C). In total, there are three statistically significant effects.
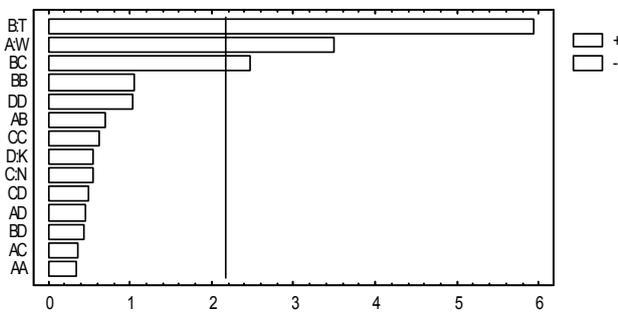


**Fig.1.** Estimated effects of regression model coefficients on the total colour difference

The residual quantity distribution for the regression model of the total colour change is uniformly distributed around zero and no values exceed two times the standard error (Fig.2).
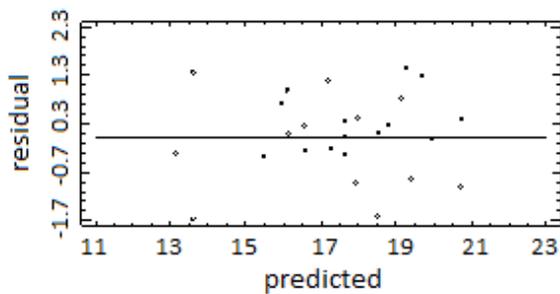


**Fig.2.** Residual distribution diagram

The effect of changes in moisture content and barrel temperature on the total colour differences of the samples is given in Fig.3. ΔE values increased with an increase in moisture content.
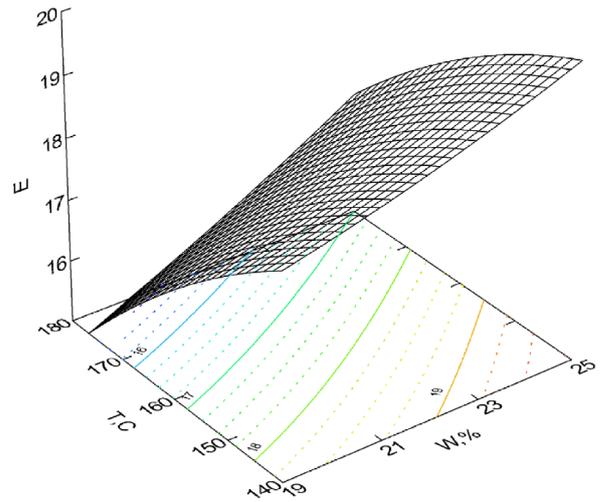


**Fig.3.** Effect of moisture content and barrel temperature on the total colour difference (ΔE) of bean-based extrudates

Our results show that the total colour difference of the extruded mixture increases by 17% ($L*$ value decreases from 71.49 to 68.08) when increasing the moisture content from 16 to 28% at barrel temperature 160ºC, screw speed 160 rpm, and screw compression ratio 3:1. Gujska and Khan [17] have extruded high starch fractions of navy, pinto, and garbanzo beans with different feed moisture contents. They have reported that increasing moisture content resulted in decreased $L*$ values of the extruded beans.

Although, the screw speed was not a significant parameter (Table 3), at low screw speeds a slight increase in colour change observed (Table 2) due to longer residence times which might increase the extent of chemical reactions. On the other hand, the increased screw speed increases the shear and temperature and could lead to more browning. The final effect being the result of the two opposite trends [13, 18].

CONCLUSION

The effect of extrusion variables on the colour of bean-based extrudates was studied. The average colour differences (*ΔE* values) between the extruded and non-extruded samples ranged from 11.92 to 21.15. Statistical analysis showed that the barrel temperature and moisture content had an effect on the total colour differences (P<0.05) whereas the screw speed and screw compression ratio had no effect on the colour.

## REFERENCES

1 A. Simitchiev, Investigation of selected process variables in extrusion of corn and wheat coextrudates, Thesis, University of Food Technologies, Plovdiv, (in Bulgarian), (2013).

2 A. Simitchiev, V. Nenov, Agri-food sciences, processes and technologies – Agri Food, 2014. Section 10. Economics, Energetics and ecology in food industry, 255, (2014).

3 A. Simitchiev, V. Nenov, *J. Food & Pack. Tech*., 2, 265, (2013).

4 L. Yu, Extrusion processing of protein rich food formulations, Thesis, McGilli University, Montreal, (2011).

5 N. Toshkov, Study of extrusion process for the preparation of food for carp (*Cyprinus carpio* L.), Thesis, University of Food Technologies, Plovdiv, (in Bulgarian), (2011).

6 V. Nenov, Investigation on the technical and technological parameters of the production of reconstituted tobacco by the extrusion-and-rolling method, Thesis, University of Food Technologies, Plovdiv, (in Bulgarian), (2007).

7 F. Francis, F. Clydesdale, Food Colorimetry: Theory and Applications, AVI Publishing Company, Inc., Westport, CT, (1975).

8 J. Berrios, D. Wood, L. Whitehand, J. Pan, *J. Food Process. Pres.*, 28, 321, (2004).

9 C. Setser, *J. Food Quality*, 6, 183, (1984).

10 R. Myers, D. Montgomery, C. Anderson-Cook, Response Surface Methodology: Process and Product Optimization Using Designed Experiment. 3rd ed. John Wiley & Sons. Inc., 704, (2009).

11 M. Leonel, T. Freitas, M.Mischan, *Sci. Agric.,* 66, 486, (2009).

12 S. Bhattacharya, V. Sivakumar, D. Chakraborty, *J. Food Eng.,* 32, 125, (1997).

13 C. Mercier, P. Linko, J. Harper. Extrusion Cooking, American Association of Cereal Chemists, St. Paul, MN, USA, 471, (1989).

14 K. Rosentrater, K. Muthukumarappan, S. Kannadhason, *J. Aqua. Feed Sci. Nutr.,* 1, 22, (2009).

15 M. Paes, J. Maga, *Revista Brasileira de Milho e Sorgo*, 3, 10, (2004).

16 A. Haber, R. Runyon. General Statistics. 3rd ed. Addison-Wesley Publishing Company, Reading, MA, 343, (1977).

17 E. Gujska, K. Khan, *J. Food Sci.*, 56, No 2, 443, (1991).

18 S. Kannadhason, K. Muthukumarappan, K. Rosentrater, *J. Aqua. Feed Sci. Nutr.,* 1, 6, (2009).

# Osmotic dehydration as a preliminary technological process for the production of dried chokeberry (Aronia melanocarpa)

M. M. Ruskova[1*], S. S. Aleksandrov[1], I. Y. Bakalov[1], E. C. Popescu[2], T. V. Petrova[1], V. G. Gotcheva[3], N. D. Penov[3]

[1]*Food Research and Development Institute, 154 Vassil Aprilov Blvd., 4000, Plovdiv, Bulgaria*
[2]*Agricultural and Stockbreeding Experimental Station, 35 Nevyastata Str., 4700, Smolyan, Bulgaria*
[3]*University of Food Technologies, 26 Maritza Blvd., 4000, Plovdiv, Bulgaria*

Black chokeberry was subjected to osmotic dehydration in a solution containing concentrated sour cherry juice (60% w:w), concentrated apple juice (20% w:w), and inulin (20% w:w). The effects of osmotic treatment temperature, solution concentration, and fruit:solution ratio on water loss (WL) and weight reduction (WR) of chokeberry fruits were studied. Response surface methodology (RSM) was applied to assess the combinations of osmotic treatment temperature (43, 50, 60, 70, and 77ºC), solution concentration (47, 50, 55, 60, and 63°Brix), and chokeberry:solution ratio (1:2, 1:3, 1:4, 1:5, and 1:6 w:w). Water loss values varied from 20.82 to 43.43% and the weight reduction values varied from 11.93 to 41.58%, respectively. Osmotic treatment temperature had the highest impact on water loss, and fruit weight reduction was mostly influenced by the osmotic solution concentration, with both effects being linear.

**Keywords**: black chokeberry, osmotic dehydration, water loss, weight reduction, response surface methodology

## INTRODUCTION

Osmotic dehydration is a pre-treatment method for the partial removal of water from plant tissues by immersion of foodstuff in hypertonic water solution [1]. Osmotic dehydration involves three mass transfer processes: (1) water transfer from the plant product to the osmotic solution, (2) incursion of solutes from the solution into the foodstuff and (3) excretion of soluble solids from the plant tissues to the osmotic solution. The third transfer is quantitatively negligible compared to the first two types of transfer but it is essential for the composition of the product [2, 3]. The different flows in and out of the plant tissue are shown in Fig.1.
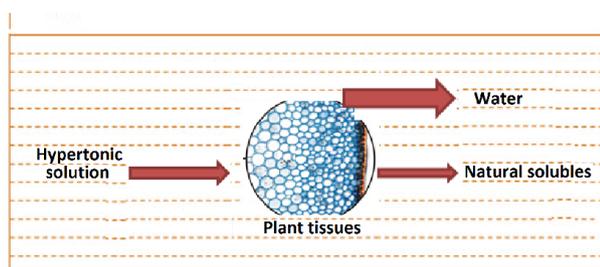


**Fig.1.** Mass transfer in fruit tissue during osmotic dehydration

The rate of osmotic dehydration and final indicators of dehydrated plant products is mainly dependent on the temperature of the osmotic solution, type and concentration of osmotic solution, and fruit to osmotic solution ratio [4, 5].

### Temperature of the osmotic solution

The most important variable affecting the kinetics of mass transfer during osmotic dehydration is temperature [4]. Increasing the temperature of the osmotic solution results in an increase in the rate of water removal and sugar uptake [5]. Diffusion of flavour and odour compounds from the fruits to the solution is also increased at high temperature. According to the literature on osmotic treatment, temperatures around 50°C have been used for fruits and vegetables for the following reasons: 1) deterioration of flavour, texture, and thermo-sensitive compounds of the materials is limited at this temperature, 2) enzymatic browning and flavour deterioration of fruits start at 49°C, and 3) this temperature proved efficient to maintain the viscosity of the solution and ensure adequate infusion time without deterioration of fruit quality [6, 7].

### Type and concentration of osmotic agent

Phisut [5] reported that low molecular weight osmotic agents penetrate easier into the fruit cells compared to high molecular weight osmotic agents. The most commonly used osmotic agents are sucrose, glucose, fructose, sorbitol, glycerol, corn syrup and fructo-oligosaccharide.

During osmotic dehydration, the increase of solute concentrations results in higher water loss

---

* To whom all correspondence should be sent:
  mmruskova@gmail.com

and solid gain rates [5]. The increased osmotic solution concentration resulted in higher water loss and weight reductions and increased drying rates [4, 8, 9].

*Fruit: osmotic solution ratio*

The increase of fruit sample:osmotic solution ratio results in higher osmosis rate up to a certain level. However, it is essential to use an optimum ratio since large ratios offer practical difficulties in handling the processing of osmotic solution and fruit mixture. A ratio of 1:2 or 1:3 sample:osmotic solution is reported as optimal for practical purposes [10].

There are some major advantages of osmotic dehydration process in the food industry: quality aspect (improvement in terms of colour, flavour, and texture), product stability and retention of nutrients during storage, energy efficiency, packaging and distribution cost reduction, chemical treatment not required, product stability during storage [11-13].

The genus Aronia (Rosaceae family, Maloidea subfamily) includes two species *A. melanocarpa*, known as black chokeberry and *A. arbutifolia* as red chokeberry. Black chokeberry fruits contain carbohydrates (10-18% wet basis), pectins (0.6-0.7% wet basis), sorbitol and parasorboside [14, 15]. Analyses showed relatively high content of K and Zn, as well as some amounts of Na, Ca, Mg and Fe [16, 17]. Chokeberry fruits are very rich in bioactive compounds, mainly total polyphenols (3.44-7.49% of dry weight), anthocyanins (0.60-2.0% of dry weight) and flavonols (0.66-5.18% of dry weight) [18-20]. Due to the high anthocyanin content, chokeberry fruit is used as an ingredient of antioxidant health-promoting juices, teas, extracts for production of syrups and dietary supplements [21-23].

Response surface methodology (RSM) is a statistical tool used in process research for evaluation of the influence of different treatment parameters on product characteristics [24]. It has also been used to determine the optimal values of process parameters in various processes [25-27]. Several studies on optimization of plant products dehydration by RSM method have been reported [28-30].

Although the process of osmotic dehydration has been extensively studied, information about the mass transfer processes of osmotic dehydration of black chokeberry is hardly found in the literature. Therefore, the present study is focused on the water loss and weight reduction as a function of process variables (osmotic treatment temperature, solution concentration and chokeberry fruits:solution ratio).

EXPERIMENTAL DETAILS

*Raw materials*

Black chokeberry (*Aronia melanocarpa*) fruits with soluble solids of 24-27°Brix were supplied by the Agricultural and stockbreeding experimental station, Bulgaria. The fresh fruits were sorted and stored in a refrigerator at 3°C until used.

Osmotic agents: concentrated sour cherry juice, concentrated apple juice, and inulin (oligofructose 87%, average degree of polymerization 8; sucrose, glucose, and fructose 12%) were purchased from Krichimfrukt Ltd. (Bulgaria), Agrobiotech Ltd. (Bulgaria), and Food consulting Ltd. (Bulgaria), respectively. The containers of concentrated sour cherry juice and concentrated apple juice were stored in a refrigerator at 3°C until used.

*Sample preparation and osmotic process*

Black chokeberry was washed with tap water, and then subjected to splitting.

Osmotic solutions were prepared in five concentrations (47, 50, 55, 60 and 63°Brix) (Table 1) using concentrated sour cherry juice with 63°Brix (60% w:w), concentrated apple juice with 72°Brix (20% w:w), and inulin (20% w:w). The concentration of the osmotic solutions was monitored by an Abbe refractometer (VEB Carl Zeiss JENA, Germany) [31].

Osmotic dehydration of fruits was performed in a water bath (VEB MLW Prüfgeräte Werk, Medingen, Sitz Freital, Germany) to achieve the necessary solution temperature according to the experimental design (Table 1). The choice of the preferred process conditions was according to survey of other researchers on osmotic dehydration [3, 32]. The berries were dipped in osmotic solution of a specified concentration for 3 hours. The fruit:solution ratio was 1:2, 1:3, 1:4, 1:5, and 1:6 (w:w) according to the experimental design (Table 1). Further, the fruits were removed from the solutions, quickly rinsed with hot water and gently blotted with paper towel to remove surface solution.

Total dry matter and drained weight (final sample weight) of the osmotic dehydrated fruits were determined [33]. Further, the samples were analyzed for the main indicators - water loss and weight reduction. Weight reduction (WR) is defined as the net difference in weight between the initial weight of the fruit sample and the weight of the osmotically dehydrated fruit based on the initial

sample weight. Water loss (WL) was defined as the net loss of water from the fresh fruits after osmotic dehydration based on the initial sample [34]. These parameters were calculated according to the following equations:

$$WR = \frac{M_o^o - M_f^o}{M_o^o} 100, \%$$ (1)

$$WL = \frac{x_o^w M_o^o - x_f^w M_f^o}{M_o^o} 100, \%$$ (2)

where $M_o^o$ – the initial sample weight (g), $M_f^o$ – the final sample weight (g), $x_o^w$ – initial moisture content (%), $x_f^w$ – final moisture content (%).

*Experimental design and data analysis*

Central composite rotatable design (CCRD) was used to prepare osmotic dehydration of black chokeberry, by response surface methodology with three variables at five levels. The actual factor values were chosen based on the literature review and the corresponding coded values (- 1.68, -1, 0, +1, +1.68) are presented in Table 1. The complete design consisted of 17 experimental runs with three replications of the center point. Experimental runs were carried out in random order.

**Table 1.** Response surface central composite design with three factors (variables) at five levels

| № | Osmotic treatment temperature | Solution concentration | Fruit : solution ratio |
|---|---|---|---|
| | X₁ (°C) | X₂ (°Brix) | X₃ (w/w) |
| 1 | 50 (-1) | 50 (-1) | 1:3 (-1) |
| 2 | 70 (+1) | 50 (-1) | 1:3 (-1) |
| 3 | 50 (-1) | 60 (+1) | 1:3 (-1) |
| 4 | 70 (+1) | 60 (+1) | 1:3 (-1) |
| 5 | 50 (-1) | 50 (-1) | 1:5 (+1) |
| 6 | 70 (+1) | 50 (-1) | 1:5 (+1) |
| 7 | 50 (-1) | 60 (+1) | 1:5 (+1) |
| 8 | 70 (+1) | 60 (+1) | 1:5 (+1) |
| 9 | 43 (-1.68) | 55 (0) | 1:4 (0) |
| 10 | 77 (+1.68) | 55 (0) | 1:4 (0) |
| 11 | 60 (0) | 47 (-1.68) | 1:4 (0) |
| 12 | 60 (0) | 63 (+1.68) | 1:4 (0) |
| 13 | 60 (0) | 55 (0) | 1:2 (-1.68) |
| 14 | 60 (0) | 55 (0) | 1:6 (+1.68) |
| 15 | 60 (0) | 55 (0) | 1:4 (0) |
| 16 | 60 (0) | 55 (0) | 1:4 (0) |
| 17 | 60 (0) | 55 (0) | 1:4 (0) |

The generalized second-order polynomial model used in the response surface analysis was the following:

$$Y = b_o + \sum_{i=1}^{n} b_i x_i + \sum_{i=1}^{n} b_{ii} x_i^2 + \sum_{i=1}^{n} \sum_{j=1}^{n} b_{ij} x_i x_j$$ (3)

where $y$ is the dependent variable (response), $x_i$ and $x_j$ are the independent variables (factors), $\beta_o$, $\beta_i$, $\beta_{ii}$, $\beta_{ij}$ are the regression coefficients for intercept, linear, quadratic, and interaction terms. SYSTAT statistical software (SPSS Inc., Chicago, USA, version 7.1) and Excel (Microsoft Office, 97-2003) were used to analyse the data.

RESULTS AND DISCUSSION

The average weight reduction (WR) and water loss (WL) values of the osmotically dehydrated black chokeberry are presented in Table 2. WR varied from 11.93 to 41.58% and WL values varied from 20.82 to 43.43%, respectively.

**Table 2.** Weight reduction and water loss values of the osmotically dehydrated black chokeberry

| № | Weight reduction Y₁ (%) | Water loss Y₂ (%) |
|---|---|---|
| 1 | 11.93 | 20.82 |
| 2 | 20.55 | 28.84 |
| 3 | 17.27 | 25.80 |
| 4 | 28.88 | 36.80 |
| 5 | 20.63 | 29.13 |
| 6 | 28.25 | 36.01 |
| 7 | 34.97 | 33.22 |
| 8 | 41.58 | 43.43 |
| 9 | 15.30 | 24.61 |
| 10 | 28.22 | 37.27 |
| 11 | 15.35 | 28.70 |
| 12 | 38.17 | 41.74 |
| 13 | 16.64 | 29.98 |
| 14 | 18.87 | 30.43 |
| 15 | 17.47 | 25.51 |
| 16 | 16.87 | 26.10 |
| 17 | 17.11 | 25.61 |

**Table 3.** Regression coefficients and analysis of variance for weight reduction of black chokeberry

| № | Regression coefficients | Sum of squares | F- value | P-value |
|---|---|---|---|---|
| Constant | 581.471 | | | |
| A:X₁ | -2.347 | 231.179 | 12.29 | 0.0099* |
| B: X₂ | -18.523 | 465.337 | 24.74 | 0.0016* |
| C:X₃ | -18.294 | 187.111 | 9.95 | 0.0161* |
| AA | 0.023 | 60.766 | 3.23 | 0.1153 |
| AB | 0.005 | 0.490 | 0.03 | 0.8763 |
| AC | -0.075 | 4.500 | 0.24 | 0.6397 |
| BB | 0.164 | 188.530 | 10.02 | 0.0158* |
| BC | 0.350 | 24.500 | 1.30 | 0.2913 |
| CC | 0.906 | 9.247 | 0.49 | 0.5058 |

*Significant at P < 0.05

Statistical analysis of variance (ANOVA) for WR and WL shows that 4 effects have p-values less than 0.05, indicating that they are significantly different from zero at the 95.0% confidence level (Table 3 and Table 4). For the indicator weight

reduction the R-squared is 0.89; the standard error of the estimate is 4.34, and the mean absolute error is 2.08. For water loss of osmotic-dehydrated fruits R-squared is 0.93; the standard error of the estimate is 2.62, and the mean absolute error is 1.33.

**Table 4.** Regression coefficients and analysis of variance for water loss of black chokeberry

| № | Regression coefficients | Sum of squares | F- value | P-value |
|---|---|---|---|---|
| Constant | 460.836 | | | |
| A:$X_1$ | -2.357 | 241.266 | 35.15 | 0.0006* |
| B: $X_2$ | -14.137 | 157.515 | 24.74 | 0.0020* |
| C:$X_3$ | -5.661 | 67.167 | 9.95 | 0.0167* |
| AA | 0.017 | 31.494 | 3.23 | 0.0694 |
| AB | 0.016 | 4.977 | 0.03 | 0.4227 |
| AC | -0.024 | 0.466 | 0.24 | 0.8020 |
| BB | 0.127 | 114.333 | 10.02 | 0.0047* |
| BC | 0.036 | 0.265 | 1.30 | 0.8525 |
| CC | 1.412 | 22.462 | 0.49 | 0.1134 |

*Significant at P < 0.05

Each of the estimated effects and interactions are shown in the standardized diagrams (Fig.2 and Fig.3). The linear effect due to the concentration of osmotic solution had the highest impact on the weight reduction. The temperature of osmotic treatment also had significant effect on weight reduction (P<0.05). Similar results were observed by Fernandes et al. [35] at osmotic dehydration of papaya in corn syrup and sugar.
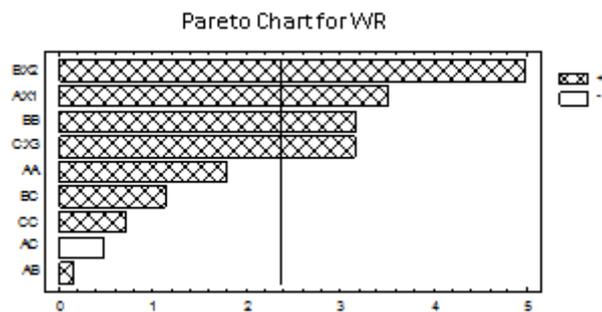


**Fig.2.** Estimated effects of regression model coefficients on the weight reduction of black chokeberry
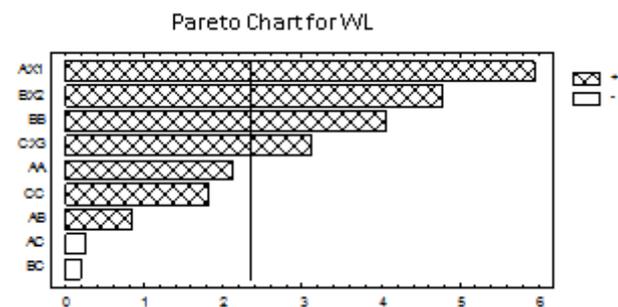


**Fig.3.** Estimated effects of regression model coefficients on the WL of black chokeberry

In agreement with Fig.3, temperature of the osmotic solution had the most significant effect on water loss, followed by the concentration of the osmotic solution and fruit to osmotic solution ratio (P<0.05). İspir and Toğrul [36], Kumar and Devi [37] also confirmed that an increase in temperature resulted in an increase in the rate of water loss.

Based on the results from ANOVA after removing the insignificant effects, the following regression equations were obtained:

$$WR = 581.47 - 2.35X_1 - 18.52X_2 - 18.29X_3 + 0.16X_2^2, \% \qquad (4)$$

$$WL = 460.84 - 2.36X_1 - 14.14X_2 - 5.66X_3 + 0,13X_2^2, \% \qquad (5)$$

The effect of osmotic dehydration conditions on the weight reduction and water loss of black chokeberry are shown on Fig.4 and Fig.5. The figures show the combined effect of two factors (temperature and concentration of osmotic solution) on the response of dependent variables.
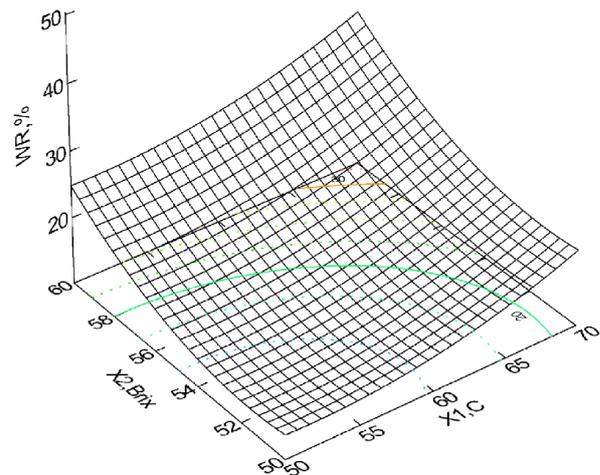


**Fig.4.** WR (%) depending on $X_1$ (°C) and $X_2$ (°Brix) at fruit:solution ratio 1:4 (w:w)

The increase in solution concentration and temperature resulted in higher water loss (Fig.5) and weight reduction (Fig,4) values throughout the osmosis period. WR and WL increase about 1.8 and 1.5 times respectively (see Table 2) with raising the osmotic treatment temperature from 43 to 77°C (at solution concentration 55ºBrix and fruit:solution ratio 1:4 (w/w). Similar results were reported by many authors [36, 38-41]. Higher temperatures seem to promote faster water loss through swelling and plasticizing of cell membranes as well as the better water transfer characteristics on the product surface due to lower viscosity of the osmotic

medium [5, 38]. Fruit sample has a porous structure so that high temperature releases the trapped air from the tissue resulting in more effective to the removal of water by osmotic pressure. This enhances the removal of water and uptake of solids [5].
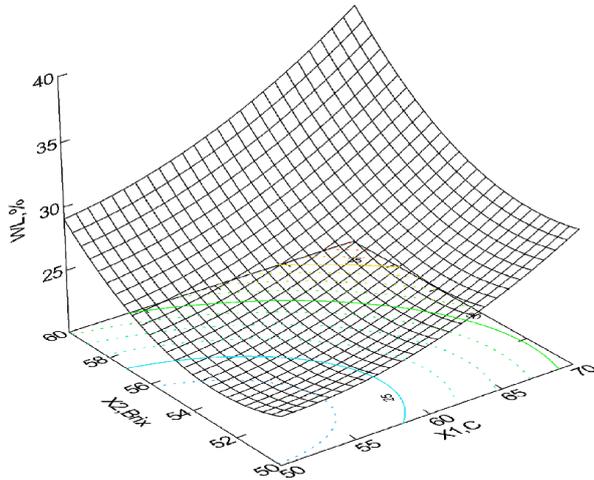


**Fig.5.** Water loss (%) depending on $X_1$ (°C) and $X_2$ (°Brix) at fruit:solution ratio 1:4 (w:w)

Our results show that WR and WL increase about 2.5 and 1.5 times respectively (see Table 2) with raising the solution concentration from 47 to 63°Brix (at osmotic treatment temperature 60°C and fruit:solution ratio 1:4 (w/w). The increase in solution concentration resulted in an increase in the osmotic pressure gradients [36, 41] and, hence, higher water loss (Fig.5) and weight reduction (Fig.4) values throughout the osmosis period were obtained. These results indicate that by choosing a higher concentration, some benefits in terms of faster water loss could be achieved.

## CONCLUSION

Combination of different osmotic agents was chosen to achieve the purpose of the study. The optimal area of combinations of osmotic agents was presented in our previous study [42]. Rich in biologically active substances fruit juices are used (concentrated sour cherry juice, concentrated apple juice) and inulin. The main advantages of fructans including inulin are: highly soluble, low degree of polymerization (8 fructose units), technological properties that are closely related to those of sugar and glucose syrups. In addition, inulin is a prebiotic food ingredient.

The choice of the preferred process conditions was according to survey of other researchers on osmotic dehydration. Response surface methodology was used for a quantitative study on the effects of the osmotic treatment temperature,

solution concentration, and fruits:solution ratio on weight reduction and water loss of osmotically dehydrated chokeberry fruits. Results show that all three main effects are statistically significant for both responses during the osmotic dehydration of fruits with osmotic solution contain cherry juice (60% w:w), concentrated apple juice (20% w:w), and inulin (20% w:w).

## REFERENCES

1  A. Sereno, R. Moreira, E. Martinez, *J. Food Eng.*, 47, 43, (2001).
2  E. Spiazzi, R. Masccheeroni, *J. Food Eng.*, 34, 384, (1997).
3  M. Akbarian, N. Chasemkhami, F. Moayedi, *Int. J. Biosci.*, 4 (1), 42, (2014).
4  Ch. Tortoe, *African J. of Food Sc.*, 4, 303, (2010).
5  N. Phisut, *Int. Food Res. J.*, 19 (1), 7, (2012).
6  M. Khan, *Pak. J. Food Sci.*, 22 (2), 71, (2012).
7  J. Shi, J. Xue, Application and development of osmotic dehydration technology in food processing. In Ratti, C. (Ed). Advances in food dehydration, CRC Press. USA, (2009).
8  J. Conway, F. Castaigne, G. Picard, X. Vovan *Canadian Institute of Food Science and Technology Journal*, 16 (1), 25, (1983).
9  M. Marcotte, C. Toupin, M. Le Maguer, *J. Food Eng.*, 13 (3), 199, (1991).
10  R. Tiwari, S. Jalali. In proceeding of First Indian Horticulture congress-2004, New Delhi, (2004).
11  P. Pant, H. Saimi. IJSTM, 1, 1, (2014).
12  M. Rahman, *Indian Food Industry*, 11 (5), 20, (1992).
13  A. Raoult-Wack, *Trends Food Sci. Technol.*, 5, 255, (1994).
14  T. Wolski, O. Lalisz, M. Rolski, *Post Fiototer*, 3, 145, (2007).
15  S. Kulling, H. Rawel, *Planta Medica*, 74, 1625, (2008).
16  M. Kane, B. Dehgan, T. Sheehan, *Proc. Fla. State Hort. Soc.*, 104, 287, (1991)
17  K. Ognik, E. Rusinek, I. Sembratowicz, J. Truchlinski. *Rocz. Panstw. Zakl. Hig.*, 57, 235-241, (2006)
18  J. Oszmiański, J. Wojdyło, *Eur. Food Res. Technol.*, 221, 809, (2005).
19  S. Hakkinen, M Heinonen, S. Karenlampi, H. Mykkaren, J. Ruuskanen, R. Torronen, *Food Res. Int.*, 32, 345, (1999).
20  X. Wu, L. Gu, R. Prior, S. McKay, *J. Agric. Food Chem.*, 52, 7846, (2004).
21  E. González-Molina, D. Moreno, C. García-Viguera, *J. Agric Food Chem.*, 23, 11327, (2008).
22  S. McKay, *N. Berry News*, 11, 4, (2004).
23  M. Soto, F. Berberán, *Eur. Food Res. Technol.*, 219, 133, (2004).
24  P. Box, S. Hunter, Estadística para Investigadores; Introducción al Diseño de Experimentos. Análisis de

Datos y Construcción de Modelos. Ed. Reverté; Barcelona. España, (2005).

25 P. Harris, S. Cuppett, L. Bullerman, *J. Food Protec.*, 53, 481, (1990).

26 S. Mannan, A. Fakhrul-Razi, Z. Alam, *Journal of Environmental Sciences,* 19, 23, (2007).

27 M. Rajasimman, R. Sangeetha, P. Karthic, *Chem. Eng. J.*, 2, 275, (2009).

28 O. Corzo, E. Gomez, *J. Food Eng.,* 64, 213, (2004).

29 I. Eren, F. Ertekin, *J. Food Eng.*, 79, 344, (2007).

30 B. Singh, P. Panesar, A. Gupta, J. Kennedy, *Eur. Food Res. Technol.*, 225, 157, (2007).

31 Fruit and vegetable juices - Estimation of soluble solids content - Refractometric method – EN 12143:2000.

32 A. Ferradji, F. Chaouche, D. Belhachat, A. Malek, *Revue des Energies Renouvelables,* 18 (4), 539, (2015).

33 Fruit and vegetable juices - Determination of total dry matter - Gravimetric method with loss of mass on drying - EN 12145:2000.

34 S. Khanom, M. Rahman, M. Uddin, *J. Bangladesh Agr. Univ.*, 12, 221, (2014).

35 F. Fernandes, S. Rodrigues, O. Gaspareto, E. Olivera, *J. Food Eng.,*77, 188, (2006).

36 A. Ispir, I. Toğrul, *Chem. Eng. Res. Des*., 87, 166, (2009).

37 P. Kumar, P. Devi, *Int. Food Res. J.,* 18, 221, (2011).

38 D. Nadia, B. Nourhène, K. Nabil, C. Francis, B. Catherine, *J. Food Process. Technol*., 4 (8), 1, (2013).

39 S. Pokharkar, S. Prasad, *J. Food Sci. Technol.*, 35 (4), 336, (1998).

40 E. Devic, S. Guyoi, J. Daudin, C. Bonazzi, *J. Agric. Food Chem.,* 58, 606, (2010).

41 M. Mundada, S. Hathan, S. Maske, *J. Food Sci.*, 76, 31, (2011).

42 M. Ruskova, Sv. Aleksandrov, A. Iliev, T. Petrova, V. Gotcheva, N. Penov, *Scientific Works of University of Food Technologies*, LXII, 371, (2015).

# Effect of extrusion conditions on breaking strength index of lentil extrudates

M. M. Ruskova[1*], T. V. Petrova[1], I. Y. Bakalov[1], G. I. Zsivanovits[1], N. G. Toshkov[2], N. D. Penov[2]

[1]*Food Research and Development Institute, 154 Vassil Aprilov Blvd., 4000, Plovdiv, Bulgaria*
[2]*University of Food Technologies, 26 Maritza Blvd., 4000, Plovdiv, Bulgaria*

Lentil semolina was extruded in a laboratory single screw extruder (Brabender 20 DN, Germany) with screw diameter 20 mm and die diameter 5 mm. A central composite rotatable design (CCRD) was adopted to study the effect of moisture content, barrel temperature, metering zone temperature, screw speed, and screw compression ratio on breaking strength index of lentil extrudates. The breaking strength index of the extrudate was determined using a texture analyser TA.XT Plus (Stable Micro Systems, England) and calculated using peak breaking force divide by extrudate diameter. The breaking strength index values varied from 12.2 to 32.87 N/mm. Analysis of variance indicates that linear effect due to the moisture content of lentil semolina had the highest impact on the breaking strength index. The regression model fitted to the experimental data showed comparatively high coefficient of determination.

**Keywords:** breaking strength index, extrusion, lentil, extrudate, texture analyser

## INTRODUCTION

Extrusion cooking is a modern high-temperature short-time processing technology, gaining ground in certain industries for various reasons. It offers several advantages over other types of cooking processes, such as faster processing times and significant reduction in energy consumed, which consequently results in lower prices for the final products. However, when they are produced by modern extrusion technology, the various types of extrudate are produced in very different shapes. These depend not only on processing conditions, but also on the size and shape of the die, and the speed of the final cutting device [1].

The quality of extrudate produced can be determined using different methods according to their applicability in a variety of food-industry sectors.

Texture testing is a well-established technique for evaluating the mechanical and physical properties of raw ingredients, food structure, and design, and for pre- and post-quality control checks [2]. Texture testing has applications across a wide range of food types, including baked goods, cereals, confectionaries, snacks, dairy, fruit, vegetables, gelatins, meat, poultry, fish, pasta and even pet food. Since texture is a property related to the sense of touch, it can be measured easily by mechanical methods in units such as force [3].

In food texture testing, standard tests such as compression, tension, and flexure are used to measure hardness, crispiness, crunchiness, softness, springiness, tackiness, and other properties of food [4-6].

For processed food, the textural properties can be used to optimize the process. Food texture analysis can highlight quality improvement opportunities throughout the supply chain and the production process. In production, food texture analysis is used for the measurement and control of process variations such as temperature, humidity and cooking time [7].

Different types of testing instrumentation available, from manual and motorized food firmness testers to fully software-controlled texture analyzers. The texture analyzers perform the test by applying controlled forces to the product and recording its response in the form of force, deformation and time [8, 9].

The purpose of this research was to investigate the effect of moisture content, barrel temperature, metering zone temperature, screw speed, and screw compression ratio on breaking strength index of lentil extrudates produced with a single screw extruder.

## EXPERIMENTAL DETAILS

### Raw material and preparation

Representative sample of commercial lentil cultivar, namely Ilina, was obtained from Dobroudja Agricultural Institute, General Toshevo, Bulgaria.

Lentil seeds were ground using a hammer mill and passed through standard sieves. Prepared particle size of lentil semolina was about 0.5 mm. Lentil semolina was mixed with distilled water to

---

* To whom all correspondence should be sent:
 mmruskova@gmail.com

be obtained various moisture contents (Table 1). The wet materials were placed and kept in sealed plastic bags for 12 h in a refrigerator at 5ºC. The samples were tempered for 2 h at room temperature prior to extrusion.

*Extrusion*

Lentil semolina was extruded in a laboratory single screw extruder (Brabender 20 DN, Germany). The compression ratio of the screw was 1:1, 2:1, 3:1, 4:1, 5:1 according to the experimental design (Table 1). The extruder barrel (476.5 mm in length and 20 mm in diameter) contained three sections and independently controlled die assembly electric heaters. The screw speed was 132, 160, 180, 200, 228 rpm. The temperature of the feed zone was 150ºC, that of the metering zone was 136, 150, 160, 170, 184ºC, and that of the extruder die was 136, 150, 160, 170, 184ºC. The feed screw speed was fixed at 70 rpm and the die diameter was 5mm.

*Hardness and breaking strength index*

Hardness and breaking strength index of the extrudates were determined using a texture analyzer TA.XT Plus (Stable Micro Systems, England), with a 50 kg load cell and a 2-bladed Kramer shear cell (2 mm thick, 32 mm high, 119 mm wide, 4 mm apart). The test settings were as follows: Pre-test speed 2 mm/s, Test speed 1 mm/s, Post-test speed 10 mm/s.

Hardness of the extrudates was the peak in the Force / Distance curve when the sample is broken (peak breaking force or collapse). Breaking strength index (BSI, N/mm) was calculated using peak breaking force (N) divided by the extrudate diameter (mm) [10, 11]. The reported values were the average of 20 determinations.

*Bulk density*

Bulk density (g/cm$^3$) of the extrudates was calculated by measuring the actual dimensions of the extrudates. The diameter and length of 10 pieces of randomly selected extrudate samples were measured by Vernier caliper. The weight of these extrudate pieces was determined by electronic weighing balance having an accuracy of 0.001 g. The bulk density was calculated using the following formula, assuming a cylindrical shape of extrudate [12, 13]:

$$Density = \frac{4W}{\pi D^2 L} \qquad (1)$$

where $W$ is weight (g), $D$ is diameter (cm), and $L$ is the length of the extrudate (cm).

*Experimental design and data analysis*

The central composite rotatable design (CCRD) is a widely adopted tool for optimization and

drastically reduces the number of experiments for studies involving more than two independent variables [14, 15]. In the present study CCRD was used to show interactions of moisture content ($X_1$), barrel temperature ($X_2$), metering zone temperature ($X_3$), screw speed ($X_4$), and screw compression ratio ($X_5$) on the extrudate in 52 runs of which 32 were for the factorial points (run № 1-32), 10 were for axial points (run № 33-42), and 10 were for replications at the central point of the design (run № 43-52). The levels of the independent variables were established according to literature information and preliminary trials. The outline of the experimental design is outlined in Table 1.

To estimate moisture content, barrel temperature, metering zone temperature, screw speed, and screw compression ratio effects each objective response, the standardized scores were fitted to a quadratic polynomial regression model by employing a least square technique [16, 17]. The model proposed for the response of Y was:

$$y = b_0 + \sum_{i=1}^{n} b_i.x_i + \sum_{i=1}^{n} b_{ii}.x_i^2 + \sum_{i=1}^{n} \sum_{j=1}^{n} b_{ij}.x_i.x_j \quad (2)$$

where y = the response (breaking strength index), $b_0$ = intercepts, $b_i$ are linear, $b_{ii}$ are quadratic, and $b_{ij}$ are interaction regression coefficient terms. Coefficients of determination ($R^2$) were computed. The adequacy of the model was tested by separating the residual sum of squares into pure error and lack of fit. For each response, response surface plots were produced from the equations, by holding the variable with the least effect on the response equal to a constant value, and changing the other two variables [17].

SYSTAT statistical software (SPSS Inc., Chicago, USA, version 7.1) and Excel were used to analyze the data results.

RESULTS AND DISCUSSION

Chemical changes taking place during extrusion influence the development of textural and mechanical properties such as hardness and breaking strength in extrudates. Breaking strength index is the measure of the strength of cell wall which is expected to affect the texture and sensory crispiness of the extruded product [18]. The mean values of breaking strength index (BSI) of the extruded lentil semolina are shown in Table 1. BSI is in the range of 12.2 – 32.87 N/mm.

The results of the statistical analysis of variance (ANOVA) for the breaking strength index show that 6 effects have p-values less than 0.05, indicating that they are significantly different from

zero at the 95.0% confidence level. The R-squared statistic is 0.82; the standard error of the estimate – 2.61, the mean absolute error – 1.58. The regression equation describing the effect of extrusion variables on the breaking strength index of extruded lentil semolina is given in Table 2. The coefficients in the regression equation can be used to examine the significance of each term relative to each other when used with coded values.

**Table 1.** Central composite rotatable design in coded form and natural units of independent variables and experimental data for breaking strength index

| Run № | Independent variables in coded form | | | | | Independent variables in natural units | | | | | BSI (Y), N/mm | |
|---|---|---|---|---|---|---|---|---|---|---|---|---|
| | $X_1$ | $X_2$ | $X_3$ | $X_4$ | $X_5$ | $X_1$ | $X_2$ | $X_3$ | $X_4$ | $X_5$ | Experi-mental | Predicted |
| 1 | -1 | -1 | -1 | -1 | -1 | 22 | 150 | 150 | 160 | 2:1 | 20.23 | 25.80 |
| 2 | +1 | -1 | -1 | -1 | -1 | 28 | 150 | 150 | 160 | 2:1 | 21.92 | 18.23 |
| 3 | -1 | +1 | -1 | -1 | -1 | 22 | 170 | 150 | 160 | 2:1 | 25.92 | 27.00 |
| 4 | +1 | +1 | -1 | -1 | -1 | 28 | 170 | 150 | 160 | 2:1 | 15.86 | 17.05 |
| 5 | -1 | -1 | +1 | -1 | -1 | 22 | 150 | 170 | 160 | 2:1 | 32.87 | 27.63 |
| 6 | +1 | -1 | +1 | -1 | -1 | 28 | 150 | 170 | 160 | 2:1 | 14.58 | 18.63 |
| 7 | -1 | +1 | +1 | -1 | -1 | 22 | 170 | 170 | 160 | 2:1 | 29.86 | 27.97 |
| 8 | +1 | +1 | +1 | -1 | -1 | 28 | 170 | 170 | 160 | 2:1 | 17.02 | 16.60 |
| 9 | -1 | -1 | -1 | +1 | -1 | 22 | 150 | 150 | 200 | 2:1 | 19.51 | 18.56 |
| 10 | +1 | -1 | -1 | +1 | -1 | 28 | 150 | 150 | 200 | 2:1 | 13.56 | 14.68 |
| 11 | -1 | +1 | -1 | +1 | -1 | 22 | 170 | 150 | 200 | 2:1 | 19.55 | 20.54 |
| 12 | +1 | +1 | -1 | +1 | -1 | 28 | 170 | 150 | 200 | 2:1 | 13.16 | 14.28 |
| 13 | -1 | -1 | +1 | +1 | -1 | 22 | 150 | 170 | 200 | 2:1 | 21.03 | 22.96 |
| 14 | +1 | -1 | +1 | +1 | -1 | 28 | 150 | 170 | 200 | 2:1 | 17.38 | 17.65 |
| 15 | -1 | +1 | +1 | +1 | -1 | 22 | 170 | 170 | 200 | 2:1 | 22.19 | 24.09 |
| 16 | +1 | +1 | +1 | +1 | -1 | 28 | 170 | 170 | 200 | 2:1 | 14.53 | 16.41 |
| 17 | -1 | -1 | -1 | -1 | +1 | 22 | 150 | 150 | 160 | 4:1 | 25.59 | 22.15 |
| 18 | +1 | -1 | -1 | -1 | +1 | 28 | 150 | 150 | 160 | 4:1 | 15.82 | 16.94 |
| 19 | -1 | +1 | -1 | -1 | +1 | 22 | 170 | 150 | 160 | 4:1 | 28.96 | 26.70 |
| 20 | +1 | +1 | -1 | -1 | +1 | 28 | 170 | 150 | 160 | 4:1 | 17.62 | 19.11 |
| 21 | -1 | -1 | +1 | -1 | +1 | 22 | 150 | 170 | 160 | 4:1 | 16.71 | 18.24 |
| 22 | +1 | -1 | +1 | -1 | +1 | 28 | 150 | 170 | 160 | 4:1 | 13.80 | 11.59 |
| 23 | -1 | +1 | +1 | -1 | +1 | 22 | 170 | 170 | 160 | 4:1 | 19.27 | 21.94 |
| 24 | +1 | +1 | +1 | -1 | +1 | 28 | 170 | 170 | 160 | 4:1 | 14.30 | 12.92 |
| 25 | -1 | -1 | -1 | +1 | +1 | 22 | 150 | 150 | 200 | 4:1 | 14.67 | 16.17 |
| 26 | +1 | -1 | -1 | +1 | +1 | 28 | 150 | 150 | 200 | 4:1 | 12.41 | 14.64 |
| 27 | -1 | +1 | -1 | +1 | +1 | 22 | 170 | 150 | 200 | 4:1 | 20.21 | 21.50 |
| 28 | +1 | +1 | -1 | +1 | +1 | 28 | 170 | 150 | 200 | 4:1 | 16.24 | 17.60 |
| 29 | -1 | -1 | +1 | +1 | +1 | 22 | 150 | 170 | 200 | 4:1 | 15.31 | 14.83 |
| 30 | +1 | -1 | +1 | +1 | +1 | 28 | 150 | 170 | 200 | 4:1 | 12.20 | 11.87 |
| 31 | -1 | +1 | +1 | +1 | +1 | 22 | 170 | 170 | 200 | 4:1 | 19.88 | 19.31 |
| 32 | +1 | +1 | +1 | +1 | +1 | 28 | 170 | 170 | 200 | 4:1 | 13.86 | 13.98 |
| 33 | -2.378 | 0 | 0 | 0 | 0 | 18 | 160 | 160 | 180 | 3:1 | 31.18 | 31.06 |
| 34 | 2.378 | 0 | 0 | 0 | 0 | 32 | 160 | 160 | 180 | 3:1 | 17.64 | 15.72 |
| 35 | 0 | -2.378 | 0 | 0 | 0 | 25 | 136 | 160 | 180 | 3:1 | 13.02 | 13.17 |
| 36 | 0 | 2.378 | 0 | 0 | 0 | 25 | 184 | 160 | 180 | 3:1 | 19.29 | 17.10 |
| 37 | 0 | 0 | -2.378 | 0 | 0 | 25 | 160 | 136 | 180 | 3:1 | 23.56 | 20.87 |
| 38 | 0 | 0 | 2.378 | 0 | 0 | 25 | 160 | 184 | 180 | 3:1 | 18.10 | 18.74 |
| 39 | 0 | 0 | 0 | -2.378 | 0 | 25 | 160 | 160 | 132 | 3:1 | 19.77 | 21.95 |
| 40 | 0 | 0 | 0 | 2.378 | 0 | 25 | 160 | 160 | 228 | 3:1 | 18.82 | 14.60 |
| 41 | 0 | 0 | 0 | 0 | -2.378 | 25 | 160 | 160 | 180 | 1:1 | 25.00 | 22.66 |
| 42 | 0 | 0 | 0 | 0 | 2.378 | 25 | 160 | 160 | 180 | 5:1 | 15.13 | 15.43 |
| 43 | 0 | 0 | 0 | 0 | 0 | 25 | 160 | 160 | 180 | 3:1 | 19.60 | 17.90 |
| 44 | 0 | 0 | 0 | 0 | 0 | 25 | 160 | 160 | 180 | 3:1 | 18.61 | 17.90 |
| 45 | 0 | 0 | 0 | 0 | 0 | 25 | 160 | 160 | 180 | 3:1 | 17.11 | 17.90 |
| 46 | 0 | 0 | 0 | 0 | 0 | 25 | 160 | 160 | 180 | 3:1 | 17.39 | 17.90 |
| 47 | 0 | 0 | 0 | 0 | 0 | 25 | 160 | 160 | 180 | 3:1 | 16.73 | 17.90 |
| 48 | 0 | 0 | 0 | 0 | 0 | 25 | 160 | 160 | 180 | 3:1 | 19.23 | 17.90 |
| 49 | 0 | 0 | 0 | 0 | 0 | 25 | 160 | 160 | 180 | 3:1 | 18.42 | 17.90 |
| 50 | 0 | 0 | 0 | 0 | 0 | 25 | 160 | 160 | 180 | 3:1 | 17.10 | 17.90 |
| 51 | 0 | 0 | 0 | 0 | 0 | 25 | 160 | 160 | 180 | 3:1 | 18.38 | 17.90 |
| 52 | 0 | 0 | 0 | 0 | 0 | 25 | 160 | 160 | 180 | 3:1 | 17.82 | 17.90 |

$X_1$ - moisture content (*W*, %), $X_2$ - barrel temperature (*$T_m$*, °C), $X_3$ - metering zone temperature (*$T_2$*, °C), $X_4$ - screw speed (rpm), $X_5$ - screw compression ratio.

**Table 2.** Regression equation coefficients and analysis of variance for BSI of lentil extrudates

| Variables | Coefficients | *DF* | *MS* | *p* values |
|-----------|--------------|------|------|------------|
| Constant | 95.7743 | | | |
| $X_1$ | -4.7449 | 1 | 450.600 | 0.0000* |
| $X_2$ | 2.0568 | 1 | 29.5114 | 0.0457* |
| $X_3$ | -0.6338 | 1 | 8.7126 | 0.2666 |
| $X_4$ | -1.2378 | 1 | 103.329 | 0.0005* |
| $X_5$ | -0.8916 | 1 | 99.9447 | 0.0006* |
| $X_1X_1$ | 0.1077 | 1 | 54.9907 | 0.0079* |
| $X_2X_2$ | -0.0049 | 1 | 14.0505 | 0.1609 |
| $X_3X_3$ | 0.0034 | 1 | 6.6256 | 0.3315 |
| $X_4X_4$ | 0.0002 | 1 | 0.2481 | 0.8499 |
| $X_5X_5$ | 0.2012 | 1 | 2.3699 | 0.5595 |
| $X_1X_2$ | -0.0198 | 1 | 11.2813 | 0.2075 |
| $X_1X_3$ | -0.0119 | 1 | 4.0613 | 0.4458 |
| $X_1X_4$ | 0.0154 | 1 | 27.1584 | 0.0546 |
| $X_1X_5$ | 0.1958 | 1 | 11.0450 | 0.2122 |
| $X_2X_3$ | -0.0021 | 1 | 1.4365 | 0.6492 |
| $X_2X_4$ | 0.0010 | 1 | 1.2246 | 0.6744 |
| $X_2X_5$ | 0.0838 | 1 | 22.4785 | 0.0789 |
| $X_3X_4$ | 0.0032 | 1 | 13.2355 | 0.1732 |
| $X_3X_5$ | -0.1436 | 1 | 65.9526 | 0.0040* |
| $X_4X_5$ | 0.0157 | 1 | 3.1626 | 0.5006 |

*Significant at 95% confidence level, *DF* – degrees of freedom, *MS* - mean square

Each of the estimated effects and interactions are shown in the standardized diagram - the Pareto diagram (Fig.1). It consists of horizontal blocks with lengths proportional to the absolute values of the estimated effects, divided by their standard errors. The vertical line in the Pareto diagram represents the value of the Student criterion at 95 % confidence level and separates factors that are significant to those that are not. The diagram shows the predominance of the moisture content (factor A). Other researchers also found that feed moisture is the main factor affecting the physicochemical properties of extrudates [12, 15]. Next in order of importance is the screw speed (factor D) and screw compression ratio (factor E). The least influential parameter is the barrel temperature (factor B). The metering zone temperature (factor C) has no significant effect on BSI.
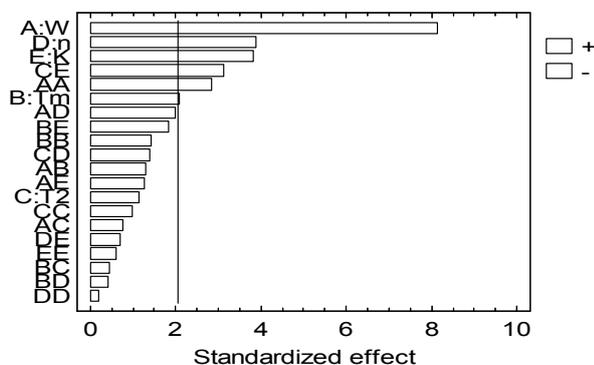


**Fig.1.** Estimated effects of regression model coefficients on breaking strength index

Response surface plots are developed based on the regression equations (see Table 2) to understand the effect of extrusion process variables on BSI. Surface plots are drawn for each of the two variables, where the other three variables are kept at the center point of the experimental design. Some important surface plots are given in Fig.2 and Fig.3.

It is well known that the decrease of moisture content in extrusion tends to increase specific mechanical energy, and consequently to favor macromolecular degradation of starch though dextrinization. The resulting melt then gives more fragile structures leading to low resistant cell walls and more structural fractures. In contrary, lentil flour (protein source) resulted in more rigid structures and elevated values of elastic modulus. Our results show that the breaking strength index of the extruded lentil semolina decreases about 2 times with raising the moisture content from 18 to 32% at barrel temperature 160ºC, metering zone temperature 160ºC, screw speed 180 rpm, and screw compression ratio 3:1. Gujska and Khan [19] have extruded high starch fractions of navy, pinto and garbanzo beans with different moisture contents. They have reported that increasing moisture content resulted in decreased density for navy and garbanzo beans and an increase for pinto bean. Decreased bulk density of extrudates was associated with high expansion index, low hardness and breaking strength [20]. Avin et al. [21] reported that density of extruded red bean is not influenced

by temperature, moisture, or screw speed. Balandran-Quintana et al. [22] have extruded pinto bean flours at three different die temperatures (140, 160, and 180ºC), feed moisture content (18, 20, and 22%), and screw speeds (150, 200, and 250 rpm). They have reported that the density was influenced by moisture and temperature and it decreased with increasing temperature for 18 and 20% moisture feed. For 22% moisture the density decreased between 140 and 160ºC and increased abruptly between 160 and 180ºC.

An increase in screw speed resulted in an extrudate with lower hardness and breaking strength (see Fig.3). It is possible that an increase in screw speed may be expected to lower the melt viscosity of the material in the extruder, resulting in a less dense, softer extrudate [12].

Breaking strength index of lentil extrudates is positively correlated with hardness ($R^2 = 0.77$, p <

0.05) (Fig.4) which is determined by measuring the maximum force required to break the extruded samples. Breaking strength index is also positively correlated with density ($R^2 = 0.77$, p < 0.05) (Fig.5). Similar results are observed by Altan et al. [23]. They investigated the effect of screw configuration and raw material on some properties of barley extrudates and established that hardness of extrudates is positively correlated with bulk density and breaking strength ($R^2 = 0.725$, $R^2 = 0.865$, p < 0.05), whereas negatively correlated with sectional expansion index ($R^2 = 0.470$, p < 0.05). High density product naturally offers high breaking strength while the increase in pore size together with a decrease in cell wall thickness results in weak extrudate structures. Breaking strength is affected by the strength of cell walls, as influenced by starch gelatinization and protein denaturation [24].
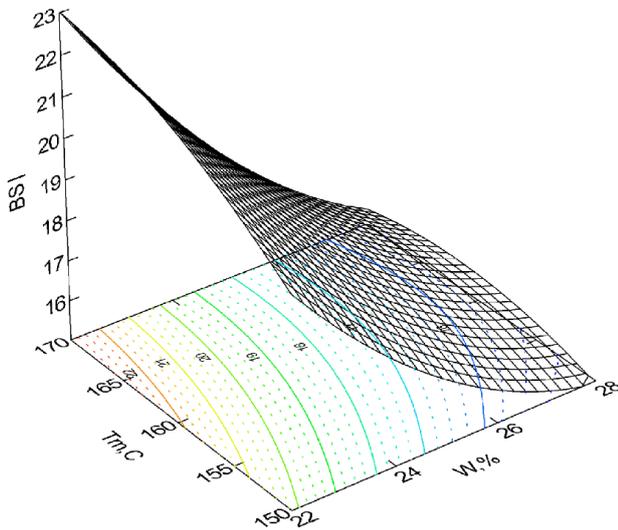


**Fig.2.** Effect of moisture content and barrel temperature on breaking strength index



**Fig.4.** Breaking strength index versus hardness



**Fig.3.** Effect of moisture content and screw speed on breaking strength index
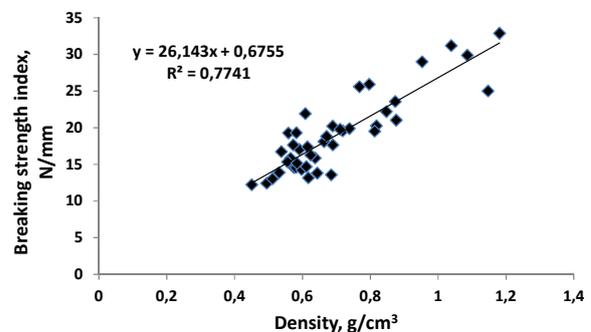


**Fig.5.** Breaking strength index versus density

## CONCLUSION

The breaking strength index of lentil extrudates produced on a laboratory single screw extruder was dependent on several process variables. Moisture content, barrel temperature, screw speed, and screw compression ratio had some significant effect on BSI. The metering zone temperature had no significant effect on BSI. The breaking strength index was found to be most dependent on moisture content. The study showed that BSI of the extruded lentil semolina decreased with raising the moisture content. An increase in screw speed resulted in an extrudate with lower breaking strength. Breaking strength index of lentil extrudates was positively correlated with hardness and bulk density.

## REFERENCES

1 M. Brnčić, B. Tripalo, D. Ježek, D. Semenski, N. Drvar, M. Ukrainczyk, *Sādhanā*, 31 (5), 527, (2006).

2 A. Simitchiev, V. Nenov, *Journal of Food and Packaging Science Technique and Technologies*, 1 (2), 265, (2013).

3 G. Zsivanovits, D. Iserliyska, *New knowledge Journal of science*, 2 (3), 111, (2013).

4 J. Bouvier, R. Bonneville, A. Goullieux, *Agro Food Industry Hi-Tech*, 8 (1), 16, (1997).

5 A. Desrumaux, J. Bouvier, J. Burri, *Cereal Chem.*, 76, 699, (1999).

6 E. Van Hecke, K. Allaf, J. Bouvier, *Journal of Texture Studies*, 29 (6), 617, (1998).

7 J. Steffe, Rheological methods in food process engineering, 2nd ed., Freeman Press, (1996).

8 A. Simitchiev, *Food Proc. Ind. Mag.*, 9-10, 37, (2013).

9 M. Maskan, A. Altan, Taylor & Francis Group, LLC, (2012).

10 S. Chaiyakul, K. Jangchud, A. Jangchud, P. Wuttijumnong, R. Winger, *LWT - Food Sci. and Technol.*, 42, 781, (2009).

11 M. Brncic, B. Tripalo, S. Brncic, S. Karlovic, A. Zupan, Z. Herceg, *Bulg. J Agric. Sci.*, 15 (3), 204, (2009).

12 Q. Ding, P. Ainsworth, A. Plunkett, G. Tucker, H. Marson, *J. Food Eng.*, 73, 142, (2006).

13 A. Sawant, N. Thakor, S. Swami, A. Divate, *Agric Eng Int: CIGR Journal*, 15 (1), 100, (2013).

14 D. Montgomery, Design and analysis of experiments, fifth ed. Wiley, New York, USA, 455, (2001).

15 S. Chakraborty, D. Singh, B. Kumbhar, S. Chakraborty, *Food Bioprod. Process.*, 89 (4), 492, (2011).

16 Jr. Gacula, J. Singh, J. Bi, St. Altan, Statistical Methods in Food and Consumer Research, 2nd Ed. Academic Press, Inc., New York, eBook ISBN 9780080920337, (2008).

17 K. Filli, I. Nkama, U. Abubakar, V. Jideani, *Afr. J. Food Sci.*, 4 (6), 342, (2010).

18 H. Doğan, M. Karwe, *Food Sci. Tech. Int.*, 9 (2), 101, (2003).

19 E. Gujska, K. Khan, *J. Food Sci.*, 56 (2), 443, (1991).

20 P. Rayas-Duarte, K. Majewska, C. Doetkott, *Cereal Chem.*, 75, 338, (1998).

21 D. Avin, C. Kim, J. Maga, *J. Food Process. Pres.*, 16, 327, (1992).

22 R. Balandran-Quintana, G. Barbosa-Canovas, J. Zazueta-Morales, A. Anzaldua-Morales, A. Quintero-Ramos, *J. Food Sci.*, 63 (1), 113, (1998).

23 A. Altan, K. McCarthy, M. Maskan, *J. Food Eng.*, 92, 377, (2009).

24 M. Martinez-Serna, R. Villota, In J. Kokini, C. Ho & M. Karwe (Eds.), Food Extr. Sci. and Technol., New York: Marcel Dekker, 387, (1992).

# Physicochemical parameters of Bulgarian yellow cheese from cow's milk (kashkaval) during the standardized manufacturing

M. Marinova*, G. Kalinova, E. Grigorova

*National Diagnostic Research Veterinary-Medical Institute, 15 Pencho Slaveikov Str., BG-1606, Sofia, Bulgaria*

We analyzed Bulgarian yellow cheese from cow's milk (kashkaval), produced for research purposes in accordance with the technology, described in BDS 14:2010. The batches of kashkaval were stored at manufacturers and delivered for analysis in three stages: immediately after blowing, on the 45-th day and 55-th day from the ripening of the kashkaval. The analyzed parameters were: water content and dry matter, content of fats in total weight, fat in dry matter, proteins, and the ash content. The water-soluble proteins and thus the degree of maturity were determined in 45-th and 55-th day from the beginning of ripening. The energy value was calculated for all samples. The physicochemical parameters of all batches after blowing were very good for the kashkaval, which have not passed the stage of ripening: the amount of dry matter was more than 56% of the total and the fat content in the dry matter was higher than 45.0%. They did not change significantly during the process of ripening. Three of the batches of kashkaval did not meet the requirements of BDS 14:2010 for ripeness (no less than 20.0%) on 45th day. On the 55th day of ripening the degree of maturity of four batches were 20.8 %; 19.4 %; 30.6 % and 16.0 %. Based on the results for physicochemical parameters the important conclusion was: the period of ripening 45 days of kashkaval from cow's milk set out in BDS 14:2010 should be change because they do not guarantee receipt of a mature product.

**Keywords:** Bulgarian yellow cheese, kashkaval, ripening, proteolysis

## INTRODUCTION

Bulgarian yellow cheese, known as "kashkaval", is a type of hard cheese, produced from milk. The technology for producing of kashkaval and all steamed cheeses has been gradually improved over many centuries. The process for manufacturing of the traditional kashkaval includes the following stages: formation of the curd (curdling the milk), initial processing and compressing the curd, cheddaring (proving) the curd, steaming, forming cakes, blowing, salting, ripening, washing and drying [1]. It is important to point at the differences between kashkaval and the yellow cheeses, known in Europe. Those yellow cheeses are manufactured with starters, which can be introduced after curdling the milk.

Essential for the development of the taste and texture of the product is the ripening process. As a biotransformation process, the ripening of the cheese leads to an accumulation of more easily digestible by the human body components. The most significant changes concern protein structure: enzyme assisted proteolysis results in hydrolysis of peptide bonds, leading to the formation of water soluble peptides [2]. It has been found that the proteolysis begins in the first few days of ripening and continues, though sustained, throughout the period of storage [3]. According to Barać et al.

[4], proteolysis during cheese ripening can be divided into two stages: First is the basic one, such that there is degradation of the casein in large well formed polypeptides and the second is the proteolytic process, during that process the formation of small polypeptides and free amino acids happens, this part of the process is when the smell and taste are forming. In the process of maturing, the amount of insoluble in water protein gradually reduces, so by monitoring the changes in the amounts of water-soluble protein the degree of ripening in the kashkaval could be detected. According to BDS 14:2010 [5], Bulgarian kashkaval of cow's milk ripens in refrigerated rooms at a temperature of 8°C to 10°C for 45 days and to 60 days for kashkaval of sheep milk.

This paper presents the changes of the quality parameters during the ripening period of kashkaval from cow's milk, produced in accordance with the technology described in BDS 14:2010 and evaluates if 45 days were sufficient time period for the maturing of the product.

## EXPERIMENTS

Kashkaval from cow's milk, produced by four leading Bulgarian manufacturers was analyzed. For the research purposes, the batches of kashkaval were produced in accordance with the technology, described in BDS 14:2010 and stored at manufacturers.

Physicochemical parameters were analyzed in three stages: immediately after blowing, on the 45-

---

* To whom all correspondence should be sent:
  magi_marinova1960@abv.bg

th day [5] and 55-th day from the ripening of the yellow cheese. For each stage the manufacturers have supplied representative samples, which were identical pieces with weight 400 g, according with requirements of sampling method [6].

*Preparation of the test sample:*

The rind was removed in such a way as to provide a test sample as it is usually consumed. The test sample was grinded by grinder and whole mass was mixed quickly. The test sample was analysed as soon as possible after grinding.

The analyzed parameters were: water content and dry matter, content of fats in total weight, fat in dry matter, proteins, ash content. The water-soluble proteins and thus the degree of maturity were determined in 45-th and 55-th day from the beginning of ripening [5].

The water content and dry matter were defined according to BDS 1109:1989 [7].

The content of fats in total weight was analyzed according to ISO 3433:2008 (IDF 222:2008) [8] and the calculation for fat in the dry matter was by following equation (Eq. 1):

*Equation 1:*

fat in the dry matter, % = (content of fats in total weight /dry matter) x 100

The total protein was determined according to BDS EN ISO 8968-1:2014 [9]. Kjeldahl digestion unit "GERHARD", type EBL was used for the incineration (acidic hydrolysis) of the sample of kashkaval. The distillation of nitrogen content was performed by distillation unit "VELP", type UDK 129.

The ash content was determined in accordance to BDS 6154:1974 [10]. The incineration of the samples was carried out in the oven at 550 °C.

The water-soluble proteins were analyzed as follows: 5.000 g homogenized sample was transferred in a volumetric flask (500 ml) with preheated (40 – 45) °C distilled water. The flask was shaken periodically for 1 hour and then allowed to cool to 20 °C. The solution was filtered through paper filter and 50 ml of the filtrate developed a procedure for determining the total protein in accordance with requirements of BDS EN ISO 8968-1:2014 [9].

The degree of maturity of the kashkaval was calculated by the following equation (Eq.2):

*Equation 2:*

Degree of maturity, % = (water-soluble protein/total protein) x 100

Energy value was determined by calculations described in Regulation 23/2001 of Ministry of Health art.10, p.3 and p.4 [11]. We used the following formula:

Energy value, kcal/100g = (4 x total proteins, %) + (9 x fat in total weight, %)

RESULTS AND DISCUSSION

The results of the analyzed physicochemical parameters of the kashkaval after blowing are presented in Table 1.

**Table 1.** Physicochemical parameters of the kashkaval after blowing

| Parameters | Water content $x \pm Sx$ % | Dry matter $x \pm Sx$ % | Content of fats in total weight $x \pm Sx$, % | Fat in dry matter $x \pm Sx$ % | Ash content $x \pm Sx$ % | Proteins $x \pm Sx$ % | Energy value $x \pm Sx$ kcal/100 g |
|---|---|---|---|---|---|---|---|
| Batch 1 | 42.65±0.08 | 57.35±0.11 | 28.0±0.5 | 48.82±0.88 | 4.09±0.06 | 24.36±0.34 | 349±9 |
| Batch 2 | 38.43±0.08 | 61.57±0.12 | 30.5±0.5 | 49.54±0.89 | 3.78±0.05 | 24.77±0.35 | 374±10 |
| Batch 3 | 42.14±0.08 | 57.86±0.12 | 25.5±0.4 | 44.07±0.79 | 4.72±0.07 | 25.50±0.36 | 332±9 |
| Batch 4 | 38.97±0.08 | 61.03±0.12 | 29.0±0.5 | 47.52±0.86 | 3.72±0.05 | 26.23±0.37 | 366±10 |

The values of all physicochemical parameters of kashkaval samples, produced by four companies were very close. That means that the milk, used for production is standardized - fat content and protein content have been similar. The amount of dry matter in the studied samples conformed to the requirements of BDS 14:2010 for kashkaval from cow's milk (not less than 56.0 %), [5]. The fat content in the dry matter of the all batches of kashkaval was higher than 45.0 % [5]. The physicochemical parameters of the samples were very good for the kashkaval, which have not passed the stage of ripening.

The water content was increased by 0.64 % to 4.07 %, due to the ongoing process of proteolysis on 45th day of ripening of the kashkaval (Table 2).

The amounts of water-soluble protein in the four batches were different and accordingly the degree of ripeness of the kashkaval was different. Only batch 3 met the requirements of BDS 14:2010 for ripeness (no less than 20.0 %) [5].

On the 55th day of ripening of the kashkaval (Table 3) the water content was increased in batch1 and 2, but it was reduced in batch 3 and 4, if compared with 45th day. The decrease of water content can be explained by the delayed process of proteolysis and moisture loss during storage.

**Table 2.** Physicochemical parameters of the kashkaval on 45th day of ripening

| Para-meters | Water content $x\pm Sx$ % | Dry matter $x\pm Sx$ % | Content of fats in total weight $x\pm Sx$ % | Fat in dry matter $x\pm Sx$ % | Ash content $x\pm Sx$ % | Proteins $x\pm Sx$ % | Energy value $x\pm Sx$ kcal/100 g | Water-soluble protein $x\pm Sx$ % | Degree of maturity $x\pm Sx$ % |
|---|---|---|---|---|---|---|---|---|---|
| Batch 1 | 43.88 ±0.09 | 56.12 ±0.11 | 27.5±0.5 | 49.00 ±0.88 | 3.92±0.05 | 23.59±0.33 | 342±9 | 4.48±0.06 | 19.0±0.4 |
| Batch 2 | 39.07±0.08 | 60.93±0.12 | 30.0±0.5 | 49.24 ±0.89 | 3.64±0.05 | 24.48±0.34 | 368±10 | 4.42±0.06 | 18.1±0.4 |
| Batch 3 | 44.84 ±0.09 | 55.16 ±0.11 | 26.0±0.5 | 47.14 ±0.85 | 4.40±0.06 | 24.06±0.34 | 330±9 | 6.56±0.09 | 27.3±0.6 |
| Batch 4 | 43.04 ±0.09 | 56.96 ±0.11 | 27.5±0.5 | 48.28 ±0.87 | 3.45±0.05 | 24.51±0.34 | 346±9 | 3.44±0.05 | 14.0±0.3 |

**Table 3.** Physicochemical parameters of the kashkaval on 55th day of ripening

| Para-meters | Water content $x\pm Sx$ % | Dry matter $x\pm Sx$ % | Content of fats in total weight $x\pm Sx$ % | Fat in dry matter $x\pm Sx$ % | Ash content $x\pm Sx$ % | Proteins $x\pm Sx$ % | Energy value $x\pm Sx$ kcal/100 g | Water-soluble protein $x\pm Sx$ % | Degree of maturity $x\pm Sx$ % |
|---|---|---|---|---|---|---|---|---|---|
| Batch 1 | 44.92±0.09 | 55.08±0.11 | 27.5±0.5 | 49.93 ±0.90 | 4.02±0.06 | 22.24±0.31 | 337±9 | 4.63±0.06 | 20.8±0.4 |
| Batch 2 | 41.12±0.08 | 58.88±0.12 | 29.5±0.5 | 50.10±0.90 | 3.66±0.05 | 23.94±0.34 | 361±10 | 4.64±0.06 | 19.4±0.4 |
| Batch 3 | 43.94±0.09 | 56.06±0.11 | 25.5±0.4 | 45.49±0.82 | 4.72±0.07 | 24.15±0.34 | 326±9 | 7.38±0.10 | 30.6±0.6 |
| Batch 4 | 42.80±0.08 | 57.20±0.11 | 27.5±0.5 | 48.08±0.86 | 3.58±0.05 | 25.01±0.35 | 348±9 | 4.01±0.06 | 16.0±0.3 |

The amounts of water-soluble protein were increased at the four batches, which leaded to an increase in the degree of maturity at all batches (Fig.1).
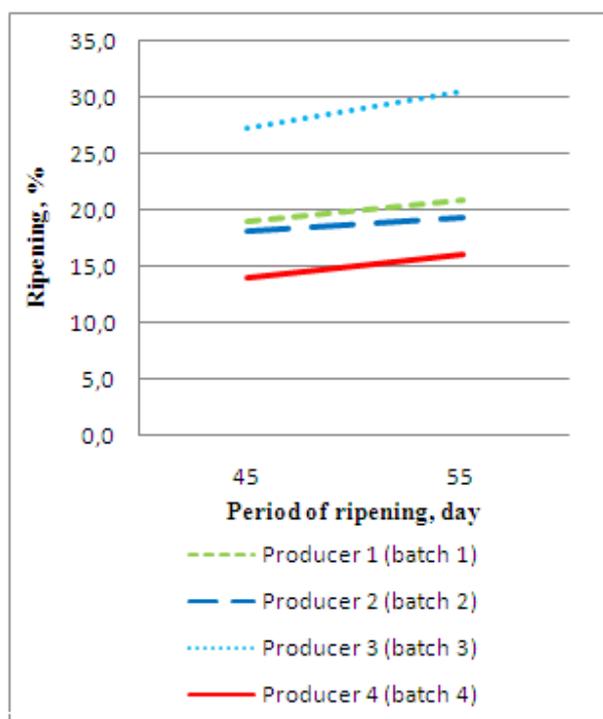


**Fig.1.** Changes in degree of maturity (%) of four batches kashkaval on 45th and 55th days

Only batch 4 did not meet the requirement of BDS 14:2010 [5] for ripeness. The different degrees of maturity of the studied kashkaval have shown, that the conditions for ripening the product were different in the four manufacturers.

The energy value of the four batches of kashkaval met the requirement of BDS 14:2010 [5]. There was a slight tendency to decrease throughout the period of study.

CONCLUSION

Based on the results for physicochemical parameters of four batches Bulgarian yellow cheese, produced in accordance the requirements of BDS 14:2010, we concluded the following:

1. The cow milk used as raw material for production of kashkaval, was standardized. Its quality was suitable for production of kashkaval, according to BDS 14:2010.

2. The physicochemical parameters of the four batches of kashkaval: dry matter (%), fat in dry matter (%) and energy value (kcal/100 g product) met the requirements of BDS 14:2010 early in the ripening process.

3. The period of ripening 45 days for kashkaval from cow's milk, set out in BDS 14:2010 [5] should be changed, since it does not guarantee the maturity of the product and its high nutritional value.

The following recommendation is acceptable for the future:

Based on the results, we will suggest to the relevant public authority to change 45 days period of ripening of kashkaval from cow's milk, set out in BDS 14:2010 and to extend it to 55 days, to ensure the completely conducted ripening process.

As a general conclusion: the quality of the produced in Bulgaria milk is good and allows manufacturing of the quality milk products.

REFERENCES

1 Tz. Zahariev, E. Dincheva, Veterinary - Sanitary Expertise of food with animal origin, Zemizdat, 177, (1991).
2 G. Ivanov, T. Balabanova, I. Ivanova, M. Baltadzhieva, Proteolysis in caw and buffalo milk bulgarian white brined cheese during refrigerated storage, Scientific Works Of University of Food Technologies – Plovdiv, LXII, 2015.
3 H. Mallatou, E. Pappa, C. Vasiliki, A. Boumba, *International Dairy Journal*, 14, 977, (2004).
4 M. B. Barać, M. Smiljanić, M. B. Pešić, S. P. Stanojević, S. T. Jovanović, O. D. Maćej, *Mljekarstvo*, 63, № 3, 122, (2013).
5 BDS 14:2010, Bulgarian Yellow Cheese.
6 ISO707: 2008(IDF 50:2008), Milk and milk products - Guidance on sampling.
7 BDS 1109:1989, Milk and milk products. Determination of water content and the dry matter.
8 ISO 3433:2008 (IDF 222:2008), Cheese – Determination of fat content – Van Gulick method.
9 BDS EN ISO 8968-1:2014, Milk – Determination of nitrogen content – Part 1: Kjeldahl method.
10 BDS 6154:1974, Milk and milk products. Determination of ash content.
11 Regulation 23 of the Ministry of Health of 19 May 2001 on the conditions and requirements for the presentation of nutrition information on food labeling, State Gazette, issue 53 of June 12, 2001, as amended in the SG number 41 of May 13, 2005, as amended in SG 74 Sept., 2009.

# Sensory and texture characterisation of plum (Prunus Domestica) fruit leather

M. Momchilova[1], G. Zsivanovits[1*], Il. Milkova-Tomova[2], D. Buhalova[2], P. Dojkova[2]

[1]*Food Research and Development Institute, Plovdiv*
[2]*University of food technologies – Plovdiv*

The dried fruit leather (pestil) is a well-known traditional healthy food in Bulgaria and Turkey with high antioxidant content. The products were produced and technology was developed based on plum with the addition of pressings (3, 5 and 10%) of Aronia melanocarpa Elliot in combination with Rubus idaeus, Rubus fruticosus and bee honey. Tasting card and intensity scales of sensory indicators were developed for the relative control of nine products. Fruit leather, with addition of 5% pressings (regardless of composition) showed the slightest differences in the organoleptic indicators compared with the control. Instrumental texture parameters were examined by texture profile analysis (TPA). Some correlations were established between the textural and sensory parameters.

**Keywords:** pestil, healthy food, new technology, waste processing, organoleptic parameters, texture profile analysis

## INTRODUCTION

**Pestils** (Fruit leather) are traditional food in some parts of Bulgaria and Turkey. These are prepared from concentrated fruit juices, mashes such as berries, apple, plum, cornel, grapes and others, which are grown regional in the countries. Traditionally used other ingredients are honey, sugar, starch or milk depending on the places. The ingredients and production technology must be studied in parallel way because they influence the physico-chemical and sensory parameters as well [1]. The dried fruit leather has high nutritional value rich in vitamins, minerals and energy. These parameters are highly related to the processing technology (process temperatures for concentration and drying) and to the quality of raw materials [2-5]. The fruit leather can be consumed like a nutritious breakfast, snack or dessert [6].

The **texture** of fruit leathers is affected by the moisture content and drying temperature [4, 7]. The longer drying or higher temperature cause usually harder texture. The differences in texture could also be due to genetic make-up of fruit, rate of water absorption from the surroundings or protein content [8] of the fruits and sugar addition as well [6, 9, 10]. The high sucrose content reinforces the sugar-acid-high methoxyl pectin gelation [6]. The added citric acid decrease the pH which supports the undissociated carboxyl groups of pectins and support the gel structure [6]. Based on the literature there are significant differences between the sensorial and instrumental texture readings [11] because the human mouth is more complex in

measuring like the penetrometers. The texture of the leather can be improved by adding maltodextrin, coconut oil or chopped nuts [9].

The drying of the leather causes **colour** and **appearance** changes of the final product. The lighter leathers tend to darker and turn to brown or lost the yellow-orange colour because the pigments are sensitive to temperature [8]. The browning of the leather could be related to the non-enzymatic vitamin C oxidation or enzymatic oxidation of polyphenols as well [12].

The **aroma** of products results from volatile substances in the fresh food such as esters, ketones, aldehydes, terpenes and others [13, 14]. The loss of these volatiles leads to a decrease in aroma detection. Based on some authors the addition of honey or sugar can be enhance the aroma of leathers [6, 9] but the sugar level above the optimum decrease the flavour rating [10].

The **taste** of the leather can be affected by the sugar level of the raw materials and by added sugar to the optimum level [10]. The aroma and the taste correlates with each other and can be improve with optimum sugar or honey addition [9, 14].

The *plum* fruits are rich in organic acids, pectin, tannins, mineral salts and vitamins and along with its taste qualities have curative effect – stimulated heart function and digestion, helping to dispose of the body of toxic substances and cholesterol. Plums prevent osteoporosis and strengthen bones [15]. *Chokeberries* are high in polyphenolic compounds, such as anthocyanins. The name "chokeberry" comes from the astringency of the fruits, which create a sensation making one's mouth pucker. Their also reduce the blood cholesterol [16, 17]. The black berries contain both soluble and

---

* To whom all correspondence should be sent:
  zsivig@yahoo.co.uk

insoluble dietary fibre, vitamin C, and vitamin K. Their seeds contain oil which is rich in omega-3 (alpha-linolenic acid) and omega-6 fats (linoleic acid) as well as protein, dietary fiber, carotenoids, ellagitannins and ellagic acid [16-20]. **Raspberries** are also high in fibre, antioxidants and in vitamin C. They have anti-inflammatory properties as well [21].

The aim of this study was develop and characterize the sensory and texture properties of new fruit pestil formulas from plum (*Prunus Domestica*) with the addition of pressings from dried fruits (3, 5 and 10%), *Aronia melanocarpa Elliot* in combination with *Rubus idaeus*, *Rubus fruticosus* and bee honey.

EXPERIMENTAL DETAILS

*Technology development*

Nine fruit leather (pestil) combination were developed from puree of plum fruit (*Prunus Domestica*), and dried fruits (3, 5 and 10%) chokeberry (*Aronia melanocarpa Elliot*) in combination with raspberry (*Rubus idaeus*),

blackberry (*Rubus fruticosus*) and bee honey (3%) (Table 1) [6].

**Table 1.** Formulation of fruit pestils[*]

| Composition | Suppl., % | Puree of plums, % | Dry content, db% | | Aw |
|---|---|---|---|---|---|
| | | | puree | pestil | |
| Plum | 0 | 74.85 | 65.80 | 77.0 | 0.502 |
| Plum+ Chokeberry | 3 | 71.85 | 55.66 | 66.9 | 0.542 |
| | 5 | 69.85 | 54.90 | 62.0 | 0.523 |
| | 10 | 64.85 | 54.44 | 60.0 | 0.476 |
| Plum + Chokeberry with blackberry | 3 | 71.85 | 52.14 | 64.0 | 0.460 |
| | 5 | 69.85 | 52.61 | 62.0 | 0.472 |
| | 10 | 64.85 | 61.56 | 71.0 | 0.486 |
| Plum + Chokeberry with raspberry | 3 | 71.85 | 52.10 | 64.0 | 0.486 |
| | 5 | 69.85 | 51.93 | 61.0 | 0.476 |
| | 10 | 64.85 | 61.41 | 74.0 | 0.462 |

* Sugar 22 %; Honey 3 %, Citric acid 0.15 %.

The puree combinations (without honey) were cooked at 80-85°C temperature up to 55-60% dry content. The prepared puree formulations were dried with convective hot air drying method [5] at 45°C for 7-8 hours to 65-70 % dry content in a laboratory drier (Fig.1).
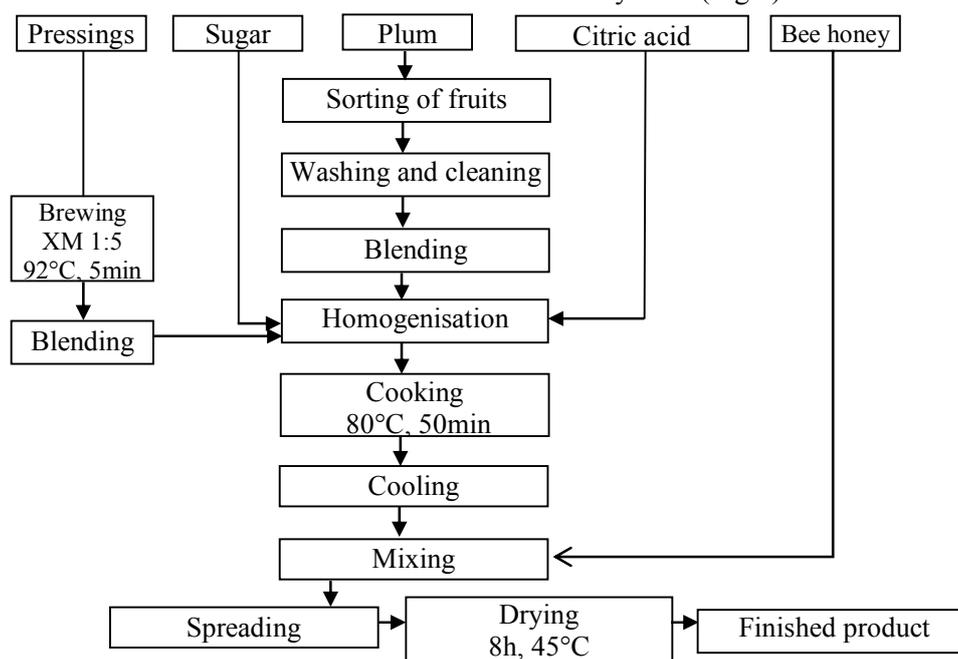


**Fig.1.** Flow diagram of the developed technology

***Water activity*** of the samples is measured by AquaLab Series 3 instrument with chilled-mirror dew-point sensor (Table1).

*Sensory analysis*

Qualitative indicators (appearance, colour, smell, taste, texture) of pestil were studied based on the Bulgarian standard of honey bee (BDS 3050-80) [22]. A consumer acceptance/preference test

was performed according to method of profiling (EN ISO 8586:2014) [23].

The test-card and acceptance scales were developed for the sensory intensities of the indicators (from 1 to 7) for relative control of the nine (9) developed products. Twelve (12) trained panelist have been selected to ensure the accuracy of the assessment. Randomly coded samples were

presented simultaneously to the evaluators. Sensory profile diagrams were formed based on the statistically analysed data.

*Texture analysis*

The texture of leather sheets was determined using a Stable Micro System texture analyzer; model TA.XT.Plus (Godalming, Surrey, UK). A texture profile curve was obtained with 2 loading and 5 s time for relaxation between them. A cylindrical probe (Ø=50 mm) was used. The instrument was set at a test speed of 1 mm·s$^{-1}$ and a strain of 70 %. (Fig.2.).
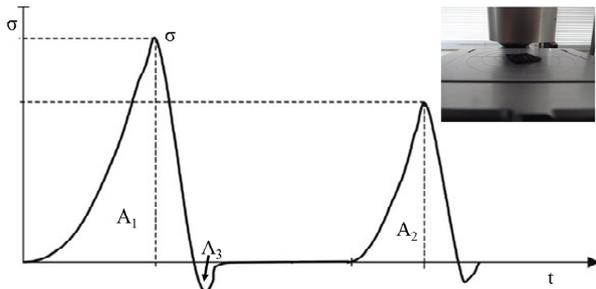


**Fig.2.** Texture profile analysis and parameters

Firmness stress (σ) is determined as the maximum stress coordinate of 1$^{st}$ peek of the curve. The adhesiveness (work of detachment – $A_3$) can be defined like the stress, necessary to pull up the measure probe after the 70 % compression (negative integrated area), cohesiveness defined as the ratio between the 2$^{nd}$ and 1$^{st}$ loading area ($A_2$/$A_1$) and gumminess was computed like cohesiveness multiplied by the firmness. (Fig.2) [24, 25].

## RESULTS AND DISCUSSION

*Sensory analysis*

The sensory parameters are one of the most important properties of food products. Fruit leather from plum with 3 % chokeberry based on the points of the panelists for the *consistence* parameters is firmer than with higher concentrations. It has glossy surface, high elasticity and is not sticky. Because of added pressings, they do not show homogeny consistency. The panelists note that these probes have attractive appearance (Fig.3).

The *aroma profile* of chokeberry is highly expressed with 10 % added pressings. The most balanced aroma of fruit leathers comes from plum and 3% dried chokeberry. The indicator of common perception in all developed formulations of chokeberry is highly pleasant (Fig.3).

Based on the *taste profile* of fruit leathers the variant with 10 % chokeberry is the sweetest and shows the nearest plum's taste like the control. The astringent taste of chokeberry is not perceptible for all concentrations and there is no sour taste (Fig.3).
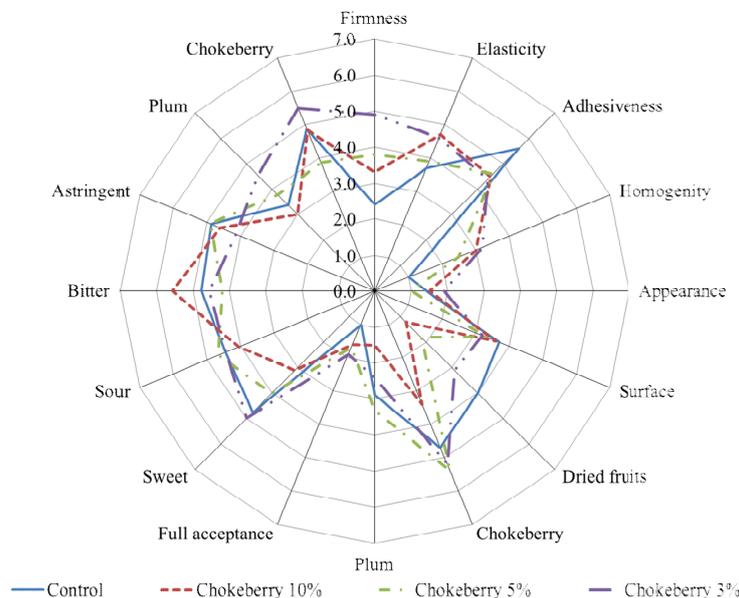


**Fig.3.** Sensory profile for fruit leather from plum with chokeberry

It has been found that the pestil probes with chokeberry and blackberry (5% and 10%) are characterized with soft *consistency* in comparison with those with 3% additive. These variants are glossy near like the control and have less elastic consistency than the sample with 10 %. The adhesiveness of these probes are smaller than the control. Although, these probes have attractive appearance (Fig.4).

It was found (Fig.4) that in plum fruit leathers with chokeberry and blackberry in at all concentrations, the *aroma* of dried fruit is strong,

but different from that of the control. Definitely, the aroma of plum prevails over that of chokeberry, while higher concentrations of blackberry flavor is more pronounced. Like samples with chokeberry the indicator of common perception, it is from highly pleasant to pleasant.

The pestils with 5% and 10% of chokeberry and blackberry have most pronounced sweet and sour *taste* but not pronounced bitter and astringent taste. All variants have taste near to the control but with higher concentration of blackberry, they show more dominant blackberry taste. The variants do not show bitter taste (Fig.4).
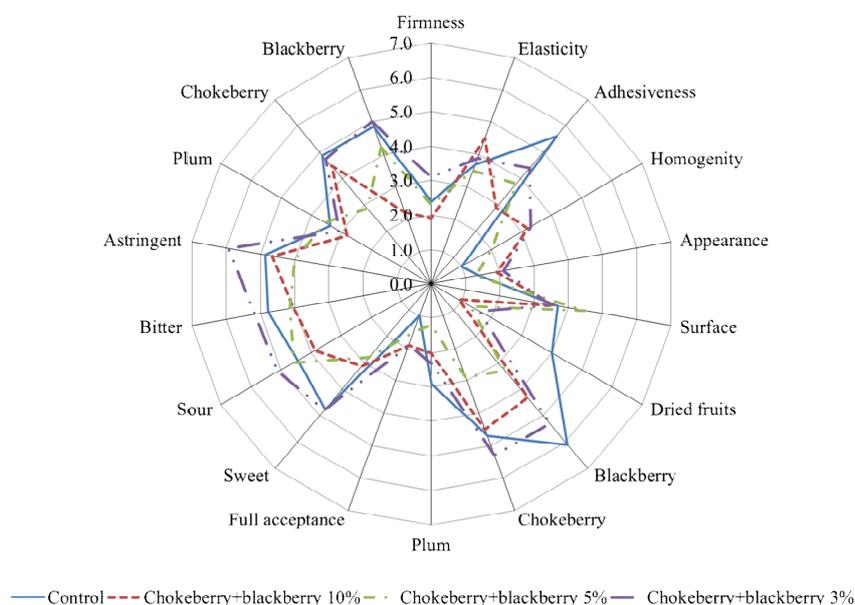


**Fig.4.** Sensory profile for fruit leather from plum with chokeberry and blackberry

The *consistency profile* (Fig.5) shows fruit leathers with 10 % chokeberry and raspberry are more in glossy and adhesiveness, but less in firmness and homogeneity like the control. Their appearance is attractive also like the control.
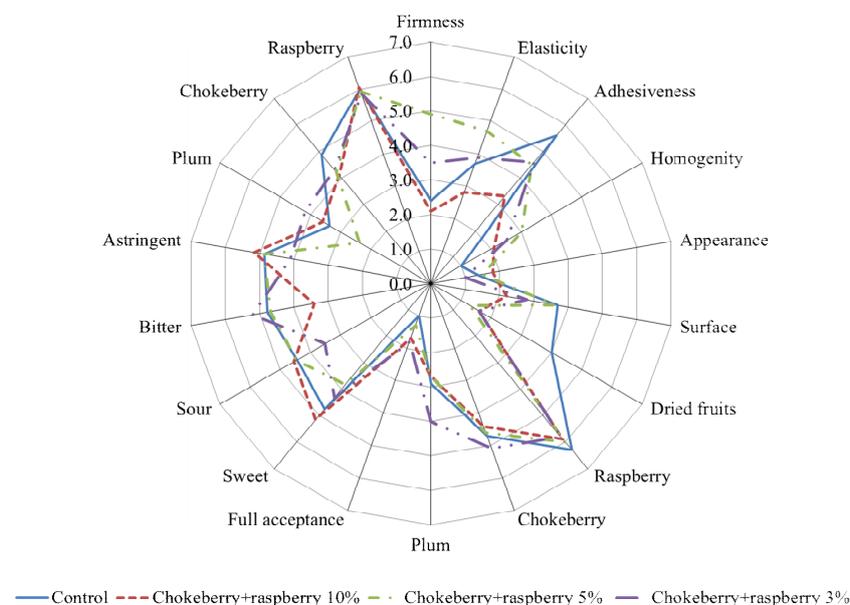


**Fig.5.** Sensory profile for fruit leather from plum with chokeberry and raspberry

The panelists note that the *aroma* of raspberry is less pronounced. In the variants with raspberry, the plum has with the dominant aroma, not like in the others. The general perception is from highly pleasant to pleasant (Fig.5).

Fruit leathers with 3% and 5% chokeberry and raspberry are sweets, near to the control. The *taste* of the plum is more pronounced for variants with 3% and 10% and pronounced for 5%. Taste of the chokeberry is also a dominant in all concentrations. The taste was stated like not astringent rather bitter for these probes, but with 10% chokeberry and raspberry the taste is not astringent and not bitter as well (Fig.5).

Based on other studies for sensory *consistency* parameters of fruit leather the harder products have with usually higher acceptance level but the adhesiveness and the elasticity are also important performers of mouth filling [1]. The addition of pressings detrimental to the homogeneity but may provide higher appearance level (attractive). The higher adhesiveness level decrease the acceptance of the products [2].

*Texture profile analysis*

The instrumental texture analysis gives a more objective results for the texture but just the complex systems of the parameters can be compare with the results of the sensory analysis [11]. These parameters can improve the descriptions of the products with goal to help the development of the technology and better quality indicators of the product.

The product with added pressings has lower *firmness* (Fig.6). It is maybe the result of the brewing during the technological procedure. Based on this result the probes with more added pressings show softer texture but just up to 5% concentration. The softest texture was reached with 5 % chokeberry+blackberry combination. That result is in correlation with the sensory analysis. The higher firmness values obtained with chokeberry is the result maybe the higher pectin content of these fruits.
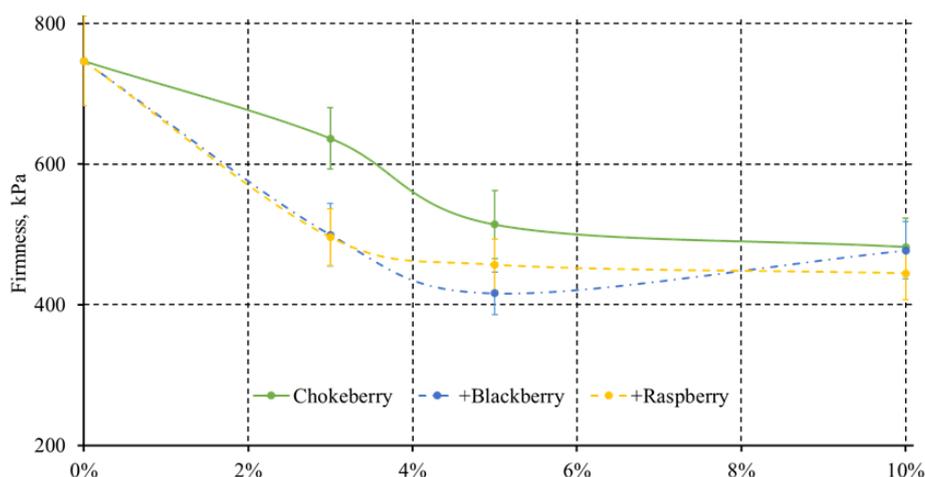


**Fig.6.** Instrumental firmness for fruit leather from plum with added chokeberry, chokeberry + blackberry and chokeberry + raspberry
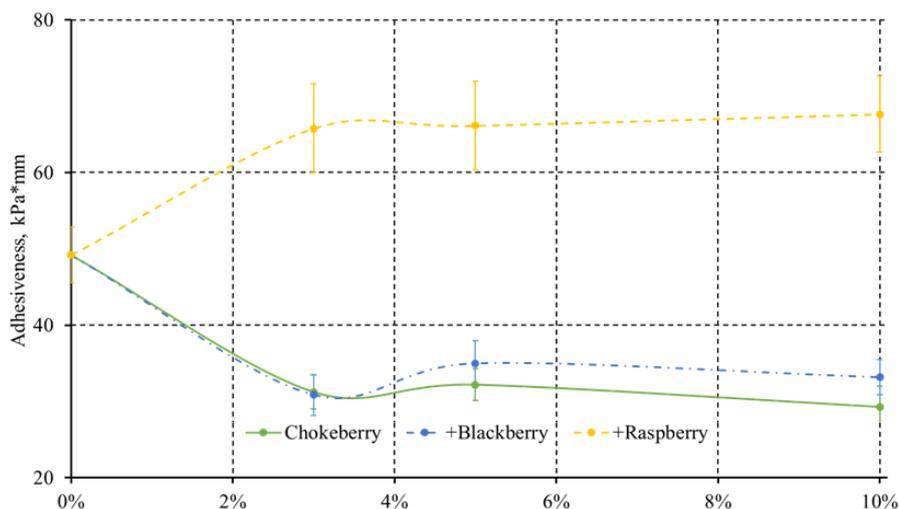


**Fig.7.** Instrumental adhesiveness for fruit leather from plum with added chokeberry, chokeberry + blackberry and chokeberry + raspberry

The adding of raspberry pressings increased the *adhesiveness* but just up to 3 % concentration. Based on our results the addition of chokeberry and blackberry pressings decreased the adhesiveness but also just in smaller concentrations. The result is very similar like the opinion of the panelists about adhesiveness (Fig.7).

The addition of pressings in smaller concentration lowered the *cohesiveness*. The highest lowering effect was encountered with 3% raspberry. With higher concentrations, the differences between the added pressings are very small. The lowering the cohesiveness means the ability for relaxation is smaller or the differences between the deformability are higher (Fig.8).
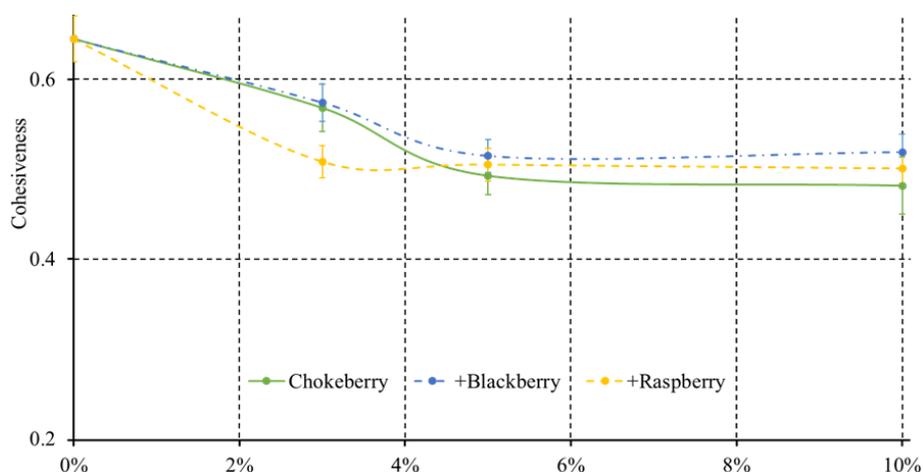


**Fig.8.** Instrumental cohesiveness for fruit leather from plum with added chokeberry, chokeberry+blackberry and chokeberry+raspberry

The effect of added pressings for *gumminess* is very similar like for the cohesiveness. There are differences between the samples just with 3 %

added pressings. Added chokeberry pressings show smallest lowering effect (Fig.9).
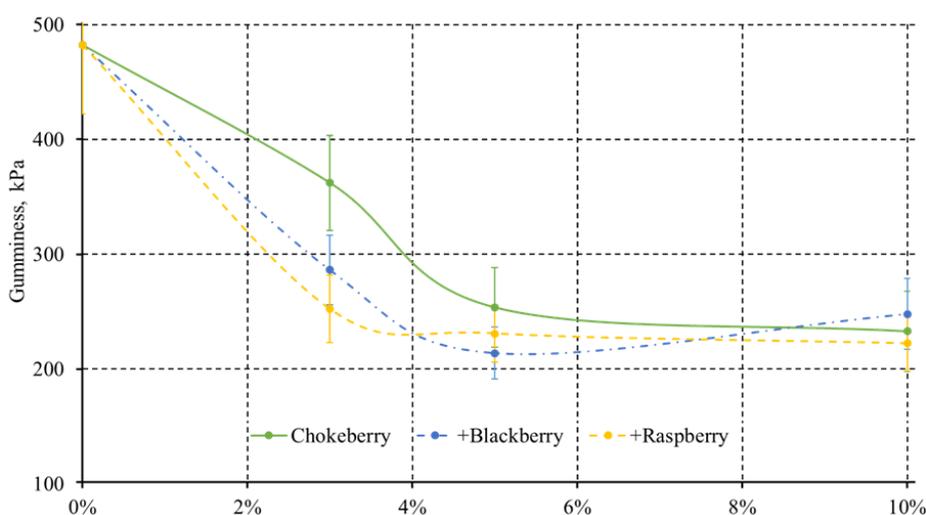


**Fig.9.** Instrumental gumminess for fruit leather from plum with added chokeberry, chokeberry+blackberry and chokeberry+raspberry

### *Correlation analysis between the parameters*

Correlation analysis between the parameters shows higher negative correlation between the concentration of added pressings and cohesiveness and gumminess ($r = -0.8171$ and $r = -0.7966$). The

adhesiveness does not show correlations with any other parameters. There are very high correlations between hardness and cohesiveness and gumminess ($r = 0.9209$ and $r = 0.9910$). These results are very similar like in the literature from Al-Hinai et.al for date-tamarind leather [11].

## CONCLUSION

The developed technology drives to stable product with low water activity.

The fruit leather is a soft product and has to be with low adhesiveness for high acceptance from the panelists.

The instrumental texture analysis also leads to a complex parameter system, which has correlation to sensorial texture parameters.

Based on literature reviews for fruit leathers there are not unified criterions about physicochemical characteristics of pestils [6]. This study gives information about texture and sensory parameters of fruit leathers. The used parameter systems can describe the correlations between the consumer acceptance and the texture, ingredients, technology parameters.

## ACKNOWLEDGEMENTS

## REFERENCES

1 Yildiz, O. (2013). Turkish Journal of Agriculture and Forestry, 37(6), 762.

2 Yılmaz, F.M. et al., Journal of the Saudi Society of Agricultural Sciences (2015), http://dx.doi.org/10.1016/j.jssas.2015.01.003

3 Denkova, R., PhD thesis, 2014.

4 Maskan, A., Kaya, S., & Maskan, M. (2002). Journal of Food Engineering, 54(1), 81.

5 Popova, A., PhD thesis, 2015.

6 Ruiz, N. A. Q., Demarchi, S. M., & August, S. A. G. A. ICEF11 Proceedings, (FPE398) Pp2041. (2014)

7 Y.B. Che Man, J. Irwandi, S. Yusof, J. Selamat, H. Sugisawa. J Food Process Press 21(5): 425. (1997).

8 S.O. Babalola, O.A. Ashaye, O.A. Babalola, J.O. Aina. Afr J Biotechnol 1 (2): 61. (2002).

9 C. Raab, N. Oehler. Fact Sheet 232, pp 1, Oregon State University Extension Service. (1999).

10 P.K. Jain, P.K. Nema. Agr. Engng. Intl. 9: 1 (2007).

11 Al-Hinai, K. Z., Guizani, N., Singh, V., Rahman, M. S., & Al-Subhi, L. (2013). Food Science and Technology Research, 19(4), 531.

12 S.M. Rahman. Handbook of food preservation. 2nd edition. CRC press. (2007).

13 D.R. Cremer, K. Eichner. J Food Chem 48 (6), 2454. (2000).

14 O.R. Fennema. Food chemistry. 3rd edn. Taylor & Francis Group, London. (1996).

15 Maria Koynova: Plums – natural cure for constipation, heart disease and osteoporosis (http://agronovinite.com/) in Bulgarian

16 Buhalova D., PhD thesis, 2015.

17 Everhart, E. (2013). Aronia – A New Crop for Iowa. Retrieved May, 24.

18 "Nutrition facts for raw blackberries". Nutritiondata.com. Conde Nast. 2012.

19 Jakobsdottir, G.; Blanco, N.; Xu, J.; Ahrné, S.; Molin, G. R.; Sterner, O.; Nyman, M. (2013). Journal of Nutrition and Metabolism 2013: 1 doi:10.1155/2013/202534. PMC 3707259. PMID 23864942.

20 Bushman BS, Phillips B, Isbell T, Ou B, Crane JM, Knapp SJ (December 2004). Journal of Agricultural and Food Chemistry 52 (26): 7982. doi:10.1021/jf049149a. PMID 15612785

21 Boryana Karamiteva: Curative properties of raspberries (http://agronovinite.com/) in Bulgarian

22 BDS 3050-80 Qualitative indicators on honey, 2014.

23 EN ISO 8586:2014, Sensory analysis - General guidelines for the selection, training and monitoring of selected assessors and expert sensory assessors (ISO 8586:2012, Corrected version 2014-06-15)

24 Shafiur Rahman, M., & Al-Mahrouqi, A. I. (2009). International journal of food sciences and nutrition, 60(sup7), 229.

25 An Overview of Texture Profile Analysis (TPA). Texture Technologies Corp and Stable Micro Systems, Ltd, 2014. Web. <http://texturetechnologies.com/texture-profile-analysis/texture-profileanalysis.php>

# Instrumental texture characterization of bread

M. Momchilova, G. Zsivanovits*

*Food Research and Development Institute, Plovdiv, Bulgaria*

Texture parameters of commercial bread samples were investigated by combined test method based on AACC 1998, modified method 74-09 – texture profile analysis (TPA) – and AIB Standard Procedure for White Pan Bread firmness – firmness measurement of bread crumb by compression with a probe. Elasticity, firmness, plastic deformation and crispness values were collected for white and semi brown Bulgarian and Hungarian breads. Combined test methods were applied with texture analyser (Stablemicrosystems TAXT2) to receive fast and precise results for several parameters. Based on the evaluated data for the texture parameters, uncertainty, limit of detection (LOD) and limit of quantification (LOQ), repeatability, intermediate precision and reproducibility of the test method were calculated. Created database will be used as a basis for validation of a method that can be applied in everyday practice of quality control laboratories.

**Keywords:** texture profile analysis (TPA), uncertainty, limit of detection (LOD), limit of quantification (LOQ), repeatability, intermediate precision and reproducibility

## INTRODUCTION

Bread is one of the most traditional and important food in the history of humankind. Today it should be already staple food with healthy claim. To reach this aim, new and traditional technologies are used in the bread industry. The mechanical and nutritional properties of breads may be related to the different performances during the chewing. The bread structure can be considered as solid foams, like cellular solids, with walls and voids [1], which has a low density ($\leq 500$ kg/m$^3$) and high porosity ($\geq 60\%$). The blended polymer (starch and proteins) matrix possesses viscoelastoplastic mechanical behaviour [2]. The most important factor of the texture is the water content. As far as the water acts as a plasticizer, it provides a plastic or rubbery soft texture to the bread crumb [3]. Other important parameters are the density and the porosity, which can explain the mechanical properties of cellular solid foams like bread crumbs. For example the modulus of elasticity can be expressed as a function of the density and known modulus for non-porous material [4]. However, the mechanical parameters, which can be extracted from a stress/strain relationship cannot be described with former equations, such as regular honeycombs formula [5], especially for the food products [3].

Most of the mechanical parameters (hardness, adhesiveness etc.) can be expressed based on the texture profile analysis (TPA) from stress - time or stress - strain diagrams [6, 7]. The parameters of TPA depends on the geometry of the used probe, on the deformation speed and on the clearance.

Although the TPA is extended for both solid and liquid (and semi-solid, semi-liquid) materials, it is not possible directly to compare the parameters observed for food samples with different textures [8]. The differences in the texture parameters which are evaluated from different measurement methods forced the identification and quantification of the potential errors – validation – for the different materials [9]. To consider the potential error parameters, all of the feasible factors should be analysed, which one should have more attention during the procedure. ISO/IEC 17025:2005 requires laboratories to evaluate and report their measurement uncertainty under specific circumstances [10, 19].

The steps of the uncertainty calculation (validation):

Step 1. Identifying the parameters of uncertainty estimation.

Step 2. Identifying all sources of uncertainty.

Step 3. Classifying the uncertainty according to type A (repeated observation) or B (other type observations).

Step 4. Estimating the standard uncertainty for each source of uncertainty

Step 5. Computing the combined uncertainty $u_c$

Step 6. Computing the expanded uncertainty U

Step 7. Reporting of results [10, 11].

The aim of this study was to analyse and simplify the TPA method to obtain informative results for most of the texture parameters of the bread. That simplified method with validation can be used later in a certified laboratory. To reach this aim, commercial Bulgarian and Hungarian breads were measured by the same instrumental methods at the FRDI, Plovdiv, Bulgaria and at the

---

* To whom all correspondence should be sent:
  zsivig@yahoo.co.uk

Department of Physics and Control at the Corvinus University of Budapest, Hungary.

### EXPERIMENTAL DETAILS

**Materials:** The study was carried out on commercial breads in Bulgaria and in Hungary (semi brown and white). Loaves of sliced bread were purchased in a local market and stored at ambient temperature in the original package until investigation. The loaves were bought from the freshest batch. The experiments were done on the purchasing day. The first three slices of the both ends of the loaves were left out of experiments. For better statistical randomization, the used slices were chosen from three loaves.

**Experimental methods:** StableMicroSystem TAXT2 texture analysers were used in both institutions (Fig.1). The instrument is supplied by the manufacturer with calibration methods for the deformation, for the force measurement, for the tare of 0 g and for the sample weight. Set of data acquisition was 200 PPS (point/second = Hz). The used method is a combination between TPA and penetration test based on AIB standard. The goal of development such a combined method, is easier

application to the product and at the same time evaluation of more parameters.



**Fig.1.** StableMicroSystem TAXT2 texture analyser

Standard test methods applied in usual laboratory practices:
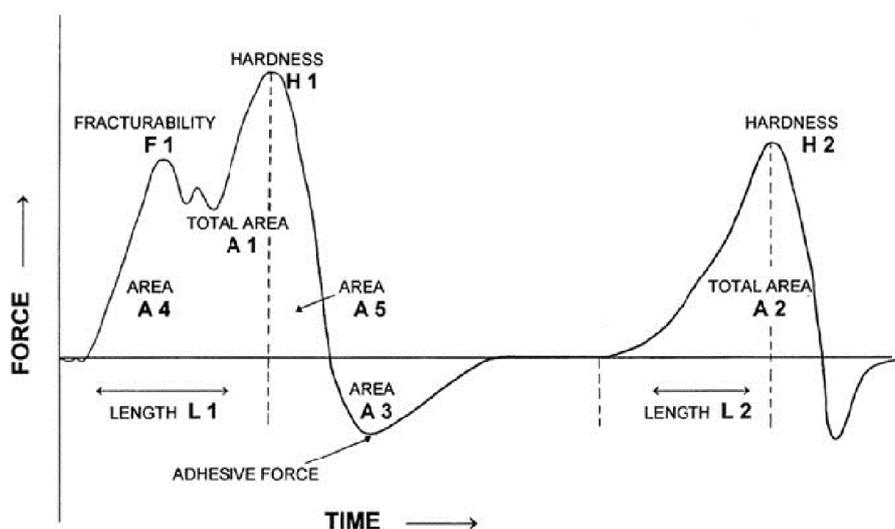


**Fig.2.** TPA method

a) AACC 1998, modified method 74-09 (TPA): Two loadings with a cylindrical probe ($\varnothing$=36 mm), the deformation speed is 1.7 mm/s, the relative deformation is 40 %, slice thickness' e.g. 25 mm or 2*12.5 mm [12]. The TPA method gives the most parameters, like hardness, springiness, cohesiveness, gumminess, chewiness, but the second loading makes the deformation analysis difficult [2, 12]. The sample preparation of cylindrical breadcrumb from softer bread is also

tricky difficult. At practical application for research, the TPA method is maybe the best but for quality control, a fast and easy way is necessary (Fig.2.).

b) AIB Standard Procedure for White Pan (trapeze shape) Bread firmness: One loading section with a cylindrical probe ($\varnothing$ = 1" = 25.1 mm), the deformation speed is 1.7 mm/s to 6.2 mm deformation on 2*0.5" ($\approx$2*12.55 mm) thick slices of bread. The used firmness value is the maximum

force, which should be the same with the force at the maximum deformation (Fig.3.) [13].
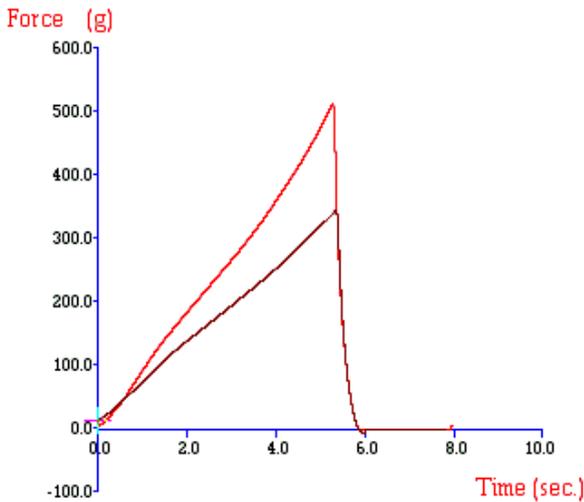


**Fig.3.** AIB standard method

The standard TPA method has more difficult sample preparation and a confusing second loading section. The AIB standard method use cylindrical probe and speed which want more difficult calculations and give just a very simple result.

**Combined test with one compression:** The method comprises the compression of two slices (2*15 mm) of bread are compressed with cylindrical probe ($\varnothing$=a 25 mm – Fig.4.). The penetration is up to 25 % of height at a crosshead speed (loading and unloading) of 1 mm/s. This loading speed simplifies the analysis of the curve. The method is the same like the first bite of the TPA [14].
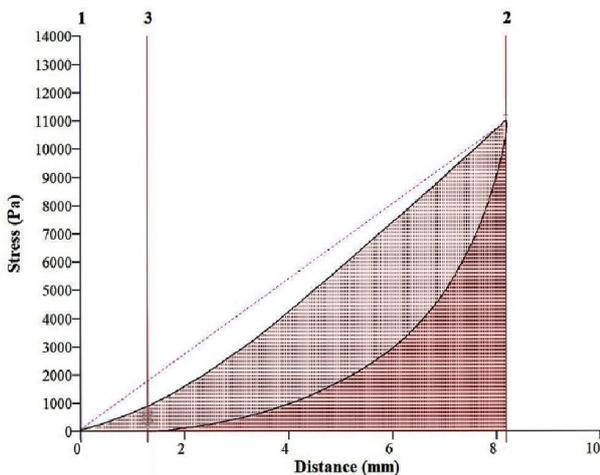


**Fig.4.** Texture test with one loading and unloading section

**Data analysis:** The variables and parameters were calculated by macros written in Texture Exponent 6.1 software. The parameters of uncertainty were calculated in Excel.

**Step by step validation:**

*Step 1*. Identifying the parameters of uncertainty estimation: In this step, the quantities were listed (measurands – Table 1) and the directly determined parameters (measurements – Table 2).

**Table 1.** List of measurands

| Measurand | Unit | Symbol |
|---|---|---|
| Area of the slices | mm$^2$ | A |
| Volume of the (double)slices | mm$^3$ | V |
| Strain during the experiment | % | ε |
| Loading stress | kPa | σ |
| Modulus of elasticity | kPa/mm | E |
| Plastic deformation | mm | $\ell_P$ |
| Crispness | kPamm | W |

**Table 2.** List of measurements

| Measurement | Unit | Symbol |
|---|---|---|
| Original thickness of the slices | mm | h |
| Original thickness of the double slices | mm | H=2*h |
| Other dimensions of the slices | mm | length; width |
| Deformation | mm | l |
| Loading force | N | F |

The original thickness and the other dimensions are measured by digital Vernier calliper. The thickness of double slices, the deformation and the loading force is measured by the texture analyser.

The area of the slices is calculated as for ellipse or trapeze based on the measured dimensions. It has effect just for the position of the experiment or the possibility of the repeatability on the same slices.

The volume of the slices is calculated as for a cylinder or column from the calculated area and thickness or double thickness.

The strain (relative deformation) is calculated from the deformation and the double thickness of the slices, as the percent of the double thickness.

Loading stress is calculated as the ratio between loading force and area of the cylindrical probe.

The modulus of elasticity is calculated as the ratio of the loading stress and loading strain. To get a reliable value the loading section should be approximately linear.

The plastic deformation is determined as inelastic deformation from the unloading section of the diagram.

The crispness is calculated as the area under the loading section of the diagram.

*Step 2*. Identifying all sources of uncertainty:

Table 3 lists the sources of uncertainty in 3 categories with their contribution (1 = major contribution, 2 = minor contribution, 0 = no contribution – zero effect), to the result. [19] For example, the height and the area of the sample are independents, but the height of the sample is one of the components of the volume. The contribution of

sample height to relative deformation maybe high, but from the viewpoint of measured loading strength, modulus of elasticity, plastic deformation or crispness it is already much smaller, because the variation interval is small for factory sliced bread. The contribution of length and width of the slides to the measured parameters is higher because these contain indirect factor to the position of investigation like the distance from the crust of the bread. The explanation of the contribution of other parameters is very similar. The parameters of the environment have high contribution to the measured strength value, but in our experiments, they had with constant value and in that case, they are not used in the calculation of combined uncertainty.

**Table 3.** Sources of uncertainty and their likely contribution to uncertainties

| Source of uncertainty | A | V | $\varepsilon$ | $\sigma$ | E | $\ell_P$ | W |
|---|---|---|---|---|---|---|---|
| 1. Test specimen | | | | | | | |
| h | 0 | 2 | 2 | 2 | 2 | 2 | 2 |
| H | 0 | 2 | 2 | 2 | 2 | 2 | 2 |
| length; width | 2 | 2 | 1 | 1 | 1 | 1 | 1 |
| l | 0 | 0-2 | 2 | 2 | 2 | 2 | 2 |
| F | 0 | 1 | 2 | 2 | 2 | 2 | 2 |
| 2. Test settings | | | | | | | |
| Loading speed | 0 | 0 | 2 | 2 | 2 | 2 | 2 |
| $\varnothing$ | 0 | 0 | 2 | 2 | 2 | 2 | 2 |
| Max. $\varepsilon$ | 0 | 0 | 2 | 2 | 2 | 2 | 2 |
| Accuracy of the instrumentation | 2 | 2 | 2 | 2 | 2 | 2 | 2 |
| Calibration of T.A. | 0 | 1 | 2 | 2 | 2 | 2 | 2 |
| 3. Environment | | | | | | | |
| Ambient T | 1 | 1 | 2 | 2 | 2 | 2 | 2 |
| Humidity | 1 | 1 | 2 | 2 | 2 | 2 | 2 |

*Accuracy and calibration of the instrumentation:* Accuracy of the digital Vernier calliper is given in the guide: measuring range: 0-150 mm; resolution: 0.01 mm; accuracy: 0.02 mm; repeatability: 0.01 mm. The measuring ranges for the texture analyser as follows: deformation 0.001 mm – 370 mm; force 0.01 N – 500 N; time 0.01 s – 1 000 000 s; and speed 0.01 mm/s – 40 mm/s. The resolutions are 0.001 mm; 0.001 N; 0.01s and 0.01 mm/s in respective. The trigger force of the instrument is 0.05 N, which means that the start point of the diagram is around 0.05 N [15]. In the way of the validation the limits of detection (LOD) and quantitation (LOQ) were computed [10]:

$$LOD = 3.3*accuracy \qquad (1)$$
$$LOQ = 10*accuracy \qquad (2)$$

The Vernier calliper has LOD = 0.066 mm; LOQ = 0.200 mm. The values of LOD and LOQ for texture analyser are partly calculated based on the measured data. LOD and LOQ of the thickness and the deformation were computed based on the measured thickness of the bread slices: LOD = 0.244 mm; LOQ = 0.739 mm. For the test of the force based on the test settings (trigger force = 0.05 N) LOD = 0.165 N; LOQ = 0.500 N. From technological viewpoint and based on our experiences the LOD and LOQ of the texture analyser are negligible in comparison with other error parameters.

*Step 3.* Classifying the uncertainty according to type A or B: All of the sources of uncertainty are type B, because they are not from repeated observation for the probes, but if the determination of texture parameters is repeated several times on the slices at different positions they become to type A. From reporting view, the experiment is repeated in more slices from the loaves and on slice of more loaves as well to have average values to characterize the type of the bread [10].

*Step 4.* Estimating the standard uncertainty for each source of uncertainty:
Measurement uncertainty is a parameter associated with the results of a measurement that characterises the dispersion of the values that could reasonably be attributed to the measurand [16]. The association of uncertainty to the results help to obtain more reliable results [11]

The standard uncertainty for each source of it was calculated from relative standard deviation:

$$U_{X_1} = \frac{C_V}{\sqrt{n}} \qquad (3)$$

where $C_v = \frac{\sigma}{\bar{x}}$

n is the number of sample pieces [10].

*Step 5.* Computing the combined uncertainty $u_c$

The combined uncertainty is computable based on the uncorrelated sources of the uncertainty:

$$U_c(y) = \sqrt{\sum_{i=1}^{N} [c_i u(x_i)]^2} \qquad (4)$$

where $c_i$ is the sensitivity coefficient associated with $x_i$. The combined uncertainty has an associated confidence level of 68.27% [18].

*Step 6.* Computing the expanded uncertainty U
The expanded uncertainty was calculated from the standard uncertainty based on the next formula:

$$U = k \sqrt{\sum_{i=1}^{n} (U_C)^2} \qquad (5)$$

where $k$ is a constant for the confidence interval (for normal distribution $k \approx 2$ at confidence probability P=95%) [10].

The normal distribution was controlled based on normal asymmetry:

$$Skewness = \frac{n}{(n-1)\cdot(n-2)}\sum\left(\frac{x_i - \bar{x}}{s}\right)^3 \quad (6)$$

and standard excess (-2<value<2):

$$Kurtosis = \left\{\frac{n(n+1)}{(n-1)(n-2)(n-3)}\sum\left(\frac{x_i - \bar{x}}{s}\right)^4\right\} - \frac{3(n-1)^2}{(n-2)(n-3)} \quad (7)$$

In equation (6) and (7) s = sample standard deviation.

*Step 7.* Reporting of results [10].

The results should be reported at P=95% confidence level in the following format for each measurand:

$$V = y \pm U \quad (8)$$

where V is the estimated value of the measurand, y is the test (or measurement) mean result, U is the expanded uncertainty associated with y.

**Repeatability, intermediate precision, reproducibility of the result:** They are smallest, middle and highest variations of the results [10].

**Repeatability:** The smallest variations are received if the experiments are repeated on identified materials, by the same person and with the same instrument.

$$r = \sqrt{2} * t * s_r \quad (9)$$

With normal distribution and 10 repeating t = 1.83:

$$s_r = \sqrt{MS_w} = \frac{\sum var}{n} \quad (10)$$

**Intermediate precision** (ISO 5725-3): Middle variations are received if the experiments are repeated in the same laboratory, by different persons and with the most different conditions.

$$R = \sqrt{2} * t * s_I \quad (11)$$

$$s_I = \sqrt{s_r^2 + s_R^2} \quad (12)$$

**Reproducibility:** The highest variation of the results is received in different laboratories by the same methods and on identified probes.

$$R = \sqrt{2} * t * s_R \quad (13)$$

$$s_R = \sqrt{\frac{MS_b - MS_w}{n}} = \hat{s} * \widehat{var} \quad (14)$$

$$s_r \leq s_I \leq s_R \quad (15)$$

Like a compromise variation the formulas (10), (12) and (14) can be used in the same laboratory with the same instrument but for different probes (e. g. different breads – semi brown and white).

## RESULTS AND DISCUSSIONS

From the viewpoint of the validation, there are no differences between the above described tests, but the values of uncertainty sources (Table 3) are strongly depend on the settings of the instrument. The loading speed and maximum deformation are maybe the most important parameters in this case. The used measure probe was selected based on our instrument set. To compare the results for the probes with different diameters it is better to evaluate the loading stress ($\sigma = F/A$; $[\sigma] = N/m^2 = Pa$) [17].

Based on Table 1 to Table 3 the most important measurements in uncertainty are *double height* (H). As reported calculated parameters the uncertainty is given for *loading stress* ($\sigma$), *elastic modulus* of E; *plastic deformation* ($\ell_P$) and *crispness* (W) [18]. These values are reported in Tables 4-6. The received uncertainty values are collected to the database and used for the calculations of results for the next clients.

**Repeatability** (Table 4) of the experimental results is given based on repeated experiments for slices of two loaves of White BG breads.

**Table 4.** Repeatability of the texture parameters

| White Bg bread | $\sigma$, kPa | E, Pa/mm | $\ell_P$, mm | W, kPamm | H, mm |
|---|---|---|---|---|---|
| $\bar{x}$ (n=10) | 14.312 | 1.724 | 1.662 | 28.008 | 31.083 |
| std | 1.370 | 0.146 | 0.120 | 2.335 | 0.375 |
| $C_V$ % | 9.570 | 8.453 | 7.211 | 8.336 | 1.208 |
| skewness | -0.050 | -0.273 | -0.725 | -0.295 | 1.066 |
| kurtosis | -0.498 | -1.071 | 0.500 | -0.376 | 1.420 |
| $U_{Xi}$ | 1.196 | 1.057 | 0.901 | 1.042 | 0.151 |
| $\bar{x}$ (n=10) | 13.623 | 1.565 | 1.638 | 28.204 | 30.469 |
| std | 1.700 | 0.201 | 0.174 | 2.277 | 0.153 |
| $C_V$ % | 12.479 | 12.839 | 10.602 | 8.073 | 0.503 |
| skewness | 0.380 | 0.384 | 0.301 | -0.783 | -2.359 |
| kurtosis | -1.002 | -1.220 | -0.494 | -0.671 | 5.958 |
| $U_{Xi}$ | 1.560 | 1.605 | 1.325 | 1.009 | 0.063 |
| U | 3.931 | 3.843 | 3.205 | 2.901 | 0.327 |
| $MS_w$ | 1.902 | 0.054 | 0.002 | 0.154 | 0.305 |
| $s_r$ | 0.493 | 0.068 | 0.040 | 1.394 | 0.347 |
| $s_I$ | 1.464 | 0.242 | 0.062 | 1.448 | 0.652 |
| r | 3.569 | 0.601 | 0.123 | 1.015 | 1.430 |

The database of repeatability is steadily growing with every client of the laboratory and the result is more and more comparable and reliable.

**The intermediate precision** (Table 5) of the results was calculated based on the experiments of white BG and semi brown BG breads in the FRDI.

**Table 5.** Intermediate precision of the texture parameters

| | σ, kPa | E, Pa/mm | $\ell_P$, mm | W, kPamm | H, mm |
|---|---|---|---|---|---|
| | | | white Bg bread | | |
| $\bar{x}$ (n=40) | 13.445 | 8.367 | 1.592 | 49.022 | 27.385 |
| std | 2.485 | 0.218 | 0.285 | 9.080 | 5.329 |
| $C_V$ % | 18.479 | 2.601 | 17.927 | 18.523 | 19.460 |
| skewness | 0.358 | 0.143 | 0.421 | 0.176 | 0.093 |
| kurtosis | -0.671 | -1.211 | -0.618 | -1.157 | -0.865 |
| $U_{Xi}$ | 0.462 | 0.065 | 0.448 | 0.463 | 0.486 |
| | | | Half brawn Bg Bread | | |
| $\bar{x}$ (n=40) | 10.350 | 1.487 | 2.046 | 20.351 | 27.759 |
| std | 1.957 | 0.297 | 0.357 | 4.017 | 1.084 |
| $C_V$ % | 18.908 | 19.967 | 17.453 | 19.738 | 3.905 |
| skewness | 0.681 | 1.930 | 1.136 | 0.445 | 0.394 |
| kurtosis | 0.228 | 6.325 | 1.587 | -0.507 | -0.438 |
| $U_{Xi}$ | 0.473 | 0.499 | 0.436 | 0.493 | 0.098 |
| U | 1.360 | 0.882 | 1.333 | 0.979 | 0.973 |
| $MS_b$= | 32.231 | 0.162 | 0.394 | 143.290 | 21.695 |
| $MS_w$= | 4.166 | 0.077 | 0.078 | 20.525 | 0.673 |
| $S_R$= | 1.675 | 0.092 | 0.178 | 3.504 | 1.450 |
| $S_I$= | 2.641 | 0.292 | 0.331 | 5.727 | 1.666 |
| R | 5.283 | 0.718 | 0.722 | 11.725 | 2.123 |

The database of the intermediate precision is also growing with every client.

**The reproducibility** (Table 6) was computed based on the results of white HU bread and white BG bread. The growing of reproducibility database also helps to obtain more comparable and reliable results.

**Table 6.** Reproducibility of the texture parameters

| | σ, kPa | E, Pa/mm | $\ell_P$, mm | W, kPamm | H, mm |
|---|---|---|---|---|---|
| | | | White Bulgarian bread | | |
| $\bar{x}$ (n=40) | 13.445 | 8.367 | 1.592 | 49.022 | 27.385 |
| std | 2.485 | 0.218 | 0.285 | 9.080 | 5.329 |
| $C_V$ % | 18.479 | 2.601 | 17.927 | 18.523 | 19.460 |
| skewness | 0.358 | 0.143 | 0.421 | 0.176 | 0.093 |
| kurtosis | -0.671 | -1.211 | -0.618 | -1.157 | -0.865 |
| $U_{Xi}$ | 0.462 | 0.065 | 0.448 | 0.463 | 0.486 |
| $U_{Xi}^2$ | 0.213 | 0.004 | 0.201 | 0.214 | 0.237 |
| | | | White Hungarian bread | | |
| $\bar{x}$ (n=40) | 7.723 | 1.022 | 3.875 | 19.619 | 0.483 |
| std | 1.485 | 0.197 | 0.335 | 3.857 | 0.045 |
| $C_V$ % | 19.228 | 19.311 | 8.643 | 19.661 | 9.238 |
| skewness | 1.746 | 1.741 | 0.168 | 0.887 | -0.174 |
| kurtosis | 4.315 | 4.273 | -0.197 | 0.337 | -0.168 |
| $U_{Xi}$ | 0.481 | 0.483 | 0.216 | 0.492 | 0.231 |
| U | 1.342 | 0.982 | 1.323 | 1.343 | 1.376 |
| $MS_b$= | 655.047 | 6.508 | 93.428 | 1206.342 | 15.975 |
| $MS_w$= | 4.189 | 0.060 | 0.079 | 21.639 | 0.338 |
| $S_R$= | 8.068 | 0.803 | 3.055 | 10.884 | 1.250 |
| $S_I$= | 8.323 | 0.840 | 3.068 | 11.837 | 1.379 |
| R | 21.540 | 2.173 | 7.941 | 30.634 | 3.569 |

Based on the results reported in tables 4-6 the repeatability of bread hardness is 3.569, the intermediate precision of it is 5.283, and the reproducibility of it is 21.540. For elastic modulus the values are r=0.601, R=0.718 and R=2.173 respectively. Based on the values, the client of the laboratory is informed about the statistical intervals of their products in comparison with similar earlier examined products. The laboratory collects the data already without information about the client and use the extended database for the next client.

The standards for texture analysis of bread suggest TPA or simple compression tests. Most of the sensory analysis parameters are related to the TPA test. The creep-recovery test is the nearest to the older instrumentation of the bread test (Elastigraph [19]). The above-applied method is fast and simple, to get minimum 4-5 parameters (Table 7), which well describe the stalling of the different breads. The used relatively small deformation is inside the elastic roles but uniform in deformation and shows the plastic properties as well [20]. The showed results

**Table 7.** The texture parameters of the breads

| | σ kPa | E kPa/mm | W kPa.mm | $\ell_P$ mm |
|---|---|---|---|---|
| White BG | 13.45±2.48 | 1.59±0.29 | 49.0±9.08 | 1.71±0.216 |
| Semi brown BG | 10.35±1.96 | 1.49±0.30 | 34.32±6.29 | 2.05±0.357 |
| White HU | 7.72±1.49 | 1.02±0.20 | 27.53±4.75 | 3.87±0.335 |
| Semi brown HU | 8.45±1.57 | 1.13±0.22 | 33.96±5.68 | 1.90±0.265 |

## CONCLUSION AND FUTURE WORK

The above described validation scheme is the beginning of database collection with aim to get a full validated method, which may be possible to use in international and national accredited laboratories and to apply it for other food products as well. The association of uncertainty help to obtain reliable results even if the measurements are not perfect. The FRDI expects to build a database for more and more Bulgarian or European breads. The validated method will be useful for other laboratories in international relation.

## REFERENCES

1 Gibson, L. J., & Ashby, M. F. (1997). Cellular solids, structure and properties. Cambridge Press University, p. 510.

2 Lambertné Meretei, A. (2012). Módszer kenyérbélzet állományjellemzőinek meghatározására (PhD dissertation), Corvinus University of Budapest, Hungary (in Hungarian).

3 Guessasma, S., Chaunier, L., Della Valle, G., & Lourdin, D. (2011). Trends in Food Science & Technology, 22(4), 142.

4 Warren, W. E., & Kraynik, A. M. (1997). Journal of Applied Mechanics-Transactions of the ASME, 64, 787e798.

5 Onck, P. R. (2003). MRS Bulletin, 279.

6 Friedman, H.H., Whitney, J.E. and Szczesniak, A. (1963). J. Food Sci., 28, 390.

7 Bourne, M. (1978). Food Technology, 32, 62 & 72.

8 Nishinari, K., Kohyama, K., Kumagai, H., Funami, T., & Bourne, M. C. (2013). Food Science and Technology Research, 19(3), 519.

9 Guideline, I. H. T. (2005). Validation of analytical procedures: text and methodology. Q2 (R1), 1.

10 B. Magnusson and U. Örnemark (eds.) Eurachem Guide: The Fitness for Purpose of Analytical Methods – A Laboratory Guide to Method Validation and Related Topics, (2nd ed. 2014). ISBN 978-91-87461-59-0. Available from www.eurachem.org.

11 da Silva, L. R. O. (2004). Evaluation of the uncertainty of measurement of mechanical properties on the tensile testing. Simposio de Metrología.

12 AACC Method 74e09.01. (1995). Measurement of bread firmness by universal testing machine. AACC International Approved Methods.

13 AIB (2001). AIB Standard Procedure White Pan Bread Firmness Measurement. *AIB Standard Procedures for Texture Measurement of Baked Products*; https://www.aibonline.org/researchand technical/services/prodqualityeval/AIBTextureAnal ysis%20Procedures.pdf.

14 Bartkiene, E., Schleining, G., Juodeikiene, G., Vidmantiene, D., Krungleviciute, V., Rekstyte, T., ... & Maruska, A. (2014). LWT-Food Science and Technology, 56(2), 445.

15 AIB Standard Procedure (2016): White Pan Bread Firmness Measurement, Manhattan, Kansas, USA. https://www.aibonline.org/aibOnline/Documents/EN /DevelopYourProductSolutions/AIBTextureAnalysi sProcedures.pdf. Accessed 15 August 2016.

16 International vocabulary of basic and general terms in metrology (VIM) - 2nd edition 1993 (ISO/BIPM/IEC/IFCC/IUPAC/IUPAP/OIML).

17 Sitkei, G. (1987). Mechanics of agricultural materials (Vol. 8). Elsevier.

18 Gabauer, W. (2000). The determination of uncertainties in tensile testing. Voest-Alpine Stahl Linz GmbH: Linz, Austria.

19 Szalai, L. (2003). Sütőiparosok, Pékek, L.3., 19. (in Hungarian).

20 Della Valle, G., Chiron, H., Cicerelli, L., Kansou, K., Katina, K., Ndiaye, A., ... & Poutanen, K. (2014). Trends in Food Science & Technology, 36(1), 5.

# Polyphenols extraction from black chokeberry wastes

M. P. Lazarova[1*], K. I. Dimitrov[2], I. S. Nikov[2], D. B. Dzhonova[1]

[1]*Institute of Chemical Engineering, Bulgarian Academy of Sciences, Acad. G. Bonchev Str., bl. 103, Sofia, Bulgaria*
[2]*Univ. Lille, INRA, ISA, Univ. Artois, Univ. Littoral Côte d'Opale, EA 7394 - ICV - Institut Charles Viollette, F-59000 Lille, France*

Polyphenols are secondary metabolites of plants and are broadly distributed in fruits and vegetables. It is demonstrated that these compounds act as strong antioxidants which determines a variety of their medicinal properties. Wastes of black chokeberry after juice recovery were used to investigate the optimal conditions for maximal yield of polyphenols applying solid-liquid extraction. Parameters such as temperature, medium acidity and type of solvent were varied. Total polyphenol content was assayed according to the Folin-Ciocalteu colorimetric reaction method. The results obtained demonstrated that water and water-ethanol mixtures were suitable for polyphenols extraction from black chokeberry wastes. The increase in temperature, regardless of the solvent, led to increasing polyphenol content in the extracts, reaching 7700 mg/L GAE with 50 % ethanol at ebullition, while acidity had clearly less effect on polyphenols extraction.

**Keywords:** aronia melanocarpa, solid-liquid extraction, Folin-Ciocalteu method

## INTRODUCTION

The importance of the diet in relation to improving human health, healthy aging and promoting quality life has increased the interest of consumers on nutraceuticals rich foods, and especially on fruits and vegetables [1]. Berries are rich sources of a wide variety of phytochemicals. Black chokeberry (*Aronia melanocarpa*) berries are widely studied for their potential as a natural product for food and medicinal use, because of their high contents of phenolic compounds such as procyanidins, anthocyanins, phenolic acids and flavonoids [2]. This phenolic content seems to correlate to the antioxidant activity reported for these berries [3, 4]. In-vitro anti-viral activity of *A. melanocarpa* against type A influenza virus as well as bacteriostatic activity against *Staphylococcus aureus* and *Escherichia coli* have been reported [5]. A very good gastroprotective effect of Aronia fruit juice in rats has been demonstrated, as well as a potential in prevention and control of diabetes mellitus type II and diabetes associated complications [6].

Extracts of *Aronia melanocarpa* have been applied as a natural anti-hypertensive and anti-atherosclerotic drug [7], have shown a pronounced anti-inflammatory effect [8] and also have shown benefits in treatment of cardiovascular disease [9]. The anthocyanin-rich extracts from black chokeberries were reported to inhibit the growth of cancer cells [10].

Berries are often processed into juices, syrups, jams. After juice extraction, many phenolic compounds and especially anthocyanins, are still present in the solid waste [11, 12] and could be valorized by suitable extraction process. Similar valorizations of food by-products by extracting antioxidant polyphenols have been reported for grape mark [13], apple pomace [14] and artichoke wastes [15], for example.

Solvent extraction is a classical technique to recover polyphenols from natural raw sources [16]. Large quantities of solvent and prolonged contact time are usually applied to obtain high extraction degree [15]. Solvents, such as methanol, acetone [17], hexane [18], propanol and ethyl acetate [19] are commonly used for the extraction of phenolics from plants. The properties of the solvent significantly affect the measured total phenolic content and antioxidant capacity [20]. An important parameter is the polarity of the solvent − highest extract yields have been obtained with polar alcohol based solvents [21], but the efficiency of the solvent is strongly dependent on the plant matrix used [13].

The objective of this work was to investigate the influence of different process parameters such as type of solvent (polarity and acidity) and temperature, in order to determine the optimal conditions for the extraction of polyphenols from black chokeberry wastes.

## MATERIALS AND METHODS

### *Reagents*

Folin-Ciocalteu reagent (2N), sodium carbonate (>99%) were supplied by Sigma–Aldrich (France);

---

ethanol (95%) was provided by Flandre Chimie (France). All other chemicals used ($H_3PO_4$, $KH_2PO_4$, $K_2PO_4$, $K_2HPO_4$, $K_3PO_4$) were of analytical grade.

## Sample preparation

Frozen *Aronia melanocarpa* berries supplied from the region around the town of Elena (Bulgaria) were used as plant material. For the studies the frozen berries were defrosted at room temperature, coarsely ground and then pressed in a small laboratory extruder to recover the juice. Finally, the waste material was washed out twice with fresh portions of distilled water and let to dry until constant weight at 60 °C in an oven. To obtain samples of the same moisture content for all extraction experiments, the chokeberry wastes were stored hermetically in a dark place at room temperature until further use.

## Total phenolic content

The Folin-Ciocalteu colorimetric reaction method was used for the analysis of total phenolics [22]. Each liquid extract was diluted and mixed with Folin-Ciocalteu reagent, and after 5 min sodium carbonate solution was added. The mixture was allowed to stand for 2 h at room temperature before the measurement of the absorbance at 765 nm. Gallic acid was used as standard and a range of gallic acid concentrations from 0 to 500 mg/L was used to prepare the calibration curve (absorbance vs. concentration). Total phenolic content was determined spectrophotometrically on a UVmini 1240 (Shimadzu) and expressed as gallic acid equivalents (GAE) in concentration units (mg/L) and as total polyphenols extraction yield (TP yield, %) from dry aronia waste. The latter was determined from the division of the calculated polyphenols weight to the weight of the waste sample, expressed in percentage.

## Experimental procedure

Solid-liquid extraction at different temperatures was studied for a period of 4 h in thermostatic shaker under moderate agitation, which maintained all particles in suspension. At ebullition the extraction of polyphenols was carried out under reflux.

As solvents water and ethanol-water mixtures were used. When necessary, the acidity of the aqueous solvent was adjusted with $H_3PO_4$ solutions and/or buffer solutions of potassium salts. The experiments were conducted at solid-solvent ratio 1:15 (2 g dry aronia wastes in 30 mL of solvent).

After extraction the two phases were separated by filtration and the liquid extracts were put to analysis by the Folin-Ciocalteu method.

## RESULTS AND DISCUSSION

### Influence of pH on the extraction of polyphenols

To determine if the acidity of aqueous solutions affects the phenolic extraction from black chokeberry, distilled water with pH 4 (its own acidity), more acidic pH 3 and alkaline pH 10 was tested as solvent. The results are presented in Fig. 1 and Table 1.
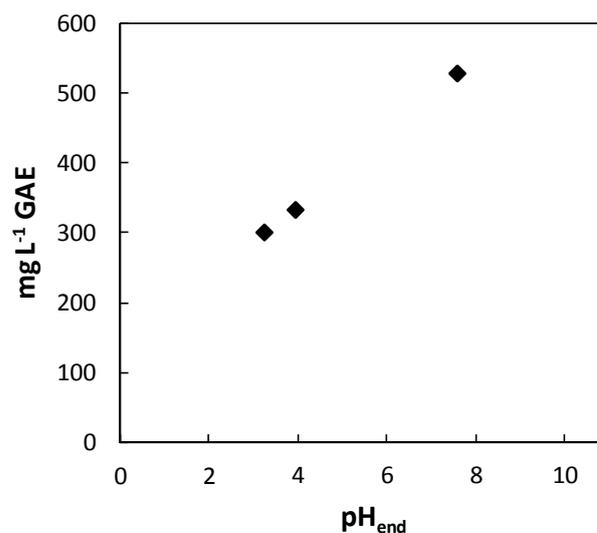


**Fig.1.** Effect of pH on polyphenols extraction from black chokeberry waste (20 °C, solid-solvent ratio 1:15, 4 h)

The obtained results demonstrate a steady increase (see Fig.1) in the content of the extracted polyphenols with decreasing acidity of the medium and 75 % increase in the extraction yield (see Table 1). The higher results in alkaline solutions could be attributed to the changes in the conformation of some phenolic compounds with pH changes.

**Table 1.** Total polyphenols extraction yield from dry black chokeberry waste depending on medium pH

| Solvent | $pH_0$, - | $pH_{end}$, - | TP yield, % |
|---|---|---|---|
| water | 3.04 | 3.25 | 0.45 |
| water | 4.05 | 3.95 | 0.50 |
| water | 10.00 | 7.59 | 0.79 |

### Influence of type of solvent

For these studies distilled water and water-ethanol solutions were chosen as solvents, which are of polar type and are non-toxic as well. It was observed that solvents with ethanol content in the

range from 40 to 60 % (vol.) are to be favourably used for extraction of polyphenols from black chokeberry waste (see Fig.2).
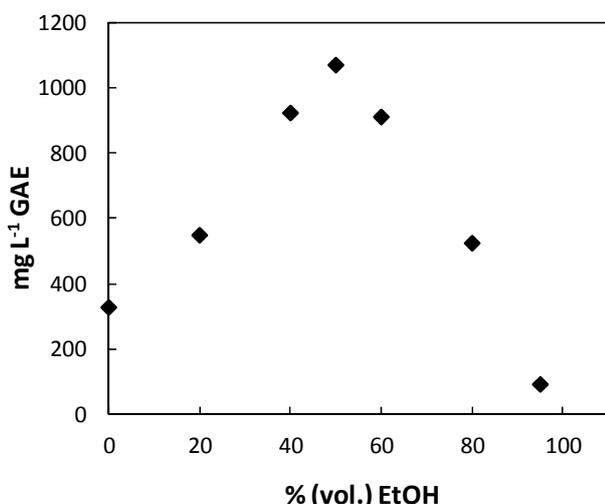


**Fig.2.** Effect of solvent on polyphenols extraction from black chokeberry waste (20 °C, solid-solvent ratio 1:15, 4 h)

Best results were obtained with 50 % (vol.) ethanol – the content of polyphenols was 3 times higher than this extracted with pure water and almost 12-fold higher than this with 95 % (vol.) ethanol. In Table 2 the extraction yield of total polyphenols from dry aronia waste is given according to the type of solvent.

Similar tendency in the results with water-ethanol solutions as solvent were observed by Galvan d'Alessandro et al. [4]. They have used directly aronia berries as material and have reported better total polyphenols extraction yield with water than with ethanol, and maximal yield with 50 % (vol.) ethanol.

**Table 2.** Total polyphenols extraction yield from dry black chokeberry waste depending on the type of solvent

| Solvent | TP yield, % |
|---|---|
| water | 0.50 |
| 20 % EtOH | 0.82 |
| 40 % EtOH | 1.38 |
| 50 % EtOH | 1.60 |
| 60 % EtOH | 1.37 |
| 80 % EtOH | 0.79 |
| 95 % EtOH | 0.14 |

*Influence of temperature*

The extraction of phenolics from plants is reported to be favourably affected by increasing temperature [4, 23]. To investigate the influence of this parameter, experiments at 20 °C, 40 °C and boiling point temperatures were undertaken. Distilled water and 50 % (vol.) ethanol were used as solvents. The obtained results showed not so distinctive difference in the amount of extracted polyphenols at 20 °C and 40 °C, especially with water as solvent (see Fig.3). Further increase in temperature had a very pronounced positive effect on phenolics extraction, in particular when 50 % (vol.) ethanol was used - almost 4.5 times higher content of polyphenols was achieved at 73.3 °C (boiling point) than at 40 °C. Pure water was also very efficient at boiling point, yet 2 times less effective than 50 % (vol.) ethanol at 73.3 °C.
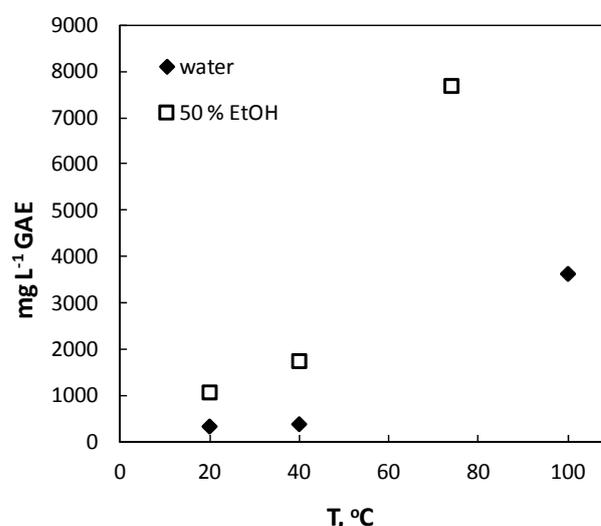


**Fig.3.** Effect of temperature on polyphenols extraction from black chokeberry waste (solid-solvent ratio 1:15, 4 h)

Higher temperatures enhance solubility of phenolic compounds and their diffusion out of the plant tissue structure, which result in higher total phenol levels [24]. In Table 3 the extraction yield of total polyphenols from dry aronia waste is given according to temperature.

**Table 3.** Total polyphenols extraction yield from dry black chokeberry waste depending on temperature

| Temperature, °C | TP yield, % (water as solvent) | TP yield, % (50 % EtOH as solvent) |
|---|---|---|
| 20 | 0.50 | 1.60 |
| 40 | 0.57 | 2.62 |
| boiling: 100 (water) | 5.44 | |
| 73.3 (50 % EtOH) | | 11.53 |

CONCLUSIONS

In this work experimental studies of the solid-solvent extraction of polyphenolic compounds from black chokeberry wastes were carried out. The change of pH of the aqueous solvent affects polyphenols extraction efficiency only in the presence of suitable buffer solutions, and the effect is evidently less than the addition of ethanol to the water. Ethanol containing solutions (20 ÷ 80 %) were found out to be more efficient for polyphenols extraction than pure water or 95 % (vol.) ethanol. The highest content of polyphenols (1070 mg/L GAE) was achieved with 50 % (vol.) ethanol. Temperature showed to be a process parameter to be reckoned with. Under high temperature water can also be efficiently used as well as ethanol containing solutions. At ebullition water and 50 % (vol.) ethanol extracted 3630 mg/L GAE and 7700 mg/L GAE, respectively. These results could contribute to the development of environmentally friendly technologies for polyphenols extraction from fruit wastes and the produced extracts to be used in pharmacy, cosmetics and food industry.

REFERENCES

1 O. Paredes-López, M. L. Cervantes-Ceja, M. Vigna-Pérez, T. Hernández-Pérez, *Plant Foods Hum. Nutr.,* 65, No 3, 299, (2010).

2 D. Rugină, Z. Sconţa, L. Leopold, A. Pintea, A. Bunea, C. Socaciu, *J Med Food*, 15, No 8, 700, (2012).

3 M. P. Kähkönen, A. I. Hopia, H. J. Vuorela, J.-P. Rauha, K. Pihlaja, T. S. Kujala, M. Heinonen, *J. Agric. Food Chem.*, 47, 3954, (1999).

4 L. Galvan D'Alessandro, K. Kriaa, I. Nikov, K. Dimitrov, *Sep. Purif. Technol.*, 93, 42, (2012).

5 S. V. Valcheva-Kuzmanova, A. Belcheva, *Folia Med.*, 48, 11, (2006).

6 S. Valcheva-Kuzmanova, K. Kuzmanov, S. Tancheva, A. Belcheva, *Methods Find. Exp. Clin. Pharmacol.,* 29, 101, (2007).

7 C. A. Domarew, R. R. Holt, G. Goldmann-Snikoff, *J. Herb. Pharmacother.,* 2, 31, (2002).

8 K. Ohgami, I. Ilieva, K. Shiratori, Y. Koyama, X.-H. Jin, K. Yoshida, S Kase, N. Kitaichi, Y. Suzuki, T. Tanaka, S. Ohno, *Invest. Ophthalmol. Vis. Sci.,* 46, No 1, 275 (2005).

9 D. R. Bell, K. Gochenaur, *J. Appl. Physiol.*, 100, No 4, 1164, (2006).

10 C. Zhao, M. M. Giusti, M. Malik, M. P. Moyer, B. A. Magnuson, *J. Agric. Food Chem.*, 52, No 20, 6122, (2004).

11 J. Oszmianski, A. Wojdylo, *Europ. Food Res. Technol.*, 221, 809, (2005).

12 P. Vauchel, L. Galvan D'Alessandro, P. Dhulster, I. Nikov, K. Dimitrov, *J. Food Eng.*, 158, 1, (2015).

13 G. Spigno, L. Tramelli, D. M. De Faveri, *J. Food Eng.,* 81, No 1, 200, (2007).

14 D. Pingret, A.-S. Fabiano-Tixier, C. L. Bourvellec, C. M. G. C. Renard, F. Chemat, *J. Food Eng.*, 111, 73, (2012).

15 G. Angelov, S. Georgieva, S. Boyadzhieva, L. Boyadzhiev, *C.R. Acad. Bulg. Sci.*, 68, No 10, 1235, (2015).

16 M. Virot, V. Tomao, C. Le Bourvellec, C.M.C.G. Renard, F. Chemat, *Ultrason. Sonochem.*, 17, No 6, 1066, (2010).

17 M. Alothman, R. Bhat, A.A. Karim, *Food Chem.,* 2009, 115, No 3, 785, (2009).

18 B. Pliszka, G. Huszcza-Ciolkowska, E. Januszewicz, I. Warminska-Radyko, *Acta Aliment.*, 42, No 2, 256, (2013).

19 T. Vatai, M. Skerget, Z. Knez, *J. Food Eng.*, 90, No 2, 246, (2009).

20 J. A. Michiels, C. Kevers, J. Pincemail, J. O. Defraigne, J. Dommes, *Food Chem.*, 130, No 4, 986, (2012).

21 L. Tomsone, Z. Kruma, R. Galoburda, *World Acad. Sci. Eng. Technol.*, 64 , 903, (2012).

22 V. L. Singleton, R. Orthofer, R. M. Lamuela-Raventos, *Methods Enzymol.*, 299, 152, (1999).

23 N. Harbourne, J. C. Jacquier, D. O'Riordan, *Food Chem.*, 116, 722, (2009).

24 T. Hofmann, E. Nebehaja, É. Stefanovits-Bányaib, L. Albert, *Ind. Crop Prod.*, 77, 375, (2015).

# Thermal behaviour of confectionary sweeteners' blends

R. Hadjikinova[1], M. Marudova[2] *

[1]*University of Food Technologies, 26 Maritsa blvd., Plovdiv, Bulgaria*
[2]*Plovdiv University "P. Hilendarski", Faculty of Physics, 24 Tsar Assen str., Plovdiv, Bulgaria margo@uni-plovdiv.bg*

The present research investigates the glass transition and melting of sucrose and some of the most commonly used in the confectionary industry sweeteners – erythritol, sorbitol, maltitol and isomalt. A comparison between the thermal properties of the studied sweeteners and the sucrose is done. It is found that the glass transition temperature and the melting temperature of the sucrose are the highest. The parameters of the maltitol were the closest to these of the sucrose probably due to their common disaccharide chemical structure. The erythritol is characterized as the sweetener with the lowest glass transition temperature and the highest enthalpy of melting. Based on the glass transition behaviour of the sugar mixtures, a miscibility between sucrose/erythritol, sucrose/sorbitol, maltitol/erythritol, maltitol/sorbitol, maltitol/isomalt, erythritol/sorbitol, erythritol/isomalt and sorbitol/isomalt was established. Intermolecular hydrogen bonding between sucrose/maltitol, sucrose/isomalt and maltitol/isomalt were demonstrated.

**Keywords***: sucrose, sweeteners, glass transition, melting, miscibility, differential scanning calorimetry*

## INTRODUCTION

Understanding and controlling the state of sugars and sweeteners is critical for making high-quality confectioneries and many other food products. The sugars and sweeteners play the main role to attaining the desired characteristics, from appearance to texture. They may be found dissolved in the water in a food, dispersed as a crystalline phase, immobilized in the amorphous or glassy state, or various combinations of these states [1]. During processing, the sugars and sweeteners in the confectionery formulations typically go through one or more phase transition, depending on the nature of the product. Changes in phase behaviour may also occur during storage, usually with a negative effect on shelf life. Therefore knowledge about the thermal behaviour of sugars and sweeteners could help in technology optimization and finding the best storage conditions. The most important transitions for the sugars and sweeteners are the melting (crystallization) and the glass transition.

The melting is endothermic first order transition wherein the crystal structure is destroyed and material goes to liquid state. Crystalline sugars melt, when they are heated to or above their melting temperature. The sugars do not have sharp melting temperatures and their melting proceeds over a temperature range. For this reason, melting endotherms are fairly broad. The melting temperatures of the sugars are sensitive to water, impurities and crystallinity [2]. Some sugars may caramelize and become brown concomitantly with the melting process and they may also decompose before melting [3].

Solid confections can either be in a crystalline state or in a thermodynamically unstable amorphous state [4]. The amorphous state can exist either as a viscous fluid-like rubbery state or as a high-viscosity glassy state with low molecular mobility [3]. The amorphous glasses are characterized by a random arrangement of the molecules with no long-scale ordering. The glass transition occurs when the glassy state converts to the rubbery state (or vice versa), with the temperature of this transition being called the glass transition temperature ($T_g$) [5]. The glass transition is a second-order state transition that results in changes in various material properties, including specific heat, dielectric constant, viscosity, molecular mobility, and mechanical properties [6]. Thus, the glass transition can be measured by tracking changes in these properties.

The sugar glasses are not completely static or unchanging [7]. Many exhibit a phenomenon known as enthalpic relaxation [8], which might loosely be defined as rearrangements of the sugar molecules while in the glassy state.

The glassy state is metastable due to the limited molecular mobility so that diffusion-based chemical reactions and physical changes (such as crystallization) are severely limited. $T_g$ is governed by the molecular composition, the degree of polymer cross-linking, and the plasticizer (such as water) concentration [9]. Among the disaccharides, $T_g$ varies from 65 °C to 70 °C for sucrose to over 100 °C for lactose, whereas the monosaccharides glucose and fructose have $T_g$ values of about 31 °C and 5 °C to 10 °C, respectively. Note the

---

\* To whom all correspondence should be sent:
  margo@uni-plovdiv.bg

significantly lower $T_g$ for most, but not all, polyols. Maltitol and isomalt, in particular, have $T_g$ values above room temperature, making them suitable for use in sugar-free hard candies.

The present work aims to investigate the thermal behaviour of sweetener's blends in respect to their miscibility.

## EXPERIMENTAL DETAILS

### *Sample preparation*

Analytical grade crystalline sucrose and sweeteners – isomalt, erythritol, sorbitol and maltitol, were purchased from Sigma-Aldrich. They were dehydrated in vacuum oven at 60 °C for 5 hours and then stored at room temperature in an exicator at 0% relative humidity (RH) (above $P_2O_5$ desiccant).

The sample mixtures were prepared by dissolving the particular sugar in distilled water (solid-water ratio 1:9). Solutions from each two sugars were mixed in weight ratios 1:3, 1:1 and 3:1 and freeze-dried to solids. The solutions were firstly frozen at -30 °C for 24 hours and then dried under vacuum (5 Pa) for more than 48 hours using TOPT-10B mini Vacuum Freeze Dryer. Subsequently dry powders were obtained. They were stored an exicator at 0% relative humidity (RH) (above $P_2O_5$ desiccant) until being used.

### *Thermal analysis*

A differential scanning calorimeter DSC 204 F1 Phoenix (NETZSCH, Germany) equipped with intracooler was used. The DSC was calibrated with indium. In order to avoid condensation of water, argon gas was used to purge the furnace chamber at 20 ml/min. Dry sample (5-10 mg) was weighed into 40 μl aluminium standard crucible and hermetically sealed with aluminium standard lead. Melting and glass transitions were analysed using Proteus® Software. All experiments were run in triplicates.

The temperature profile of the DSC experiments is illustrated in Fig.1 [10]. All the investigated samples were initially melted in a DSC pan by heating from room temperature ($T_1 = 25$ °C) to $T_0 = 200$ °C at a heating rate of 20 °C/min. The temperature and the enthalpy of melting were determined from the first heating run. The molten sample was cooled at a cooling rate of 20 °C/min to a temperature that was about 60 °C below its glass transition temperature $T_g$, which was defined as inflection point in the specific heat capacity – temperature dependence, in order to form an amorphous glass. The sample was then reheated at 4 °C/min to a temperature about 40 °C above $T_g$. Through the experiments, the glass transition temperatures and the relaxation enthalpy were determined.
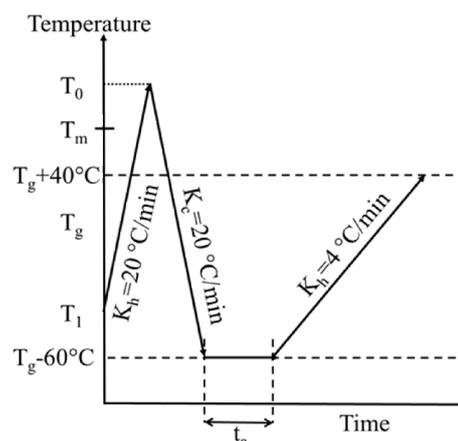


**Fig.1.** DSC temperature profile

## RESULTS AND DISCUSSION

### *Melting*

The results about melting behaviour of the sucrose and the investigated sweeteners are presented in Fig.2 and Table 1. They are in good agreement with previously reported data [11, 12].
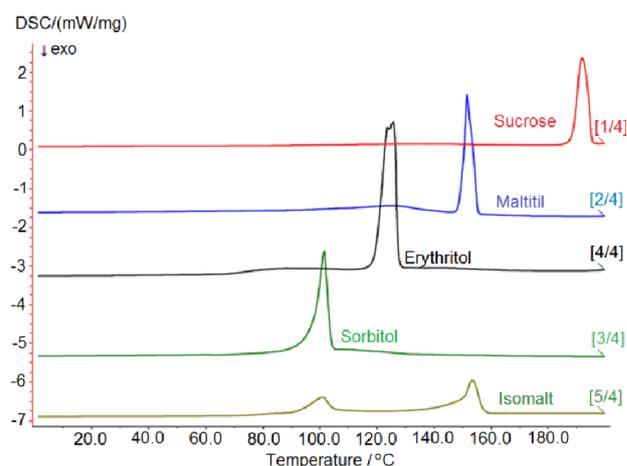


**Fig.2.** Melting temperatures of sugars

**Table 1.** Melting point and enthalpy of fusion of the investigated sugars

| Sugar/ sweetener | Glass transition $T_g$, °C | Melting point $T_m$, °C | Enthalpy $\Delta H$, J/g |
|---|---|---|---|
| Sucrose | 61.93 | 189.1 | 126.4 |
| Maltitol | 43.10 | 149.6 | 160.8 |
| Isomalt | 32.00 | 98.0/155.0 | 143.0 |
| Sorbitol | -9.20 | 97.4 | 187.4 |
| Erythritol | -42.50 | 119.6/125.7 | 313.0 |

It is interesting to note that the sucrose, which is a disaccharide, possesses the highest melting temperature and the lowest enthalpy of fusion. The melting temperature of maltitol – the other disaccharide, is the closest to that of the sucrose,

but its enthalpy of fusion is about 27 % higher than the sucrose enthalpy of fusion. The other tree sweeteners, which are sugar alcohols, are characterized with lower melting temperatures. The erythritol is found to be the sweetener with the highest enthalpy of fusion. The double melting peak of the erythritol could be due to different crystal size and a crystal size distribution [13]. As far as isomalt is a mixture of two sugar alcohols - gluco-mannitol and gluco-sorbitol, it is characterized with two melting temperatures – 98 °C and 155 °C respectively. The differences, which are found in the melting behavior of the investigated sugars, are interesting in the terms of their application in the food industry and are related to the optimization of the treatment processes.

*Glass transition*

The glass transition temperatures $T_g$ of the sucrose and the investigated sweeteners are presented in Table 1. The disaccharides – sucrose and maltitol – are characterized with the highest values of $T_g$ (61.93 °C and 43.10 °C respectively), and the glass transitions of the alcohols vary in a wide temperature range – from -42.5 °C to 32 °C. The received data are similar to these reported in the literature [12].

Usually the glass transition of a mixture is between the glass transition temperatures of the components and can be expressed by Gordon-Taylor equation:

$$T_g = \frac{\omega_1 T_{g1} + K\omega_2 T_{g2}}{\omega_1 + K\omega_2},$$ (1)

Here $T_g$, $T_{g1}$, $T_{g2}$ are the glass transition temperatures of the binary mixture, component 1, and component 2 respectively, $\omega_1$ and $\omega_2$ are the weight fractions of component 1 and component 2 respectively, $K$ is a constant, which according to the free volume theory is related to the free volumes of the two components [14] and can be calculated using Simha-Bouer rule [15]:

$$K \approx \frac{T_{g1} \cdot \rho_1}{T_{g2} \cdot \rho_2},$$ (2)

where $\rho$ is the density of each component.

Figures 3(a) – 3(j) show the glass transition temperatures of the sugar mixtures. Each mixture shows a single glass transition temperature, which means that the components are miscible in the mixture. The free volume theory predicted the mixing of most of the sugar pairs – sucrose/ erythritol, sucrose/sorbitol, maltitol/ erythritol, maltitol/sorbitol, isomalt/sorbitol, isomalt/ rythritol and sorbitol/erythritol. The values of the K constant were calculated in these cases using the regression of the experimental data by the equation (1). These values are shown in Table 2. In cases of sugar mixtures between sucrose/isomalt, sucrose/maltitol and isomalt/maltitol, the glass transition temperatures of the mixtures are lower than these of the pure sugars.

It is interesting to note that the glass transition temperatures of sugars whose mixtures do not obey the Gordon-Taylor equation, are very close to each other and their ratio is near to one. These results are similar to the behaviour of co-lyophilized binary mixtures of sucrose and another component – amorphous tapioca starch syrup [10], lactose, dextran [16], etc. where the $T_g$ values of the mixtures are lower than the values, predicted from the free volume theory. The differences could be attributed to non-uniform distribution of the free volume between the components or to interaction between the components through hydrogen bonding and formation of new network [17].

a)


b)
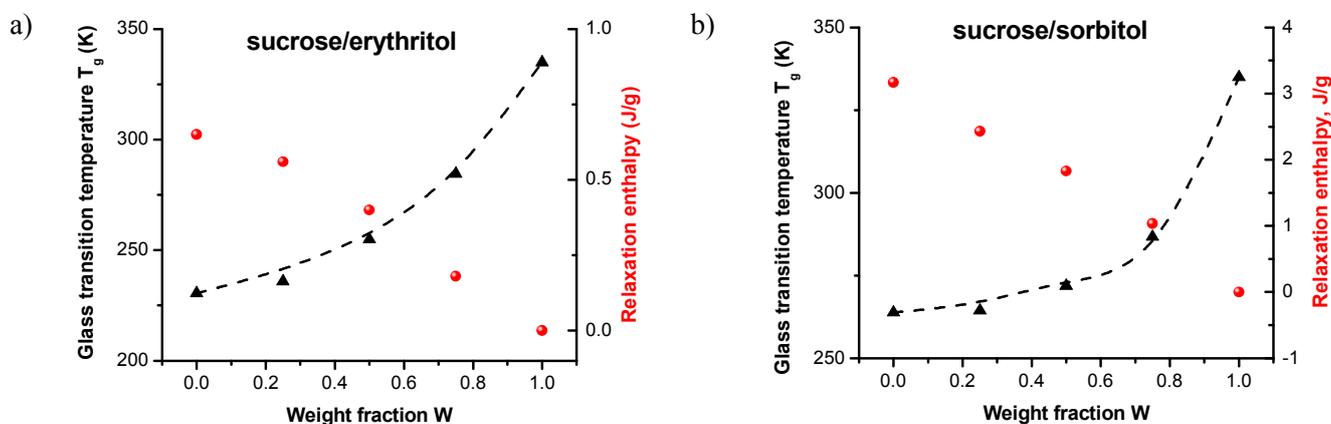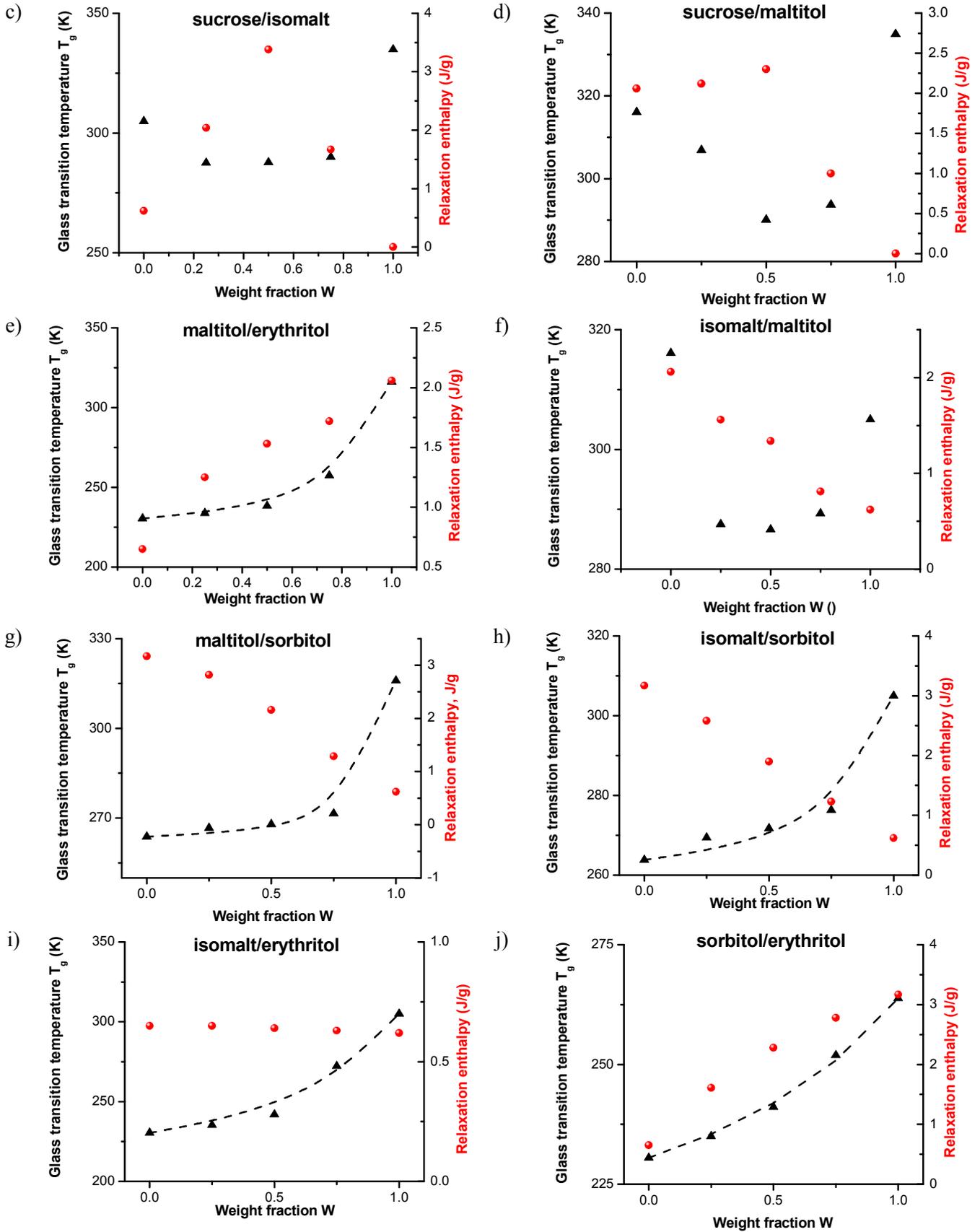
**Fig.3.** Glass transitions temperatures and relaxation enthalpies of sugar mixtures: ▲ - experimental data for the glass transition temperature, ----- theoretical model for glass transition temperatures of the sweeteners' blends, ● - experimental data for the relaxation enthalpy at glass transition

It is known from the literature [18, 19] that the maltitol and isomalt show in aqueous solutions a fully extended conformation without intramolecular hydrogen bonds. All hydroxyl groups are involved in intermolecular hydrogen-bond. It could be assumed that the maltitol and isomalt interact with the sucrose and each other to form hydrogen bond network. Therefore the blends sucrose/maltitol, sucrose/isomalt and maltitol/isomalt disobey the Gordon-Taylor equation.

**Table 2.** K values of the sweeteners' blends

| Mixture | K | $\frac{T_{g1}}{T_{g2}}$ |
|---|---|---|
| Sucrose/erythritol | 3.09 | 1.45 |
| Sucros/sorbitol | 6.80 | 1.27 |
| Sucrose/isomalt | - | 1.09 |
| Sucrose/ maltitol | - | 1.06 |
| Maltitol/erythritol | 6.8 | 1.37 |
| Maltitol/isomalt | - | 1.04 |
| Maltitol/sorbitol | 15.68 | 1.20 |
| Isomalt/sorbitol | 5.68 | 1.16 |
| Isomalt/erythritol | 3.16 | 1.32 |
| Sorbitol/erythritol | 1.91 | 1.14 |

The relaxation enthalpy at the glass transition was calculated for the pure and mixed sugars – Fig.3. It was found out that the sucrose does not undergo any relaxation process at glass transition and the relaxation enthalpy is zero. All the sweeteners tend to approach towards the most stable state and undergo through structural relaxation. The relaxation enthalpy of binary mixtures changes almost linearly except in the cases of mixtures between the sucrose and maltitol and sucrose and isomalt. In these cases the relaxation enthalpy of the mixtures is higher than the relaxation enthalpies of the pure sugars and it coincides with glass transition temperatures, which are lower than the predicted from the theory. The phenomena might be due to a bit net loss of hydrogen bonding that resulted in a loose glassy structure. However further studies need to be done in support of this assumption.

CONCLUSION

Thermal properties of confectionary sugars were investigated in respect to characterize their behaviour during processing and to clarify their miscibility. Among the investigated sugars the sucrose possesses the highest glass transition and melting temperature and the lowest enthalpy of fusion. The glass transition undergoes without relaxation process. The thermal transitions of the investigated sweeteners vary in a wide temperature range and their enthalpies of fusion are higher than sucrose's. Therefore different process conditions should be developed for product with replaced sucrose. Based on the single glass transition of the sweetenrs' blends a miscibility between sucrose/erythritol, sucrose/ sorbitol, maltitol/ erythritol, maltitol/ sorbitol, maltitol/ isomalt, erythritol/ sorbitol, erythritol/ isomalt and sorbitol/ isomalt was confirmed. Intermolecular interactions were found to exist between sucrose/maltitol, sucrose/isomalt and maltitol/isomalt and as a result the thermal bahaviour of these blends does not match the Gordon-Taylor.

REFERENCES

1 R. W. Hartel, E.Roja, V. Sarah, *Comprehensive Reviews in Food Science and Food Safety*, **10**, 17, (2011).
2 M. Hurtta, I. Pitkänen, J. Knuutinen, Carbohydrate Research, 33, 2267, (2004).
3 Y. Roos, Phase Transitions in Foods; Academic: San Diego, (1995).
4 R. Ergun, R.W. Hartel, *Manufact. Confect.*, 89(10), 51, (2009).
5 L. Slade, H. Levine, Crit Rev. Food Sci Nutr., 30, 115, (1991).
6 L. H. Sperling, Introduction to physical polymer science, New York: Wiley-Inter-Science, (1986).
7 C. A. Angell, Chem. Rev., 102, 2627, (2002).
8 B. R. Bhandari, R. W. Hartel, Kinetics of enthalpy relaxation in corn syrup-sucrose mixtures. In: Reid DS, Sajjaanantukul T, Lillford PJ, Charoenrein S, editors. ISOPOW 10, Ames, Iowa: Wiley. 419, (2008).
9 E. M. de Graaf, H. Madeka, A. M. Cocero, J. L. Kokini., Biotechnol Prog., 9, (1993).
10 Y. Liu, , B. Bhandari, W. Zhou, Journal of food engineering, 81, 3 599, (2007).
11 S. T. Beckett, , et al., Carbohydrate research, 341, 2591, (2006).
12 K. O'Donnell, M. Kearsley, Sweeteners and Sugar Alternatives in Food Technology, John Wiley & Sons, (2012).
13 O. Tyapkova, S. Bader-Mittermaier, U. Schweiggert-Weisz, Journal of food research, 1, 207, (2012).
14 M. Gordon and J. S. Taylor, Journal of Applied Chemistry, 2, 493, (1952).
15 R. Simha, R. F. Boyer, The Journal of Chemical Physics, 37, 1003, (1962).
16 S. L. Shamblin, G. Zografi, Pharmaceutical research, 15, 1828, (1998).
17 E. P. W. Kets, et al. Cryobiology, 48, 46, (2004).
18 S. Ohno, M. Hirao, M. Kido, Carbohydrate Research, 108, 163, (1982).
19 A. Bensouissi, B. Roge, M. Mathlouthi, Food chemistry, 122, 443, (2010).

# Intensification of extraction of bioactive substances from artichoke wastes

S. S. Georgieva[*], S. S. Boyadzhieva, G. Angelov

*Institute of Chemical Engineering, Bulgarian Academy of Sciences, Acad. G. Bonchev Str., Bl. 103, 1113, Sofia, Bulgaria*

Artichoke (Cynara scolymus L.) is a traditionally cultivated and highly appreciated food in the Mediterranean region. The edible parts are only the heart and inner leaves (bracts). The external bracts, leaves and stems are non-edible by-products considered as wastes. They represent about 60% of the plant, and could be used as raw material for production of useful substances. This article examines potential intensification of the process of extraction of bioactive substances from artichoke wastes through the application of a widely used production process – conventional batch extraction. The target components to be extracted are compounds with high antioxidant activity - polyphenols and flavonoids. The study results in selection of optimal operational parameters that intensify the mass transfer and produce maximum yield of bioactive substances while minimizing the processing costs.

**Keywords:** artichoke, batch extraction, process intensification, polyphenols, antioxidants

## INTRODUCTION

Artichoke *(Cynara cardunculus L. var. Scolymus (L.) Fiori)* is an ancient herbaceous perennial plant, originating from the Mediterranean area, which today is widely cultivated all over the world. Artichoke has been known since 4th century B.C. as a food and remedy, and has been recognized for its healing effects on hepato-biliary diseases and as a digestive aid [1]. In South European countries, the globe artichoke plays an important economic role where its production represents 45% of world production, of which 550 kt are produced in Italy, 200 kt in Spain, and 55 kt in France in 2013 [2]. Only the inner leaves (bracts) and heart of this vegetable are considered edible, whereas external bracts, leaves and stems are non-edible by-products which represent about 60% of the plant. Numerous studies have focused on its beneficial health and antioxidant properties. It appears that they could be related to the phenolic compounds, also known as polyphenols, mainly composed of mono- and dicaffeoylquinic acids and flavonoids. These properties are consistent with a well-known dual role of phenolic compounds as antioxidants and as substrates for oxidative browning reactions, mainly in the presence of high iron concentrations [3-6].

Polyphenols are a class of plant secondary metabolites characterized by the presence of a hydroxyl group attached to a benzene ring or to more complex aromatic structures. Humans cannot synthesize polyphenols and therefore have to rely on their intake to meet dietary needs. This has led to campaigns for promoting the consumption of fruit and vegetables as well as to the idea of enriching common foods with phenolic compounds [7].

Dietary plant polyphenols have received attention for their significant biological functions as antioxidants, anticarcinogens or antimutagens, which have led to their recognition as potential nutraceuticals [8]. In the gastrointestinal tract the polyphenol antioxidant compounds can protect nutrients, such as proteins, lipids and vitamins, from oxidation. In addition, they can also interact with proteins, protecting them from precipitation and loss of nutritional value, enzymatic activity, and other biological effects. It is confirmed that polyphenols have many potential bioactivities in the human body due to interactions with other macromolecules [9].

The extraction of substances from solids using a solvent is applied in many chemical, biotechnological, and pharmaceutical processes for extraction of valuable ingredients. It is the first and important step in isolating and purifying bioactive components from plant materials. The extraction efficiency is influenced by several factors, such as the type and concentration of solvent, solid–solvent ratio, time, temperature, pH, etc. However, in most studies the influence of a single factor has been explained while the interactions among factors have not been examined thoroughly [10]. Prospective and future trends in production processes are indicating new strategies for reducing expenses (energy, time, reprocessing, etc.) without affecting product quality. One such strategy is process intensification: a systematic organization to boost and enhance the mass transfer, optimizing in parallel the use of chemicals and energy, expenses or other benefits through development of efficient techno-

economical systems [11].

The aim of this article is to determine optimal operational conditions for conventional batch extraction of artichoke wastes (stems and leaves) that intensify the mass transfer and produce maximum yield at reduced solvent consumption and shorter processing time. The target components to be extracted are compounds with high antioxidant activity - polyphenols and flavonoids.

EXPERIMENTAL

*Plant material*

Stems and leaves of artichoke cultivated in the region of Troyan, Bulgaria (vintage 2014) were used as a raw material. Dry stems and leaves were ground in a household electric grinder, sieved (fraction less than 1 mm was used) and stored in a cold and dark place.

*Extraction protocol*

A sample of ground raw material (10 g) was mixed in a flask with solvent (ethanol-water mixtures containing 0, 20, 35, 50, 70, 96% ethanol). The extractions were carried out in a thermostatic water bath shaker (Gyrotory Water Bath Shaker, model G76, New Brunswick Scientrific, USA) at 160 rpm. The influence of the main process parameters on the yield was determined by performing extractions with different solvents at different temperatures and different solvent-to-solid ratio (hydromodule). Long contact time was applied in order to await the process completion. The development of the process over time (extraction kinetics) was observed by making parallel extractions of identical samples, each one analyzed after different contact time. After extraction, the mixture was filtered, and the filtrate was collected and stored at $4^0$C for analyses. Each test was repeated in duplicate or in triplicate in case of big variances between two analyses. Mean values were used. The range of deviation of parallel experiments was 2.5 -7.5 %. Generally, the deviation was greater for smaller measured values.

Single factor ANOVA statistical test was applied to the kinetic results in order to determine whether they are statistically equal (null hypothesis) or significantly different one from another.

*Chemicals and reagents*

Analyses for total content of polyphenols, flavonoids and antioxidant capacity were made using Folin-Ciocalteu reagent (2N), quercetin, gallic acid, anhydrous $Na_2CO_3$, DPPH*, methanol and $AlCl_3$ (Sigma). Ethanol-water solvents were prepared by using 96% ethanol (Valerus) in different proportions.

*Analyses*

**1. Determination of total phenolic content**

Total polyphenolic content (TPC) of the extracts was determined by the Folin–Ciocalteu method [12] using UV-VIS spectrophotometer (UNICAM®-Helios β). The absorbance of samples was measured at 765 nm. TPC was expressed as mg of gallic acid equivalent (GAE) per 1 gram of raw material (mg GAE/g rm).

**2. Determination of total flavonoids content**

The total flavonoids content (TFC) was determined using aluminum chloride colorimetric assay [13]. Absorbance was measured at 420 nm and results were expressed as mg of quercetin equivalents (QE) per one gram of raw material (mg QE/g rm).

**3. Antioxidant capacity (AOC)**

AOC is determined as described by Brand-Williams [14]. The method is based on a color reaction between the nitrogen atom (from DPPH) and the hydrogen atom of hydroxyl group of the antioxidant compound. 1 ml extract was mixed with 4 ml solution of DPPH in methanol (0.004%). After keeping the sample 60 min in the dark at room temperature, the absorbance was measured at 517 nm. AOC was expressed as IC50 (quantity of extract neutralizing 50% of DPPH amount).

Graphically, antioxidant capacity is expressed as mg DPPH which is neutralized by the corresponding amount (one gram) of dry extract.

**4. Dry extract yield**

It was determined by drying and weighting of liquid extracts at mild temperature until stagnant weight is achieved. Analytical balance Sartorius with 0.1 mg precision was used.

RESULTS

*Solid-liquid batch extraction*

The mass transfer in solid-solvent systems is affected by several parameters, the main among them being solvent type and concentration, solid/liquid ratio, and temperature. In order to define appropriate conditions the influence of the main parameters has to be studied to select the optimal combination resulting in highest process efficiency. In this study, the process efficiency is quantified by the mass of extracted substance from unit of raw material and by the concentration of target substance in the extract. Higher values indicate higher process efficiency.

The selection of optimal operational parameters is made by applying a four-step experimental approach. Initially, an appropriate solvent has to be used. As known, the extraction of bioactive substances from plants is highly influenced by the solvent nature. Polar solvents such as water and ethanol are widely recognized as adequate for extraction of antioxidant phenolic compounds, which are also of polar type [15]. Consequently, ethanol and water in pure state as well as their mixtures were used as solvents in this study.

The first step was to determine the best solvent concentration. It was done by making extractions with a number of ethanol/water mixtures (0, 20, 35, 50, 70, 96% ethanol) at 70°C near to the ethanol boiling point, which is supposed to ensure better solubility. Abundant solvent was applied (liquid-solid ratio at least 20:1) in order to ensure sufficient amount of liquid phase for good wetting of the solid and for dissolving all extractable matter. Agitation (160 rpm) and long contact time (2 hours) were applied to provide good phase mixing and enough time for attaining pseudo-equilibrium state, at which the mass transfer process should practically complete.

**Table 1.** Yields of substances extracted with different solvent concentrations

| % ethanol | TPC | | TFC | | Yield of dry extract |
|---|---|---|---|---|---|
| | (mg GAE/g rm) | (mg GAE/g de) | (mg QE/g rm) | (mg QE/g de) | (mg de/g rm) |
| 0 | 12.4 | 36.6 | 2.4 | 7.2 | 320.0 |
| 20 | 13.3 | 41.0 | 2.9 | 9.1 | 323.6 |
| 35 | 14.8 | 45.7 | 3.2 | 9.8 | 324.5 |
| 50 | 16.3 | 56.00 | 4.0 | 11.5 | 336.9 |
| 70 | 15.6 | 56.5 | 4.1 | 14.9 | 275.5 |
| 96 | 8.5 | 46.1 | 2.8 | 15.1 | 183.9 |

TPC – total polyphenolic content; TFC – total flavonoids content; GA– acid equivalent; QE – quercetin equivalent; rm– raw material; de – dry extract

According to Table 1, maximum yield of total extract and polyphenols is obtained with 50% ethanol. Regarding extracted flavonoids, they are better extracted with more concentrated ethanol. However, they are in minor quantity compared with total polyphenols and do not contribute significantly to the total concentration of the antioxidant substances. Also, yield of polyphenols is the same at 50% and 70% ethanol. Thus, a cheaper 50% ethanol solvent was chosen for further experiments.

Concerning the total extracted mass (yield of dry extract), it is the same up to 50% ethanol and decreases afterwards i.e. water is a better solvent than an ethanolic solvent with concentration more than 50% ethanol.

**Table 2.** Extraction yield at different temperature

| Temp (°C) | TPC | | TFC | | Yield of dry extract |
|---|---|---|---|---|---|
| | (mg GAE/g rm) | (mg GAE/g de) | (mg QE/g rm) | (mg QE/g de) | (mg de/g rm) |
| 20 | 12.7 | 46.0 | 2.6 | 9.3 | 276.1 |
| 50 | 14.8 | 50.2 | 3.2 | 11.0 | 295.9 |
| 70 | 16.3 | 56.0 | 4.0 | 11.5 | 336.9 |

The second step was to identify the appropriate temperature. In general, higher temperature will increase the solubility. However, some substances might be thermally unstable, which will be manifested by lower yield at higher temperature indicating that substance degradation exists. Three temperatures have been tested: 20, 50 and 70°C, and the results are depicted in Table 2.

As it is seen, the extraction yield becomes better with higher temperature. Consequently, temperature of 70°C is selected as it results in more intensive mass transfer and highest yield.

The third step is to identify the appropriate liquid-to-solid ratio. In the previous experiments, high ratio was used to ensure sufficient amount of unsaturated solvent to dissolve all extractable matter. However, operation with excessive amount of solvent generates additional expenses for heating, evaporation, recovery and recycling and thus optimization is appropriate.

Extractions at different hydromodules were performed (Fig.1). The other process parameters were tuned at their optimal values (50% ethanolic solvent, temperature 70°C). Again, long contact time (2 hours) was applied in order to ensure equilibrium state.

The results in Fig.1 show that the polyphenols and flavonoids concentration in the dry extracts

rises up to hydromodule 10, while addition of more solvent beyond that does not bring improvement. Therefore, to maximize the active components content with minimum costs, the optimal choice is solvent-to-solid ratio equal to 10.
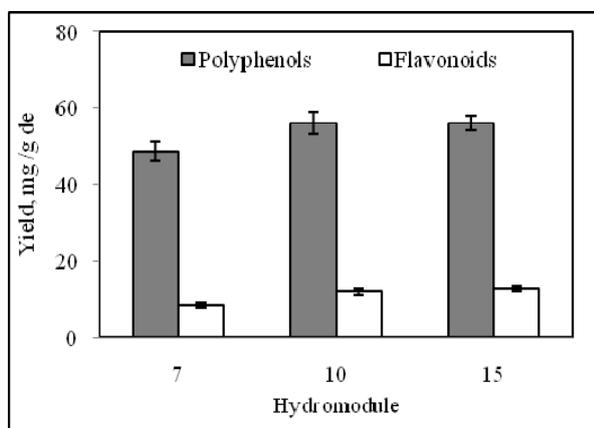


**Fig.1.** Influence of hydromodule

The fourth step is to determine the minimum time necessary to complete the process. As noted, in all previous experimental runs the phase contact was prolonged to ensure equilibrium state. A long contact time might have some disadvantages, such as: longer and more expensive technological process; increased probability for thermal destruction of unstable active components because of longer exposition at high temperature; unnecessary occupation of reactors, which could be used for production of other goods, etc. Optimization can be done by examination of the process development over time. Extractions were carried out for different contact time at the established optimal process parameters, the obtained yields being plotted against extraction time. The resulting kinetic curves are shown in Fig.2.
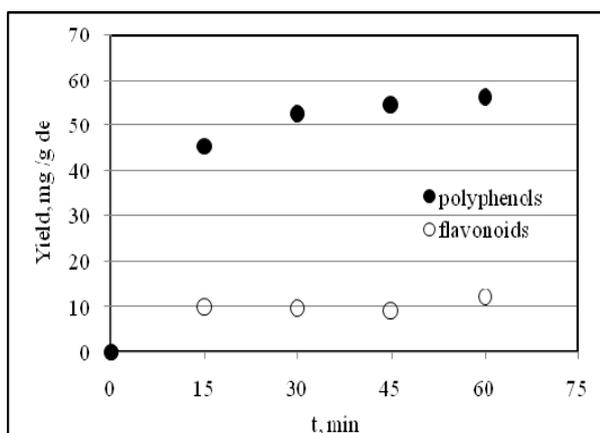


**Fig.2.** Extraction kinetics

Important increase of the amount of extracted major substances (polyphenols) is observed during the initial period from 0 to about 30 minutes contact time. If the process is run for longer time, minor

and insignificant additional amount is extracted (about 3.5%). Thus, further processing might be useless as it does not materially improve the yield, and the processing cost might be higher than the cost of the additional product.

The choice of contact time for polyphenols extraction is justified also by the results of single factor ANOVA tests with significance level 0.05. Statistically, similar (not significantly different) yields of polyphenols are obtained in the interval 30-60 min, i.e. no need to prolong the contact time for more than 30 min.

*Antioxidant capacity (AOC)*

Fig.3 illustrates the antioxidant capacity of extracts obtained for different contact time at optimal conditions.
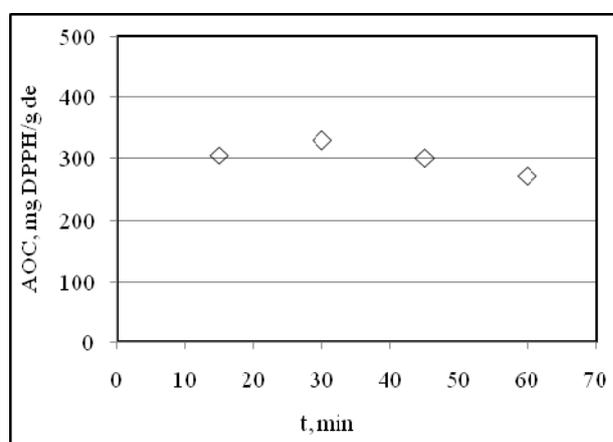


**Fig.3.** Antioxidant capacity

It is seen that 15-30 min processing results in extracts with maximum AOC. The ANOVA test shows statistically similar values of AOC in the range 15-60 min, which determines 15 min contact as the optimal choice for maximizing AOC. However, in view of the whole extraction process, it seems better to recommend 30 min process duration, because the extract will contain more polyphenols (see Fig.2), although the AOC does not increase proportionally to polyphenol content.

Some decrease of AOC is observed at prolonged contact (more than 30 min). As the yield of polyphenols and flavonoids is not reduced (see Fig.2), the lower AOC can probably be assigned to thermal destruction of non-phenolic antioxidant compounds.

CONCLUSIONS

The extraction of some bioactive compounds (polyphenols and flavonoids) from artichoke wastes was studied with the aim to intensify the process. Operational conditions were determined, at which the mass transfer was improved and yield maximized while minimizing processing costs. In

summary, the optimal operational conditions for the particular case studied here are:

- Solvent composition – 50% ethanol;
- Processing temperature 70°C;
- Solvent-to-solid ratio 10;
- Processing time 30 minutes.

They can be used as basic process parameters necessary for development of technological schemes for production of extracts from artichoke wastes.

## REFERENCES

1  L. Vincenzo, P. A. Kroon, V. Linsalata, A. Cardinali, J. Funct. Foods, 1, 131, (2009).
2  http://faostat3.fao.org.
3  L. Ruiz-Aceituno, M. J. García-Sarrió, B. Alonso-Rodriguez, L. Ramos, M. L. Sanz, Food Chem., 196, 1156, (2016).
4  G. Pandino, S. Lombardo, G. Mauromicale, Ind. Crops Prod., 44, 44, (2013).
5  D. Negro, V. Montesano, S. Grieco, P. Crupi, G. Sarli, A. De Lisi, G. Sonnante, J. Food Sci., 77, 2, 244, (2012).
6  F. Fratianni, M. Tucci, M. De Palma, R. Pepe, F. Nazzaro, Food Chem., 104, 1282, (2007).
7  A. Zuorro, G. Maffei, R. Lavecchia, J. Clean. Prod., 111, 279, (2016).
8  A. Bose, Food Chem., 126, 417, (2011).
9  L. Jakobek, Food Chem., 175, 556, (2015).
10  N. Cujic, Šavikin K., Jankovic T., Pljevljakušic D., Zdunic G., Ibric S., Food Chem., 194, 135, (2016).
11  G. L. Zabot, M. N. Moraes, P. I. N. Carvalho, M. Angela A. Meireles, Ind. Crops Prod., 77, 758, (2015).
12  V. Singleton, J. A. Rossi, Amer. J. Enol. Viticult., 16, 144, (1965).
13  A. A. L. Ordonez, J. D. Gomez, .A. Vattuone, M. Isla, Food Chem., 97, 452, (2006).
14  W. Brand-Williams, M. E. Cuvelier, C. Berset, Lebensmit.-Wissensch. und Technol., 28, 25, (1995).
15  M. Naczk, F. Shahidi, J. Chromatogr. A, 1054, 95, (2004).

# BIOTECHNOLOGIES

# Optimizing enzymatic extraction from rose petals (Rosa Damascena Mill.)

K. D. Kalcheva – Karadzhova[1*], K. M. Mihalev[2], D. P. Ludneva[1], V. T. Shikov[2], R. H. Dinkova[2],
N. D. Penov[2]

[1]*Food Research and Development Institute – Plovdiv, bul. Vasil Aprilov 154, Bulgaria*
[2]*University of Food Technology – Plovdiv, bul. Marica 26, Bulgaria*

Response surface methodology (RSM) has been used to optimize the extraction conditions of antioxidants and anthocyanins from rose petals (*Rosa Damascena* Mill.) by using enzyme - assisted extraction. A ternary enzyme combinations included pectinolytic, cellulolytic and hemicellulolytic preparation was used. The variation in enzyme dosage (0.052 - 0.132%) and maceration time (125 - 205 min) define the optimal maceration conditions to prepare extracts with high antioxidant and anthocyanins content

**Keywords:** Response surface methodology (RSM), polyphenols, anthocyanins, enzyme-assisted extraction, Rosa Damascena Mill

## INTRODUCTION

The interest in drug–and product derived from plants has made it important to search for effective extraction method to maximize the yield of bioactive component such as vitamin C, anthocyanin and phenolic compounds [1]. Response surface methodology (RSM) is an effective statistic technique which uses quantitative data in an experimental design to optimize a process [2].

RSM was demonstrated to be a potent tool in optimizing experimental parameters maximizing numerous responses [3]. Central composite design, which is one of the most common designs, has been widely used to optimize phenolic compounds extraction [4].

Optimal central composite design (OCCD) is an experimental approach to define empirical models or equations for describing the effect of test variables and th3ir interactions on the respective responses [5, 6, 7].

In previous investigations the efficiency of enzyme-assisted extraction with three components enzyme mixture (pectinolytic, cellulolytic and hemicellulolytic preparation) on the recovery of polyphenols from *Rosa damascena* petals using a simplex centroid experimental design was evaluated [8].

So the purpose of this study is to optimize enzymatic treatment conditions from rose petals (*Rosa Damascena* Mill.) using variation in dosage obtained extract can be used in food and parapharmaceutical industry.

## MATERIALS AND METHODS

### Chemicals

For analytical purposes the following reagents were used: DPPH [2,2-diphenyl-1-picrylhydrazyl] and Trolox [(+/−)-6-hydroxy-2,5,7,8- tetramethyl-chroman-2-carboxylic acid] (Sigma-Aldrich, Steinheim, Germany); TPTZ [2,4,6-tripyridyl-s-triazine] and gallic acid monohydrate (Fluka, Buchs, Switzerland); Folin-Ciocalteau's reagent (Merck, Darmstadt, Germany). All the other reagents and solvents used were of analytical grade.

### Enzyme preparations

The following commercial enzyme preparations were used: pectinolytic preparation Pectinex Ultra Color (Novozymes A/S, Bagsvaerd, Denmark); cellulolytic preparation Rohament CL (AB Enzymes GmbH, Darmstadt, Germany); hemicellulolytic preparation Xylanase AN (Biovet JSC, Peshtera, Bulgaria). Plant material:

Rose (*Rosa damascena* Mill.) petals, harvest year 2013, were supplied by Ecomaat Ltd. (Mirkovo, Bulgaria). The petals were dried in a thin layer at room temperature (25-27°C) for one week before final hot air drying (50°C, 1 h). Dried rose petals were stored in a desiccator in dark until used.

### Enzyme - assisted extraction

Extracts from *Rosa damascena* petals were processed according to the flow diagram shown in Fig.1.

### Sample preparation

An aliquot (5 g) of filtered extract was transferred into 50 mL volumetric flask using 40 ml of acidified (0.1% HCl) methanol. After extraction for 24 h at 10°C, the flask was filled up to the mark with acidified methanol and filtered through a paper filter. Extraction was performed in triplicate.

---

\* To whom all correspondence should be sent:
   krasimiradecheva@abv.bg
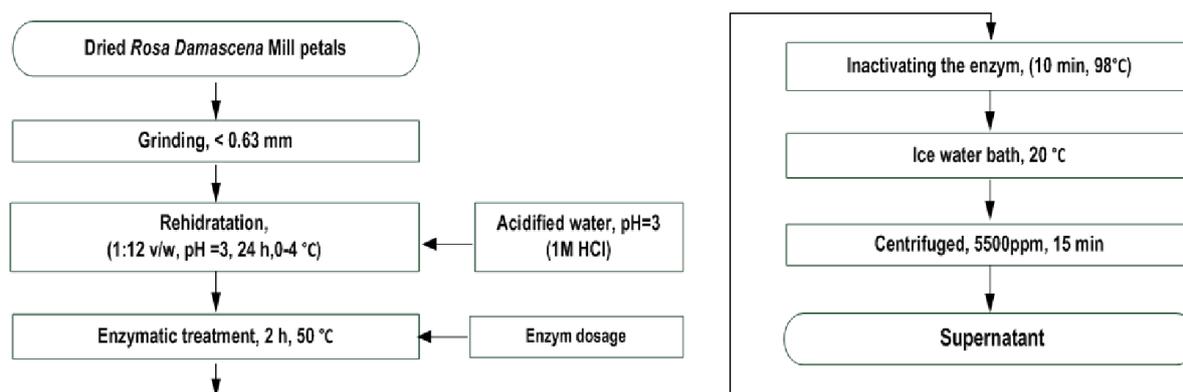
**Fig.1.** Process flowchart for extraction of rose petals (*Rosa Damascena* Mill.)

*Analytical methods*

All measurements were performed with a Helios Omega UV-Vis spectrophotometer equipped with VISIONlite software (all from Thermo Fisher Scientific Inc., Waltham, MA, USA) using 1 cm path length cuvettes.

The contents of total polyphenols (TPP) and total monomeric anthocyanins (TMA) were determined by the method of Singleton and Rossi [9] and the pH-differential method [10], respectively, modified as described by [11].

The total antioxidant capacity was determined by the DPPH (free radical scavenging activity) and FRAP (ferric reducing antioxidant power) assay, following the methods of Brand-Williams et al. [12] and Benzie and Strain [13], respectively, with some modifications [11].

*Statistical analysis*

The results reported in the present study are the mean values of at least three analytical determinations and the coefficients of variation, expressed as the percentage ratios between the standard deviations and the mean values, were found to be < 5% in all cases. SYSTAT statistical software (SPSS Inc., Chicago USA, version 7.1) and Excel were used to analyze the data.

*Experiment design*

An OCCD of the type $2^n + 2n + n_0$ was applied. The influence of the independent variables was determined by means of the RSM [2, 14].

Table 1 shows the levels of the two independent variables – enzyme dose (0.02–0.18%E/S) and reaction time (30–210 min).

Considering two parameters and a response, experimental data were fitted to obtain a second-degree regression equation of the form:

$$y = b_0 + \sum_{i=1}^{n} b_i x_i + \sum_{i=1}^{n} b_{ii} x_i^2 + \sum_{i=1}^{n}\sum_{j=1}^{n} b_{ij} x_i x_j \quad (1)$$

where y is the predicted responses for TMA, TPP, DPPH, FRAP, yield of extract, respectively; $X_1$ is the enzyme concentration and $X_2$ is the incubation time; $b_0$ is the value of the fitted response at the centre point of the design and $b_i$, $b_{ii}$ and $b_{ij}$ are the coefficients of the regression equation

**Table 1.** Independent variable values and corresponding levels

| Factor | Minima | Center point | Maxima | Axial piont, α |
|---|---|---|---|---|
| Enzyme dose (%E/S[a]) – $X_1$ | 0.02 | 0.1 | 0.18 | $-\alpha = -1$ $+\alpha = +1$ |
| Time (min) – $X_2$ | 30 | 120 | 210 | $-\alpha = -1$ $+\alpha = +1$ |

[a] ml enzyme preparation per 100 g substrate

RESULTS

The statistical combinations of variables in coded and actual values along with the predicted and experimental responses are presented in Table 2. There is an increase in the values of TMA and TPP (Table 2 and Fig.2) by prolong the time of processing, leading to reduction of enzyme dosage mixture.

The positive effect of prolonged treatment means that the enzyme mixture possess the pectolytic, cellulitic and hemicellulitic activities that are able to catalyze the degradation of the polysaccharides in the cell wall, resulting in increased extraction of polyphenols and anthocyanins.

Higher content of enzyme mixture dosage leads to increased values of bioactivities compounds and yield in a short time of processing. The effect of enzyme dosage decrease with decreasing of time treatment.

The regression equation characterizing the influence of different variables on extraction process is obtained (2-6). The high values of the

coefficient of determination ($R^2$) indicate a reasonable agreement of the corresponding model with the experimental results [16].

Pareto chart Fig.3, was used to visualize the interaction effects of all factors to the response variable.

**Table 2.** Experimental design matrix and results for the optimal central composite design

| № | Coded values | | Enzyme dose (%E/S[a]) | Time (min) | TMA[b] (mgCGE/100g) | TPP[c] (mgGAE/100g) | DPPH[d] (mgTE/100g) | FRAP[e] (mgTE/100g) | Yield[f], % |
|---|---|---|---|---|---|---|---|---|---|
| | | | $X_1$ | $X_2$ | $Y_1$ | $Y_2$ | $Y_3$ | $Y_4$ | $Y_5$ |
| 1 | - | - | 0.02 | 30 | 14.4 | 302.5 | 1880.0 | 1493.0 | 34.0 |
| 2 | + | - | 0.18 | 30 | 15.7 | 424.5 | 2637.0 | 1808.0 | 45.5 |
| 3 | - | + | 0.02 | 210 | 18.3 | 494.2 | 2796.0 | 2180.0 | 34.5 |
| 4 | + | + | 0.18 | 210 | 18.5 | 481.3 | 2950.0 | 2237.0 | 37.0 |
| 5 | - | 0 | 0.02 | 120 | 17.6 | 561.1 | 3242.0 | 1830.0 | 42.6 |
| 6 | + | 0 | 0.18 | 120 | 18.4 | 615.6 | 3697.0 | 2012.0 | 49.1 |
| 7 | 0 | - | 0.1 | 30 | 14.0 | 245.3 | 1965.0 | 1538.0 | 32.2 |
| 8 | 0 | + | 0.1 | 210 | 17.3 | 369.5 | 2579.0 | 2085.0 | 29.5 |
| 9 | 0 | 0 | 0.1 | 120 | 17.6 | 473.6 | 3187.0 | 1740.0 | 42.0 |
| 10 | 0 | 0 | 0.1 | 120 | 17.2 | 458.2 | 3157.0 | 1798.0 | 42.0 |
| 11 | 0 | 0 | 0.1 | 120 | 15.9 | 478.6 | 3185.0 | 1868.0 | 42.0 |

[a] ml enzyme preparation per 100 g substrate.
[b] Results are presented as mg cyanidin 3-glucoside equivalents (CGE) per 100 g
[c] Results are presented as mg gallic acid equivalents (GAE) per 100 g
[d] Results are presented as mg trolox equivalents (TE) per 100 g
[e] Results are presented as mg trolox equivalents (TE) per 100 g
[f] Results are presented as % per 100 g



a



b



c



d



e
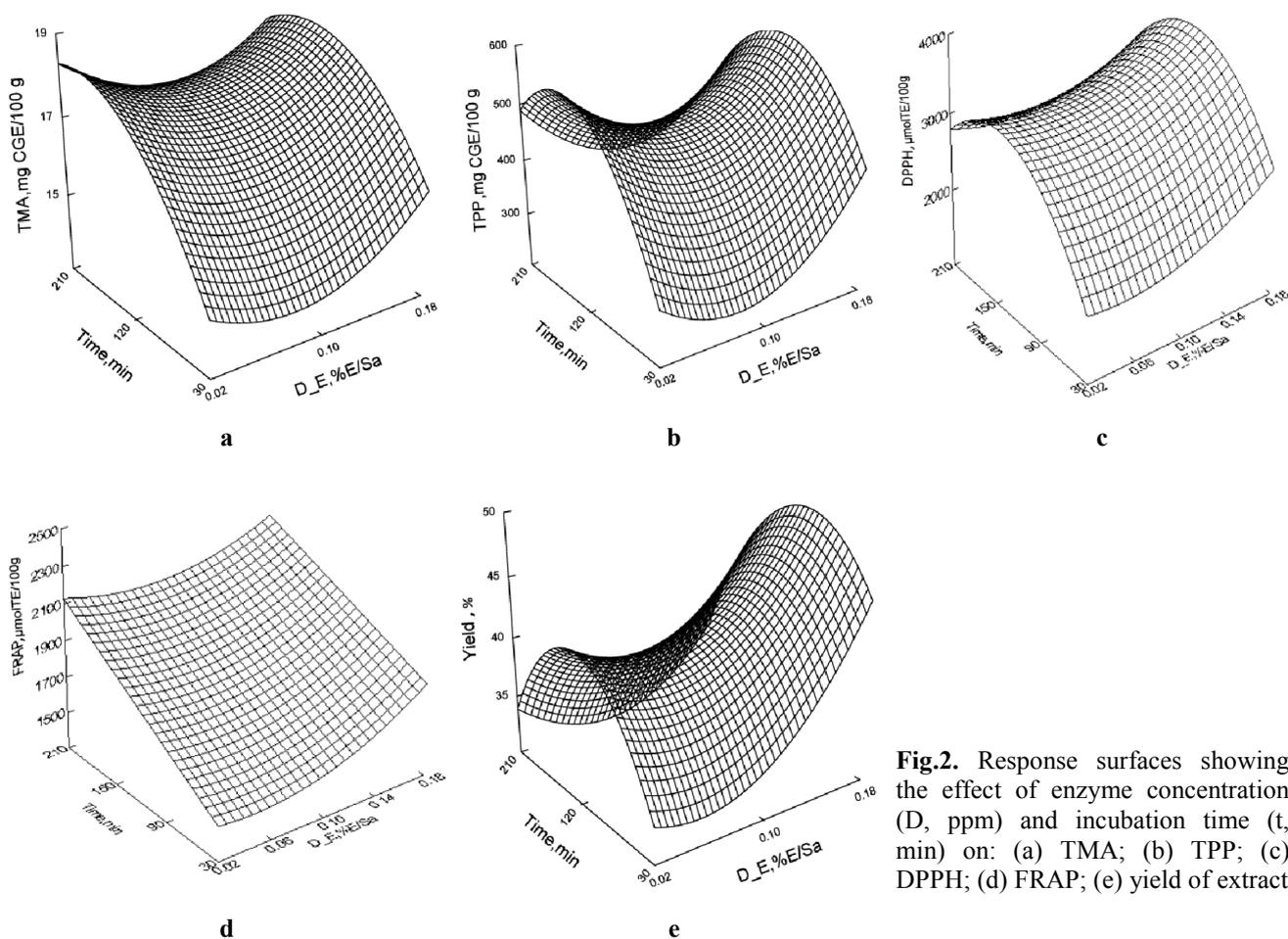
**Fig.2.** Response surfaces showing the effect of enzyme concentration (D, ppm) and incubation time (t, min) on: (a) TMA; (b) TPP; (c) DPPH; (d) FRAP; (e) yield of extract

$$Y_1 = 13.191 - 25.030.X_1 + 0.06.X_2 + 171.505.X_1^2 - 0.038.X_1.X_2 - 0.0002.X_2^2, \, mg \, CGE/100 \, g; \, R^2 = 0.937 \quad (2)$$

$$Y_2 = 190.88 - 2390.52.X_1 + 5.57.X_2 + 16525.5.X_1^2 - 4.68.X_1.X_2 - 0.01.\, X_2^2, \, mg \, GAE/100 \, g; R^2 = 0.993 \quad (3)$$

$$Y_3 = 1082.22 - 3812.72.X_1 + 32.29.X_2 + 45855.3.X_1^2 - 20.94.X_1.X_2 - 0.11.X_2^2, \, \mu molTE/100g; \, R^2 = 0.999 \quad (4)$$

$$Y_4 = 1410.81 - 1473.14.X_1 + 3.71.X_2 + 18511.5.X_1^2 - 8.96.X_1.X_2 + 0.001 \, X_2^2, \, \mu molTE/100g; \, R^2 = 0.986 \quad (5)$$

$$Y_5 = 26.978 - 66.10.X_1 + 0.27.X_2 + 745.07X_1^2 - 0.31.\, X_1.X_2 - 0.001.X_2^2, \%; \, R^2 = 0.96 \quad (6)$$



**a- TMA**    **b- TPP**    **c- DPPH**

**d- FRAP**    **e-yield**
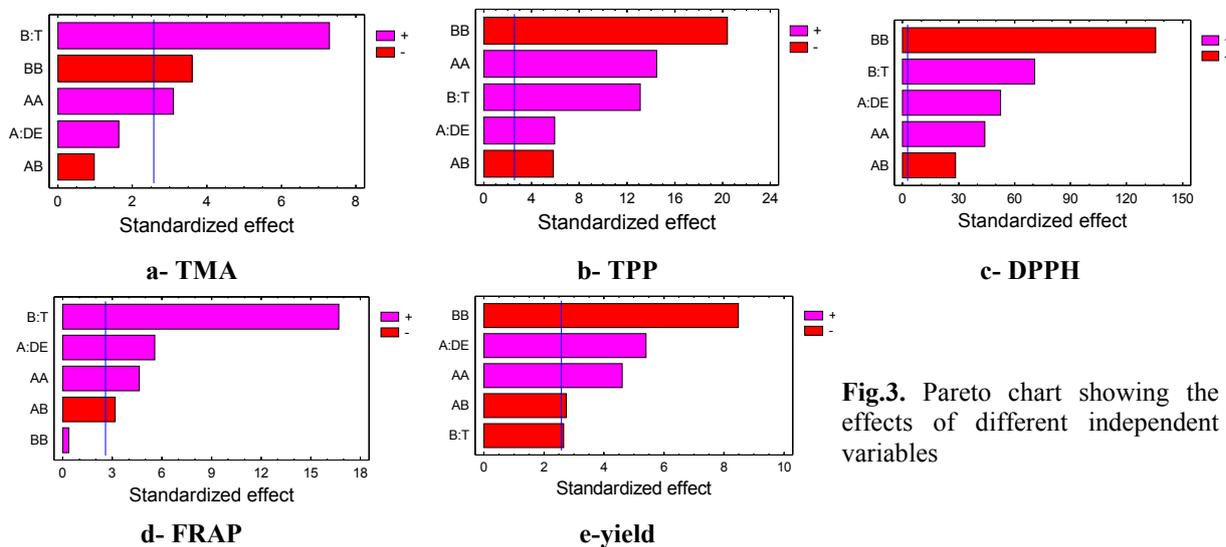
**Fig.3.** Pareto chart showing the effects of different independent variables

The model shows that time of enzymatic treatment influence the greatest selected dependent variables, such as the yield of extracts, TPP and radical scavenging activities (DPPH - test) the effect is quadratic. The effect is linear to the TMA and ferric reducing antioxidant power (FRAP).

In order to prepare the extract with high polyphenol and anthocyanin content graphical optimization was made (Fig.4).
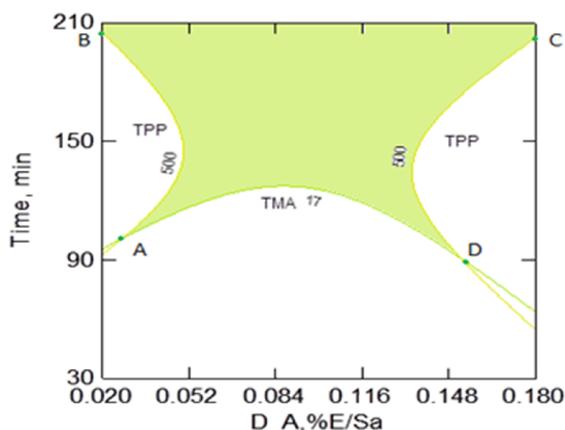


**Fig.4.** Graphics optimization of enzymatic extraction of rose petals as a function of extraction time and enzyme dosage

Optimization was carried out by the superposition of several contour surfaces of competing responses. The response surface plots were generated for interaction of two independent variables. The limits of target functions for optimization of enzymatic extraction of rose petals (*Rosa damascena* Mill.) were presented in Table 3.

**Table 3.** Limits of target functions for optimization of enzymatic extraction of rose petals

| Equation № | Target function | Limits of target function |
|---|---|---|
| 2 | TMA,mg CGE/100 g | TMA > 17.0 |
| 3 | TPP,mg GAE/100 g | TPP > 500.0 |

Intervals of variations of the enzyme mixture dosage (0.052 to 0.132%) and enzymatic treatment time (125-205 min) determine the field for obtaining the extracts with high content of total polyphenols and anthocyanins content.

CONCLUSIONS

The effect of ternary enzyme combinations included pectolytic, cellulytic and hemicellulytic preparation were investigated to optimize the extraction conditions of antioxidants and anthocyanins from rose petals (*Rosa Damascena* Mill.). The OCCD results show that the increment

of incubation time significantly affects the contents of total polyphenols and anthocyanins. A decrease in the time of enzyme treatment could be achieved with increasing of dosage of enzyme mixture.

The optimization process was focused on the total anthocyanins and total polyphenols content. Intervals of variations in the enzyme mixture dosage (0.052 to 0.132%) and the time of enzymatic treatment (125-205 min) determine the best conditions for preparing rose petals extracts with high content of total polyphenols and anthocyanins content.

## ACKNOWLEDGEMENTS

## REFERENCES

1 R. Dibazar, Optimization of ultrasound - assisted extraction of anthocyanins from Nova Scotian lowbush blueberries (*Vaccinium Angustifolium Aiton* L.), Dalhousie University Halifax, Nova Scotia November, (2014).

2 A. Lambrev, Bases of the Engineering Experiment in the Investigation of Machines and Devices for the Food Industry. "Ch. G. Danov", Plovdiv, (In Bulgarian), 211 pp. (1994).

3 J. E. Cacace, G. Mazza, Optimization of Extraction of Anthocyanins from Black Currants with Aqueous Ethanol, *Journal of Food Science*, Vol. 68, No. 1, pp. 240-248, (2003).

4 Y. El.Hajj, N. Louka, C. Nguyen and R. G. Maroun, "Low Cost Process for Phenolic Compounds Extraction from Cabernet Sauvignon Grapes (Vitisvinifera L. cv. Cabernet Sauvignon). Optimization by Response Surface Methodology", *Food and Nutrition Sciences*, Vol. 3, No. 1, pp. 89-103, (2012).

5 Y. S. Sun, Z. Wang, J. Wu , F. Chen, X. Liao, X. Hu, Optimising enzymatic maceration in pretreatment of carrot juice concentrate by response surface methodology. *International Journal of Food Science and Technology*, 41, 1082, (2006).

6 T. Petrova, Study of Extrusion Process of Lentil Semolina, Dissertation, UHT - Plovdiv (2011), in Bulgarian

7 M. Ruskova, Study the extrusion technology for utilization of organic losses in the processing of fruit (apples). , Dissertation, FRDI - Plovdiv, (2014), in Bulgarian

8 K. Kalcheva-Karadzhova, V. Shikov, K. Mihalev, G. Dobrev, D. Ludneva and N. Penov, Enzyme-assisted extraction of polyphenols from rose (*Rosa damascena* Mill) petals; Acta universitatis Cibiniesis Series E: Food technology, 18, 2, 65-72, (2014).

9 V. Singleton, J. Rossi, Colorimetry of total phenolics with phosphomolybdic- phosphotungstic acid reagents. *American Journal of Enology and Viticulture*, 50, 3828-3834, (1963).

10 M. Giusti, R. Wrolstad, Anthocyanins. Characterization and measurement with UVvisible spectroscopy. In R. E. Wrolstad (Ed.), Current Protocols in Food Analytical Chemistry. New York: Wiley, Unit F1.2.1-13, (2001).

11 R. Dinkova, V. Shikov, K. Mihalev, Z. Velchev, H. Dinkov, P. Mollov, Changes in the total anthocyanins and polyphenols during processing af wild berries into freshly pressed juices. *Journal of EcoAgriTourism*, 8 (1), 254, (2012).

12 W. Brand – Williams, M. Cuvelier, C. Berst, Use of a free radical method to evaluate antioxidant activity. *Lebensmittel Wissenschaft and Technologie*, 28, 25-30, (1995).

13 I. Benzie, J. Strain, The Feric reducing ability of plasma (FRAP) as a measure of antioxidant activity. The FRAP assay. *Analytical Biochemistry*, 189, 70-76, (1996).

14 B. Bojanov , I. Vuchkov, Statistical methods for modelling and optimizing multi-factorial objects. State Publishing Company "Technology", Sofia, (In Bulgarian), 530 pp. (1973).

15 N. K. Rastogi, K. R. Rashmi, Optimization of enzymatic liquefaction of mango pulp by response surface methodology. *European Food Research and Technology*, 209, 57, (1999).

# Effect of pectolytic enzyme preparation on antioxidant capacity and color characteristic of rose petals extract (Rosa Damascena Mill.)

K. D. Kalcheva – Karadzhova[1*], K. M. Mihalev[2], D. P. Ludneva[1], V. T. Shikov[2], R. H. Dinkova[2],

I. Y. Bakalov[1]

*[1]Food Research and Development Institute – Plovdiv, bul. Vasil Aprilov 154, Bulgaria*
*[2]University of Food Technology – Plovdiv, bul. Marica 26, Bulgaria*

The influence of three commercial pectolytic enzyme preparations (Pectinex Ultra Color, Panzym Pro Color and Panzym BE XXL) on the yield of total polyphenols, anthocyanins, antioxidant activities and color characteristic of extracts from rose petals (*Rosa Damascena* Mill) was investigated. As a result of the enzymatic treatment, the content of total polyphenols and anthocyanins general increase, by 18% and 15%, respectively. There is an overall increase up to 2.2 times in the antioxidant activity and an enhancement on the red color component intensity of the extracts.

**Keywords:** Rosa Damascena Mill., enzyme-assisted extraction, antioxidants, polyphenols, color

## INTRODUCTION

Damask rose (*Rosa damascena* Mill.) is one of the most important medicinal and ornamental plants grown mainly for it's essential oil and medicinal aspects in many areas of the world, such as Bulgaria, Turkey, India and Iran [1].

Antioxidant compounds like phenolic acids, polyphenols such as peroxide, hydro- peroxide or lipid peroxyl inhibit the oxidative mechanisms that lead to degenerative diseases [2].

*Rosa damascena* is a plant rich in terpenes, glycosides, flavonoids, and anthocyanins but also contains carboxylic acid, myrcene, vitamin C, kaempferol and quarcetin [3, 4, 5, 6]. Its ability to be strengthening the heart, treatment of menstrual bleeding, digestive problems [7, 8]. and reduction of inflammation [3]. It also healing depression, grief, nervous stress and tension [3, 8].

The application of cell-wall degrading enzymes represents another novel approach in spice production. Enzyme-assisted extraction is an effective method for improving and recovery of bioactive compounds from plants and algae [9, 10]. Enzymatic hydrolysis of plant materials is currently being used for a variety of reasons, e.g. improving yields in juice processing [11], enhanced release of secondary plant metabolites [12], recovery of functional food ingredients [13].

To facilitate the extraction of polyphenols by destroying the cell wall matrix food industry is commonly used widely used pectolytic enzyme preparations. The use of pectolytic enzyme preparations cause destruction of the cell wall matrix, resulting in with maximizing juice yield and increased extraction of phenolic compounds, especially anthocyanins [14].

The purpose of this paper was to investigate the possibilities for achieving enhanced extraction using of three commercial pectolytic enzyme preparations (Pectinex Ultra Color, Panzym Pro Color and Panzym BE XXL) on the juice yield, yield of total polyphenols, anthocyanins, antioxidant activities and color characteristic of extracts from rose petals (*Rosa Damascena* Mill). The obteined extract will be a good base to used in different areas of the food industry.

## MATERIALS AND METHODS

### Chemicals

For analytical purposes the following reagents were used: DPPH [2,2-diphenyl-1-picrylhydrazyl] and Trolox [(+/−)-6-hydroxy-2,5,7,8- tetramethyl-chroman-2-carboxylic acid] (Sigma-Aldrich, Steinheim, Germany); TPTZ [2,4,6-tripyridyl-s-triazine] and gallic acid monohydrate (Fluka, Buchs, Switzerland); Folin-Ciocalteau's reagent (Merck, Darmstadt, Germany). All the other reagents and solvents used were of analytical grade.

### Enzyme preparations

The following three commercial pectinolytic enzyme preparations were used: Pectinex Ultra Color (Novozymes A/S, Bagsvaerd, Denmark),

* To whom all correspondence should be sent:
krasimiradecheva@abv.bg

Panzym BE XXL and Panzym Pro Color were provided from Begerow GmbH& Co, Langenlonsheim, Germany.

### Plant material

Rose (*Rosa damascena* Mill.) petals, harvest year 2012, were supplied by Ecomaat Ltd. (Mirkovo, Bulgaria). The petals were dried in a thin layer at room temperature (25-27°C) for one week before final hot air drying (50°C, 1 h). Dried rose petals were stored in a desiccator in dark until used.

### Enzyme - assisted extraction

Enzyme-assisted extraction: Finely ground (particle size < 0.63 mm) rose petals were mixed with water (12:1, v/w), acidified (pH 3.0) with 1 M HCl, and left overnight for rehydration at 10 C. After pH adjustment (pH 3.0), the suspension (100.0 g) was placed in a 50°C water bath for 20 min before 10 mL of an acidified water solution (1.0%, v/v) of enzyme preparation were added. After incubation for 2 h at 50°C, the sample was placed in a boiling water bath for 10 min to inactivate enzymes, then immediately cooled in an ice bath and centrifuged (4200 g × 15 min, 25°C). The supernatant obtained was filtered through a paper filter.

### Sample preparation

An aliquot (5 g) of filtered extract was transferred into 50 mL volumetric flask using 40 ml of acidified (0.1% HCl) methanol. After extraction for 24 h at 10 °C, the flask was filled up to the mark with acidified methanol and filtered through a paper filter. Extraction was performed in triplicate. The resulting extracts where analysing.

### Analytical methods

All measurements were performed with a Helios Omega UV-Vis spectrophotometer equipped with VISIONlite software (all from Thermo Fisher Scientific Inc., Waltham, MA, USA) using 1 cm path length cuvettes.

The contents of total polyphenols (TPP) and total monomeric anthocyanins (TMA) were determined by the method as described by Singleton et al. [15] and the pH-differential method [16], respectively, modified as described by Dinkova et al. [17].

The total antioxidant capacity was determined by the DPPH (free radical scavenging activity) and FRAP (ferric reducing antioxidant power) assay, following the methods of Brand-Williams et al.

[18] and Benzie and Strain [19] respectively, with some modifications [Dinkova et al.].

The content of total dry matter (%) in the extract from *Rosa Damascena* petals was determined by weight moisture analyzer (Kern "MLB-50-3, Kern & Sohn GmBH, Germany).

The yield of the extract wre determined by a measuring cylinder after centrifugation and filtration of the sample.

### Statistical analysis

The results reported in the present study are the mean values of at least three analytical determinations and the coefficients of variation, expressed as the percentage ratios between the standard deviations and the mean values, were found to be < 5% in all cases. The means were compared using one-way ANOVA, performed with Microsoft Excel, and Tukey's test at a 95% confidence level.

## RESULTS AND DISCUSSIONS

The results show (table 1) that the use of other pectinolytic enzyme preparations does not affect the extraction of phenolic compounds, anthocyanins, yield of extract and dry matter.

As a result of the enzymatic treatment, the content of total polyphenols and anthocyanins general increase, by 18% and 15% respectively.

The values of antioxidant capacity of enzymaticaly treated samples were 1.1 - 1.2 times, and 1.6 - 2.2 times higher, for the DPPH- and FRAP -test, compared the control. This is with positive correlation with the increased values of polyphenols.
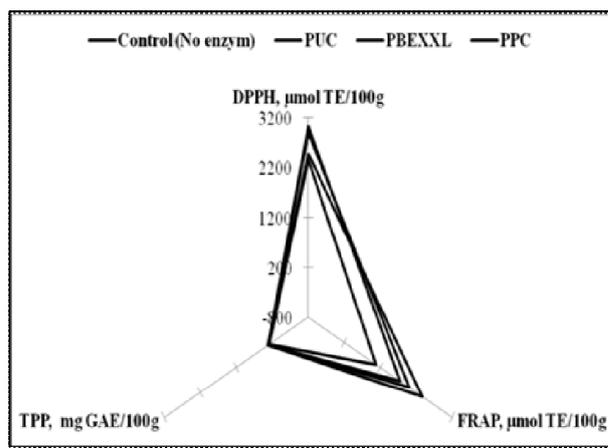


**Fig.1.** Radar chart of the antioxidant capacity of the extract of rose petals depending on processing different pectinolytic preparations

The radar diagram (Fig.1) of Terashima et al. [20] was used for characterization of total antioxidant capacity. The polyphenols antioxidants, acting as both a donor of electrons (FRAP-test) and hydrogen atoms (DPPH-test) are essential for the activities of extracts from rose petals (*Rosa Damascena* Mill.).

The color indicators in CIE*Lab* and CIE*Lch* system were given in Fig.2.

Enhance of the red color component intensity of the extracts, evaluated in the CIE*Lab* and CIE*Lch* system, was reported by the increase in the value of the red component (*a**) and decrease the hue angle (*h*°). Results are consistent with an increase in anthocyanin content as a result of enzymatic treatment (Table 1).

**Table 1.** Treatment variants and results for the extracts (supernatant) from Rosa Damascena petals (*Rosa Damascena* Mill.)

| Treatment variant | TMA[1], mgCGE/100g | TPP[2], mgGAE/100g | DPPH[3], µmolTE/100g | FRAP[3], µmolTE/100g | Yield, % | Dry matter,% |
|---|---|---|---|---|---|---|
| **Control (no enzyme)** | 6.7 ± 0.3a | 271.0 ± 12a | 2463.0 ± 111a | 1078.0 ± 47a | 30.5 ± 1a | 3.2 ± 0.1a |
| **PUC** | 7.7 ± 0.3b | 320.0 ± 14b | 2720.0 ± 122b | 1750.0 ± 79b | 48.5 ± 2b | 4.0 ± 0.2b |
| **PBEXXL** | 7.7 ± 0.4b | 320.0 ± 14b | 2882.0 ± 130b | 2002.0 ± 90c | 47.0 ± 2b | 4.1 ± 0.2c |
| **PPC** | 7.7 ± 0.3b | 318.0 ± 14b | 2865.0 ± 129b | 2367.0 ± 107d | 50.0 ± 2b | 4.3 ± 0.2d |

[a] Means ± standard deviations (n = 3). Different letters within a column indicate significant differences (Tukey's test, $P < 0.05$).
[1] Results are expressed as mg Cyanidin 3-glucoside equivalents (CGE) per 100 g.
[2] Results are expressed as mg gallic acid equivalents (GAE) per 100 g.
[3] Results are expressed as µmol Trolox equivalents (TE) per 100 g.
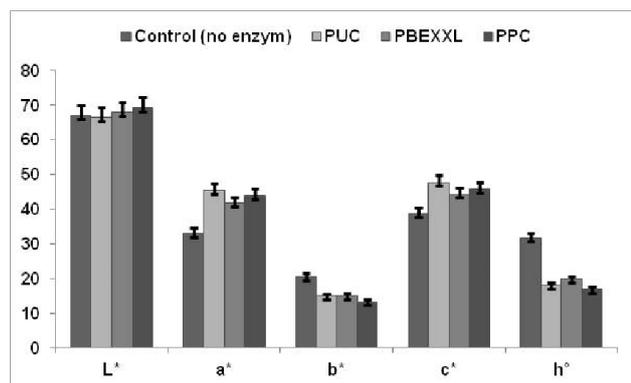


**Fig.2.** Color indicators in CIE*Lab* and CIE*Lch* system on extracts from petals of *Rosa damascena* depending on the various pectinolytic enzyme preparations (mean ± SD; n= 3)

## CONCLUSIONS

The results demonstrate that enzyme-assisted extraction enhances the recovery of polyphenolic antioxidants from rose petals (*Rosa Damascena* Mill.), with all types of pectolytic enzyme preparations. This new process may offer an environmentally-friendly alternative to the conventional organic solvent extraction. Due to the high extraction yields, and high total polyphenols content of extracts from rose petals it could be used in food, cosmetic and pharmaceutical industries.

## REFERENCES

1 S. Tabaei-Aghdaei, H. Hosseini Monfared, H. Fahimi et al., Genetic variation analysis of different population of Rosa damascena Mill. in NW. Iran using RAPD markers. *Iranian Journal of Botany*, 12, 121-127, (2006).
2 R. D. Jacobs, L. J. Slavin, Whole Grains and Health: An Overview. *J Am Coll Nutr.* 19 (3), 289-290, (2000).
3 A. Zargari, Medicinal plants. Vol 2. 5th ed. TehranUniversity Press, Tehran, 281-284, (1992).
4 A. Schiber, K. Mihalev,N. Berardini, P. Mollov, R. Carle. Flavonol glycosides from distilled petals of Rosa damascena Mill. *Z. Naturforsch*, 60, 379-384, (2005).
5 M. Moeina, F. Karamib, H. Tavallalib, Y. Ghasemia. Composition of the Essential Oil of Rosa damascena Mill. from South of Iran. Iranian Journal of Pharmaceutical Sciences, 6 (1), 59-62, (2010).
6 M. H. Boskabady, M. N. Shafei, Z. Saberi, S. Amini, Pharmacological Effects of Rosa Damascena. *Iranian Journal of Basic Medical Sciences*, 14 (4), 213-218, (2011).
7 M. N. Shafei, H. Rakhshandahb, M. H. Boskabady, Antitussive effect of Rosa damascena in Guinea pigs. IJPR, 2, 231–234, (2003).

8  M. Libster, Delmar's Integrative Herb Guide for Nurses. Albany: Delmar Thamson Learning, pp. 360–370, (2002).

9  M. Puri, D. Sharma, C. Barrow, Enzyme-assisted extraction of bioactives from plants. *Trends in Biotechnology*, 30 (1), 37-44, (2012).

10 W. Wijesinqhe, Y. Jeon, Enzyme-assistant extraction (EAE) of bioactive components: a useful approach for recovery of industrially important metabolites from seaweeds; a review. *Fitoterapia*, 83 (1), 6–12, (2012).

11 R. Urlaub, Modern use of enzymes in fruit processing. *Fruit Processing*, 12, 360–361, (2002).

12 R. D. Kammerer, A. Claus, A. Schieber, R. Carle, A novel process for the recovery of polyphenols from grape (*Vitis vinifera* L.) pomace. *Journal of Food Science*, 70, C157–C163, (2005).

13 T. Stoll, U. Schweiggert, A. Schieber, R. Carle, Process for the recovery of a carotene-rich functional food ingredient from carrot pomace by enzymatic liquefaction. *Innovative Food Science and Emerging Technologies*, 4, 415–423, (2003).

14 R. Dinkova, V. Shikov, K. Mihalev, Z. Velchev, N. Penov, H. Dinkov, P. Mollov, Optimizing enzymatic maceration of bilberry mash by response surface methodology, *Journal of Mountain Agriculture on the Balkans*, 16 (1), 327-339, (2013).

15 V. Singleton, J. Rossi, Colorimetry of total phenolics with phosphomolybdic- phosphotungstic acid reagents. *American Journal of Enology and Viticulture*, 50, 3828-3834, (1963).

16 M. Giusti, R. Wrolstad, Anthocyanins. Characterization and measurement with UVvisible spectroscopy. In R. E. Wrolstad (Ed.), Current Protocols in Food Analytical Chemistry. New York: Wiley, Unit F1.2., 1-13, (2001).

17 R. Dinkova, V. Shikov, K. Mihalev, Z. Velchev, H. Dinkov, P. Mollov, Changes in the total anthocyanins and polyphenols during processing af wild berries into freshly pressed juices. *Journal of EcoAgriTourism*, 8 (1), 254, (2012).

18 W. Brand – Williams, M. Cuvelier, C. Berst, Use of a free radical method to evaluate antioxidant activity. *Lebensmittel Wissenschaft and Technologie*, 28, 25-30, (1995).

19 I. Benzie, J. Strain, The Feric reducing ability of plasma (FRAP) as a measure of antioxidant activity. The FRAP assay. *Analytical Biochemistry*, 189, 70-76, (1996).

20 M. Terashima, I. Nakatani, A. Harima, S. Nakimura, M. Shiiba, New method to evaluate water-soluble antioxidant activity based on protein structural change. *Journal of Agricultural and Food Chemistry*, 55 (1), 165-169, (2007).

# Nanostructured polyelectrolyte multilayer drug delivery systems for buccal administration

M. Marudova[1*], I. Bodurov[1], S. Sotirov[1], Y. Uzunova[2], B. Pilicheva[2], I. Avramova[3], A. Viraneva[1], I. Vlaeva[4], G. Exner[1], T. Yovcheva[1]

[1]*Plovdiv University "P. Hilendarski", Faculty of Physics, 24 Tsar Assen str., Plovdiv, Bulgaria*
[2]*Medical University Plovdiv, Faculty of Pharmacy, 15A Vassil Aprilov blvd., Plovdiv, Bulgaria*
[3]*Institute of General and Inorganic Chemistry, Bulgarian Academy of Sciences, Acad G. Bonchev Blvd., Block 11, Sofia, Bulgaria*
[4]*University of Food Technologies, 26 Maritsa blvd., Plovdiv, Bulgaria*

Polyelectrolyte multilayers (PEMs) are well-defined nanoarchitectures with many potential applications, usually as biomaterial coatings. They possess excellent characteristics, such as fine tuning of thickness, stiffness, stability, morphology and topography. Hence they may exhibit special biological properties, such as mucoadhesion and local drug delivery. We present our recent investigations on layer-by-layer assembled polyelectrolyte multilayers from chitosan and xanthan on preliminary corona charged substrates from poly-ε-caprolacton. Polyelectrolyte multilayers were deposited by two different techniques – dip-coating and spin-coating. The presence of PEMs on the substrates was proved by ATR FT-IR spectroscopy. The surface chemical composition was established by X-ray photoelectron spectroscopy (XPS). Further investigations on the morphology and topography of the samples were done by scanning electron microscopy (SEM) and atomic force microscopy (AFM). All the experimental data confirmed differences in the structure and surface properties of the PEMs assembled by dip-coating and spin-coating. An interfusion of the polyelectrolyte layers was observed in dip-coated PEMs, while flat and clearly separated layers were deposited by spin-coating. The ability to control the inner structure of the PEMs enables to manipulate the physical properties or chemical activity of the functionalized thin films. In this way tunable mucoadhesion and drug release properties could be achieved.

**Keywords:** polyelectrolyte multilayers, drug delivery, mucoadhesion, chitosan, xanthan, charged poly-ε-caprolacton substrates

## INTRODUCTION

The fabrication of thin polyelectrolyte layers by the electrostatic assembly of oppositely charged polyelectrolytes (LbL self-assembly) has recently attracted much interest [1, 2]. The formation of these films is electrostatically driven, and favoured by the release of counterions. During the assembly, polyelectrolytes from solutions form electrostatically bound complexes with polyelectrolyte functional groups of opposite charges that are present on the surface, leaving excess charges upon adsorption due to charge overcompensation. Therefore, the surface charge of the outermost layer is altered between the anionic and cationic state, and this charge reversal offers a driving force for the sequential build-up of multilayers in the assembly. As a result, one can obtain a more or less irreversibly adsorbed polyelectrolyte multilayer of which thickness and interpenetration can be readily manipulated with varying the type of adsorbing species, type of deposition technique and processing conditions such as polyelectrolyte charge, ionic strength, salt concentration and adsorption time [3-5].

LbL self-assembly usually leads to a linear growth of film thickness [6, 7]. However, some authors have reported cases of LbL assemblies in which the film thickness grows exponentially with increasing the number of polyelectrolyte deposition layers [8, 9]. Usually this phenomenon is observed for weakly charged polyelectrolyte multilayer systems. It can be attributed to the reversible interdiffusion of at least one of the polyelectrolyte species that constitute the film.

Structure and topography of LbL assemblies influence propertieshe such as adhesion, biocompatibility, and drug reliese [10]. Quantitative characterization of the multilayers surfaces made from various polymer components is important both for practical purposes e.g. for evaluating the biocompatibility, and for the comparison of the influence of the polymer constituents on the multilayer features.

The aim of the present study is characterisation of the chemical composition, structure and surface topography of weak polyelectrolyte multilayers from chitosan and xanthan on biodegradable substrates in respect to their use for buccal drug delivery.

---

EXPERIMENTAL

*Substrate formation*

Poly(ε-caprolacton) (PEC) with ester end groups and intrinsic viscosity (1-1.3) dL/g was purchased from Lactel Absorbable Polymers (USA) and used for the preparation of biodegradable substrates. The PEC substrates were casted from 2% w/v PEC solution in chloroform and dried at 35°C for 48 hours. Their thickness was (40 ± 5) μm. They were then kept in an exicator, at room temperature, and 54% relative humidity (RH). Before the deposition process, the substrates were charged in a corona discharge system, consisting of a corona electrode (needle), a grounded plate electrode and a metal grid placed between them. A voltage of ± 5 kV was applied to the corona electrode and a voltage of ± 1 kV to the grid. The polarity of the corona electrode and the grid electrode was one and the same. The samples were charged under standard room conditions (T = (21÷23) °C and RH = 45-55%) for 1 minute.

*Polyelectrolyte multilayers deposition*

Layer-by-layer (LbL) deposition technique was applied for multilayer build-up. Chitosan (low molecular weight) and xanthan gum were purchased from Sigma-Aldrich and were used without further purification or characterization. For the LbL assembly 0.1% w/v chitosan and 0.05% w/v xanthan solutions in acetate buffer (pH 4.5 and ionic strength 0.1 M) were prepared. The deposition was done in two ways – dip-coating and spin-coating. In both cases, the first built-up layer always possessed opposite to the substrate electric charge.

For dip-coating assembly a slide stainer (Poly Stainer IUL, Spain) was used with the deposition program: 15 min adsorption of polyelectrolyte solution, followed by 5 min washing step in the acetate buffer. The procedure was repeated until reaching the desired even numbers of layers (8, 14 or 20 xanthan/chitosan or chitosan/xanthan). After the last layer deposition the film was dried with hot air.

For the spin-coating assembly a DDR Labortechnik T54 spin-coater was used. Polyelectrolyte solutions of chitosan and xanthan were alternately spun coated (15 s at 1000 rpm) onto the preliminary charged substrates with an intermediate washing step (acetate buffer) before the deposition of each consecutive layer.

Ready multilayer structures were stored in an exicator at RH 54%.

*ATR-FTIR spectroscopy*

The ATR-FTIR spectra were collected by means of a Thermo ScientificTM NicoletTM iSTM 10 FT-IR spectrometer, equipped with a diamond ATR accessory in the range (650-4000) cm$^{-1}$, giving a 4 cm$^{-1}$ resolution and 64 scans. The integral intensity was measured using an OMNIC software package.

*XPS analysis*

The X-ray photoelectron spectroscopy was used for investigation of the surface chemical states of polyelectrolyte multilayers. For that purpose an Axis Supra (Kratos Analytical Ltd, GB) electron spectrometer was used. The survey, C1s, O1s, and N1s photoelectron lines had been recorded with monochromatic Al Kα radiation (1486.6 eV) under $10^{-7}$ Pa base pressure and total instrumental resolution of ~0.48 eV. The binding energies (BE) were determined utilizing the C1s line (from an adventitious carbon) as a reference with energy of 285.0 eV. All data were recorded at a 90° take-off angle. High resolution C1s, O1s, N1s, F1s, Na1s, S2p, Si2p spectra were collected at a pass energy of 20 eV. The concentration of the elements on the surface of polymers had been calculated.

*Scanning electron microscopy (SEM)*

The morphology of the obtained polyelectrolyte multilayer structures was examined by means of SEM. A scanning electron microscope Lyra 3 XMU (Tescan) was employed. The working voltage was 30 kV. Prior to the measurements, the samples were covered with a thin film of gold (about 30 nm).

*Atomic force microscopy (AFM)*

The polyelectrolyte multilayer topography was analysed by a Nanosurf Flex AFM (Switzerland). The surface images were obtained in tapping mode with a standard cantilever Tap190Al-G with a 10 nm tip radius. The viewing field consisted of 256x256 pixels, revealing the morphology of a 10 μm x 10 μm area from the sample surface. The line scan time was 1 s. Based on the AFM images, the surface roughness and PSD spectra were calculated using a Gwyddion software.

RESULTS AND DISCUSSION

Attenuated total reflection (ATR) FT-IR spectroscopy was used to confirm the polyelectrolyte deposition. Typical spectra of positively and negatively charged substrates with 8, 14 and 20 polyelectrolyte layers deposited by dip-coating assembly are shown in the Fig.1 and Fig.2. Slightly intense bands of CH groups stretching

vibrations at 2880 cm$^{-1}$ and 2946 cm$^{-1}$ are observed in both substrate and polyelectrolyte multilayers spectra. The broad band between 3000 and 3700 cm$^{-1}$ is due to a combination of two vibrations: OH groups and amine groups, which is present in the chitosan [11]. A band at 1594 cm$^{-1}$, which corresponds to an amino group [12], is present only in the spectra of the polyelectrolyte multilayer structures and its intensity increases with increasing the number of the deposited layers.
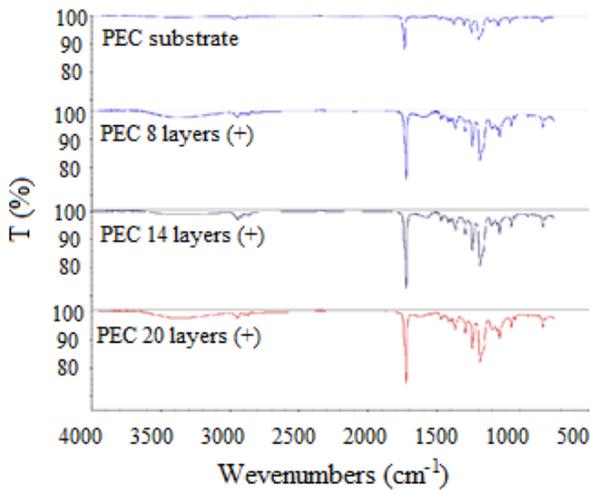


**Fig.1.** ATR FT-IR spectra of xanthan/chitosan multilayers deposited on positively charged PEC substrate
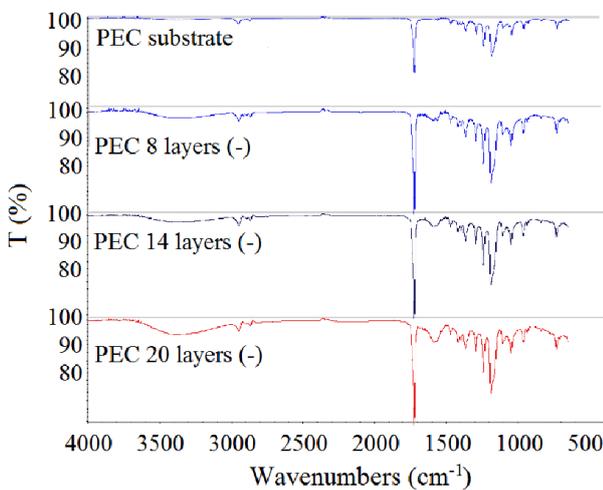


**Fig.2.** ATR FT-IR spectra of chitosan/xanthan multilayers deposited on negatively charged PEC substrate

Peaks corresponding to the vibrations of NH$^{3+}$ (1632 cm$^{-1}$ and 1522 cm$^{-1}$) of chitosan and ionized carboxyl group (COO$^{-}$) of xanthan at 1620 cm$^{-1}$ are not observed in the spectra, which suggests the formation of a complex between the deposited polyelectrolytes by ionic interactions between the

NH$^{3+}$ groups of chitosan and ionized carboxyl group COO$^{-}$ of xanthan [13].

Similar ATR-FTIR spectra were collected for xanthan/chitosan multilayers, assembled by spin-coating (the data are not shown). In that case the peak intensities were less pronounced than these for the dip-coated samples.

Based on the ATR-FTIR analysis the following conclusions can be derived:

- Both dip-coating and spin-coating assemblies lead to irreversible deposition of xanthan and chitosan on pre-charged PEC substrates.
- The increase of the number of layers leads to a higher amount of deposited hydrocolloids.
- Chitosan and xanthan molecules interact predominantly by ionic interactions to form polyelectrolyte complexes.

Further investigations on the surface chemical composition of the polyelectrolyte multilayers were done by X-ray photoelectron spectroscopy (XPS). The N1s spectra, collected from the surfaces of multilayers, assembled by dip-coating and spin-coating on both positively and negatively charged substrate (i.e. structures finishing with chitosan or xanthan layer respectively) are shown in Fig.3a and Fig.3b.



a)



b)
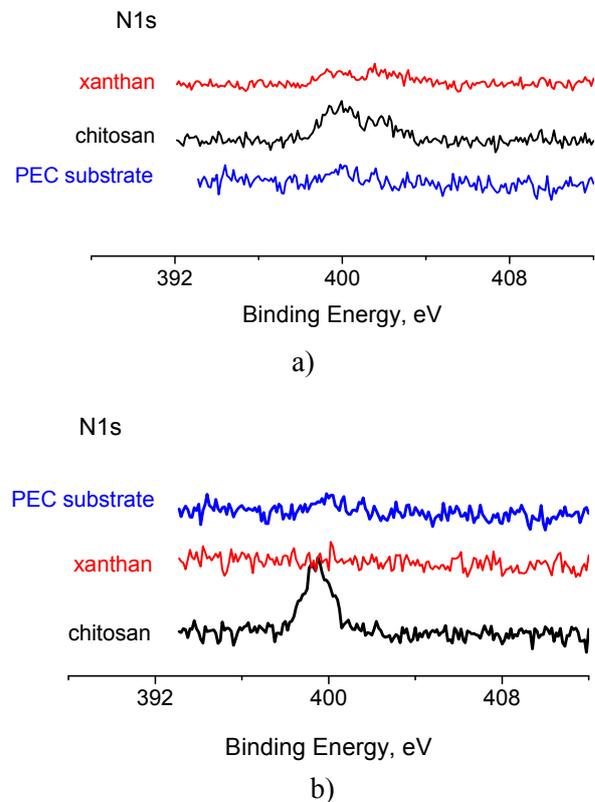
**Fig.3.** N1s XPS spectra of polyelectrolyte multilayers, assembled by dip-coating (a) and spin-coating (b)

Quantity analysis of the nitrogen concentration on the multilayer surfaces is presented in Table 1.

As nitrogen appears just in the structure of chitosan, the following conclusions can be derived:

**Table 1.** Nitrogen surface atomic concentration of chitosan/xanthan polyelectrolyte multilayers

| Atomic concentration [%] | Dip-coating | | Spin-coating | |
|---|---|---|---|---|
| Last layer | Chitosan | Xanthan | Chitosan | Xanthan |
| Nitrogen | 1.95 | 1.93 | 0.69 | 0.00 |

- The amount of the deposited polyelectrolytes is bigger in the case of the dip-coating assembly.
- Diffusion of chitosan and interlayer penetration is observed in the polyelectrolyte multilayer structures, assembled by dip-coating. This is the reason that nitrogen appears on the surface of structures finishing with a xanthan layer.
- There is no nitrogen detected in the xanthan layer in the spin-coated samples, therefore no interpenetration is observed and clear separated layers were formed.

These observations are in agreement with previous investigations on the deposition process of weakly charged polyelectrolytes [14, 15]. Shear forces arising during the spin-coating assembly lead to smaller amounts of adsorbed polyelectrolytes within LbL films, resulting in a higher degree of internal film order, and dramatically improved stability of assemblies in salt solutions as compared to dip-coated LbL assemblies.
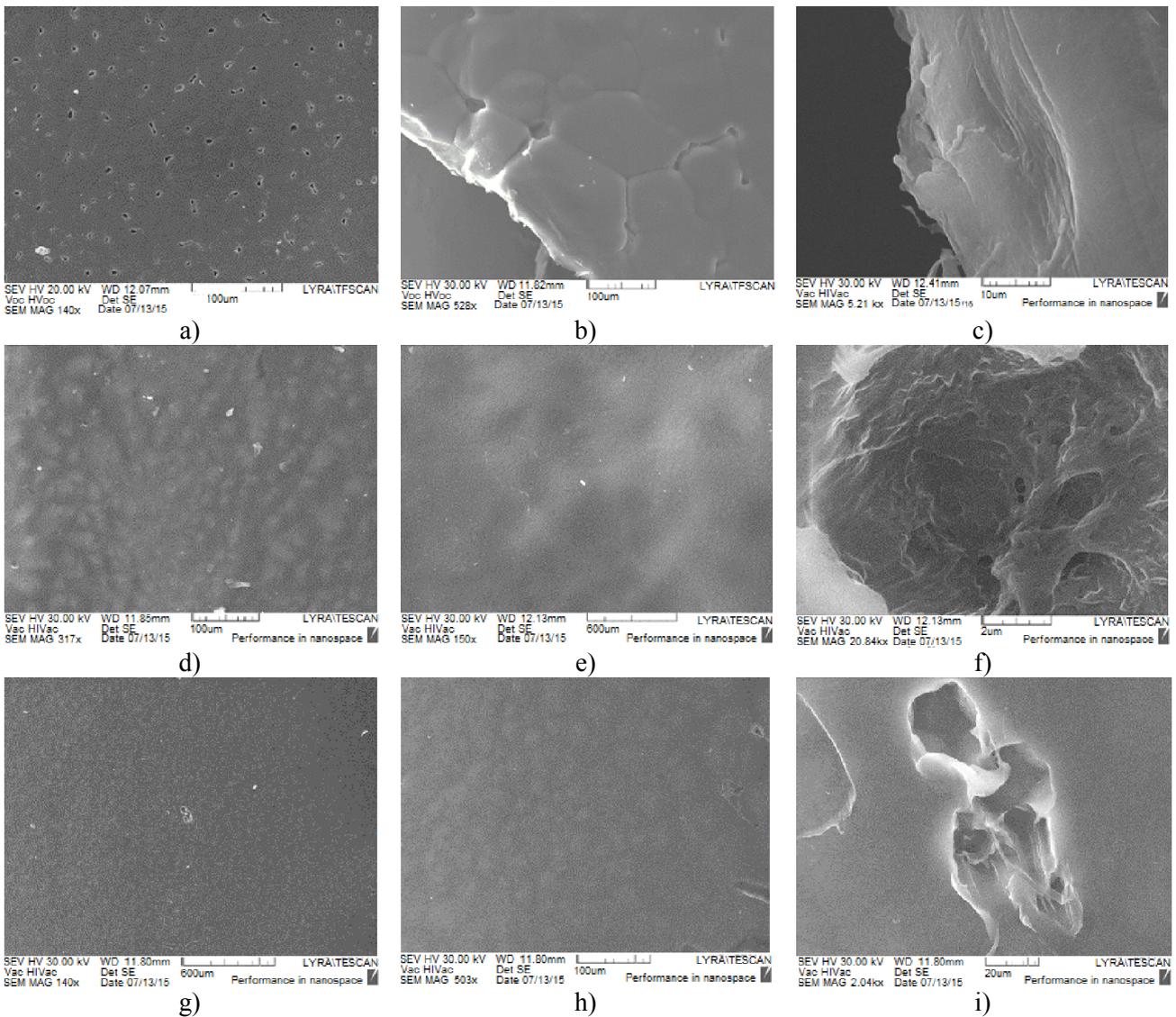


**Fig.4.** SEM micrographs of PEC substrates (a-c); PEC substrates, coated with 10 (d) and 20 (e, f) layers, ending with xanthan; PEC substrates, coated with 10 (g) and 20 (h, i) layers, ending with chitosan

The surface morphology of the PEC substrates and dip-coated chitosan/xanthan polyelectrolyte multilayers with different number of layers and different end layers are presented in Fig.4.

It is important initially to study the morphology of the substrate, since it largely determines the mode and the type of the deposited thereon thin layers.

During the fabrication of the poly ($\varepsilon$-caprolactone) substrate from solution, the long time for evaporation of the solvent facilitates the preparation of large (size of about 200 $\mu$m) spherulites (Fig.4a-b). Spherulites are composed of lamellae, which are well observed at larger magnifications (Fig.4c).

LbL deposition of the polyelectrolyte layers by dip-coating on a negatively charged substrate leads to a gradual change of the morphology of the surface thereby the general characteristics of the substrate are retained (Fig.4d-f). In case of a negatively charged substrate (multilayers ending with xanthan) the morphological units increase in size by increasing the number of layers – Fig.4d-e. This interesting finding is explained by the porous

structure of the deposited chitosan/xanthan complexes – Fig.4f. Porous complexes are typical for stiff macromolecules like xanthan. The observation is in agreement with the reported one in the literature data about a toroid morphology of xanthan/chitosan complexes reported [16]. Significant difference is observed in positively charged substrates (multilayers ending with chitosan, where the morphological units remain the same size, even at 20 deposited layers – Fig.4g-h. As shown in the Fig.4i the morphology of the deposited complexes in that case is dense lamella.

Presented microphotographs show the successful deposition of polyelectrolyte multilayer structures on PEC substrates. The observed differences in the morphology could be relevant to the different size and flexibility of xanthan and chitosan, which resulted in varied extent of macromolecular interdiffusion and multilayer penetration.

More detailed analysis of the surface topography was carried out by AFM for samples with various number of polyelectrolyte layers - Fig.5.



a) Dip-coating - 8 layers    b) Dip-coating - 14 layers    c) Dip-coating - 20 layers

d) Spin-coating - 8 layers    e) Spin-coating - 14 layers    f) Spin-coating 20 layers
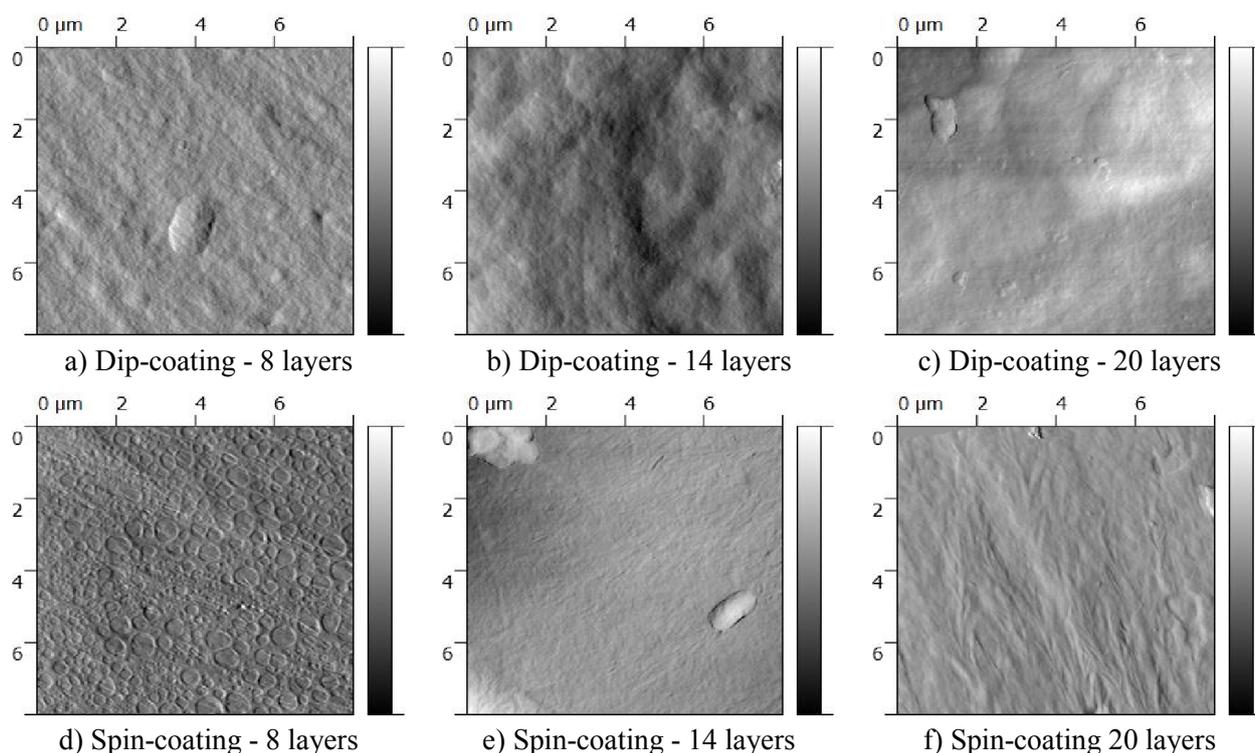
**Fig.5.** AFM micrographs of polyelectrolyte multilayers ending with xanthan, which are deposited by dip-coating (a-c) and spin-coating (d-f) technique

The polyelectrolytes, which are deposited by dip-coating technique, revealed a network-like structure for all samples with different number of

layers – Fig.5a-c. However for the 20 layer samples there were additional regions on the surface where polymer had accumulated on the top of the network

structure – Fig.5c. The dimensions of the network voids increased in size with the increase of the number of layers.

The polyelectrolytes, which are deposited by spin-coating, revealed a pattern structure, which is more pronounced for 14 and 20 layers samples – Fig.5e-f. Most probably it is related to molecular orientation due to the centrifugal forces.

Based on the AFM micrografs the following conclusions could be formulated:

- The surface roughness Rms shows an increase with the increase of the numbers of deposited layers for both deposition techniques – Table 2. This is similar to the trend reported for similar systems [17, 18].
- The spin-coated layers are smoother than the dip-coated ones.

**Table 2.** Roughness of dip-assembled and spin-assembled polyelectrolyte multilayers ending with xanthan

| Sample | Rms [nm] | | |
|---|---|---|---|
| | 8 layers | 14 layers | 20 layers |
| Dip-coating | 63.2 | 118.3 | 133.2 |
| Spin-coating | 22.8 | 77.7 | 90.9 |

The low roughness for spin-coated samples suggested flat and clearly separated interfaces between the layers which could be interpreted as lack of interpenetration in the case of spinning assembly. On the contrary, the surfaces topography of dipping-assembled films consists of rough patterns, indicating loose interpenetrating structures.

Additional quantity analysis of the multilayer surface topography is done by evaluating the power spectral density (PSD) spectra The PSD function is useful in analysing surface roughness. This function provides a representation of the amplitude of a surface's roughness as a function of the spatial frequency of the roughness. The dependence of PSD (W) on the spatial frequency (k) for dip-coated and spin-coated multilayers, ending with xanthan are presented in Fig.6.

Three different characteristic regions could be identified in the PSDs. First, the PSDs display a frequency independent plateau at low spatial frequencies. This is followed by a transition to a power law dependence at higher frequencies. Additionally, a peak at even higher frequencies was observed in the PSDs. The transition space frequency in both dip- and spin-coating mode is the same and gives the surface pore-size of about 1 μm. Two high-frequency peaks at about 300 nm and 200 nm could be detected for the dipping-mode.

The dimensions of 200 nm and 300 nm are relevant to the xanthan radius of gyration [19] and therefore it could be assumed that in multilayers, which are deposited by dip-coating, the polyelectrolytes are in a random coil conformation. A series of peaks in the PSD spectra are recognized for the spin-assembled multilayers. Probably the pattern is due to the centrifugal force, which dominates during the deposition process.



a)



b)
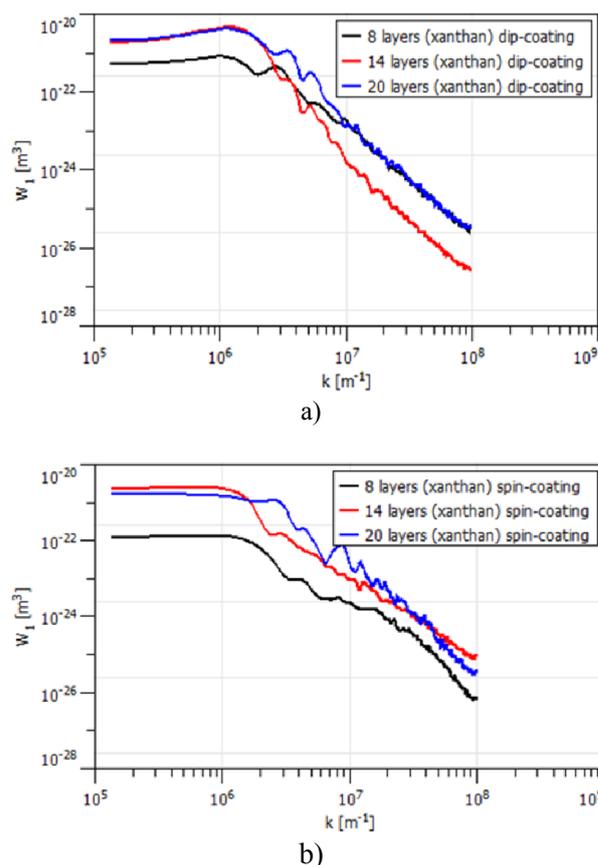
**Fig.6.** PSD spectra of dip-coated (a) and spin-coated (b) multilayers, ending with xanthan

In Fig.7 the PSD spectra of dip-coated and spin-coated samples with 20 layers ending with chitosan and xanthan respectively are compared.

The multilayers ending with xanthan are characterized with higher roughness in both coating modes. The transition frequency corresponds to surface pore-size of 1 micron. The surfaces of multilayers ending with chitosan are smoother and the pore size is about 300 nm. The observed differences could be explained by different characteristics sizes and chain flexibility of xanthan and chitosan. In case of xanthan the molecular mass is higher and the functional carboxyl groups are situated in the branches. Therefore looser network is formed.

a)



b)
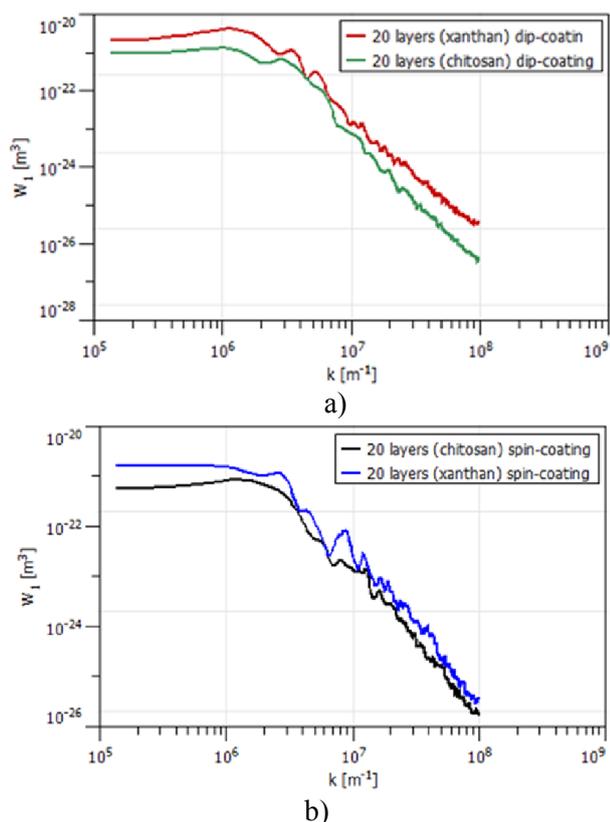
**Fig.7.** PSD spectra of dip-coated (a) and spin-coated (b) multilayers, ending with xanthan or chitosan respectively

## CONCLUSIONS

This study shows that dip-coating and spin-coating techniques are successfully applied for the deposition of chitosan and xanthan multilayers on PEC corona charged substrates. In both methods of assembly the binding of polyelectrolytes to the substrate is irreversible and multilayer growth is predominantly due to ionic interactions and formation of polyelectrolyte complexes.

The surface roughness and surface chemical compositions of dip-coating multilayers indicate the presence of inter-polymer diffusion and interpenetration. The polyelectrolytes are in random-coil conformation.

Spin-coating process causes fabrication of flat clearly separated multilayers with orientated pattern topography.

## ACNOWLEDGEMENTS

## REFERENCES

1 G. Decher, J.B. Schlenoff (Eds.), Multilayer Thin Films. Sequential Assembly of Nanocomposite Materials, 2nd Edition, Wiley-VCH, (2012).
2 C. Picart, F. Caruso, J.-C. Voegel, G. Decher Layer-by-Layer Films for Biomedical Applications, Wiley-VCH, (2014).
3 Y. M. Lee et al., *Journal of nanoscience and nanotechnology*, 9, 7467, (2009).
4 S. S. Shiratori and M. F. Rubner, *Macromolecules*, *33*, 4213, (2000).
5 M. Losche, J. Schmitt, G. Decher, W. G. Bouwman, and K. Kjaer, *Macromolecules*, 31, 8893, (1998).
6 K. Glinel, A. Moussa, A. M. Jonas, and A. Laschewsky, *Langmuir*, 18, 1408, (2002).
7 B. Schoeler, G. Kumaraswamy, and F. Caruso, *Macromolecules*, 35, 889, (2002).
8 P. Lavalle, C. Gergely, F. J. G. Cuisinier, G. Decher, P. Schaaf, J. C. Voegel, and C. Picart, *Macromolecules* 35, 4458, (2002).
9 C. Picart, J. Mutterer, J. L. Richert, Y. Luo, G. D. Prestwich, P. Schaaf, J. C. Voegel, and P. Lavalle, *P. Natl. Acad. Sci*. USA, 99, 12531, (2002).
10 E.Marken, M. Gjertrud, and B. T. Stokke, *Thin Solid Films*, 516, 7770, (2008).
11 P. Katugampola, and W. Cherese, *International Journal of Pharmaceutical Science Invention*, 3, 24, (2014).
12 N. Kulkarni, P. Wakte, J. Naik, *International Journal of Pharmaceutical Investigation*, 5(2), 73, (2015).
13 M. Fukuda, N.A. Peppas, J.W. McGinity, *International Journal of Pharmaceutics*, 310, 90, (2006).
14 Y. M. Lee, D. K. Park, W-S. Choe, S. M. Cho, G. Y. Han, J. Y. Park, J. Pil, *Journal of Nanoscience and Nanotechnology*, 9, 7467, (2009).
15 Zhuk, Aliaksandr, et al., *Langmuir*, 31, 3889, (2015).
16 G. Maurstad, S. Danielsen, and B. T. Stokke, *The Journal of Physical Chemistry B*, 107, 8172, (2003).
17 G. Maurstad, et al., *Macromolecular Symposia*, 227, 161, (2005).
18 R. F. M. Lobo, M. A. Pereira-da-Silva, M. Raposo, R. M. Faria, O. N. Oliveira, *Nanotechnology*, 14, 101, (2003).
19 E. Dickinson, M. E. Leser (Eds.), Food Colloids : Self-Assembly and Material Science, Royal Society of chemistry, (2007).

# BULGARIAN CHEMICAL COMMUNICATIONS

## Instructions about Preparation of Manuscripts

**General remarks:** Manuscripts are submitted in English by e-mail or by mail (in duplicate). The text must be typed double-spaced, on A4 format paper using Times New Roman font size 12, normal character spacing. The manuscript should not exceed 15 pages (about 3500 words), including photographs, tables, drawings, formulae, etc. Authors are requested to use margins of 3 cm on all sides. For mail submission hard copies, made by a clearly legible duplication process, are requested. Manuscripts should be subdivided into labelled sections, e.g. **Introduction, Experimental, Results and Discussion**, *etc*.

**The title page** comprises headline, author's names and affiliations, abstract and key words.

Attention is drawn to the following:

a) **The title** of the manuscript should reflect concisely the purpose and findings of the work. Abbreviations, symbols, chemical formulas, references and footnotes should be avoided. If indispensable, abbreviations and formulas should be given in parentheses immediately after the respective full form.

b) **The author**'s first and middle name initials, and family name in full should be given, followed by the address (or addresses) of the contributing laboratory (laboratories). **The affiliation** of the author(s) should be listed in detail (no abbreviations!). The author to whom correspondence and/or inquiries should be sent should be indicated by asterisk (*).

**The abstract** should be self-explanatory and intelligible without any references to the text and containing not more than 250 words. It should be followed by key words (not more than six).

**References** should be numbered sequentially in the order, in which they are cited in the text. The numbers in the text should be enclosed in brackets [2], [5, 6], [9–12], etc., set on the text line. References, typed with double spacing, are to be listed in numerical order on a separate sheet. All references are to be given in Latin letters. The names of the authors are given without inversion. Titles of journals must be abbreviated according to Chemical Abstracts and given in italics, the volume is typed in bold, the initial page is given and the year in parentheses. Attention is drawn to the following conventions:

a) The names of all authors of a certain publications should be given. The use of "*et al.*" in the list of references is not acceptable.

b) Only the initials of the first and middle names should be given.

In the manuscripts, the reference to author(s) of cited works should be made without giving initials, e.g. "Bush and Smith [7] pioneered...". If the reference carries the names of three or more authors it should be quoted as "Bush *et al*. [7]", if Bush is the first author, or as "Bush and co-workers [7]", if Bush is the senior author.

**Footnotes** should be reduced to a minimum. Each footnote should be typed double-spaced at the bottom of the page, on which its subject is first mentioned.

**Tables** are numbered with Arabic numerals on the left-hand top. Each table should be referred to in the text. Column headings should be as short as possible but they must define units unambiguously. The units are to be separated from the preceding symbols by a comma or brackets.

Note: The following format should be used when figures, equations, *etc*. are referred to the text (followed by the respective numbers): Fig., Eqns., Table, Scheme.

**Schemes and figures**. Each manuscript (hard copy) should contain or be accompanied by the respective illustrative material as well as by the respective figure captions in a separate file (sheet). As far as presentation of units is concerned, SI units are to be used. However, some non-SI units are also acceptable, such as °C, ml, l, etc.

The author(s) name(s), the title of the manuscript, the number of drawings, photographs, diagrams, etc., should be written in black pencil on the back of the illustrative material (hard copies) in accordance with the list enclosed. Avoid using more than 6 (12 for reviews, respectively) figures in the manuscript. Since most of the illustrative materials are to be presented as 8-cm wide pictures, attention should be paid that all axis titles, numerals, legend(s) and texts are legible.

The authors are asked to submit **the final text** (after the manuscript has been accepted for publication) in electronic form either by e-mail or mail on a 3.5'' diskette (CD) using a PC Word-processor. The main text, list of references, tables and figure captions should be saved in separate files (as *.rtf or *.doc) with clearly identifiable file names. It is essential that the name and version of

the word-processing program and the format of the text files is clearly indicated. It is recommended that the pictures are presented in *.tif, *.jpg, *.cdr or *.bmp format, the equations are written using "Equation Editor" and chemical reaction schemes are written using ISIS Draw or ChemDraw programme.

The authors are required to submit the final text with a list of three individuals and their e-mail addresses that can be considered by the Editors as potential reviewers. Please, note that the reviewers should be outside the authors' own institution or organization. The Editorial Board of the journal is not obliged to accept these proposals.

## EXAMPLES FOR PRESENTATION OF REFERENCES

### REFERENCES

1. D. S. Newsome, *Catal. Rev.–Sci. Eng.*, **21**, 275 (1980).
2. C.-H. Lin, C.-Y. Hsu, *J. Chem. Soc. Chem. Commun.*, 1479 (1992).
3. R. G. Parr, W. Yang, Density Functional Theory of Atoms and Molecules, Oxford Univ. Press, New York, 1989.
4. V. Ponec, G. C. Bond, Catalysis by Metals and Alloys (Stud. Surf. Sci. Catal., vol. 95), Elsevier, Amsterdam, 1995.
5. G. Kadinov, S. Todorova, A. Palazov, in: New Frontiers in Catalysis (Proc. 10th Int. Congr. Catal., Budapest, 1992), L. Guczi, F. Solymosi, P. Tetenyi (eds.), Akademiai Kiado, Budapest, 1993, Part C, p. 2817.
6. G. L. C. Maire, F. Garin, in: Catalysis. Science and Technology, J. R. Anderson, M. Boudart (eds), vol. 6, Springer-Verlag, Berlin, 1984, p. 161.
7. D. Pocknell, *GB Patent* 2 207 355 (1949).
8. G. Angelov, PhD Thesis, UCTM, Sofia, 2001.
9. JCPDS International Center for Diffraction Data, Power Diffraction File, Swarthmore, PA, 1991.
10. CA **127**, 184 762q (1998).
11. P. Hou, H. Wise, *J. Catal.*, in press.
12. M. Sinev, private communication.
13. http://www.chemweb.com/alchem/articles/1051611477211.html.

# CONTENTS

## PART E1

### SOLAR AND HYBRID THERMAL SYSTEMS

## SOLAR PHOTOVOLTAIC SYSTEMS

## STORAGES WITH PHASE CHANGE MATERIALS

## PART E2

## ENERGY EFFICIENCY

## MATERIALS SCIENCE

FOOD ENGINEERING AND TECHNOLOGIES

## BIOTECHNOLOGIES